Dielectrophoresis of sub-micrometre particles

by

Nicolas Gavin Green

A thesis submitted to
the Faculty of Engineering,
University of Glasgow
for the degree of
Doctor of Philosophy

Department of Electronics and Electrical Engineering
University of Glasgow
Scotland, UK

January, 1998

Summary

A polarisable particle in a non-uniform electric field experiences a force arising from the interaction of the field and the dipole induced in the particle; the movement resulting from this force is termed Dielectrophoresis (DEP). The magnitude and direction of the dielectrophoretic force depends on the dielectric properties of the particle and the medium it is suspended in, as well as the frequency and amplitude of the applied field. Under suitable conditions, the particle experiences a force towards either high field regions or low field regions, referred to as positive or negative DEP respectively. This technique can be used to study or move biological particles, such as cells and bacteria and as a non-invasive method to characterise the dielectric properties of the particles. Knowledge of these properties can then be used to develop DEP for use in practical applications.

The aim of this PhD project was to develop the technology of dielectrophoresis on the sub-micrometre scale and to use DEP to manipulate sub-micrometre particles and measure their dielectric properties. Of particular interest was the application of DEP to viruses, the largest of which is approximately 250nm in diameter. A system for virus characterisation, identification and separation based on DEP would be a major milestone in this field of research, as well as having beneficial medical and biotechnological uses.

Particles with a diameter between 1nm and 1μm are referred to as *colloidal particles* and the dynamics of their movement are complicated by the effects of thermal energy and Brownian motion. High electric fields are required to dominate these effects but signals with high potentials and high frequencies are difficult to generate. Semiconductor manufacturing techniques can be used to fabricate micro-electrode structures which can produce high electric fields from relatively low potentials.

Lithography based manufacturing techniques were developed to produce suitable electrodes for dielectrophoresis on a scale small enough to manipulate sub-micrometre particles. Detailed electric field patterns were numerically calculated for these electrodes, so that the dielectrophoretic force could be simulated, predicted and compared with experimental measurements of particle movement. The dielectric properties of latex spheres with diameters from 93nm to 557nm were determined through observation and measurement of the DEP movement; new theories were postulated to account for the results which did not conform to accepted theories.

A rod shaped plant virus, Tobacco Mosaic Virus (TMV) was also studied and its dielectric properties determined from the experimental results. TMV is 300nm long with a cylindrical radius of 9nm, a shape of particle which is very different from a sphere and one which has not been studied by this method previously. An expression for the frequency dependent dielectrophoretic force on such a particle was derived and values of the dielectrophoretic force on the particle were measured and compared with the theoretical model.

A new perspective on the use of Brownian motion theory to describe the movement of particles under dielectrophoresis was formulated and a method was proposed for the stochastic integration of Langevin's equation.

During the course of this project, observations of fluid movement and its effect on the motion of particles were made. The types of fluid movement were categorised and attempts made to relate observations to probable causes.

The practical possibilities of this project were demonstrated through the separation of sub-micrometre and nano-scale particles using dielectrophoresis. A new technique based on a combination of DEP and electrically induced fluid flow was also developed for separation purposes.

A summary of work carried out on the design of travelling wave dielectrophoresis electrode arrays and separators is presented.

Acknowledgements

I would like to thank Dr. Hywel Morgan, for giving me the opportunity to study for my PhD and for providing enthusiastic guidance and supervision. I would also like to thank Professor Jim Hough for pointing me in the right direction and the Engineering and Physical Sciences Research Council for providing financial support.

For their invaluable assistance with my project, I would like to thank Dr Joel Milner and Ms Fiona MacDonald, Professor John Coggins and Ms Sharon Hardie, Professor Ron Pethig, Dr Julian Burt and Professor Chris Wilkinson. For advice and discussion, I am grateful to the following people: Bill Monaghan, Mary Robertson, Dr Alun Griffith, Dr Mike Hughes, Dr Ka Lok Chan, Steffen Archer, Dave Bakewell, Pam Foreman, Chris Cotton, Brendan Casey, May McCallum, Mark Dragnes, Steve Broadfoot, Dave Gourlay, Helen McLelland, Chris Hardy, Dave Clifton, Bill Ward and all the technical staff of the cleanroom facilities.

I would also like to thank my friends for putting up with the mad scientist, especially Neil, Louise, Lesley, Kirsten, Dougie and James.

Finally, I would like to thank my family, for helping me get through university and their continuing support.

Table of Contents

Chapter One

Introduction

1.1 Introduction

The term Dielectrophoresis (DEP) was first used to describe the motion of particles in non-uniform fields by Pohl [1]. Later the subject of a book by the same author [2], DEP has been reviewed in several journal articles [3-5] and been described in texts [6,7]. The DEP force depends on the dielectric properties of the particle and the suspending medium and, as a result, the fundamentals are based on dielectric theory and electromagnetism (described in the theory chapters in this thesis).

In brief, the DEP force on a particle suspended in a dielectric medium depends on the effective polarisability of the particle, a value which is related to the difference between the complex permittivities of the particle and the suspending medium. A detailed derivation of the governing equations can be found in Chapters Three and Four. The effective polarisability can be either positive or negative so that the resulting force is either towards high field regions or towards low field regions respectively. The polarisation of a sphere in an electric field and the difference between positive and negative DEP are shown schematically in Figure (1.1).

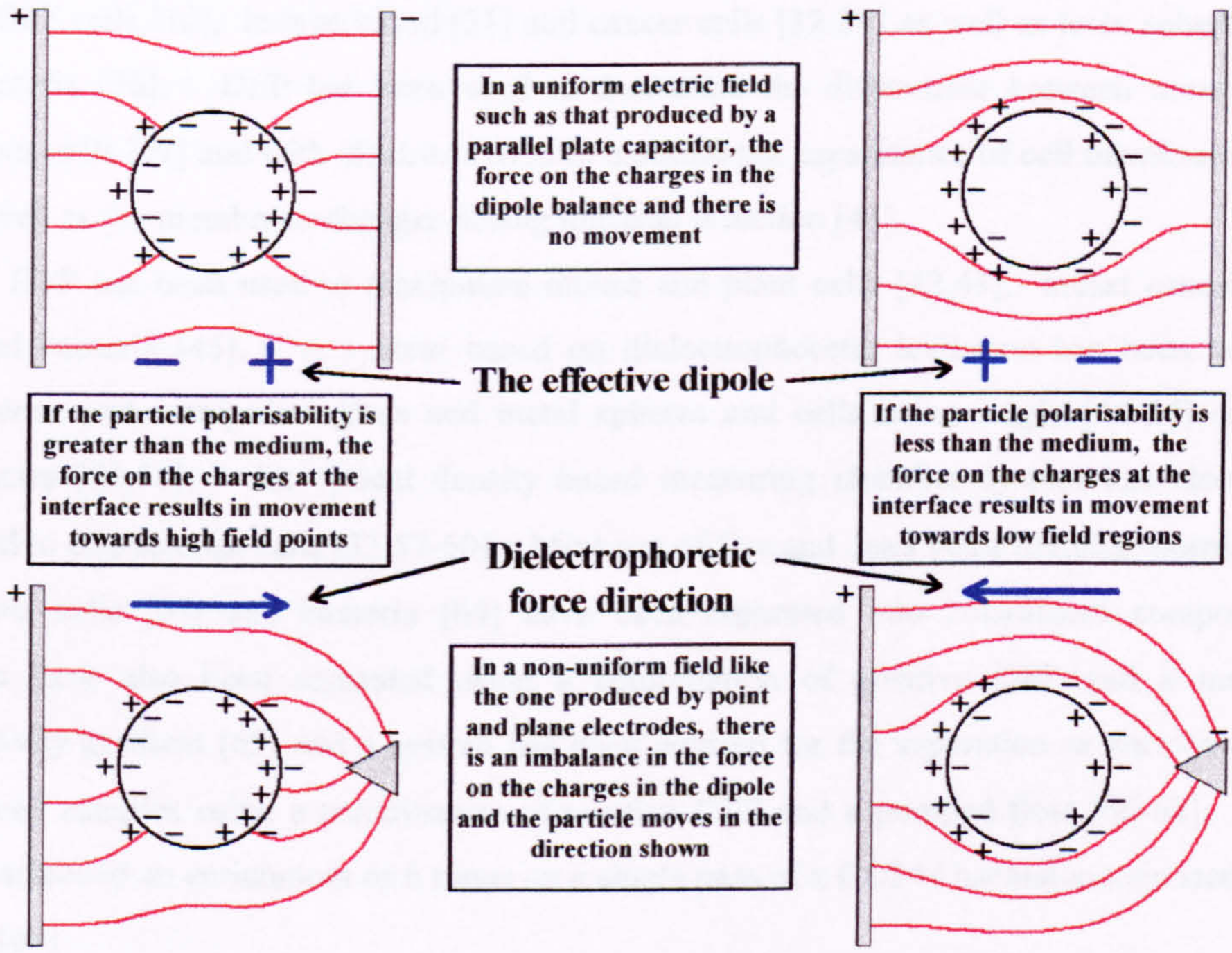

Figure (1.1) Schematic of the polarisation of a spherical particle in a dielectric medium in a uniform and a non-uniform electric field. The case of a particle with polarisability α_p, greater than the medium polarisability α_m, is shown on the left and the case where $\alpha_p < \alpha_m$ is shown on the right. Both cases are detailed with the relative amounts of charge on either side of the particle/medium interface, the effective dipole and the direction of the dielectrophoretic force.

The magnitude and the direction of the dielectrophoretic force depend on the particle permittivity and conductivity, the medium permittivity and conductivity and the field strength and frequency. The fact that the DEP force is dependent on such a variety of parameters, makes Dielectrophoresis a powerful tool for particle, especially biological particle, characterisation, manipulation and separation.

1.2 Overview of research in Dielectrophoresis

A great deal of work has been carried out to elucidate the nature of the DEP force [8-10], linking the force derivation to Maxwell stress tensors [11] and to torque related effects viz. electrorotation [12,13] and travelling-wave dielectrophoresis [14]. The specific case of two interacting cells has been examined [15], as well as the multipolar force [16-22] and the potential non-Laplacian nature of the cell membrane [23].

Specifically designed DEP electrodes [24-26] have been used to characterise the dielectric properties of cells, starting with Pohl's pioneering work on the differences between live and dead yeast cells [27,28]. Further work has been carried out on yeast [25,26,29], mouse SP2 cells [30], human blood [31] and cancer cells [32-34] as well as latex spheres [35] and bacteria [36]. DEP has been used to determine the differences between normal and cancerous cells [37] and with electrorotation to measure the capacitance of cell membranes [38-40] as well as the membrane changes during malarial infection [41].

DEP has been used to manipulate mouse and plant cells [42,43], breast cancer cells [44] and bacteria [45]. A system based on dielectrophoretic levitation has been used to characterise and manipulate glass and metal spheres and cells using single [46-54] or dual frequencies [55,56]. An optical density based measuring chamber system has also been designed to characterise cells [33,57-60]. Mixtures of live and dead yeast [61,62], normal and cancerous cells [63] and bacteria [64] have been separated into constituent components. Bacteria have also been separated using a combination of positive DEP and a medium conductivity gradient [65] and a system has been devised for the separation or enrichment of cancer cell samples using a combination of positive DEP and a pumped flow [66-68]. This system achieved an enrichment of 6 times on a single pass of a CD34+ haematopoetic stem cell sample [69]

Simulations of the electric fields in DEP electrodes and the DEP force expected on a particle in these electrodes have been carried out numerically for planar [70-72] and 3D [73,74] electrodes and also, analytical solutions have been derived for certain electrode shapes [25,75].

It had been supposed that dielectrophoretic manipulation of sub-micrometre or colloidal particles would be difficult to achieve [2,76] due to the high potentials required to generate

strong enough electric fields. High potentials are difficult to generate at the high frequencies that DEP manipulation sometimes requires. However, recent advances in semiconductor manufacturing techniques means smaller electrodes can be manufactured, resulting in stronger electric fields for the same potential and enabling DNA [77,78], latex spheres [79]. Sendai virus [80] and protein macromolecules [76] to be manipulated. The characterisation of latex spheres [81] and small plant viruses has been achieved [82-84] as well as the separation of a mixture of virtually identical 93nm diameter dielectric spheres [85].

1.3 Thesis outline

The first three chapters contain an outline of the theory relevant to the experimental results presented subsequently. Chapter Two is an outline of basic dielectric theory, the polarisation of an interface and relaxations. Chapter Three expands the basics to the special case of the effective dipole induced on a dielectric particle in a dielectric medium. Particular attention is paid to surface charge effects and the electrical double layer polarisation. Chapter Four describes the forces on sub-micrometre particles, including the dielectrophoretic force derived from the effective dipole equations in Chapter Three. A method for the numerical simulation of the electric field and the DEP force is discussed, as well as a method for solving the equation of motion for the particle including random thermal effects (Brownian motion).

Chapter Five presents and discusses the results of the development of fabrication techniques and the manufacture of electrodes for Dielectrophoresis experiments. Chapter Six contains the result of electric field and force simulation specifically for the electrodes described in the previous chapter. Chapter Seven presents and discuss the dielectrophoresis experiments performed on sub-micrometre latex spheres and the calculation of the particle dielectric properties. Special attention is paid to the low frequency effects which have not been accurately explained in previous literature. Chapter Eight describes the dielectrophoresis of Tobacco Mosaic Virus and the determination of this particle's dielectric properties. Chapters Nine and Ten discuss the other forces involved in sub-micrometre dielectrophoresis and the application of all the experimental effects described previously in the thesis to the practical problem of separation.

References

1. H.A.Pohl (1958)
   Journal of Applied Physics **22** 869-871
2. H.A.Pohl (1978) *Dielectrophoresis*
   Cambridge University Press, New York
3. E.Barnaby, G.Bryant and J.Wolfe (1988)
   Bioelectrochemisty and Bioenergetics **19** 347-352
4. R.Pethig (1991)
   Institute of Physics Conference Series No.**118** 13-26
5. R.Pethig (1996)
   Critical Reviews in Biotechnology **16** 331-348
6. R.Pethig (1979) *Dielectric and electronic properties of biological materials*
   Wiley, Chichester
7. T.B.Jones (1995) *Electromechanics of particles*
   Cambridge University Press, Cambridge
8. T.B.Jones (1979)
   Journal of Electrostatics **6** 69-82
9. L.Benguigui and I.J.Lin (1986)
   American Journal of Physics **54** 447-450
10. I.Turcu and C.M.Lucaciu (1989)
    Journal of Physics A: Mathematical and General **22** 985-993
11. V.Denner and H.A.Pohl (1982)
    Journal of Electrostatics **13** 167-174
12. X-B.Wang, R.Pethig and T.B.Jones (1992)
    Journal of Physics D: Applied Physics **25** 905-912
13. X-B.Wang, Y.Huang, R.Holzel, J.P.H.Burt and R.Pethig (1993)
    Journal of Physics D: Applied Physics **26** 312-322
14. X-B.Wang, Y.Huang, F.F.Becker and P.R.C.Gascoyne (1994)
    Journal of Physics D: Applied Physics **27** 1571-1574
15. K.R.Foster and A.E.Sowers (1995)
    Biophysical Journal **69** 777-784
16. T.B.Jones (1985)
    IEEE Transactions on Industry Applications **21** 930-934
17. T.B.Jones (1986)
    Journal of Electrostatics **18** 55-62

18. M.Washizu (1992)
Journal of Electrostatics **29** 177-188

19. M.Washizu and T.B.Jones (1994)
Journal of Electrostatics **33** 187-198

20. T.B.Jones and M.Washizu (1994)
Journal of Electrostatics **33** 199-212

21. T.B.Jones and M.Washizu (1996)
Journal of Electrostatics **37** 121-134

22. M.Washizu and T.B.Jones (1996)
Journal of Electrostatics **38** 199-211

23. C.Grosse and H.P.Schwan (1992)
Biophysical Journal **63** 1632-1642

24. H.A.Pohl and K.Pollock (1978)
Journal of Electrostatics **5** 337-342

25. Y.Huang and R.Pethig (1991)
Measurement Science and Technology **2** 1142-1146

26. R.Pethig, Y.Huang, X-B.Wang and J.P.H.Burt (1992)
Journal of Physics D: Applied Physics **24** 881-888

27. J.S.Crane and H.A.Pohl (1968)
Journal of the Electrochemical Society **115** 584-586

28. H.A.Pohl and J.S.Crane (1971)
Biophysical Journal **11** 711-727

29. Y.Huang, R.Holzel, R.Pethig and X-B.Wang (1992)
Phys. Med. Biol. **37** 1499-1517

30. T.L.Mahaworasilpa, H.G.L.Coster and E.P.George (1994)
Biochimica et Biophysica Acta **1193** 118-126

31. I.C.Tsoneva, D.V.Zhelev and D.S.Dmitrov (1986)
Cell Biophysics **8** 89-101

32. M.Mischel, F.Rouge, I.Lamprecht, C.Aubert and G.Prota (1983)
Arch. Dermatol. Res. **275** 141-143

33. J.P.H.Burt, R.Pethig, P.R.C.Gascoyne and F.F.Becker (1990)
Biochimica et Biophysica Acta **1034** 93-101

34. X-B.Wang, Y.Huang, P.R.C.Gascoyne and F.F.Becker (1997)
IEEE Transactions on Industry Applications **33** 660-669

35. H.Watari, T.Sakamoto and S.Tsukahara (1997)
Langmuir **13** 2417-2420

36. G.P.Archer, W.B.Betts and T.Haigh (1993)
Microbios **73** 165-172

37. P.R.C.Gascoyne, J.Noshari, F.F.Becker and R.Pethig (1994)
IEEE Transactions on Industry Applications **30** 829-834

38. P.Marszalek, J.Zielinsky, M.Fikus and T.Y.Tsong (1991)
Biophysical Journal **59** 982-987

39. Y.Huang, X-B.Wang, F.F.Becker and P.R.C.Gascoyne (1996)
Biochimica et Biophysica Acta **1282** 76-84

40. P.R.C.Gascoyne, R.Pethig, J.P.H.Burt and F.F.Becker (1993)
Biochimica et Biophysica Acta **1149** 119-126

41. P.R.C.Gascoyne, R.Pethig, J.Satayavivad, F.F.Becker and M.Ruchirawat (1997)
Biochimica et Biophysica Acta **1323** 240-252

42. G.Fuhr, H.Glasser, T.Muller and T.Schnelle (1994)
Biochimica et Biophysica Acta **1201** 353-360

43. N.Matsumoto, T.Matsue and I.Uchuda (1995)
Bioelectrochemistry and Bioenergetics **34** 199-202

44. X-B.Wang, Y.Huang, X.Wang, F.F.Becker and P.R.C.Gascoyne (1997)
Biophysical Journal **72** 1887-1899

45. M.Washizu, Y.Kurahashi, H.Iochi, O.Kurosawa, S-i.Aizawa, S.Kudo, Y.Magariyama and H.Hotani (1993)
IEEE Transactions on Industry Applications **29** 286-294

46. T.B.Jones and G.A.Kallio (1979)
Journal of Electrostatics **6** 207-224

47. T.B.Jones and M.J.McCarthy (1981)
Journal of Electrostatics **11** 71-83

48. K.Kaler and H.A.Pohl (1983)
IEEE Transactions on Industry Applications **IA-19** 1089-1093

49. I.J.Lin and T.B.Jones (1984)
Journal of Electrostatics **15** 53-65

50. T.B.Jones and J.P.Kraybill (1986)
Journal of Applied Physics **60** 1247-1252

51. K.V.I.S.Kaler and T.B.Jones (1990)
Biophysical Journal **57** 173-182

52. T.B.Jones and T.N.Tombs (1991)
Institute of Physics Conference Series **118** 39-44

53. T.N.Tombs and T.B.Jones (1993)
IEEE Transactions on Industry Applications **29** 281-285

54. M.Washizu, T.B.Jones and K.V.I.S.Kaler (1993)
Biochimica et Biophysica Acta **1158** 40-46

55. K.V.I.S.Kaler, J-P.Xie, T.B.Jones and R.Paul (1992)
Biophysical Journal **63** 58-69

56. S.F.Paddison, R.Paul and K.V.I.S.Kaler (1996)
Journal of Colloid and Interface Science **183** 78-90

57. J.A.R.Price, J.P.H.Burt and R.Pethig (1988)
Biochimica et Biophysica Acta **964** 221-230

58. T.Inoue, R.Pethig, T.A.K.Al-Ameen, J.P.H.Burt and J.A.R.Price (1988)
Journal of Electrostatics **21** 215-223

59. J.P.H.Burt, T.A.K.Al-Ameen and R.Pethig (1989)
Journal of Physics E: Scientific Instrumentation **22** 952-957

60. M.S.Talary and R.Pethig (1994)
IEEE Proceedings: Sci. Meas. Technol. **141** 395-399

61. G.H.Markx, M.S.Talary and R.Pethig (1994)
Journal of Biotechnology **32** 29-37

62. G.H.Markx and R.Pethig (1995)
Biotechnology and Bioengineering **45** 337-343

63. P.R.C.Gascoyne, Y.Huang, R.Pethig, J.Vykoukal and F.F.Becker (1992)
Measurement Science and Technology **3** 439-445

64. G.H.Markx, Y.Huang, X-F.Zhou and R.Pethig (1994)
Microbiology **140** 585-591

65. G.H.Markx, P.A.Dyda and R.Pethig (1996)
Journal of Biotechnology **51** 175-180

66. F.F.Becker, X-B.Wang, Y.Huang, R.Pethig, J.Vykoukal and P.R.C.Gascoyne (1994)
Journal of Physics D: Applied Physics **27** 2659-2662

67. F.F.Becker, X-B.Wang, Y.Huang, R.Pethig, J.Vykoukal and P.R.C.Gascoyne (1995)
Proceedings of the National Academy of Sciences **92** 860-964

68. P.R.C.Gascoyne, X-B.Wang, Y.Huang and F.F.Becker (1997)
IEEE Transactions on Industry Applications **33** 670-678

69. M.S.Talary, K.I.Mills, T.Hoy, A.K.Burnett and R.Pethig (1995)
Medical and Biological Engineering and Computing **33** 235-237

70. X-B.Wang, Y.Huang, J.P.H.Burt, G.H.Markx and R.Pethig (1993)
Journal of Physics D: Applied Physics **26** 1278-1285

71. M.P.Hughes, X-B.Wang, F.F.Becker, P.R.C.Gascoyne and R.Pethig (1994)
Journal of Physics D: Applied Physics **27** 1564-1570

72. X-B.Wang, M.P.Hughes, Y.Huang, F.F.Becker and P.R.C.Gascoyne (1995)
Biochimica et Biophysica Acta **1243** 185-194

73. T.Schnelle, R.Hagedorn, G.Fuhr, S.Fiedler and T.Muller (1993)
Biochimica et Biophysica Acta **1157** 127-140

74. G.Fuhr, T.Muller, R.Hagedorn and S.G.Shirley (1995)
Journal of Cellular Engineering **1** 47-57

75. X.Wang, X-B.Wang, F.F.Becker and P.R.C.Gascoyne (1996)
Journal of Physics D: Applied Physics **29** 1649-1660

76. M.Washizu, S.Suzuki, O.Kurosawa, T.Nishizaka and T.Shinohara (1994)
IEEE Transactions on Industry Applications **30** 835-843

77. M.Washizu and O.Kurosawa (1990)
IEEE Transactions on Industry Applications **26** 1165-1172

78. K.Morishima, T.Fukuda, F.Arai, H.Matsuuro and K.Yoshikawa (1996)
Proc: 1996 International Conference on Robotics and Automation 2214-2219

79. T.Muller, A.Gerardino, T.Schnelle, S.G.Shirley, F.Bordoni, G.de Gasperis, R.Leoni and G.Fuhr (1996)
Journal of Physics D: Applied Physics **29** 340-349

80. T.Schnelle, T.Muller, S.Fiedler, S.G.Shirley, K.Ludwig, A.Hermann, G.Fuhr, B.Wagner and U.Zimmerman (1996)
Naturwissenschaften **83** 172-176

81. N.G.Green and H.Morgan (1997)
Journal of Physics D: Applied Physics **30** 2626-2633

82. N.G.Green, H.Morgan and J.J.Milner (1997)
Biophysical Journal **72** MP448

83. N.G.Green, H.Morgan and J.J.Milner (1997)
Journal of Biochemical and Biophysical Methods **35** 89-107

84. H.Morgan and N.G.Green (1997)
Journal of Electrostatics **42** 279-293

85. N.G.Green and H.Morgan (1997)
Journal of Physics D: Applied Physics **30** L41-L44

Chapter Two

Theory: Dielectrics and polarisation

2.1 Introduction

For most of this century, the effects of electric fields on dielectric materials has been a subject of major interest and research for scientists from many fields. The early work of Maxwell [1] and Wagner [2] prepared the groundwork for understanding the properties of interfaces and particles [3-5]. Subsequently, interest in applications of dielectric spectroscopy to the understanding of the interior of biological particles grew [6-8] as well as the apparently simpler but less well understood charged dielectric sphere [9-12].

Dielectrophoresis is governed by the combined dielectric properties of a particle and the medium it is suspended in. As a consequence, the theory for the dielectrophoretic force, discussed in Chapter Four, is based on particle dielectric theory (Chapter Three).

This chapter discusses the basics of dielectric theory.

2.2 Dielectrics, polarisation and permittivity [13]

A dielectric material has the intrinsic property that it possesses bound charges. In a true or ideal dielectric, the charges are bound to the atoms and molecules and can only move minute distances under the influence of an externally applied electric field. When positive and negative charges in a dielectric are displaced in opposite directions, the dielectric is said to be *polarised.*

2.2.1 Three basic polarisation processes

(a) *Electronic.*

Under an applied electric field, the centre of charge of the electron cloud in a molecule moves slightly with respect to the centre of charge of the nucleus. With an applied field of the order of 10^{6}-10^{7} Vm^{-1} (compared to the internal field of the atom which is of the order of $10^{11}Vm^{-1}$), the displacement is of the order of 10^{-8} times the diameter of an atom. This is referred to as *electronic polarisation.*

(b) *Orientational.*

In some dielectrics, the molecules possess a permanent dipole moment and are said to be polar. The polar molecules both align with and become further polarised in an applied electric field. This is referred to as *orientational polarisation.*

(c) *Atomic.*

In a solid such as crystalline Potassium Chloride, the ions of different sign move in different directions when subjected to an electric field. This is referred to as *atomic polarisation.*

2.2.2 The polarisation, $\underline{\mathbf{P}}$

In a dielectric consisting of N molecules per cubic metre, where the average vector dipole moment per molecule is $\underline{\mathbf{p}}$ (Cm), in the neighbourhood of an arbitrary point, then

$$\underline{\mathbf{P}} = N\,\underline{\mathbf{p}} \tag{2.1}$$

is the electric *polarisation* or dipole moment per unit volume (in Cm^{-2}) at that point. The unit of electric dipole moment is the *Debye* equal to 3.336×10^{-30} Cm [14].

Polarisation causes charges to gather, either at points within the dielectric or at the surface. These charges are related to the polarisation and are referred to as bound. The bound volume charge density ρ_b is given by:

$$\rho_b = -\nabla.\underline{\mathbf{P}} \tag{2.2}$$

2.2.3 Gauss's Law, Poisson's and Laplace's equations

A surface S encloses a volume which contains a variety of dielectrics and a total charge $Q = Q_f + Q_b$. Q_f is the free charge, Q_b is the bound charge and there are no charges on the surface S. *Gauss's law* relates the outward flux of the electric field $\underline{\mathbf{E}}$ due to these charges through S:

$$\int_s \underline{\mathbf{E}}.\underline{d\mathbf{s}} = \frac{Q}{\varepsilon_o} \tag{2.3}$$

where $\underline{d\mathbf{s}}$ is a small element of the surface and ε_o is the permittivity of free space.

If the volume is entirely contained within the dielectric, application of the divergence theorem gives Gauss's Law in differential form:

$$\nabla.\underline{\mathbf{E}} = \frac{\rho_f + \rho_b}{\varepsilon_o} \tag{2.4}$$

where ρ_f is the free charge density and ρ_b is the bound charge density.

Substituting $\underline{\mathbf{E}} = -\nabla V$ into equation (2.4) gives *Poisson's equation* for the electrical potential V in a dielectric of constant permittivity:

$$\nabla^2 V = -\frac{\rho}{\varepsilon} \tag{2.5}$$

In regions where the total charge density $\rho = \rho_f + \rho_b$ is zero the particular form of this equation is given by *Laplace's equation*

$$\nabla^2 V = 0 \tag{2.6}$$

The finite element method outlined in Chapter (3) for calculation of the electric field uses these equations to determine the solution of the electric potential.

2.2.4 The electric flux density $\underline{\mathbf{D}}$

The free charge density in a dielectric can be found by substituting equation (2.2) into equation (2.4) to give:

$$\nabla.(\varepsilon_o \underline{\mathbf{E}} + \underline{\mathbf{P}}) = \rho_f \tag{2.7}$$

The vector $\underline{\mathbf{D}}$ defined by

$$\underline{\mathbf{D}} = \varepsilon_o \underline{\mathbf{E}} + \underline{\mathbf{P}} \tag{2.8}$$

is called the *electric flux density* (in Cm^{-2}) and its divergence is equal to the free volume charge density

$$\nabla.\underline{\mathbf{D}} = \rho_f \tag{2.9}$$

2.2.5 Electric susceptibility and the relative permittivity

Most dielectrics are linear and isotropic, and $\underline{\mathbf{P}}$ is proportional to $\underline{\mathbf{E}}$ such that

$$\underline{\mathbf{P}} = \varepsilon_o \chi_e \underline{\mathbf{E}} \tag{2.10}$$

where χ_e is the *electric susceptibility* of the dielectric.

Therefore, for a linear and isotropic dielectric, from equation (2.8):

$$\underline{\mathbf{D}} = \varepsilon_o \underline{\mathbf{E}} + \underline{\mathbf{P}} = \varepsilon_o (1 + \chi_e) \underline{\mathbf{E}} = \varepsilon_o \varepsilon_r \underline{\mathbf{E}} \tag{2.11}$$

where $\varepsilon_r = (1 + \chi_e)$ is a dimensionless number referred to as the *relative permittivity* of the dielectric.

2.2.6 AC fields, real dielectrics and complex permittivity

As a simple means of illustrating more involved polarisation effects, a good example is the parallel plate capacitor of area A and plate separation d, connected to an alternating potential V of angular frequency ω, as shown in Figure (2.1).

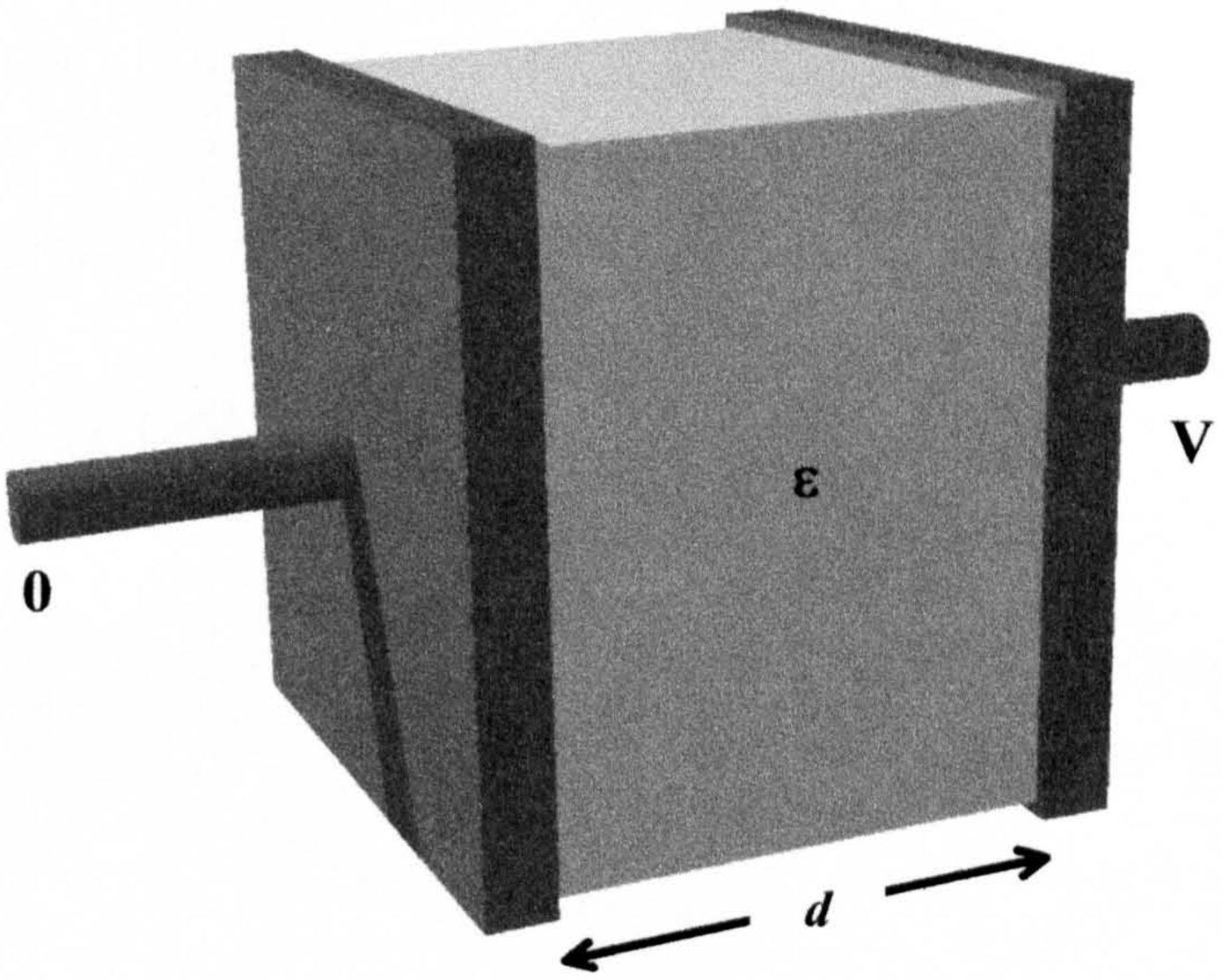

Figure (2.1) Parallel plate capacitor of plate separation d and area A containing a dielectric of permittivity $\varepsilon = \varepsilon_o \varepsilon_r$, and with an applied alternating potential of V.

With an ideal, loss-free dielectric filling the gap, the impedance is:

$$Z = \frac{1}{j\omega C} \tag{2.11}$$

where $j = \sqrt{(-1)}$ and the capacitance C is given by:

$$C = \varepsilon_o \varepsilon_r \frac{A}{d} \tag{2.12}$$

Some dielectrics are close to being ideal i.e., they are homogeneous, linear, isotropic and have a conductivity close to zero. For present purposes, they can be considered to have a constant permittivity. However, most real dielectrics, referred to as lossy, have a non-zero conductivity and the permittivity is dependent on the frequency of the applied electric field.

Consider the capacitor in Figure (2.1) with the ideal dielectric replaced with a real dielectric of conductivity σ. The current in the circuit is the same as if the circuit were replaced with a capacitor (capacitance C_1) containing an ideal dielectric, together with a resistor in parallel of resistance R_1 given by:

$$R_1 = \frac{d}{\sigma A} \tag{2.13}$$

The total impedance of the circuit is:

$$Z = \frac{1}{1/R_1 + j\omega C_1} = \frac{R_1}{1 + j\omega R_1 C_1} \tag{2.14}$$

Equating this impedance with the impedance of a capacitor as given in equation (2.11) and replacing the capacitance C_1 and resistance R_1 according to equations (2.12) and (2.13) respectively, gives:

$$C = \varepsilon^* \frac{A}{d} \tag{2.15}$$

where the permittivity $\varepsilon = \varepsilon_o \varepsilon_r$ from equation (2.13) has been replaced by:

$$\varepsilon^* = \varepsilon_o \varepsilon_r - j\frac{\sigma}{\omega} \tag{2.16}$$

This is the *complex permittivity* of the dielectric.

2.3 Polarisation processes [15,16]

In general, the behaviour of a dielectric is more complicated than the descriptions in previous sections. Polarisation mechanisms have a frequency dependent nature and where the dielectric is non-homogeneous, the complications are multiplied. This section briefly describes the principle of a Debye relaxation and the phenomenon of Maxwell-Wagner interfacial polarisation. The latter is fundamental to the origin of the dielectrophoretic force.

2.3.1 Dielectric relaxations and Debye.

Polarisation mechanisms in dielectrics involve the movement of charge to create dipoles. As the rate of this movement is finite, each mechanism has an associated characteristic time constant which is the time necessary for the polarisation to reach its maximum value. As the frequency of the applied alternating field increases, the period over which the dipole moment is able to 'relax' and then follow the field decreases. Therefore, there is a frequency at which these two periods are the same and beyond which the polarisation no longer reaches its maximum. At much higher frequencies, the mechanism virtually ignores the field and no polarisation occurs. This fall in polarisability causes a decrease in energy storage, and therefore permittivity, and is referred to as a dielectric relaxation.

Of the three basic polarisation mechanisms outlined in section (2.2.1), orientational polarisation has the longest relaxation time. Atomic and electronic polarisation will align with the field up to frequencies of the order of 10^{14} Hz and can be considered constant for the purposes of this work. The polarisation due to these mechanisms is therefore of the form of equation (2.10):

$$\underline{\mathbf{P}}_a = \varepsilon_o \chi_a \underline{\mathbf{E}} \tag{2.17}$$

The orientational polarisation has a characteristic '*relaxation time*' τ_{or} associated with the time taken for the permanent dipoles to reorient with the field. The polarisation is given by:

$$\underline{\mathbf{P}}_{or} = \frac{\varepsilon_o \chi_{or} \underline{\mathbf{E}}}{1 + j\omega\tau_{or}} \tag{2.19}$$

where χ_{or} is the low frequency or static field limit for orientational polarisation. The total frequency dependent polarisation is then:

$$\underline{\mathbf{P}}_{tot} = \varepsilon_o \left(\chi_a + \frac{\chi_{or}}{1 + j\omega\tau_{or}} \right) \underline{\mathbf{E}} \tag{2.20}$$

From equation (2.20), at the low frequency limit:

$$\chi = \chi_a + \chi_{or} = \varepsilon_s - 1 \tag{2.21}$$

where ε_s is the relative permittivity measured in a static electric field.

At the high frequency limit:

$$\chi = \chi_a = \varepsilon_\infty - 1 \tag{2.22}$$

where ε_∞ is the relative permittivity at sufficiently high frequency that there is no orientational polarisation. χ_{or} is therefore given by $\varepsilon_s - \varepsilon_\infty$ and equation (2.20) can be rewritten:

$$\underline{P}_{tot} = \varepsilon_o (\varepsilon^* - 1) \underline{E} \tag{2.23}$$

where ε^* is a complex term given by:

$$\varepsilon^* = \varepsilon_\infty + \frac{\varepsilon_s - \varepsilon_\infty}{1 + j\omega\tau_{or}} \tag{2.24}$$

This complex permittivity is independent of the complex permittivity of the dielectric (equation (2.17)) and is usually re-written:

$$\varepsilon^* = \varepsilon' - j\varepsilon'' \tag{2.25}$$

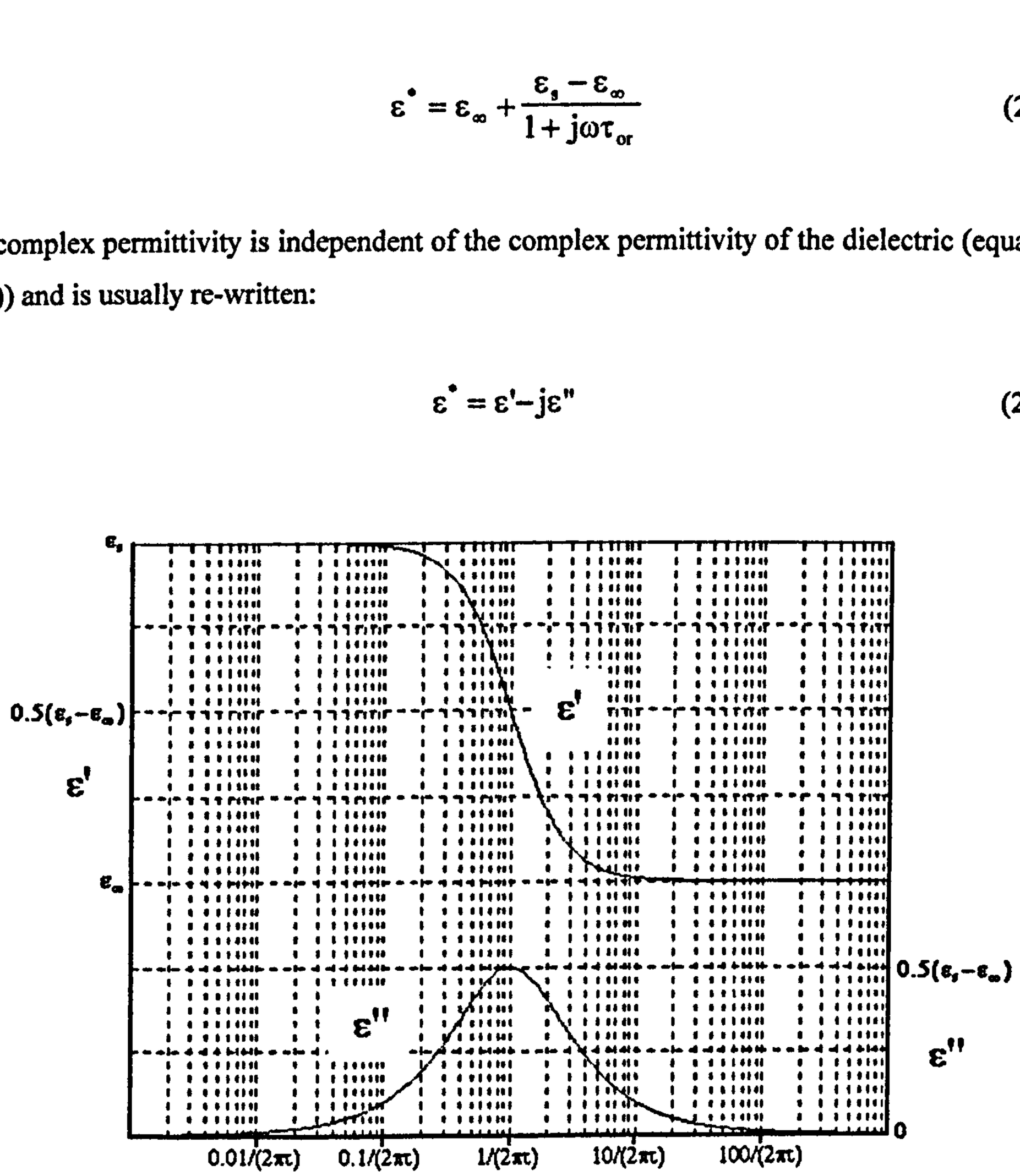

Figure (2.2) Plot of the variation of ε' and ε'' with frequency of the applied field. The axis on the left gives the values for ε' and the axis on the right, the values for ε''.

ε' and ε'' are given by the Debye formulations [15]:

$$\varepsilon' = \varepsilon_\infty + \frac{\varepsilon_s - \varepsilon_\infty}{1+\omega^2\tau_{or}^2} \tag{2.26}$$

$$\varepsilon'' = \frac{\omega\tau_{or}(\varepsilon_s - \varepsilon_\infty)}{1+\omega^2\tau_{or}^2} \tag{2.27}$$

The variation of ε' and ε'' with ω results in a dispersion in the relative permittivity as the frequency of the applied field is increased as shown in Figure (2.2).

2.3.2 Interfacial Polarisation

Experimental systems are further complicated by the presence of many dielectrics with differing properties. Under an applied field, the difference in these properties causes charges to build up at the discontinuities or interfaces between the dielectrics. As the polarisabilities of each dielectric are frequency dependent, so the surface charge density at the interface is also frequency dependent. As a result, the permittivity and conductivity of the whole system exhibit additional dispersions due solely to the polarisation of the interfaces. The study of such heterogeneous dielectrics was first discussed by Maxwell and extended by Wagner and the dispersion in permittivity arising because of an interface has come to be referred to as Maxwell-Wagner interfacial polarisation.

The simplest case is a parallel plate capacitor with two dielectrics as shown in Figure (2.3). This system can be described in a similar fashion to the capacitor in section (2.2.6) as two capacitors in series, both containing a real dielectric. The two dielectrics have permittivities ε_1 and ε_2 and conductivities σ_1 and σ_2, respectively. Each capacitor can be represented by a resistor and capacitor in parallel with resistance and capacitance given by equations (2.13) and (2.14) respectively. The impedance of the equivalent circuit is given by:

$$Z = Z_1 + Z_2 = \frac{R_1}{1+j\omega R_1 C_1} + \frac{R_1}{1+j\omega R_2 C_2} \tag{2.28}$$

Again, equating this to equation (2.11), the capacitance of the whole system is:

$$C = \varepsilon^* \frac{A}{d} \tag{2.29}$$

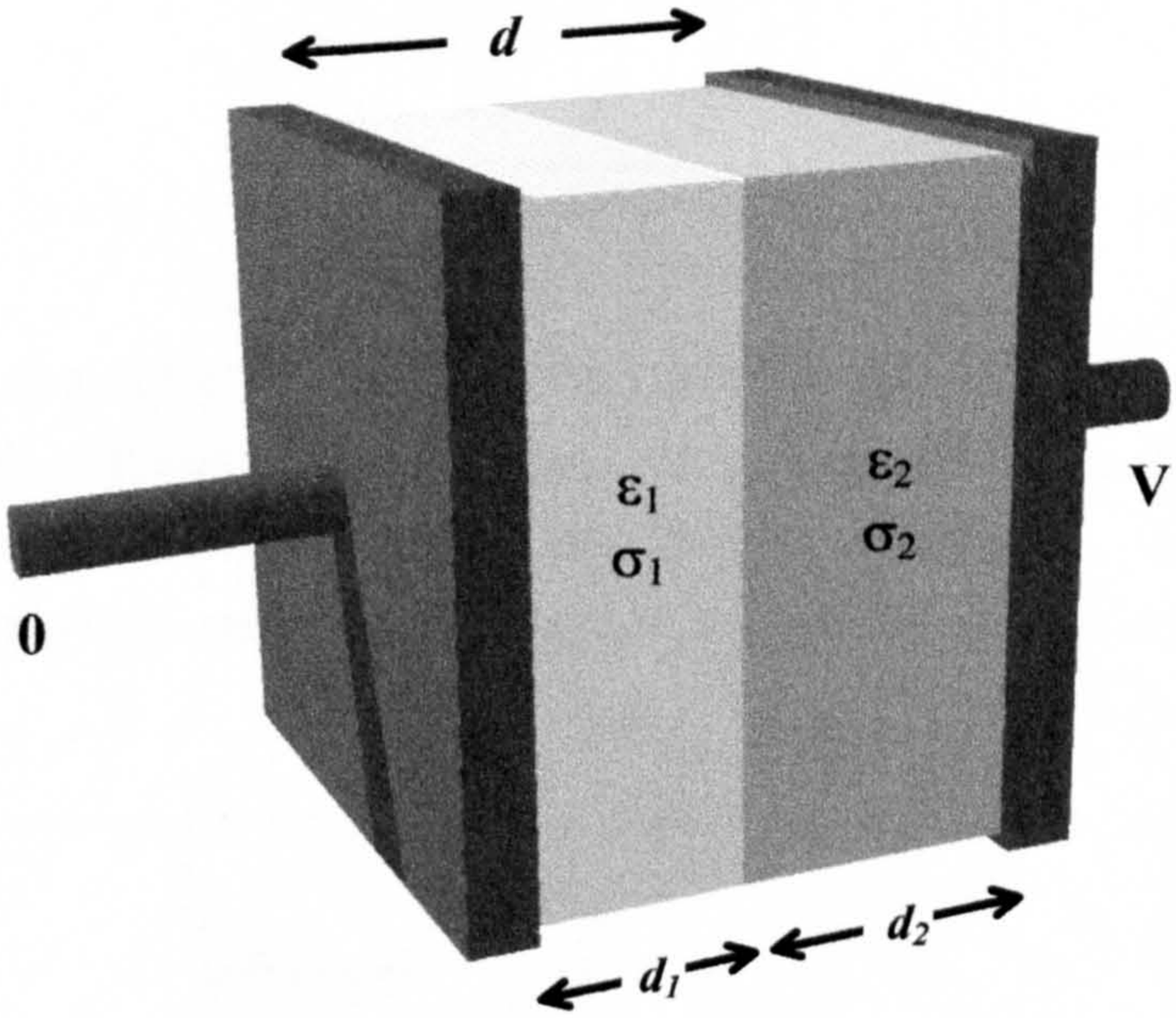

Figure (2.3) Parallel plate capacitor completely filled by two dielectrics, with permittivities ε_1, ε_2, conductivities σ_1, σ_2 and widths d_1 and d_2. The plate area is A, the plate separation is d and the applied voltage is V.

The complex permittivity ε^* in this case is given by:

$$\varepsilon^* = \varepsilon_o\varepsilon' - j\varepsilon_o\varepsilon'' - j\frac{\sigma}{\omega} \tag{2.30}$$

ε' and ε" are given by the Debye formulations (equations (2.26) and (2.27)) with:

$$\varepsilon_\infty = \frac{d\varepsilon_1\varepsilon_2}{d_1\varepsilon_2 + d_2\varepsilon_1} \tag{2.31}$$

$$\varepsilon_s = \frac{d(d_1\varepsilon_1\sigma_2^2 + d_2\varepsilon_2\sigma_1^2)}{(d_1\sigma_2 + d_2\sigma_1)^2} \tag{2.32}$$

$$\tau = \varepsilon_o \frac{d_1\varepsilon_2 + d_2\varepsilon_1}{d_1\sigma_2 + d_2\sigma_1} \tag{2.33}$$

σ is the conductivity of the whole system, given by:

$$\sigma = \frac{d\sigma_1\sigma_2}{d_1\sigma_2 + d_2\sigma_1} \tag{2.34}$$

The permittivity of the capacitor shown in Figure (2.3) has a dispersion due to a Debye type relaxation as well as the imaginary loss term. In general, relaxations due to interfacial polarisation occur at lower frequencies than for orientational polarisation and a plot of the complex permittivity of the system as a whole would be of the form of Figure (2.4).

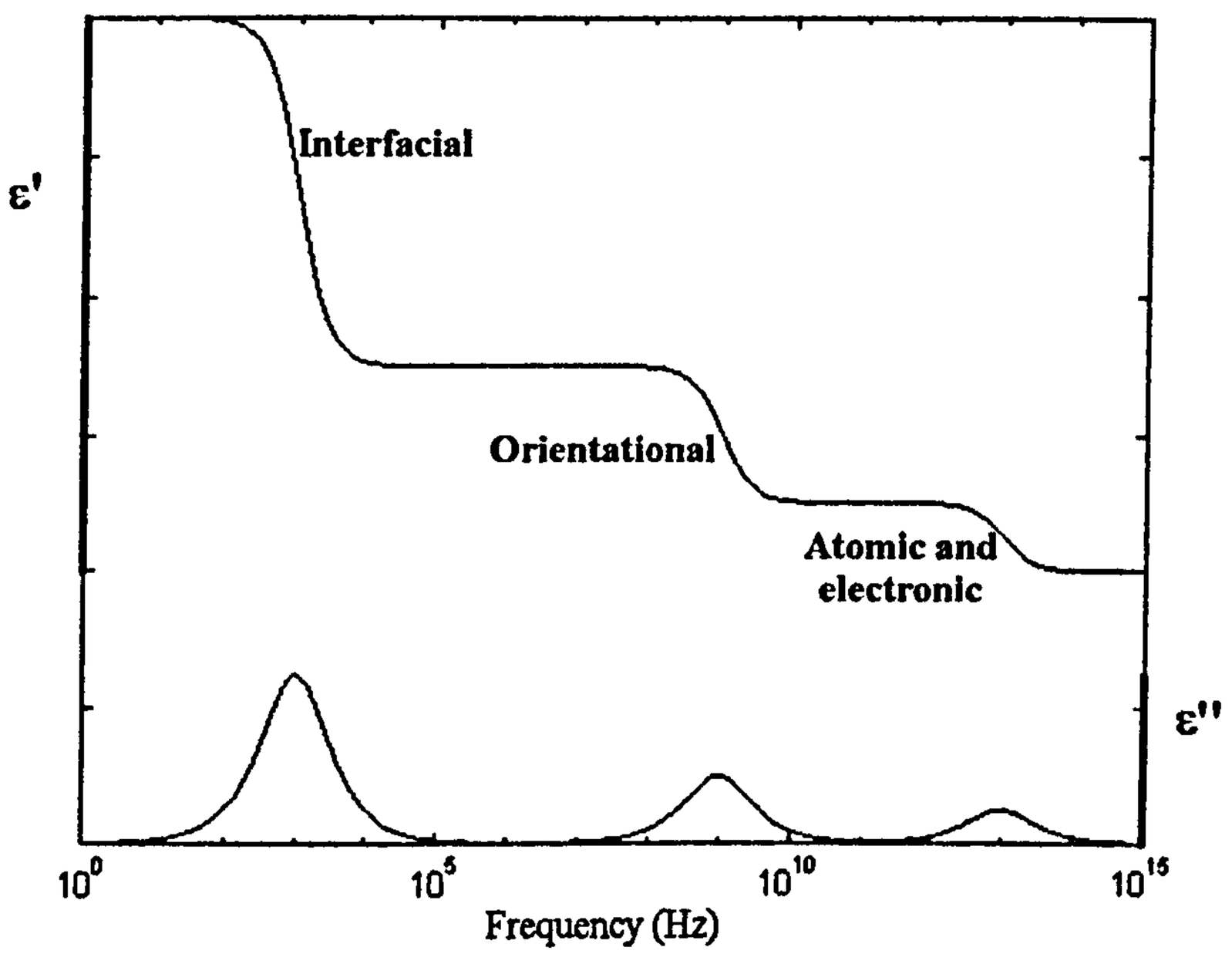

Figure (2.4) Schematic showing the variation of the real and imaginary parts of the permittivity for a system of dielectrics. The frequencies shown are the orders of magnitude for each type of relaxation.

References

1. J.C.Maxwell (1892) *A Treatise on Electricity and Magnetism*
   Clarendon Press, Oxford
2. K.W.Wagner (1914)
   Arch. Elektrotech. **2** 378
3. H.Fricke and H.J.Curtis (1937)
   Journal of Physical Chemistry **41** 729-745
4. J.B.Miles and H.P.Robertson (1932)
   Physical Review **40** 583-591
5. H.Pauly and H.P.Schwan (1959)
   Z.Naturforsch **14b** 125-131
6. H.Pauly and H.P.Schwan (1966)
   Biophysical Journal **6** 621-639
7. T.Hanai, N.Koizumi and A.Irimajiri (1975)
   Biophys. Struct. Mechanism **1** 285-294
8. A.Irimajiri, T.Hanai and A.Inouye (1979)
   Journal ofTheoretical Biology **78** p251-259
9. C.T.O'Konski (1960)
   Journal of Physical Chemistry **64** 605-619
10. H.P.Schwan, G.Schwarz, J.Maczuk and H.Pauly (1962)
    Journal of Physical Chemistry **66** 2626-2635
11. G.Schwarz (1962)
    Journal of Physical Chemistry **66** 2636-2642
12. J.M.Schurr (1964)
    Journal of Physical Chemistry **68** 2407-2413
13. P.Lorrain, D.R.Corson and F.Lorrain (1988) *Electromagnetic Fields and Waves 3rd ed*
    W.H.Freeman and Company, New York
14. B.I.Bleaney and B.Bleaney (1962) *Electricity and Magnetism*
    Oxford University Press, London
15. R.Pethig (1979) *Dielectric and electronic properties of biological materials*
    Wiley, Chicester
16. H.A.Pohl (1978) *Dielectrophoresis*
    Cambridge University Press, New York

Chapter Three

Theory: Dielectric particles

3.1 Introduction

A dielectric particle polarises under the influence of an electric field as outlined in Chapter Two. For a particle suspended in a liquid, the particle/liquid interface is polarised by Maxwell-Wagner interfacial polarisation (section (2.3.2)) and a surface charge density is induced at the interface. As a consequence, the particle has an induced dipole moment and an effective permittivity which depends not only on its internal properties but also the properties of the medium. This chapter outlines the derivation of the dipole moment for a spherical particle and the more general ellipsoidal particle.

3.2 The effective dipole moment of a spherical particle

In the following subsections, the simple model of the dielectric sphere shown in Figure (3.1) is considered. To determine the surface charge density and the resulting dipole moment of the particle, Laplace's equation for the electrical potential (equation (2.6)) is solved.

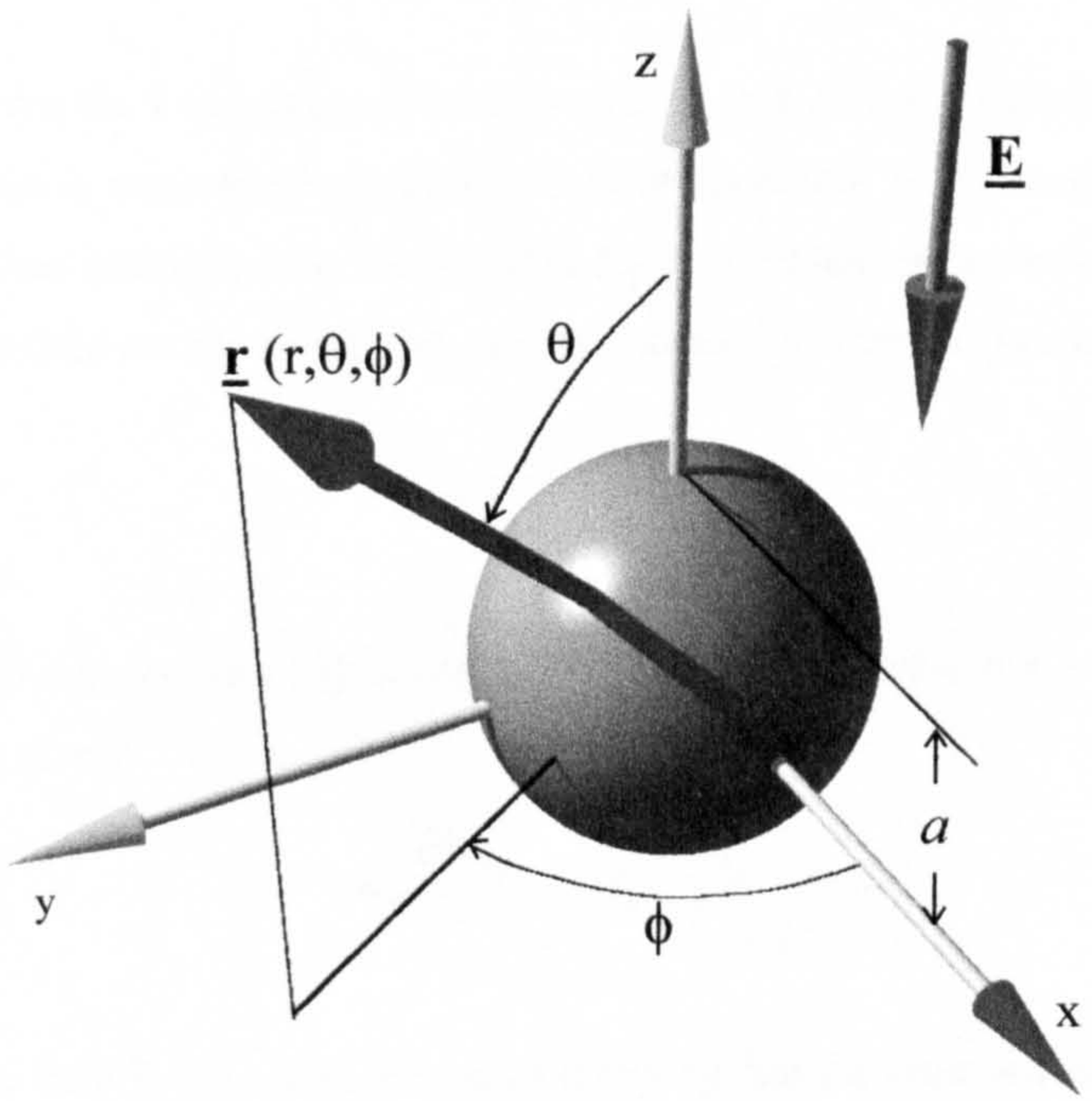

Figure (3.1) Dielectric sphere, radius a and permittivity ε_p, suspended in a medium of permittivity ε_m, under the influence of an electric field $\underline{\mathbf{E}}$.

Initially, the model as shown above is solved using spherical harmonics and the solution for the potential and dipole moment are easily obtained. Experimentally however, the dielectric particles are usually suspended in an electrolyte consisting of a solution of mobile

ions. In this case, the surface charge built up at the interface attracts the ions and an electrical double layer forms (see Appendix 3a). This effect complicates the model and different theories must be used to solve for the potential around the particle.

3.2.1 The simple dielectric sphere [1]

The solution for the case of an ideal dielectric is simply an application of spherical harmonic functions to solve Laplace's equation (equation (2.6)) to find the electric potential V. Further details of the solution method can be found in reference [1]. If the co-ordinate axes are arranged so that the sphere is centred on the origin and the applied field $\underline{\mathbf{E}}$ lies along the z-axis (i.e. $\underline{\mathbf{E}} = \mathrm{E}\hat{\underline{\mathbf{z}}}$ where $\hat{\underline{\mathbf{z}}}$ is the unit vector along the z-axis), the problem becomes axially symmetric. Therefore, in spherical polar co-ordinates (r,θ,ϕ), the solution is independent of ϕ and Laplace's equation becomes two dimensional. The general solution for the potential is given by:

$$V = \sum_{0}^{\infty} (A_n r^n + B_n r^{-(n+1)}) P_n(\cos\theta) \tag{3.1}$$

where $P_n(\cos\theta)$ are the Legendre polynomials and A_n and B_n are constants [1]. The potential inside the particle is considered separately from the potential in the medium. The boundary conditions and their restrictions on the solution for the problem are as follows[1]:

(a.) The electric field cannot be infinite, so the potential V is continuous at $r = a$.

$$V_m\big|_{r=a} - V_p\big|_{r=a} = 0 \tag{3.2}$$

(b.) The normal component of $\underline{\mathbf{D}}$ is continuous at $r = a$. Application of Gauss's Law (from equation 2.3) gives:

$$\varepsilon_m \frac{\partial V_m}{\partial r}\bigg|_{r=a} - \varepsilon_p \frac{\partial V_p}{\partial r}\bigg|_{r=a} = 0 \tag{3.3}$$

(c.) The electric field $\underline{\mathbf{E}}$ lies along the z-axis implying that the potential with no sphere present must be $V = -E r\cos\theta$. This must still be true at large r for the case of the potential around the sphere since the contributions to the electric field from the charges in and around the sphere are inversely proportional to r. As a consequence, the particular solution for the potential in the medium must contain the term $-Er\cos\theta$ and no other positive power of r. The solution for the potential in the medium V_m is therefore:

---

[1] The subscripts m and p refer to the medium and the particle respectively.

$$V_m = -\mathrm{Er}\cos\theta + \sum_{o}^{\infty}(B_n \mathrm{r}^{-(n+1)})\mathrm{P_n}(\cos\theta) \tag{3.4}$$

(d.) The electric field must also remain finite inside the particle. As a consequence, V must be finite as $r \rightarrow 0$ implying that the particular solution for the potential inside the sphere must contain no negative powers of r. The solution for the potential inside the particle V_p is therefore:

$$V_p = \sum_{o}^{\infty}(A_n \mathrm{r}^{n})\mathrm{P_n}(\cos\theta) \tag{3.5}$$

Equations (3.2) and (3.3) can be solved to find the values of the constants A_n and B_n [1]. Substitution of these values into equations (3.4) and (3.5) gives the particular solution for the potential in the medium and in the particle:

$$V_m = \mathrm{Er}\cos\theta\left[\frac{a^3}{\mathrm{r}^3}\left(\frac{\varepsilon_\mathrm{p} - \varepsilon_\mathrm{m}}{\varepsilon_\mathrm{p} + 2\varepsilon_\mathrm{m}}\right) - 1\right] \tag{3.6}$$

$$V_p = -\frac{3\varepsilon_\mathrm{m}}{\varepsilon_\mathrm{p} + 2\varepsilon_\mathrm{m}}\mathrm{Er}\cos\theta \tag{3.7}$$

3.2.2 The effects of conductivity - lossy dielectrics [2]

If the dielectrics in the above model are lossy, the same boundary conditions and general solutions hold. The difference is the presence of conductivity terms and charge transport to the interface. Conductivity affects $\underline{\mathbf{D}}$ in the different dielectrics and therefore the second boundary condition is also affected. Applying Gauss's Law in this case gives:

$$\varepsilon_\mathrm{p}\left.\frac{\partial \mathrm{V_p}}{\partial \mathrm{r}}\right|_{\mathrm{r=a}} - \varepsilon_\mathrm{m}\left.\frac{\partial \mathrm{V_m}}{\partial \mathrm{r}}\right|_{\mathrm{r=a}} = \rho^s \tag{3.8}$$

where ρ^s is the free surface charge density at the interface. This surface charge density is governed by the time dependent nature of free charge transport in the dielectrics. The charge conservation equation:

$$\frac{\partial q}{\partial t} = -\nabla.\underline{J} \tag{3.9}$$

relates the rate of change of charge in a volume to the flux of charges through the surface bounding the volume. In a dielectric, Ohm's law relates the flux of charges to the applied electric field:

$$\underline{J} = \sigma\underline{E} \tag{3.10}$$

For a small volume through the surface of the dielectric sphere, the rate of change of the surface charge density is related to the flux of charges in the medium and in the sphere. Using the divergence theorem and substituting equation (3.10) into equation (3.9) gives the continuity equation for the transport of charge carriers to and from the surface:

$$\frac{\partial \rho^s}{\partial t} = \sigma_m \left.\frac{\partial V_m}{\partial r}\right|_{r=a} - \sigma_p \left.\frac{\partial V_p}{\partial r}\right|_{r=a} \tag{3.11}$$

If the field is periodic, i.e. $E = E_o e^{j\omega t}$, then V and ρ^s are also periodic and the time derivative of ρ^s is $j\omega \rho^s$. Equations (3.8) and (3.11) can therefore be combined to give:

$$\varepsilon_p^* \left.\frac{\partial V_p}{\partial r}\right|_{r=a} - \varepsilon_m^* \left.\frac{\partial V_m}{\partial r}\right|_{r=a} = 0 \tag{3.12}$$

where ε_p^* and ε_m^* are the complex permittivities (equation (2.16)) for the particle and medium respectively. As the differences between equation (3.12) and equation (3.3) are independent of position, the solution for the potential is given by the equations:

$$V_m = E r \cos\theta \left[\frac{a^3}{r^3}\left(\frac{\varepsilon_p^* - \varepsilon_m^*}{\varepsilon_p^* + 2\varepsilon_m^*}\right) - 1\right] \tag{3.13}$$

$$V_p = -\frac{3\varepsilon_m^*}{\varepsilon_p^* + 2\varepsilon_m^*} E r \cos\theta \tag{3.14}$$

The factor

$$\frac{\varepsilon_p^* - \varepsilon_m^*}{\varepsilon_p^* + 2\varepsilon_m^*} \tag{3.15}$$

is the Clausius-Mossotti factor and describes the frequency dependent variation of the potential around the sphere.

3.2.3 The effective dipole moment [3]

The potential generated by a dipole consisting of two charges, +q and -q, separated by a distance *d* is given by [3]:

$$V = \frac{q d \cos\theta}{4\pi\varepsilon_m r^2} \tag{3.16}$$

Comparison of this and equation (3.13) shows that the potential in the medium is the sum of the original uniform field and a dipole moment $\underline{\mathbf{p}}$ where:

$$\underline{\mathbf{p}} = 4\pi\varepsilon_m \left(\frac{\varepsilon_p^* - \varepsilon_m^*}{\varepsilon_p^* + 2\varepsilon_m^*} \right) a^3 \underline{\mathbf{E}} \tag{3.17}$$

This is the effective dipole moment of the sphere. The size of the effective dipole moment is frequency dependent and undergoes a dispersion because of Maxwell-Wagner interfacial polarisation. It is sometime re-written in terms of the volume of the sphere and an effective polarisability u_p where:

$$\underline{\mathbf{p}} = \frac{4}{3}\pi a^3 u_p \underline{\mathbf{E}} \tag{3.18}$$

The effective polarisability of a spherical dielectric particle is therefore:

$$u_p = 3\varepsilon_m \left(\frac{\varepsilon_p^* - \varepsilon_m^*}{\varepsilon_p^* + 2\varepsilon_m^*} \right) \tag{3.19}$$

This solution is correct under the condition that the size of the sphere is small compared with a characteristic distance associated with the electric field. However, experiments conducted in order to determine the internal properties of particles by measuring their effective dipole moments showed that the theory did not describe dielectric spheres under certain conditions [4-7]. This implied that a modification to the theory was required in order to describe the differences between expected and measured properties.

3.3 Surface effects and surface conductance

In the majority of cases, experiments are performed on dielectric spheres suspended in an ionic salt solution. A charge at the particle/medium interface will attract ions to the surface forming an electrical double layer (Appendix 3a). The situation is further complicated if the particle being studied has a fixed surface charge. In this case, the fixed surface charge creates a double layer which is independent of the applied field and interacts with it. Miles and Robertson [4] first proposed the idea that the double layer would affect the dielectric properties of the medium around the particle and, as a direct consequence, the effective dipole moment. The experimental results, in general, showed two unexplained phenomena: the apparent conductivity of the particle was higher than expected [5] and there was a second large dispersion at a frequency lower than the Maxwell-Wagner relaxation frequency [6,7].

O'Konski [8] presented a theory to explain the apparent increase in the conductivity of the particle in terms of a surface conductance. It postulates that the flux due to the transport of charge carriers associated with the fixed charge on the surface, must be added to the flux due to transport of bulk charges to and from the surface. The latter flux is the one which gives rise to interfacial polarisation.

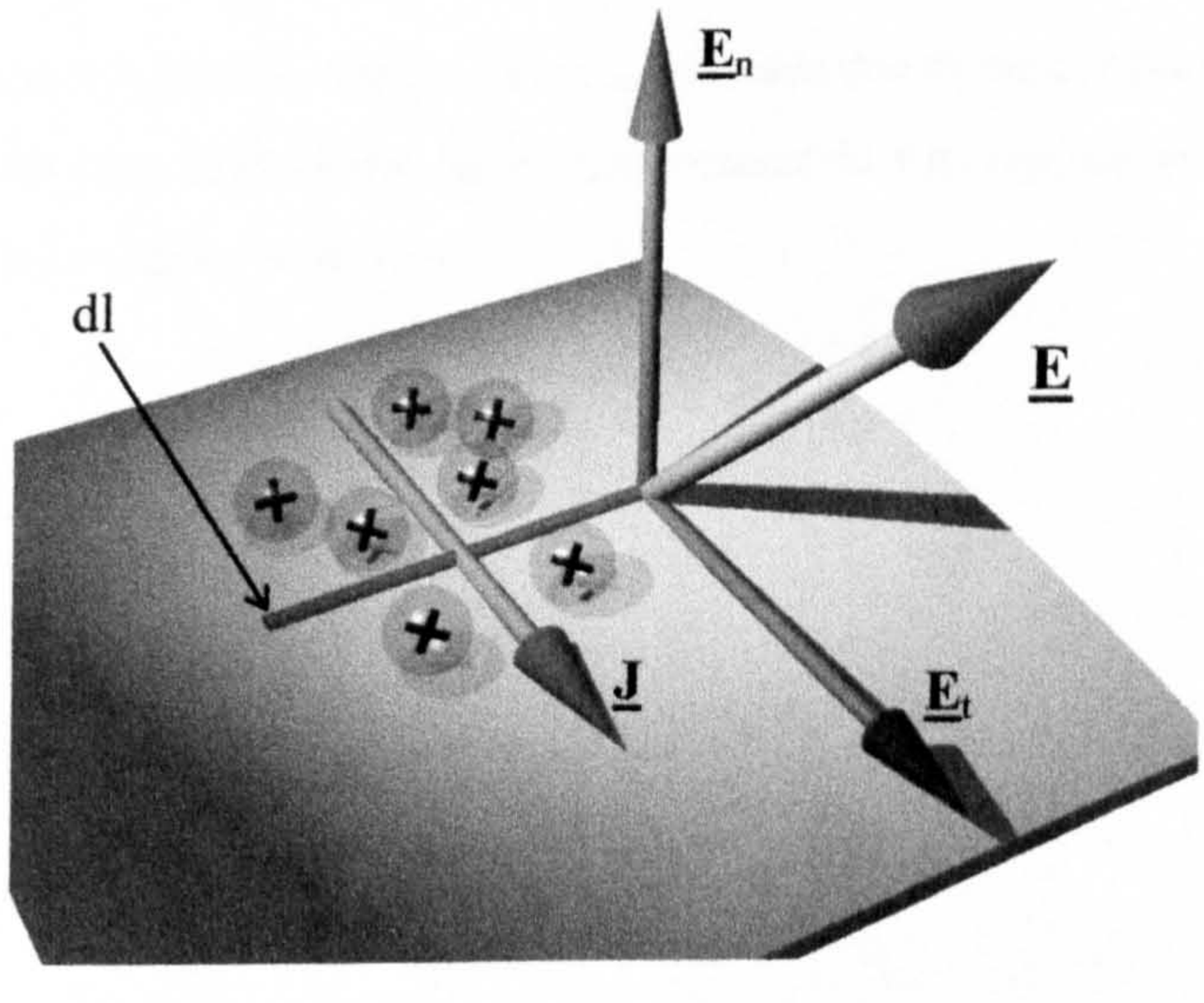

Figure (3.2) Diagram of a surface of specific conductance λ. The flux of charge carriers **J** through line element dl is governed by the component of the electric field **E** tangential to the surface

Assuming these carriers are restricted to movement only along a surface, the surface conductance is defined as the rate of transfer of charge:

$$J = \frac{dq}{dt} = \lambda E_t dl \tag{3.20}$$

along a surface of specific conductance λ through a line element of length dl in an electric field $\underline{E}$ with component E_t along the surface and perpendicular to dl as shown schematically in Figure (3.2). The contribution of the charge carriers in the medium is given by the sum:

$$\lambda = \sum_i N_i \mu_i z_i \tag{3.21}$$

where N_i is the number of carriers per unit surface area, μ_i is the mobility and z_i the valency for carrier of type i. For a single type of counterion, this can be simplified to $\rho^s \mu$ where μ is the mobility of the ion and ρ^s is, again, the surface charge density.

The total surface charge density ρ^s is the sum of two components:

$$\rho^s = \rho_a^s + \rho_b^s \tag{3.22}$$

where ρ_a^s is the component due to transport to and from the surface and ρ_b^s is the component related to the transport of charge carriers along the surface due to the conductance λ.

The two transport mechanisms have an associated flux as represented in Figure (3.3) and are governed by the continuity equations:

$$\frac{\partial \rho_a^s}{\partial t} = \sigma_m \left.\frac{\partial V_m}{\partial r}\right|_{r=a} - \sigma_p \left.\frac{\partial V_p}{\partial r}\right|_{r=a} \tag{3.23}$$

and:

$$\frac{\partial \rho_b^s}{\partial t} = \frac{\lambda}{a^2 \sin\theta} \frac{\partial}{\partial \theta}\left(\sin\theta \left.\frac{\partial V_p}{\partial \theta}\right|_{r=a} \right) \tag{3.24}$$

This assumes an axially symmetric system as for section (3.2.3). The continuity equation for ρ^s is therefore:

$$\frac{\partial \rho^s}{\partial t} = \frac{\lambda}{a^2 \sin\theta} \frac{\partial}{\partial \theta}\left(\sin\theta \left.\frac{\partial V_p}{\partial \theta}\right|_{r=a} \right) + \sigma_m \left.\frac{\partial V_m}{\partial r}\right|_{r=a} - \sigma_p \left.\frac{\partial V_p}{\partial r}\right|_{r=a} \tag{3.25}$$

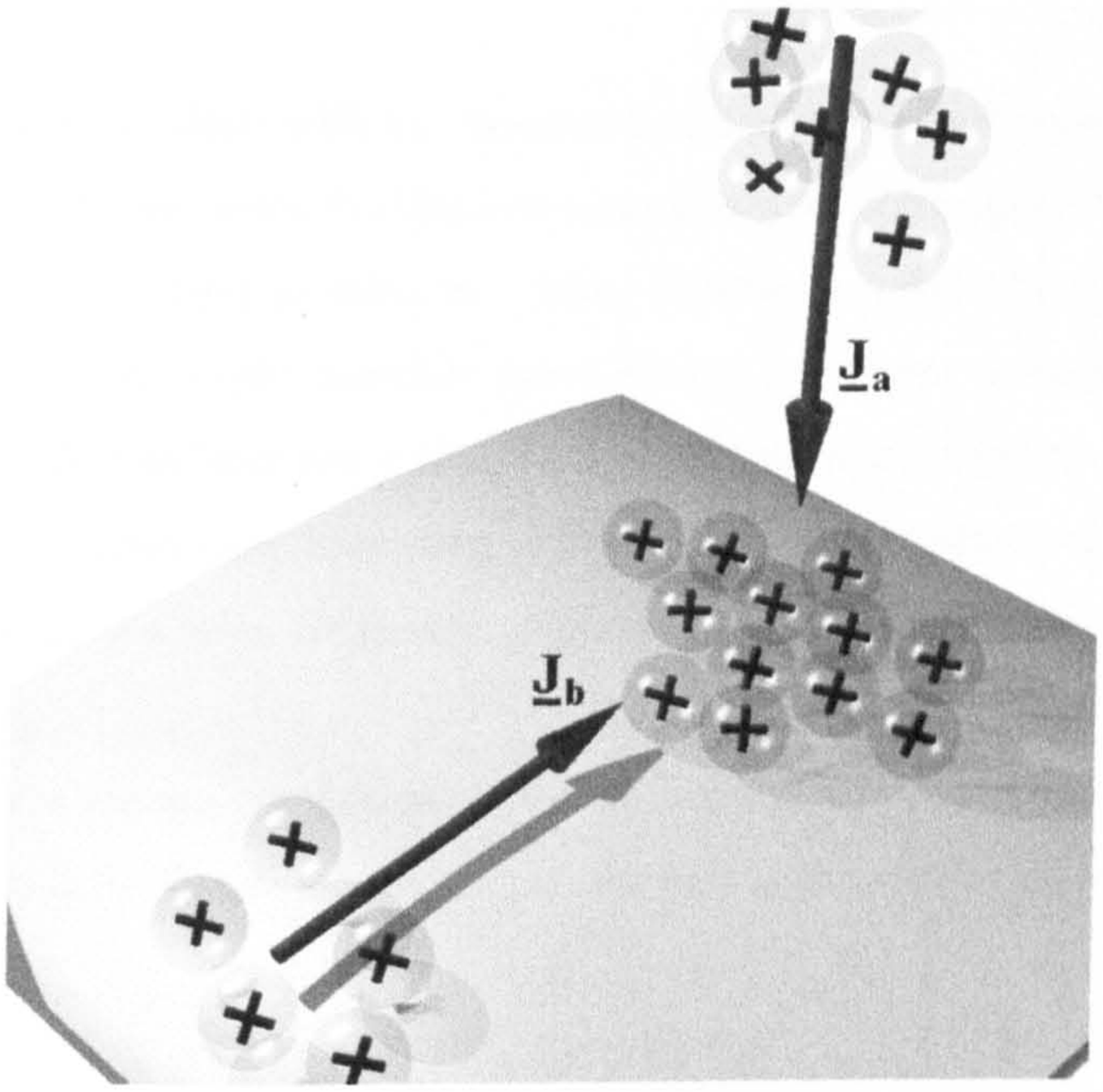

Figure (3.3) A schematic representation of the movement of charge carriers at the surface of a sphere in response to an applied field. The flux $\underline{\mathbf{J}}_a$ is due to ohmic conductivity in the medium and $\underline{\mathbf{J}}_b$ is due to the surface conductivity.

Assuming a periodic electric field as before, manipulation of this equation and equation (3.8) gives a solution for the potential which is identical to equations (3.13) and (3.14) and a solution for the dipole identical to equation (3.17), with the complex permittivity of the particle given by:

$$\varepsilon_p^* = \varepsilon_o \varepsilon_p - j\frac{\sigma_p'}{\omega} \quad \text{where} \quad \sigma_p' = \sigma_p + \sigma_s \quad \text{and} \quad \sigma_s = \frac{2\lambda}{a} \tag{3.26}$$

This theory successfully explained the larger than expected value for the particle conductivity at low frequencies. However, further experiments revealed the presence of another dispersion in the complex permittivity of these types of particle. This dispersion is generally referred to as the α-relaxation and occurs at a lower frequency than the Maxwell-Wagner relaxation (called the β-relaxation). The cause of the low-frequency dispersion is generally assumed to be caused by polarisation of the electrical double layer.

3.4 The α–relaxation I: Schwarz [9] and Schurr [10]

O'Konski's theory deals with the movement of the counterions normal to the surface of the sphere. Schwarz [9] presented the idea that these ions were quite tightly bound to the surface and, as a result, were unlikely to move in a radial direction but were free to move tangentially around the particle. Ions would therefore move around the sphere in response to the electric field, polarising the double layer and adding to the effective dipole moment. This polarisation would have a longer relaxation time than an interfacial mechanism and the corresponding dispersion would occur at a lower frequency, explaining the low frequency α–relaxation reported experimentally [6,7].

Briefly, there are two components to the surface flux of counterions moving around the sphere. First, there is the flux of ions moving in response to the applied field:

$$\underline{\mathbf{J}}_{\mathrm{E}} = -\frac{\rho^{s}\mu}{a}\frac{\partial V^{s}}{\partial\theta} \tag{3.27}$$

where ρ^s is the surface counterion density, μ is the mobility of the counterion and V^s is the potential at the surface. The second term is the diffusion flux acting against the first term :

$$\underline{\mathbf{J}}_{\mathrm{D}} = -\frac{\mu \mathrm{kT}}{a\mathrm{e}_{\mathrm{o}}}\frac{\partial\rho^{s}}{\partial\theta} \tag{3.28}$$

where T is the temperature, k is the Boltzman constant and e_o is the charge of the electron. Diffusion is discussed in more detail in section (4.2.4).

The rate of change of the surface charge density is given by the divergence of the flux:

$$\frac{\partial\rho^{s}}{\partial \mathrm{t}} = \nabla.(\underline{\mathbf{J}}_{\mathrm{E}} + \underline{\mathbf{J}}_{\mathrm{D}}) \tag{3.29}$$

The surface charge density can be represented as the original undisturbed counterion distribution ρ_o^s which is a constant, and a time varying perturbation ρ_t^s such that:

$$\rho^{s} = \rho_{o}^{s} + \rho_{t}^{s} \tag{3.30}$$

Substitution of equations (3.27) and (3.28) into (3.29) gives the partial differential continuity equation:

$$\frac{\partial \rho^s}{\partial t} = \frac{\mu kT}{a^2 e_o \sin\theta} \frac{\partial}{\partial \theta}\left(\sin\theta \frac{\partial \rho^s}{\partial \theta} + \frac{e_o}{kT} \frac{\partial V^s}{\partial \theta} \rho^s \sin\theta \right) \tag{3.31}$$

To help solve this equation, Schwarz introduced a quantity γ such that:

$$\gamma = \frac{e_o a E}{kT} \tag{3.32}$$

where E is the electric field. Schwarz assumed that $\gamma << 1$ for all cases and also made the reasonable assumption that the electric field along the surface is of the same order of magnitude as the external field. As a consequence, the second term in the brackets in equation (3.31) is also small compared to unity and ρ^s varies only a little from ρ_o^s. This implies that $\rho_t^s << \rho_o^s$ and that equation (3.31) can be modified by substituting: ρ_t^s for ρ^s on the left hand side and in the first term in the brackets, and ρ_o^s for ρ^s in the second term in the brackets. The equation can then be solved for an alternating field of angular frequency ω using Legendre polynomials to give:

$$\frac{dq}{dt} = \lambda E_t dl \tag{3.33}$$

where the surface conductance term introduced by O'Konski has been replaced by a frequency dependent surface conductivity λ such that:

$$\lambda = \frac{j\omega\tau_{\alpha s}}{1 + j\omega\tau_{\alpha s}} \lambda_o \tag{3.34}$$

where λ_o is the surface conductance as given by equation (3.21). The relaxation time $\tau_{\alpha s}$, associated with the frequency dependent part is given by:

$$\tau_{\alpha s} = \frac{e_o a^2}{2\mu kT} = \frac{a^2}{2D} \tag{3.35}$$

where D is the diffusion coefficient for the ions (see section (4.2.4)).

The solutions for the potential and effective dipole moment are, again, exactly the same as given in section (3.3.3) with the surface conductance, in this case, given by equation (3.34). The effective complex permittivity of the particle is:

$$\varepsilon_p^* = \varepsilon_o\varepsilon_p + \frac{2\lambda_o}{a}\frac{\tau_{\alpha S}}{(1+\omega^2\tau_{\alpha S}^2)} - j\left(\frac{\sigma_p}{\omega} + \frac{2\lambda_o}{a}\frac{\omega\tau_{\alpha S}^2}{(1+\omega^2\tau_{\alpha S}^2)}\right) \qquad (3.36)$$

According to this equation, the electric and diffusion flux terms cancel each other and the total current due to surface ions disappears as $\omega \to 0$. However, for a steady state DC field, there is still a current term due to the surface counterions. Schurr [10] found this to be equivalent to the surface conductance described by O'Konski and resolved the problem using Schwarz's method and O'Konski's boundary conditions. This solution for the interaction of potential and diffusion driven surface fluxes does not have the limitation that the counterions are bound to the surface. Again, the equations for the potential and dipole moment are given by equations (3.13) and (3.17) respectively, where the effective permittivity of the particle is given by [10]:

$$\varepsilon_p^* = \varepsilon_o\varepsilon_p + \frac{2\lambda_o}{a}\frac{\tau_{\alpha S}}{(1+\omega^2\tau_{\alpha S}^2)} - j\left(\frac{\sigma_p}{\omega} + \frac{2\lambda_o}{a} + \frac{2\lambda_o}{a}\frac{\omega\tau_{\alpha S}^2}{(1+\omega^2\tau_{\alpha S}^2)}\right) \qquad (3.37)$$

Unfortunately, these theories did not describe the experimental results adequately. Further experimental research indicated that under most experimental conditions, the assumptions made to simplify the initial equations in order obtain a solution were not valid.

3.5 The α-relaxation II: Duhkin [11], Lyklema [12-15] and Minor [16]

Lyklema [12-14] summarised the results given in sections (3.3) and (3.4) and outlined the problems with these theories. As previously stated, O'Konski's theory adequately explained the apparent increase in the particle conductivity in terms of a surface conductance. In doing so, the assumption was made that there was free exchange of charge between the surface conductance layer and the bulk. However, this does not explain the measured low-frequency dispersion. The theory presented by Schwarz and modified by Schurr was also unsuitable because of certain assumptions made and resulting limitations in the solution. The assumption that the charges are bound to the surface is only true at very high frequencies. However, charges bound to the surface would have a much lower mobility than the bulk and therefore the relaxation time for the associated polarisation mechanism (equation (3.35)) would be much longer than for bulk values. By inference, the interpretation of the physical basis of this mechanism is flawed and the theory cannot apply. Also, the assumption that γ, as given by equation (3.32), is much smaller than one is not true under most circumstances. More fundamentally, this theory only considers

bound counterions and does not take into account the effects of ions in the diffuse part of the double layer (see Figure (3.4) and Appendix 3a).

Lyklema, following the work of Duhkin [11], presented several theories for polarisation mechanisms in the double layer. In [12], a generalisation of the Schwarz model was published which takes into account the effects of the diffuse part of the double layer. A model for the polarisation of a double layer consisting only of a diffuse part was also presented. In his book [15], Lyklema published a more up to date model for the polarisation of the double layer as a whole.

3.5.1 Polarisation of the bound layer according to Lyklema

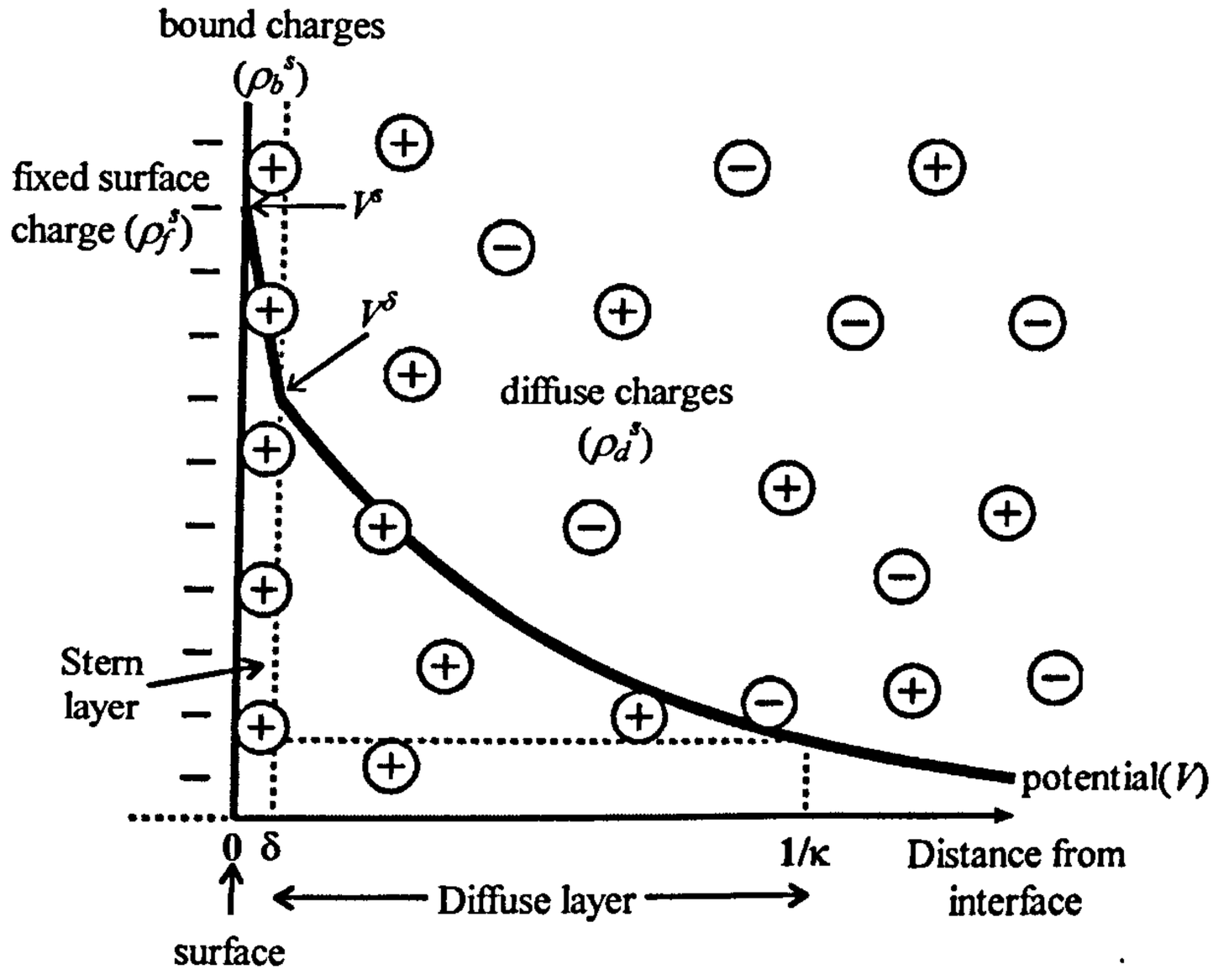

Figure (3.4) Schematic diagram of the electrical double layer. The surface charge and the related surface potential V^s results in an increase in the volume density of the counterion (the ion in the solution with opposite charge) near the interface between the surface and the fluid. As a result of the redistribution of charge and the physical size of the ions, the potential V falls linearly across the bound or Stern layer and then as 1/r across the diffuse layer.

Figure (3.4) shows a schematic diagram of an electrical double layer with approximate distributions of the charges and the size of the potential with distance from the surface. Close to the surface, which has a fixed negative charge, there are bound positive counterions which form the Stern layer, across which the potential falls linearly. Farther from the surface, in the diffuse layer, the counterion density is less and they have a mobility approximately equal to the bulk. A detailed description of the double layer can be found in Appendix (3a).

In deriving a general model for the behaviour of the bound layer, Lyklema took into account three types of charges as shown in Figure (3.4):

a. fixed surface charges such as covalently bound ionic groups $-\rho_f^s$

b. charges in the bound layer $-\rho_b^s$

c. charges in the diffuse layer $-\rho_d^s$

For the purposes of this derivation, a fixed charge is taken to be a charge with negligible surface mobility. Counterions with a surface diffusion coefficient $D_s < D$ may be considered as fixed for frequencies $\omega >> 2D_s a^{-2}$ and mobile if $\omega \leq 2D_s a^{-2}$.

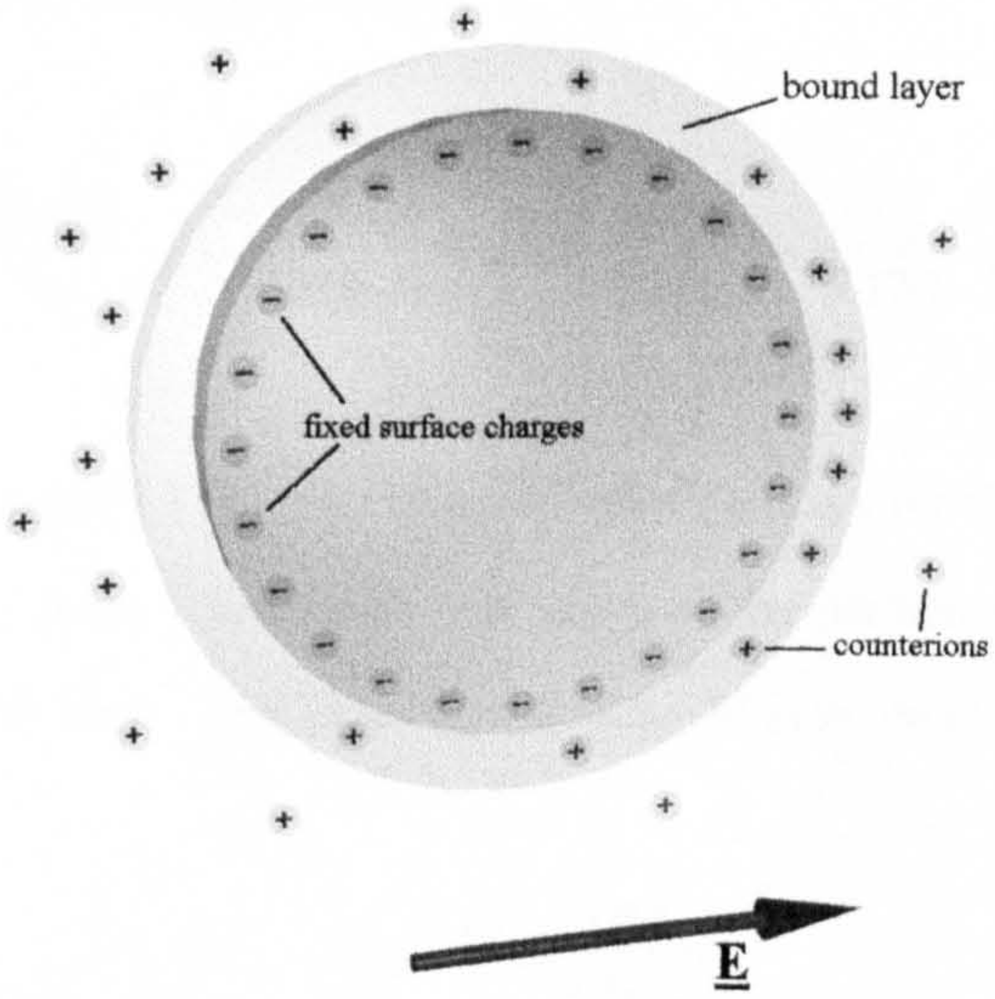

Figure (3.5) A cross-section through a spherical dielectric particle showing the positions of fixed surface charges and counterions in the double layer. Under the influence of the electric field **E**, the counterions in the bound layer enrich the positive side of the particle. In order to maintain electroneutrality, the counterions outside the bound layer move in the opposite direction.

Figure (3.5) shows, in cross-section, the position and movement of charges in and around a dielectric sphere which is assumed to have a net negative surface charge. At low frequencies, the bound ions move under the influence of an applied electric field to enrich the negative side (to the right of the diagram). However, the diffuse ions outside the bound layer can exchange with the bulk and attempt to maintain electroneutrality by enriching the positive side (on the left). The mobility of counterions in the bound layer is less than the ions in the diffuse part of the double layer. For thin double layers, the diffuse ions can redistribute fast enough to be able to almost maintain equilibrium between the bound and diffuse parts of the double layer. Therefore, the bound and surface charges are almost continually screened by the diffuse ions and the polarisation of the diffuse layer cannot be ignored. This extra polarisation

reduces the relaxation time of the bound ions and, as a consequence, the frequency of the α-dispersion is higher in this case than for the double layer model of Schwarz (section 3.4)

Lyklema introduced a differential capacitance C_d to account for this effect:

$$C_d = \varepsilon_m \kappa \cosh\left(\frac{F\zeta}{2RT}\right) \tag{3.38}$$

where ε_m is the permittivity of the bulk medium, κ is the reciprocal Debye length, F is the Faraday, R is the gas constant, T is the temperature and ζ is the zeta potential.

The continuity equation for this mechanism is:

$$\frac{\partial \Delta\rho_{bE}^{s}}{\partial t} = \frac{F D_b M}{a^2 \sin\theta} \frac{\partial}{\partial\theta}\left(\sin\theta\left(\frac{\partial \Delta\rho_{bE}^{s}}{\partial\theta} + \frac{F\rho_b^{s}}{RTM}\frac{\partial V^{s}}{\partial\theta}\right)\right) \tag{3.39}$$

which is similar to equation (3.31). D_b is the diffusion constant for the ions in the bound layer, ρ_b^s is the charge density in the bound layer and $\Delta\rho_{bE}^{s}$ is the perturbation in this charge density due to the applied electric field. The modification factor M is given by:

$$M = 1 + \frac{F\rho_b^{s}}{RTC_d} \tag{3.40}$$

Lyklema then solved this equation using the same procedure as Schwarz and obtained a relaxation time for the polarisation mechanism of:

$$\tau_{\alpha L} = \frac{a^2}{2D_b M} \tag{3.41}$$

3.5.2 Polarisation of the diffuse layer

The theory presented for the relaxation of the diffuse double layer in reference [12] by Lyklema, Shilov and Dukhin is a straight transcription of the theory published by Dukhin in his book [11]. Both are based on electro-osmotic flow around the particle in the absence of a Stern layer. No attempt was made to explain the derivation of the equations which are summarised here. The suspending medium is assumed to be an electrolye solution consisting of positive and

negative ions, with diffusion coefficients D^+ and D^- respectively. For simplicity it is assumed that $D^+ = D^- = D$.

The induced dipole moment of the particle is:

$$\underline{\mathbf{p}} = -\frac{3}{2}\left(\frac{a_1(1+W)+j(a_1W+a_2W^2)}{A_1(1+W)+j(A_1W+A_2W^2)}\right)a^3\underline{\mathbf{E}} \tag{3.42}$$

where a is the radius of the particle and $\underline{\mathbf{E}}$ is the electric field as before. The other terms in the equation are given by a complicated series of equations which are outlined in Appendix (3b).

3.5.3 The relaxation of the double layer as a whole

In his book [15], Lyklema presented a complete theory for the dielectric dispersion caused by the relaxation of the electrical double layer. The theory describes the contribution of charge currents, the surface potential and electro-osmosis in the diffuse layer to the surface conduction of the particle.

The far field solution for the perturbation in the potential outside the spherical particle is:

$$\Delta V_m = \left[-Er\cos\theta + \frac{d_e a^3}{r^2}E\cos\theta\right]e^{j\omega t} \tag{3.43}$$

Comparing this to equation (3.13) shows that the d_e is an equivalent term to the Clausius-Mossotti factor (equation (3.15)) for a Maxwell-Wagner relaxation. This term is given by the following set of equations:

$$d_e = -\frac{1}{2} + \frac{3Du^d}{2(1+Du^d(\gamma+1))} \tag{3.44}$$

where Du^d is a "*Duhkin number*" for the diffuse layer, given by:

$$Du^d = \frac{2}{\kappa a}\left(1+\frac{3m}{z^2}\right)\left[\cosh\left(\frac{zF|\zeta|}{2RT}\right)-1\right] \tag{3.45}$$

The Duhkin number is the ratio of the surface conductance to the bulk.

The assumption has been made, as in the previous section, that the electrolyte is symmetrical and that the diffusion coefficients for the ions are equal. The factor γ is:

$$\gamma = 1 - \frac{(\omega\tau)^{3/2} - j\omega\tau}{(1+\sqrt{\omega\tau})(1+\omega\tau)} \tag{3.46}$$

and the electro-osmotic contribution to the polarisation, m is given by:

$$m = \left(\frac{RT}{F}\right)^{\frac{3}{2}} \frac{2\varepsilon_m}{3\eta D} \tag{3.47}$$

The relaxation time for this mechanism is identical to the relaxation time given by Schwarz (equation (3.35)). Using the same manipulation outlined in section (3.2.3), the effective dipole from this polarisation mechanism is:

$$\underline{p}_D = 4\pi\varepsilon_m d_e a^3 \underline{E} \tag{3.48}$$

This theory can be considered to supersede the theory outlined in section (3.5.2).

3.6 The effective polarisability of an ellipsoidal particle

In some cases, the more general case of an ellipsoidal particle must be considered. Several references [17,18] contain the method of derivation for the effective polarisability of such particles. This section summarises the resulting equations and simplifies for the case of a long thin particle as a suitable approximation to a rod.

Consider the homogeneous, ellipsoidal, dielectric particle shown in Figure (3.5), the half lengths of the major axes are a, b and c and the particle has permittivity ε_p and conductivity σ_m. The medium has permittivity ε_m and conductivity σ_m. Without loss of generalisation, the major axis of half length a can be assumed to lie along the x-axis.

The effective polarisability u_α of the particle along an arbitrary axis α (where α is one of x, y, z) is given[18] by:

$$u_\alpha = \varepsilon_m \chi_\alpha \tag{3.49}$$

where the susceptibility χ_α is given by:

$$\chi_\alpha = \frac{\varepsilon_p^* - \varepsilon_m^*}{(\varepsilon_p^* - \varepsilon_m^*)A_\alpha + \varepsilon_m^*} \tag{3.50}$$

and ε^*_m and ε^*_p are the complex permittivities of the medium and particle respectively as given by equation (2.17).

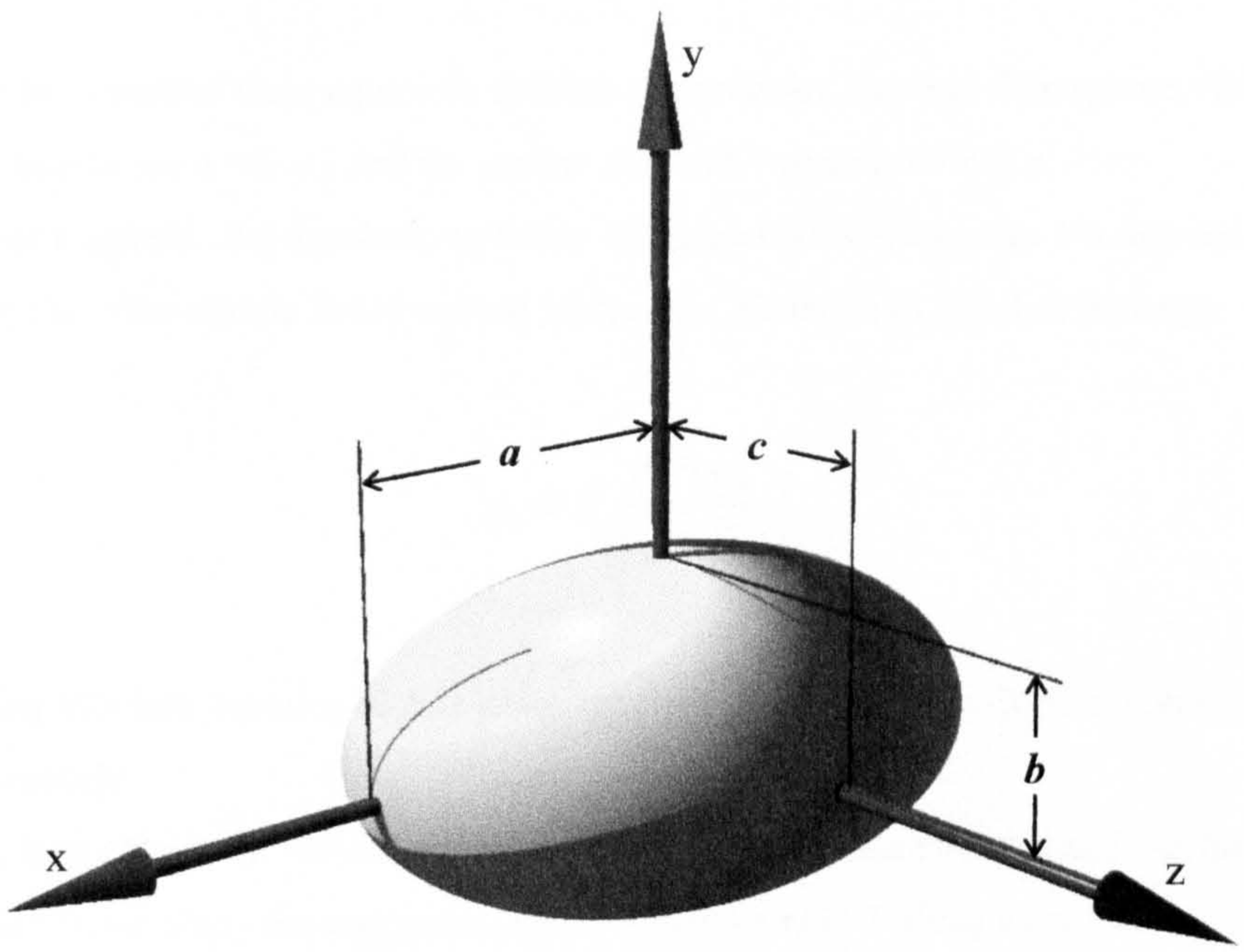

Figure (3.6) An ellipsoidal particle of half axis lengths *a*, *b*, *c* oriented with major axis a along the x-axis.

A_α is referred to as the depolarising factor along the axis α and is given by:

$$A_\alpha = \frac{1}{2}abc\int_0^\infty \frac{ds}{(s + l_\alpha^2)R} \tag{3.51}$$

where

$$R = \sqrt{(s + a^2) + (s + b^2) + (s + c^2)}$$

s is an arbitrary distance and l_α is the half length of the ellipsoid along the axis α. With some manipulation, equation (3.50) can be shown to have characteristic relaxation times associated with it, given by:

$$\tau_\alpha = \frac{A_\alpha \varepsilon_p + (1 - A_\alpha)\varepsilon_m}{A_\alpha \sigma_p + (1 - A_\alpha)\sigma_m} \tag{3.52}$$

The dipole moment along the axis α can be found from the polarisability by using the relationship outlined in section (3.2.3). The volume of an ellipsoid is ($4/3\pi abc$) and the dipole moment along α is the component of the electric field along α multiplied by the volume times the polarisability:

$$\underline{\mathbf{p}}_{\alpha} = \frac{4}{3}\pi abc\varepsilon_{m}\chi_{\alpha}\underline{\mathbf{E}}_{\alpha} \tag{3.53}$$

There are two cases of these equations that are of particular interest: The sphere, for which the axes half lengths are $a = b = c$ and the prolate ellipsoid, where $a >> b = c$.

For a sphere, the depolarising factor along each axis is equal to 1/3 and the orientation of the particle to the electric field becomes irrelevant. Equation (3.50) then becomes:

$$\chi_{\alpha} = 3\left(\frac{\varepsilon_{p}^{*} - \varepsilon_{m}^{*}}{\varepsilon_{p}^{*} + 2\varepsilon_{m}^{*}}\right) \tag{3.54}$$

Substituting this into equation (3.53) gives equation (3.19) for the effective polarisability of a spherical particle.

A long cylindrical particle can be approximated a prolate ellipsoid and, in this case, the depolarising factor along the major axis a tends to zero and to 1 along axes b and c. Therefore, when the major axis is aligned with the field, equation (3.50) tends to:

$$\chi_{\alpha} = \frac{\varepsilon_{p}^{*} - \varepsilon_{m}^{*}}{\varepsilon_{m}^{*}} \tag{3.55}$$

along the major axis. The situation is complicated by a torque which can align different axes with the field. If the major axis is no longer aligned with the field, equation (3.55) no longer holds. This is discussed further in the analysis section of Chapter Eight.

Appendix (3a) The electrical double layer [19,12]

At the interface between a solid dielectric particle and a liquid dielectric containing free charge carriers, a surface charge density can develop for a number of reasons. This charge creates an electrostatic potential local to the interface which falls off with distance from the particle. The electrostatic potential attracts ions of opposite charge (called counterions) from the solution and repels ions with like charge (co-ions). The resulting change in the distribution of ions near the surface is governed by the spatial distribution of the surface electrostatic potential.

The region of space in the liquid near the interface has a higher density of counterions and a lower density of co-ions than the bulk. This region is referred to as the electrical double layer. The variation in the potential across this region is shown in figure (3.4).

In the Stern layer, the ions are assumed to be bound to or at least tightly associated with the surface. This is what is generally referred to as the bound part of the double layer and the potential falls across the width δ of the Stern layer linearly from the surface value of V^{s} to V^{δ}. In the diffuse part of the double layer, the counterions are not bound to the particle and the potential falls off as 1/r where r is the distance from the surface. The outer limit of the double layer is taken to be at the Debye length which is generally denoted as a reciprocal κ. For a symmetrical electrolyte consisting of two type of ions whose valencies z^{+} and z^{-} are equal to z, the reciprocal Debye length is given by:

$$\kappa = \left(\frac{2z^2 e_o^2 n}{\varepsilon_m kT} \right)^{\frac{1}{2}}$$

where e_o is the charge on the electron, n is the equilibrium volume density of the ions, ε_m is the permittivity of the liquid dielectric, k is the Boltzmann constant and T is the temperature.

Appendix (3b) Equations from section (3.5.2)

The induced dipole moment is given by [12]:

$$\underline{\mathbf{p}} = -\frac{3}{2}\left(\frac{\mathrm{a}_1(1+\mathrm{W})+\mathrm{j}(\mathrm{a}_1\mathrm{W}+\mathrm{a}_2\mathrm{W}^2)}{\mathrm{A}_1(1+\mathrm{W})+\mathrm{j}(\mathrm{A}_1\mathrm{W}+\mathrm{A}_2\mathrm{W}^2)}\right)a^3\underline{\mathbf{E}}$$

where:

$$\mathrm{W} = a\sqrt{\frac{\omega}{2D}}$$

$$\mathrm{a}_1 = \alpha^+(1+\alpha_c^-)-\alpha^-(1+\alpha_c^+)$$

$$\mathrm{a}_2 = \alpha^+(1+\alpha_1^-)-\alpha^-(1+\alpha_1^+)$$

$$\mathrm{A}_1 = (z^- -\alpha^-)(1+\alpha_c^+)+(z^+ +\alpha^+)(1+\alpha_c^-)$$

$$\mathrm{A}_2 = (z^- -\alpha^-)(1+\alpha_1^+)+(z^+ +\alpha^+)(1+\alpha_1^-)$$

z^+ and z^- are the valencies of the ions.

$$\alpha^+ = \frac{1}{\kappa a}\left(\frac{3}{2}\mathrm{m}\mathrm{I}_2^+ - z^+\mathrm{I}_1^+\right)$$

$$\alpha^- = \frac{1}{\kappa a}\left(\frac{3}{2}\mathrm{m}\mathrm{I}_2^- + z^-\mathrm{I}_1^-\right)$$

$$\alpha_c^+ = \frac{1}{\kappa a}\left(\frac{3}{2}\mathrm{m}\mathrm{I}_{2c}^+ - \mathrm{I}_1^+\right)$$

$$\alpha_c^- = \frac{1}{\kappa a}\left(\frac{3}{2}\mathrm{m}\mathrm{I}_{2c}^- - \mathrm{I}_1^-\right)$$

$$\alpha_1^+ = \frac{z^+}{\kappa a}\left(\mathrm{I}_1^+ + \mathrm{I}_3^+\right)$$

$$\alpha_1^- = \frac{z^-}{\kappa a}\left(\mathrm{I}_1^- + \mathrm{I}_3^-\right)$$

For a symmetrical electrolyte, i.e. $z^+ = z^- = z$,

$$\mathrm{I}_1^+ = -2\mathrm{e}^{-\left(\frac{zF\phi_d}{RT}+1\right)}$$

$$I_1^- = -2e^{\left(\frac{zF\phi_d}{RT}-1\right)}$$

$$I_2^+ = \frac{2F\zeta}{RT} - \frac{4}{z}\left(1-e^{-\frac{zF\zeta}{2RT}}\right)$$

$$I_2^- = \frac{2F\zeta}{RT} + \frac{4}{z}\left(1-e^{\frac{zF\zeta}{2RT}}\right)$$

$$I_{2c}^+ = \frac{2F\zeta}{zRT} - \frac{4}{z^2}\left(1-e^{-\frac{zF\zeta}{2RT}}\right) - 16\ln\left[\cosh\left(\frac{zF\zeta}{4RT}\right)\right]$$

$$I_{2c}^- = \frac{2F\zeta}{zRT} - \frac{4}{z^2}\left(1-e^{\frac{zF\zeta}{2RT}}\right) - 16\ln\left[\cosh\left(\frac{zF\zeta}{4RT}\right)\right]$$

$$I_3^+ = -\frac{3\cosh\left(\frac{zF\phi_d}{2RT}\right) - e^{-\left(\frac{zF\phi_d}{RT}\right)} - 2}{\cosh\left(\frac{zF\phi_d}{2RT}\right)}$$

$$I_3^- = -\frac{3\cosh\left(\frac{zF\phi_d}{2RT}\right) - e^{\left(\frac{zF\phi_d}{RT}\right)} - 2}{\cosh\left(\frac{zF\phi_d}{2RT}\right)}$$

$$m = \frac{2\varepsilon_m}{3\eta D}\left(\frac{RT}{F}\right)^2$$

References

1. P.Lorrain, D.R.Corson and F.Lorrain (1988) *Electromagnetic Fields and Waves 3rd Ed*
   WH Freeman and Company, New York
2. A.R.Von Hippel (1954) *Dielectrics and Waves*
   Wiley, New York
3. T.B.Jones (1995) *Electromechanics of Particles*
   Cambridge University Press, Cambridge
4. J.B.Miles and H.P.Robertson (1932)
   Physical Review **40** 583-591
5. H.Fricke and H.J.Curtis (1937)
   Journal of Physical Chemistry **41** 729-745
6. H.P.Schwan, G.Schwarz, J.Macjuk and H.Pauly (1962)
   Journal of Physical Chemistry **66** 2626-2635
7. H.P.Schwan and J.Macjuk (1959)
   Proceedings 1st National Biophys. Conf. Columbus, Ohio 1957, Yale Uni Press
8. C.T.O'Konski (1960)
   Journal of Physical Chemistry **64** 605-619
9. G.Schwarz (1962)
   Journal of Physical Chemistry **66** 2636-2642
10. J.M.Schurr (1964)
    Journal of Physical Chemistry **68** 2407-2413
11. S.S.Duhkin (1974) *Dielectric phenomena and the double layer in disperse systems and polyelectrolytes*
    John Wiley and Sons, New York
12. J.Lyklema, S.S.Duhkin and V.N.Shilov (1983)
    Journal of Electroanalytical Chemistry **143** 1-21
13. M.M. Springer, A.Korteweg and J.Lyklema (1983)
    Journal of Electroanalytical Chemistry **153** 55-66
14. J.Lyklema, M.M.Springer, V.N.Shilov and S.S.Duhkin (1986)
    Journal of Electroanalytical Chemistry **198** 19-26
15. J.Lyklema (1991) *Fundamentals of Interface and Colloid Science*
    Academic Press, London
16. Marcel Minor (1997) *Thesis: Published and unpublished work*
    Wageningen Agricultural University, The Netherlands

17. Stratton (1941) *Electromagnetic theory*
McGraw Hill, New York
18. T.Kakutani, S.Shibatani and M.Sugai (1993)
Bioelectrochemistry and Bionenergetics **31** 131-145
19. P.C.Hiemenz (1986) *Principles of Colloid and Surface Chemistry*
Marcel Dekker, New York

Chapter Four

Theory: Forces on a particle

4.1 Introduction

The movement of a particle in solution is a complicated system to model theoretically. There are many forces which are intrinsic to the system, such as Brownian motion and diffusion, as well as externally imposed forces, such as gravity and the dielectrophoretic force. The dielectrophoretic force arises from the interaction of a non-uniform field with the effective dipole of the particle (Chapter Three). There is also often fluid motion, arising from electrothermal effects, which exerts a force on the particle through viscous drag.

This chapter outlines the forces other than the EHD and electrothermal, and the numerical methods which can be used to calculate a particle trajectory under these conditions.

4.2 Forces on particles in solution

The forces described in this section are those which occur in the solution in the absence of an applied electric field. Some of these forces, such as gravity and buoyancy are governed by the densities of the liquid and particle and are related to the physical constants of the system. The other force of note is the randomising effect of Brownian motion on single particles. In considering the movement of a particle in solution, the effects of each of these forces must summed.

4.2.1 Gravity and buoyancy [1]

Consider a particle of volume υ and mass density ρ_p suspended in a fluid of mass density ρ_m. The particle experiences a force $\underline{\mathbf{F}}_g$ due to gravity and a buoyancy force $\underline{\mathbf{F}}_b$ which acts in the opposite direction. The vector sum of $\underline{\mathbf{F}}_g$ and $\underline{\mathbf{F}}_b$ gives the net force on the particle:

$$\underline{\mathbf{F}}_{tot} = \underline{\mathbf{F}}_g - \underline{\mathbf{F}}_b = \upsilon(\rho_p - \rho_m)\underline{\mathbf{g}} \tag{4.1}$$

where $\underline{\mathbf{g}}$ is the acceleration due to gravity. This force acts with $\underline{\mathbf{g}}$ if $\rho_p > \rho_m$ and against $\underline{\mathbf{g}}$ if $\rho_p < \rho_m$.

4.2.2 Viscous drag [1,2]

A particle moving in solution experiences a force acting in opposition to its direction of travel due to the viscous nature of the fluid. This is called the drag force and in the steady state, is proportional to the velocity $\underline{\mathbf{v}}$ of the particle and a constant referred to as the friction factor *f*.

$$\underline{\mathbf{F}}_v = f\,\underline{\mathbf{v}} \tag{4.2}$$

f depends on the viscosity η of the fluid and the shape of the particle. For a spherical particle, this factor is given by Stoke's Law, derived in 1850:

$$f = 6\pi\eta a \tag{4.3}$$

where a is the radius of the particle. An ellipsoidal particle with axes half lengths a, b, and c, is referred to as *prolate* when $a > b = c$. The friction factor can be represented as a ratio with respect to the friction factor of a sphere of the same volume [1]:

$$\frac{f_{ell}}{f_o} = \frac{(1-e^2)^{1/2}}{e^{2/3}\ln\left(\frac{1+(1-e^2)^{1/2}}{e}\right)} \tag{4.4}$$

where f_{ell} is the friction factor of the ellipsoid, f_o is the friction factor of a sphere and e is the ratio b/a.

4.2.3 Sedimentation in a fluid [1]

The combined effects of gravity and viscous drag describe the rate at which particles settle or sediment out of a solution. If $\rho_p > \rho_m$, the particles quickly reach the steady state and sediment with a velocity $\underline{\mathbf{v}}$. This velocity can easily be calculated for the case of a sphere in the steady state since the gravitational and drag forces are balanced:

$$\frac{4}{3}\pi a^3(\rho_p - \rho_m)\underline{\mathbf{g}} = 6\pi\eta a\underline{\mathbf{v}} \tag{4.5}$$

At any point, these forces act along the same unit vector. As a consequence, the vector nature can be neglected and equation (4.5) can be re-written in terms of a sedimentation velocity:

$$\mathrm{v} = \frac{2}{9}a^2(\rho_p - \rho_m)\frac{\mathrm{g}}{\eta} \tag{4.6}$$

Alternatively, by re-writing in terms of a, and using equation (4.3), the friction factor for this situation can be found to be:

$$f = 6\pi\eta\left(\frac{9\eta v}{2(\rho_p - \rho_m)g}\right)^{\frac{1}{2}} \tag{4.7}$$

4.2.4 Brownian motion [3,4]

Particles in solution experience a force due to thermal energy which causes them to move in random manner. The physical origin of this force is due to collisions between the vibrating molecules of the solution and the much larger particle. This random motion was first observed by Robert Brown in 1827, who studied the movement of pollen in liquid, and is referred to as Brownian motion. The theory describing this effect was published by Einstein in 1905 and gives the distribution of the probability of finding a single particle at any point after a given time. If at time t = 0, the position of the particle is known, the probability distribution after a time dt is a Gaussian distribution with zero first moment (mean) and mean (time averaged) squared displacement in three dimensions given by:

$$\langle \underline{x}^2 \rangle = 6\frac{kT}{f}t \tag{4.8}$$

The second moment about the mean or standard deviation σ_x, with a zero first moment, is given by the square root of equation (4.8). The force which gives rise to Brownian motion can also be represented by a Gaussian distribution $\underline{F}_{rand}(t)$ with zero mean. Combining this with the viscous drag force $\underline{F}_v$ (equation 4.2) gives the equation of motion, allowing for viscous and random thermal effects, of a single particle under the influence of an arbitrary external force $\underline{F}_{ext}$:

$$m\frac{d\underline{v}}{dt} = \underline{F}_{ext} - f\underline{v} + \underline{F}_{rand}(t) \tag{4.9}$$

This is the Langevin equation and the solution gives the probability distribution of the particle velocity. If $\underline{F}_{ext}$ is zero, then the velocity also has a Gaussian distribution with zero mean. The important information to draw from this is that the time averages: $\langle \underline{x} \rangle, \langle \underline{v} \rangle$ and $\langle \underline{F}_{rand} \rangle$ all equal zero and that over long time intervals, Brownian motion produces no net displacement of a particle from its origin.

4.2.5 Diffusion [1,3]

If there is more than one particle, the interaction between the particles must be considered. For a system composed of a large number of particles, the thermodynamics requires the system to increase its entropy until the energy density is uniform. The system is therefore in a stable equilibrium when the particles are distributed in a random but uniform manner. As a consequence, if a non-uniform distribution is created by the application of an external force, the particles will also experience an opposing force tending to restore uniformity.

Considering a simple one dimensional case, the flux of particles across a small area element is related to the concentration gradient at that point by Fick's first law:

$$J = -D\frac{\partial c}{\partial x} \tag{4.10}$$

where c is the particle concentration and D is defined to be the diffusion coefficient. The corresponding force is given by:

$$F_{diff} = \frac{kT}{c}\frac{\partial c}{\partial x} \tag{4.11}$$

where T is the temperature and k is the Boltzmann constant. For a particle, the steady state velocity can be found using equation (4.2) and equation (4.11):

$$v = \frac{kT}{fc}\frac{\partial c}{\partial x} \tag{4.12}$$

As a consequence, the diffusion coefficient for the particle is:

$$D = \frac{kT}{f} \tag{4.13}$$

which can be substituted into equation (4.8) to give $\left\langle |\underline{x}|^2 \right\rangle = 6Dt$.

An example of naturally induced diffusion gradients is the balance of sedimentation and diffusion for particles in solution. For a solution of particles (ignoring electrostatic particle-particle interactions), the only external force in the system is the gravitational force, which acts

downwards, pulling particles from solution. The resulting increase in concentration of particles at the bottom of the vessel creates a diffusion force acting upwards [1]. This reaches a steady state with particles either suspended in the bulk in a distribution related to the forces on the particles, or else complete sedimentation occurs. Another example is an ion of charge q in a uniform electric field $\underline{\mathbf{E}}$. The Coulomb force on the particle $q\underline{\mathbf{E}}$ gives rise to a steady state velocity (equation 4.2):

$$\underline{v} = \frac{q\underline{E}}{f} \tag{4.14}$$

The mobility μ is defined to be the velocity per unit field which in this simple case is:

$$\mu = \frac{v}{E} \tag{4.15}$$

Substituting equation (4.13) and (4.14) into (4.12), gives the Einstein relation:

$$D = \frac{kT}{q}\mu \tag{4.16}$$

which relates the diffusion coefficient to movement in an electric field.

4.3 Force on a polarisable particle in an electric field: Dielectrophoresis [5-11]

In an electric field, the interface between the particle and the medium polarises according to Maxwell-Wagner interfacial polarisation as described in section (2.3.2). As a consequence, the particle has an effective polarisability and the polarisation of the interface creates an effective dipole moment (Chapter Three). The particle then experiences a force due to the interaction of the field and the charges in the dipole. In a uniform field, the net force is zero but in a non-uniform field, there is a force imbalance and as a result the particle moves. This section outlines a theoretical description of the force on a dipole in a non-uniform electric field.

The simplest way to assign a force to a particle in a field is to consider the force exerted on a dipole by an electric field. The dipole, shown in Figure (4.1) (where the two equal and opposite charges +q and -q are separated by the vector $\underline{\mathbf{d}}$), experiences a net force due to the non-uniform electric field $\underline{\mathbf{E}}$. The force can be represented as a sum of the forces on the two charges:

$$\underline{\mathbf{F}} = q\,\underline{\mathbf{E}}(\underline{\mathbf{r}} + \underline{\mathbf{d}}) - q\,\underline{\mathbf{E}}(\underline{\mathbf{r}}) \tag{4.17}$$

where $\underline{\mathbf{r}}$ can be taken to be the position vector of -q without loss of generalisation. This equation can be simplified if $|\underline{\mathbf{d}}|$ is much smaller than $|\underline{\mathbf{r}}|$ by expanding the electric field using a Taylor Series expansion about $\underline{\mathbf{r}}$, to give:

$$\underline{\mathbf{E}}(\underline{\mathbf{r}} + \underline{\mathbf{d}}) = \underline{\mathbf{E}}(\underline{\mathbf{r}}) + \underline{\mathbf{d}}.\nabla\underline{\mathbf{E}}(\underline{\mathbf{r}}) + \ldots \tag{4.18}$$

where all terms of order d^2 or higher have been neglected.

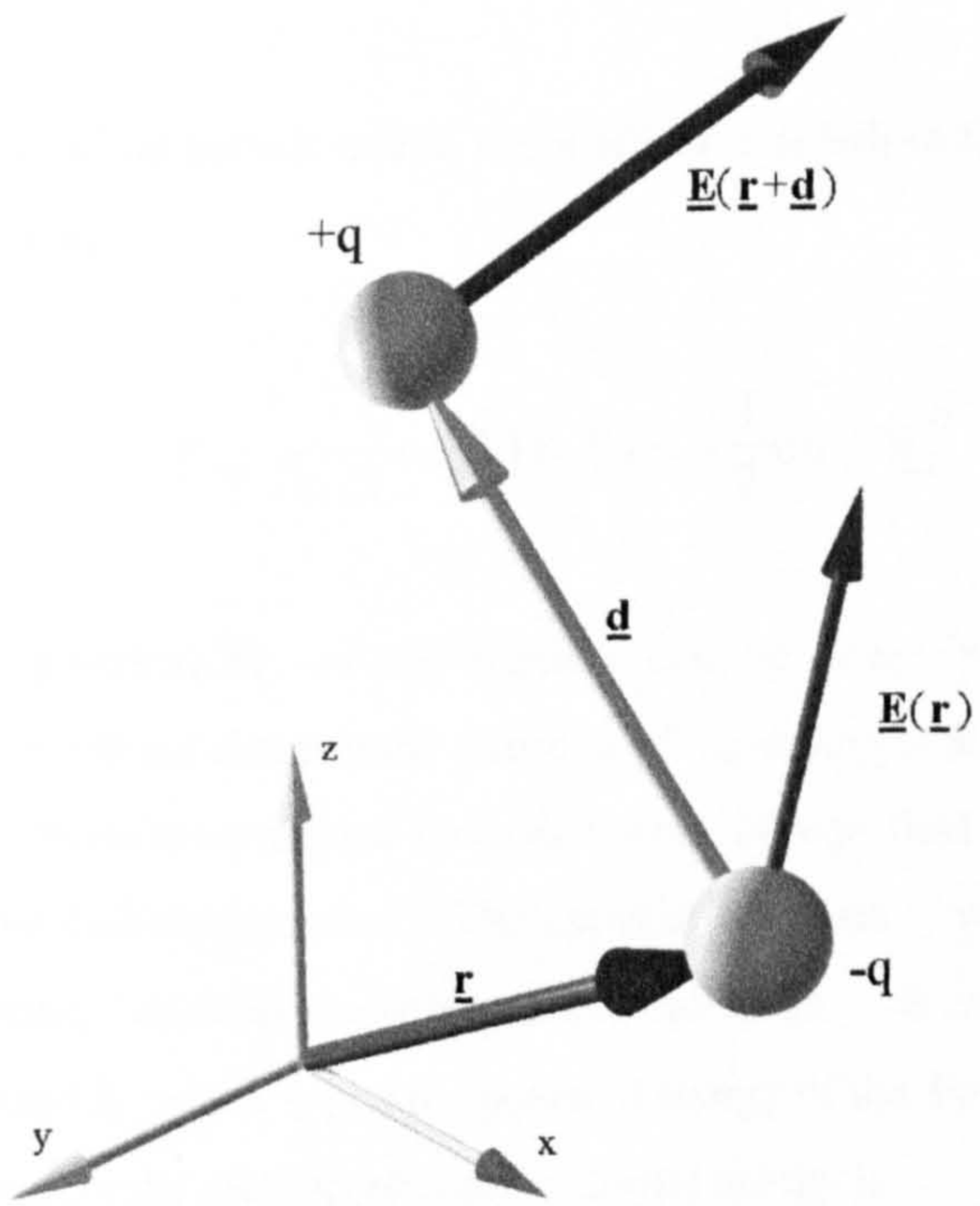

Figure (4.1) A schematic representation of a dipole consisting of two charges, +q and -q, separated by the distance vector $\underline{\mathbf{d}}$. In a non-uniform field, the force on each charge due to the electric field is different, giving rise to a net force acting on the dipole as a whole.

If the dipole moment $\underline{\mathbf{p}} = q\underline{\mathbf{d}}$ remains finite in the limit $|\underline{\mathbf{d}}| \to 0$, then substituting equation (4.18) into (4.17) gives the first order force on an infinitesimal dipole:

$$\underline{\mathbf{F}} = \underline{\mathbf{p}}.\nabla\underline{\mathbf{E}} \tag{4.19}$$

Only in a non-uniform field does this force have a non-zero net value. The resulting movement of particles is referred to as Dielectrophoresis (DEP) [5] and the force referred to as the dielectrophoretic force. This equation is restricted to cases where the gradient of the field across the particle can be assumed to be constant. In cases where the field is very non-uniform across a distance comparable in size to the particle, the higher order terms can no longer be ignored. For the purposes of this work, this equation is assumed to be valid.

The dielectrophoretic force on a particle is found by substituting the effective dipole moment (Chapter three) into equation (4.19). This approximation is valid as long as the electric field is linear across the diameter of the particle. Performing the substitution gives:

$$\underline{\mathbf{F}}_{dep} = \upsilon u_p \underline{\mathbf{E}}.\nabla\underline{\mathbf{E}} \tag{4.20}$$

where υ is the volume of the particle and u_p is the effective polarisability. This can be re-written using a vector identity as:

$$\underline{\mathbf{F}}_{dep} = -\frac{1}{2}\upsilon u_p \nabla(\underline{\mathbf{E}}.\underline{\mathbf{E}}) = -\frac{1}{2}\upsilon u_p \nabla|\underline{\mathbf{E}}|^2 \tag{4.21}$$

Since the effective polarisability of the particle can be either positive or negative, the dielectrophoretic force can act either in the direction of increasing field strength or in the opposite direction. Where particles are attracted towards regions of high field strength, the movement is referred to as positive dielectrophoresis. The opposite situation, where particles are repelled from high field regions, is called negative dielectrophoresis. It is also useful to derive the dielectrophoretic potential, which is just the potential energy of the dipole in the electric field. In this case, the equation for the dielectrophoretic potential energy is:

$$U_{dep} = \frac{1}{2}\upsilon u_p |\underline{\mathbf{E}}|^2 \tag{4.22}$$

4.4 Simulation of forces

The velocity of a particle is described by an equation of motion. Solving this equation analytically is often difficult and numerical methods have to be used instead. This section discusses the equation of motion for a particle in a viscous medium and describes a method for solving it.

4.4.1 Stochastic Integration of the Langevin equation

Analytical solutions for the Langevin equation are difficult to obtain in most situations. Some phenomena like the dielectrophoretic force depend on position but do not have an analytical representation. Instead, a simple numerical technique can be applied to solve the Langevin equation as a set of increments. The numerical equations in this section were derived for this thesis from basic equations in references 3 and 4.

Consider the movement of the particle to consist of a series of steps with time increment Δt and use the simple Euler system to integrate. The particle starts each step at time t and position $\underline{x}(t)$ moving with velocity $\underline{v}(t)$. Over the step Δt, the particle experiences a number of forces as outlined by the Langevin equation, each of which is treated in independently. After Δt, the particle is in a new position $\underline{x}(t+\Delta t)$ moving with velocity $\underline{v}(t+\Delta t)$.

The drag force is represented as the friction factor times the average of the old and the new velocity. The external forces in general are not dependent on the velocity of the particle and are either constant, such as sedimentation, or dependent on the position of the particle, such as the dielectrophoretic force (which may or may not have an analytical expression). Constant forces can simply be added but where there is a position dependent force, the position of the particle must be calculated prior to the next calculation of the velocity. This repeated calculation of position also gives the path of the particle: a set of vectors representing the position of the particle over time. For the purpose of numerical simulation, the random force can be represented by a random number generated by the computer in a Gaussian set of unity standard deviation multiplied by a constant. The constant is derived from the thermal energy of the system to be $f\sqrt{3kT/m}$ [4], where k is Boltzman's constant, T is the temperature and m is the mass of the particle.

The new velocity is found from the Langevin equation re-written in the form:

$$m\frac{\underline{v}(t+\Delta t)-\underline{v}(t)}{\Delta t} = \underline{F}_{ext} - f\left[\frac{\underline{v}(t+\Delta t)+\underline{v}(t)}{2}\right] + \underline{F}_{rand} \qquad (4.23)$$

which can be re-written in terms of the new velocity as:

$$\underline{v}(t+\Delta t)\left(1+\frac{f\Delta t}{2m}\right) = \underline{v}(t)\left(1-\frac{f\Delta t}{2m}\right) + \left[\underline{F}_{ext}+\underline{F}_{rand}\right]\frac{\Delta t}{m} \qquad (4.24)$$

where $\underline{\mathbf{F}}_{ext}$ are external forces like gravity and dielectrophoresis. After time Δt, due to velocity $\underline{\mathbf{v}}(t)$, the particle reaches the new position $\underline{\mathbf{x}}(t+\Delta t)$ given by:

$$\underline{\mathbf{x}}(t+\Delta t) = \underline{\mathbf{x}}(t) + \underline{\mathbf{v}}(t)\Delta t \tag{4.25}$$

and is now moving with velocity $\underline{\mathbf{v}}(t+\Delta t)$. This is then taken as the starting position $\underline{\mathbf{x}}(t)$ for the next step and the complete set of position vectors $\underline{\mathbf{x}}(t)$ gives the path of the particle over time.

4.4.2 Electric field simulation: The finite element method [12]

Gravity, buoyancy and sedimentation can be added to the Langevin equation simply by inserting the force terms. The position-independent analytical form for these forces can be considered accurate for the purposes of simulating particle movement. However, the dielectrophoretic force, which is the most important force for deterministic motion, is dependent on the electric field which varies noticeably with position. In most cases, there is no analytical expression for the position dependence of the electric field and a numerical method must be used.

The finite element method was developed in 1956 in the area of structural mechanics and quickly became widely used as a means of solving non-linear systems. It has also become important in the simulation of electromagnetic devices, with significant work being carried out on the mathematics of the method. In this project, a commercial finite element solver called Maxwell (Ansoft, Pittsburg) was used and the background to the method is included in summary only.

For the purpose of particle movement, a static field approximation can made. The equation that must be solved in this case is Poisson's equation (equation (2.5)) in its most general form:

$$\nabla.\varepsilon\nabla V = -\rho^{v} \tag{4.26}$$

where V is the potential in the interior of a domain which denotes the solution space and ρ^{v} is the free volume charge density. Over the surface of the domain, two boundary conditions hold, either, (a.) the Dirichlet boundary condition, where the electrical potential is a constant and the electric field is perpendicular to the surface:

$$V = V_o \tag{4.27}$$

or (b.), the Neumann boundary condition, where the electric field is tangential to the surface:

$$\frac{\partial V}{\partial \mathrm{n}} = \mathrm{k} \tag{4.28}$$

V_o and k are constants. The differentiation with respect to n indicates differentiation along the normal to the surface. Another allowed boundary condition is a combination of (a.) and (b.):

$$\mathrm{k}_1 V + \mathrm{k}_2 \frac{\partial V}{\partial \mathrm{n}} = \mathrm{k}_3 \tag{4.29}$$

where the k_i are again constants. In addition to these constraints, the solution must take into account any variation in ε with position, such as a boundary between one dielectric and another.

The problem space is broken up into elements and the electric potential in these elements is approximated to a simple linear function. Each element has a number of points or 'nodes' in it, such as corners or mid points of edges. These nodes are used to construct a finite matrix for the problem space which is then solved to give the potential at each node. Increasing the number of elements, makes the problem computationally more intense, but improves the accuracy of the final solution.

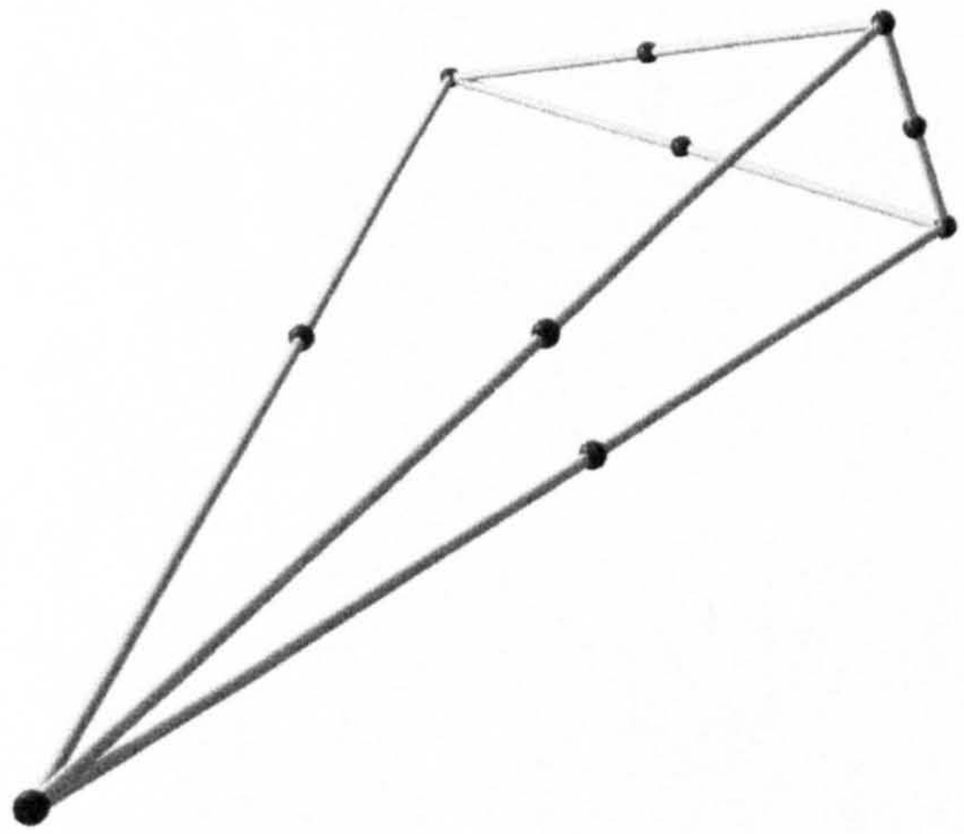

Figure (4.2) A tetrahedral element typical of those used by Maxwell to divide the problem space into a mesh. The ten known defining points allow any second order function to be calculated anywhere in the element.

In Maxwell, a 3-D problem space is divided into a series of tetrahedra (Figure 4.2). The four corner points and the six points in the middle of the edges gives ten nodes for each

element. Therefore, the equation for the potential at any point inside the tetrahedra can be approximated to the general second order function:

$$V(x,y,z) = a_1 + a_2x + a_3y + a_4z + a_5xy + a_6yz + a_7xz + a_8x^2 + a_9y^2 + a_{10}z^2$$

and the individual constants a_i can be found from the known potential at each node.

The usual procedure in solving the problem is to divide the problem space into a coarse mesh of elements and solve. The resulting solution is not accurate and error analysis is performed on the elements. Maxwell then refines the mesh where the error is greatest, adding elements only where improvement in accuracy is required. The problem is then solved for the new mesh and the error analysis performed again. This procedure is referred to as adaptive refinement and continues until the error over the whole problem space reduces to a value pre-set by the user.

Once a suitable solution for the electric potential is obtained, the electric field can be calculated across each element using $\underline{\mathbf{E}} = -\nabla V$.

References

1. P.C.Hiemenz (1986) *Principles of Colloid and Surface Chemistry*
   Marcel Dekker, New York
2. P.D.Grossman and D.S.Soane (1990)
   Analytical Chemistry **62** 1592-1596
3. C.Kittel (1965) *Elementary Statistical Physics*
   Wiley, New York
4. J.Lyklema (1991) *Fundamentals of Interface and Colloid Science*
   Academic Press Ltd, London
5. H.A.Pohl (1978) *Dielectrophoresis*
   Cambridge University Press, Cambridge
6. T.B.Jones (1979)
   Journal of Electrostatics **6** 69-82
7. V.Denner and H.A.Pohl (1982)
   Journal of Electrostatics **13** 167-174
8. X-B.Wang, R.Pethig and T.B.Jones (1992)
   Journal of Physics D: Applied Physics **25** 905-912
9. T.B.Jones (1995)
   Institute of Physics, Conference Series **143** 135-144
10. T.B.Jones and M.Washizu (1996)
    Journal of Electrostatics **37** 121-134
11. T.B.Jones (1995)
    Cambridge University Press, Cambridge
12. O.C.Zienkiewicz and R.L.Taylor (1989) *The Finite Element Method 4th Ed*
    McGraw Hill Book Company, London

Chapter Five

Technological considerations for dielectrophoresis devices

Results and discussion: Device fabrication

5.1 Introduction

Until recently, dielectrophoretic manipulation and separation of particles smaller than one micrometre in diameter had been assumed to be an unattainable goal because of the magnitude of the thermal forces acting on such a particle [1]. As the volume of the particle decreases, the dielectrophoretic force decreases proportionately (equation 4.17) but the magnitude of the movement due to Brownian motion increases. Equation (4.17) also shows that since the size of the force depends on the gradient of the electric field squared, increasing the field strength around the particle provides a means of overcoming the stronger thermal forces.

Using energy balance arguments, field strengths of the order of 10^6-10^7 Vm^{-1} have been quoted in the literature [2] as necessary for providing a large enough dielectrophoretic force to cause deterministic movement of particles of the order of 100nm in diameter. Generating such high field strengths over a wide range of frequencies is not a simple matter. For example, in order to move a cell of the order of 10μm in diameter requires a field strength of 10^4Vm^{-1} which can be provided by two electrodes 1mm apart with a potential difference of 10volts. To generate a field strength high enough to control the movement of a 100nm particle in the same electrodes would require a potential difference of 10^3-10^4volts. As signals of this magnitude are difficult to generate, another method of increasing the field strength must be found.

Advances in micro and nano fabrication techniques allow small electrodes of the order of 1μm in size to be manufactured with relative ease. The two electrodes outlined above manufactured with a gap of 1μm with an applied potential difference of 10volts would generate a field strength of 10^7Vm^{-1}. Therefore, microelectrode structures can provide sufficient field strengths to move sub-micrometre particles without requiring high voltage signal generators.

This chapter outlines the design of electrode structures capable of generating optimum non-uniform electric fields, the fabrication techniques used to manufacture them, together with the resulting structures. The technology used to generate suitable AC signals is also discussed, along with the measured electrical properties of the manufactured devices.

5.2 Dielectrophoresis electrode designs: literature review

There were two main considerations affecting the design of devices for use in dielectrophoretic experiments in the sub-micrometre range:

- To move particles with diameters in this range, field strengths of the order of 10^6 Vm^{-1} are required.

- As the field gradient is important, the geometric shape of the electrodes generating the field is important. Different shapes of electrodes can be designed to move particles in different directions or hold them in place.

Three electrode designs were used in this project, developed from designs found in the literature [3-8]. All the designs involved planar electrodes manufactured in two dimensions on a flat surface. The feature sizes of the electrodes were varied in order to determine if the dielectrophoretic movement of particles was improved by adjusting the size of the electrodes relative to the size of the particle. Arbitrary comparisons between size of particle and necessary size of electrode features have been quoted in the literature but without any detail being provided.

(a.) Hyperbolic "polynomial" electrodes

This design, consisting of four electrodes, is one of a group called "polynomial electrodes" [3-5] based on the idea that "isomotive" electrodes can produce constant forces over significant areas [6]. The general case consists of 2n electrodes, but the simplest useful case is the four electrode system shown in Figure (5.1). This design has been used because of the low field "trap" in the centre of the electrode. The voltage signal is applied to two of the electrodes diametrically opposite each other, with the inverse of the signal applied to the remaining two electrodes. As a result, the edges of the electrodes define high field regions which are potential minima for positive dielectrophoresis. The symmetry of the design means that there is also a deep potential minimum for negative dielectrophoresis in the centre of the four electrodes which can trap and hold particles. The curved part of the electrode is defined by the hyperbolic function [3]:

$$xy = \frac{d^2}{8} \tag{5.1}$$

where d is the separation of the opposing electrodes diagonally across the centre, and the focus of the hyperbola is at the centre of the four electrodes. For practical use, the curve was cut off at an arbitrary distance limited by the capabilities of the manufacturing procedure. Beyond this point the edges of adjacent electrodes were mutually parallel to the limit of the active area. The active area need not be larger than can be observed during a experiment and the electrodes are connected by thin wires to the signal source.

The hyperbolic function is used because the electric field resulting from the electrodes is isometric and has a uniform gradient over most of the central area. This simplifies the measurement and comparison of particle velocities for determining the dielectrophoretic force.

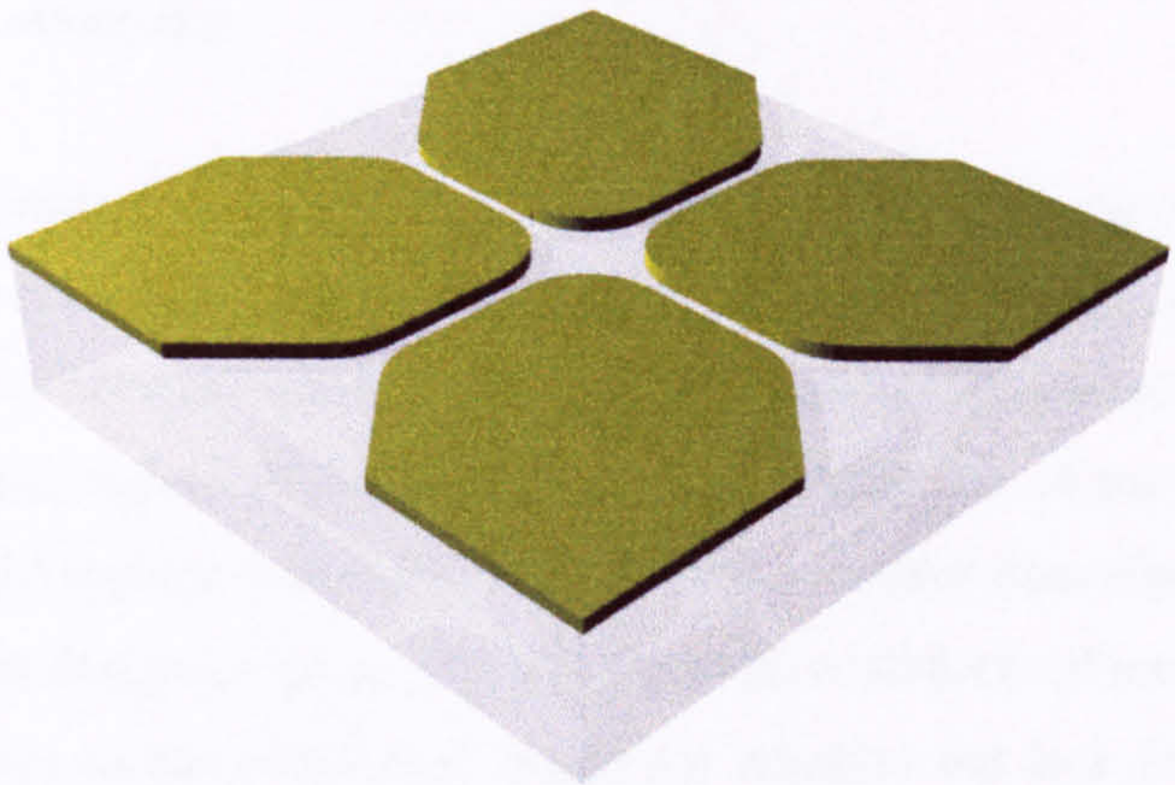

Figure (5.1) Schematic of the centre part of a set of hyperbolic electrodes. The curve in the middle is defined by the hyperbola given in equation (5.1).

(b.) Triangular electrodes

The arrangement shown in Figure (5.2) of triangular features arranged symmetrically along parallel wires is similar to a design used by Washizu for manipulating biopolymers [2] and to a design used for paired alignment of cells [7].

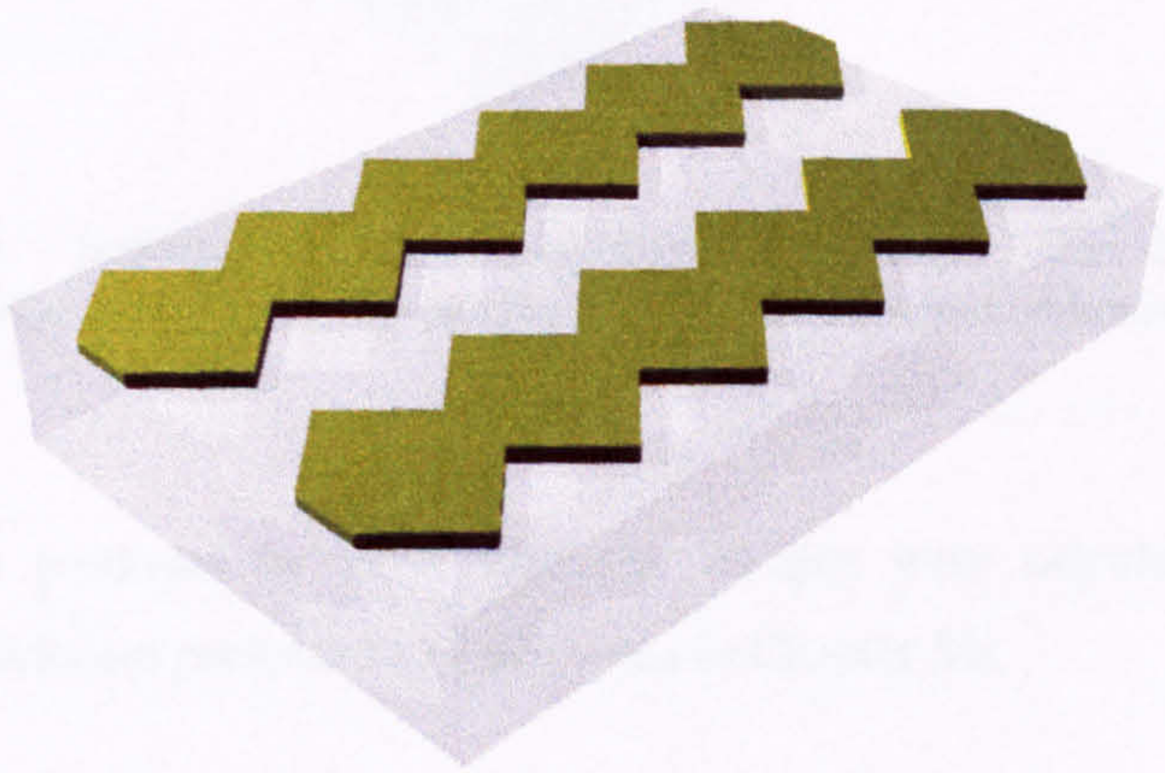

Figure (5.2) Schematic of the triangular electrodes. This design produces high fields between the points and can be repeated over large areas.

This design can be repeated over large areas, with the voltage signal and its inverse being applied to alternate electrodes. The advantage of this design is the high field strengths and the very high field gradients generated around the tips of the features and it is therefore ideal for observing positive dielectrophoresis.

(c.) Castellated electrodes.

The third design, consisting of square features on parallel wires as shown in figure (5.3), has been widely used [4,8] and is referred to as "castellated". Again, the signal and its inverse are applied to alternate electrodes and the design can be repeated over a large area. The resulting field has regions of high field magnitude at the tips of the square features and well-defined low field regions in the 'bays' between the squares (described in more detail in section (5.5.4). This design is not as effective for positive dielectrophoresis as the triangular design nor as effective as the polynomial design for negative but is a good compromise for observing both types of dielectrophoresis at the same time. The castellated design can also be repeated over a large area making it ideal for a large scale separator.

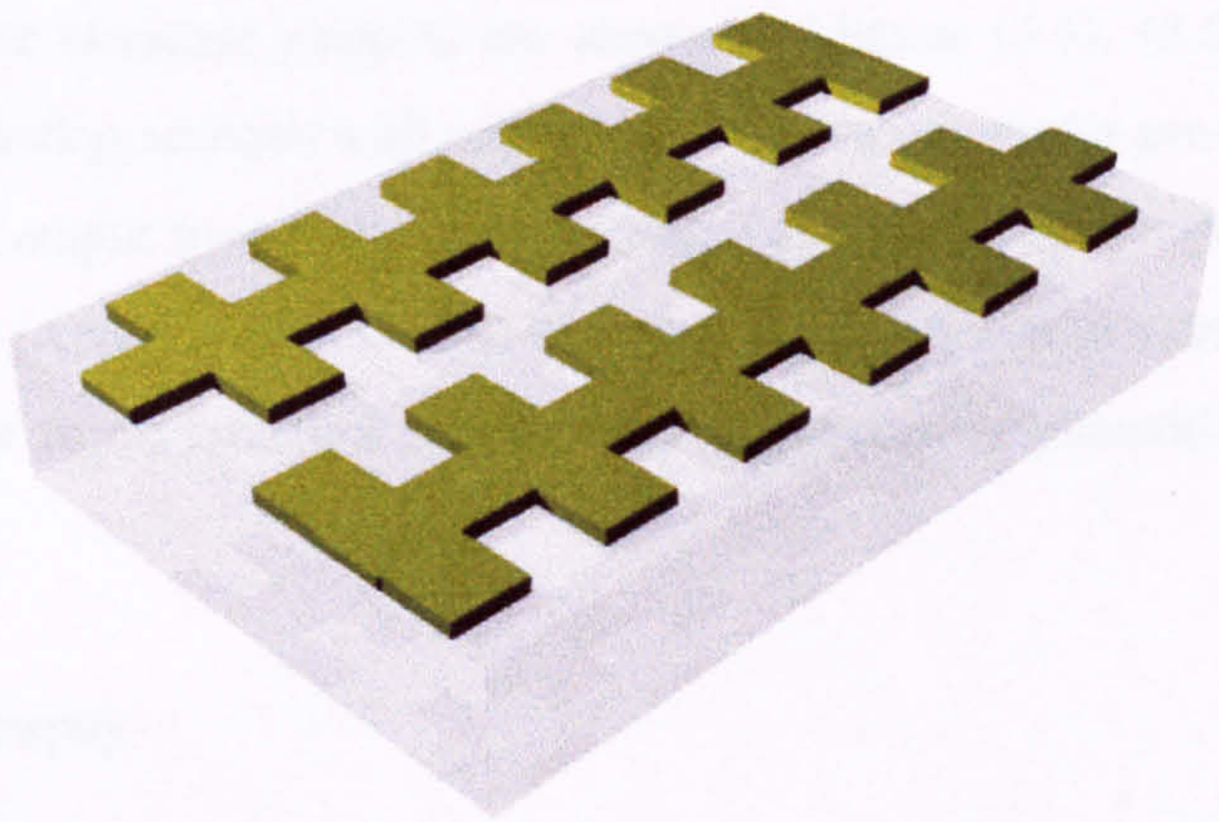

Figure (5.3) Schematic of the castellated electrodes. This design has well defined trapping areas for both positive and negative dielectrophoresis

The electric fields produced by these electrode designs were calculated using numerical methods and the results are presented and discussed in Chapter Six.

5.3 Device fabrication: results and discussion

This section describes the design and fabrication procedures used to manufacture devices for this project. A complete description of each individual procedure is contained in Appendix (5a) and referred to by name in the text. The results of the fabrication tests are presented and discussed with a view towards solving the problems encountered and the limitations of the individual procedures.

5.3.1 Electrode design and signal source considerations.

The electrodes were designed using the computer aided design feature of a microwave simulation program called WAveMaker (WAM). Practical considerations required electrode arrays that were small, along the guidelines discussed in the previous section, easy to manufacture and easy to use. The last consideration was important since the aim of the project was to use these devices in experimental work. As a consequence, it would be an advantage to have robust arrays that could be used many times.

Another consideration was that the signal source output was passed along, on this scale, large wires typically 1mm in diameter. The easiest means of connecting the signal source to the electrodes was to attach a connector to the electrodes by means of soldering or silver paint. In order to achieve this simply and quickly, large connection areas were included in the designs.

The complete electrode patterns are shown in Figures (5.4), (5.5) and (5.7) and are discussed in the following sections with reference to the manufacturing procedures and limits on size. The graphical output from WAM was processed and passed to the control program for the electron beam-writer (Appendix 5a.1). The beam-writer was then used either to manufacture the electrodes directly or to manufacture a mask used in subsequent photolithographic fabrication procedures.

5.3.2 Photolithography

The electrode patterns used for the early experiments were manufactured using photolithography (Appendix 5a.3) with masks fabricated using electron beam lithography (Appendix 5a.2). Two electrode designs were manufactured on glass substrates using this fabrication procedure.

The first (design A) is shown in Figure (5.4) and consisted of a set of three hyperbolic electrodes in the centre and twelve large bonding pads along the edge. The size of the complete design was 35x25mm and was intended to be fabricated onto half a microscope slide. The polynomials were manufactured with centre separations d (equation (5.1)) of 5, 7.5, 10, 20, 50 and 100 micrometres. The gaps between adjacent electrodes was kept to a minimum of 2μm but varied with the centre separation. The minimum separation was chosen to ensure reliable and efficient fabrication.

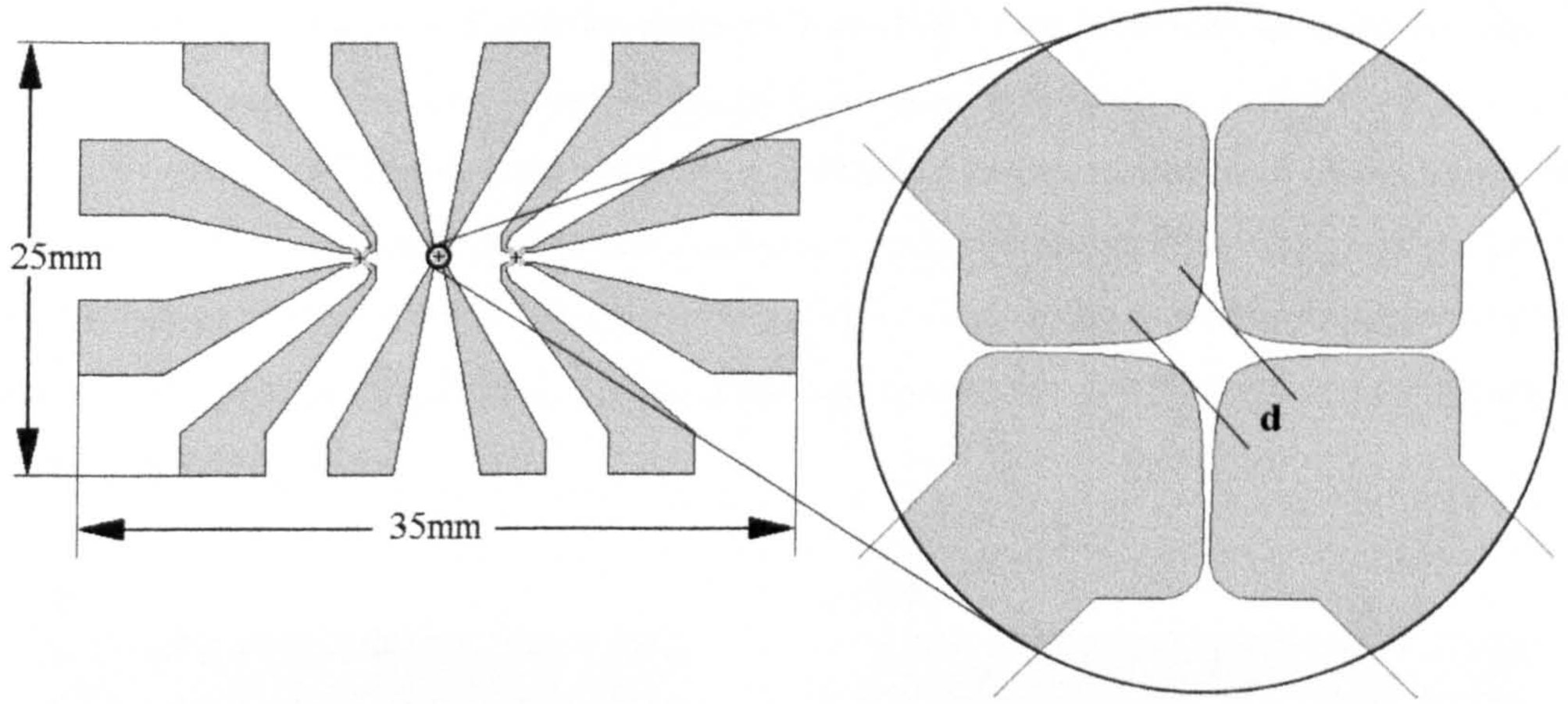

Figure (5.4) Schematic of electrode array design A. The total design size was 25x35mm with hyperbolic centre separations in the range 5 - 100μm.

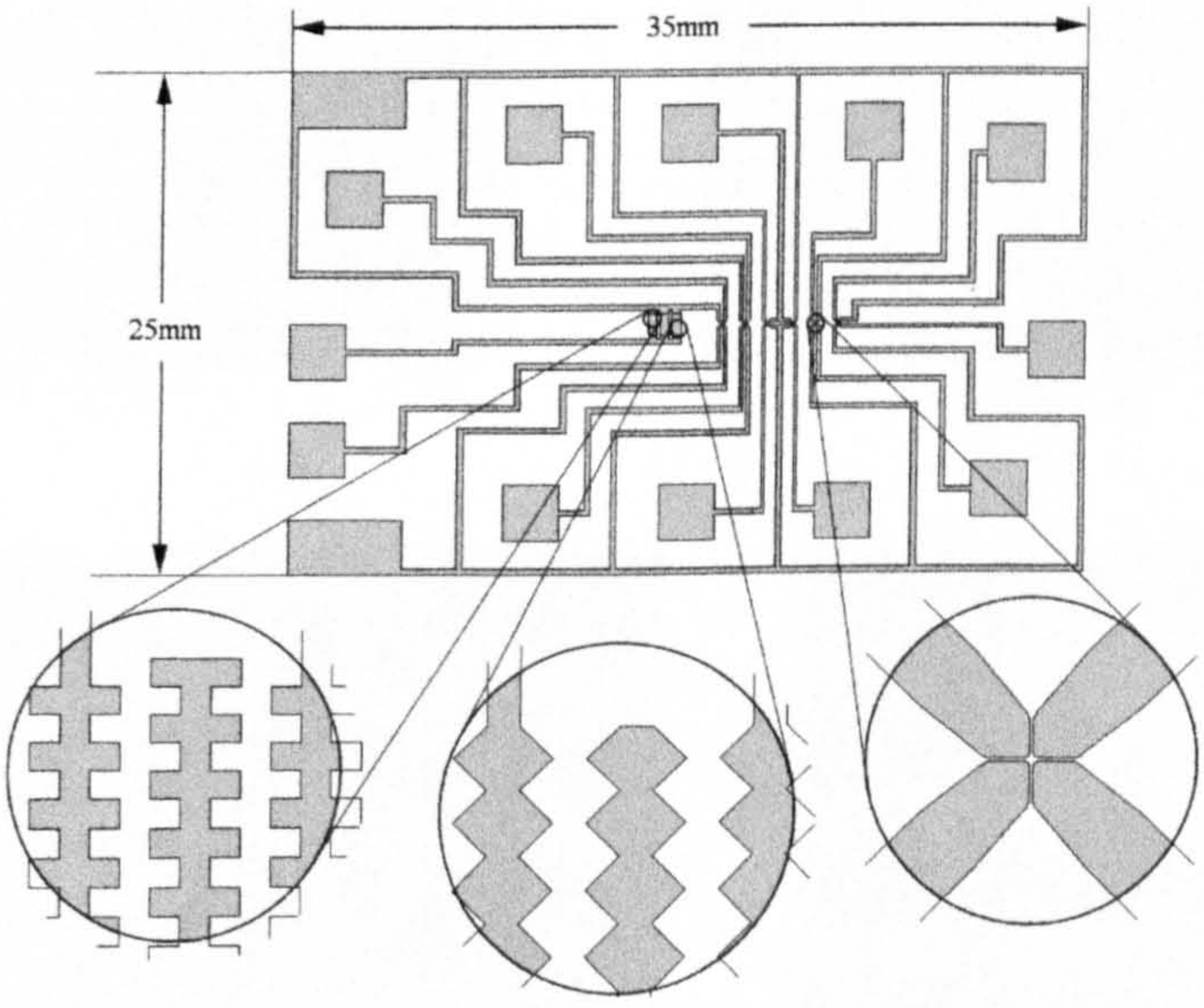

Figure(5.5) Schematic of array design B, with areas of all three types of electrode patterns. The castellated feature sizes were 4 and 5μm and the triangular feature size was 4μm. The centre separation of the six hyperbolic electrodes was 6μm.

The second design (B) is shown schematically in Figure (5.5) and consisted of six hyperbolic electrodes with separations d equal to 6 micrometres. The minimum separation was again chosen to be 2μm. In addition to the hyperbolic electrodes, there were two areas of castellated electrodes with feature sizes of 4 and 5 μm and one of triangular electrodes with feature sizes of 4μm. This design was intended to be able to demonstrate dielectrophoresis over a wide range of experimental conditions.

For fabrication, a S1400-31 resist (1.3μm thick) was used with an exposure time of 10.5 seconds and 60 seconds for development time were established as giving the best results. The evaporated metal layer consisted of 10nm titanium, 10nm palladium and 100nm gold. The gold layer is essential because of its low resistance and its biocompatible nature, but it does not adhere well to a glass surface. Titanium, on the other hand, adheres well to the glass substrate and was used to improve adhesion. The palladium layer acts as a diffusion barrier between the titanium and the gold.

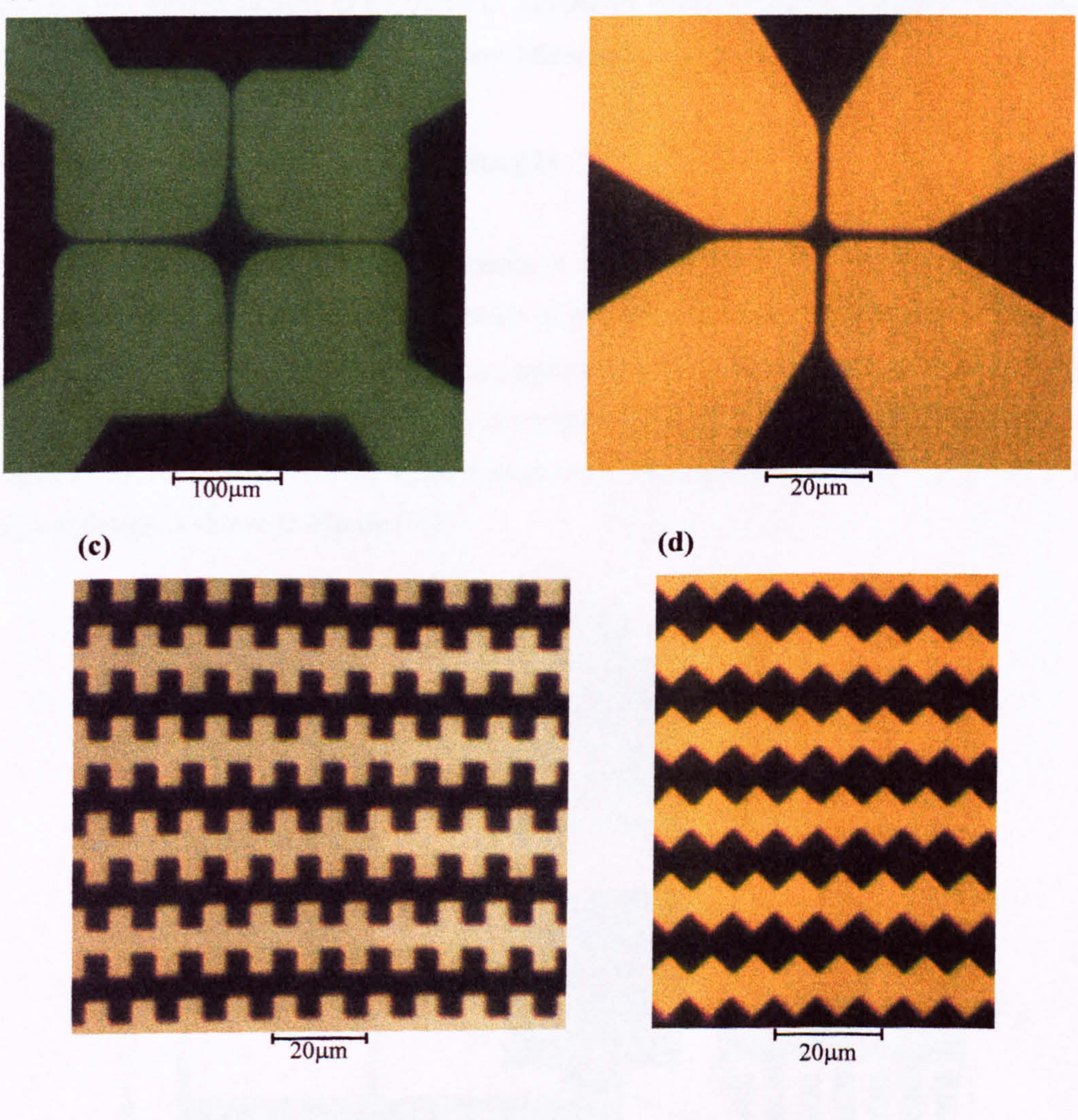

Figure (5.6) Scanned photographs of electrodes manufactured using photo-lithography. Hyperbolic electrodes from design (A) are shown in (a) and the three electrode patterns from design (B) are shown in (b) - (d).

Figure (5.6) shows photographs of electrodes taken with a camera mounted on a microscope (Nikon Microphot). Figures (5.6a) and (5.6b) show polynomial electrodes of

centre separations 50 and 6 μm. Figures (5.6c) and (5.6d) show castellated and triangular electrodes fabricated according to design B with feature sizes of 5 and 4 μm respectively.

Using photolithography, the polynomial electrodes could be fabricated reproducibly. However, the castellated and triangular electrodes proved to be more difficult to manufacture with any degree of reproducibility. The figures show the best set of electrodes manufactured using this method but most of the fabricated electrodes had rounded edges where sharp corners were present on the mask. For optimum manufacture, it was established that the exposure and development times needed to be accurate to less than 0.1 seconds and the contact between the mask and the sample needed to be perfect, neither of which could be managed reproducibly using the available facilities. Electron-beam lithography was therefore used.

5.3.3 Direct-write electron beam lithography

Electron-beam lithography (Appendices 5a.4 and 5a.5) is capable of producing electrodes with feature resolutions of the order of the spot size of the electron beam. The beam spot diameter can be reduced to improve the feature resolution but at the expense of increasing the time taken to write the pattern into the resist. Arrays with a grid of castellated and triangular electrodes with varying feature sizes were manufactured using this process. The complete design is shown in Figure (5.7).

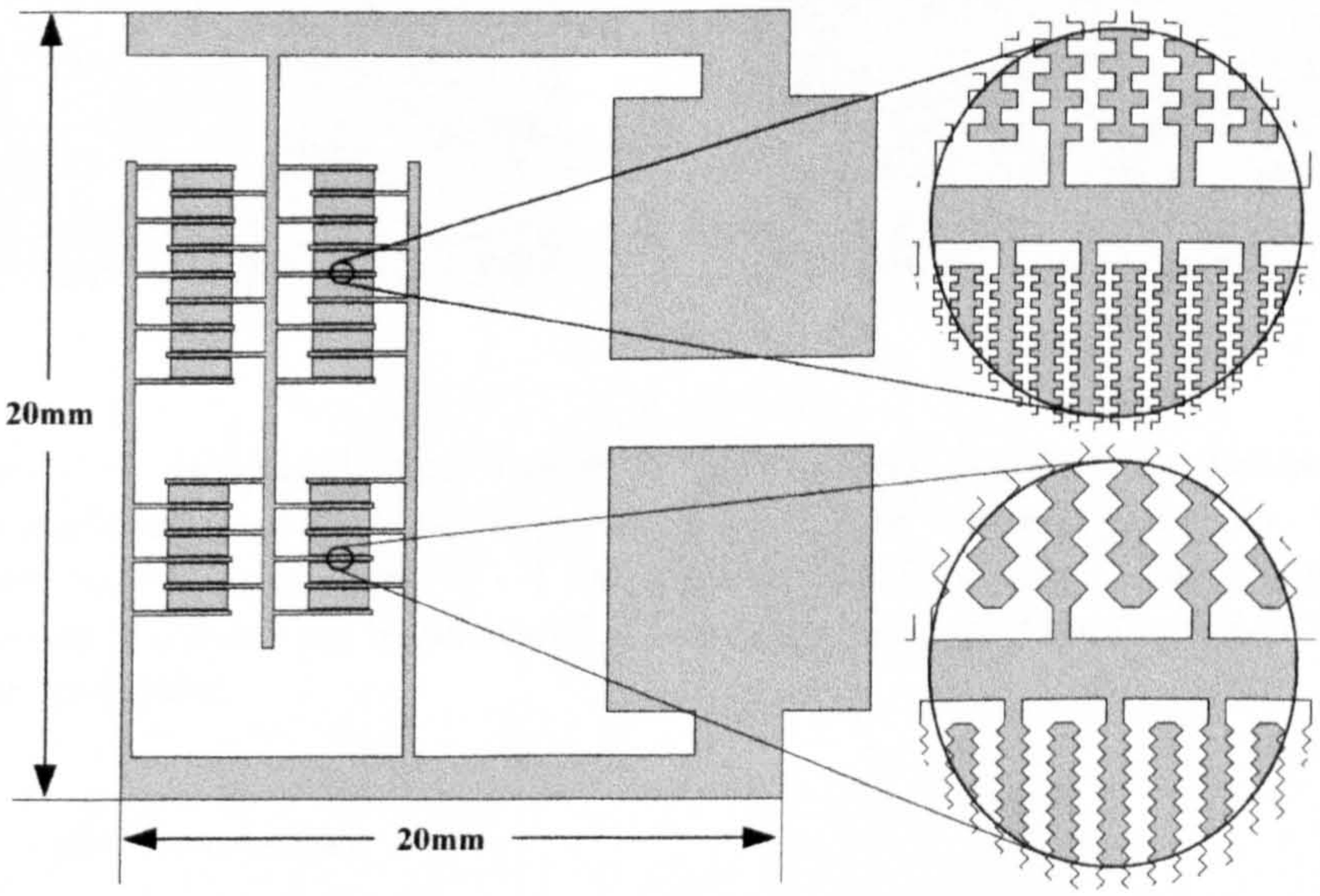

Figure (5.7) Design schematic of the electron-beam design. The upper castellated areas have feature sizes in the range 1-5μm and gap sizes ranging from 1-10μm. The triangular areas have feature in the range 1-4μm and gaps in the range 1-8μm.

Both the two-layer resist layer procedure (Appendix 5a.4) and the mask plate procedure (Appendix 5a.5) were used to manufacture arrays of this design, but the second procedure was found to be more efficient and to have a higher feature reproducibility. Figure (5.8) shows photographs of the electrodes. The castellated electrodes in Figures (5.8a), (5.8b) and (5.8c) have features sizes of 1, 3 and 4 μm and separations of 2, 3 and 5 μm respectively. Figure (5.8d) shows triangular electrodes with a feature size of 4μm and a gap of 2μm.

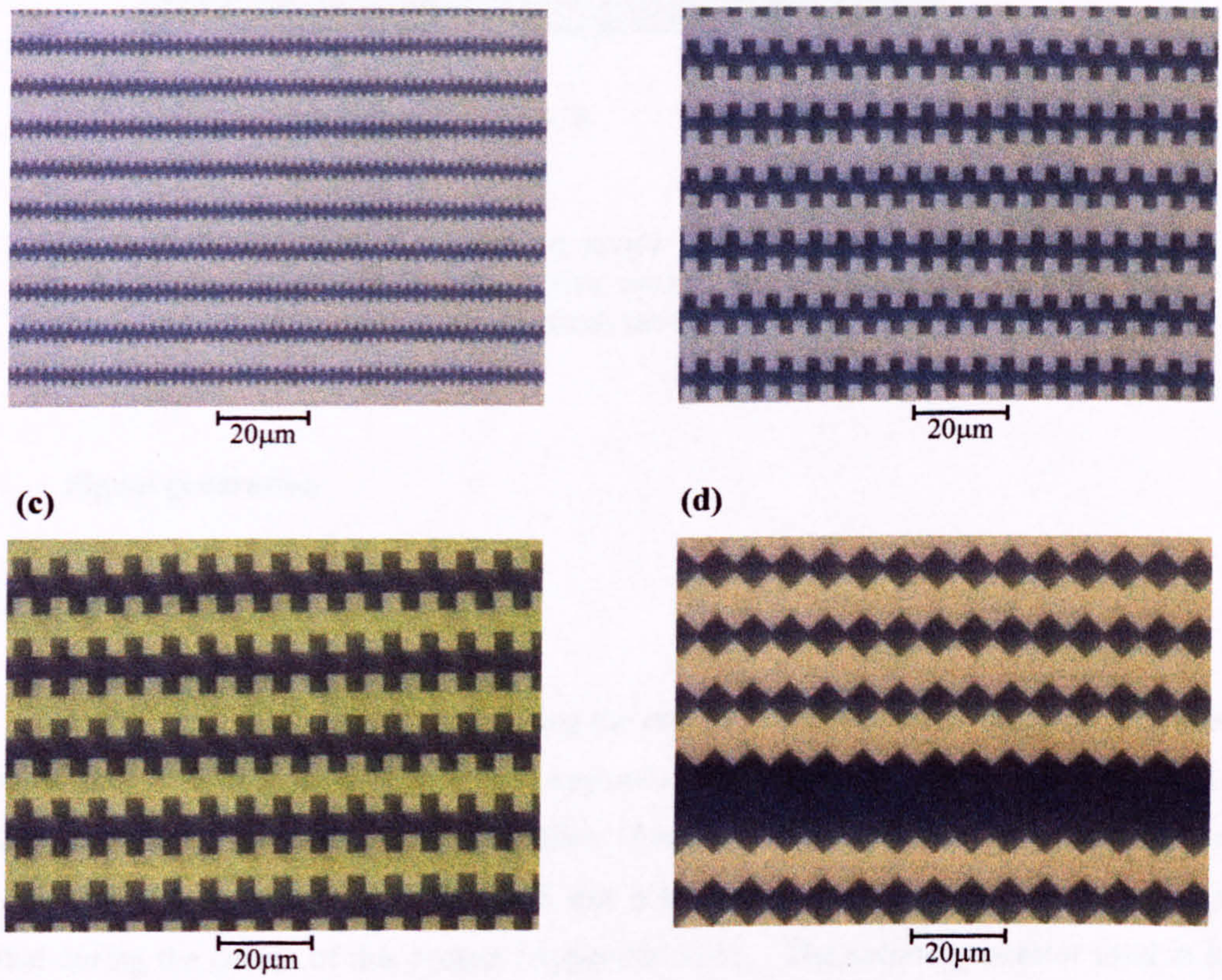

Figure (5.8) Captured video images of electron-beam manufactured electrodes. The castellated sizes are: (a) - 1μm features with 2μm electrode gaps, (b) - 3μm features with 3μm gap and (c) - 4 μm features with 5 μm gap. The triangular electrodes (d) have 4 μm features with a 2 μm gap at the top of the figure and 3 μm gap at the bottom.

5.3.4 Signal/device interface

The electrode arrays were mounted on specially designed printed circuit boards (PCBs). The complete devices, consisting of the array and the PCB, were designed in such a way that the necessary connectors were mounted on the PCB. Pads were arranged on the PCB to match the bonding pads on the electrode array and wires used to connect the two. Solder was used to

attach the wire to the PCB and silver paint to attach the wire to the electrode array. A diagram of a completed device is shown in Figure (5.9).

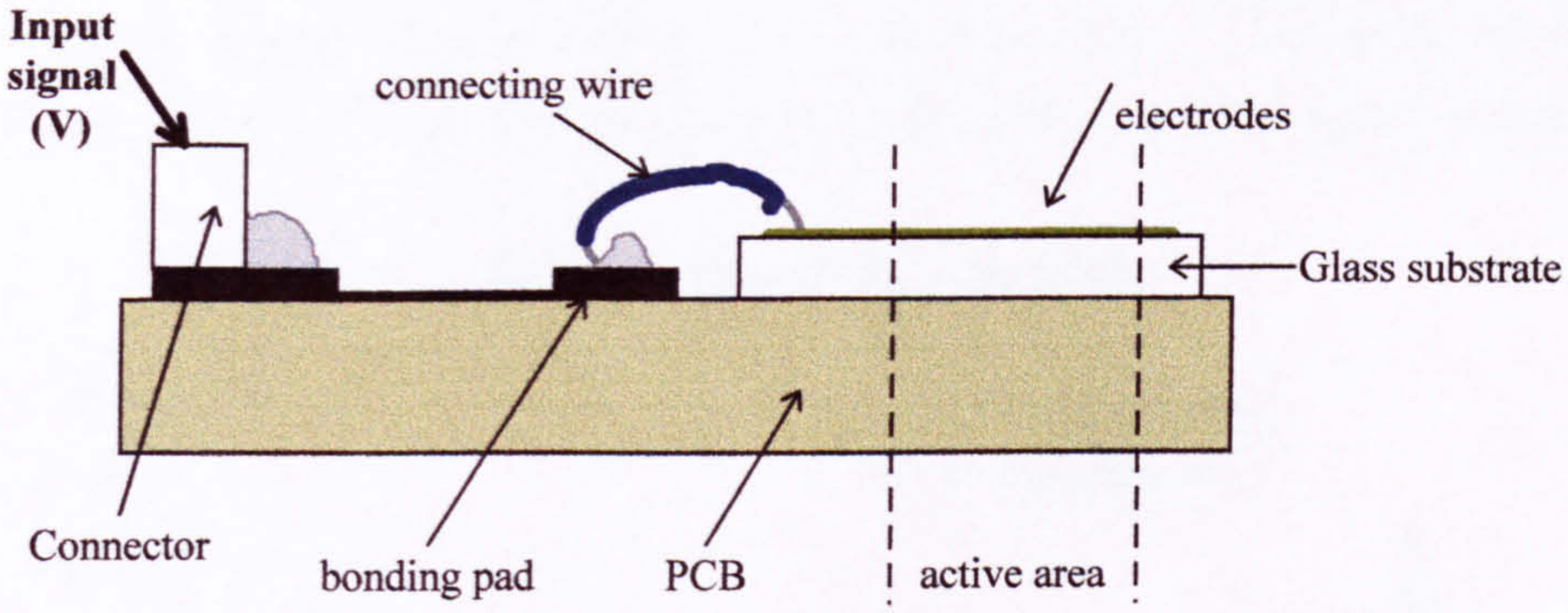

Figure (5.9) Diagram of a complete device. The PCB and the connecting wires to the electrodes ensure that the active area of the device is removed from the wiring and connectors necessary to attach the signal generator.

5.4 Signal generation

5.4.1 Signal generators

Two signal sources were used during the course of experimentation. The first was an in-house manufactured digital generator (Appendix 5b.4) which used direct digital synthesis (DDS) to produce a four phase analogue signal. For dielectrophoresis experiments, only the 0^{o} and the 180^{o} signals were used. The DDS was controlled by a PC running a control program written during the course of this project (Appendix 5a.5). The second generator used in later experiments was a simple analogue source (Appendix 5a.3).

The maximum operating frequency of both generators was 20 MHz. The DDS produced both a signal and its inverse at a requested frequency whereas the analogue generator produced only the single phase with earth being used as the second connection. This meant that for a given signal amplitude, the DDS produced twice the potential difference on a pair of electrodes than the analogue generator. However, the analogue generator could provide higher signal amplitudes. For example, in 100mM KCl, the maximum potential on the electrodes from the DDS is approximately 1volt peak to peak but the analogue generator could produce a maximum of 10 volts peak to peak. In 1mM KCl, the DDS can produce 12 volts peak to peak and the analogue generator 20 volts peak to peak.

5.4.2 Device characteristics: results and discussion

The impedance of the devices described in section (5.3) was measured as a function of frequency in air using a vector impedance meter (Appendix 5b.2). The results are shown in Figures (5.10) as plots of the magnitude and phase angle of the impedance against frequency.

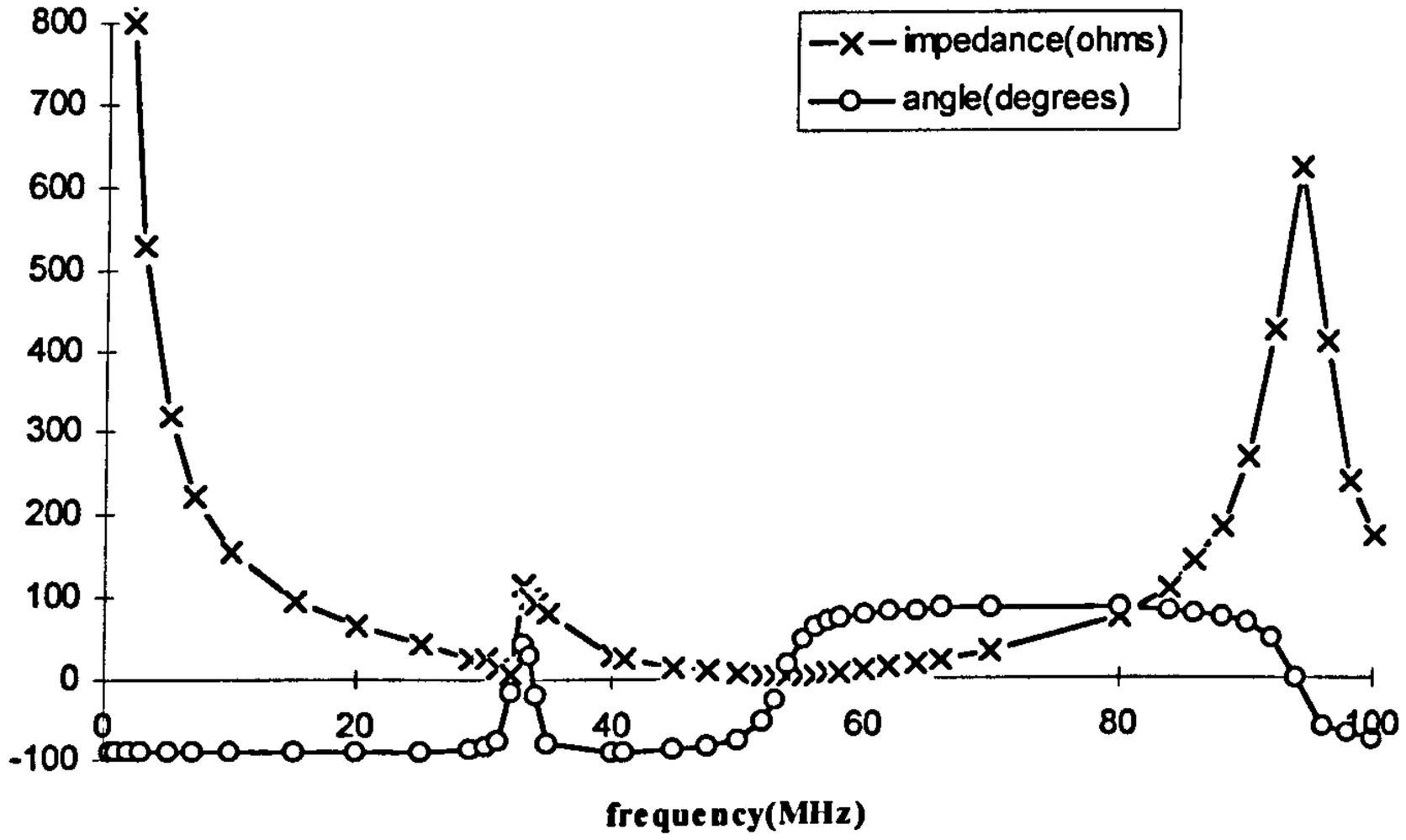

Figure (5.10a) Characteristic behaviour of the design A electrodes (section 5.3.2).

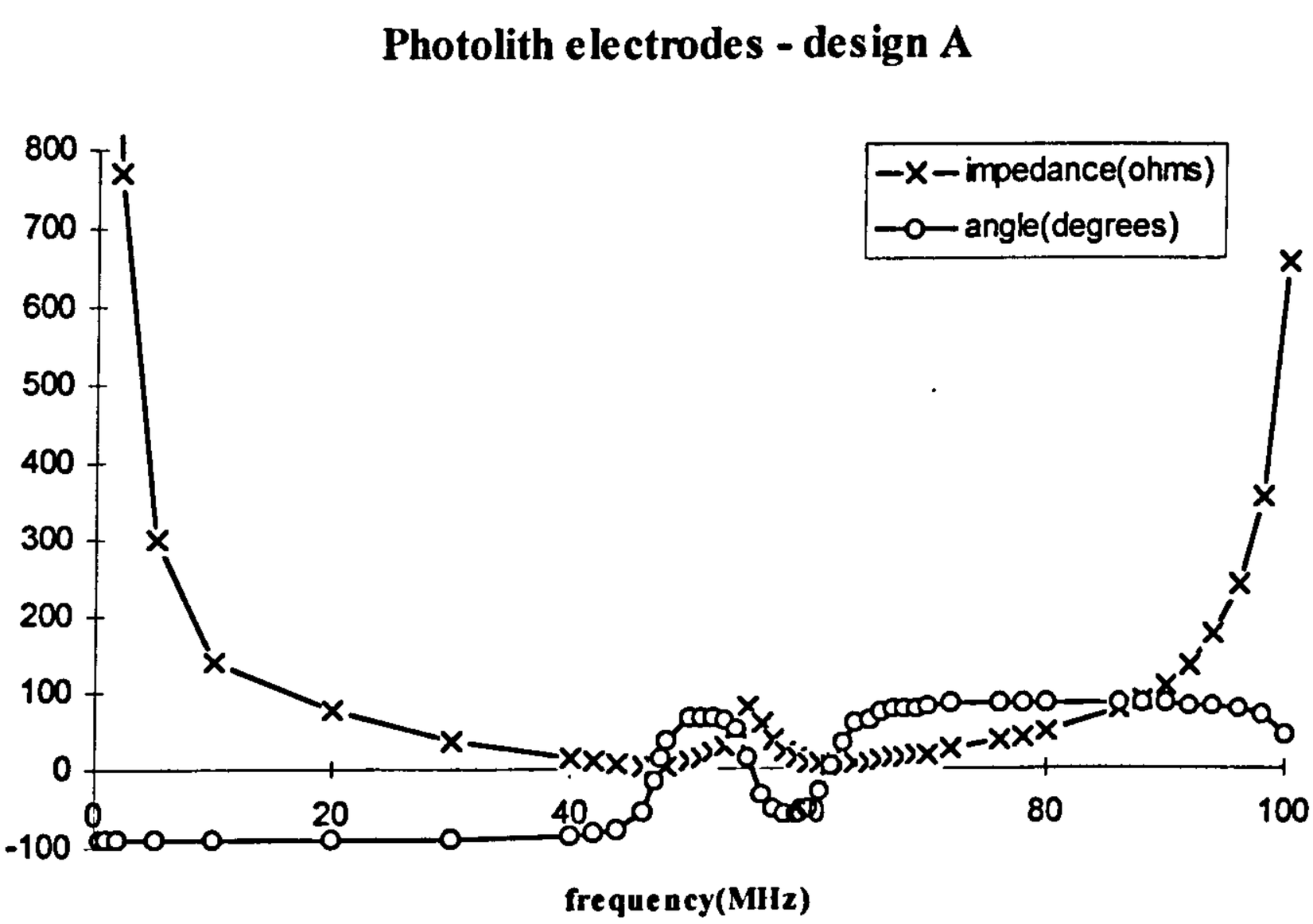

Figure (5.10b) Characteristic behaviour of the design B electrodes (section 5.3.2).

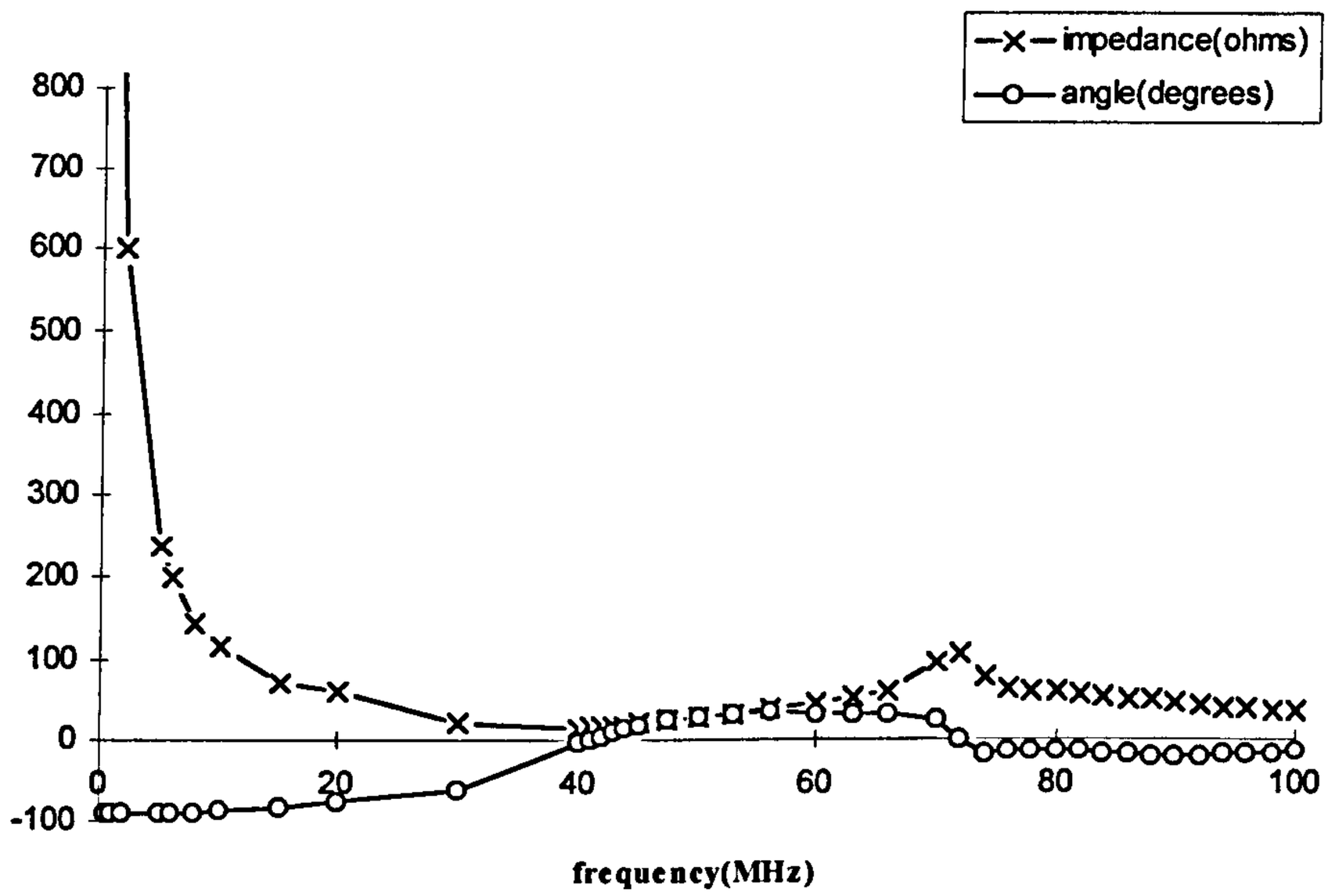

Figure (5.10c) Characteristic behaviour of the e-beam electrodes (section 5.3.3).

The results shown graphically in Figures (5.10a-c) demonstrated for each of the devices that, although the behaviour was complicated, in the frequency range of the signal generators the behaviour was equivalent to a capacitor. There was little change in the phase angle with frequency and no resonance below 20MHz. As a result, the amplitude of the signal on the electrodes in the devices could be expected to remain constant. This was confirmed by measuring the voltage on the electrodes as a function of frequency up to 20MHz in a range of conductivities.

Appendix (5a) Electrode manufacturing procedures

5a.1 Electrode design software

The electrode patterns were designed in the CAD section of a microwave waveguide simulation package called WAveMaker (WAM). This particular package saved files in GDSII format, allowing multiple overlayed layers to be included in the design. This was especially useful for electron-beam lithography where the electrodes could be separated into different sections with different resolutions and spot-sizes. As the write-time is inversely proportional to the spot-size squared (which varies with resolution), sections which do not require accurate features are better written with large spot sizes.

The saved GDSII file was transferred to a VAX workstation and converted to a file type specific to the CAD package used to process pattern files for the beamwriter (CATS). CATS translates the multiple levels of the GDSII file into separate pattern files for the beam-writer. The GDSII file describes solid shapes in terms of the points that delineate the edge of the shape whereas the CATS output to the beamwriter describes shapes in terms of blocks. CATS divides the shape into squares and parallelograms on the basis of the desired resolution for the final product. A low resolution results in poorly defined curves. A GDSII pattern for an electrode can be separated into two overlapping levels which can have separate resolutions. Areas which do not require a high resolution can therefore be written with a larger spot size then the areas with fine detail, reducing the write-time for the pattern. Alternatively for multi-layer patterns (Chapter Ten), the individual patterns, which are overlapped in WAM to ensure matching between distinct layers, can be separated in CATS and written on different masks.

The control file for the beam-writer was written in a program called BWL. Each pattern to be written on a sample (mask or glass substrate) is referenced in this file in terms of its name, position on the sample, resolution, spot-size (usually double the resolution) and the dose. The last parameter controls the electron beam current and is critical in correct exposure of the pattern on the sample. Typically, test exposures at multiple doses are run in order to determine the correct dose/ resolution/spot-size for a particular feature shape or size and resist.

The control file and the pattern files were then sent to the beam-writer control workstation to be written into a mask or a prepared sample. The following sections describe the preparation and manufacturing processes involved in fabrication of electrodes.

5a.2 Mask manufacture

Pre-prepared slide (Hoya corporation)

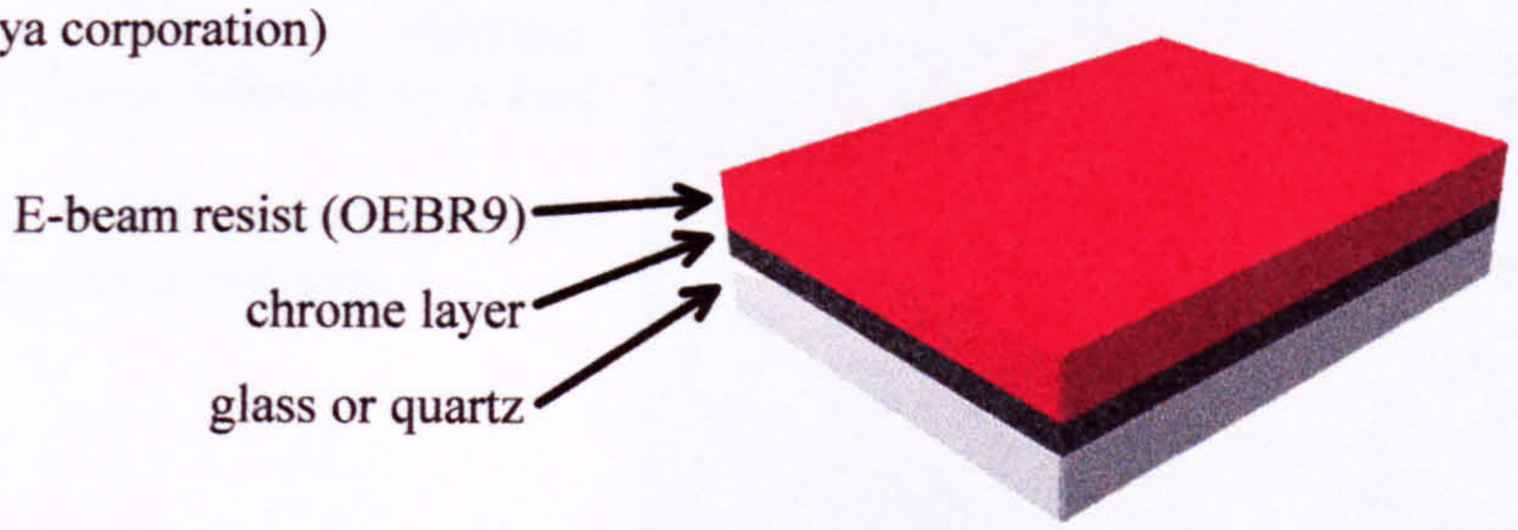

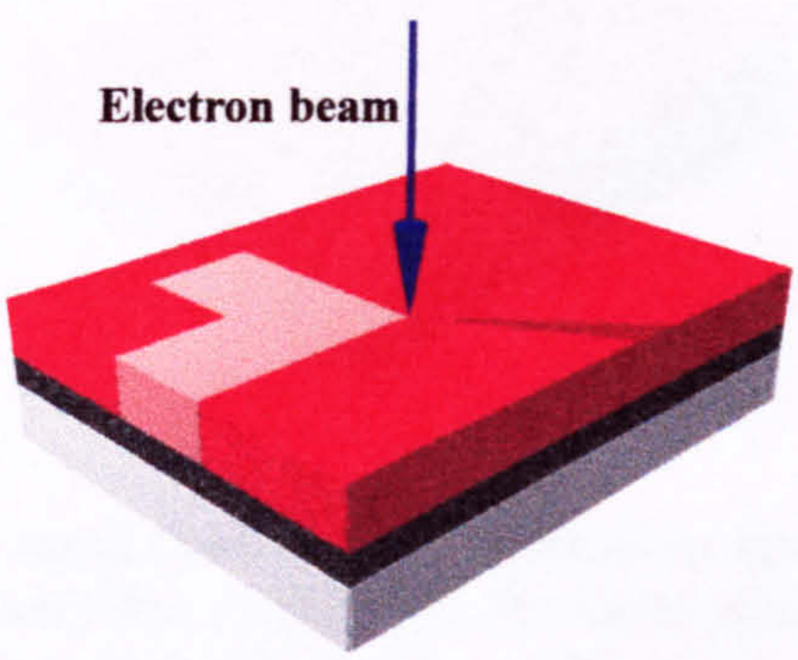

Electron beam exposes resist according to BWL control program and CATS pattern file.

The spot size was approximately double the pattern resolution and the dose for OEBR9 resist was always 30 $\mu C/cm^2$ regardless of spot size

The pattern in the resist was developed in isobutyl methyl ketone (MiBK).

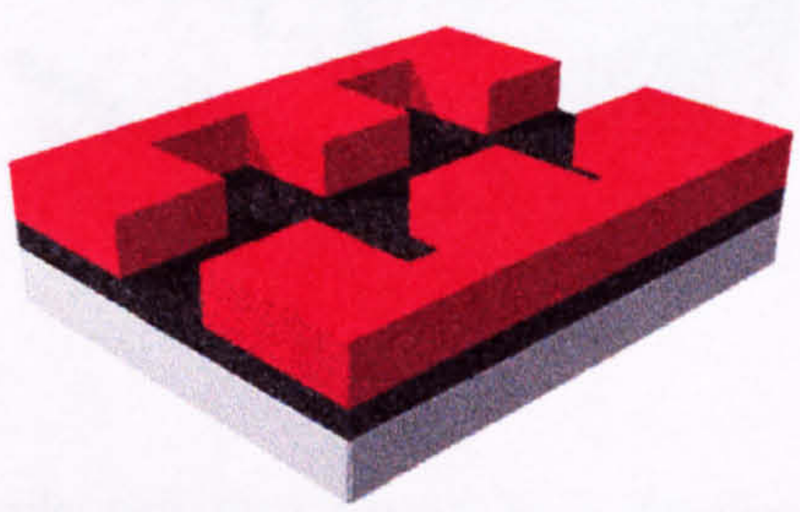

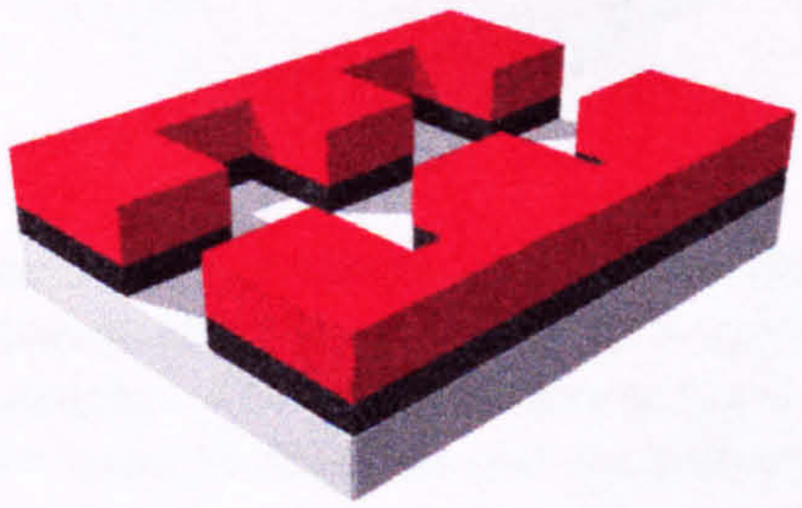

The mask was then placed in an etching solution composed of ceric ammonium nitrate in acetic acid for 80 seconds and the chrome etched where the resist was exposed, transferring the pattern to the chrome layer.

Finally, the resist was removed by warm acetone to leave a chrome negative copy of the original pattern on the glass. This mask could be copied using photolithography (appendix 5a.3)

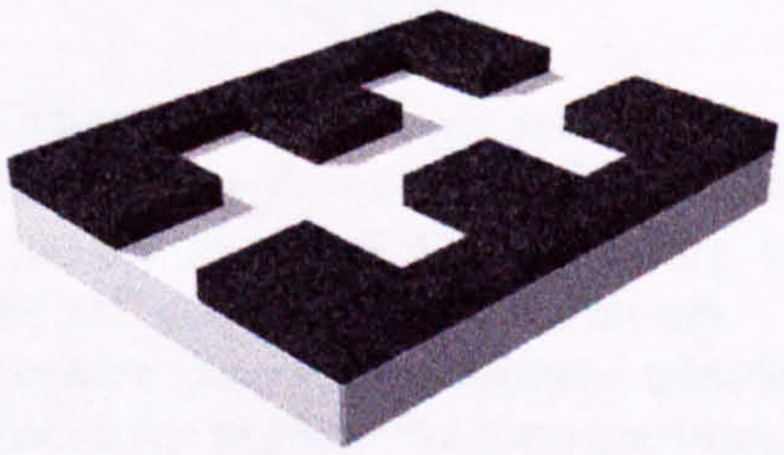

5a.3 Photolithography

The substrate (glass) was cleaned by immersion and ultrasonication sequentially in: opticlear, water, acetone, and methanol followed by a final rinse in purified water.
Hitachi resist (S1400-31 or S1818) was spun onto the substrate at 4000 rpm for 30 seconds.

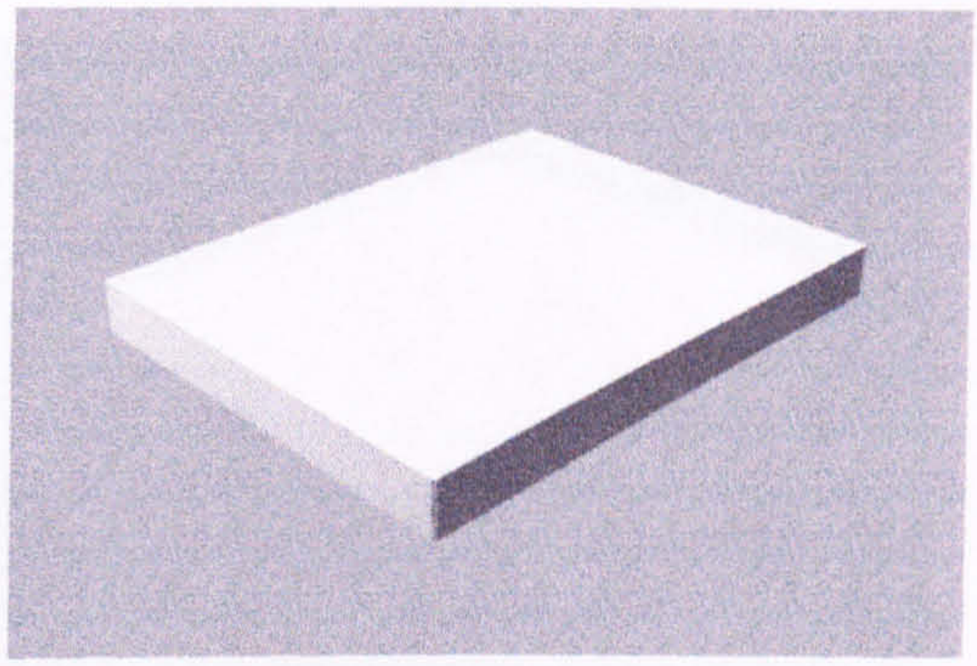

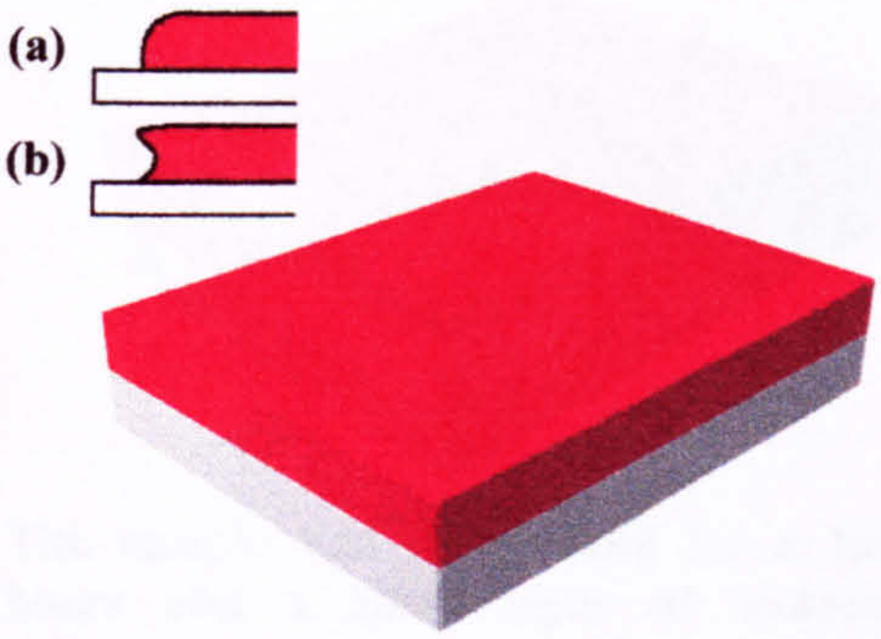

The sample was then either (a) baked for 30 minutes at 90°C or (b) baked for 15 minutes at 90°C, soaked in chlorobenzene for 15 minutes and baked again for 15 minutes at 90°C. The post-development resist profiles for (a) and (b) are shown in the diagram.

The mask (fabricated as outlined in the previous section) was placed with the metal side in direct contact with the resist. The resist was then exposed to ultraviolet light through the mask for a set period of time determined from experimental data. Large features required longer exposure times and the smaller features were covered with a red filter during the extra exposure.

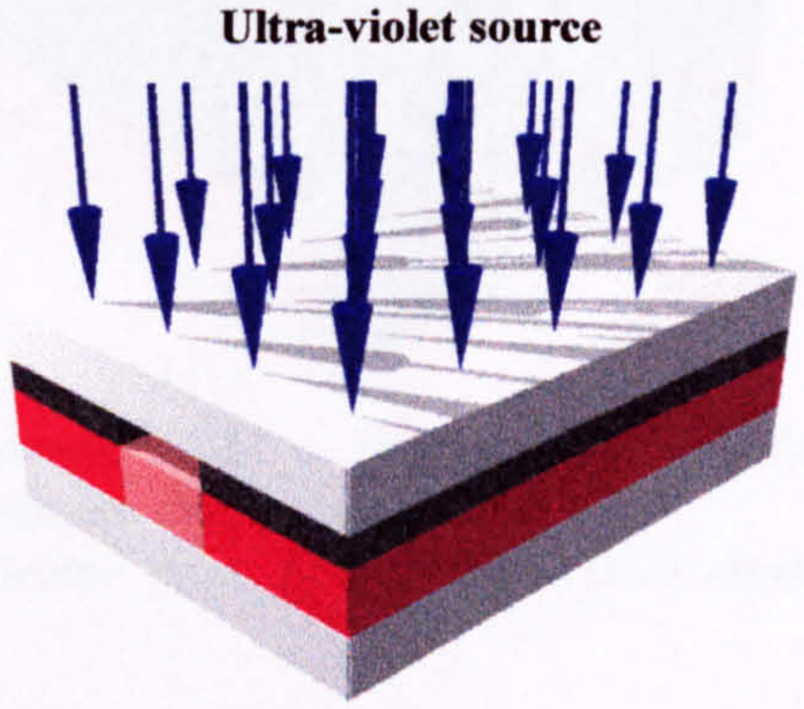

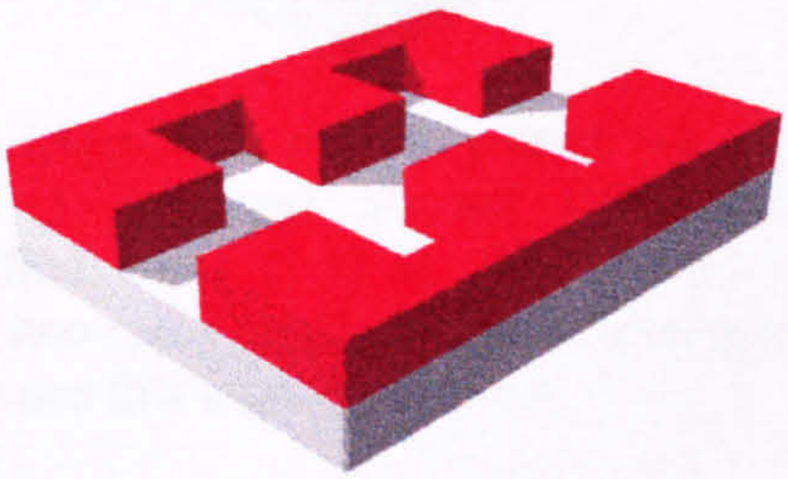

The sample was then placed in a developing solution of Hitachi developer and purified water in a 1:1 mix. The development time was 60 seconds.

A metal layer consisting of 10nm titanium, 10nm palladium and 100nm gold was evaporated onto the sample. The titanium ensured good adhesion of the metal to the glass and the palladium acted

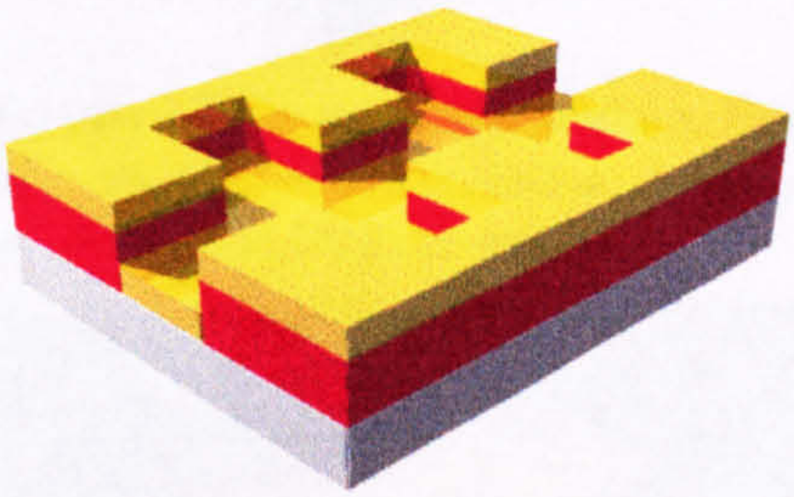

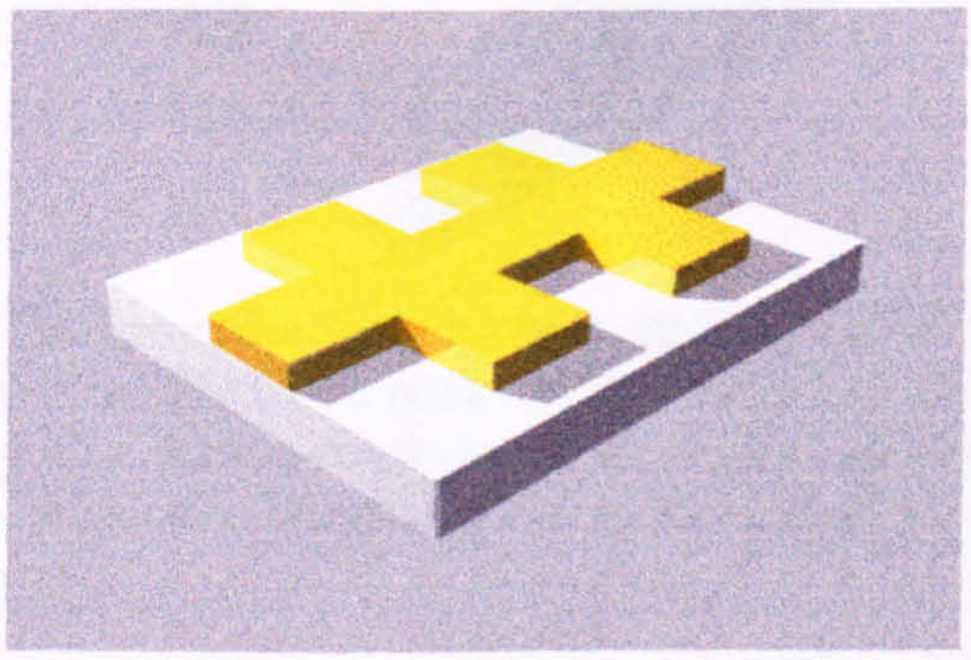

as a diffusion barrier between the titanium and the gold. The sample was then placed in warm acetone which dissolved the remaining resist and 'lifted off' the unwanted metal on top.
This procedure results in a negative transfer of the pattern on the mask to the glass substrate.

5a.4 Direct-write electron beam lithography - process (a)

The glass substrates were cleaned as described in Appendix (5a.3). Two layers of resist were spun onto the sample, both at 5000 rpm for 60 seconds.

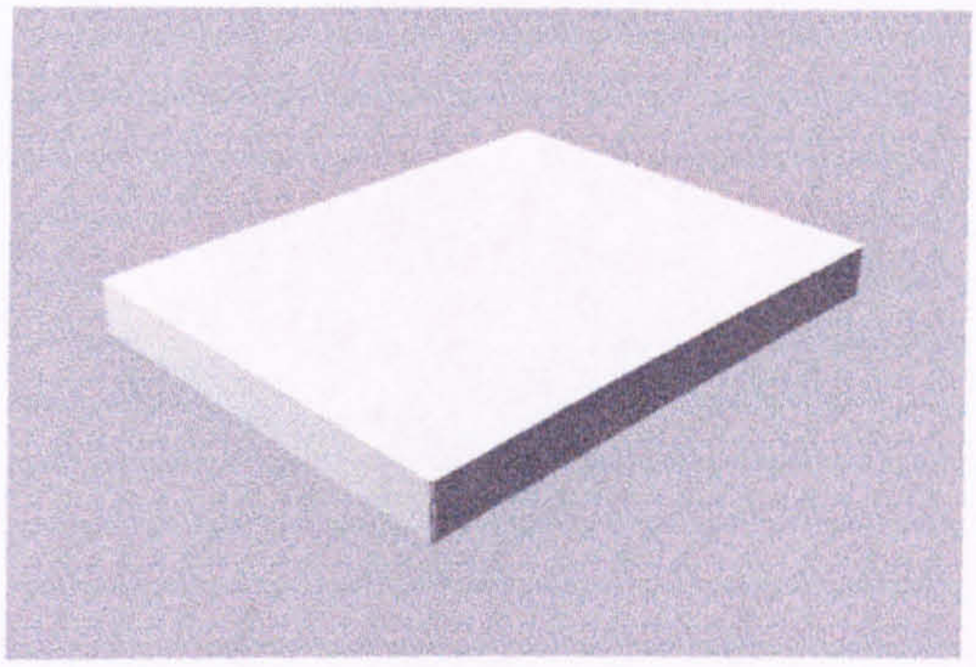

The first layer (8% polymethylmethacrylate (PMMA) 200μm) was baked for 2 hours before the second layer (4%PMMA 100μm) was added.

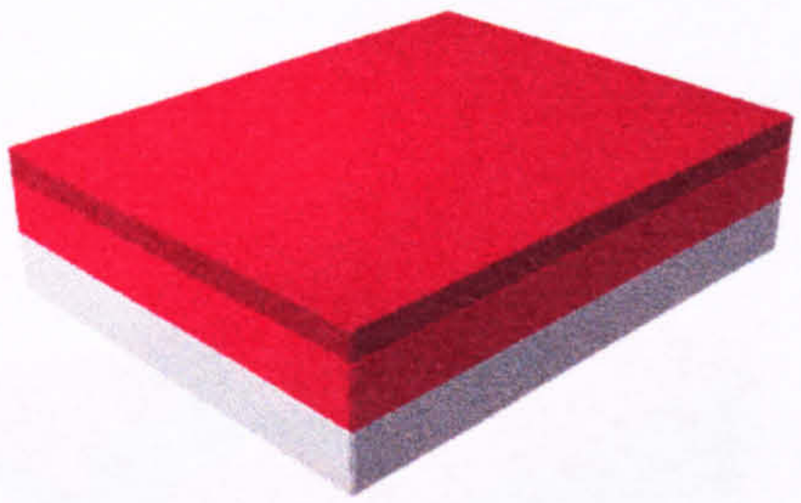

The sample was then baked for a further 22 hours and a 50nm layer of nichrome was evaporated on top to act as an earth layer during the electron-beam exposure.
The sample was then directly written by the beam writer according to a control and pattern

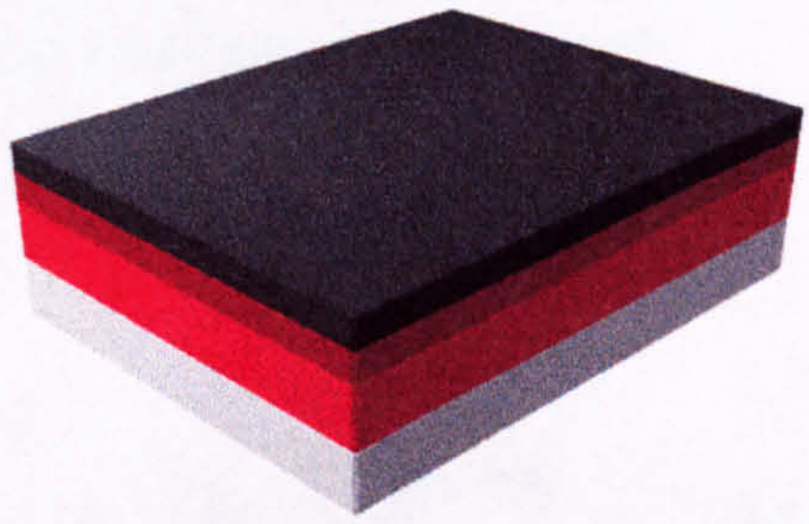

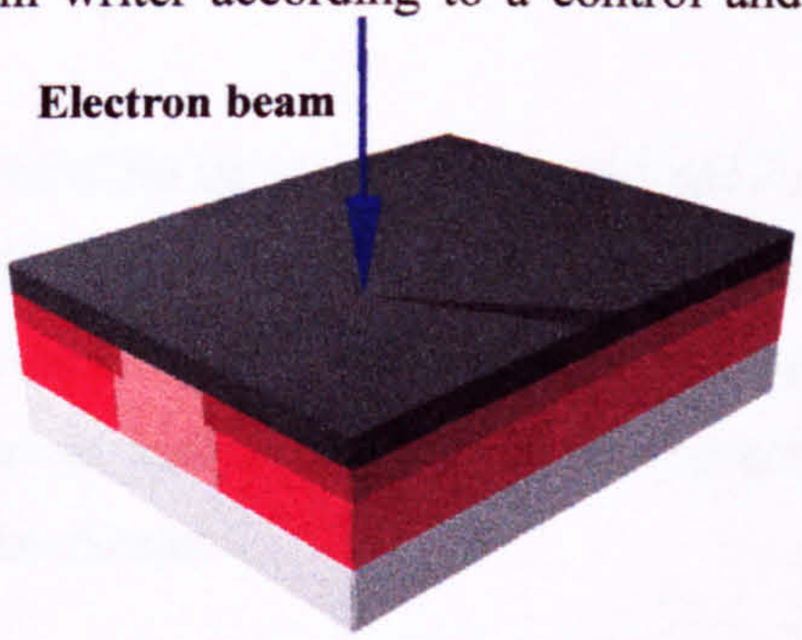

file (Appendix 5a.1). The spot size and dose varied with the feature resolution.
The nichrome layer was removed with chrome etch (App 5a.2) and the pattern was developed in 1:1 isopropyl alcohol (IPA)/MiBK and purified water (1:1) at 23^{0}C for 31 seconds. The two-resist profile had an overhang as shown here and this improved lift-off.

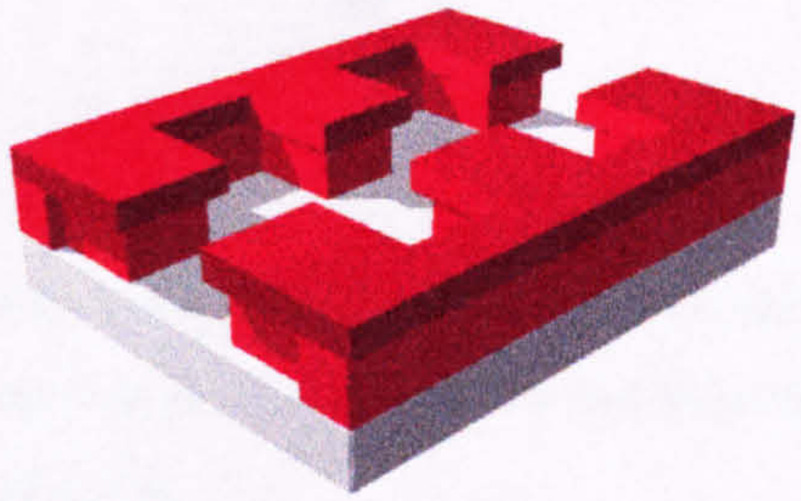

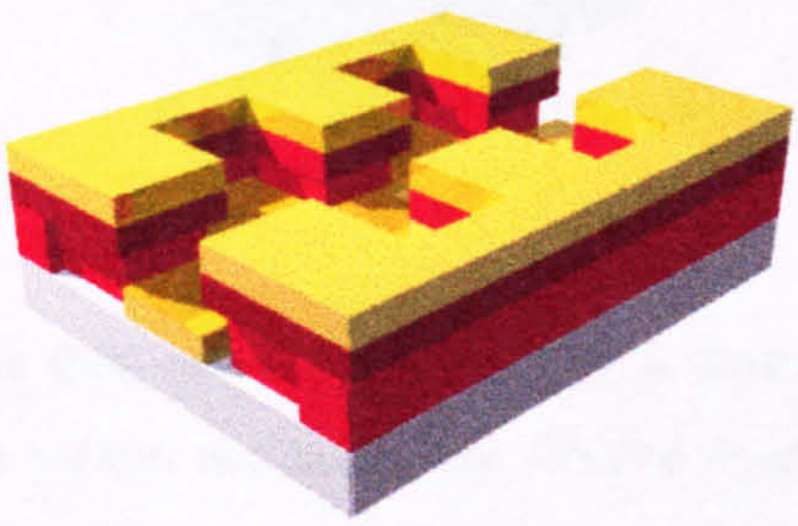

A Ti/Pd/Au metal layer was evaporated as before and lift-off was performed in warm acetone to remove the unwanted resist and metal.

This procedure results in a direct transfer of the pattern file to the resist and produces a metal copy with a feature resolution equal to the resolution of the electron beam used during the exposure step.

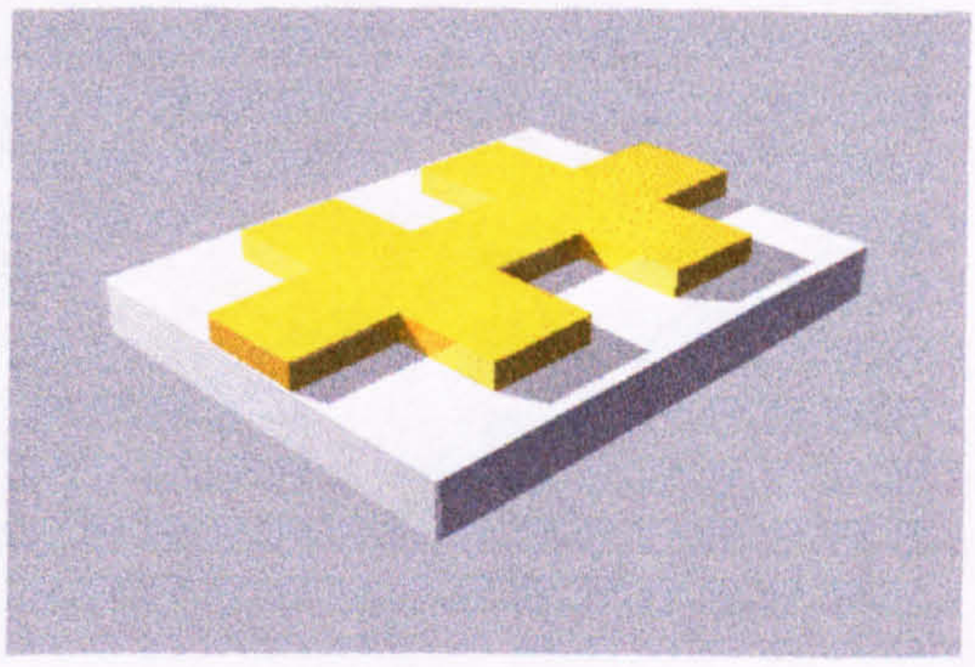

5a.5 process (b) - manufacturing electrodes on a mask plate

This procedure started with a mask plate (Hoya corporation). The pattern was written into the resist and etched into the metal as outlined in Appendix (5a.2).

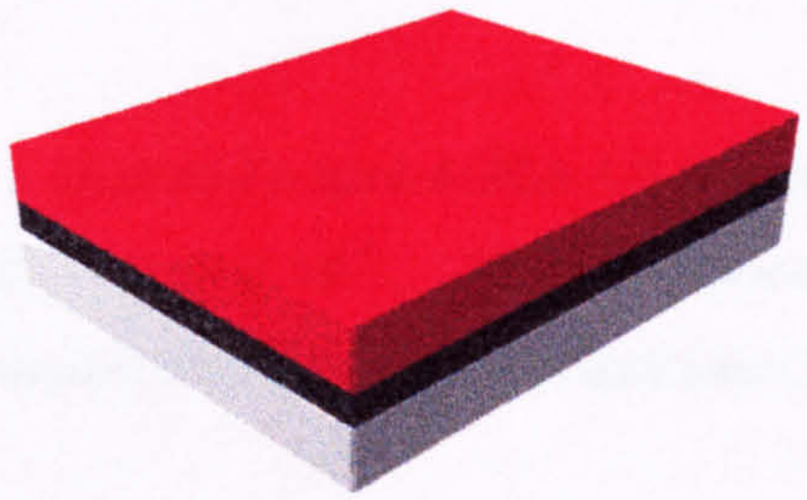

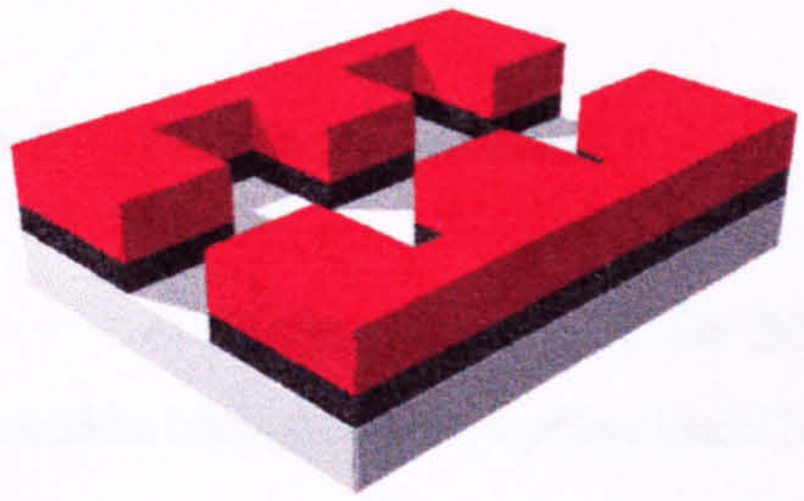

The mask manufacture process was halted after the chrome etch. The resist in this case was fast acting (low dose) and had an almost vertical profile making it ideal for good lift-off.

A Ti/Pd/Au layer was evaporated onto the mask as before. Lift-off was performed in warm acetone and the unwanted resist and metal removed leaving the gold in the pattern etched in the chrome.

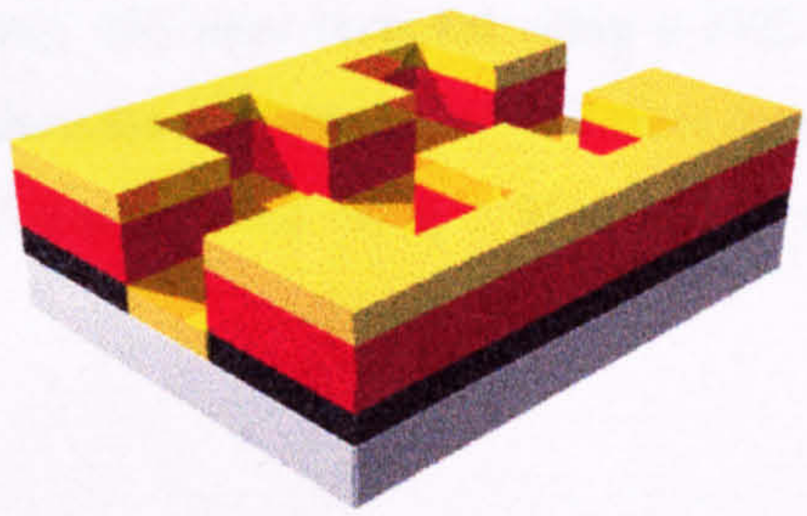

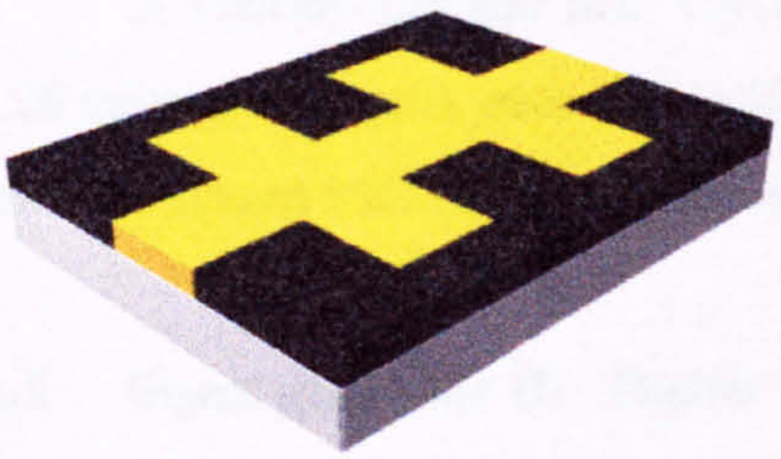

The sample was immersed in chrome etch until all the chrome had been removed and was then rinsed in purified water.

The final electrode pattern was a direct copy of the pattern written by the electron beam, again with a feature resolution equal to the resolution of the beam. However, this procedure was more efficient than process (a) and more complicated patterns could be written.

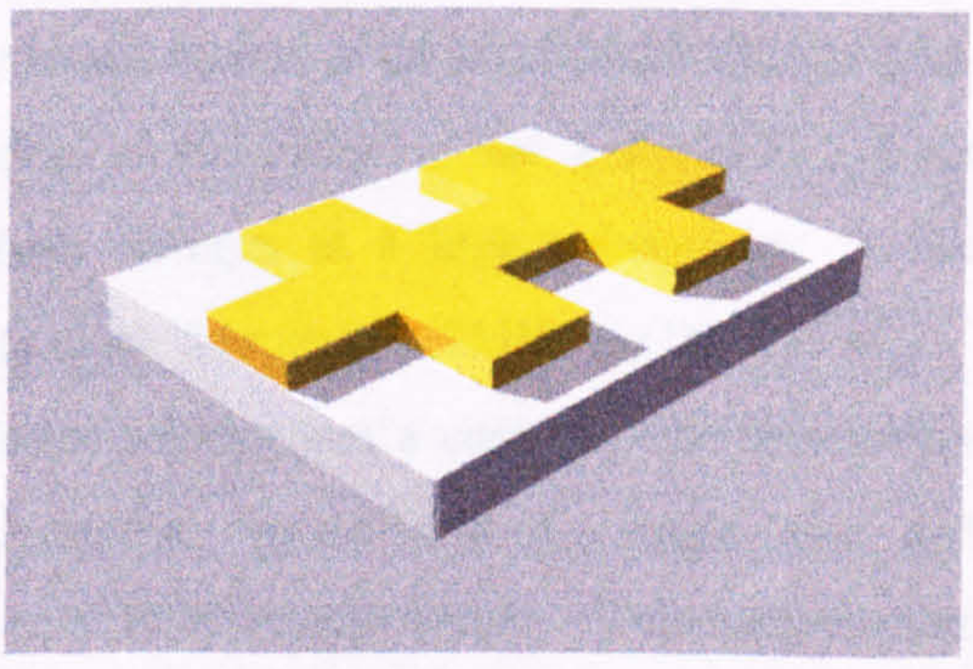

Appendix (5b) Experimental equipment details

5b.1 Conductivity measurements - the bridge

Solution conductivities were measured using a Hewlett-Packard 4192A LF Impedance analyser with a measuring cell (Sentec, UK) with cell constant $0.1m^{-1}$. The capacitance and resistance were determined by comparison with the equivalent circuit as given by equations (2.12) to (2.16).

5b.2 Impedance analyser

A Hewlett-Packard 4815A RF Vector Impedance Meter was used to determine the impedance magnitude and phase angle of dielectrophoresis devices.

5b.3 Video capture and imaging system

Images from the microscope (Nikon Microphot 5A) were recorded using a JVC TK-C1380 Colour video CCD camera onto super-VHS video cassettes using a S-VHS recorder (JVC HR-75000). The transfer to computer for analysis was handled using a Miro DC30 video capture card (Miro, Germany).

5b.4 Signal generator I: Analogue

A Thurlby-Thandar Inst. TG120 20MHz function generator was used to provide signals of 20 volts peak to peak over 1Hz to 20MHz into 50 ohms. The signals were measured using a Hewlett-Packard 500MHz digital oscilloscope.

5b.5 Signal generator II: Digital

A synthesiser was manufactured in-house based around a QUALCOMM Q2334 Dual Direct Digital Synthesiser. Digital Synthesis works on the principle that a signal at a given frequency can be generated by accumulating phase changes at a higher frequency. The maximum frequency is limited to one half of the chip clock frequency (50MHz for the Q2334).

The Q2334 DDS has two phase accumulators which share a common interface with a microprocessor. The interface receives signal information, in the form of a single byte, and stores it in one of four increment registers (two for each DDS output signal). This byte remains

in the register until the computer sends a different value and is added to the value stored in the phase accumulator once per clock period. The accumulated value is then modulated to a desired phase offset (in this case set to 90 degrees) and applied to a sine lookup table to turn the phase into a sinusoidal amplitude. Spurs in the signal produced by repetition of the amplitude error are removed by a noise reduction circuit and the two output signals (one form each phase accumulator) are passed into a Q2150 digital to analogue converter (DAC) which gives sine wave outputs which are then passed through low pass filters to remove harmonics and aliasing errors.

The output from this part of the circuit is two sinewave signals, identical apart from the 90 degrees phase difference. The signals are then passed through two EL2082 current mode multipliers which are used as voltage controlled variable attenuators. The computer addresses two AD557 DACs (6 bit locations) with a single byte which gives the DAC output voltage which in turn provides the control voltage for the attenuators. The computer control over the DDS output voltage removes the frequency dependence of the voltage produced by the entire circuit. The modulated signals from the attenuators are then passed through two EL2030 current feedback op-amps. Each amplified signal then drives two EL2030 output amplifiers, one inverting and one non-inverting.

The generator produces four signals of 200Hz to 20MHz and phases 0, 90, 180 and 270 degrees, with maximum voltages of 6Vpk-pk into 50 ohms and 12Vpk-pk into high impedance.

5b.6 DDS control program

A computer control program written to enable the user to have single frequency entry, frequency hopping or frequency/amplitude sweeps was written. It is included here.

```
program logandds;

{*****************************************************************
*  Program to control the specific DDS four phase signal  *
*  generator ED1101. Started 15/10/94. This version is 002  *
*              date 9/11/94                *
* Developed by Nicolas "Rogue" Green from a concept program *
*   written by Chris Hardy. Version supplied 10/10/94     *
*****************************************************************}

uses
 crt, dos;

const
 base = $200;   { Base address of the 8255 24 bit port. Value
          assigned 200(hex), 512(dec), 1000000000(bin) }
 control = $80;  { Control byte to configure mode 0 with :
          Port A              output
          Port B              output.
          Port C (bits 0-3)       output.
          Port C (bits 4-7)       output. }

{*****************************************************************
 * The program has quite a bit of elementary picture drawing with special *
 * extended characters making up the boxes.                *
*****************************************************************}

 hlinesngl  = #196;        hlinedbl  = #205;
 vlinesngl  = #179;        vlinedbl  = #186;
 upleftsngl = #218,        upleftdbl = #201,
 loleftsngl = #192;        loleftdbl = #200;
 uprightsngl = #191;       uprightdbl = #187;
 lorightsngl = #217;       lorightdbl = #188,

 arrow_l  = #27;           arrow_u  = #24,
 arrow_r  = #26,           arrow_d  = #25,
 Tdowndbl  = #203,

 yes1 = #89; yes2 = #121; no1 = #78, no2 = #110;

 Ls = #115, Lf = #102,  La = #97; Lv = #118, L_p = #112,
 US = #83;  UF = #70;   UA = #65, UV = #86,  U_P = #80;
 Lx = #120; Lm = #109;  Lr = #114; Lo = #111; Ll = #108,
 UX = #88,  UM = #77;   UR = #82, UO = #79;  UL = #76;

 escape = #27, enter = #13; space = #32; null = #0;
 left  = #75, right = #77; up  = #72; down = #80;


{*****************************************************************
 * The program uses byte values to communicate to the generator the value *
 * for amplitude required The user communicates this value by means of a *
 * voltage, so a conversion table is required              *
*****************************************************************}

 V1 = 0.01;  b1 = 10;
 V2 = 0.02,  b2 = 13,
 V3 = 0.05;  b3 = 20;
 V4 = 0.1;   b4 = 28,
 V5 = 0.2;   b5 = 39;
 V6 = 0.5;   b6 = 61;
 V7 = 1;     b7 = 85,
 V8 = 2,     b8 = 120;
 V9 = 5;     b9 = 187,
 V10 = 6,    b10 = 210;

{*****************************************************************
```

```
 * Another problem arises in the form of decreasing gain with frequency  *
 * The variation is non linear and so, reference points are required for *
 * the purpose of correcting this problem.                                *
*************************************************************************}
 f1 = 10;   A1 = 1 00;
 f2 = 11;   A2 = 0.98,
 f3 = 12,   A3 = 0 94,
 f4 = 13;   A4 = 0 91;
 f5 = 14;   A5 = 0 91;
 f6 = 15,   A6 = 0 93;
 f7 = 16,   A7 = 0.93,
 f8 = 17,   A8 = 0 85,
 f9 = 18,   A9 = 0.74,
 f10 = 19;   A10 = 0 70;
 f11 = 20;   A11 = 0.75;
 f12 = 21,   A12 = 0 425;

{*************************************************************************
 * As an addition to this version of the program, a range of default     *
 * settings are available to the user. These are detailed as constants *
 * here and converted to an array later.                                  *
*************************************************************************}
 lrd1 = 0 0005;  urd1 = 1;    id1 = 0 00005;
 lrd2 = 0.001;   urd2 = 1;    id2 = 0 0001;
 lrd3 = 0 001;   urd3 = 5;    id3 = 0 0005;
 lrd4 = 0 1;     urd4 = 5;    id4 = 0 001;
 lrd5 = 0 01;    urd5 = 10;   id5 = 0 005;
 lrd6 = 0.1;     urd6 = 10;   id6 = 0 01;
 lrd7 = 0 1;     urd7 = 15;   id7 = 0 05;
 lrd8 = 1;       urd8 = 15;   id8 = 0 1,
 lrd9 = 0 1;     urd9 = 20;   id9 = 0 5;
 lrd10 = 1;      urd10 = 20;  id10 = 1,
 special1 = 0 0001;          special2 = 2;

type
 show = string[3],
 nicolas = array[1..2] of integer;

var

{*************************************************************************
 * Here we have an example of major conflict between programmers. *
 * I dislike long variable and function names since they are a    *
 * bugger to type all the time and since they disrupt the flow of *
 * reading the program. Anyone reading the program from the start *
 * is going to remember the names anyway, so I keep them short    *
 * AND relevant.                                                  *
*************************************************************************}

 A : integer;                    { Amplitude }
 bam, bam_bam : real;
 fq, Vout_pp : real,             { frequency, output voltage peak to peak }
 L_array : array[1..10,1..2] of real,   { linearising array }
 fA_array : array[1..12,1..2] of real;  { frequency/amplitude correction array }
 dummyy : string[20],            { This is a dummy variable to check
                                   for character entries }
 d_array : array[1..10,1..3] of real;   { The default values array }
 DS_array : array[1..10] of real;       { single freq array }
 realvalue : real,
 fancy : integer;
 Hstart, Vstart : Nicolas;

procedure byte_table; forward,
procedure freq_table, forward,
function correction(fq : real) : real, forward,
function A_byte(Vout : real) : real ; forward,
function phase_inc(fq : real) : longint, forward,
function byte(fq : real, i : integer) . integer; forward;
function screen_freq(bam : real) : real, forward;
function show_range(bam_bam : real) . show; forward,
procedure send_addr(addr : integer); forward;
procedure send_data(data : integer); forward;
procedure write_pulse, forward,
procedure instruct(addr,data : integer); forward,
procedure generate; forward,
procedure initialise; forward,
procedure option_sfa; forward,
procedure option_sfva; forward,
procedure option_vfsa, forward,
procedure option_vfa, forward,
procedure man_auto(var k : integer); forward;
procedure man_sfva(var k : integer); forward;
procedure man_vfsa(var k : integer); forward;
procedure auto_sfva(var k : integer); forward;
procedure auto_vfsa(var k : integer); forward,
procedure exit, forward;
procedure error1(g, h : integer); forward;
procedure pulse, forward,

{*************************************************************************
* Procedures Group ( 0 ) extras                                          *
*  These routines are especially for particular strange *
* requirements in the program.                                           *
*************************************************************************}

procedure buffer;

{ It has come to my attention that the function Keypressed reacts to the
keyboard buffer rather than to the keyboard itself which means that there are still
values in there every time any key is pressed.  Readkey clears ONE value from
the buffer but there may still be values in there from extended keys and so
keypressed will be true  Even readkey may react to the wrong value
This routine clears the buffer and should be called EVERY time a keyboard
entry is required. }

var
 Cout : char;  { A purely dummy variable. Idiotic, in fact }
begin
 while keypressed do
  Cout := readkey,
end,

procedure reset,
{ As the name might suggest this is to reset the DDS to
safer values instantly. }
begin
 fq := 5,
 Vout_pp := 0 001,
 generate,
end,

{*************************************************************************
* Procedures Group ( 1.) Conversion of tables to arrays  *
*************************************************************************}

procedure byte_table;  { Converts the byte/voltage table to an array }
begin
 L_array[1,1] := V1,   L_array[1,2] := b1;
 L_array[2,1] := V2;   L_array[2,2] := b2,
 L_array[3,1] := V3,   L_array[3,2] := b3;
 L_array[4,1] := V4,   L_array[4,2] := b4,
 L_array[5,1] := V5;   L_array[5,2] := b5,
 L_array[6,1] := V6,   L_array[6,2] := b6,
 L_array[7,1] := V7;   L_array[7,2] := b7;
 L_array[8,1] := V8,   L_array[8,2] := b8,
 L_array[9,1] := V9;   L_array[9,2] := b9;
 L_array[10,1] := V10;  L_array[10,2] := b10;
end,

procedure freq_table; { Converts the frequency correction table to an array }
begin
 fA_array[1,1] := f1,    fA_array[1,2] := A1,
 fA_array[2,1] := f2,    fA_array[2,2] := A2,
 fA_array[3,1] := f3;    fA_array[3,2] := A3,
 fA_array[4,1] := f4,    fA_array[4,2] := A4;
 fA_array[5,1] := f5,    fA_array[5,2] := A5,
 fA_array[6,1] := f6,    fA_array[6,2] := A6;
 fA_array[7,1] := f7,    fA_array[7,2] := A7;
 fA_array[8,1] := f8,    fA_array[8,2] := A8,
 fA_array[9,1] := f9;    fA_array[9,2] := A9;
 fA_array[10,1] := f10;   fA_array[10,2] := A10;
 fA_array[11,1] := f11;   fA_array[11,2] := A11;
 fA_array[12,1] := f12;   fA_array[12,2] := A12,
end,

procedure default_array; { Converts default table to an array }
begin
 d_array[1,1] := lrd1,  d_array[1,2] := urd1,  d_array[1,3] := id1;
 d_array[2,1] := lrd2;  d_array[2,2] := urd2;  d_array[2,3] := id2;
 d_array[3,1] := lrd3,  d_array[3,2] := urd3;  d_array[3,3] := id3;
 d_array[4,1] := lrd4,  d_array[4,2] := urd4,  d_array[4,3] := id4,
 d_array[5,1] := lrd5,  d_array[5,2] := urd5,  d_array[5,3] := id5,
 d_array[6,1] := lrd6;  d_array[6,2] := urd6;  d_array[6,3] := id6;
 d_array[7,1] := lrd7,  d_array[7,2] := urd7,  d_array[7,3] := id7,
 d_array[8,1] := lrd8,  d_array[8,2] := urd8;  d_array[8,3] := id8,
 d_array[9,1] := lrd9;  d_array[9,2] := urd9;  d_array[9,3] := id9;
 d_array[10,1] := lrd10; d_array[10,2] := urd10; d_array[10,3] := id10;
DS_array[1] := special1,
 DS_array[2] := lrd1,
 DS_array[3] := lrd2,
 DS_array[4] := lrd4,
 DS_array[5] := lrd8,
 DS_array[6] := special2;
 DS_array[7] := urd3;
 DS_array[8] := urd5,
 DS_array[9] := urd7;
 DS_array[10] := urd9;
end;

{*************************************************************************
*
* Functions Group ( 1 ) Data correction and conversion.      *
* Two functions, one to apply the gain correction, contained *
* inside the other, which converts the given, corrected value *
* to a byte value                                            *
*************************************************************************}

function correction(fq . real) : real,
{ Here fA_array is used to compensate for changes in the output amplitude with
frequency  It corrects based on the values in the constant section at the start,
using interpolation for values falling in between the given points. }
var
 n : integer;
 A_hi, A_lo, f_hi, f_lo, A_value : real,
begin
 if fq < fA_array[1,1] then
```

```
    begin
     A_value := fA_array[1,2], {if below min value set A to min value (1.0)}
    end
   else
    begin
     if fA_array[12,1] <= fq then
      begin
       A_value := fA_array[12,2]; { if above max set A to max (0 425) }
      end
     else
      begin
       for n := 1 to 11 do
        if (fA_array[n,1] <= fq) and (fq < fA_array[n+1,1]) then
         begin
          A_hi := fA_array[n+1,2],
          A_lo := fA_array[n,2],
          f_hi := fA_array[n+1,1];
          f_lo := fA_array[n,1],
         end,
       A_value := (fq-f_lo)*((A_hi-A_lo)/(f_hi-f_lo)) + A_lo;
      end,
    end,
  correction := A_value;
end,

function A_byte(Vout : real) : real ;
{ Converts peak to peak output voltage requested by user to a byte value to be
assigned to the gain DACs by interpolating between the points in the L_array.
The function for the curve between the points on either side of the requested
voltage is calculated and used to derive a fairly accurate value for the control
byte. }
var
 n : integer;
 hi_byte, lo_byte, hi_volt, lo_volt, A_trans : real;
B, C, D, E, F : real ;   { B,C,D,E,F are purely dummy variables for altering the
                           data (the first bit I don't understand). }
begin
B := Vout/2,             { compensates for x2 attenuation when using 50R
                  termination (used to produce table) }
 C := B/correction(fq);    { correction due to gain fall off with frequency. }
 if C < L_array[1,1] then
  begin
   A_trans := sqrt(C/L_array[1,1])*L_array[1,2];
  end
 else
  begin
   if C >= L_array[10,1] then
    begin
     A_trans := sqrt(C/L_array[10,1])*L_array[10,2];
    end
   else
    begin
     for n := 1 to 9 do
      if (L_array[n,1] <= C) and (C < L_array[n+1,1]) then
       begin
        hi_byte := L_array[n+1,2],
        lo_byte := L_array[n,2],
        hi_volt := L_array[n+1,1];
        lo_volt := L_array[n,1],
       end;
     D := ln(hi_byte/lo_byte);
     E := ln(hi_volt/lo_volt);
     F := ln(C/lo_volt);
     A_trans := exp((D/E)*F)*lo_byte,
    end,
  end;
 if A_trans > 255.9 then
  begin
   A_trans := 255 9;
  end,
 A_byte := A_trans,
end,

{**************************************************************
* Functions Group ( 2 ) Phase changes                         *
* These functions apparently produce the required changes     *
* in the phase for the different outputs. I may amend this    *
* comment when I have some idea of how they do it.            *
**************************************************************}

function phase_inc(fq : real) : longint;
{ This function is responsible for it all. It is called
by all the byte functions for an unknown purpose.
According to the original program notes, this function
derives the 32 bit phase from the frequency given }
begin
 phase_inc := trunc(fq*4294967295 0 /50);
end,

function byte(fq : real, i : integer) : integer;
{ produces byte * of the phase increment from frequency
given in MegaHertz. }
begin
 case i of
  0: byte := phase_inc(fq) and $000000FF;
  1: byte := (phase_inc(fq) DIV $100) and $000000FF,
  2. byte := (phase_inc(fq) DIV $10000) and $000000FF;
  3: byte := (phase_inc(fq) DIV $1000000) and $000000FF;
end,
```

```
 end,

{**************************************************************
* Procedures Group ( 2.) Writing to the I/O board.            *
* These physically(electronically) send the data to the generator *
**************************************************************}
procedure send_addr(addr : integer); { writes address value to Port C }
begin
 port[base+2] := addr;
end,

procedure send_data(data . integer); { writes data value to Port B }
begin
 port[base+1] := data,
end,

procedure write_pulse,   { writes +ve 10ms pulse to Port A bit 0 }
{ The equipment requires that the signal be held at the
"on" position for at least the 10ms registered here to
ensure receipt of the information. }
begin
 port[base+0] := 1;
 delay(10),
 port[base+0] := 0;
end,

procedure instruct(addr,data : integer),
{ Sends address, data abd write pulse to the dds. }
begin
 delay(10),
 send_addr(addr);
 send_data(data);
 delay(10);
 write_pulse;
end,

procedure generate,
{ sets all the necessary registers in the dds chip and the
gain DACs for any value required }
var
 i : integer;
begin
 instruct(12,0);              { address accum reset1. }
 instruct(28,0);              { address accum reset2. }
 instruct(8,2),               { set synch mode cntrl1 to 2
                              ext phase mod established. }
 instruct(10,140);            { set asynch mode cntrl1 to 12, 10 bit
                              offset bin invert DAC strobe. }
 for i := 0 to 3 do
  begin
   instruct(i,byte(fq, i)),   { as far as I can tell at this point,
                              this should have the effect of four
                              lines of code  Sets phase inc A1
                              (bits 0-7, 8-15, 16-23) to 0 and
                              A1 (bits 24-31) to 33, @6 445 MHz }
  end,
 instruct(24,0);              { set synch mode cntrl2 to 0 }
 instruct(26,140);            { set asynch mode cntrl2 to 12, 10 bit
                              offset bin invert DAC strobe. }
 for i := 0 to 3 do
  begin
   instruct(16+i,byte(fq, i)),  { set phase inc A2 (bits 0-7,8-15,16-23)
                              to 0 and (bits 24-31) 33 @6.445MHz}
  end;
 instruct(32,0);              { strobe hopclk 1&2 in sync with the
                              system clock. }
 instruct(39,64);             { set external mod1 bit1 to 1 (90 deg)
                              and clock. }
 instruct(40,trunc(A_byte(Vout_pp))); { set real(X ch) gain D-A. }
 instruct(41,trunc(A_byte(Vout_pp))); { set imag(Y ch) gain D-A. }
end,

procedure initialise; { configures the 8255 PPI chip on the interface board. }
begin
 port[base+3] := control;     { configures ports to i/o determined
                              by control. }
 port[base+0] := 0;           { clear port A to 0. }
 port[base+1] := 0;           { clear port B to 0. }
 port[base+2] := 0;           { clear port C to 0. }
 end,

{**************************************************************
* Procedures Group ( 3 ) new routines                         *
* These are the routines that I have added to make            *
* a more versatile and user friendly program                  *
**************************************************************}

procedure box(j : integer);
{ This program draws a box on the screen defined by the variables
Hstart and Vstart. The integer just tells the computer what the lines are,
and especially what the corners are. I have decided to change the sub-
heading box to a double line all the way around. }
var
 up_l, up_r, down_l, down_r, hor_line, ver_line : char;
 i, row, col . integer;
begin
 case j of
  1 :
   begin
```

```
    up_l := upleftdbl,     up_r := uprightdbl,
    down_l := loleftdbl;   down_r := lorightdbl;
    hor_line := hlinedbl;  ver_line := vlinedbl,
   end,
  2:
   begin
    up_l := upleftsngl,    up_r := uprightsngl;
    down_l := loleftsngl;  down_r := lorightsngl,
    hor_line := hlinesngl; ver_line := vlinesngl,
   end,
  3:
   begin
    up_l := Tdowndbl,     up_r := Tdowndbl;
    down_l := loleftdbl,  down_r := lorightdbl;
    hor_line := hlinedbl; ver_line := vlinedbl,
   end,
end,
for i := 1 to 2 do
 begin
  gotoXY((Vstart[1]+1),Hstart[i]);
  for col := (Vstart[1]+1) to (Vstart[2]-1) do
   begin
    write(hor_line),
   end,
  for row := (Hstart[1]+1) to (Hstart[2]-1) do
   begin
    gotoXY(Vstart[i], row);
    write(ver_line),
   end,
  end,
 gotoXY(Vstart[1],Hstart[1]);  write(up_l);
 gotoXY(Vstart[2],Hstart[1]),  write(up_r);
 gotoXY(Vstart[1],Hstart[2]);  write(down_l);
 gotoXY(Vstart[2],Hstart[2]),  write(down_r);
end;

procedure screen01;  { draws the introductory screen. }
{ This routine is the basis of all the others. It draws a box using the
box routine, then fills in the text itself. }
begin
 Hstart[1] := 10;   Hstart[2] := 14,
 Vstart[1] := 20;   Vstart[2] := 60;
 box(1);
{ Now that the box is finished, we add the text. }
gotoXY(23,11);  write('Frequency/Amplitude Control Program');
 gotoXY(34,12);  write('for GUED1101');
 gotoXY(22,13);  write('Four-phase Direct Digital Synthesizer'),
 delay(9000),
end,

procedure screen02;  { To draw the second screen, as you might expect. }
var
 cat : char;
begin
 Hstart[1] := 10;   Hstart[2] := 15;
 Vstart[1] := 18,   Vstart[2] := 62;
 box(1);
gotoXY(25,11);  write('Please ensure that the DDS is');
 gotoXY(27,12);  write('connected and switched on');
 gotoXY(20,13);  write('otherwise the INITIALISING procedure will');
 gotoXY(23,14);  write('not work. Press any key when ready.');
 buffer;
 cat := readkey,
end;

procedure screen03;   { Need I say more. }
var
 n : integer;
begin
 Hstart[1] := 12,   Hstart[2] := 14,
 Vstart[1] := 32;   Vstart[2] := 47;
 box(1);
textattr := 16*black+white+blink;
 gotoXY(34,13);  write('INITIALISING');
 delay(4000),
 textattr := 16*black+lightgray;
 initialise;   { very important line }
 fq := 5,
 Vout_pp := 0.1,
 for n := 1 to 2 do
  begin
   generate,
   gotoXY(34,13),  write('INITIALISING');
  end,
end,

procedure screen;   { This procedure is responsible for the bar
                      that appears at the top of every screen. }
begin
 clrscr;
 Hstart[1] := 1;   Hstart[2] := 3,
 Vstart[1] := 3,   Vstart[2] := 78,
 box(1);
 gotoXY(5,2),  write('GUED1101 4-phase Digital Synthesizer
Frequency/Amplitude Control Program');
end,

procedure screen04,    { Draws the fourth screen. }
var
 cat : char;
begin
 Hstart[1] := 10;   Hstart[2] := 16;
 Vstart[1] := 21;   Vstart[2] := 60;
 box(1);
gotoXY(29,11);  write('Initialisation complete');
 gotoXY(23,12),  write('As long as DDS was connected during');
 gotoXY(23,13);  write('procedure, test output signal should ');
 gotoXY(28,14);  write('be 100 millivolts at 5 MHz');
 gotoXY(28,15),  write('Press any key to continue');
 buffer;
 cat := readkey,
 reset;
end,

procedure screen05;   { Ergo et go. However, this asks for whether the
                        user would like instructions on using the prog.}
var
 cat : char;
begin
 repeat
  Hstart[1] := 11,   Hstart[2] := 14,
  Vstart[1] := 25;   Vstart[2] := 55,
  box(2),
  gotoXY(27,12);  write('Do you require Introduction');
  gotoXY(29,13),  write('and Instructions (y/n)');
  buffer;
  cat := readkey;
  if (cat = yes1) or (cat = yes2) then
   begin
    { usually this part would call the intro routine
     but as this has not been written, it can't. }
    clrscr;
    gotoXY(20,13);   write('Sorry, not available ');
    delay(5000),
    screen,
   end
  else
   begin
    if (cat = no1) or (cat = no2) then
     begin
     end
    else
     begin
      gotoXY(29,18);   write('Invalid response.');
      delay(5000);
      screen;
     end,
   end;
until (cat = no1) or (cat = no2);
end,

procedure bar(k : integer);  { this adds in the parts of the bar
                               that other beers cannot reach. }
var
 write_start : integer;
 big_word : string[52],
begin
 Hstart[1] := 3,   Hstart[2] := 5,
 case k of
  1 : begin
       big_word := 'options menu',
       Vstart[1] := 33;     Vstart[2] := 48;
      end,
  2 : begin
       big_word := 'static frequency and amplitude';
       Vstart[1] := 24,     Vstart[2] := 57,
      end,
  3 : begin
       big_word := 'static frequency and variable amplitude';
       Vstart[1] := 20;     Vstart[2] := 62;
      end,
  4 : begin
       big_word := 'static frequency and variable amplitude - automatic';
       Vstart[1] := 13,     Vstart[2] := 67;
      end,
  5 : begin
       big_word := 'static frequency and variable amplitude - manual',
       Vstart[1] := 15,     Vstart[2] := 66,
      end,
  6 . begin
       big_word := 'variable frequency and static amplitude';
       Vstart[1] := 20;     Vstart[2] := 62,
      end,
  7 : begin
       big_word := 'variable frequency and static amplitude - automatic';
       Vstart[1] := 13,     Vstart[2] := 67;
      end,
  8 : begin
       big_word := 'variable frequency and static amplitude - manual',
       Vstart[1] := 15;     Vstart[2] := 66;
      end;
  9 : begin
       big_word := 'variable frequency and amplitude';
       Vstart[1] := 23;     Vstart[2] := 58,
      end,
 10 : begin
       big_word := 'introduction';
       Vstart[1] := 33,     Vstart[2] := 48,
```

```
      end,
   11 : begin
        big_word := 'instructions';
        Vstart[1] := 33,      Vstart[2] := 48,
      end,
   12 : begin
        big_word := 'pulse';
        Vstart[1] := 36,      Vstart[2] := 44;
      end,
  end,
  gotoXY((Vstart[1]+2),4),   write(big_word);
  box(3),
end,

procedure menu01;
var
  cat : char;
begin
  repeat
    screen,
    bar(1),
    Hstart[1] := 10;    Hstart[2] := 17;
    Vstart[1] := 18,    Vstart[2] := 64;
    box(2);
    gotoXY(20,11);  write('s - static frequency and amplitude');
    gotoXY(20,12),  write('f - static frequency and variable amplitude');
    gotoXY(20,13);  write('a - variable frequency and static amplitude');
    gotoXY(20,14),  write('v - variable frequency and amplitude');
    gotoXY(20,15),  write('p - pulse'),
    gotoXY(20,16),  write('x - exit program'),
    buffer;
    cat := readkey,
    case cat of
     Ls  : option_sfa;
     US  : option_sfa,
     Lf  : option_sfva,
     UF  : option_sfva,
     La  : option_vfsa;
     UA  : option_vfsa,
     Lv  : option_vfa,
     UV  : option_vfa,
     L_p : pulse;
     U_P : pulse;
     Lx  : exit;
     UX  : exit;
    else
     gotoXY(27,20),  write('Invalid response '),
     delay(5000);
     gotoXY(27,20);  write('                 '),
    end,
   until (cat = Lx) or (cat = UX),
  end;

{**********************************************************************
* This is where it all begins. Here are all the entry procedures *
* and the display procedures for the running of the program.     *
**********************************************************************}
procedure single_freq(var fq : real),
{ This function accepts a single frequency value }
var
  limits : boolean,
  cat : char;
  numstr : string[15],
  i : integer;
begin
  limits := false;
  while not limits do
    begin
      gotoXY(3,8);  write('Enter frequency (in MHz): ');
      fq := DS_array[1];
      i := 1,
      str(fq:9:6, numstr),
      gotoXY(30,8); write(numstr);
      repeat
        buffer;
        cat := readkey;
        if cat = null then
  begin
    cat := readkey;
    case cat of
     left :
      begin
        if i <= 1 then
          begin
            i := 1;
          end
        else
          begin
            i := i-1;
          end,
      end,
     right :
      begin
        if i >= 11 then
          begin
            i := 11;
          end
        else
          begin
            i := i+1,
          end,
      end;
    end,
   end;
  if i = 11 then
    begin
      fq := 1234;
      gotoXY(29,8),  write('         ');
      gotoXY(30,8),  write('other'),
    end
  else
    begin
      fq := DS_array[i];
      str(fq:9:6, numstr);
      gotoXY(29,8),  write('         '),
      gotoXY(30,8);  write(numstr);
    end;
  until cat = enter;
  if fq = 1234 then
    begin
      repeat
        gotoXY(29,8), write('                 ');
        gotoXY(3,8);  write('Enter frequency (in MHz): ');
        readln(dummyy),
        error1(29,8),
      until fancy = 0;
      fq := realvalue,
      if (fq <= 0) or (fq > 20) then
        begin
          gotoXY(29,8);  write('                         ')
        end
      else
        begin
          limits := true;
        end,
    end
  else
    begin
      limits := true,
    end;
  end;
end,

procedure enter_frequency(var lower_f, upper_f, f_incr : real);
{ This procedure allows the user to enter all the values required by the
variable frequency part of the program  }
var
  fish, chips : boolean;
  numstr1, numstr2 : string[15],
  i : integer;
  cat : char;
begin
  fish := false,
  while not fish do
    begin
      gotoXY(3,10);  write('Enter minimum frequency (in Mhz): '),
      gotoXY(3,11);  write('Enter maximum frequency (in MHz): ');
      lower_f := d_array[1,1];
      upper_f := d_array[1,2];
      i := 1;
      str(lower_f:9:6, numstr1);
      str(upper_f:9:6, numstr2),
      gotoXY(38,10);  write(numstr1);
      gotoXY(38,11);  write(numstr2),
      repeat
        buffer;
        cat := readkey;
        if cat = null then
          begin
            cat := readkey;
            case cat of
              left :
                begin
                  if i <= 1 then
                    begin
                      i := 1;
                    end
                  else
                    begin
                      i := i-1;
                    end,
                end,
              right :
                begin
                  if i >= 11 then
                    begin
                      i := 11;
                    end
                  else
                    begin
                      i := i+1;
                    end,
                end;
            end,
          end,
        if i = 11 then
          begin
            lower_f := 1234,
```

```
    gotoXY(37,10), write('          ');
    gotoXY(37,11); write('          '),
    gotoXY(38,10), write('other');
    gotoXY(38,11); write('other');
   end
  else
   begin
    lower_f := D_array[i,1],
    upper_f := d_array[i,2];
    str(lower_f:9:6, numstr1);
    str(upper_f:9:6, numstr2),
    gotoXY(37,10), write('          ');
    gotoXY(37,11); write('          ');
    gotoXY(38,10), write(numstr1);
    gotoXY(38,11); write(numstr2);
   end,
until cat = enter;
if lower_f = 1234 then
 begin
  chips := false,
  while not chips do
   begin
    repeat
     gotoXY(37,10); write('                ');
     gotoXY(37,11); write('                ');
     gotoXY(3,10), write('Enter minimum frequency (in Mhz): '),
     readln(dummyy);
     error1(37,10),
    until fancy = 0;
    lower_f := realvalue,
    if (lower_f <= 0) or (lower_f > 20) then
     begin
      gotoXY(37,10); write('                    ')
     end
    else
     begin
      chips := true,
     end;
   end;
chips := false;
while not chips do
 begin
  repeat
   gotoXY(37,11); write('                ');
   gotoXY(3,11); write('Enter maximum frequency (in MHz): ');
   readln(dummyy);
   error1(37,11);
  until fancy = 0;
  upper_f := realvalue;
  if (upper_f <= 0) or (upper_f > 20) then
          begin
           gotoXY(37,11), write('                    ')
          end
         else
          begin
           if upper_f <= lower_f then
            begin
             gotoXY(37,11); write('Try max larger than min ');
             delay(4000);
             gotoXY(37,11); write('                    ');
            end
           else
            begin
             chips := true;
             fish := true;
            end,
          end,
       end;
    end
   else
    begin
     fish := true;
    end;
 end,
fish := false;
while not fish do
 begin
  gotoXY(3,12); write('Enter frequency increment (in MHz). '),
  f_incr := D_array[1,3],
  i := 1;
  str(f_incr:9:6, numstr1);
  gotoXY(40,12); write(numstr1);
  repeat
   buffer;
   cat := readkey;
   if cat = null then
    begin
     cat := readkey;
     case cat of
      left :
       begin
        if i <= 1 then
         begin
          i := 1;
         end
        else
         begin
          i := i-1,
         end,
       end;
      right :
       begin
        if i >= 11 then
         begin
          i := 11;
         end
        else
         begin
          i := i+1,
         end;
       end,
     end;
    end,
  if i = 11 then
   begin
    f_incr := 1234;
    gotoXY(39,12); write('          ');
    gotoXY(40,12), write('other');
   end
  else
   begin
    f_incr := d_array[i,3],
    str(f_incr:9:6, numstr1),
    gotoXY(39,12), write('          ');
    gotoXY(40,12); write(numstr1);
   end,
  until cat = enter;
  if f_incr = 1234 then
   begin
    repeat
     gotoXY(39,12); write('                    ');
     gotoXY(3,12); write('Enter frequency increment (in MHz): ');
     readln(dummyy);
     error1(39,12),
    until fancy = 0;
    f_incr := realvalue;
    if f_incr < 0 then
     begin
      gotoXY(39,12); write('Cannot be negative.');
      delay(4000),
      gotoXY(39,12); write('                    ');
     end
    else
     begin
      if f_incr > 1 then
       begin
        gotoXY(39,12); write('Try something < 1.');
        delay(4000),
        gotoXY(39,12); write('                    ');
       end
      else
       begin
        fish := true;
       end,
      end
     else
      begin
       fish := true,
      end;
    end,
  end,
end,

procedure single_amp(j : integer; var Vout_pp : real);
{ This function accepts a single amplitude value }
var
 limits : boolean;
 i : integer;
begin
 case j of
  1 : i := 12,
  2 : i := 15,
  3 : i := 16;
 end,
 limits := false,
 while not limits do
  begin
   repeat
    gotoXY(3,i); write('Enter amplitude (in volts): ');
    readln(dummyy);
    error1(31,i);
   until fancy = 0;
   Vout_pp := realvalue;
   if (Vout_pp <= 0) or (Vout_pp > 12) then
    begin
     gotoXY(31,i), write('                    ')
    end
   else
    begin
     limits := true,
    end;
  end,
end;

procedure enter_amplitude(var lower_v, upper_v, a_incr : real),
{ This procedure allows the user to enter all the values required by the
variable amplitude part of the program. }
```

```
var
 fish, chips : boolean,
begin
 fish := false,
 while not fish do
  begin
   chips := false,
   while not chips do
    begin
     repeat
      gotoXY(3,13); write('Enter minimum amplitude (in volts): ');
      readln(dummyy);
      error1(39,13);
     until fancy = 0;
     lower_v := realvalue;
     if (lower_v <= 0) or (lower_v > 12) then
      begin
       gotoXY(39,13); write('                    ')
      end
     else
      begin
       chips := true,
      end,
    end;
  chips := false;
  while not chips do
   begin
    repeat
     gotoXY(3,14); write('Enter maximum amplitude (in volts): ');
     readln(dummyy);
     error1(39,14);
    until fancy = 0;
    upper_v := realvalue;
    if (upper_v <= 0) or (upper_v > 12) then
     begin
      gotoXY(39,14); write('                    ')
     end
    else
     begin
      if upper_v <= lower_v then
       begin
        gotoXY(39,14); write('Try max larger than min.');
        delay(4000);
        gotoXY(39,14); write('                    ');
       end
      else
       begin
        chips := true;
        fish := true,
       end,
     end,
  fish := false;
  while not fish do
   begin
    repeat
     gotoXY(3,15); write('Enter amplitude increment (in volts): '),
     readln(dummyy);
     error1(41,15),
    until fancy = 0;
    a_incr := realvalue;
    if a_incr < 0 then
     begin
      gotoXY(41,15), write('Cannot be negative.');
      delay(4000),
      gotoXY(41,15), write('                    ');
     end
    else
     begin
      if a_incr > 1.0 then
       begin
        gotoXY(41,15); write('Try something < 1.');
        delay(4000);
        gotoXY(41,15); write('                    ');
       end
      else
       begin
        fish := true;
       end,
      end;
    end;
  end;

procedure enter_pause(j : integer; var seconds : real);
var
 hello : boolean;
 i : integer;
begin
 case j of
  1 : i := 16,
  2 : i := 13,
 end,
 hello := false,
 while not hello do
  begin
   repeat
    gotoXY(3,i); write('Enter time increment (in seconds). ');
    readln(dummyy);
    error1(38,i);
   until fancy = 0;
   seconds := realvalue,
   if seconds < 0 then
    begin
     gotoXY(38,i); write('Try something > 0 ');
     delay(4000),
     gotoXY(38,i); write('                    ');
    end
   else
    begin
     if seconds > 20 then
      begin
       gotoXY(38,i); write('Try something < 20 ');
       delay(4000);
       gotoXY(38,i); write('                    ');
      end
     else
      begin
       hello := true;
      end,
    end,
  end,
end;

procedure error1(g, h : integer),
begin
 val(dummyy, realvalue, fancy);
 if fancy = 1 then
  begin
   gotoXY(g,h); write('Invalid - character entered');
   delay(3000);
   gotoXY(g,h); write('                    ');
  end,
end,

procedure log_lin(var w : integer);   { choice of two options and return an
integer }
var
 mouse : char;
begin
 repeat
  Hstart[1] := 11;   Hstart[2] := 14,
  Vstart[1] := 31;   Vstart[2] := 49;
  box(2),
  gotoXY(33,12);  write('l - logarithmic');
  gotoXY(33,13);  write('r - linear'),
  buffer;
  mouse := readkey;
  case mouse of
   Ll : w := 1;
   UL : w := 1;
   Lr : w := 2,
   UR : w := 2;
  else
   w := 0;
   gotoXY(27,20),  write('Invalid response '),
   delay(5000),
   gotoXY(27,20); write('                '); end,
 until (w = 1) or (w = 2),
end;

{*****************************************************************
* These two functions control the new improved incrementation. The  *
* purpose was to introduce logarithmic incrementing into the frequency *
* part of the program. Extension is possible to the amplitude : it is  *
* simply a matter of altering the a_incr to exactly the same functions *
* and putting a_incr as the parameter instead of f_incr.            *
*****************************************************************}
function incr_up(u : integer; curvalue, incrvalue : real) : real,
var
 trans01, trans02, trans03, trans04, trans05, trans06 : real;
begin
 case u of
  1 :
   begin
    trans01 := (1+(incrvalue)),
    trans02 := ln(trans01);
    trans03 := (curvalue*1000000);
    trans04 := ln(trans03);
    trans05 := (trans02+trans04),
    trans06 := exp(trans05);
   end,
  2 :
   begin
    trans06 := curvalue+incrvalue,
   end,
 end,
 incr_up := (trans06/1000000);
end,

function incr_down(u : integer; curvalue, incrvalue : real) : real,
var
 trans01, trans02, trans03, trans04, trans05, trans06 . real,
begin
 case u of
  1 :
   begin
    trans01 := (1+(incrvalue)),
```

```
      trans02 := ln(trans01);
      trans03 := (curvalue*1000000);
      trans04 := ln(trans03),
      trans05 := (trans04-trans02);
      trans06 := exp(trans05),
     end,
   2 :
    begin
     trans06 := curvalue-incrvalue,
    end,
  end,
  incr_down := (trans06/1000000);
end;

procedure pulse,   { this is the pulse option }
var
 cat, mouse : char;
begin
 repeat
  screen,
  bar(12);
  gotoXY(3,21); write('This routine will send a 100ms pulse at the set values,
then will set the');
  gotoXY(3,22); write('amplitude to a minimum and return the frequency to the
test frequency ');
  gotoXY(3,7),  write('The lower limit on the frequency is 0 and the upper limit
is 20MHz.'),
  gotoXY(3,11); write('The lower limit on the amplitude is 0 and the upper limit
is 12 volts ');
  repeat
   single_freq(fq);
   single_amp(1, Vout_pp);
   repeat
    gotoXY(25,24);   write('Are these values correct (y/n)?');
    readln(cat);
    if (cat = no1) or (cat = no2) then
     begin
      gotoXY(29,8);  write('                          ');
      gotoXY(31,12); write('                          ');
      gotoXY(56,24); write('             ');
     end
    else
     begin
      if (cat <> yes1) and (cat <> yes2) then
       begin
        gotoXY(25,24);   write('    Invalid response         ');
        delay(4000),
       end;
     end,
   until (cat = yes1) or (cat = yes2) or (cat = no1) or (cat = no2);
   until (cat = yes1) or (cat = yes2),
   screen;
   bar(12);
   gotoXY(22,13);
   write('Now sending a ',Vout_pp 6.3,'V ',screen_freq(fq).6 3,show_range(fq),'
signal.'),
   generate;  { It's amazing how simple it is to actually do the thing.}
   delay(100), { A little delay, then... }
   reset;
   repeat
    screen;
    bar(12);
    Hstart[1] := 11;    Hstart[2] := 15;
    Vstart[1] := 13;    Vstart[2] := 68,
    box(2);
    gotoXY(15,12);  write('r - repeat with different frequency and/or amplitude');
    gotoXY(15,13),  write('o - return to the options menu');
    gotoXY(15,14);  write('x - exit program');
    buffer;
    mouse := readkey;
    if (mouse = Lx) or (mouse = UX) then
     begin
      exit,
     end
    else
     begin
      if (mouse <> Lo) and (mouse <> UO) and (mouse <> Lr) and (mouse <>
UR) then
       begin
        gotoXY(27,20),  write('Invalid response.');
        delay(5000);
        gotoXY(27,20);  write('             ');
       end,
      end;
   until (mouse = Lo) or (mouse = UO) or (mouse = Lr) or (mouse = UR);
  until (mouse = Lo) or (mouse = UO);
end,

procedure option_sfa;   { this is the single value option }
var
 cat, mouse : char;
begin
 repeat
  screen;
  bar(2);
  gotoXY(3,21);  write('<esc> acts as both exit and panic button, reducing signal
amplitude to a');
  gotoXY(3,22),  write('minimum and returning the frequency to the test
frequency.'),
  gotoXY(3,7);  write('The lower limit on the frequency is 0 and the upper limit
is 20MHz.');
  gotoXY(3,11);  write('The lower limit on the amplitude is 0 and the upper limit
is 12 volts.');
  repeat
   single_freq(fq);
   single_amp(1, Vout_pp),
   repeat
    gotoXY(25,24);   write('Are these values correct (y/n)?'),
    readln(cat),
    if (cat = no1) or (cat = no2) then
     begin
      gotoXY(29,8);  write('                          ');
      gotoXY(31,12); write('                          ');
      gotoXY(56,24), write('             ');
     end
    else
     begin
      if (cat <> yes1) and (cat <> yes2) then
       begin
        gotoXY(25,24);   write('    Invalid response         ');
        delay(4000),
       end,
     end,
    until (cat = yes1) or (cat = yes2) or (cat = no1) or (cat = no2);
   until (cat = yes1) or (cat = yes2);
   screen;
   bar(2),
{ It just struck me that the best way to display these values
   is limited by the method of display.  You have to specify the
   number of decimal places etc.  But what if your number is too
   small to be shown?  Well then, you add more decimal places to
   your variable display but then it just looks stupid. }
gotoXY(48,24);   write('<esc> - exit and panic button');
   gotoXY(22,13);
   write('Now sending a ',Vout_pp 6 3,'V ',screen_freq(fq) 6.3,show_range(fq),'
signal.'),
   generate;  { It's amazing how simple it is to actually do the thing }
   buffer;
   repeat
    cat := readkey;
   until cat = escape;
   { This is the point when a user realises he's in }
   { deep kimshee and panics, but NEVER FEAR!! }
   reset,
   { this last part is the menu at the end of the routine. }
   repeat
    screen,
    bar(2);
    Hstart[1] := 11;    Hstart[2] := 15,
    Vstart[1] := 13,    Vstart[2] := 68,
    box(2),
    gotoXY(15,12);   write('r - repeat with different frequency and/or amplitude');
    gotoXY(15,13);   write('o - return to the options menu');
    gotoXY(15,14);   write('x - exit program');
    buffer;
    mouse := readkey;
    if (mouse = Lx) or (mouse = UX) then
     begin
      exit,
     end
    else
     begin
      if (mouse <> Lo) and (mouse <> UO) and (mouse <> Lr) and (mouse <>
UR) then
       begin
        gotoXY(27,20);   write('Invalid response.');
        delay(5000),
        gotoXY(27,20),   write('             ');
       end,
      end;
   until (mouse = Lo) or (mouse = UO) or (mouse = Lr) or (mouse = UR);
  until (mouse = Lo) or (mouse = UO),
end,

procedure option_sfva,
var
 k : integer;
begin
 repeat
  k := 0;
  screen;
  bar(3);
  man_auto(k);
  case k of
   1 : man_sfva(k);
   2 . auto_sfva(k),
  end;
 until k = 3;
end,

procedure option_vfsa;
var
 k : integer;
begin
 repeat
  k := 0;
  screen,
  bar(6);
```

```
   man_auto(k);
   case k of
    1 : man_vfsa(k);
    2 : auto_vfsa(k);
   end,
  until k = 3,
end,

procedure man_auto(var k : integer);    { choice of three options and return an
integer }
var
 mouse : char;
begin
 repeat
  Hstart[1] := 11,    Hstart[2] := 15,
  Vstart[1] := 26;    Vstart[2] := 55;
  box(2),
  gotoXY(28,12);   write('a - automatic');
  gotoXY(28,13);   write('m - manual');
   gotoXY(28,14),   write('o - return to options menu');
   buffer;
   mouse := readkey;
   case mouse of
    Lm : k := 1;
    UM : k := 1;
    La . k := 2;
    UA . k := 2;
    Lo . k := 3;
    UO : k := 3;
   else
    k := 0;
    gotoXY(27,20);   write('Invalid response ');
    delay(5000),
    gotoXY(27,20);  write('                ');   end,
  until (k = 1) or (k = 2) or (k = 3);
end;

procedure auto_sfva(var k : integer);
var
 cat, mouse : char;
 seconds, a_incr : real,
 upper_v, lower_v, A1, A2 : real;
begin
 repeat
  screen,
  bar(4),
  gotoXY(3,21);  write('<esc> acts as both exit and panic button, reducing signal
amplitude to a');
  gotoXY(3,22),  write('minimum and returning the frequency to the test
frequency ');
  gotoXY(3,7);   write('The lower limit on the frequency is 0 and the upper limit
is 20MHz.'),
  gotoXY(3,10),  write('This routine scans automatically in a range of amplitudes
within the limits');
  gotoXY(3,11);  write('0 and 12 volts.');
  gotoXY(3,12);  write('An amplitude increment and a time increment (pause)
must also be entered ');
  gotoXY(3,18);  write('<space> stops scan and holds at current frequency.');
  gotoXY(3,19),  write('<enter> resumes scan.');
  repeat
   single_freq(fq);
   enter_amplitude(lower_v, upper_v, a_incr);
   enter_pause(1, seconds);
   repeat
    gotoXY(25,24);
    write('Are these values correct (y/n)?');
    readln(cat);
    if (cat = no1) or (cat = no2) then
     begin
      gotoXY(29,8),  write('                    ');
      gotoXY(39,13); write('                    ');
      gotoXY(39,14); write('                    ');
      gotoXY(41,15); write('                    ');
      gotoXY(38,16); write('                    ');
      gotoXY(56,24), write('          ');
     end
    else
     begin
      if (cat <> yes1) and (cat <> yes2) then
       begin
        gotoXY(25,24); write('    Invalid response        ');
        delay(4000),
       end,
     end,
    until (cat = yes1) or (cat = yes2) or (cat = no1) or (cat = no2);
   until (cat = yes1) or (cat = yes2),
   screen,
   bar(4);
   gotoXY(48,24);   write('<esc> - exit and panic button');
   gotoXY(11,11);
   write('Now sending a ',screen_freq(fq):6:3,show_range(fq),' signal scanning
from ',lower_v:6:3,'V to ',upper_v:6:3,'V');
   { Now we have the iteration part of the program.
   The means I use to run the program is to change variables
   to short dummy names and work with those. }
   buffer;
   A1 := lower_v;
   A2 := lower_v;
   gotoXY(29,13);   write('Amplitude = ',lower_v:6:3,'volts');
   repeat
    buffer;
    gotoXY(28,15);   write('<space> holds amplitude');
    repeat,
     buffer,
     repeat
      if A2 >= A1 then
       begin
        if A2 >= upper_v then
         begin
          A2 := upper_v;
          Vout_pp := A2,
          gotoXY(29,13);  write('Amplitude = ',Vout_pp:6:3,'volts');
          generate,
          delay(trunc(1000*seconds)),
          A1 := A2;
          A2 := A1-a_incr;
         end
        else
         begin
          Vout_pp := A2,
          gotoXY(29,13);  write('Amplitude = ',Vout_pp:6:3,'volts');
          generate,
          delay(trunc(1000*seconds)),
          A1 := A2;
          A2 := A1+a_incr;
         end;
       end
      else
       begin
        if A2 <= lower_v then
         begin
          A2 := lower_v;
          Vout_pp := A2,
          gotoXY(29,13);  write('Amplitude = ',Vout_pp:6:3,'volts');
          generate,
          delay(trunc(1000*seconds)),
          A1 := A2,
          A2 := A1+a_incr;
         end
        else
         begin
          Vout_pp := A2,
          gotoXY(29,13);  write('Amplitude = ',Vout_pp:6:3,'volts');
          generate,
          delay(trunc(1000*seconds)),
          A1 := A2,
          A2 := A1-a_incr;
         end,
       end,
     until keypressed,
     cat := readkey;
    until (cat = space) or (cat = escape);
    if cat = space then
     begin
      repeat
       buffer;
       gotoXY(28,15);  write('  <enter> resumes scan    ');
       cat := readkey,
      until cat = enter;
     end,
   until cat = escape;
   reset;
   { The menu at the end of the option
   K the integer is definitely a factor here so I have gone back to add it }
   repeat
    screen,
    bar(4);
    Hstart[1] := 10;    Hstart[2] := 15,
    Vstart[1] := 15,    Vstart[2] := 66,
    box(2);
    gotoXY(17,11);   write('r - repeat with different frequency and/or range');
    gotoXY(17,12);   write('m - try manual scan');
    gotoXY(17,13);   write('o - return to options menu');
    gotoXY(17,14);   write('x - exit program');
    buffer;
    mouse := readkey;
    case mouse of
     Lx : exit;
     UX : exit,
     Lm . k := 0;
     UM : k := 0;
     Lo : k := 3,
     UO : k := 3;
    else
     if (mouse <> Lr) and (mouse <> UR) then
      begin
       gotoXY(29,20);  write('Invalid response');
       delay(4000),
       gotoXY(29,20);  write('                ');
      end;
    end,
   until (k = 0) or (k = 3) or (mouse = Lr) or (mouse = UR);
  until (k = 0) or (k = 3);
end,

procedure auto_vfsa(var k : integer);
var
 cat, mouse : char;
```

```
  seconds, f_incr : real;
  upper_f, lower_f, F1, F2 : real,
  w : integer;
begin
  repeat
    screen;
    bar(7);
    log_lin(w);
    screen;
    bar(7);
    gotoXY(3,21);  write('<esc> acts as both exit and panic button, reducing signal
amplitude to a');
    gotoXY(3,22);  write('minimum and returning the frequency to the test
frequency.');
    gotoXY(3,15);  write('The lower limit on the amplitude is 0 and the upper limit
is 12volts.');
    gotoXY(3,7);   write('This routine scans automatically in a range of frequencies
within the limits');
    gotoXY(3,8);   write('0 and 20 MHz.');
    gotoXY(3,9),  write('A frequency increment and a time increment (pause)
must also be entered.');
    gotoXY(3,18);  write('<space> stops scan and holds at current frequency.');
    gotoXY(3,19);  write('<enter> resumes scan ');
  repeat
   enter_frequency(lower_f, upper_f, f_incr);
   single_amp(3, Vout_pp);
   enter_pause(2, seconds);
   repeat
    gotoXY(25,24);
    write('Are these values correct (y/n)?');
    readln(cat);
    if (cat = no1) or (cat = no2) then
     begin
      gotoXY(37,10);  write('                    ');
      gotoXY(37,11);  write('                    ');
      gotoXY(39,12);  write('                    ');
      gotoXY(38,13);  write('                    ');
      gotoXY(31,16);  write('                    ');
      gotoXY(56,24),  write('          ');
     end
    else
     begin
      if (cat <> yes1) and (cat <> yes2) then
       begin
        gotoXY(25,24);  write('    Invalid response        ');
        delay(4000);
       end;
     end,
   until (cat = yes1) or (cat = yes2) or (cat = no1) or (cat = no2),
until (cat = yes1) or (cat = yes2),
    screen;
    bar(7);
    gotoXY(48,24);   write('<esc> - exit and panic button');
    gotoXY(11,11);
    write('Now sending a ',Vout_pp:6:3,'V signal scanning from');
    gotoXY(53,11);
    write(' ',screen_freq(lower_f):6:3,show_range(lower_f),' to
',screen_freq(upper_f):6:3,show_range(upper_f));
    { Now we have the iteration part of the program.
    The means I use to run the program is to change variables
    to short dummy names and work with those. }
    buffer;
    F1 := lower_f;
    F2 := lower_f;
    gotoXY(29,13),  write('Frequency = ',screen_freq(fq):6:3,show_range(fq)),
    repeat
     buffer;
     gotoXY(28,15);   write('<space> holds frequency');
     repeat;
      buffer;
      repeat
       if F2 >= F1 then
        begin
         if F2 >= upper_f then
          begin
           F2 := upper_f;
           fq := F2;
           gotoXY(29,13);  write('Frequency =
',screen_freq(fq):6:3,show_range(fq)),
           generate,
           delay(trunc(1000*seconds)),
           F1 := F2,
           F2 := incr_down(w, F1, f_incr);
          end
         else
          begin
           fq := F2;
           gotoXY(29,13);  write('Frequency =
',screen_freq(fq):6:3,show_range(fq)),
           generate,
           delay(trunc(1000*seconds));
           F1 := F2;
           F2 := incr_up(w, F1, f_incr);
          end,
        end
       else
        begin
         if F2 <= lower_f then
          begin
           F2 := lower_f;
           fq := F2,
           gotoXY(29,13);  write('Frequency =
',screen_freq(fq):6:3,show_range(fq)),
           generate,
           delay(trunc(1000*seconds));
           F1 := F2,
           F2 := incr_up(w, F1, f_incr),
          end
         else
          begin
           fq := F2,
           gotoXY(29,13);  write('Frequency =
',screen_freq(fq):6:3,show_range(fq)),
           generate,
           delay(trunc(1000*seconds));
           F1 := F2;
           F2 := incr_down(w, F1, f_incr);
          end;
        end;
      until keypressed,
      cat := readkey;
     until (cat = space) or (cat = escape);
     if cat = space then
      begin
       repeat
        buffer;
        gotoXY(28,15);  write(' <enter> resumes scan   '),
        cat := readkey;
       until cat = enter;
      end;
  until cat = escape;
  reset;
  { The menu at the end of the option
  K the integer is definitely a factor here so I have gone back to add it }
  repeat
   screen,
   bar(7);
   Hstart[1] := 10;    Hstart[2] := 15;
   Vstart[1] := 15,    Vstart[2] := 66,
   box(2),
   gotoXY(17,11);   write('r - repeat with different range and/or amplitude');
   gotoXY(17,12),   write('m - try manual scan');
   gotoXY(17,13);   write('o - return to options menu');
   gotoXY(17,14),   write('x - exit program');
   buffer;
   mouse := readkey;
   case mouse of
    Lx : exit;
    UX : exit,
    Lm : k := 0;
    UM : k := 0;
    Lo : k := 3,
    UO : k := 3;
   else
    if (mouse <> Lr) and (mouse <> UR) then
     begin
      gotoXY(29,20);  write('Invalid response'),
      delay(4000),
      gotoXY(29,20),  write('                ');
     end,
    end,
   until (k = 0) or (k = 3) or (mouse = Lr) or (mouse = UR);
  until (k = 0) or (k = 3),
end,

procedure man_sfva(var k : integer);
var
  cat, mouse : char;
  seconds, a_incr : real,
  upper_v, lower_v, A1, A2 : real;
begin
  repeat
    screen;
    bar(5),
    gotoXY(3,21);  write('<esc> acts as both exit and panic button, reducing signal
amplitude to a');
    gotoXY(3,22),  write('minimum and returning the frequency to the test
frequency.');
    gotoXY(3,7);   write('The lower limit on the frequency is 0 and the upper limit
is 20MHz.');
    gotoXY(3,10);  write('This routine allows manual scanning in a range of
amplitudes within the limits');
    gotoXY(3,11);  write('0 and 12 volts ');
    gotoXY(3,12);  write('An amplitude increment must also be entered ');
    gotoXY(3,18);  write('The arrow keys control the amplitude ');
    gotoXY(3,19);  write(arrow_l,' decreases and ',arrow_r,' increases the
amplitude.');
    repeat
     single_freq(fq);
     enter_amplitude(lower_v, upper_v, a_incr);
     repeat
      gotoXY(25,24);
      write('Are these values correct (y/n)?');
      readln(cat);
      if (cat = no1) or (cat = no2) then
       begin
        gotoXY(29,8);   write('                    ');
        gotoXY(39,13);  write('                    ');
```

```
      gotoXY(39,14); write('                    ');
      gotoXY(41,15); write('                    ');
      gotoXY(56,24); write('          ');
     end
    else
     begin
      if (cat <> yes1) and (cat <> yes2) then
       begin
        gotoXY(25,24); write('    Invalid response        ');
        delay(4000),
       end,
     end,
  until (cat = yes1) or (cat = yes2) or (cat = no1) or (cat = no2);
 until (cat = yes1) or (cat = yes2);
 screen;
 bar(5);
 gotoXY(48,24);  write('<esc> - exit and panic button');
 gotoXY(11,11);
 write('Now sending a ',screen_freq(fq):6:3,show_range(fq),' signal scanning
from ',lower_v:6:3,'V to ',upper_v:6:3,'V');
 { Now we have the alteration part of the program.
 The means I use to run the program is to change variables
 to short dummy names and work with those }
 gotoXY(21,15);  write('arrow keys ',arrow_l,' and ',arrow_r,' control the
amplitude');
 buffer;
 A1 := lower_v;
 gotoXY(28,13);  write('Amplitude = ',lower_v:6:3,'volts');
 Vout_pp := lower_v;
 generate;
 repeat
  buffer;
  cat := readkey;
  if cat = null then
   begin
    cat := readkey;
    if cat = left then
     begin
      A2 := A1-a_incr;
      if A2 <= lower_v then
       begin
        A2 := lower_v;
       end;
      Vout_pp := A2;
      gotoXY(28,13);  write('Amplitude = ',Vout_pp:6:3,'volts');
      generate;
     end
    else
     begin
      if cat = right then
       begin
        A2 := A1+a_incr;
        if A2 >= upper_v then
         begin
          A2 := upper_v;
         end;
        Vout_pp := A2;
        gotoXY(28,13);  write('Amplitude = ',Vout_pp:6:3,'volts');
        generate;
       end;
     end;
    A1 := A2;
   end;
until cat = escape;
reset;
{ The menu at the end of the option
K the integer is definitely a factor here so I have gone back to add it }
repeat
 screen;
 bar(5);
 Hstart[1] := 10;   Hstart[2] := 15;
 Vstart[1] := 15,   Vstart[2] := 66;
 box(2);
 gotoXY(17,11);  write('r - repeat with different frequency and/or range');
 gotoXY(17,12);  write('a - try automatic scan');
 gotoXY(17,13);  write('o - return to options menu');
 gotoXY(17,14);  write('x - exit program');
 buffer;
 mouse := readkey;
 case mouse of
  Lx : exit;
  UX : exit;
  La : k := 0;
  UA : k := 0;
  Lo : k := 3;
  UO : k := 3;
 else
  if (mouse <> Lr) and (mouse <> UR) then
   begin
    gotoXY(29,20);  write('Invalid response');
    delay(4000);
    gotoXY(29,20);  write('          ');
   end;
 end;
 until (k = 0) or (k = 3) or (mouse = Lr) or (mouse = UR);
until (k = 0) or (k = 3);
end;

procedure man_vfsa(var k : integer);

var
 cat, mouse : char;
 seconds, f_incr : real;
 upper_f, lower_f, F1, F2 : real;
 w : integer;
begin
 repeat
  screen;
  bar(8);
  log_ln(w);
  screen;
  bar(8);
  gotoXY(3,21);  write('<esc> acts as both exit and panic button, reducing signal
amplitude to a');
  gotoXY(3,22);  write('minimum and returning the frequency to the test
frequency.');
  gotoXY(3,14);  write('The lower limit on the amplitude is 0 and the upper limit
is 12volts '),
  gotoXY(3,7);  write('This routine manual scanning in a range of frequencies
within the limits');
  gotoXY(3,8);  write('0 and 20 MHz.');
  gotoXY(3,9);  write('A frequency increment must also be entered.');
  gotoXY(3,18);  write('The arrow keys control the frequency.');
  gotoXY(3,19);  write(arrow_d,' decreases and ',arrow_u,' increases the
frequency.');
  repeat
   enter_frequency(lower_f, upper_f, f_incr);
   single_amp(2, Vout_pp);
   repeat
    gotoXY(25,24);
    write('Are these values correct (y/n)?');
    readln(cat);
    if (cat = no1) or (cat = no2) then
     begin
      gotoXY(37,10);  write('                    ');
      gotoXY(37,11);  write('                    ');
      gotoXY(39,12);  write('                    ');
      gotoXY(31,15);  write('                    ');
      gotoXY(56,24);  write('          ');
     end
    else
     begin
      if (cat <> yes1) and (cat <> yes2) then
       begin
        gotoXY(25,24);  write('    Invalid response        ');
        delay(4000),
       end;
     end;
   until (cat = yes1) or (cat = yes2) or (cat = no1) or (cat = no2);
  until (cat = yes1) or (cat = yes2);
  screen;
  bar(8);
  gotoXY(48,24);  write('<esc> - exit and panic button');
  gotoXY(11,11);
  write('Now sending a ',Vout_pp:6:3,'V signal scanning from');
  gotoXY(43,11);
  write(' ',screen_freq(lower_f):6:3,show_range(lower_f),' to
',screen_freq(upper_f):6:3,show_range(upper_f));
  { Now we have the alteration part of the program.
  The means I use to run the program is to change variables
  to short dummy names and work with those. }
  gotoXY(21,15);  write('arrow keys ',arrow_d,' and ',arrow_u,' control the
amplitude');
  buffer;
  F1 := lower_f;
  F2 := lower_f;
  gotoXY(30,13);  write('Frequency = ',screen_freq(F1):6:3,show_range(F1));
  generate;
  repeat
   buffer;
   cat := readkey;
   if cat = null then
    begin
     cat := readkey;
     if cat = down then
      begin
       F2 := incr_down(w, F1, f_incr);
       if F2 <= lower_f then
        begin
         F2 := lower_f;
        end;
       fq := F2;
       gotoXY(30,13);  write('Frequency =
',screen_freq(fq):6:3,show_range(fq));
       generate;
      end
     else
      begin
       if cat = up then
        begin
         F2 := incr_up(w, F1, f_incr);
         if F2 >= upper_f then
          begin
           F2 := upper_f;
          end;
         fq := F2;
         gotoXY(30,13);  write('Frequency =
',screen_freq(fq):6:3,show_range(fq));
```

```
        generate;
       end;
     end,
    F1 := F2,
   end;
until cat = escape;
reset;
{ The menu at the end of the option
K the integer is definitely a factor here so I have gone back to add it }
repeat
 screen,
 bar(8);
 Hstart[1] := 10;   Hstart[2] := 15,
 Vstart[1] := 15;   Vstart[2] := 66,
 box(2),
 gotoXY(17,11);  write('r - repeat with different range and/or amplitude');
 gotoXY(17,12);  write('a - try automatic scan');
 gotoXY(17,13);  write('o - return to options menu');
 gotoXY(17,14);  write('x - exit program');
 buffer;
 mouse := readkey,
 case mouse of
   Lx : exit;
   UX : exit;
   La : k := 0;
   UA : k := 0;
   Lo : k := 3,
   UO . k := 3;
  else
   if (mouse <> Lr) and (mouse <> UR) then
    begin
     gotoXY(29,20);  write('Invalid response');
     delay(4000),
     gotoXY(29,20);  write('                ');
    end,
  end,
 until (k = 0) or (k = 3) or (mouse = Lr) or (mouse = UR);
until (k = 0) or (k = 3);
end;

procedure option_vfa;
var
 cat, mouse : char;
 seconds, f_incr, a_incr : real,
 upper_f, lower_f, F1, F2, upper_v, lower_v, A1, A2 : real,
 w : integer;
begin
 repeat
  screen;
  bar(9),
  log_lin(w);
  screen;
  bar(9),
  gotoXY(3,21);  write('<esc> acts as both exit and panic button, reducing signal
amplitude to a');
  gotoXY(3,22);  write('minimum and returning the frequency to the test
frequency ');
  gotoXY(3,7);  write('This routine allows manual scanning in, a range of
frequencies within the');
  gotoXY(3,8),  write('limits 0 and 20 MHz, and a range of amplitudes within
the limits 0 and 12V '),
  gotoXY(3,9);  write('A frequency increment and an amplitude increment must
also be entered.');
  gotoXY(3,17),  write('The arrow keys control the frequency.');
  gotoXY(3,18);  write(arrow_d,' decreases and ',arrow_u,' increases the
frequency ');
  gotoXY(3,19);  write(arrow_l,' decreases and ',arrow_r,' increases the
amplitude.');
  repeat
   enter_frequency(lower_f, upper_f, f_incr);
   enter_amplitude(lower_v, upper_v, a_incr);
   repeat
    gotoXY(25,24);
    write('Are these values correct (y/n)?');
    readln(cat);
    if (cat = no1) or (cat = no2) then
     begin
      gotoXY(37,10);  write('                    ');
      gotoXY(37,11);  write('                    ');
      gotoXY(39,12);  write('                    ');
      gotoXY(39,13);  write('                    ');
      gotoXY(39,14);  write('                    ');
      gotoXY(41,15),  write('                    ');
      gotoXY(56,24);  write('          ');
     end
    else
     begin
      if (cat <> yes1) and (cat <> yes2) then
       begin
        gotoXY(25,24);  write('    Invalid response      ');
        delay(4000),
       end,
     end;
   until (cat = yes1) or (cat = yes2) or (cat = no1) or (cat = no2);
  until (cat = yes1) or (cat = yes2);
  screen;
  bar(9),
  gotoXY(48,24);  write('<esc> - exit and panic button');
   gotoXY(11,9);   write('Now sending a signal with amplitude between
',lower_v:6 3,'V and ',upper_v:6 3,'V'),
   gotoXY(33,10);  write('and frequency between
',screen_freq(lower_f) 6.3,show_range(lower_f)),
   gotoXY(64,10);  write(' and ',screen_freq(upper_f) 6 3,show_range(upper_f));
   { Now we have the alteration part of the program.
   The means I use to run the program is to change variables
   to short dummy names and work with those. }
   gotoXY(21,16);  write('arrow keys ',arrow_d,' and ',arrow_u,' control the
frequency'),
   gotoXY(31,17);  write(arrow_l,' and ',arrow_r,' control the amplitude');
   buffer;
   F1 := lower_f;
   A1 := lower_v;
   gotoXY(30,12);  write('Frequency =
',screen_freq(lower_f) 6 3,show_range(lower_f));
   gotoXY(30,14);  write('Amplitude = ',lower_v:6 3,'volts');
   vout_pp := lower_v;
   fq := lower_f;
   generate;
   repeat
    buffer;
    cat := readkey;
    if cat = null then
     begin
      cat := readkey;
      case cat of
       down :
        begin
         F2 := incr_down(w, F1, f_incr);
         if F2 <= lower_f then
          begin
           F2 := lower_f;
          end;
         fq := F2,
         gotoXY(30,12);  write('Frequency =
',screen_freq(fq) 6 3,show_range(fq),'    ');
         generate,
        end,
       up   :
        begin
         F2 := incr_up(w, F1, f_incr);
         if F2 >= upper_f then
          begin
           F2 := upper_f;
          end,
         fq := F2;
         gotoXY(30,12),  write('Frequency =
',screen_freq(fq) 6 3,show_range(fq),'    ');
         generate;
        end,
       left :
        begin
         A2 := A1-a_incr;
         if A2 <= lower_v then
          begin
           A2 := lower_v;
          end,
         Vout_pp := A2,
         gotoXY(30,14);  write('Amplitude = ',Vout_pp 6.3,'volts    '),
         generate;
        end,
       right :
        begin
         A2 := A1+a_incr;
         if A2 >= upper_v then
          begin
           A2 := upper_v;
          end;
         Vout_pp := A2,
         gotoXY(30,14);  write('Amplitude = ',Vout_pp 6.3,'volts    ');
         generate,
        end,
      end,
     A1 := A2;
     F1 := F2,
    end,
  until cat = escape;
  reset;
  { The menu at the end of the option }
  repeat
   screen;
   bar(9),
   Hstart[1] := 11;   Hstart[2] := 15;
   Vstart[1] := 23;   Vstart[2] := 58,
   box(2),
   gotoXY(25,12);  write('r - repeat with different ranges');
   gotoXY(25,13);  write('o - return to options menu');
   gotoXY(25,14);  write('x - exit program'),
   buffer;
   mouse := readkey;
   if (mouse = Lx) or (mouse = UX) then
    begin
     exit,
    end
   else
    begin
     if (mouse <> Lr) and (mouse <> UR) and (mouse <> Lo) and (mouse <>
UO) then
```

```
        begin
         gotoXY(29,20);  write('Invalid response');
         delay(4000);
         gotoXY(29,20),  write('                ');
        end,
      end,
   until (mouse = Lr) or (mouse = UR) or (mouse = Lo) or (mouse = UO);
  until (mouse = Lo) or (mouse = UO),
end;

{*****************************************************************
* Procedures/Functions Group ( X) Miscellaneous                  *
* Here are contained the odd little functions and procedures     *
* that make up the program, especially those that do odd little *
* things.                                                        *
*****************************************************************}
function screen_freq(bam : real) : real,
{ This function takes the value for fq and returns an appropriate
value in the Mhz or the kHz range depending on the size of the
current value of fq. }
 var
  F_trans : real,
 begin
  if bam >= 0 01 then
   begin
    F_trans := bam;
   end
  else
   begin
    F_trans := bam*1000;
   end;
  screen_freq := F_trans;
end,

function show_range(bam_bam : real) : show;
{ This function takes the value for fq and returns either 'kHz' or
'MHz' as a string for the displaying of. }
var
 trans : show;
begin
 if bam_bam >= 0 01 then
  begin
   trans := 'MHz';
  end
 else
  begin
   trans := 'kHz';
  end;
 show_range := trans,
end,

procedure exit,
var
 mouse : char;
begin
 repeat,
  clrscr;
  gotoXY(23,13),   write('Are you sure you want to exit (y/n)?');
  mouse := readkey;
  case mouse of
   yes1 :
    begin
     { It's here that the anime2 would go }
     clrscr;
     halt,
    end,
   yes2 :
    begin
     { Ditto about anime02 }
     clrscr;
     halt,
    end,
   no1 :
    begin
     clrscr;
     gotoXY(29,13),   write('Rightyho! Going back in.');
     delay(3000),
     clrscr;
    end,
   no2 .
    begin
     clrscr;
     gotoXY(29,13);   write('Rightyho! Going back in.');
     delay(3000);
     clrscr;
    end,
   else
    begin
     clrscr;
     gotoXY(33,13),   write('Invalid response'),
     delay(3000);
     clrscr;
    end,
   end;
  until (mouse = no1) or (mouse = no2);
 end,

{*****************************************************************
*****************************************************************
**                                                             **
**                THE MAIN PROGRAM                             **
**                                                             **
*****************************************************************
*****************************************************************}

begin
 clrScr,
 byte_table;
 freq_table;
 default_array;
 screen01,
 clrscr,
 delay(500),
 screen02,
 clrscr;
 screen03,
 screen;
 screen04,
 screen;
 screen05,
 menu01;
 exit,
end.
```

References

1. H.A.Pohl (1978) *Dielectrophoresis*
   Cambridge University Press, Cambridge
2. M.Washizu, S.Suzuki, O.Kurosawa, T.Nishizaki and T.Shinohara (1994)
   IEEE Transactions on Industry Applications **30** 835-843
3. Y.Huang and R.Pethig (1991)
   Measurement Science and Technology **2** 1142-1146
4. X-B.Wang, Y.Huang, J.P.H.Burt, G.H.Markx and R.Pethig (1993)
   Journal of Physics D: Applied Physics **26** 1278-1285
5. M.P.Hughes, X-B.Wang, F.F.Becker, P.R.C.Gascoyne and R.Pethig (1994)
   Journal of Physics D: Applied Physics **27** 1564-1570
6. H.A.Pohl and K.Pollock (1978)
   Journal of Electrostatics **5** 337-342
7. N.Matsumoto, T.Matsue and I.Uchida (1994)
   Bioelectrochemistry and Bioenergetics **34** 199-202
8. R.Pethig, Y.Huang, X-B.Wang and J.P.H.Burt (1992)
   Journal of Physics D: Applied Physics **24** 881-888

Chapter Six

Results and discussion: Electric field simulation

6.1 Introduction

The dielectrophoretic behaviour of particles in an electrode array is governed by the electric field in the array through the dielectrophoretic force equation (equation 4.20 and 4.21):

$$\underline{\mathbf{F}}_{dep} = -\frac{1}{2}\upsilon u_p \nabla |\underline{\mathbf{E}}|^2 \tag{6.1}$$

This force is the gradient of the dielectrophoretic potential energy which is the potential energy of the dipole in the electric field. This is the work required to bring the dipole from infinity to its current position and can be represented by equation (4.22):

$$U_{dep} = \frac{1}{2}\upsilon u_p |\underline{\mathbf{E}}|^2 \tag{6.2}$$

In order to properly understand the movement of a particle an expression, analytical or numerical, must be first found for the electric field. Previous work on electric field calculation for dielectrophoresis includes analytical work on simple electrode geometries [1,2], numerical simulation for the castellated and polynomial geometries [3,4] and simulation of more complicated "field cages" [5].

Most of the electric field simulation that has been published previously has been to determine the nature of particle trapping rather than movement. The most common example of this is the polynomial electrodes. In the centre of the electrodes there is a negative dielectrophoretic potential well or "trap" which is a region of low field strength surrounded completely by high field strength regions (a local minimum in the field strength). The presence of a negative DEP trap can be determined by considering the electric field magnitude, since the dielectrophoretic potential is proportional to the field strength squared. By analogy, if a particle experiences positive dielectrophoresis, it will be trapped in a potential minimum at a high field point surrounded completely by low field points (a local maximum in field strength). This case is slightly different in that high field points are always found at electrode edges and they are not usually completely surrounded by low field points. The negative dielectrophoretic traps are always found away from electrode surfaces.

Apart from this difference, the idea of "trapping" is valid for both positive and negative dielectrophoresis. Positive dielectrophoretic "traps" will be found at local high field maxima and negative "traps" will be found at local low field minima.

In order to determine the electric field in a system, Poisson's equation (equation 4.26) must first be solved for the electric potential. However, it is difficult to solve Poisson's equation analytically unless the boundary and initial conditions have a continuously differentiable analytical representation. If such representations do not exist, it is easier to obtain the electric potential by a numerical method.

This chapter outlines the methods used to simplify and model the electrode structures, then presents and discusses the results of the electric field simulations. Plots of the electric field strength are used to determine regions where dielectrophoretic trapping is likely to occur. In order to determine the direction of particle movement in the electrode arrays, the dielectrophoretic force vector is also calculated.

6.2 Electrode models, simplification and symmetry boundaries

The first step in modelling the electric field was to create a numerical model of the problem space, which in this case was the electrode array. Maxwell uses a Computer Aided Design package to create three dimensional shapes representing the electrodes, the glass substrate and the solution placed on the array. Each of these shapes is assigned the electrical properties of the appropriate material and the boundary formed by the surface of the electrode is assigned a constant potential. Maxwell then divides the problem space into tetrahedral elements and solves for the potential at every node (section 4.4.2).

However, there are difficulties associated with modelling large electrode patterns. The software cannot easily solve problems where high aspect ratios exist between the electrodes and the whole solution space. The electrodes are 120nm thick which limits the size of the problem space to approximately 1000 times larger. Also, the more complicated the shape, the higher the required number of elements to give a high degree of accuracy to the solution. Therefore in order to accurately solve problems, the problem space must be kept as small as possible.

The models can be simplified using the boundary conditions (section 4.4.2), the symmetry of the electrodes and the method of images. The array is reduced to its smallest repeated shape, which is used as a basic cell, and symmetry boundaries are then used to create images of the cell. Figure (6.1) shows a schematic outline of one of the four electrodes in the hyperbolic design with two symmetry boundaries creating the complete design.

There are two different boundary conditions which can be applied to the symmetry planes. The Dirichlet boundary condition with a constant potential of zero (equation(4.25)) creates a plane of odd symmetry and the image object has a potential equal to the negative of the original. The Neumann boundary condition (equation (4.26)) creates a plane of even symmetry and the resulting image object has the same potential as the original. Combinations of these

symmetry planes can be used to map the basic cell repeatedly to form the complete electrode array. The improvement in the solution follows automatically: the numerical analysis is performed on a much smaller problem space with a smaller aspect ratio and the solution is correspondingly more accurate.

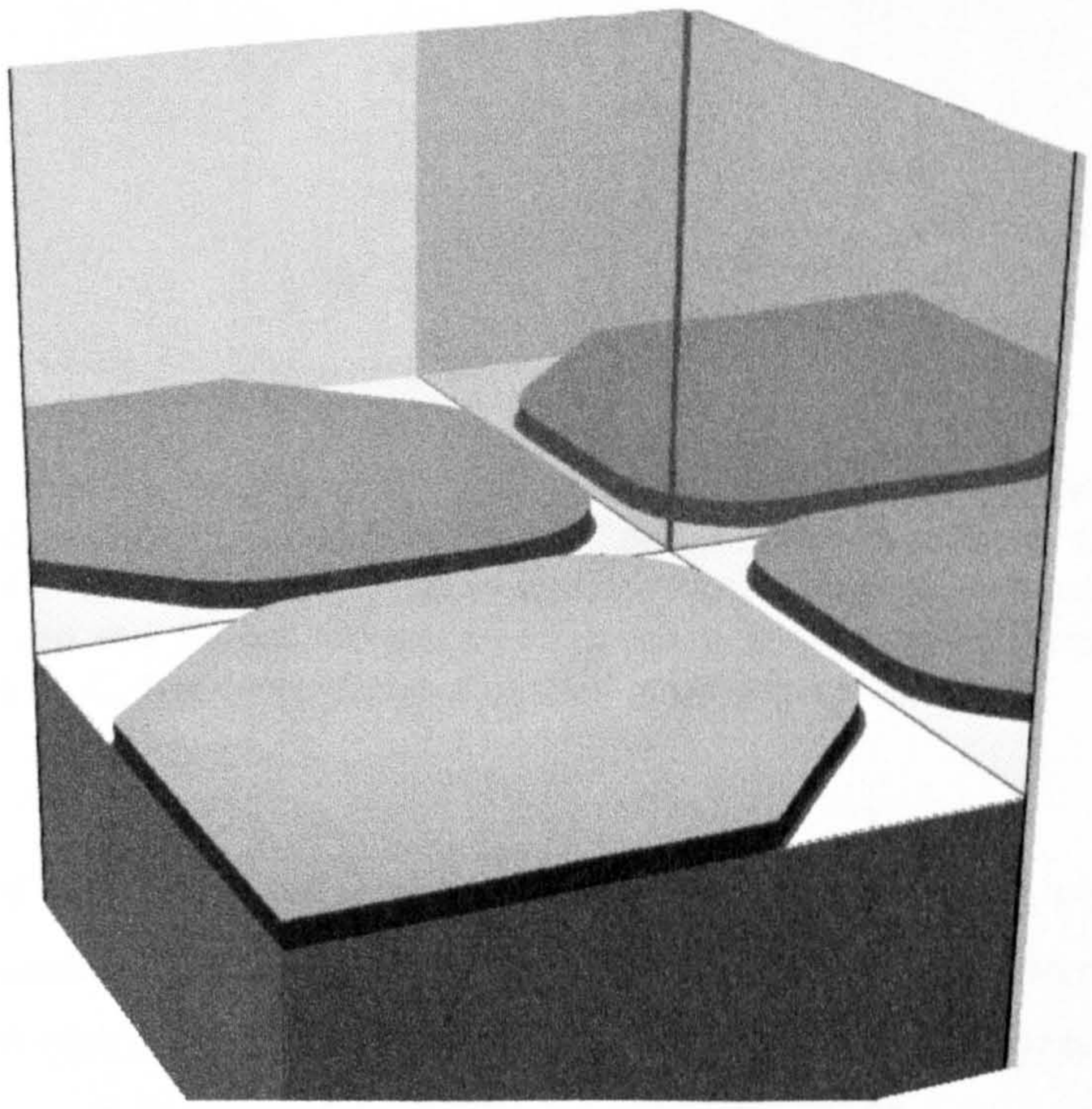

Figure (6.1) Schematic diagram of one quarter of the hyperbolic polynomial design with two "mirror" symmetry planes, creating the image of the complete electrode array.

6.3 Results and discussion

6.3.1 Results I: hyperbolic electrodes

The hyperbolic polynomial electrode design was reduced to the basic cell shown in Figure (6.2). The edges of the problem space were defined to be symmetry boundaries as shown. The top and bottom of the cell were defined to be Neumann boundaries which, in combination with the other boundaries, resulted in the cell being mapped infinitely. However, the area of interest was restricted to the centre of the electrodes within ten micrometres of the surface of the glass substrate. This region was not noticeably affected by inaccuracies due to the boundary conditions on the upper surface of the problem space.

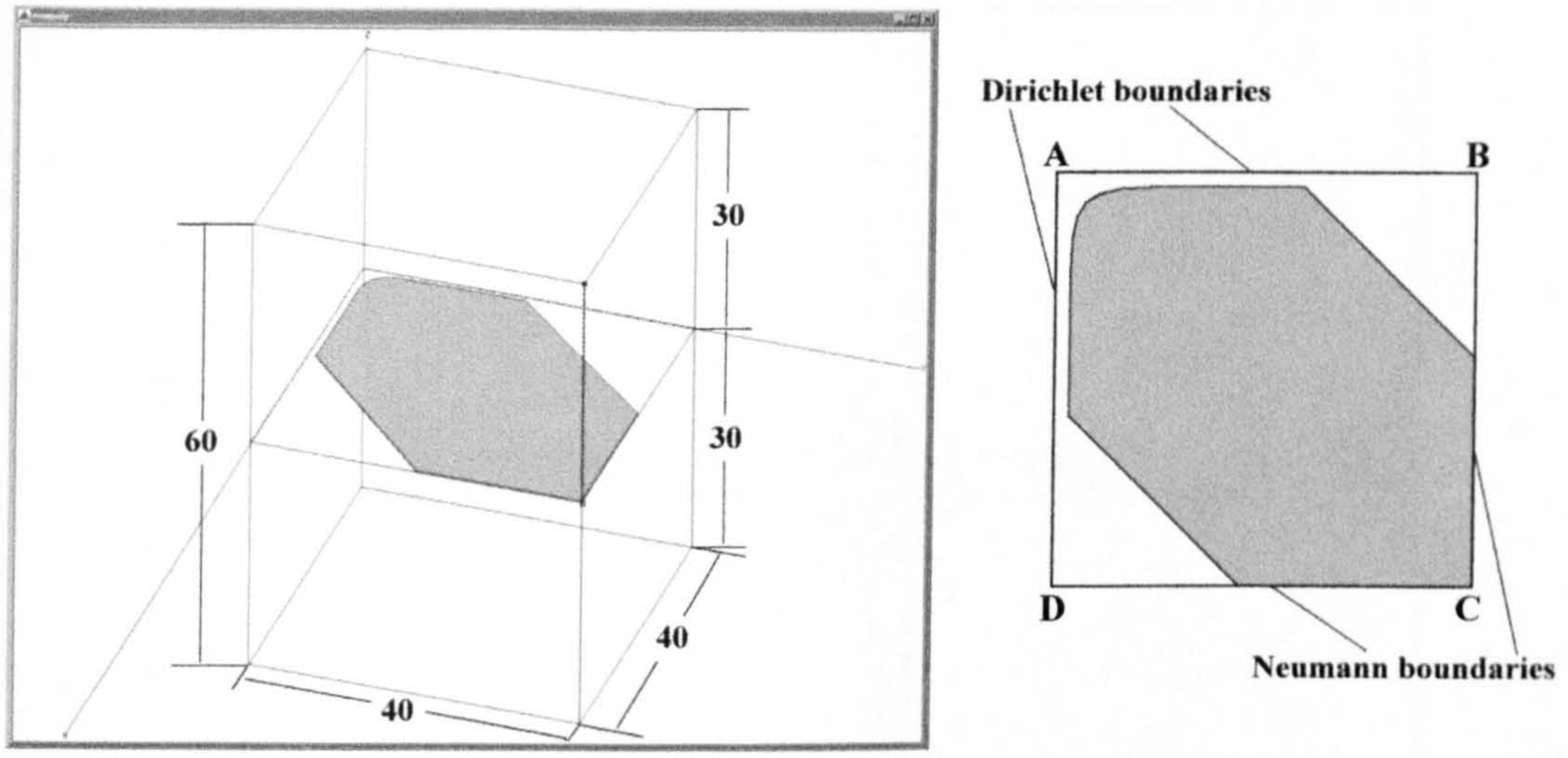

Figure (6.2) Schematic diagram of the basic cell used in solving the electric field in the hyperbolic electrodes. The dimensions of the problem space are as shown on the left in units of micrometres. The boundaries were defined as shown on the right with the top and bottom of the problem space defined to be Neumann boundaries. **A**, **B**, **C**, **D** are reference points used in subsequent diagrams

The surface of the electrode was defined to be a Dirichlet surface with a potential of 5volts, which is equivalent to it being a perfect conductor with the same potential. The potential difference between adjacent electrodes was therefore 10 volts. The upper half of the problem space was assigned the dielectric properties of water ($\varepsilon_r = 78.54$ and $\sigma = 2\text{x}10^{-5}$ Sm^{-1}) and the lower half was assigned the dielectric properties of glass ($\varepsilon_r = 5.5$ and $\sigma = 1\times10^{-12} Sm^{-1}$).

The problem was solved to an accuracy of 0.388% error in the total energy of the solution. Figure (6.3a-d) show the magnitude of the electric field in slices across the problem space parallel to the upper electrode surface with the mirror images generated to show the potential trap in the centre. (6.3a) shows the field magnitude in a plane cutting through the electrode at the midpoint in the height (50nm below the upper surface). (6.3c-d) shows the field in planes at heights of 100nm, 1μm and 5μm above the upper surface of the electrode respectively. The maximum values for the field magnitudes in each of theses planes was found to be 1.26×10^7, 8.55×10^6, 2.48×10^6 and 6.32×10^5 Vm^{-1} respectively. The maximum field strength in the complete solution was 1.48×10^7 Vm^{-1} and was found on the edge of the electrode on the upper surface. This value for the electric field is unlikely to be accurate as real electrodes would have a certain amount of curvature at the edges and the model has sharp edges. However, in solving the electric field from the potential, Maxwell can only approximate across the size of the mesh elements near the electrode and the solution is therefore not that of a sharp edge either.

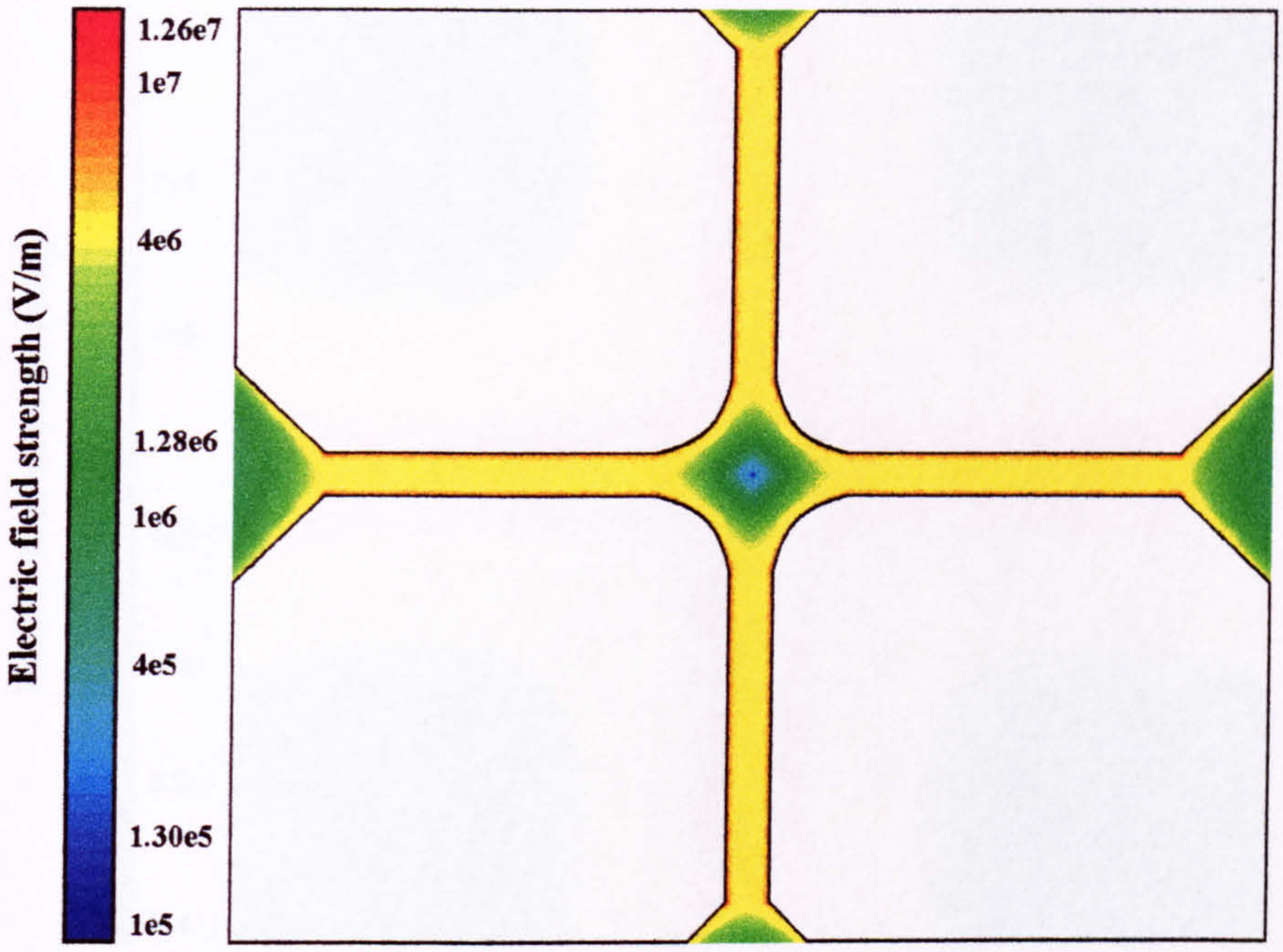

Figure (6.3a) Electric field magnitude in a plane through the middle of the polynomial electrodes parallel to the upper surface. The potential difference between adjacent electrodes was 10 volts and the maximum field strength in this plane was $1.26\times10^{7}\ Vm^{-1}$.

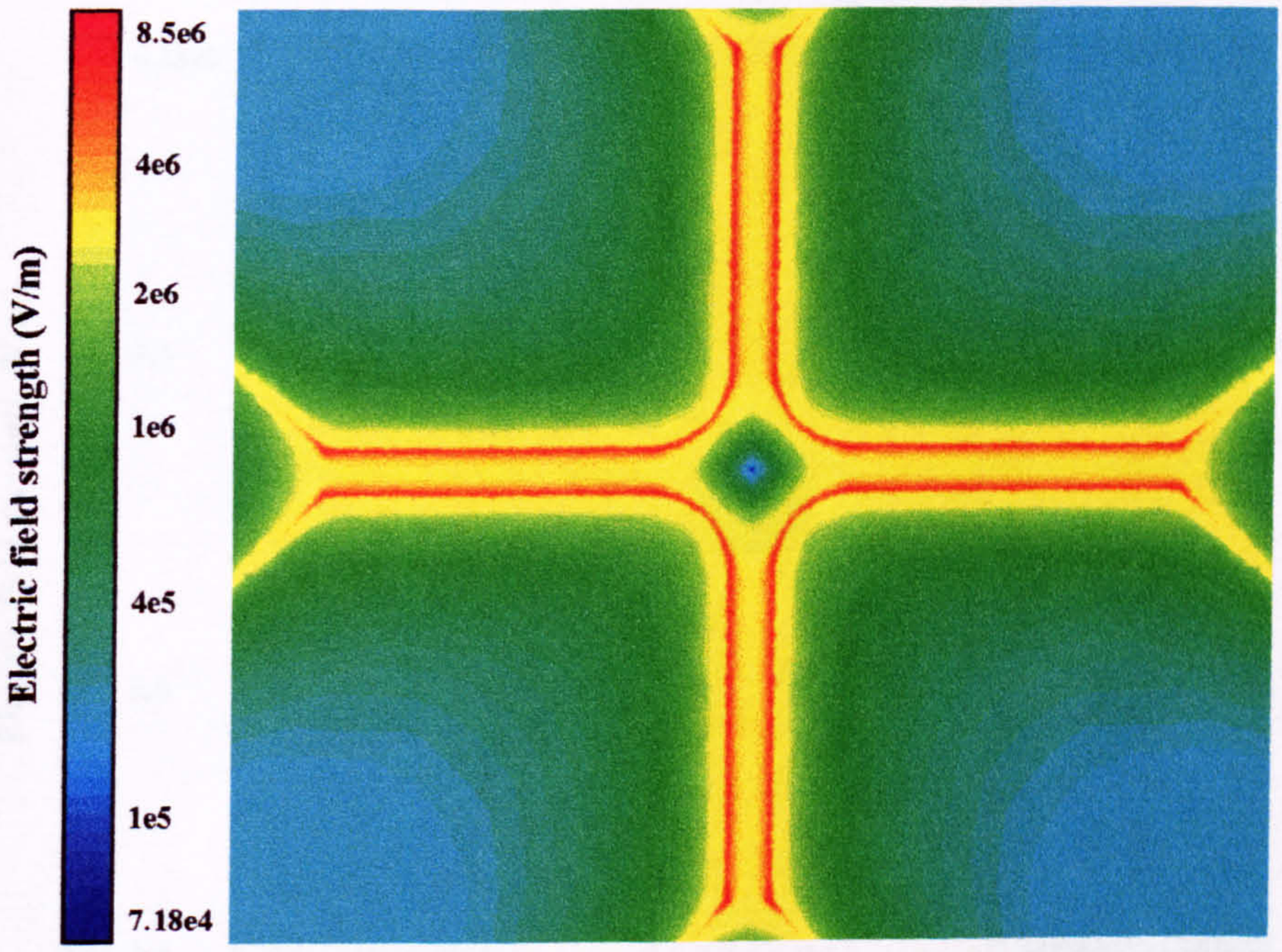

Figure (6.3b) Electric field magnitude in a plane 100nm above and parallel to the upper surface of the electrodes. The potential difference between electrodes was 10 volts and the maximum field strength in this plane was $8.55\times10^{6}\ Vm^{-1}$.

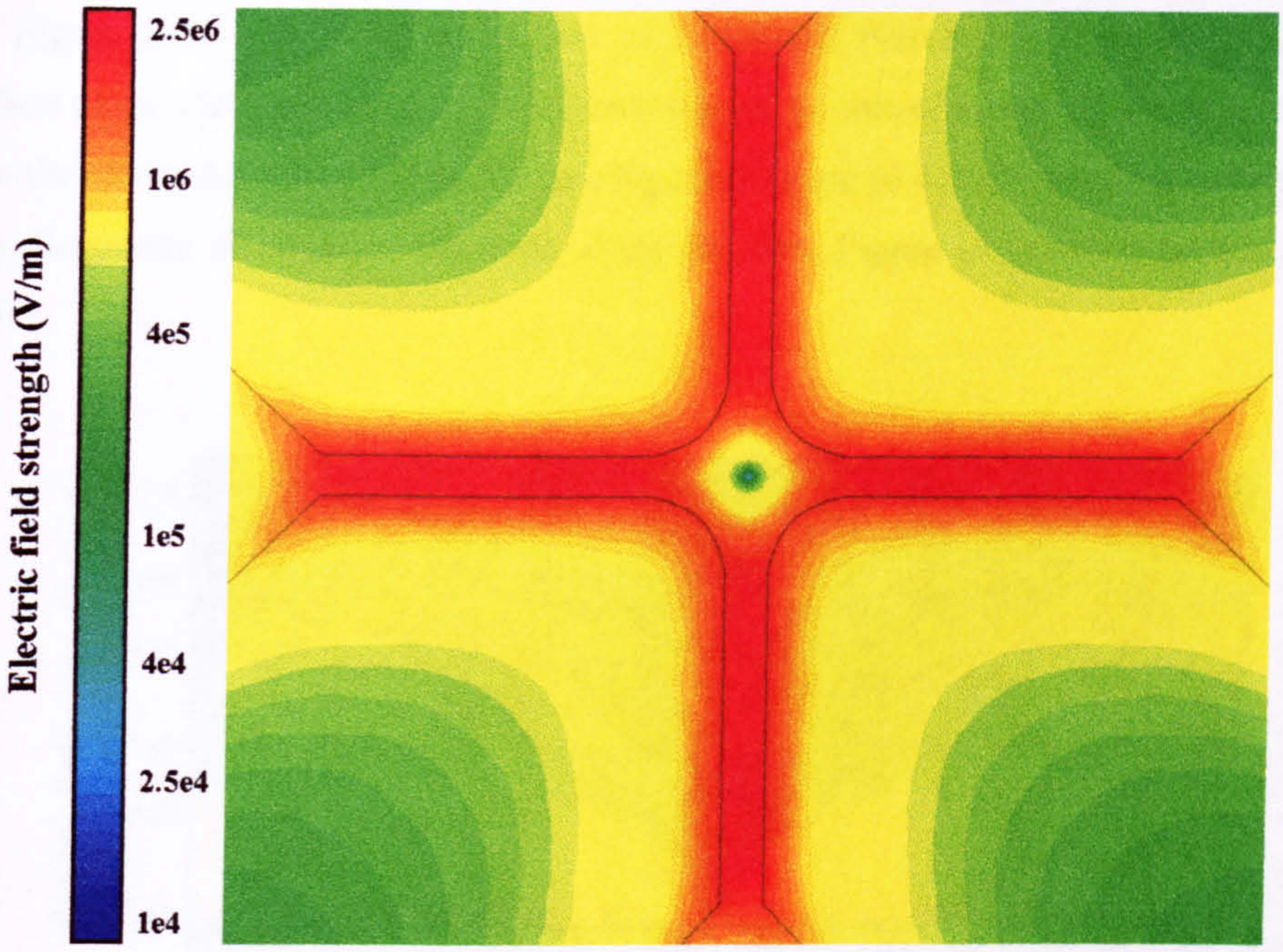

Figure (6.3c) Electric field magnitude in a plane 1μm above and parallel to the upper surface of the electrodes. The potential difference between electrodes was 10 volts and the maximum field strength in this plane was $2.48\times10^{6}\ Vm^{-1}$.

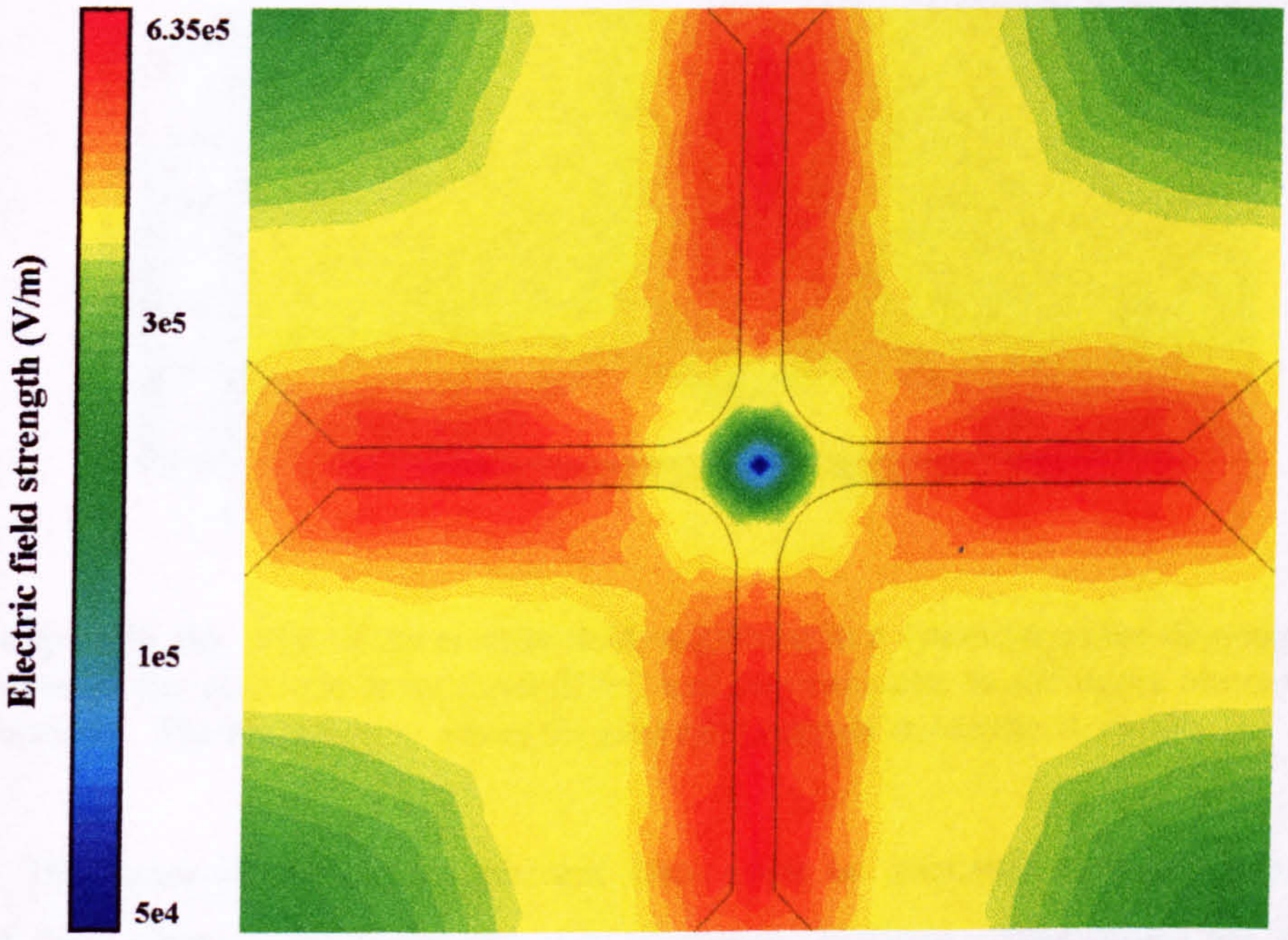

Figure (6.3d) Electric field magnitude in a plane 5μm above and parallel to the upper surface. The potential difference between electrodes was 10 volts and the maximum field strength in this plane was $6.32\times10^{5}\ Vm^{-1}$.

Figure (6.4a) and (6.4b) shows plots of the electric field in two planes perpendicular to the surface of the electrodes. (6.4a) represents one of the mirror symmetry boundaries running between the electrodes along AD or AB (see Figure 6.2) and (6.4b) represents a symmetry plane running diagonally through an electrode along AC (see Figure (6.2) for reference to points A,B,C,D).

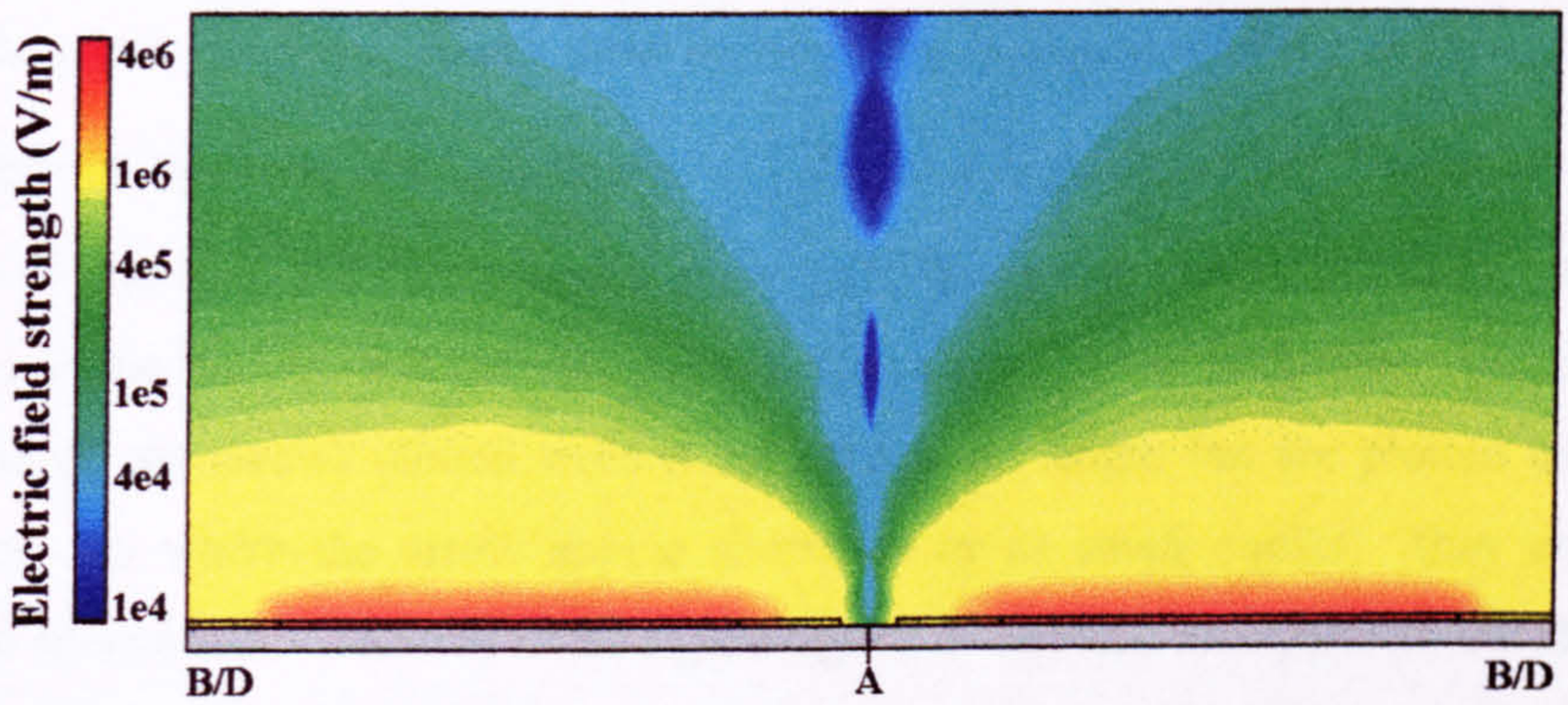

Figure (6.4a) Plot of the electric field magnitude in the symmetry boundaries AD or AB as shown in Figure(6.2). The image demonstrates the 3D nature of the electric field "trap" between the electrodes. A cross section of the electrodes is also shown for reference.

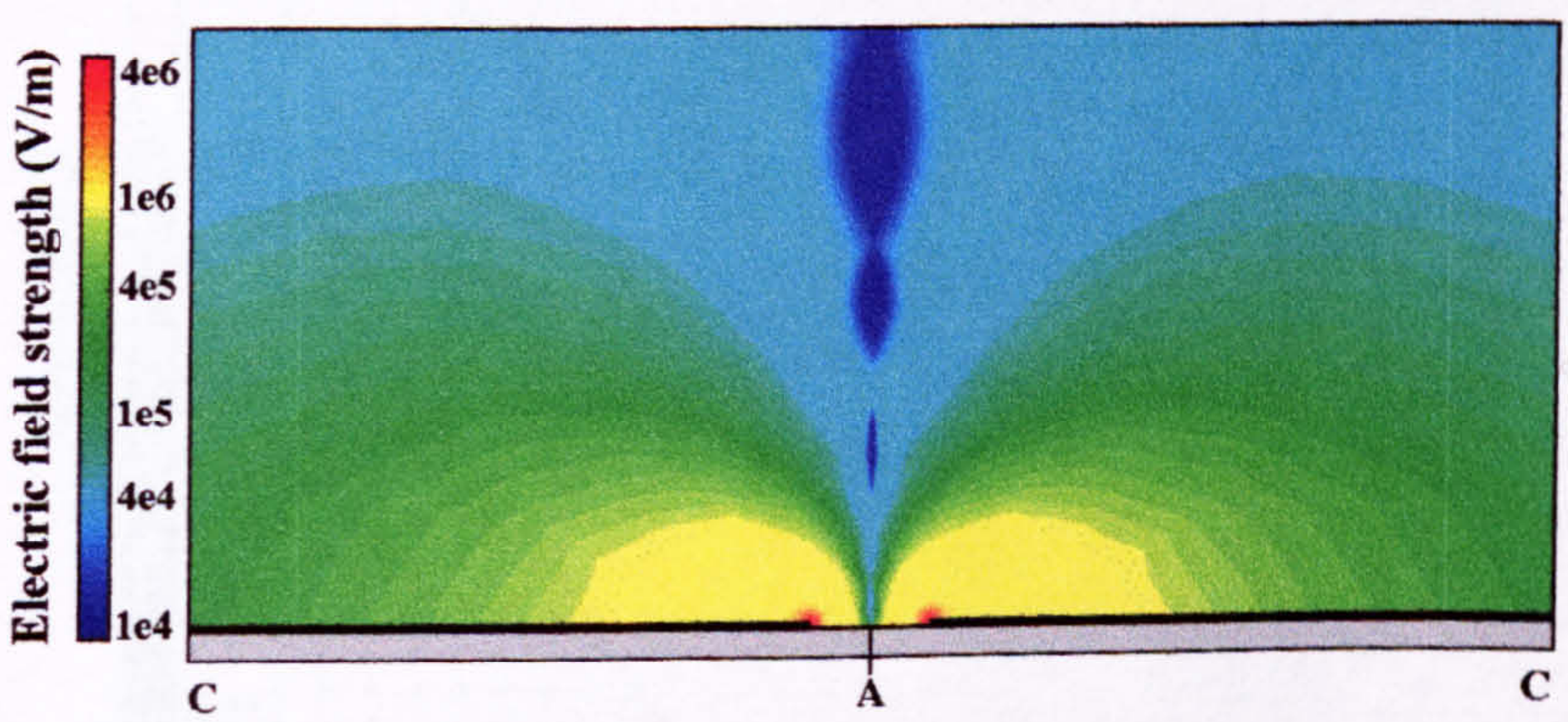

Figure (6.4b) Plot of the electric field magnitude in a symmetry plane diagonally through the electrode array through AC and perpendicular to the upper electrode surface. The black region marks the zero field regions inside the electrode.

The vector for the dielectrophoretic force given by (equation 6.1) was calculated in each of these planes using Maxwell's post processing facilities. The results are shown in Figures (6.5), (6.6) and (6.7). Figures (6.5a-d) show the positive DEP vector direction in planes parallel to the upper electrode surface at heights of -50nm, 100nm, 1μm and 5μm as well as a colour coded plot of the magnitude of $\nabla|\underline{\mathbf{E}}|^2$. Figures (6.6a-d) show the negative

DEP vector direction and $\left|\nabla\left|\underline{\mathbf{E}}\right|^2\right|$ in the same four planes. The maximum value of $\left|\nabla\left|\underline{\mathbf{E}}\right|^2\right|$ in each of the four planes was 2×10^{22}, 1×10^{21}, 8.1×10^{18} and 2.3×10^{17} V^2m^{-3}. The maximum value for $\left|\nabla\left|\underline{\mathbf{E}}\right|^2\right|$ in the entirety of the problem space was 5×10^{22} V^2m^{-3} and was found on the edge of the electrode. The figures show only the solution in the basic cell i.e. one quarter of the complete solution and represent the dielectrophoretic force as direction and magnitude plots. The arrow diagrams simply show the variation in direction of the force and the colour coded diagrams represent the magnitude of $\nabla\left|\underline{\mathbf{E}}\right|^2$ on a logarithmic scale at each point. In Figures (6.5) and (6.6) the colour coded section and the arrow section are mirror images in a plane through the line AC and perpendicular to the surface of the electrodes. Another point of note is that all the arrows plotted were exactly the same length but are plotted in true three dimensions, so where the arrow appear shortened or as small circles, they are pointing upwards or downwards. The text in the figure legend is intended to expand on the diagram and describe the vertical direction where appropriate, not merely describe what is in the figure.

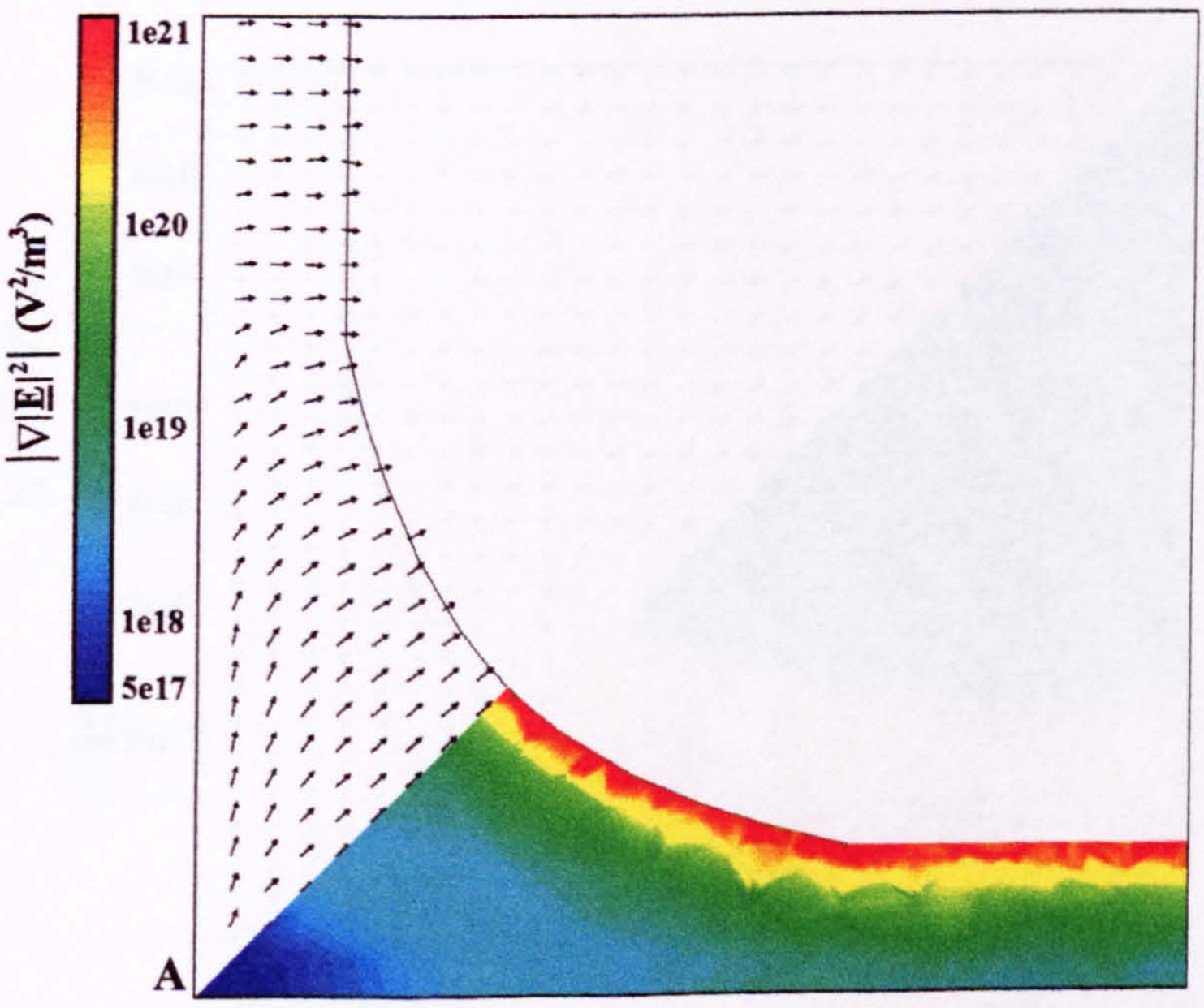

Figure (6.5a) The positive DEP force vector direction and magnitude of $\nabla\left|\underline{\mathbf{E}}\right|^2$ in the plane of the hyperbolic polynomial electrodes (ABCD). In this plane there is no solution for the dielectrophoretic force in the area covered by the electrodes as the field is zero inside a conductor. Where there is a solution, the DEP force vector tends to point towards the edge of the electrode and increases in magnitude as the distance to the electrode edge decreases.

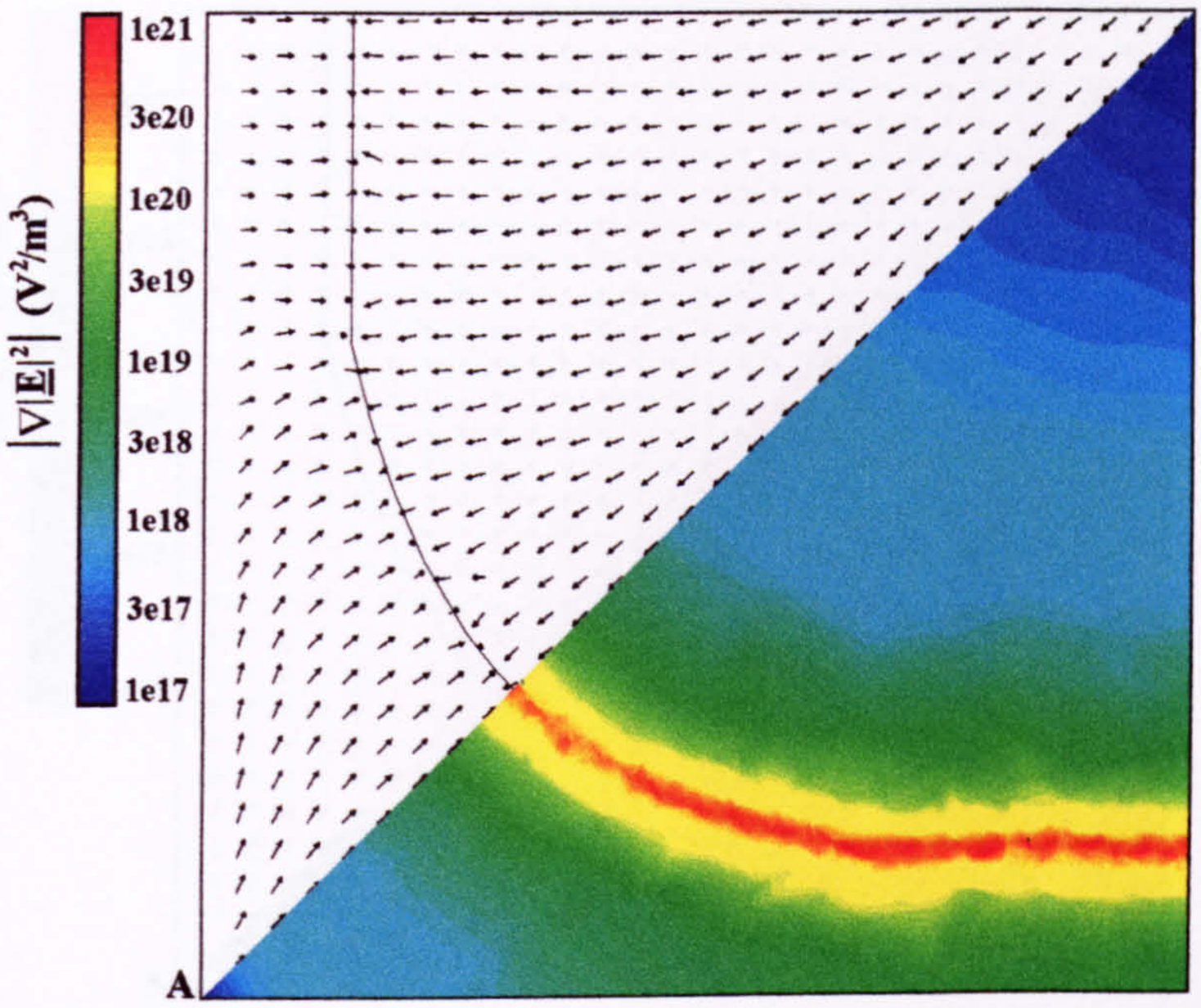

Figure (6.5b) The positive DEP force vector direction and magnitude of $\nabla|\underline{\mathbf{E}}|^2$ in a plane 100nm above the upper surface of the electrodes and parallel to ABCD. The vectors point towards the electrode edge both on top of the electrode and in the gap. The maximum values of the magnitude are found over the electrode edges where the vectors point downwards.

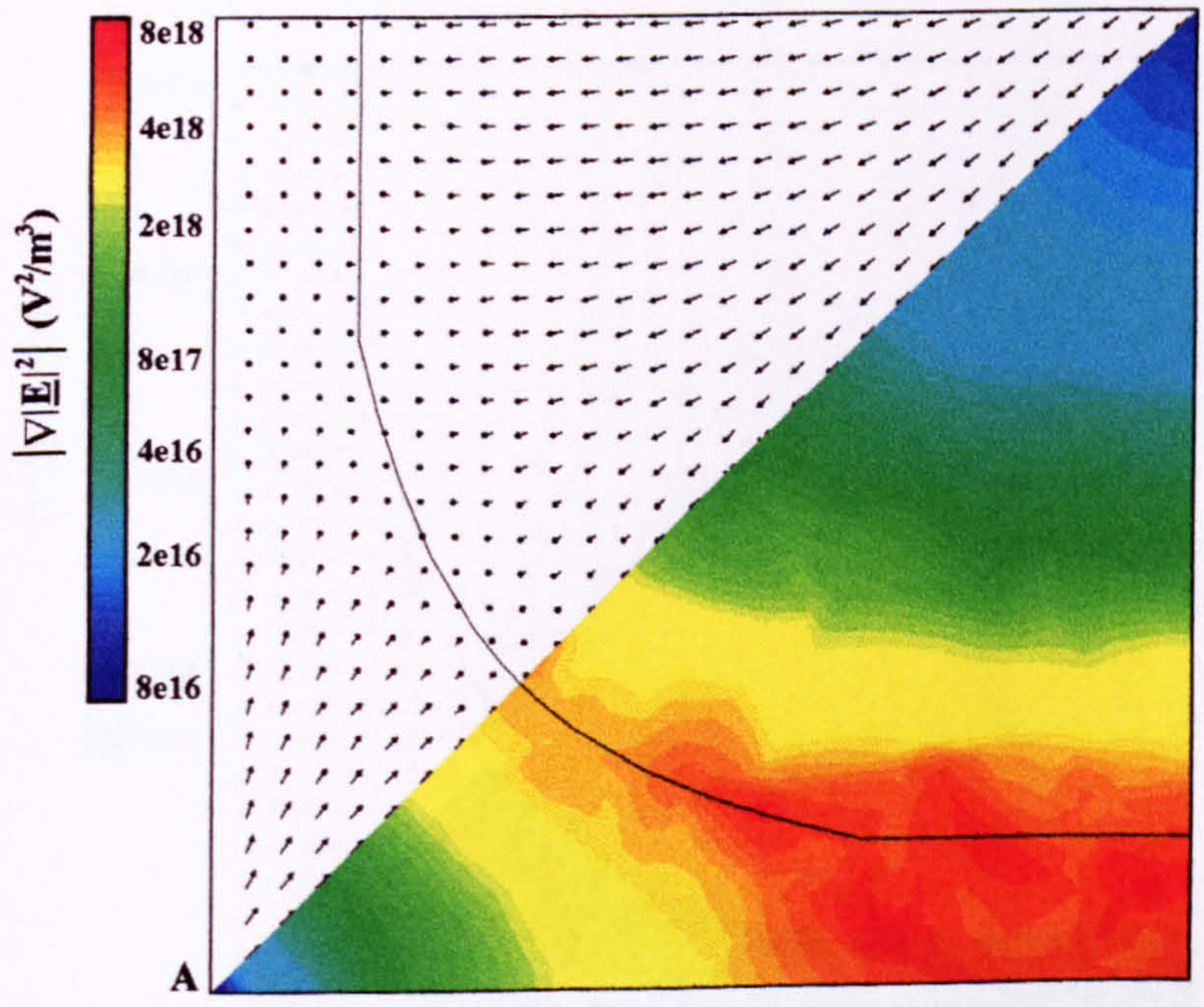

Figure (6.5b) The positive DEP force vector direction and magnitude of $\nabla|\underline{\mathbf{E}}|^2$ in a plane 1μm above the electrodes and parallel to ABCD. The vectors tend to point towards the electrode edge both on top of the electrode and in the gap which in this plane means that over a noticeable region, the vectors point downwards. In this plane, the maximum values of the magnitude are found over the electrode edges.

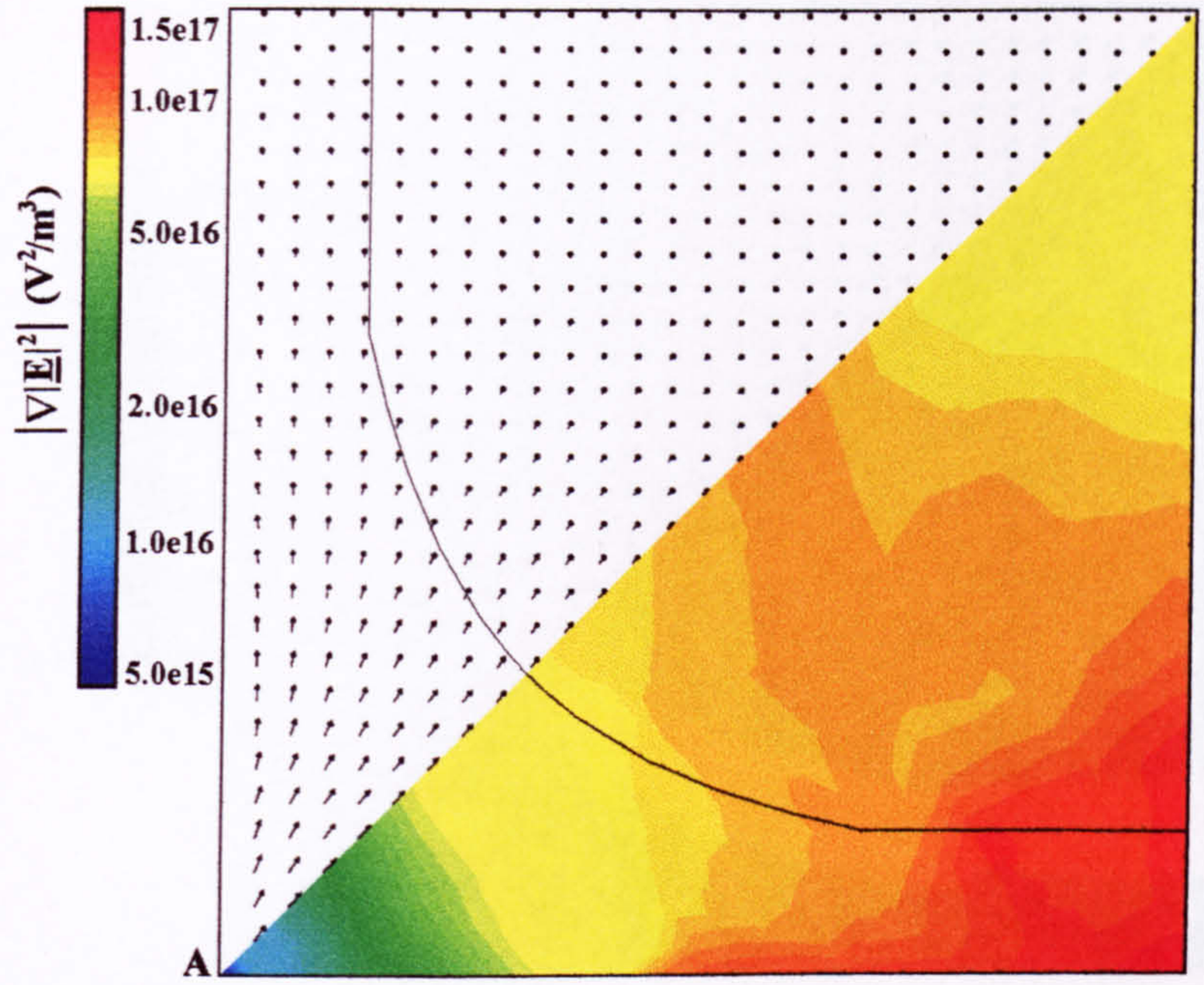

Figure (6.5d) The positive DEP force vector direction and magnitude of $\nabla|\underline{\mathbf{E}}|^2$ in a plane 5μm above the upper surface of the electrodes and parallel to ABCD. The vectors over the electrode and over the parallel gap region all point straight down and without much variation in magnitude. In the centre of the electrodes, the vectors point out from the centre towards the electrode edges with a logarithmic rise in magnitude until close to the electrode.

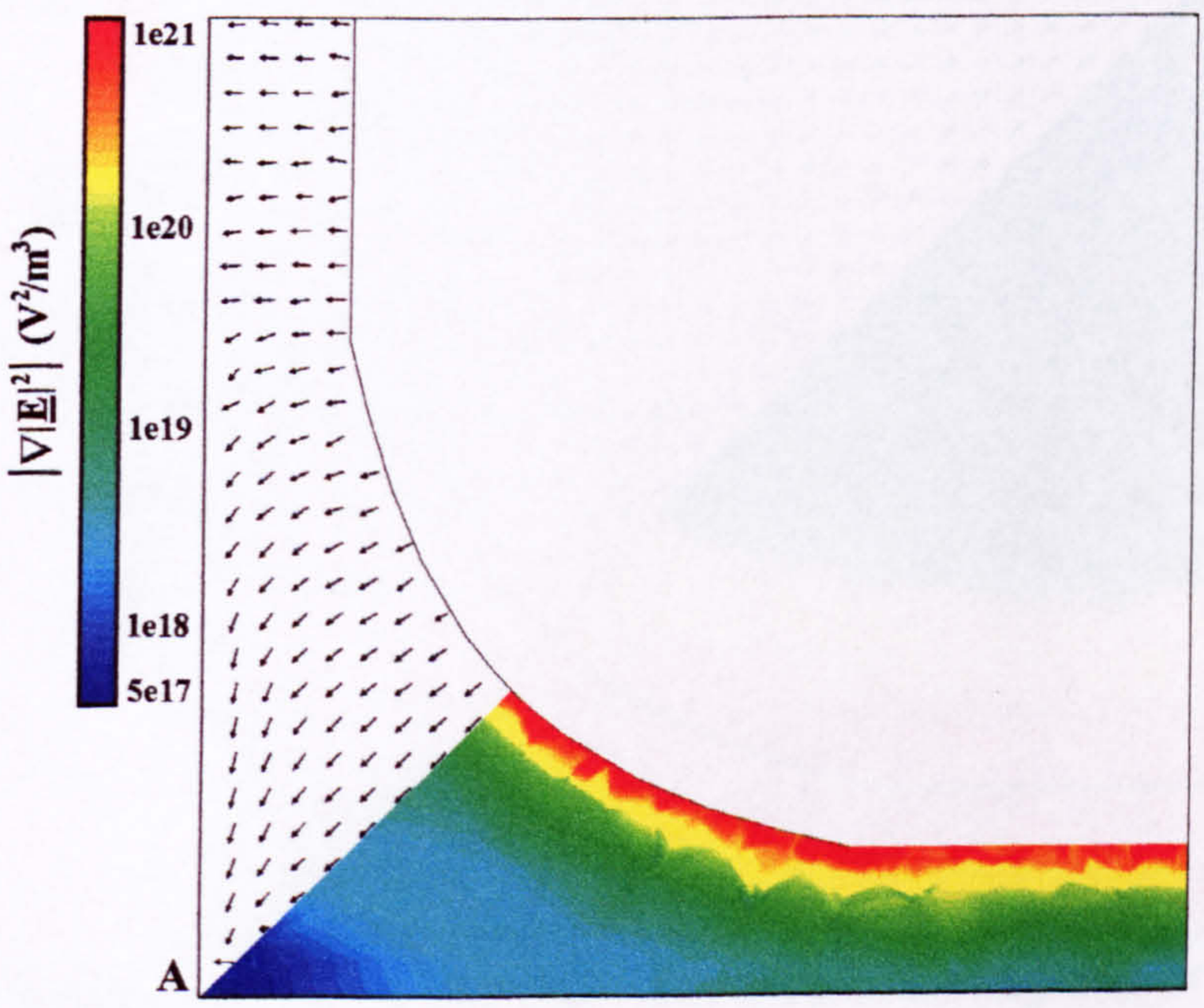

Figure (6.6a) The negative DEP force vector direction and magnitude of $\nabla|\underline{\mathbf{E}}|^2$ 50nm below the upper surface of the electrodes Away from the electrode, the vectors tend to point away from the electrode edge and decrease in magnitude rapidly to a minimum in the centre of the four electrodes. The negative DEP trap can be seen in the centre where all the vectors point towards A.

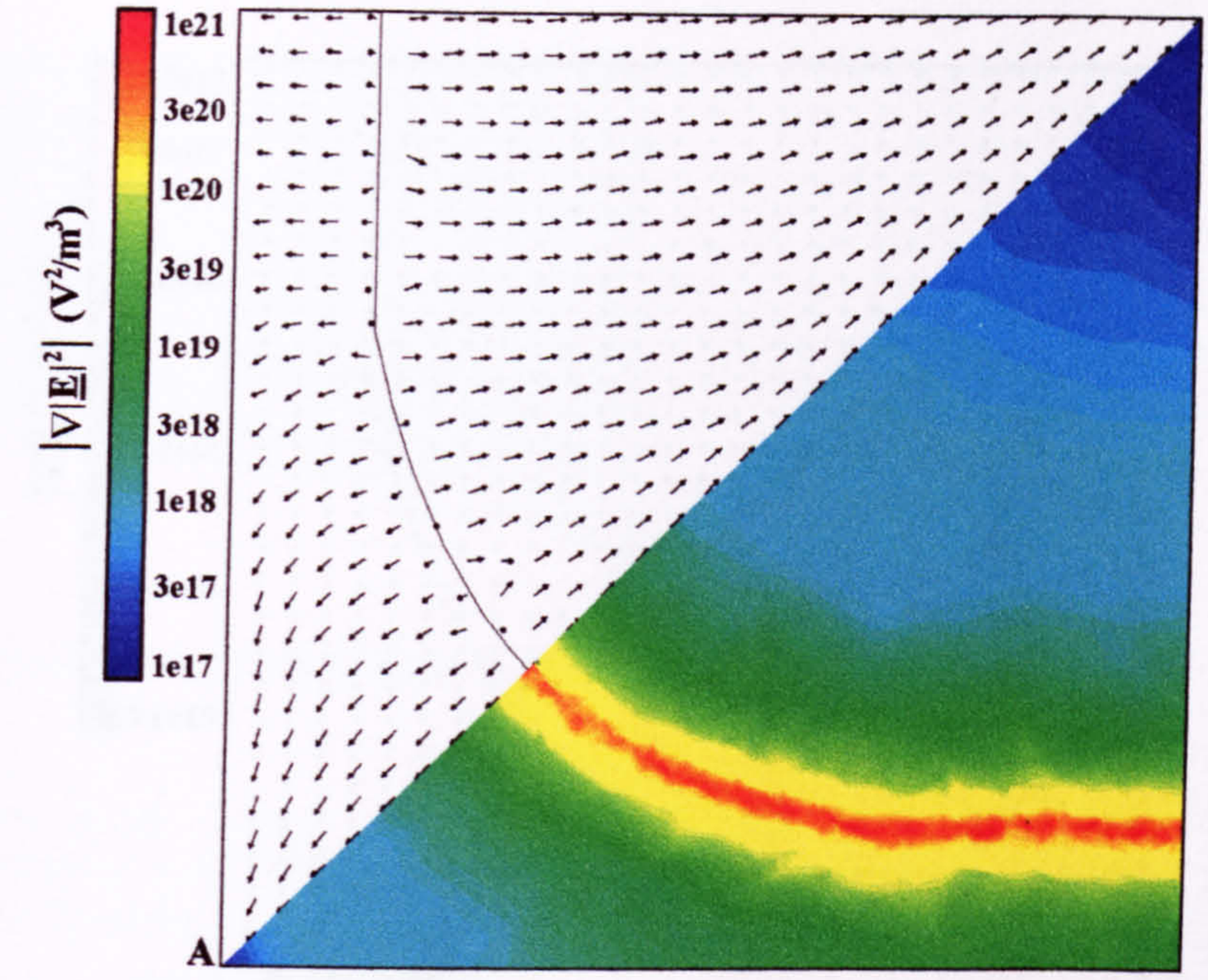

Figure (6.6b) The negative DEP force vector direction and magnitude of $\nabla|\underline{\mathbf{E}}|^2$ in a plane 100nm above the upper surface of the electrodes and parallel to ABCD. The vectors point away from the electrode edge both on top of the electrode and in the gap. The maximum values of the magnitude are found over the electrode edges where the vectors tend to point upwards. The negative DEP trap can be seen as an enclosure of vectors surrounding and pointing towards the centre (A).

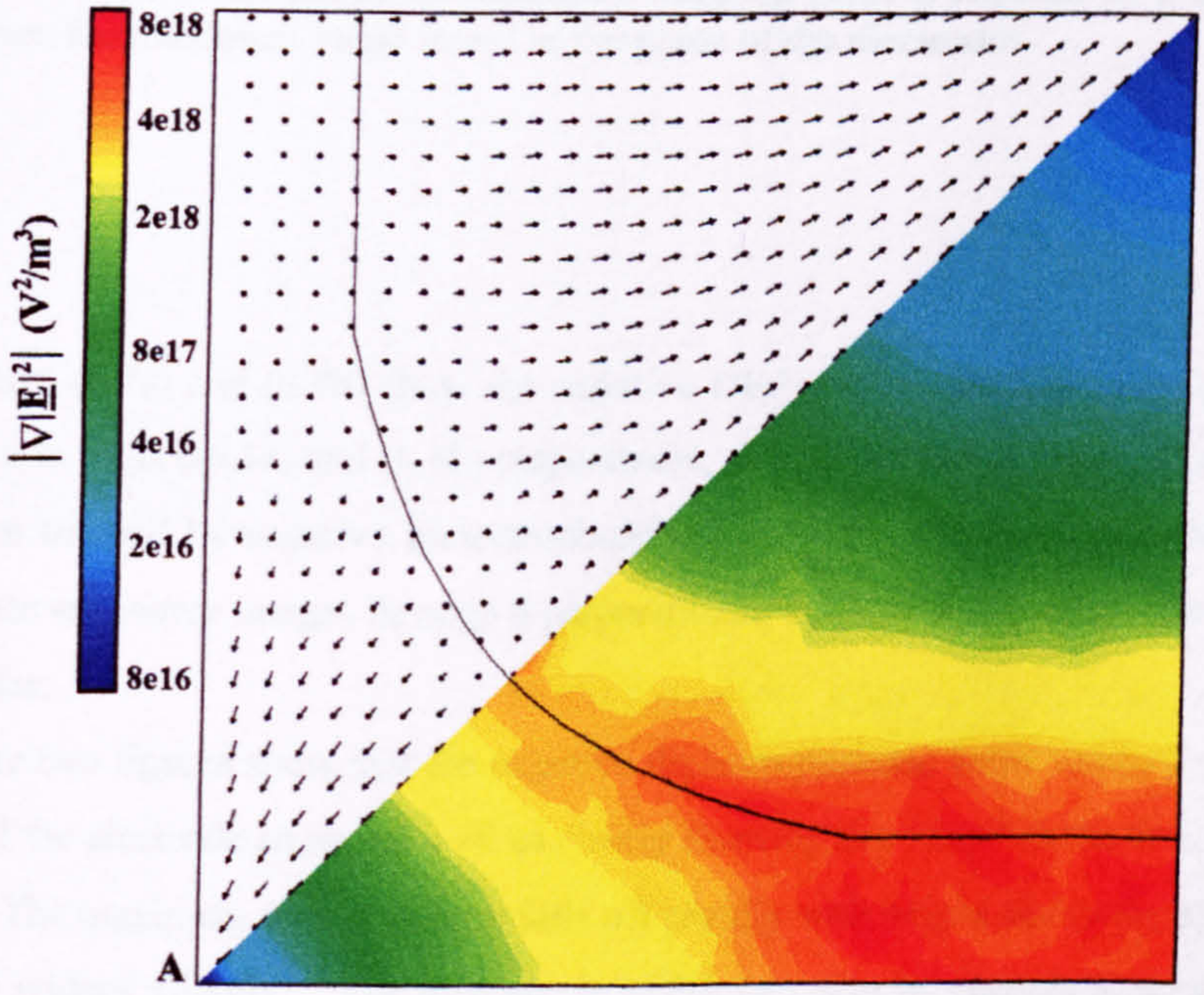

Figure (6.6c) The negative DEP force vector direction and magnitude of $\nabla|\underline{\mathbf{E}}|^2$ in a plane 1μm above the upper surface of the electrodes and parallel to ABCD. The vectors tends to point away from the electrode edge, pointing upwards over a noticeable area. In this plane, the maximum values of the magnitude are found over the electrode gap where the vectors point straight upwards. The trap is still present in the centre of the electrodes.

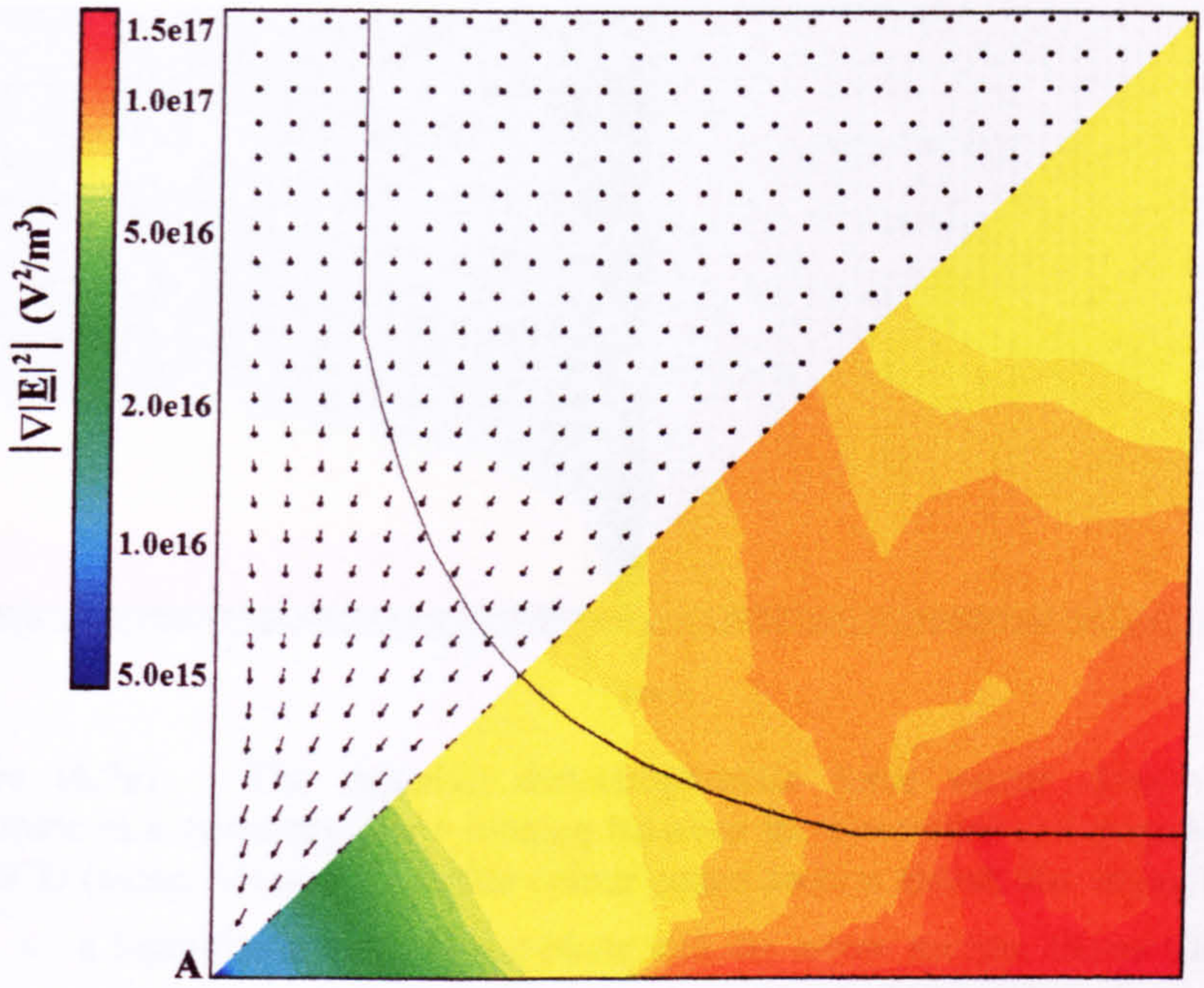

Figure (6.6d) The negative dielectrophoretic force vector direction and magnitude of $\nabla|\underline{\mathbf{E}}|^2$ in a plane 5μm above the upper surface of the electrodes and parallel to ABCD. The vectors over the electrode and over the parallel gap region all point upwards with little variation in magnitude. The trap is present in the centre of the electrodes but the maximum trapping force is reduced by a factor of 10^5 from the maximum value found in the plane of the electrodes.

Figures (6.7a) and (6.7b) show the negative DEP vector direction in the perpendicular planes shown in Figure(6.4a) and (6.4b) respectively, indicating the direction of the force on a particle when trapped by negative dielectrophoresis. In Figure (6.7), the arrow and colour coded sections are mirror images through a perpendicular running line through the centre of the four electrodes.

These two figures show that the negative dielectrophoretic force vector points upwards over much of the electrode array, as well as clearly showing the "trap" in the centre of the four electrodes. The maximum trapping force falls off rapidly with height above the electrodes and the trap also widens slightly. The increase in width can also be seen in successive steps in Figures (6.3a-d) and (6.6a-d).

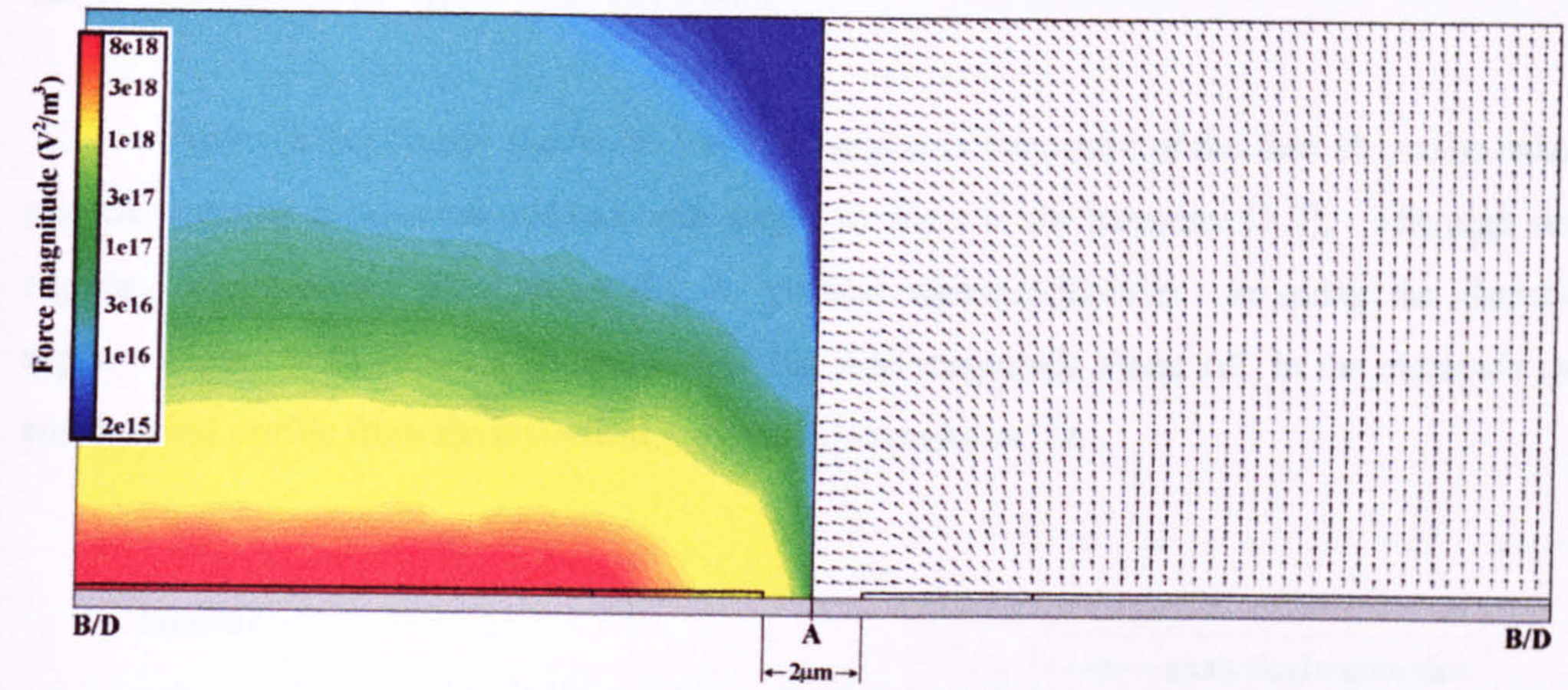

Figure (6.7a) The negative dielectrophoretic force vector direction and magnitude in a symmetry plane running between the electrodes and perpendicular to ABCD (along AB or AD). The colour coded section shows the magnitude of $\nabla|\underline{\mathbf{E}}|^2$ on a logarithmic scale in the plane and the arrow section shows the force direction. The two sections are mirror images of each other about a vertical line running through the centre of the electrodes.

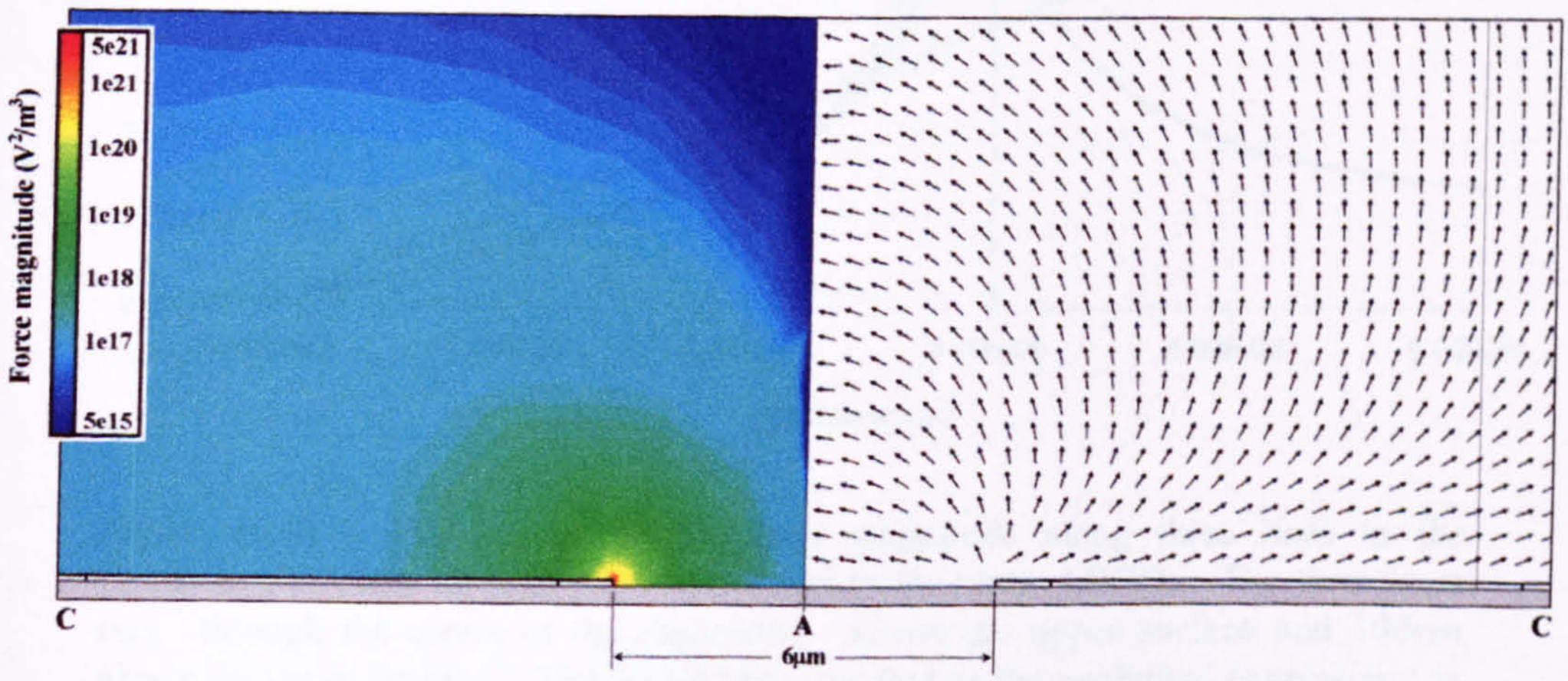

Figure (6.7b) The negative dielectrophoretic force vector direction and magnitude in a symmetry plane running between the electrodes and perpendicular to ABCD (along AC). The colour coded section shows the magnitude of $\nabla|\underline{\mathbf{E}}|^2$ on a logarithmic scale in the plane and the arrow section shows the force direction. The two sections are mirror images of each other about a vertical line running through the centre of the electrodes.

6.3.2 Discussion I: hyperbolic electrodes

Figure (6.3a) clearly shows the low field region in the centre of the four electrodes where particle trapping is expected and has been shown to occur in the literature [1,4]. The high field regions, which attract particles moving by positive dielectrophoresis, lie along the electrode edges. Figure (6.8) shows a comparison of the field magnitude along AC in the electrode gap and the field profile from the analytical polynomial expression [1].

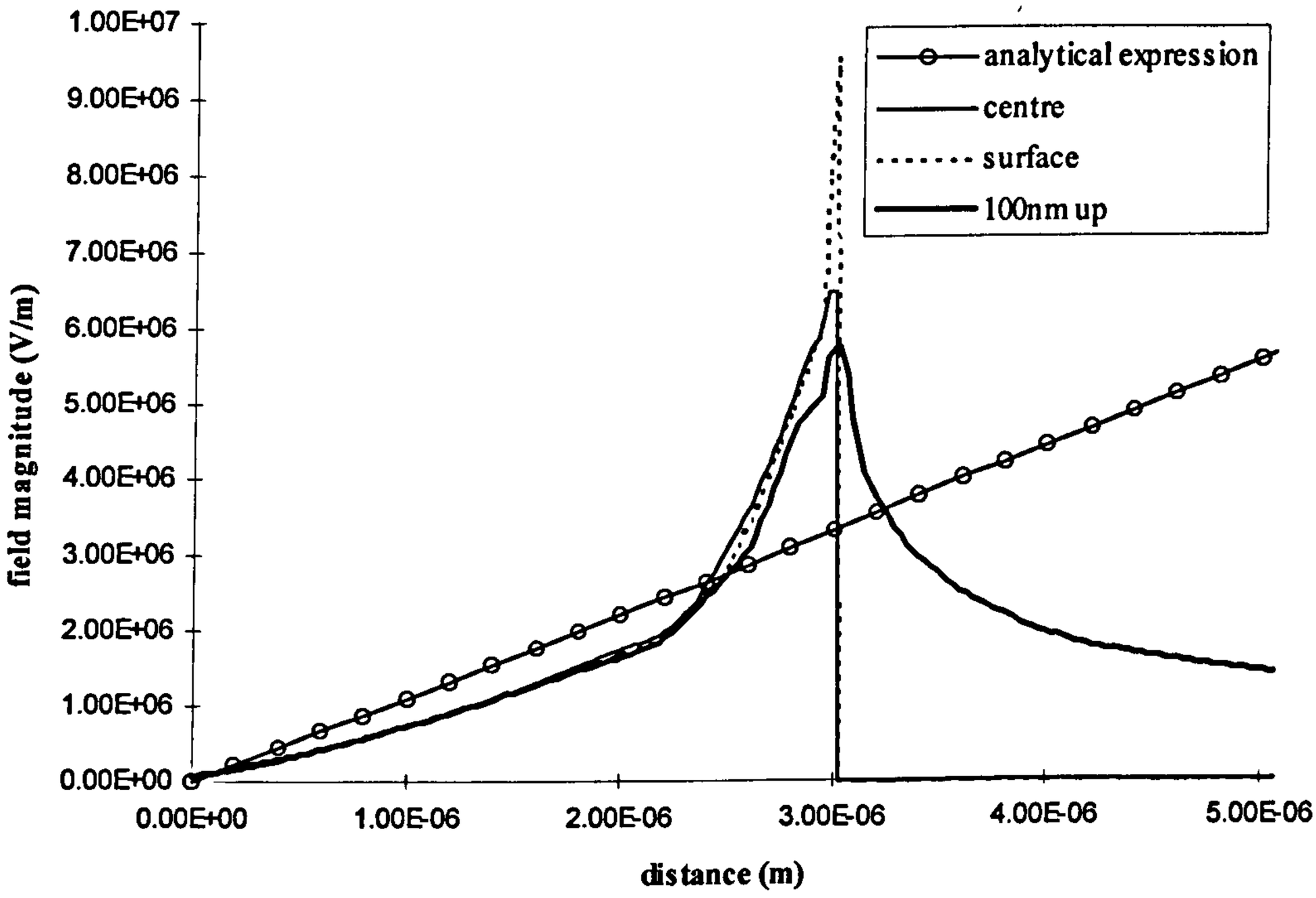

Figure (6.8) Plot of the electric field magnitude along three lines in the perpendicular plane through AC and parallel to the plane ABCD. The three lines run, through the centre of the electrodes, across the upper surface and 100nm above the upper surface. The fourth line, marked as the analytical expression, is the theoretical line from reference 1 for comparison.

This figure shows that the estimate of the electric field strength from the analytical expression is a fairly good approximation, although not exact, out to a distance of approximately 2.2μm from the centre of the 6μm electrodes. It does not accurately represent the sharp increase in the electric field close to the electrode edge, or that the field is zero inside the electrode. However, the agreement of the numerical solution with the established result is good in the centre of the electrodes.

The size of the low field region, defined by a full enclosure of high field regions, increases as the height above the electrodes increases (Figures (6.3a-d)). Figure (6.4b) demonstrates this variation in a vertical plane through the line AC (see Figure (6.2)) where the high field region only occurs over the edge of the electrode and Figure (6.4a) shows the variation in a vertical plane through the line AB (or AD) where the high field region extends along the length of the electrode gap. This shows that the potential 'trap' defined by $|\underline{\mathbf{E}}|^2$ has a wide wall in the direction of the electrode gap (AB, AD) reducing to a comparatively thin wall across the electrode (AC). This implies directly that the probability of escaping from the trap is greater along the path AC than along either AB or AD. The trap is open at the top but when gravitational potential is added to the system, the trap becomes fully enclosed if the mass density of the particle is greater than the medium (section 4.2.1).

The dielectrophoretic force (equation 6.1) is given by a frequency dependent term multiplied by $\nabla|\underline{\mathbf{E}}|^2$. Figure (6.4a) shows that in the plane of the electrodes the force is towards the electrode and strongest at the edge (1.26×10^7 V/m). At a height of 100nm, the size of the force has fallen off slightly and particles moving in this plane would remain in the plane (horizontal vectors) except very close to the electrode edges where the force vectors point straight down. In the 1μm plane (Figure 6.5c) the pattern is similar with a downward slant to the vectors across the whole plane and a wide bend above the electrode edges where the vectors point downwards and have a large magnitude. In the 5μm plane, except for the 'trap' region, the positive DEP vector points downwards with a maximum of 2×10^{17} V^2m^{-3} over the electrode edge. The pattern of the vectors suggest that, above a height of approximately 10μm and over the electrode surface, particles which are experiencing positive DEP would descend straight towards the electrode to a height of approximately 3-4μm. Below this height, the particles would then experience a force tending to direct them towards the edges of the electrodes. If the particles are not over the electrode surface but over the electrode gap, the path they follow as they descend is similar but they do not experience a noticeable force component towards the electrode edge until they are within 1μm of the surface. Above the 'trap', the force directs the particles towards space above the electrodes even at 5μm and above, and the magnitude increases as the height decreases.

The negative dielectrophoretic force is the negative of the positive dielectrophoretic force: equal in magnitude and opposite in direction. In the plane of the electrodes (Figure 6.6a), the plot shows that a particle would be pushed into the centre of the four electrodes by a force that falls off rapidly with distance from the electrode edge. In the 100nm plane (Figure 6.6b), the pattern in the centre is similar except that a particle on top of the electrode would also be pushed

away from the edge into the middle of the electrode. At 1μm, (Figure 6.6c), the negative DEP force has fallen off to a maximum value of 8×10^{18} V^2m^{-3} and the force vectors in a wide region over the electrode edges point upwards. As the distance from the electrode edges increases, the force vectors become more horizontal but the magnitude of the force falls off considerably. In the 5μm plane (Figure 6.6d), the centre 'trap' is still present, represented here by converging arrows in the central area between the electrodes, but over the rest of the electrode area, the force vectors point almost straight up. Figures (6.7a) and (6.7b) show the negative dielectrophoretic vector in vertical planes through the lines AB and AC, demonstrating the variation in the force direction and in $\left|\nabla|\underline{E}|^2\right|$. In these symmetry planes, the DEP vector lies entirely in the plane and these plots show completely the expected force on a particle lying in either of the planes. Comparison of the six plots of the negative DEP vectors shows the movement of a particle in the region above the hyperbolic electrode designs. The "trap" can be defined as a volume with a cross-section defined, at the level of the substrate, by the centre of the electrode array and above the electrodes by a circle which expands as height increases. Within this volume, particles which experience negative DEP are pushed towards the centre of the 'trap' and buoyancy acts either to push them upwards or downwards. Outside the volume, particles are pushed away from the 'trap' and away from the central region of the electrodes altogether. The magnitude of the negative DEP force is a maximum at the boundary of this volume in any horizontal plane but the magnitude of the force also falls off rapidly with increasing height, from a value of approximately 1×10^{22} V^2m^{-3} in the electrode plane to 1×10^{17} V^2m^{-3} at a height of 5μm.

The simulation of the electric field and the dielectrophoretic force show that the hyperbolic electrodes provide a good stable negative dielectrophoretic trapping region (with the assistance of gravity) in agreement with the literature [1]. The calculated values of $\left|\nabla|\underline{E}|^2\right|$, indicate that a hyperbolic polynomial electrode with a gap separation of 2μm and a centre separation of the order of 6μm, can produce a large dielectrophoretic force on sub-micrometre particles. Based on the arguments discussed in the introduction to Chapter Five (section 5.1), the values of the electric field strength produced by the electrodes certainly indicates that dielectrophoretic trapping, both positive and negative, should be achievable using this modelled electrode array.

6.3.3 Results II: triangular electrodes

The basic cell for the triangular electrode design is shown in Figure (6.9). The edges of the problem space were defined as symmetry boundaries (as shown) with the top and bottom set to Neumann boundaries. The feature and gap sizes of the particular cell presented in this section were 5μm. Again, the boundaries resulted in the solution for an infinite mirroring of this basic cell and the area of interest was restricted to within 10μm of the substrate surface.

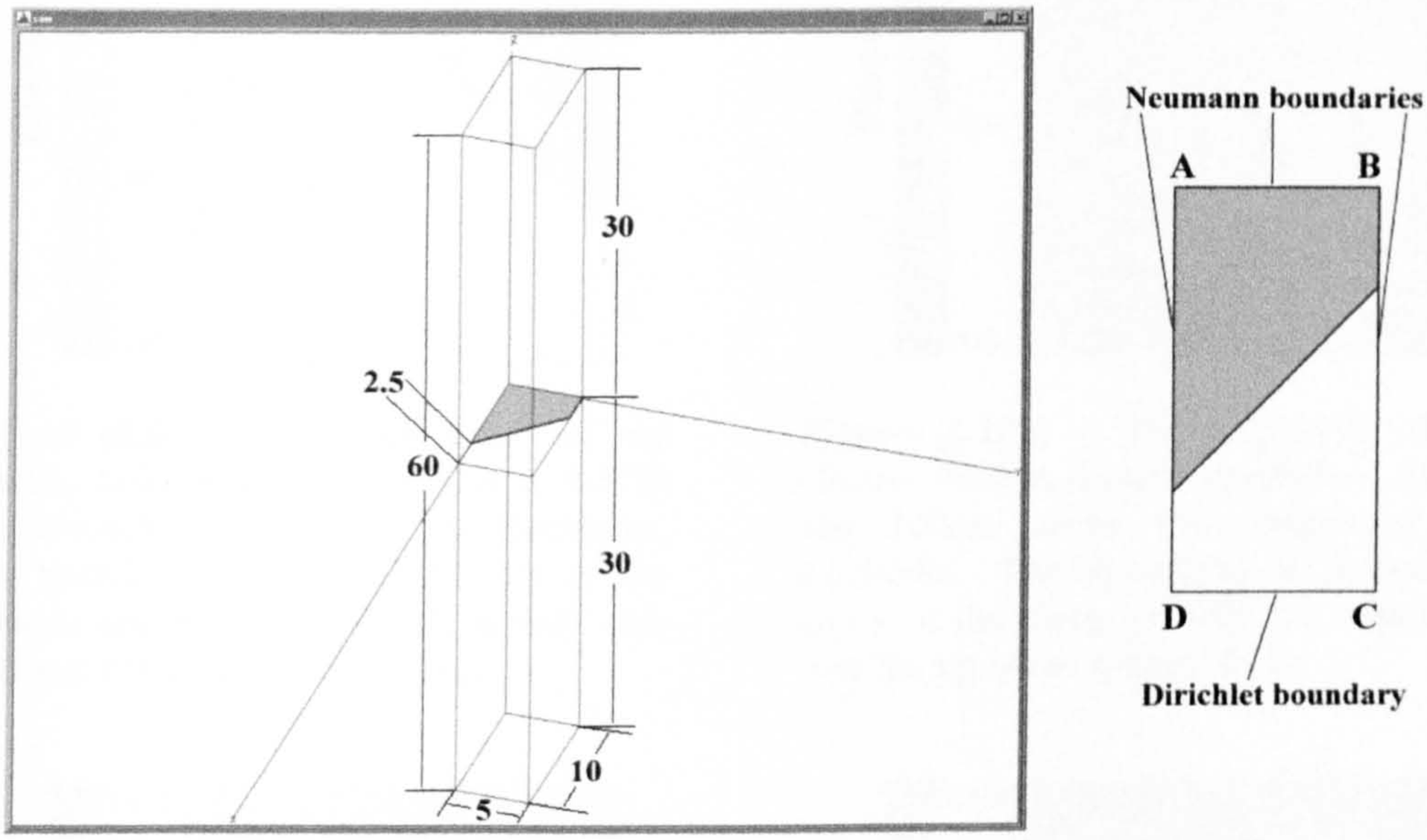

Figure (6.9) Schematic diagram of the basic cell used in solving the electric field in the triangular electrodes. The dimensions of the problem space were as shown in units of micrometres. The boundaries were defined as shown on the right with the top and bottom of the solution space also set to Neumann boundaries. A, B, C, D are reference points used in subsequent parts of the section.

The surface of the electrode was defined to be a Dirichlet surface with a potential of 5volts, giving a potential difference of 10 volts between alternate electrodes. The dielectric properties of the upper and lower halves of the problem were defined to be the same as in Section (6.3.1). The problem was solved to an accuracy of 0.09% error in the total energy in the solution. Figure (6.10a-d) show the magnitude of the electric field in slices across the problem space parallel to the plane ABCD with the mirror images generated to show the potential trap in the centre. Figure (6.10a) shows the field magnitude in a plane cutting through the electrode at the midpoint in the height, in this case 50nm below the upper surface. Figures (6.10b-d) shows the field in planes at heights of 100nm, 1μm and 5μm above the electrodes respectively. The maximum values for the field magnitudes in each of these planes was found to be 2.63×10^7, 6.64×10^6, 1.42×10^6 and 4.35×10^5 Vm^{-1} respectively. The maximum field strength in the solution was 4.57×10^7 Vm^{-1} and was found on the edge of the electrode on the upper surface.

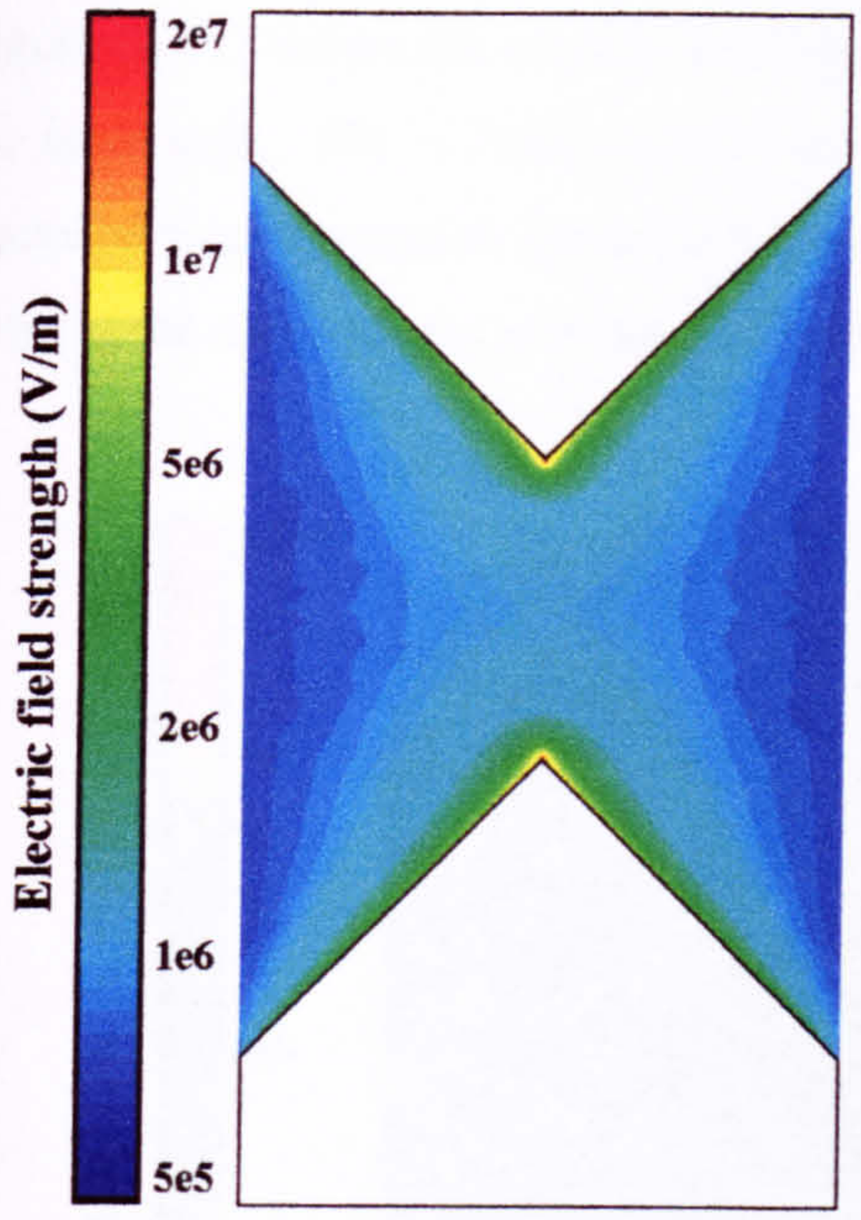

Figure (6.10a) The magnitude of the electric field in a plane parallel to ABCD and through the middle of the electrodes. The maximum value is at the tip of the triangle and the field falls off rapidly with distance from the electrode edge.

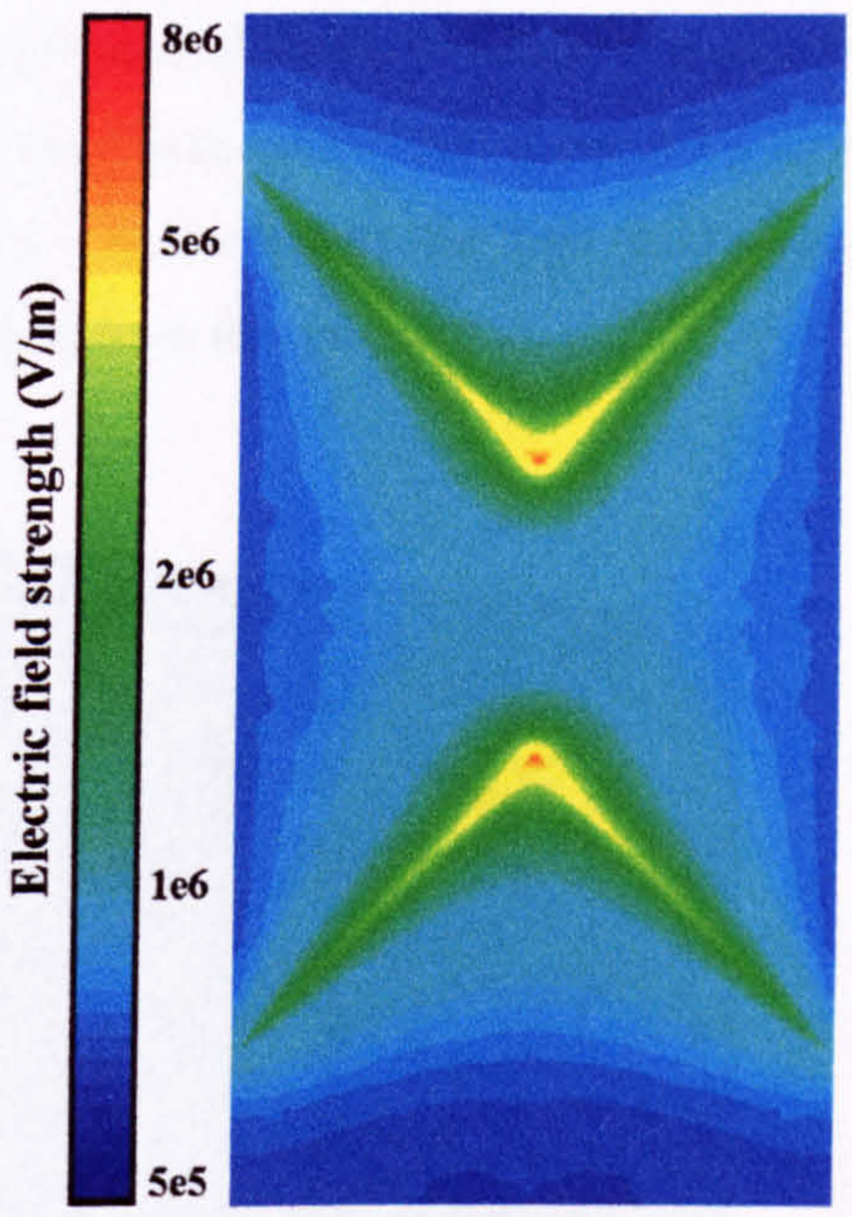

Figure (6.10b) The magnitude of the electric field in a plane parallel to ABCD and 100nm above the surface of the electrodes. The highest values are over the edges of the electrode with the maximum over the tip of the triangulation.

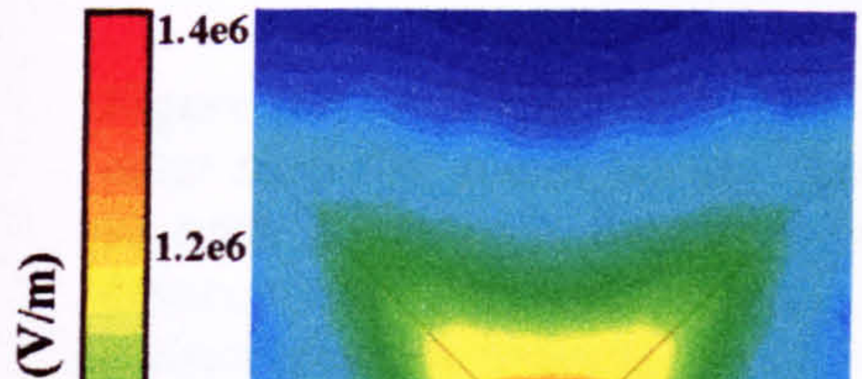

Figure (6.10c) The magnitude of the electric field in a plane parallel to ABCD and 1μm above the electrode surface. The distribution of the field is similar to (6.10b) but more spread out.

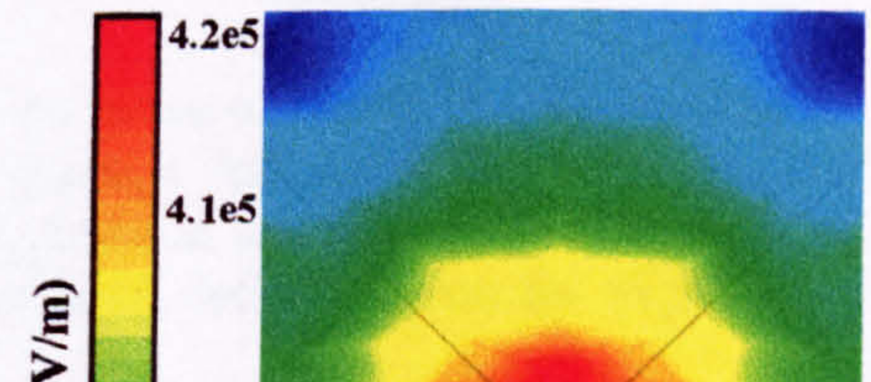

Figure (6.10d) The magnitude of the electric field in a plane parallel to ABCD and 5μm above the electrodes. There is a general high field region over the point of closes approach and low field away from this point but the variation is not large.

Figure (6.11) shows the electric field magnitude in three mutually perpendicular planes across the basic cell. The reference points are marked and the figure shows that there is no tightly enclosed trapping region for negative dielectrophoresis. It also shows the high field trapping point at the electrode tip and that the field falls off rapidly from this point.

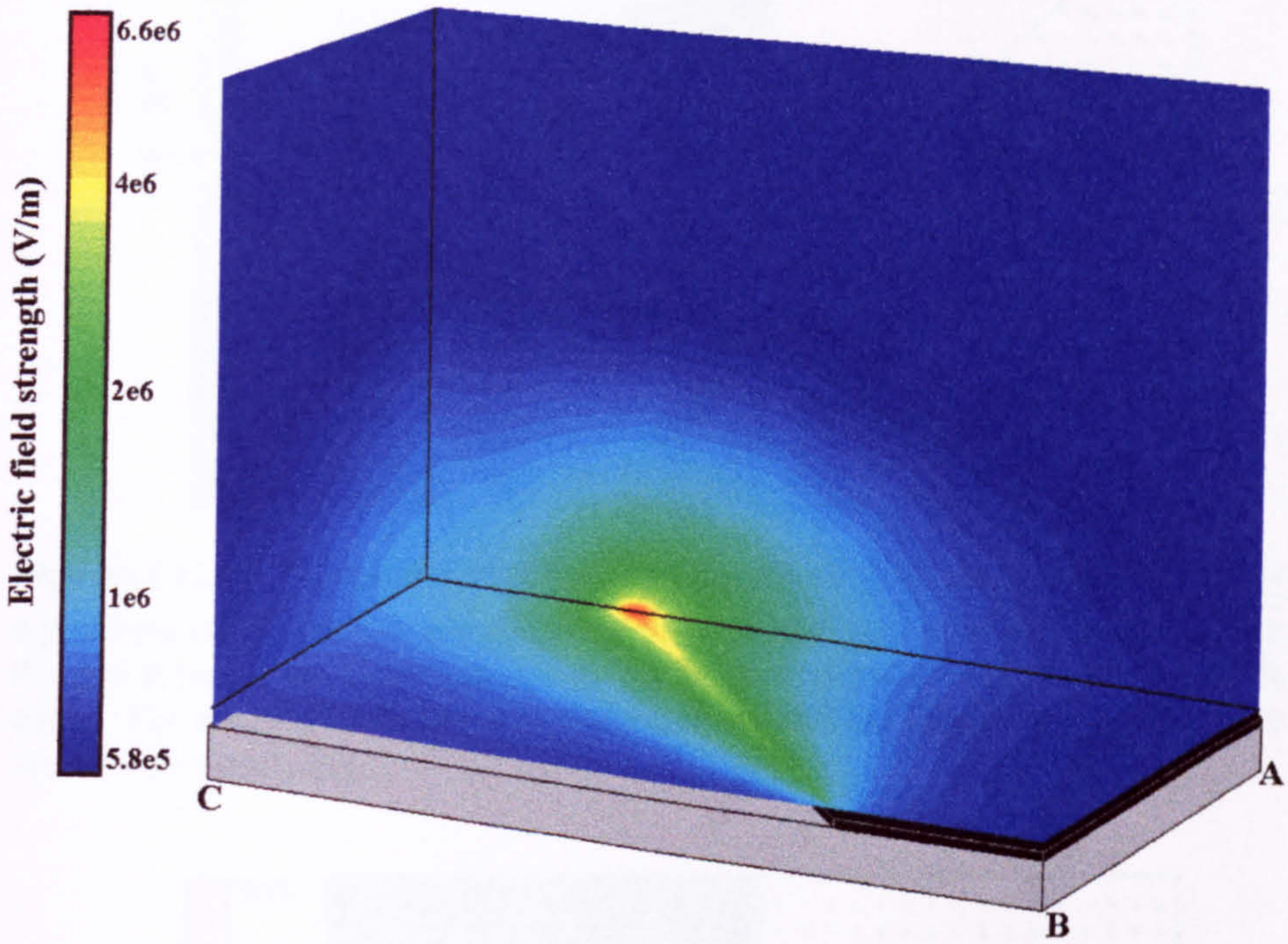

Figure (6.11) The electric field magnitude in the plane of Figure (6.10b) and two other mutually perpendicular vertical planes through AD and CD. The field strength is very high around the tip of the triangulation and falls off rapidly with distance from the electrode edge. There is no well defined region for negative dielectrophoretic trapping.

The vector for the dielectrophoretic force, $\nabla|\underline{\mathbf{E}}|^2$, was calculated in the four horizontal planes and the vertical plane through AD. The results are shown in Figure (6.12), (6.13) and (6.14). Figures (6.12a-d) show the positive DEP vector direction in planes parallel to ABCD at heights of -50nm, 100nm, 1μm and 5μm above the electrode surface. Figures (6.14a-d) show the negative DEP vector direction in the same planes. The maximum value of $\left|\nabla|\underline{\mathbf{E}}|^2\right|$ in each of the four planes was $2.8\text{x}10^{22}$, $8.3\text{x}10^{20}$, $4.8\text{x}10^{18}$ and $7.1\text{x}10^{16}$ V^2m^{-3}. The maximum value in the whole solution was $2.8\text{x}10^{22}$ V^2m^{-3}, found at the tip of the electrode. Figure (6.13) shows the positive DEP vector through the tip of the triangular feature in the vertical plane of symmetry through AD. The vector is represented in each figure by an arrow plot showing the vector direction, and a colour coded plot showing the magnitude at all points in the plane. The arrows in these plots are all the same length and 3D, shorter arrows indicate a direction into or out of the plane.

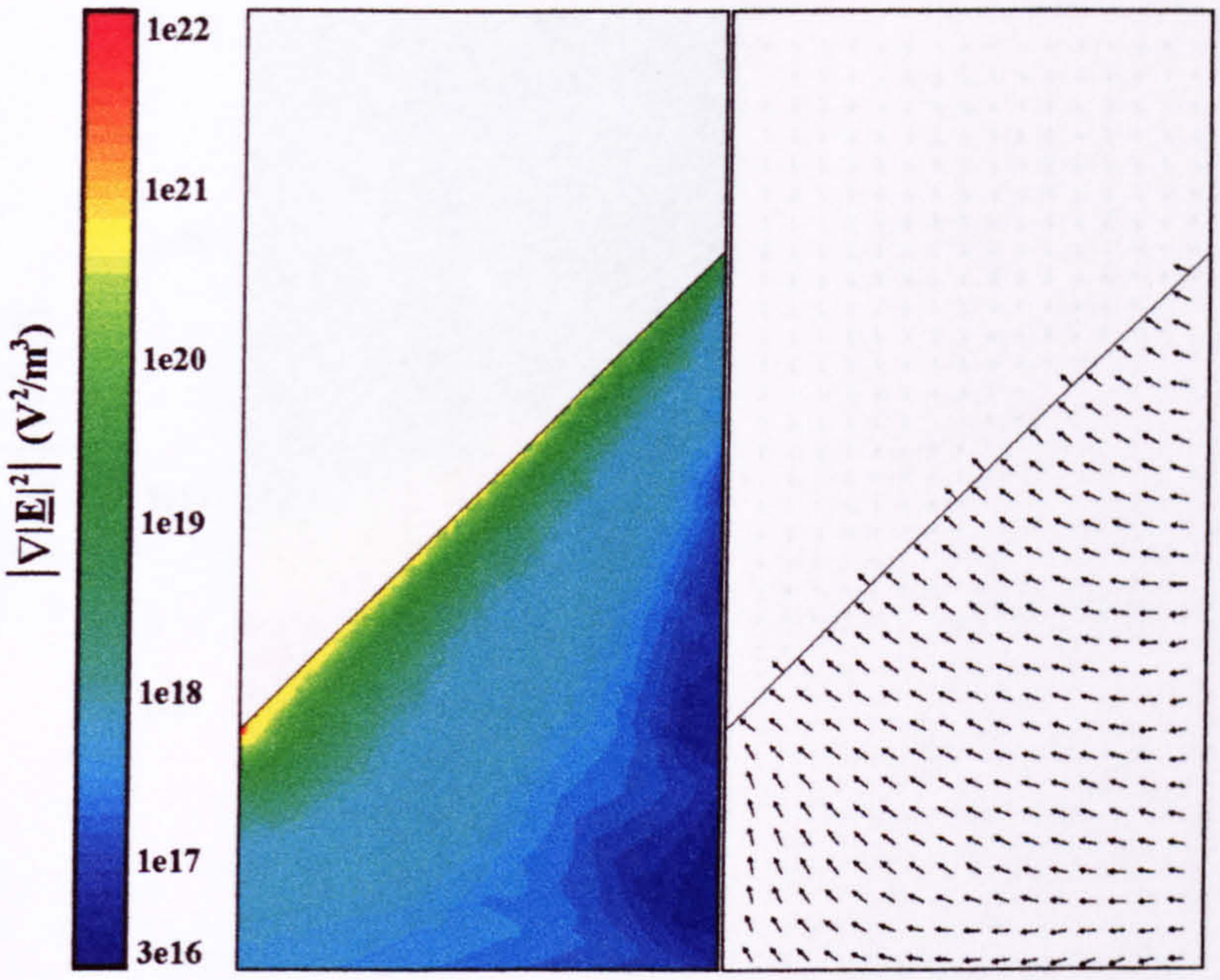

Figure (6.12a) The positive DEP force vector direction and magnitude of $\nabla|\underline{\mathbf{E}}|^2$ in a plane parallel to ABCD and 50nm below the upper surface of the electrode. In the gap between the electrodes, the vectors tend to point towards the electrode edge. The magnitude of the vector increases towards the edge and at the edge the vector is perpendicular.

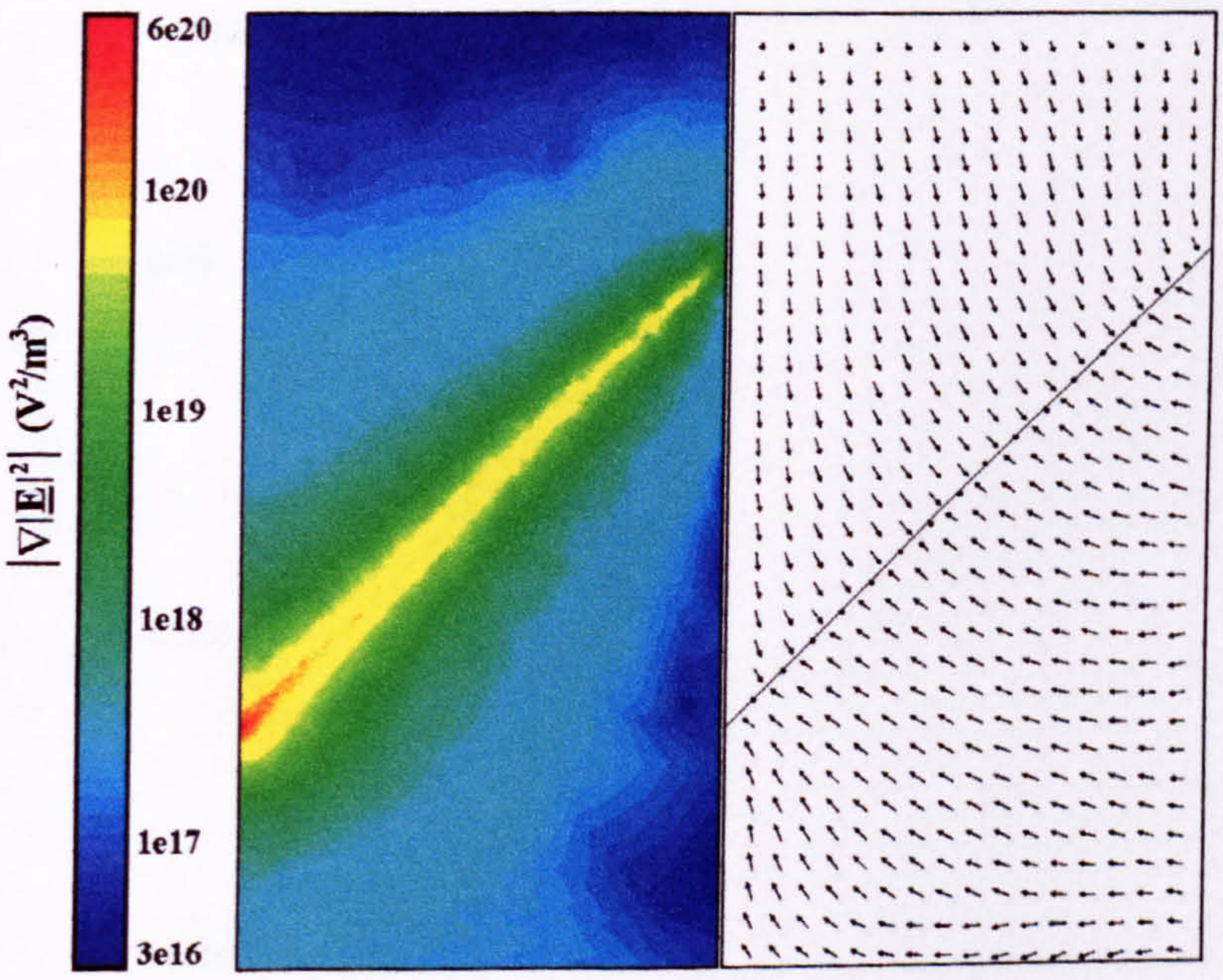

Figure (6.12b) The positive DEP force vector direction and magnitude of $\nabla|\underline{\mathbf{E}}|^2$ in a plane parallel to ABCD and 100nm above the electrode surface. Above the electrode the vectors point towards the electrode edge and the force magnitude again increases with decreasing distance. The maximum value of the vector is $8.3\text{x}10^{20}$ V^2m^{-3} and is found over the tip of the triangulation. Directly above the electrode edge, the vectors point straight downwards.

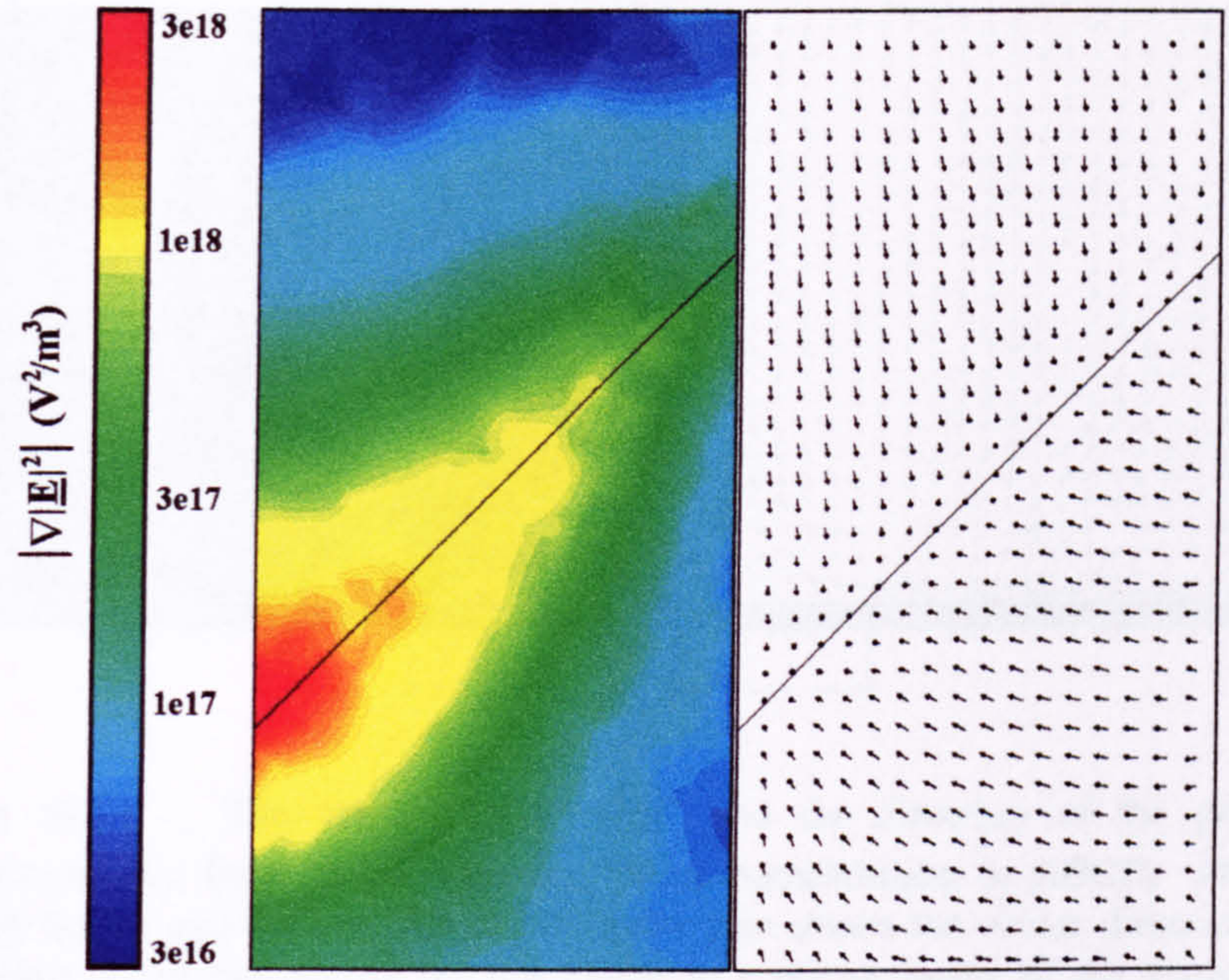

Figure (6.12c) The positive DEP force vector direction and magnitude of $\nabla|\underline{\mathbf{E}}|^2$ in a plane parallel to ABCD and 1μm above the surface of the electrodes. The vector direction is towards the electrode edge, which means that over the edge, the vectors tend to point downwards. The magnitude of the vector is highest over the tip of the triangulation and lowest over the middle of the electrode.

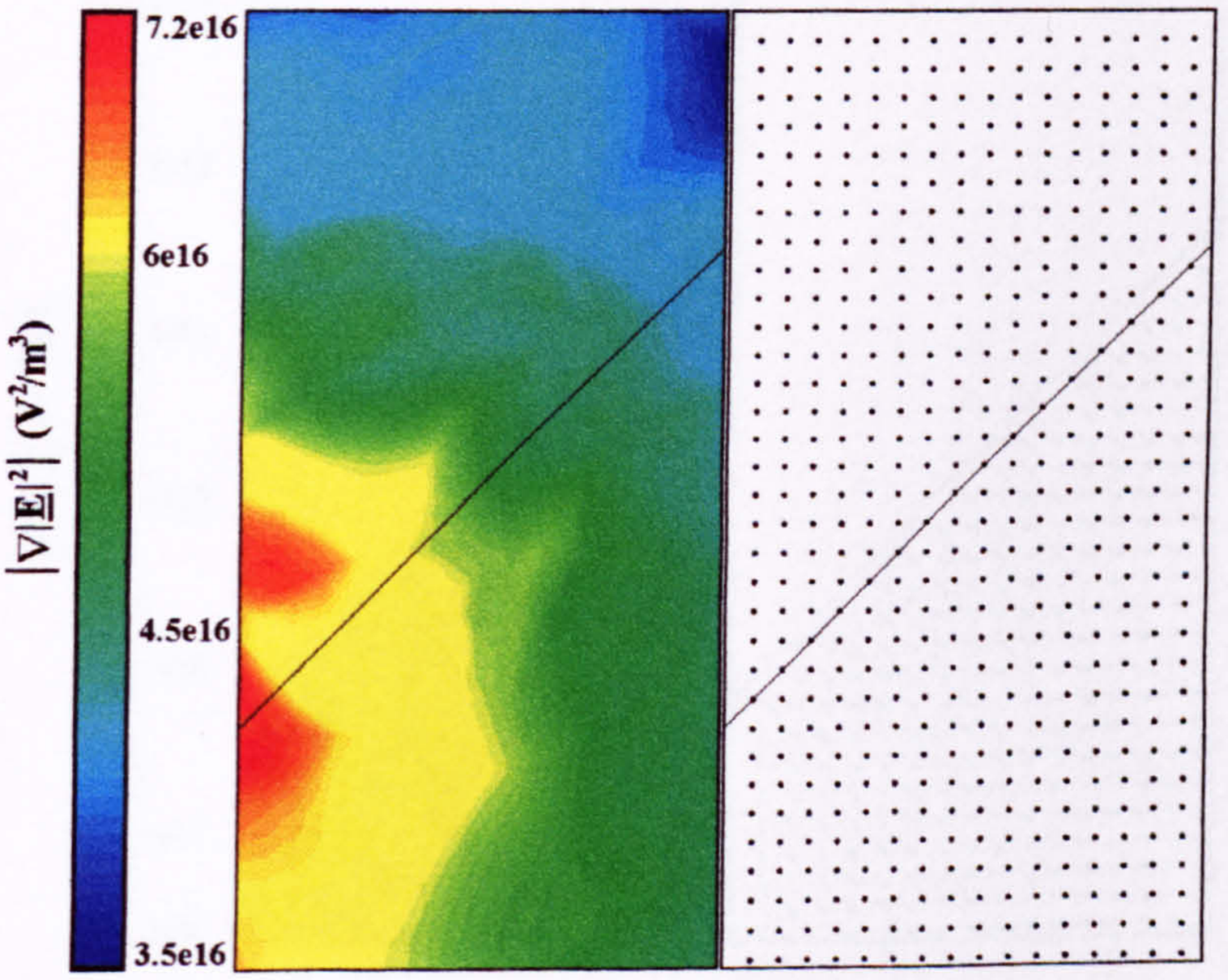

Figure (6.12d) The positive DEP force vector direction and magnitude of $\nabla|\underline{\mathbf{E}}|^2$ in a plane parallel to ABCD and 5μm above the electrode surface. The vectors all point downwards and the magnitude has a maximum over the tip of the electrode but does not vary by much across the plane. This figure indicates that the path of a particle would be vertical at this height.

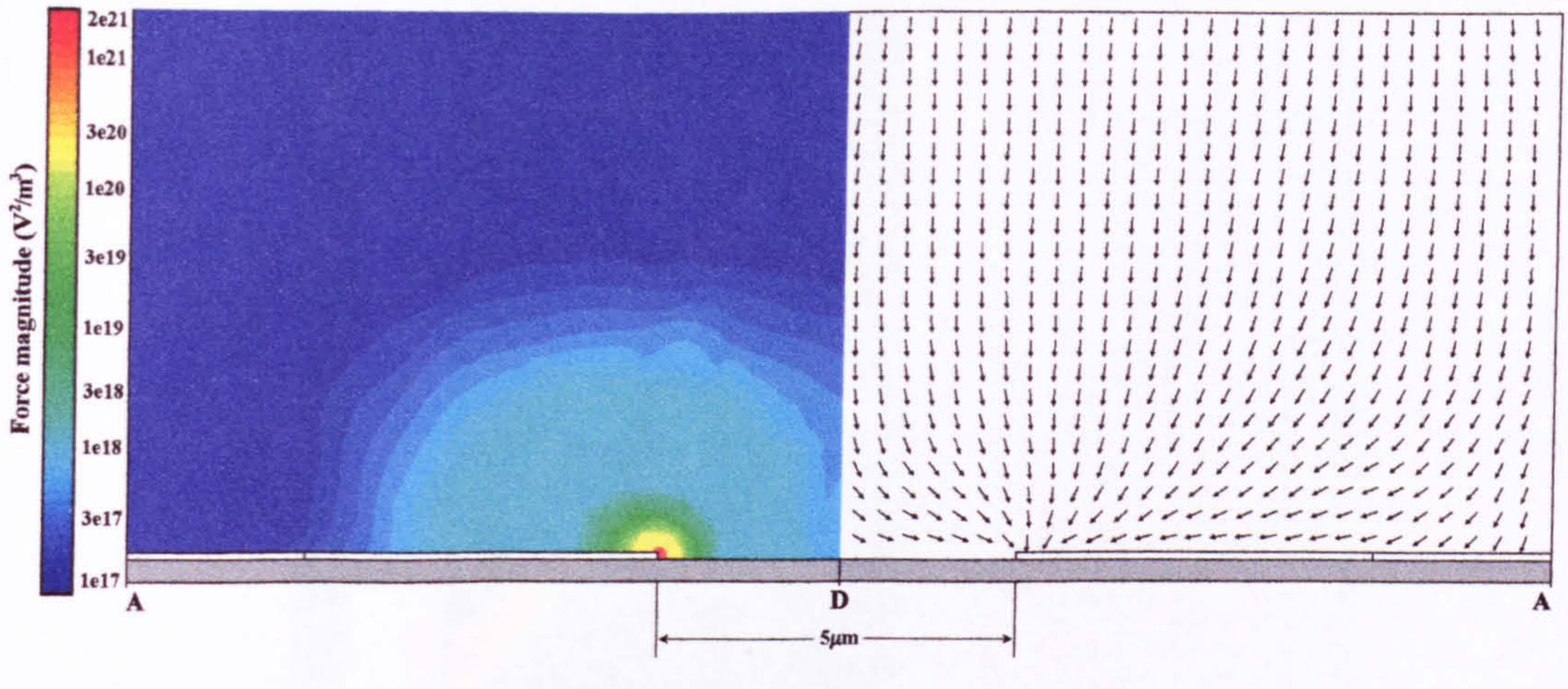

Figure (6.13) The magnitude of $\nabla|\underline{\mathbf{E}}|^2$ and the direction of the positive dielectrophoretic force in the symmetry plane perpendicular to ABCD, running through the tip and the line AD. The arrow plot shows the vector direction and the colour coded plot shows the magnitude in a mirror image of the arrow plot about the vertical line through D. Above approximately 4μm, the arrows all point straight down and below 4μm, they tend to point towards the tip of the electrode. The magnitude rises sharply, from approximately 1×10^{18} V^2m^{-3} at a distance of 2μm to the maximum value of 2×10^{22} V^2m^{-3} on the electrode surface at the tip.

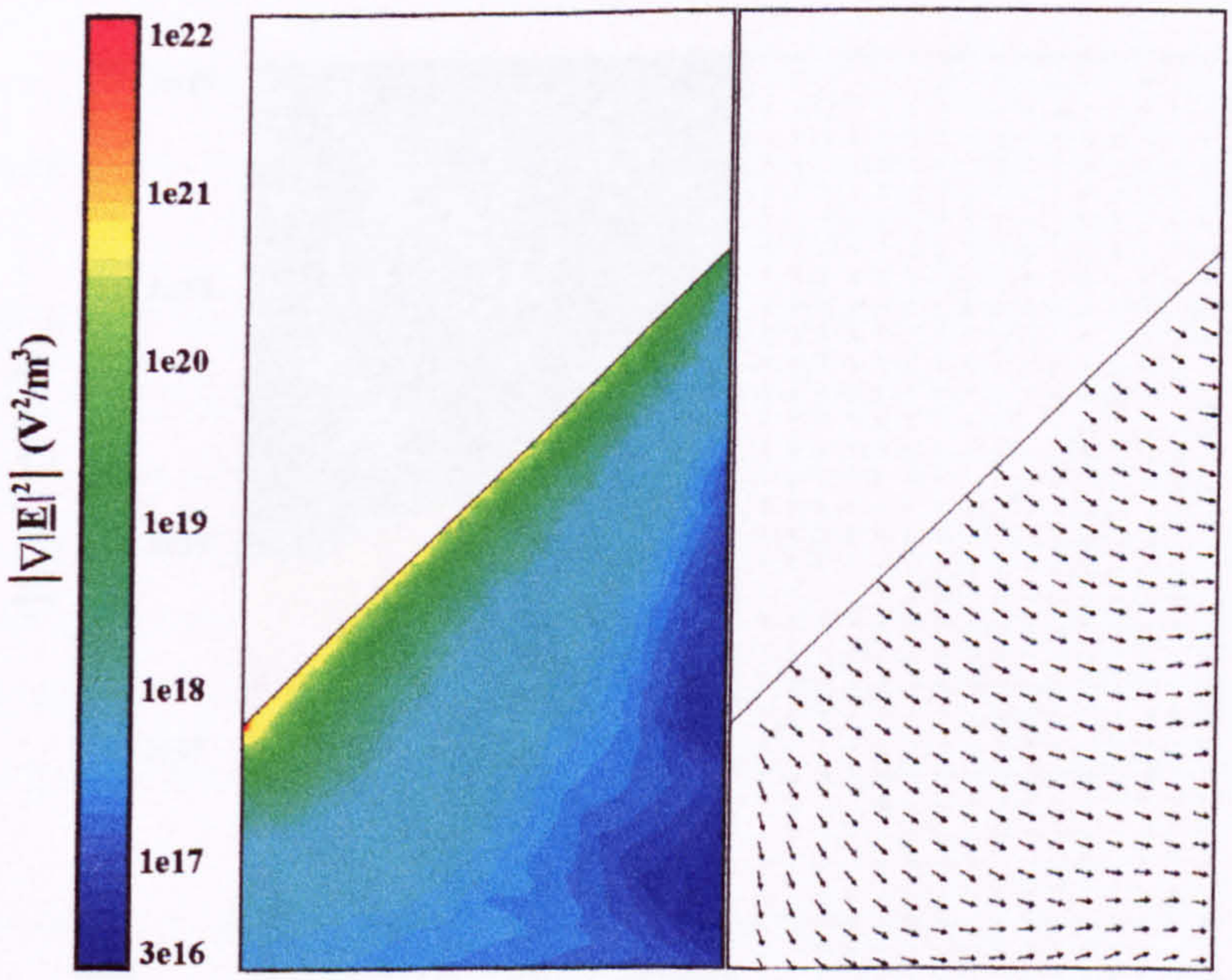

Figure (6.14a) The negative DEP force vector direction in a plane parallel to ABCD and 50nm below the upper surface of the electrode. In the gap between the electrodes, the vectors tend to point away from the electrode edge. The magnitude of $\nabla|\underline{\mathbf{E}}|^2$ decreases rapidly with increasing distance from the electrode edge and the highest value is found at the tip of electrode.

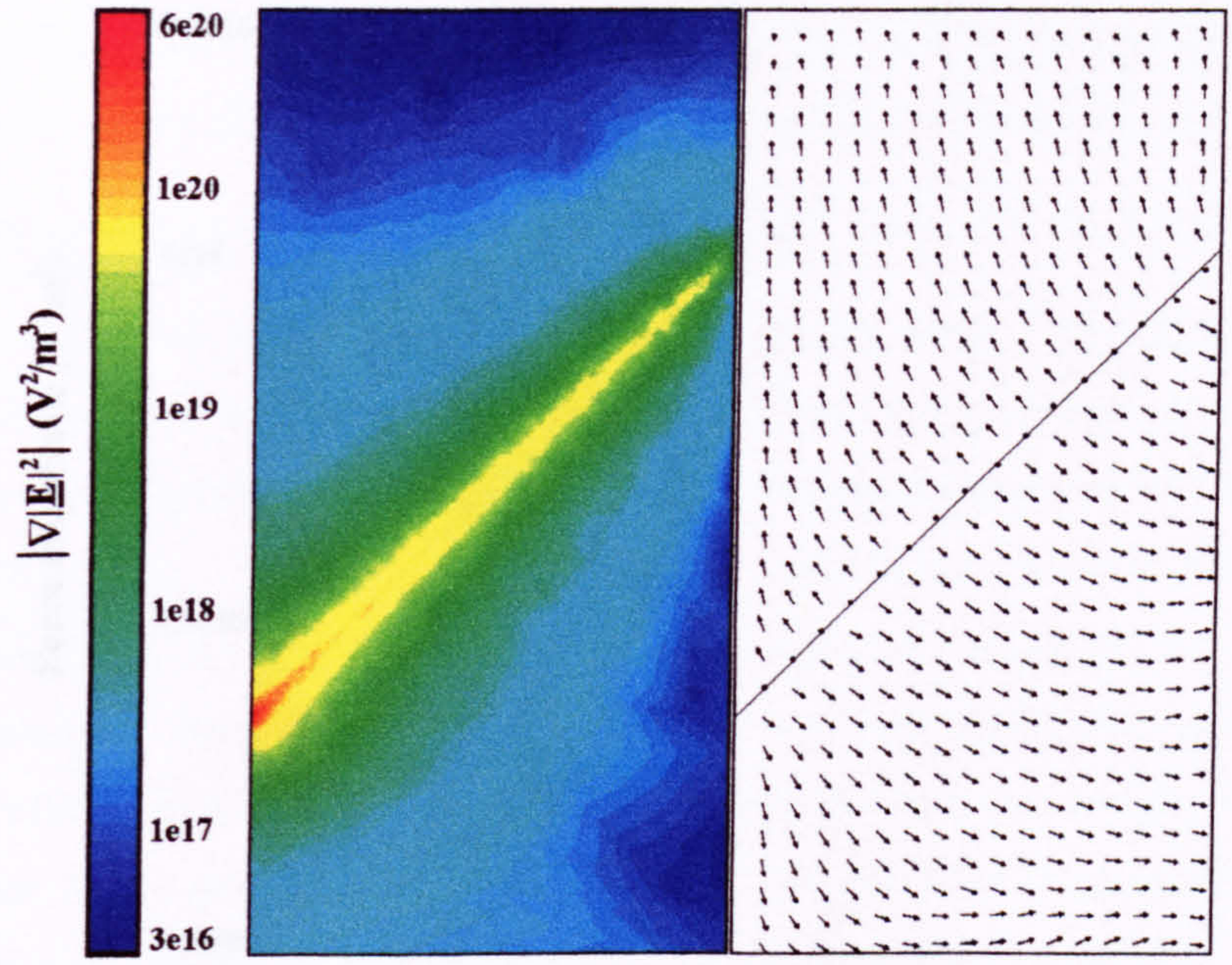

Figure (6.14b) The negative DEP force vector direction in a plane parallel to ABCD and 100nm above the electrode surface. Above the electrode the vectors point away from the electrode edge and the magnitude of $\nabla|\underline{\mathbf{E}}|^2$ again increases with decreasing distance. The maximum value is found over the tip of the triangulation and above the electrode edge, the vectors point straight upwards.

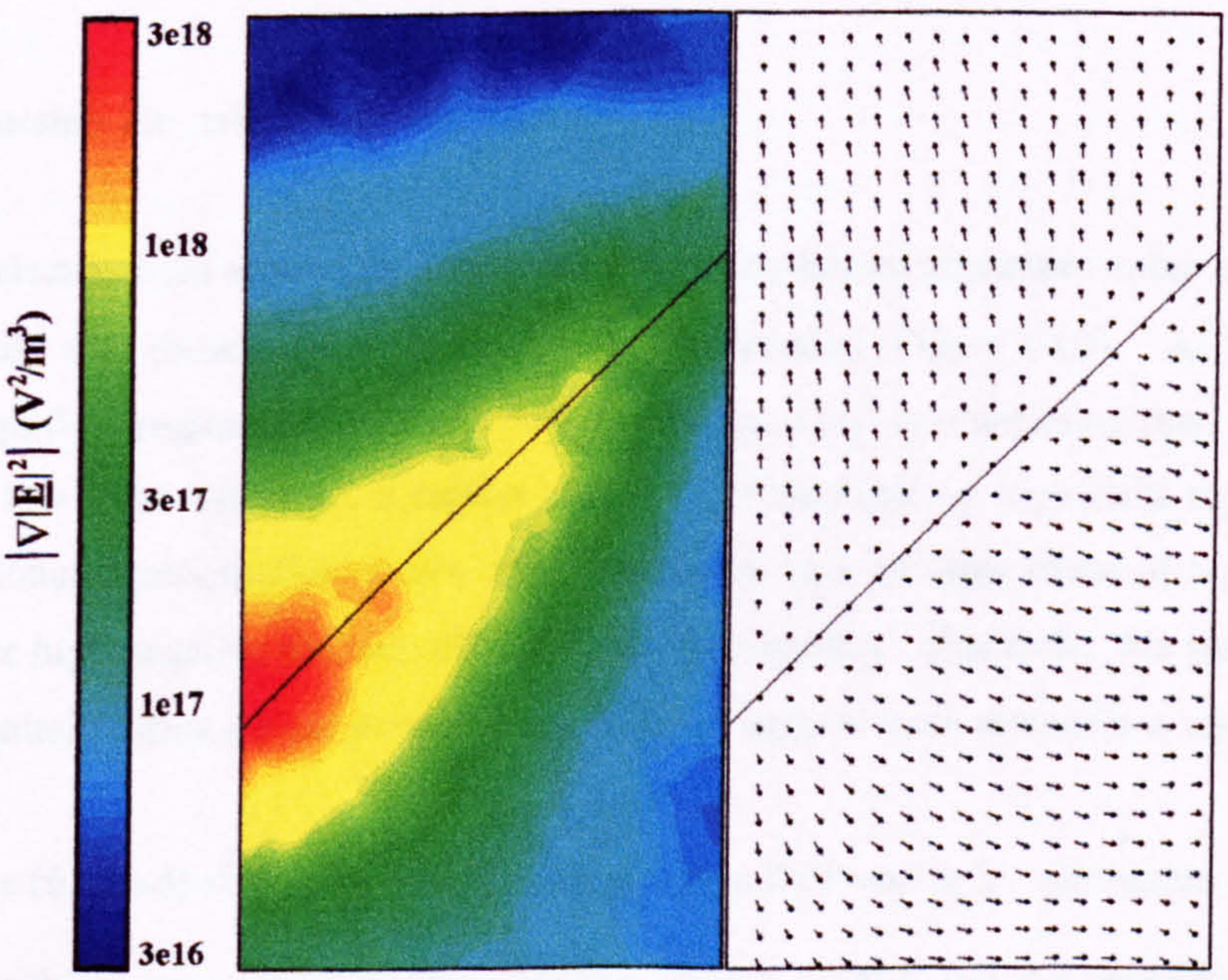

Figure (6.14c) The negative DEP force vector direction in a plane parallel to ABCD and 1μm above the surface of the electrodes. The vector direction is away from the electrode edge, which means that in the region over the edge, the vectors point upwards. The magnitude of $\nabla|\underline{\mathbf{E}}|^2$ is highest over the tip of the triangulation and lowest over the middle of the electrode.

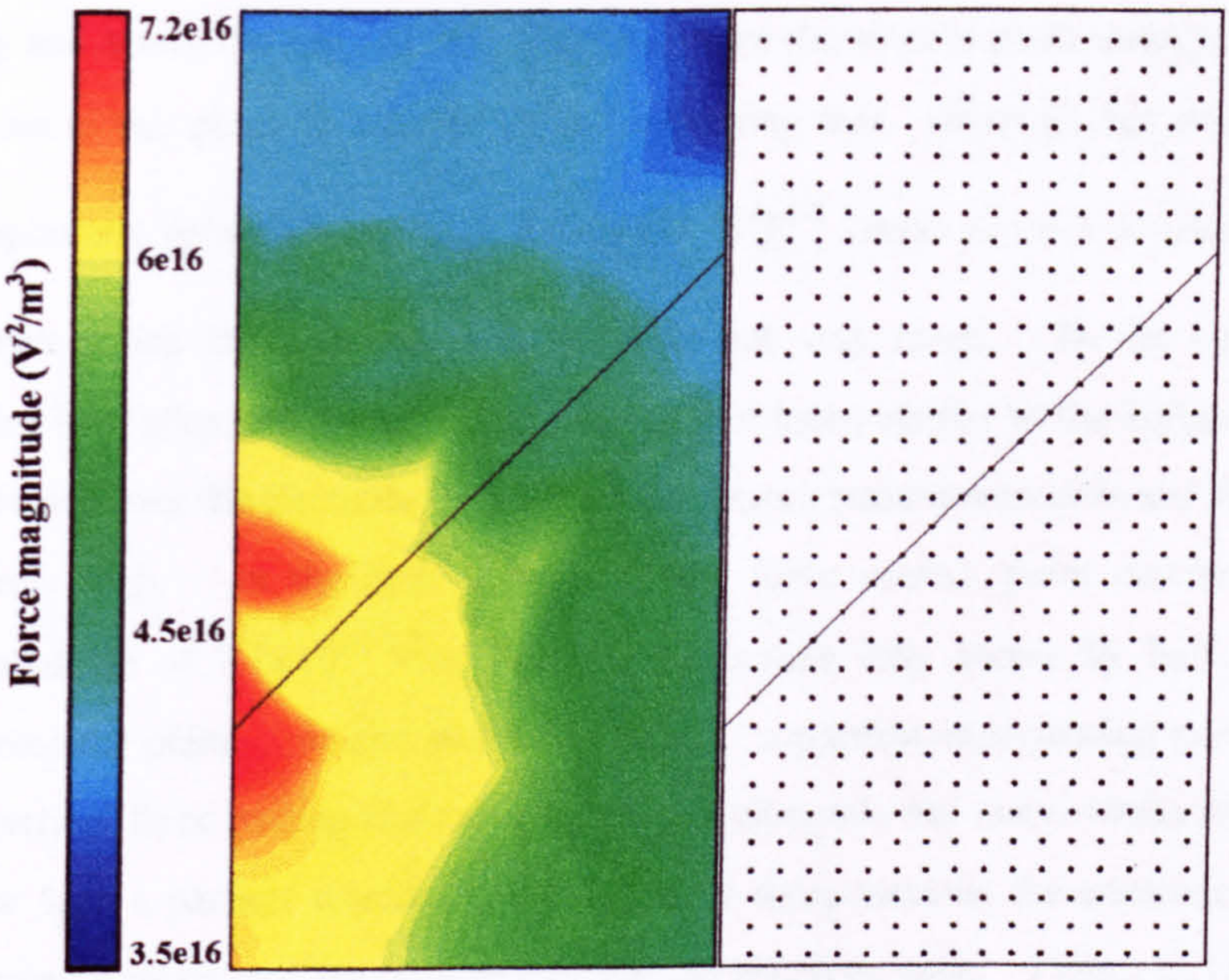

Figure (6.14d) The negative DEP force vector direction and magnitude of $\nabla|\underline{\mathbf{E}}|^2$ in a plane parallel to ABCD and 5μm above the electrode surface. The vectors all point vertically upwards and the magnitude has a maximum over the tip of the electrode but is fairly constant across the plane.

6.3.4 Discussion II: triangular electrodes

The electric field around the triangular electrodes has its maximum value at the tip and falls off rapidly with distance from this point in any direction (Figure 6.10). At 5μm (Figure 6.9d), the high field region is diffuse and covers the region between opposing tips. There is no well-defined low field region i.e. a region of low field bounded by high field regions. The three dimensional representation shows more clearly the lack of large areas of high field that could generate high negative dielectrophoretic potential minima. However, the very high field at the tip definitely forms a local maximum in field strength in three dimensions and is an ideal positive trap.

Figure (6.12a-d) shows the nature of the positive DEP vector in four planes horizontally through the problem space showing the direction (with a vector) and the magnitude of $\nabla|\underline{\mathbf{E}}|^2$ (with a colour coded plot). In the plane of the electrode (Figure 6.12a), the force is directed towards the electrode edge with the largest value of 2.8×10^{22} V^2m^{-3} at the tip. 100nm above the upper surface of the electrode, the picture is similar with the force vector both on and off the electrode pointing towards the electrode edge. The maximum force magnitude is in the region

running along and above the edge of the electrode where the vectors point straight down. The maximum value in this plane is 8.3×10^{20} V^2m^{-3} indicating that, although this design produces high dielectrophoretic potentials and high values of $\left|\nabla|\underline{\mathbf{E}}|^2\right|$ (these are not necessarily related), the volume over which the high gradients occur is not very large. In the 1μm plane the maximum value has fallen to 4.8×10^{18} V^2m^{-3} and the plot looks similar to the 100nm plot, with a more diffuse region over the electrode edge where the vectors point downwards and the magnitude is comparatively high. In the 5μm plane, all the force vectors point downwards with a maximum magnitude of 7.1×10^{16} V^2m^{-3} but the magnitude only varies by half an order of magnitude across the plane. At and above this height, a particle experiencing positive DEP is subject to a vertical force pulling it down towards the electrode but not towards any particular point. Below 5μm a particle would also experience a force towards the electrode surface but with an increasing translational component towards the electrode edge. Figure (6.13) shows the positive DEP vector in the symmetry plane through the tip and along the line AD, demonstrating the variation in the magnitude and direction of force vertically. Particles falling towards the electrode surface experience an increasing attractive force towards the tip. The magnitude of the force also increases rapidly as the distance between the particle and the tip decreases.

Figure (6.14a-d) show the nature of the negative DEP force vector in the same four horizontal planes. Although the maximum force in each plane is the same as for positive DEP, the volumes over which the large values occur is very small. There are no well-defined points of negative DEP collection, only regions where particles would be repelled from by negative DEP. The particles would then move to a distance at which the dielectrophoretic force is balanced by other forces.

6.3.5 Results III: castellated electrodes

The basic cell for the castellated electrode design is shown in Figure (6.15). The solution shown in this section is for a set of castellated electrodes with feature and gaps sizes equal to 5μm. All the external boundaries of the problem space were defined to be Neumann. Again, the boundaries resulted in the solution for an infinite mirroring of this basic cell and the area of interest was restricted to within 10μm of the substrate surface.

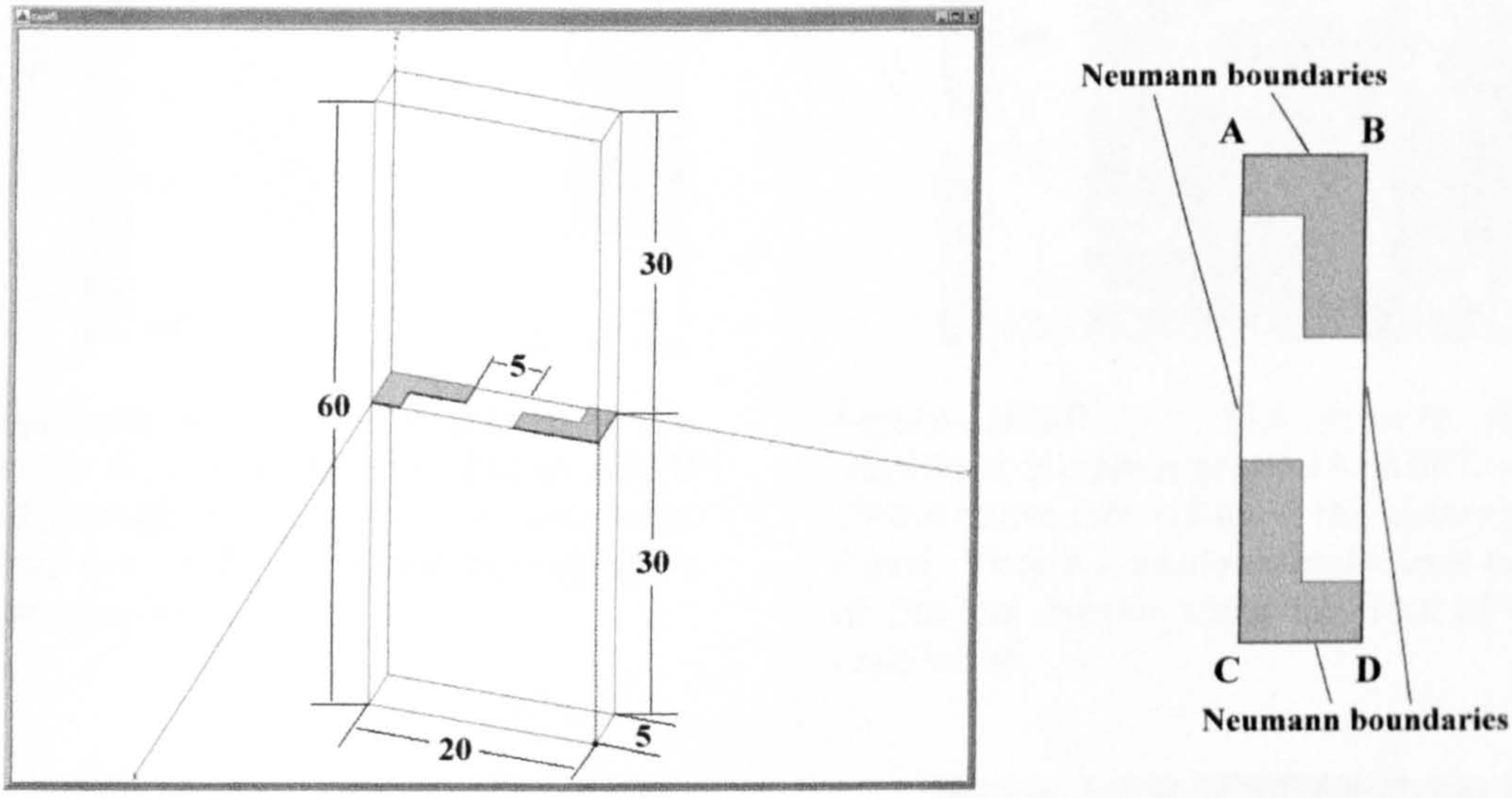

Figure (6.15) Schematic diagram of the basic cell used in solving the electric field in the castellated electrodes. The dimensions of the problem space were as shown on the right in units of micrometres. All boundaries were defined to be Neumann and A, B, C, D are reference points.

The surface of the electrodes were defined to be Dirichlet surfaces with potentials of 5volts and -5volts giving a potential difference between the electrodes of 10volts. The dielectric properties of the upper and lower halves of the problem space were defined as in section 6.3.1. The problem was solved to an accuracy of 0.26% error in the total energy in the solution. Figure (6.16a-d) show the magnitude of the electric field in slices across the problem space parallel to the upper electrode surface with the mirror images generated to show the potential trap in the centre. (6.16a) shows the field magnitude in a plane cutting through the electrode at the midpoint in the height (50nm below the upper surface). (6.16b-d) shows the field in planes at heights of 100nm, 1μm and 5μm above the electrode surface respectively. The maximum values for the field magnitudes in each of theses planes was found to be 2.11×10^7, 6.35×10^6, 1.5×10^6 and 4.35×10^5 Vm^{-1} respectively. The maximum field strength in the solution was 3.04×10^7 Vm^{-1} and was found on the edge of the electrode on the upper surface.

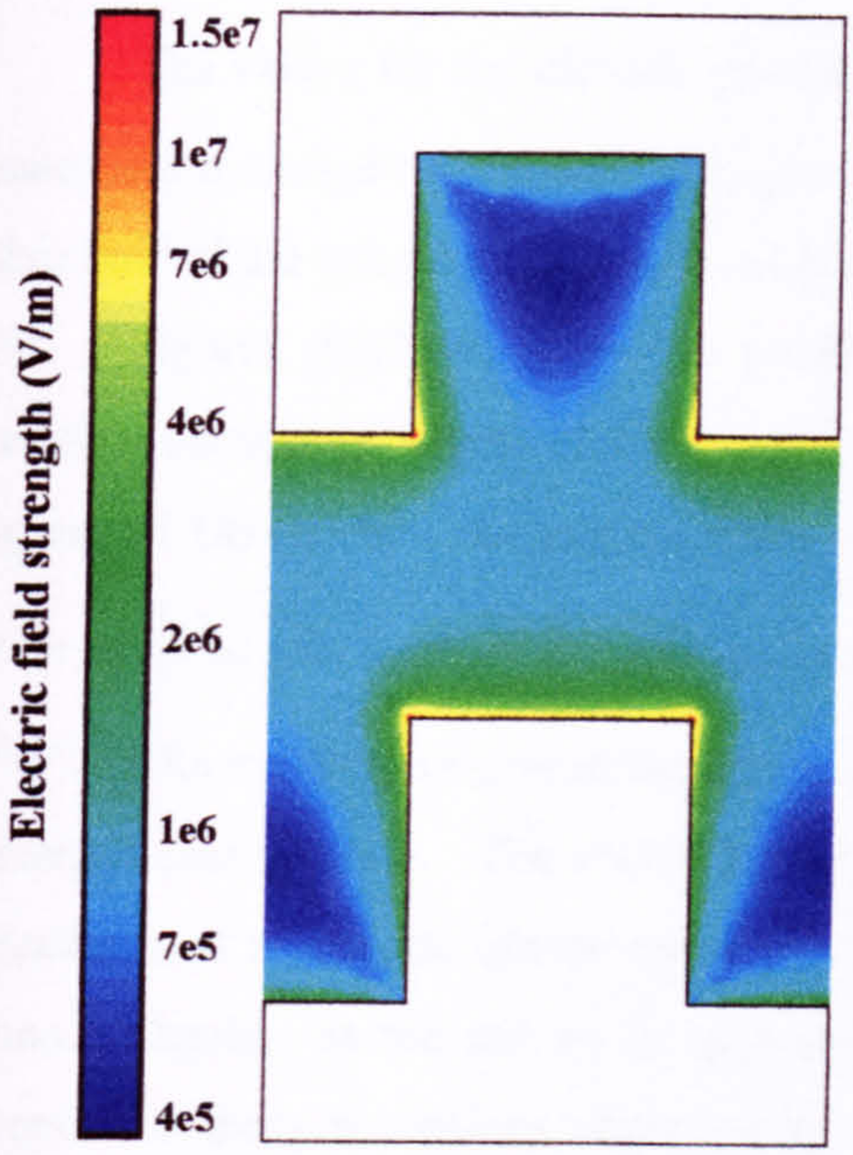

Figure (6.16a) The magnitude of the electric field in a plane parallel to ABCD and through the middle of the electrodes. There is a local maximum at each tip and a local minimum in the bays.

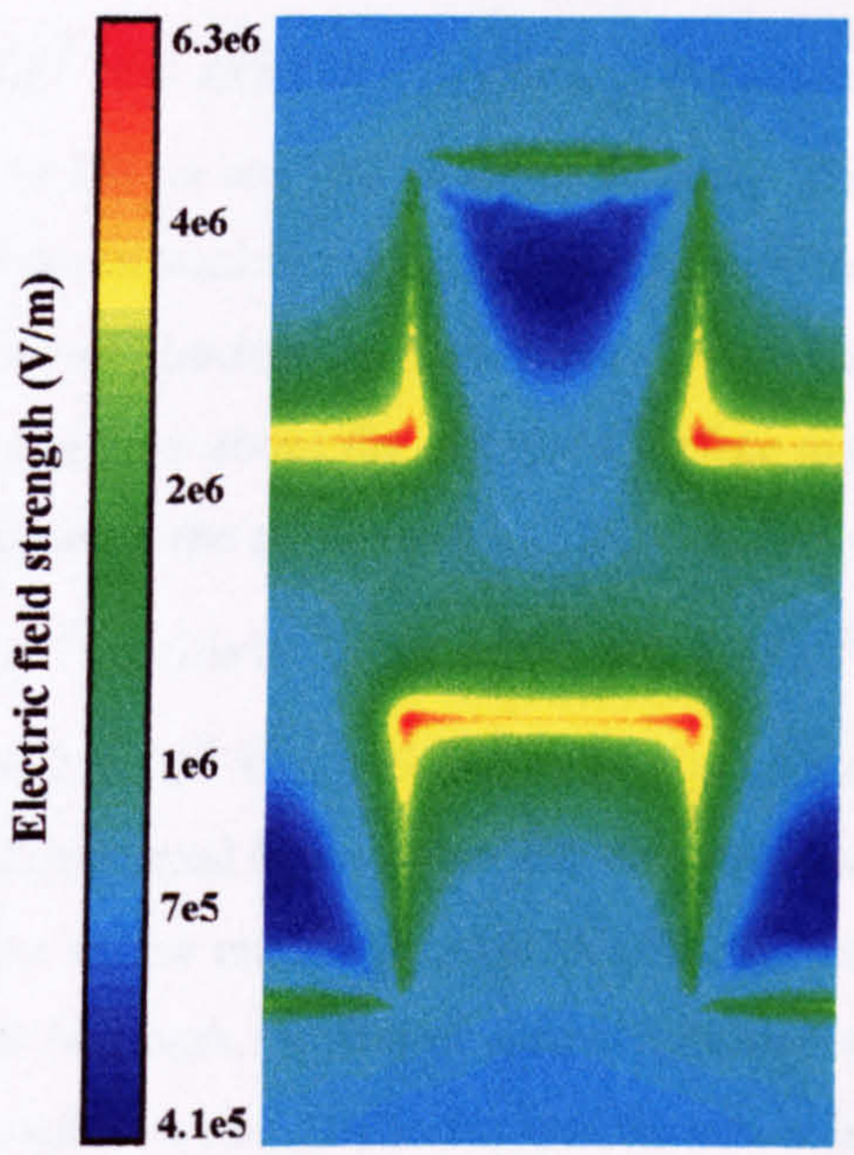

Figure (6.16b) The electric field magnitude in a plane parallel to ABCD and 100nm above the surface of the electrodes. Again, there is a local maximum over each tip but this extends along the front of the castellation.

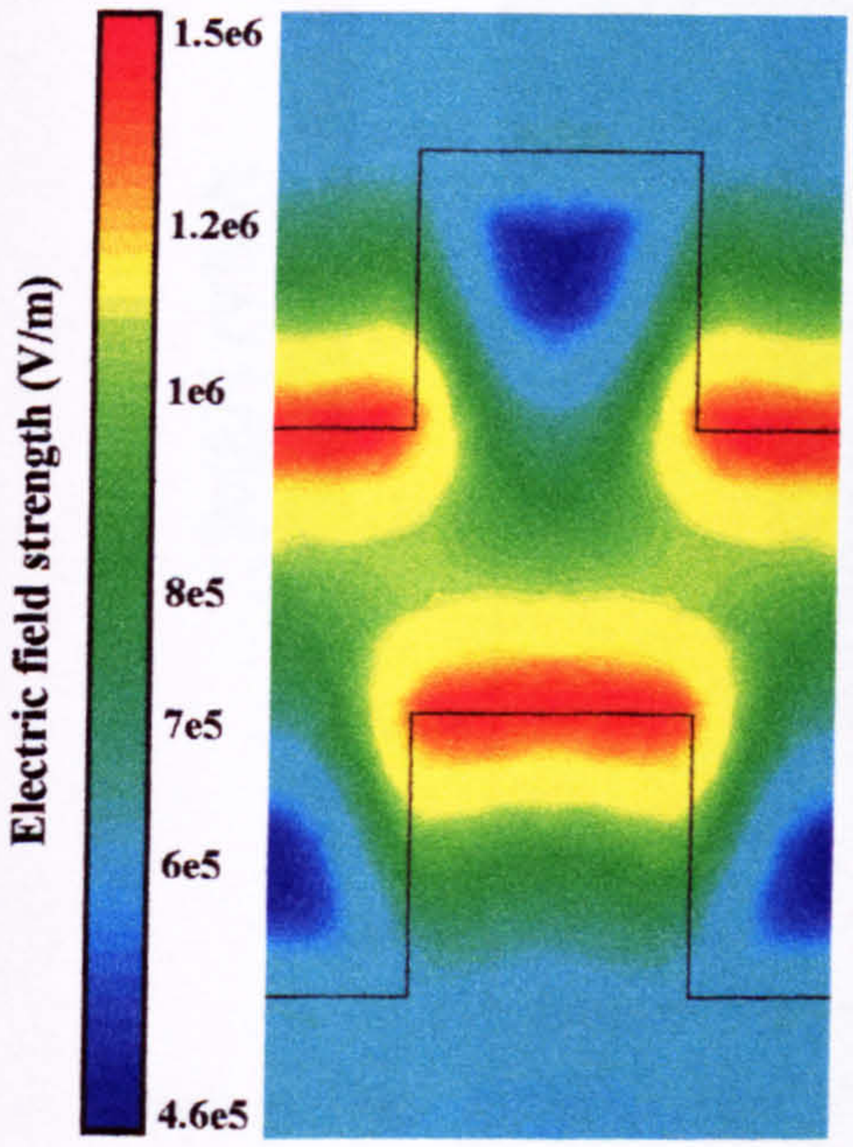

Figure (6.16c) The magnitude of the electric field in a plane parallel to ABCD and 1μm above the surface of the electrodes. There are high field regions over the fronts of the castellations and the low field regions in the bays have decreased in size.

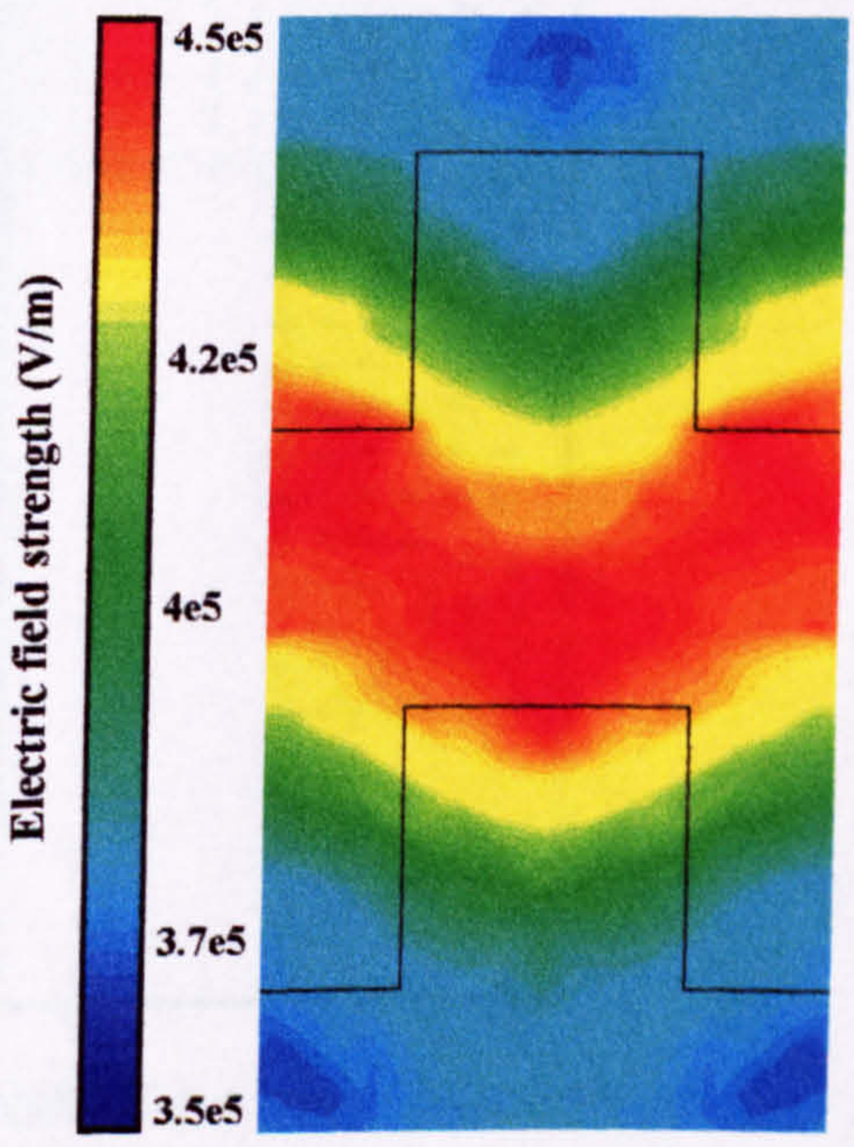

Figure (6.16d) The electric field magnitude in a plane parallel to ABCD and 5μm above the surface of the electrodes. There is a general high field region over the gap between the electrodes and a low field region over the electrodes but there is a very small difference in magnitude.

The vector for the dielectrophoretic force, $\nabla|\underline{\mathbf{E}}|^2$ was calculated in the four horizontal planes and the results are shown in Figure (6.17) and (6.18) for one half of the basic cell. The other half of the solution is a rotational image around the vertical line through the centre of the cell. Figures (6.17a-d) show the positive DEP vector direction in planes parallel to the electrode surface at heights of -50nm, 100nm, 1μm and 5μm above the electrode surface and Figures (6.18a-d) show the negative DEP vector direction in the same planes. The maximum value of $\left|\nabla|\underline{\mathbf{E}}|^2\right|$ in each of the four planes was $2.5\text{x}10^{22}$, $6.76\text{x}10^{20}$, $3.25\text{x}10^{18}$ and $8.4\text{x}10^{16}$ V^2m^{-3}. The maximum value in the whole solution was $2.5\text{x}10^{22}$ V^2m^{-3}, found at the tips of the electrode castellations. The vector in each figure is represented by an arrow plot showing the direction and a separate colour coded plot showing the vector magnitude at each point in the plane. Again, as the arrows in each plot are equal in length, a shorter arrow indicates a direction in three dimensions either into or out of the page. A circle indicates that the arrow is pointing in a direction perpendicular to the page.

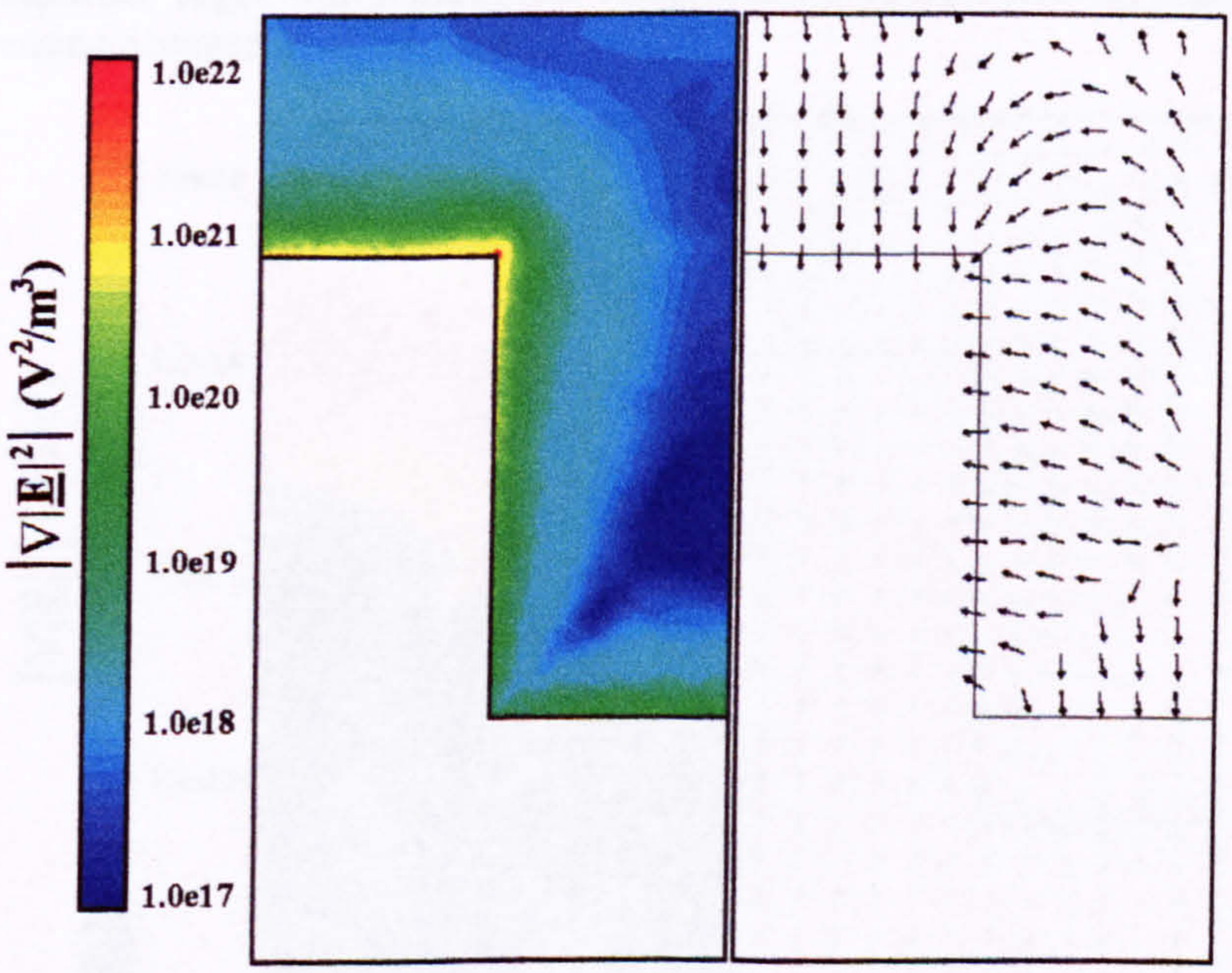

Figure (6.17a) The positive dielectrophoretic force vector direction and magnitude of $\nabla|\underline{\mathbf{E}}|^2$ in a plane parallel to ABCD and through the electrodes 50nm below the upper surface. In the gap between the electrodes, the vectors point towards the electrode edge. The magnitude is maximum at the tip of the electrode, in general high along the electrode edge and a minimum in the low electric field region in the bay.

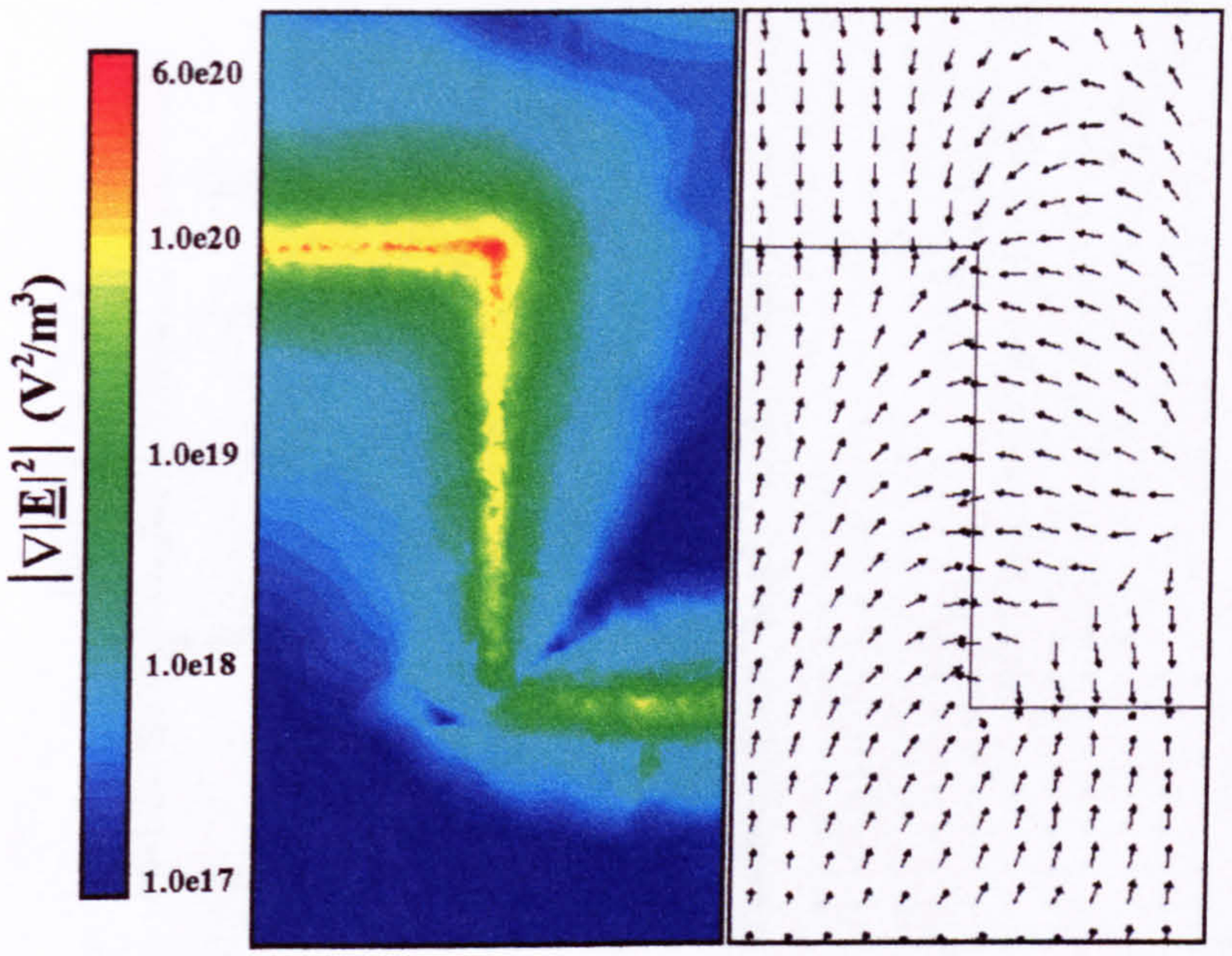

Figure (6.17b) The positive dielectrophoretic force vector direction and magnitude of $\nabla|\underline{\mathbf{E}}|^2$ in a plane parallel to ABCD and 100nm above the electrode surface. In the gap between the electrodes and above the electrode surface, the vectors point towards the electrode edge. The magnitude of the force is high over the electrode edges with a maximum value over the tip and falls off rapidly with increasing distance from the edge.

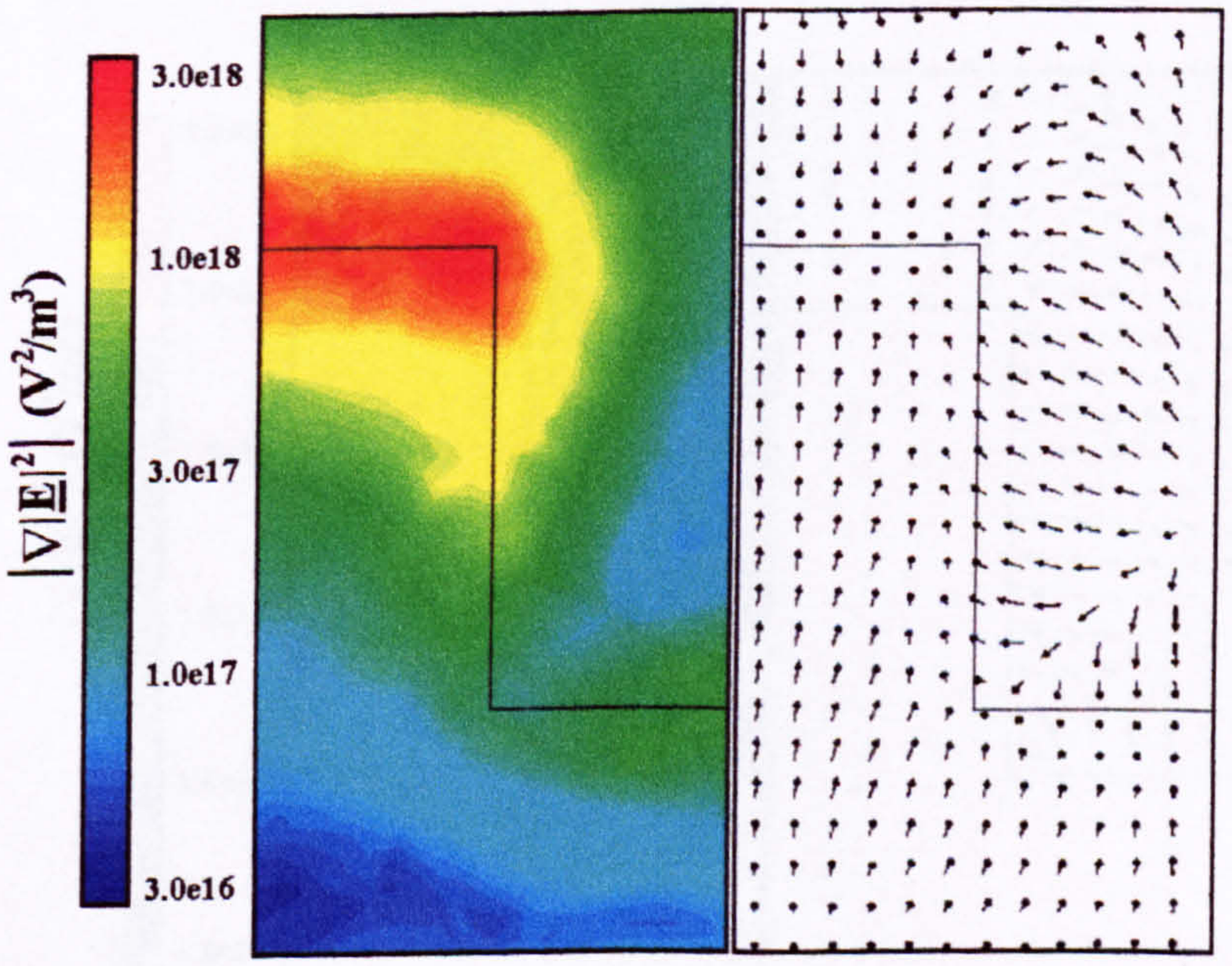

Figure (6.17c) The positive dielectrophoretic force vector direction and magnitude of $\nabla|\underline{\mathbf{E}}|^2$ in a plane parallel to ABCD and 1μm above the electrode surface. In the gap between the electrodes and above the electrode surface, the vectors point towards the electrode edge. The magnitude of the force is high over the front edge of the castellation and gap between the electrodes and lowest over the electrode surface.

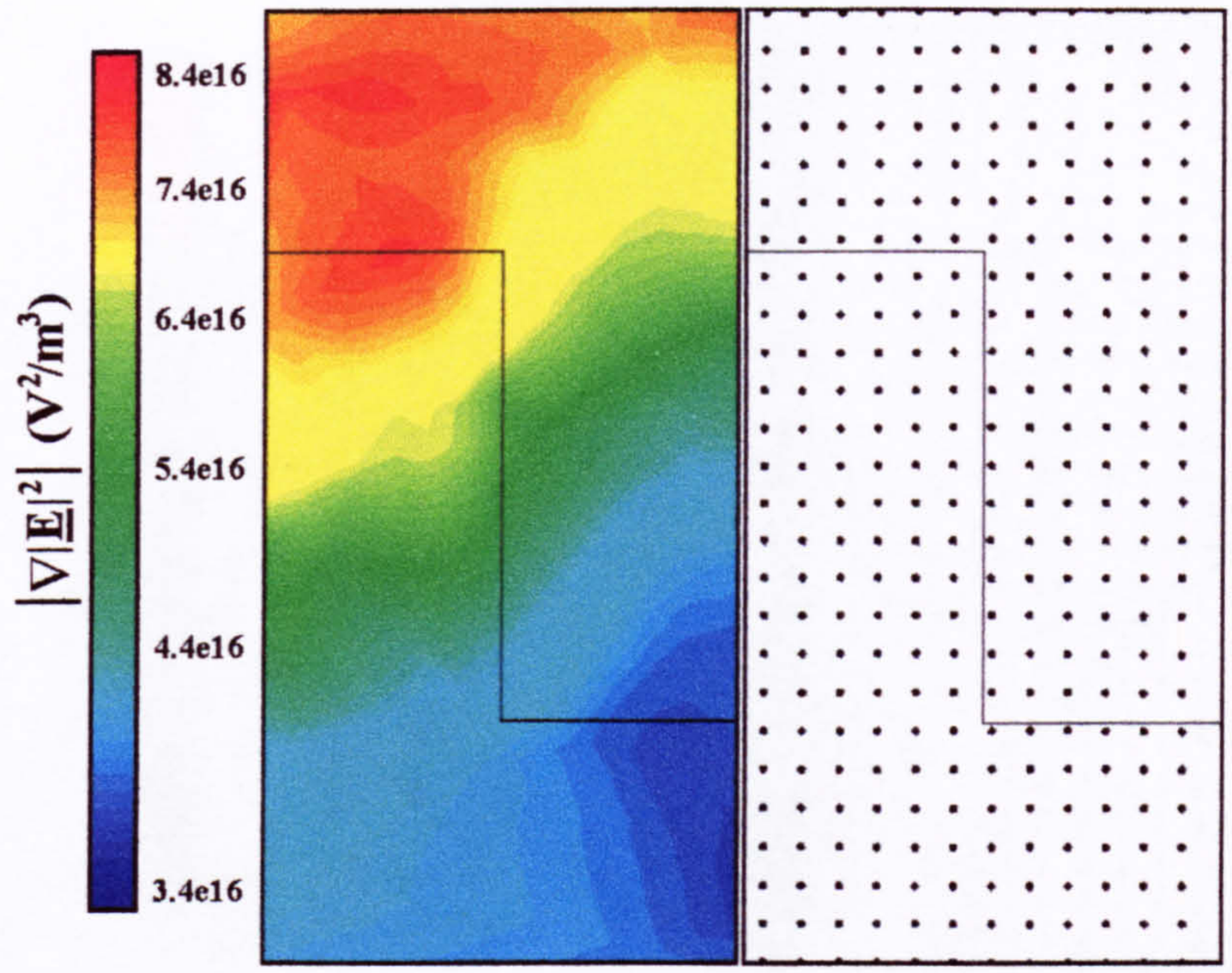

Figure (6.17d) The positive DEP vector direction and magnitude of $\nabla|\underline{\mathbf{E}}|^2$ in a plane parallel to ABCD and 5μm above the surface of the electrodes. The vectors all point downwards and the magnitude has a maximum over the electrode gap and a minimum over the narrowest part of the electrode but only varies by half an order of magnitude in this plane.

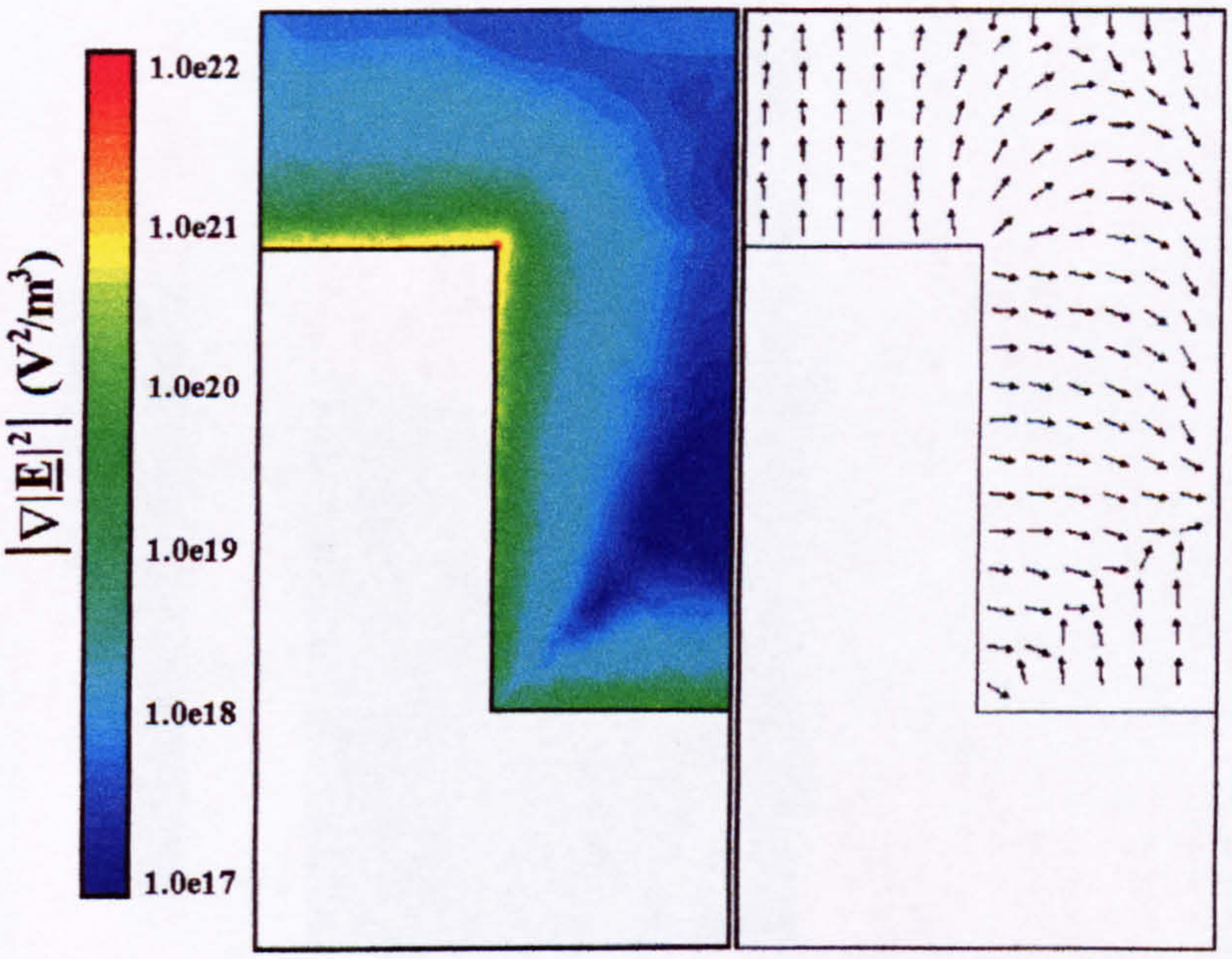

Figure (6.18a) The negative DEP force vector direction and magnitude of $\nabla|\underline{\mathbf{E}}|^2$ in a plane parallel to ABCD and through the electrodes 50nm below the upper surface. The vectors in the gap point away from the electrode edge and in the bay, they can be seen to converge on the low field trap. The vector magnitude falls with distance from the electrode edge to a minimum at the low field point.

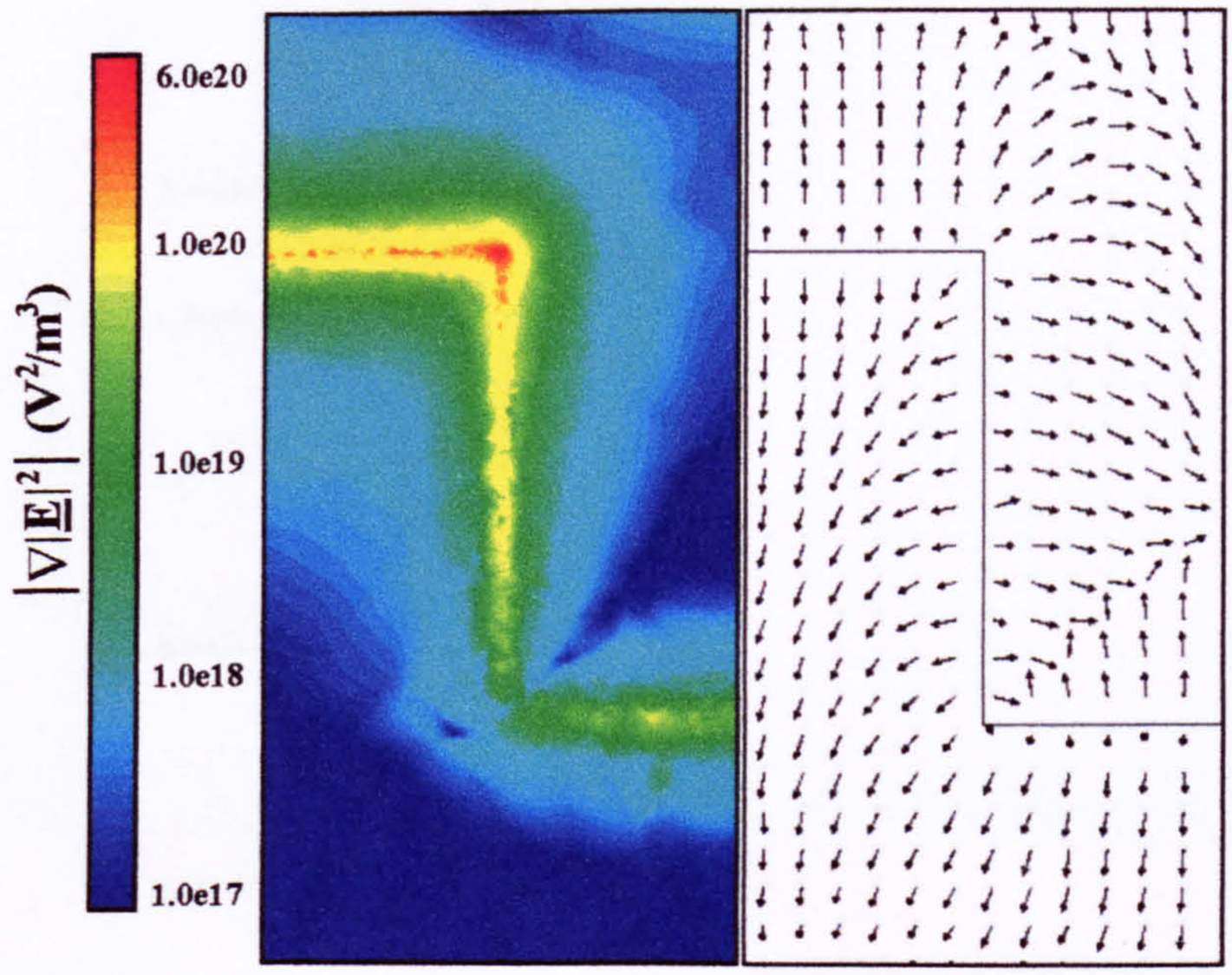

Figure (6.18b) The negative DEP force vector direction in a plane parallel to ABCD and 100nm above the electrode surface. Across the whole plane, the vectors point away from the electrode edge and in the bay, they again converge on the low field trap. The magnitude of $\nabla|\underline{\mathbf{E}}|^2$ falls with distance from the electrode edge to a local minimum at the low field point and also over the electrode surface.

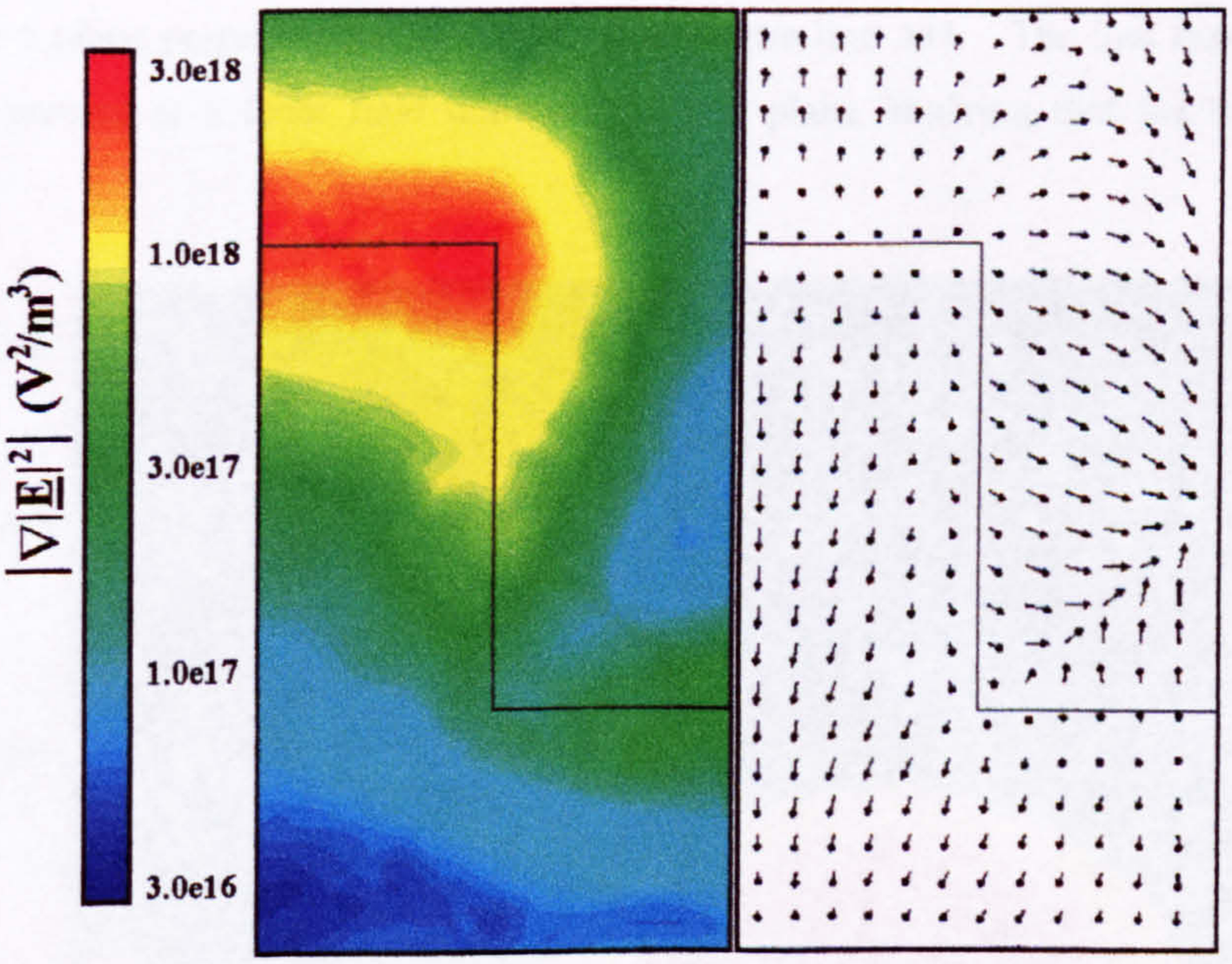

Figure (6.18c) The negative DEP force vector direction in a plane parallel to ABCD and 1μm above the surface of the electrodes. The vector direction again points away from the electrode edge which means that over the gap, and to a certain extent over parts of the electrode, the vectors point upwards. In the bay, the vectors still converge on the trap. The magnitude of the force vector is a maximum over the front of the castellation and a minimum over the electrode.

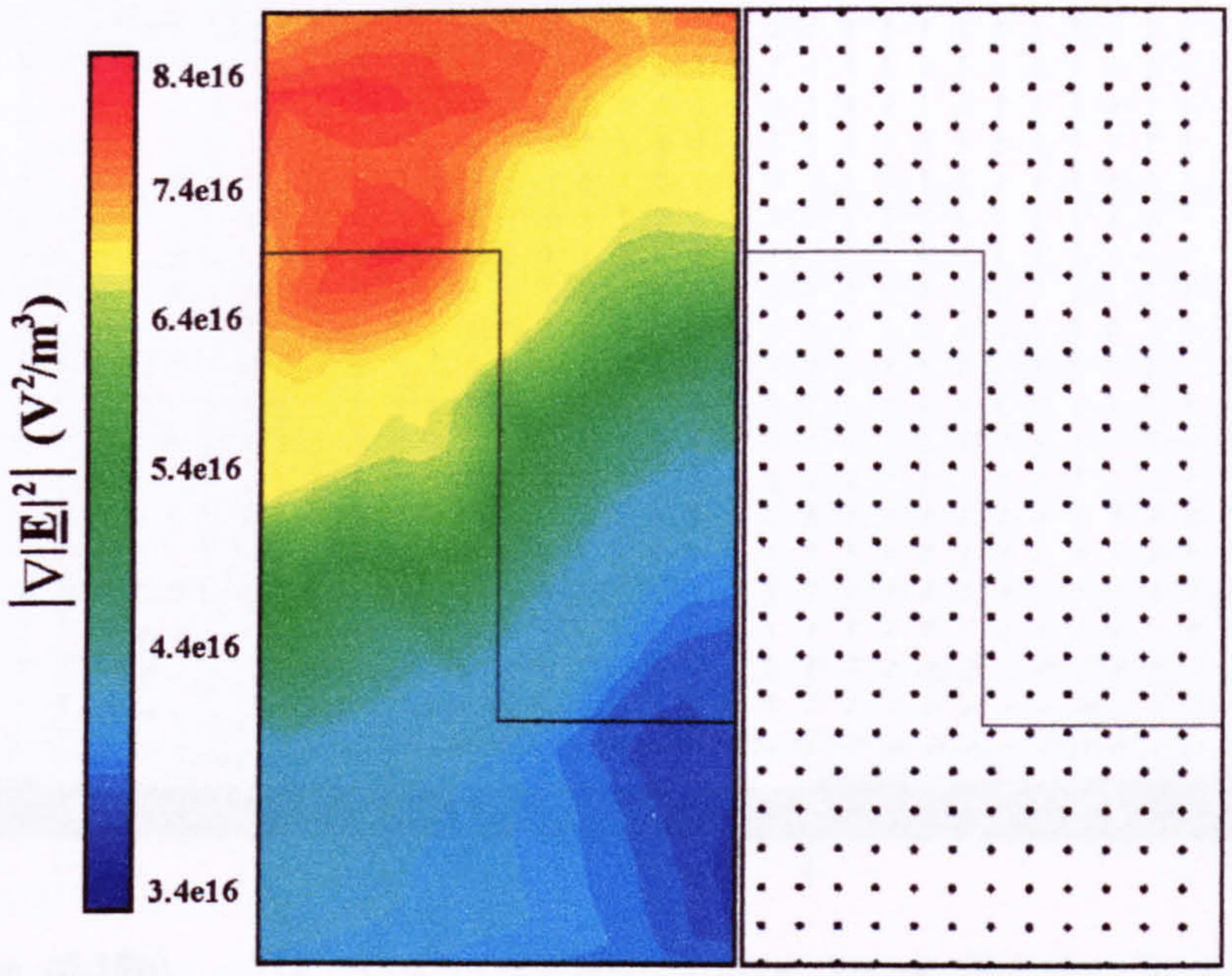

Figure (6.18d) The negative DEP force vector direction and magnitude of $\nabla|\underline{\mathbf{E}}|^2$ in a plane parallel to ABCD and 5μm above the surface. The force vectors point vertically upwards and the force magnitude has a maximum value over the gap and a minimum over the narrowest part of the electrode. The variation, however, is only a half of an order of magnitude.

Figure (6.19) shows the field strength and negative dielectrophoretic force vector direction for a plane perpendicular to ABCD through the line AD. The low field trap in the bay is also present as a local field minimum in this plane implying that the trap is three-dimensional.

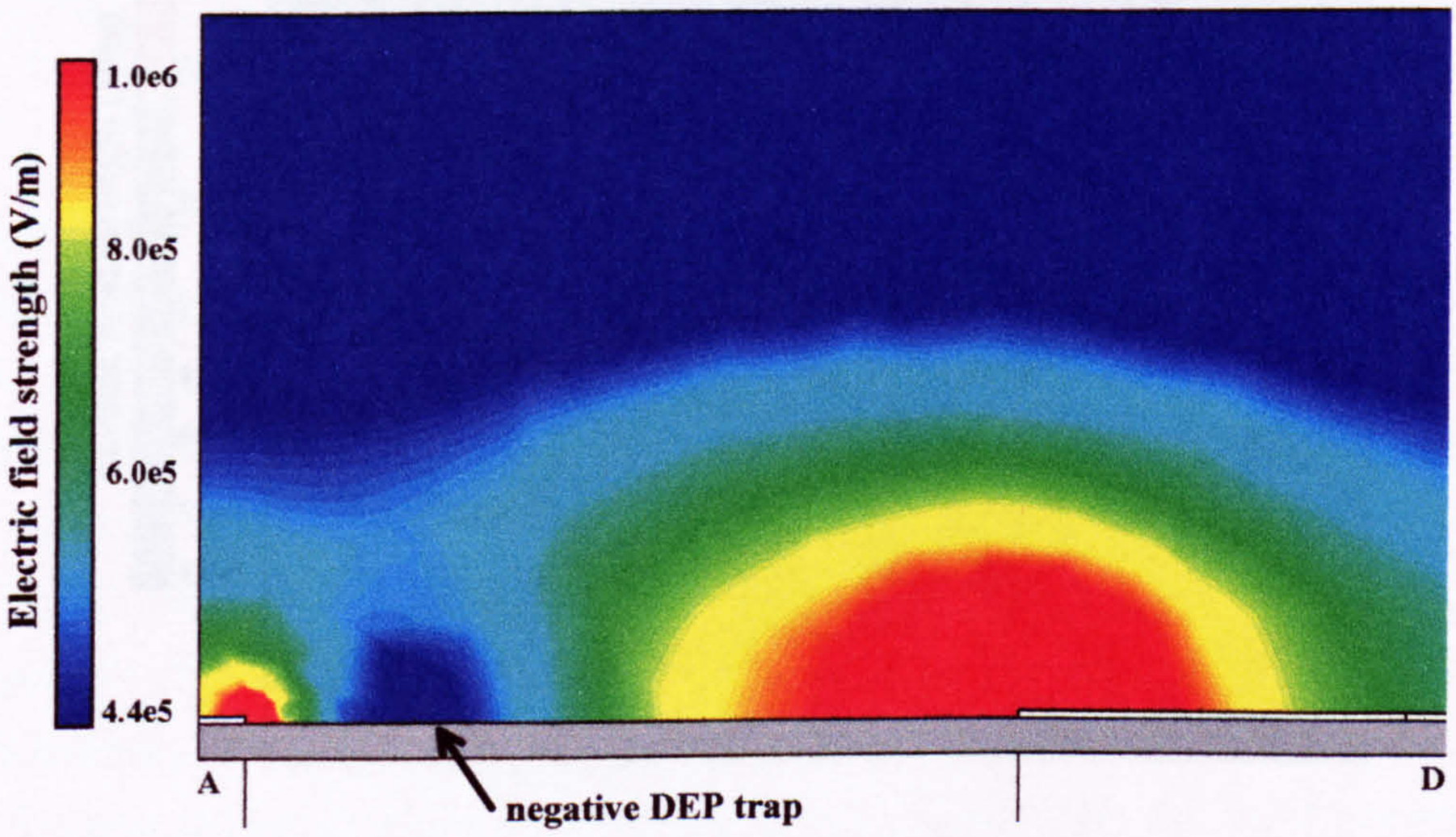

Figure (6.19a) The electric field strength in a plane perpendicular to ABCD through the line AD. There is a local field minimum in the field strength in this plane located in the bay between adjacent castellations.

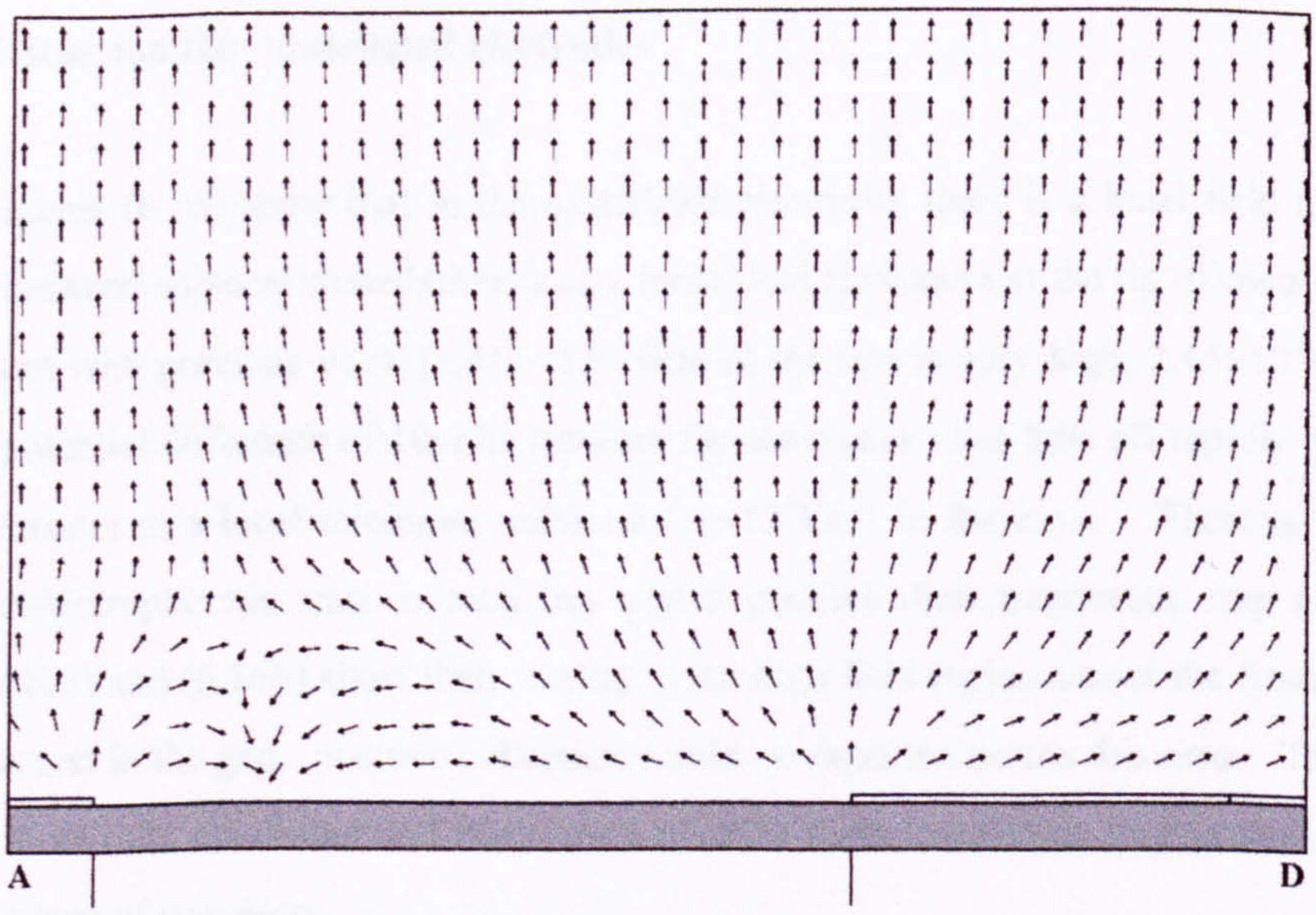

Figure (6.19b) The negative dielectrophoretic vector direction in a plane perpendicular to ABCD through the line AD. The vectors point vertically upwards above approximately 3μm but below this height in the bay, they converge on the local field minimum

Figure (6.20) shows the field magnitude in the vertical plane through AD, the plane ABCD and a mutually perpendicular plane through the electrode bay demonstrating the 3D local minimum.

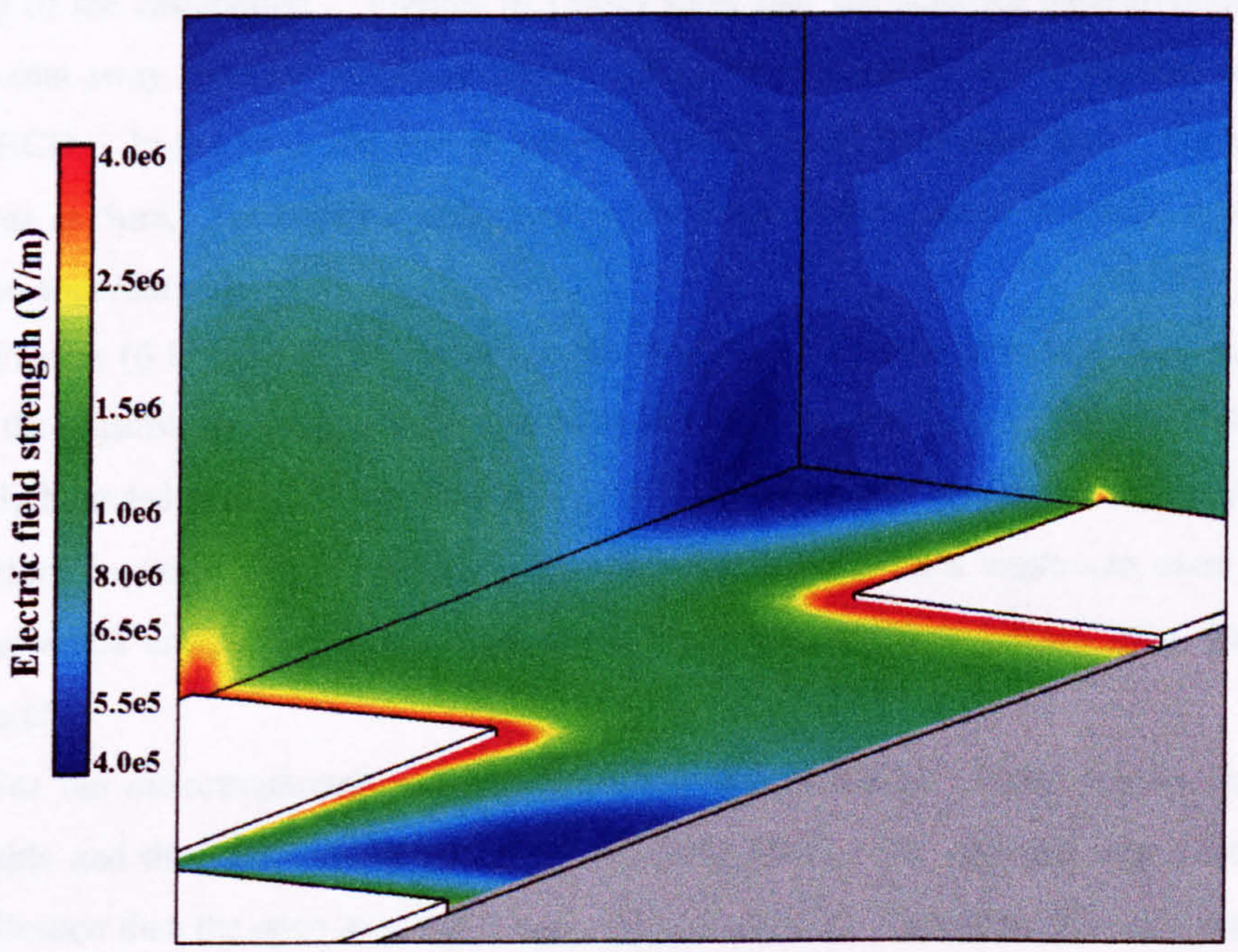

Figure (6.20) The field magnitude in the plane ABCD, a plane perpendicular through the line AD and a plane mutually perpendicular to both, running through the electrode bay. The field has a local minimum in the bay in three dimensions.

6.3.6 Discussion III: castellated electrodes

Figures (6.16) show that in the castellated electrodes there is a local field minimum in each bay between adjacent castellations and a local field maximum at the tip of each castellation in agreement with previous work [3,4]. The field at the tips is very high, $2.45\times10^{7}Vm^{-1}$ for an electrical potential difference of 10volts between the electrodes, but falls off rapidly in the plane of the electrodes to a local minimum value of $4.1\times10^{5}Vm^{-1}$ in the bays. There is therefore a negative dielectrophoretic trap in each bay and a positive dielectrophoretic trap at each tip. Figures (6.16a) and (6.16b) show that, owing to the high field region across the front end of the castellation and in the gap, positive collection would be expected across this area. There is also a smaller local field maximum and therefore a positive dielectrophoretic trap at the back of the bay in the plane of symmetry.

Figure (6.17d) show that particles, in the 5μm plane and higher, undergoing positive dielectrophoresis, experience an almost uniform $\nabla|\underline{E}|^2$ of the order of $5\times10^{16}V^2m^{-3}$ acting vertically downwards towards the plane of the electrodes (ABCD). From Figures (6.17a-c), it can be seen that below 5μm there is an increasing translational component in the force vector which pulls the particles towards the electrode edge. The magnitude of the vector increases rapidly with decreasing distance from the electrode edge, rising to a maximum of $2.55\times10^{22}V^2m^{-3}$ at the tip of the castellation. Figures (6.18a-c) show that the negative dielectrophoretic force vector points away from the electrode edges, with a vertical component increasing with height above ABCD. In the bay, the vectors converge on the local field minimum. Figure (6.18d) shows that at 5μm, the negative dielectrophoretic force vector points vertically upwards and there is no apparent trap.

Figures (6.19) and (6.20) show that the local field minimum is in fact three dimensional and that the negative dielectrophoretic trap is in fact a "field cage" [5]. The low field point is completely bounded in three dimensions by higher field regions and the negative dielectrophoretic force vectors converge on the middle. This demonstrates that field cages can exist in planar electrodes which are easier to manufacture on this scale than complicated three dimensional structures [5].

For the dielectrophoretic movement of colloidal particles, where thermal effects are considerable and the force due to gravity is relatively small, the enclosed trap would ensure better collection than the open trap of the hyperbolic electrodes. However, it is also important to note that the trap does not extend to a great height above the electrodes and would therefore not be able to collect particles in suspension above a height of approximately 4μm for a 5μm set of electrodes. This limit scales with the feature size of the electrodes.

References

1. Y.Huang and R.Pethig (1991)
   Measurement Science and Technology **2** 1142-1146
2. X.Wang, X-B.Wang, F.F.Becker and P.R.C.Gascoyne (1996)
   Journal of Physics D: Applied Physics **29** 1649-1660
3. R.Pethig, Y.Huang, X-B.Wang and J.P.H.Burt (1992)
   Journal of Physics D: Applied Physics **24** 881-888
4. X-B.Wang, Y.Huang, J.P.H.Burt, G.H.Markx and R.Pethig (1993)
   Journal of Physics D: Applied Physics **26** 1278-1285
5. T.Schnelle, R.Hagedorn, G.Fuhr, S.Fiedler and T.Muller (1993)
   Biochimica et Biophysica Acta **1157** 127-140

Chapter Seven

Results and discussion: Latex spheres

7.1 Introduction

Simple dielectric spheres have been used extensively in dielectric and dielectrophoretic experiments as test particles. However the dielectric properties of charged spheres are complicated and, as yet, unsatisfactorily explained.

Latex spheres, consisting of polymers of carboxylate modified styrene, were purchased from Molecular Probes (Leiden, The Netherlands). The spheres were purchased pre-loaded with fluorescent dye and had a high negative surface charge at neutral pH because of the carboxylate groups. In order to illustrate the variation of dielectric and surface parameters with particle size, several different diameter spheres were used in this project and the manufacturer's supplied data is included in Appendix (7a). Figure (7.1) shows scanning electron micrographs of the 282nm and 557nm diameter latex spheres.

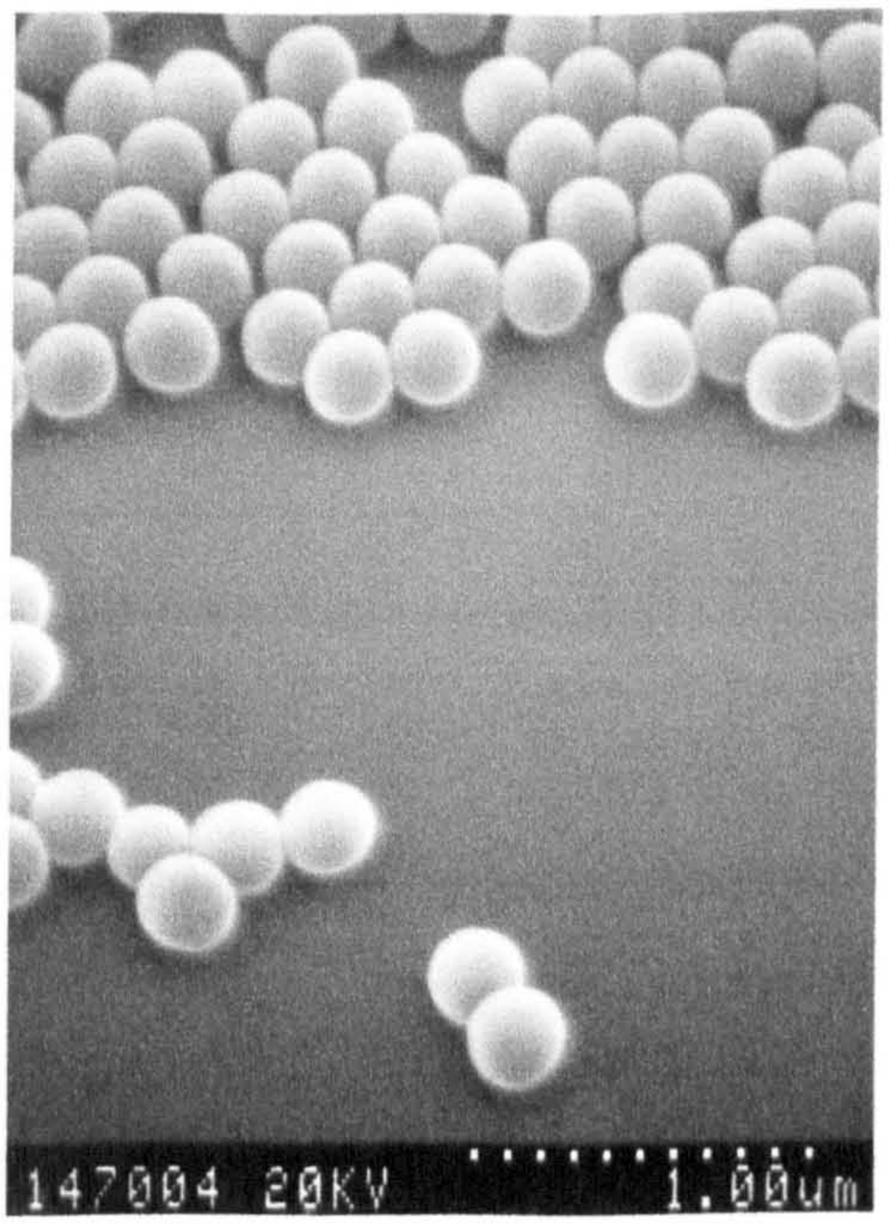

(7.1a) 282nm diameter spheres

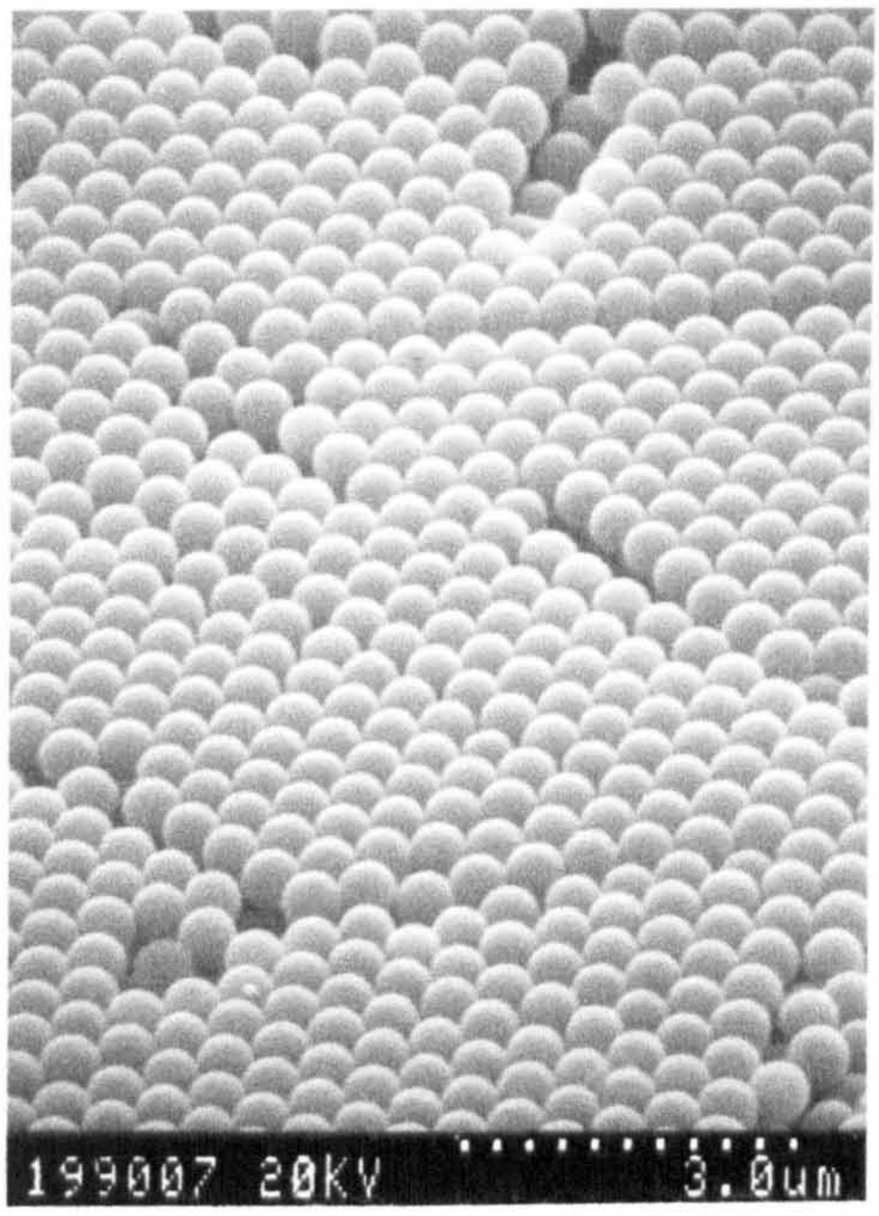

(7.1b) 557nm diameter spheres

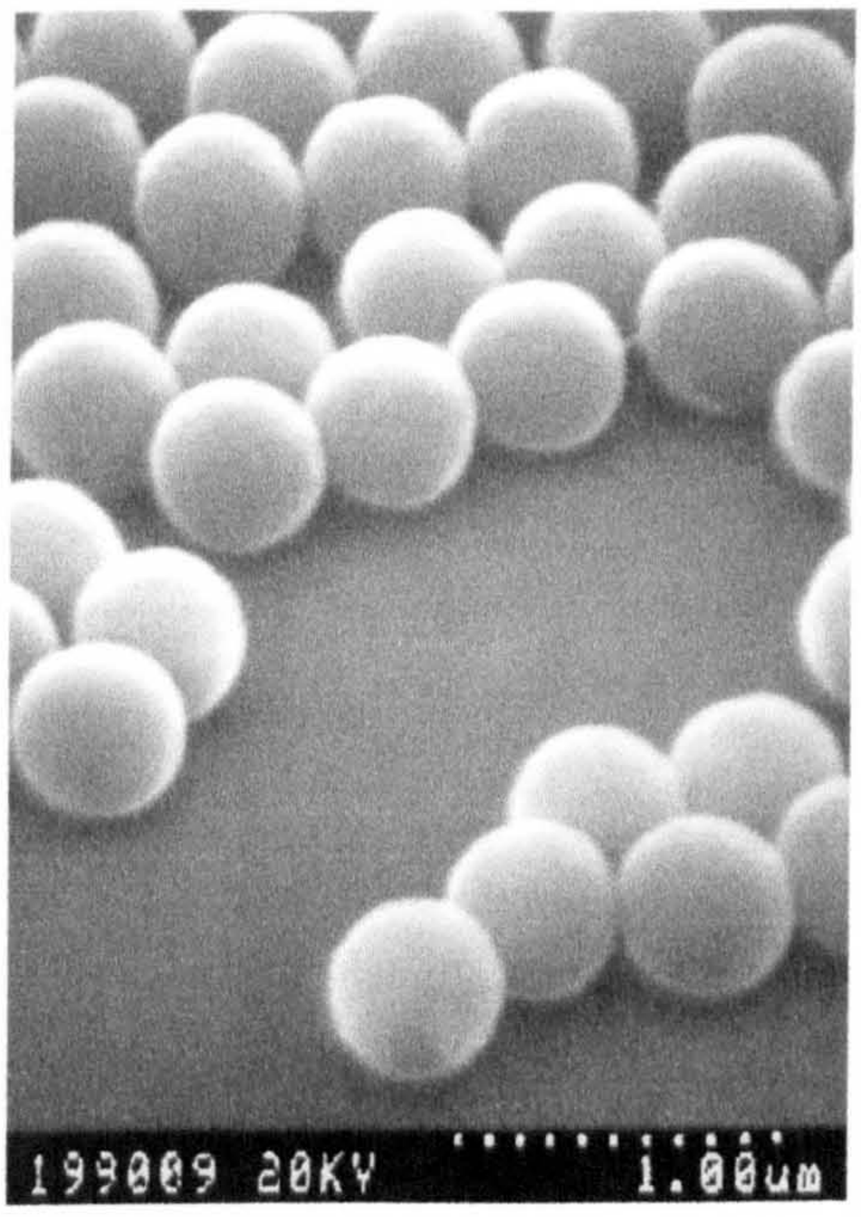

(7.1c) 557nm diameter spheres

Figure (7.1) Scanning electron microscope images of the latex spheres used for dielectrophoresis experiments in this chapter.

This chapter presents the results of dielectrophoresis experiments performed on latex spheres in order to determine their dielectric properties. Some of the preliminary results were published in an article in the Journal of Physics D: Applied Physics [1].

Subsequent sections of this chapter expand on this preliminary article with more detailed results and discussion in light of the theories set out in Chapters Three and Four. The experimental results consistently deviate from the established theory and attempts are made to explain this in terms of accepted ideas. The double layer α–relaxation theories are also applied to the dielectrophoretic measurements.

7.2 Sample preparation

The suspending media for the dielectrophoresis experiments described in this Chapter were made using three different salts. The salt used most frequently in the literature is potassium chloride (KCl) and is as a symmetrical electrolyte. KCl is symmetrical both in terms of charge, i.e. the two ions have equal valency and also in terms of mobility: the potassium ion and the chloride ion have less than a 4% difference in mobility. The theories that govern the double layer and related phenomena are simplified considerably if the electrolyte is symmetrical. Two other salts were used: sodium chloride (NaCl) was used in order to determine if changing the mobility of the positive ion changed the behaviour of the α–relaxation, and potassium phosphate (KPO_4) was used to determine if altering the mobility of the negative ion would have an effect on the results. 1M stock solutions of KCl and NaCl were freshly prepared before each series of experiments, autoclaved and stored at 4°C. The 1M stock solution of KPO_4 was prepared from 1M monopotassium dihydrogen phosphate (Sigma) and 1M dipotassium monohydrogen phosphate (Sigma) mixed in a 1:1 ratio. The stock solution was then sterilised by autoclave and the pH was measured at 7.2 ± 0.1. Different concentrations of the solutions were prepared by serial dilution.

The spheres were supplied in a 2mM azide solution in sealed containers to prevent contamination. Samples were prepared by first diluting the manufacturer's supplied solution either 1:1000 or 1:10000 in each different salt solution. Samples of the 557 and 282nm spheres were centrifuged and resuspended in the appropriate solution three times. The 216nm and 93nm spheres would only pellet if they were spun down in a Sorval ultracentrifuge at 50krpm (200,000g) but the pellet would not remain long enough to perform the resuspension. However, a 1:1000 dilution was considered sufficient to ensure removal of the azide from the spheres. Also, the smaller spheres had a tendency to remain aggregated after spinning down and resuspension in high salt concentrations solutions (>20-50mM) with ultra-sonication failing to separate the aggregates therefore centrifugation was not used.

For SEM analysis, samples of the spheres were placed on slides, dried, metallised by sputtering and imaged to determine both if the solutions were contaminated and to check the manufacturer's data on sphere size. The samples were uncontaminated and the variation in size of the spheres was within the uncertainty quoted by the manufacturer (see Appendix 7a).

7.3 Results

This section sets out the results of the measurements of medium conductivity, describes the observed dielectrophoretic behaviour of the latex spheres and presents the data from measurements of the change in behaviour with applied field frequency and conductivity.

7.3.1 Solution conductivity measurements

The conductivity of the different solutions was measured using the HP impedance analyser or a conductivity meter (Appendix 5b.1).

Initially, the conductivity of a cross-sectional set of the concentrations of the three salts was measured across a range of temperatures in order to determine if the textbook value of +2% per degree Celsius change in conductivity with temperature was correct. Figures (7.2a-c) show as examples, the results for the conductivity of three salt solutions (100mM KCl, 1mM NaCl and 100μM KPO_4) as a function of temperature. The best linear fit shown in the figures indicate that in the experimental range (10-30°C) the variation of conductivity with temperature can be assumed to be linear.

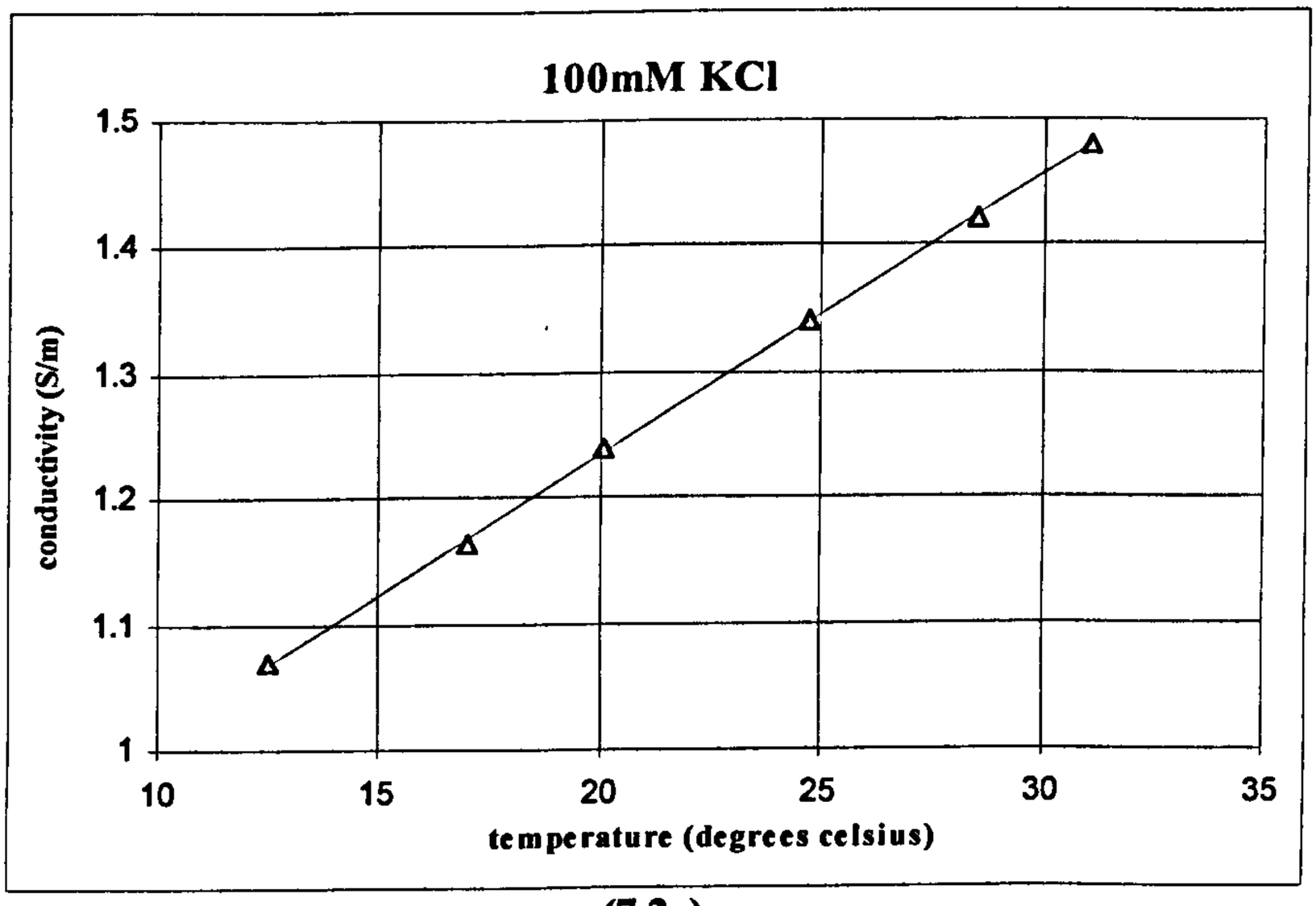

(7.2a)

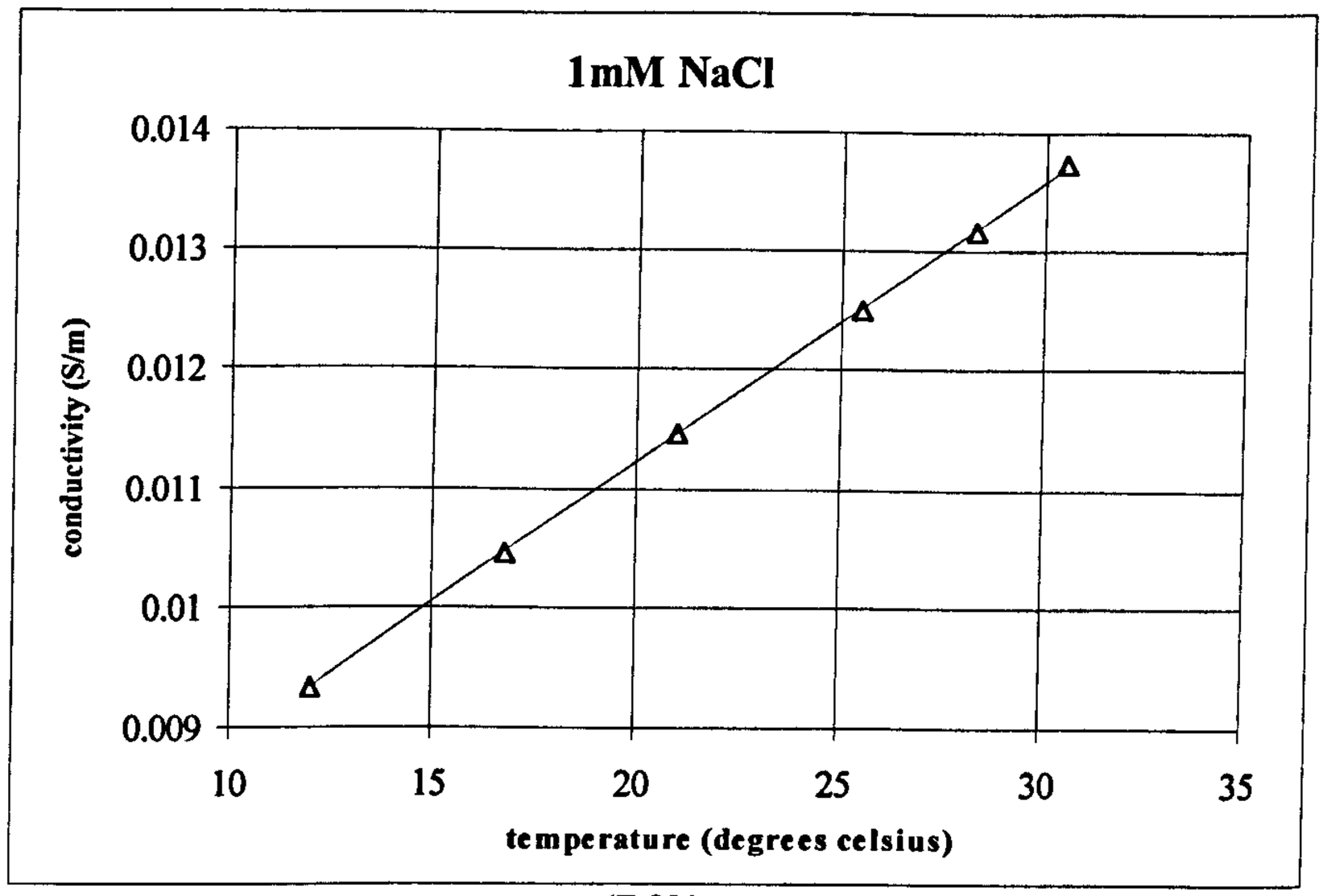

(7.2b)

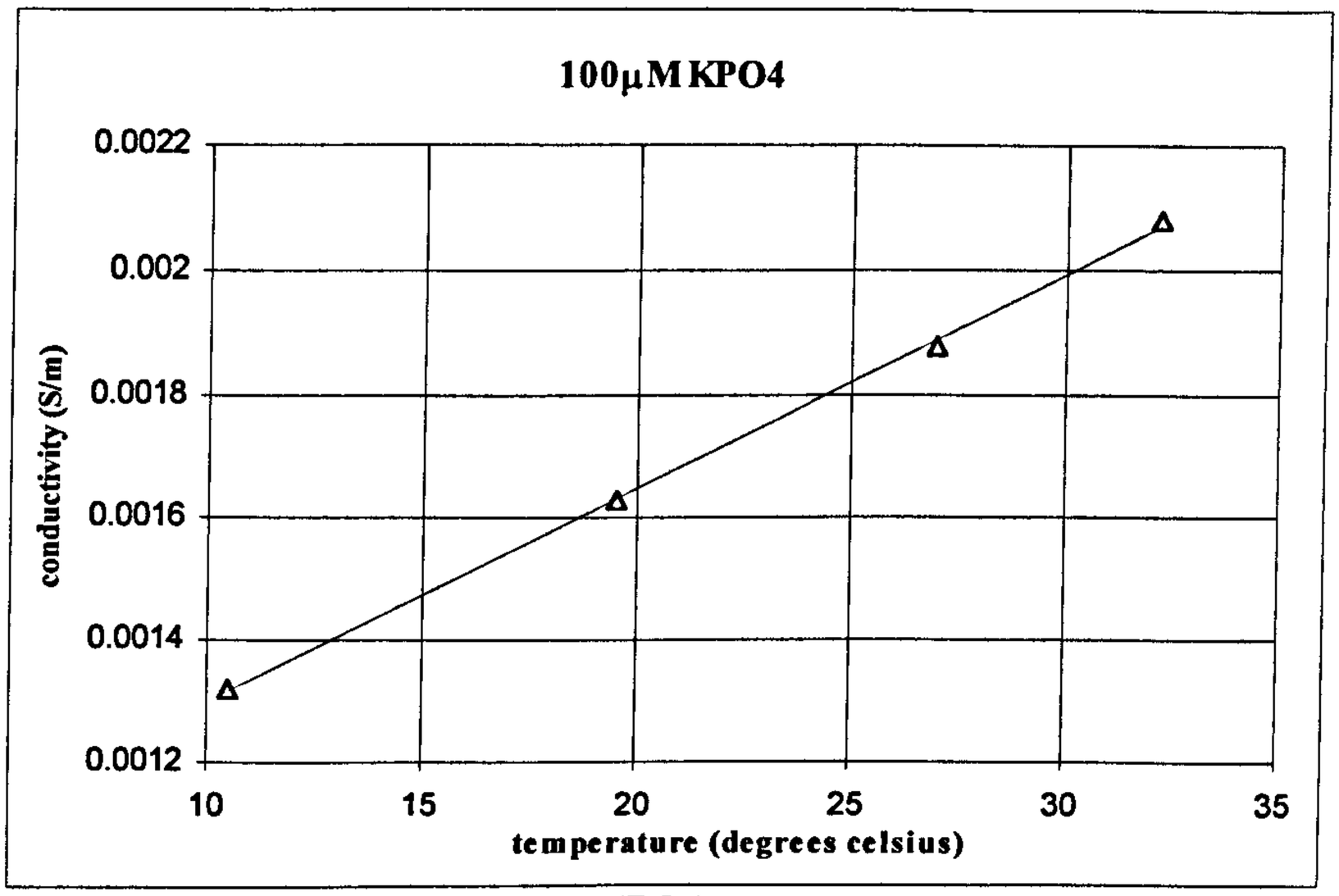

(7.2c)

Figure (7.2) Plots of the change in conductivity with temperature for **(a)** 100mM KCl, **(b)** 1mM NaCl and **(c)** 100μM KPO_4. The triangles mark measured values and the lines are best fit linear trends which indicate, for each of the three solutions shown, that in the range 10-30°C the variation in conductivity with temperature is linear.

Experimental measurements of conductivities were made at a temperature of 15 ± 1°C. The temperature of the device when performing dielectrophoresis experiments was at room temperature which was measured in the range 20-22°C. Owing to the small volume of the sample used in the experiments, the temperature of the samples will rapidly reach the temperature of the device. The temperature rise from 15°C to 21°C was calculated for each of

the three salts and the results are plotted in Figure (7.3) for each salt as a function of concentration. From these results, the change in conductivity from 15°C to 21°C was determined and used to correct the measured values more accurately than assuming a +2% per degree rise.

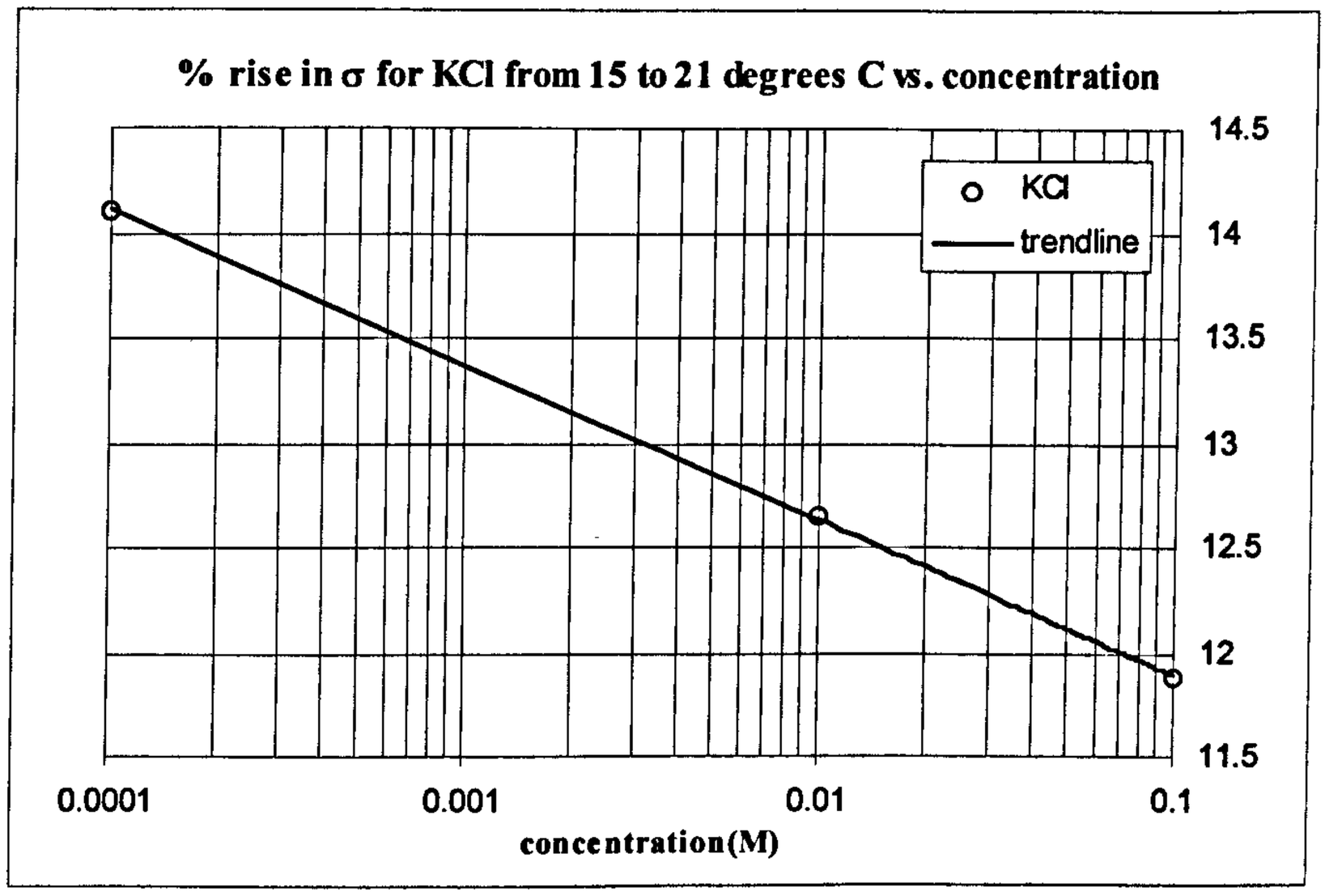

(7.3a)

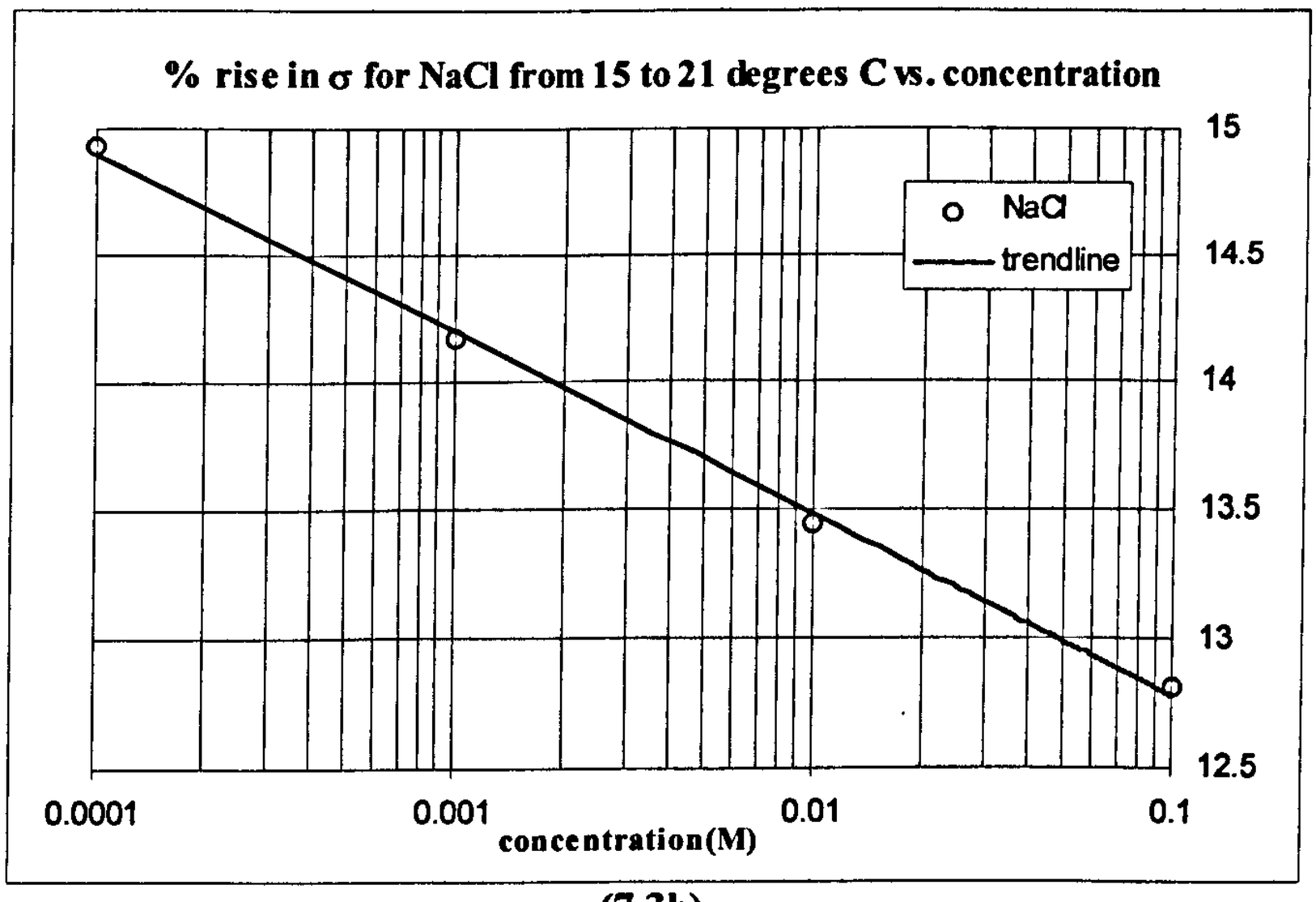

(7.3b)

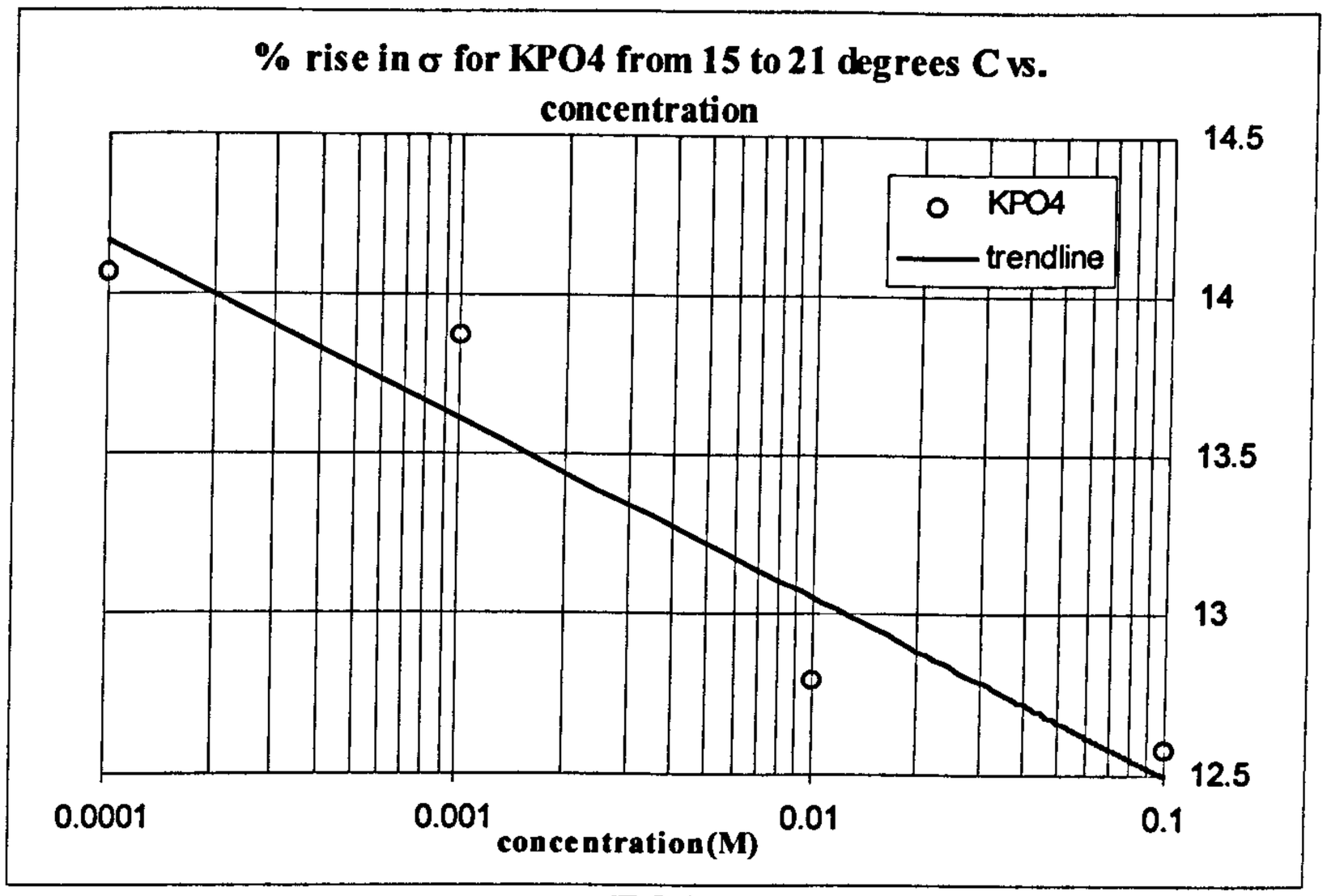

(7.3c)

Figure (7.3) Plots of the percentage rise in solution conductivity as the solution temperature is increased from 15 to 21°C for different concentrations of **(a)** KCl, **(b)** NaCl and **(c)** KPO_4. The lines plotted through the data points are best fit logarithmic lines which indicate the variation across the complete range of salt concentrations.

The percentage variation in conductivity per degree at 21°C was also calculated from the original temperature variation data (examples shown in Figure 7.2) for the three different salts to ascertain the accuracy of the textbook value of 2% per degree. The results are shown in Figure (7.4) for the three different salts. As these results show, the value of 2% is close to the measured value and would serve as a rough first approximation but there is a definite variation in the percentage change with salt concentration.

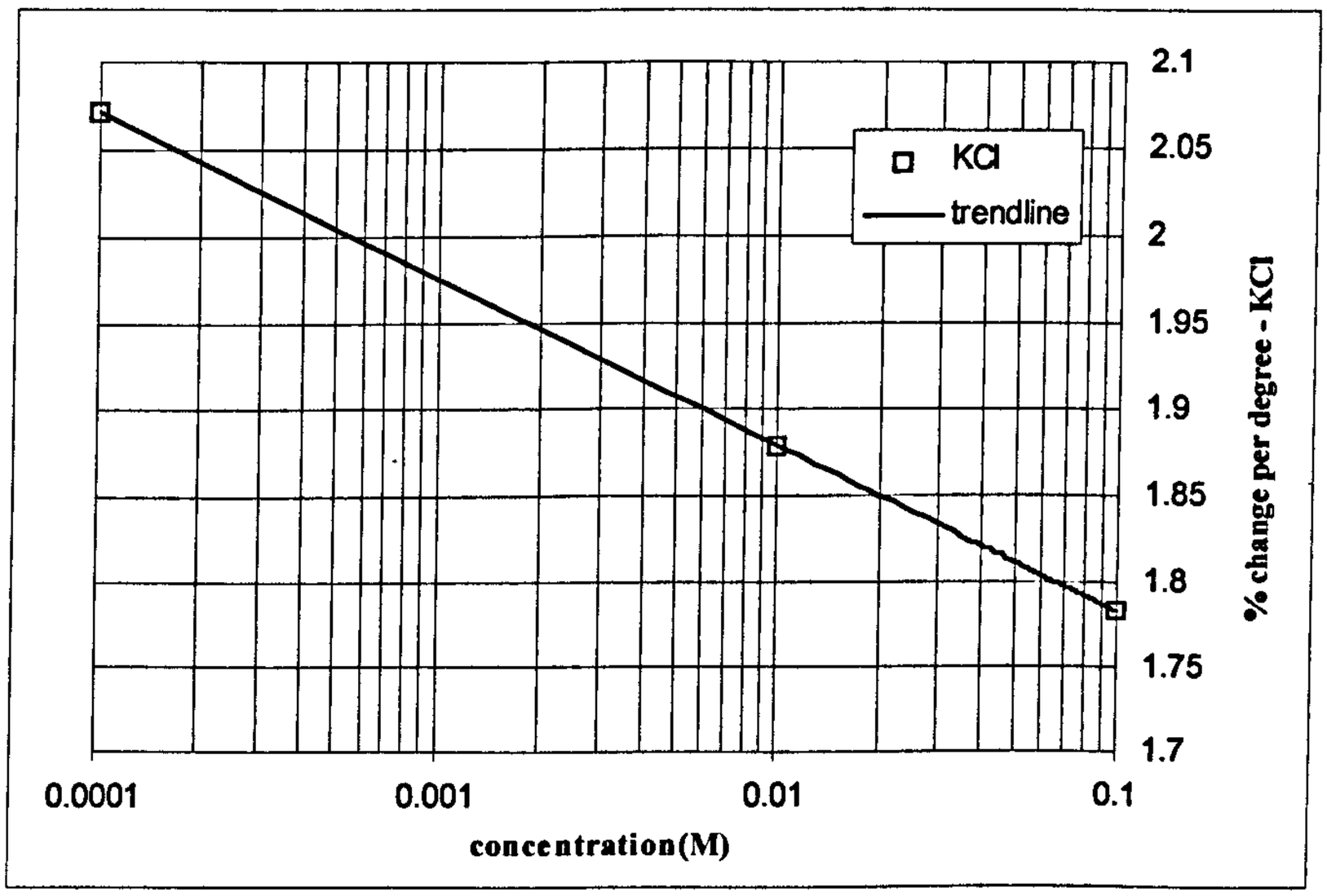

(7.4a)

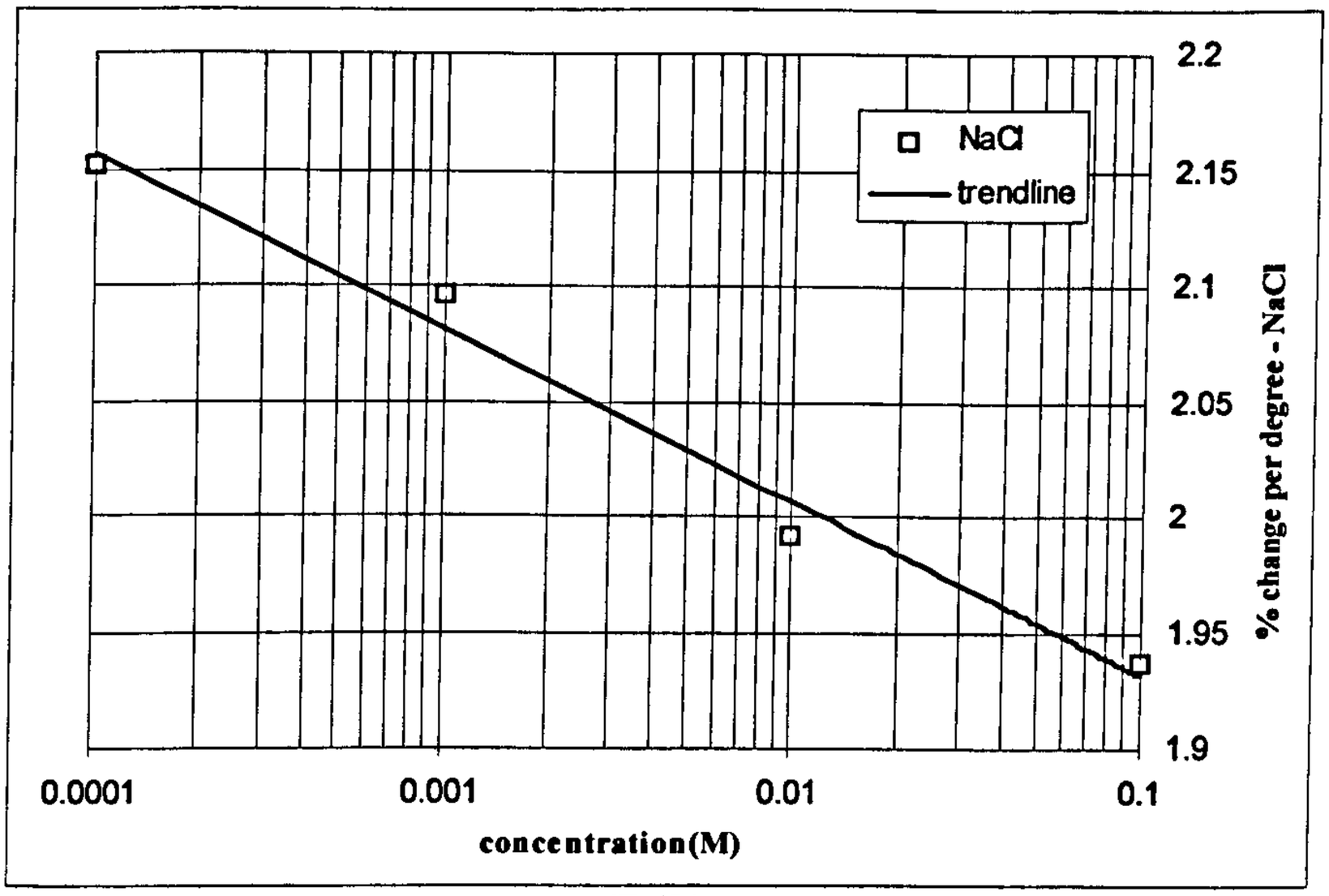

(7.4b)

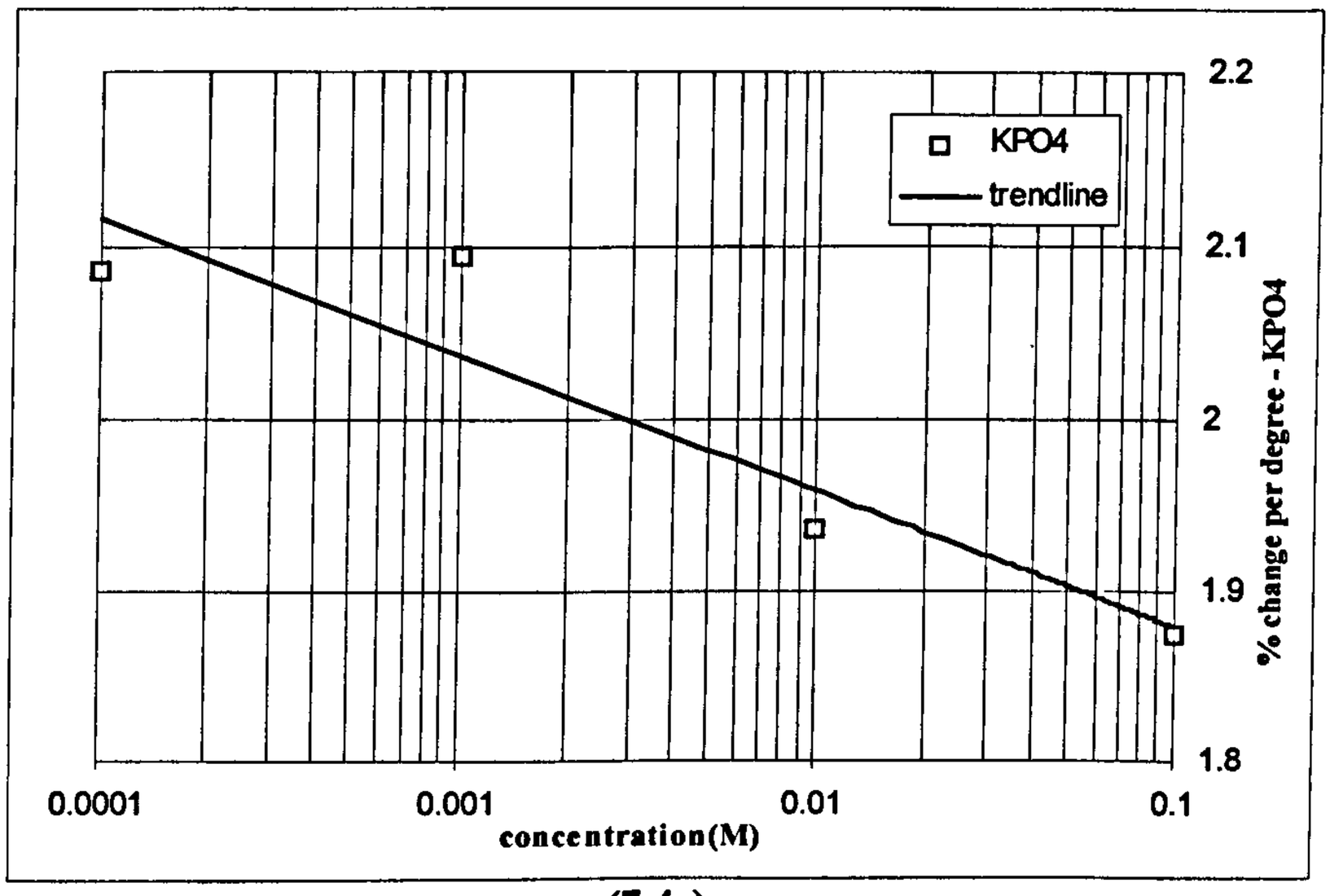

(7.4c)

Figure (7.4) Variation in the percentage solution conductivity change per degree celsius at a solution temperature of 21°C for **(a)** KCl, **(b)** NaCl and **(c)** KPO_4. The lines are again best fit logarithmic trend lines.

The conductivity of each different solution was measured and then adjusted to the room temperature value using the data shown in Figure (7.3). An experimental uncertainty in the conductivity value based on the measurement errors was introduced using the data in Figures (7.4). The results are plotted in Figures (7.5) for the three salts. The experimental uncertainty of approximately 4% is too small to be visible on this graph.

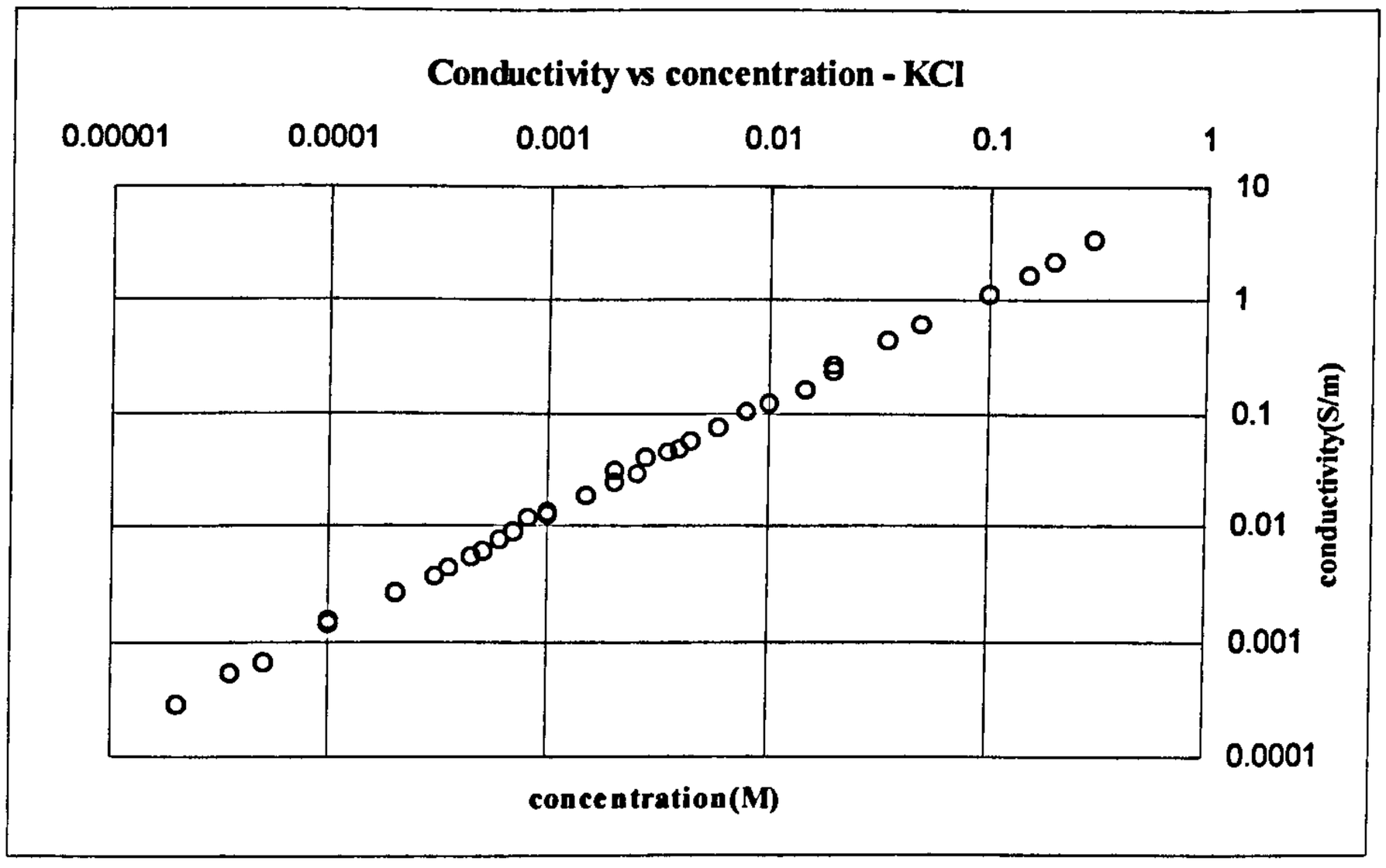

Figure (7.5a) Conductivity in Siemens per metre against concentration in Moles at 21°C (room temperature) for potassium chloride.

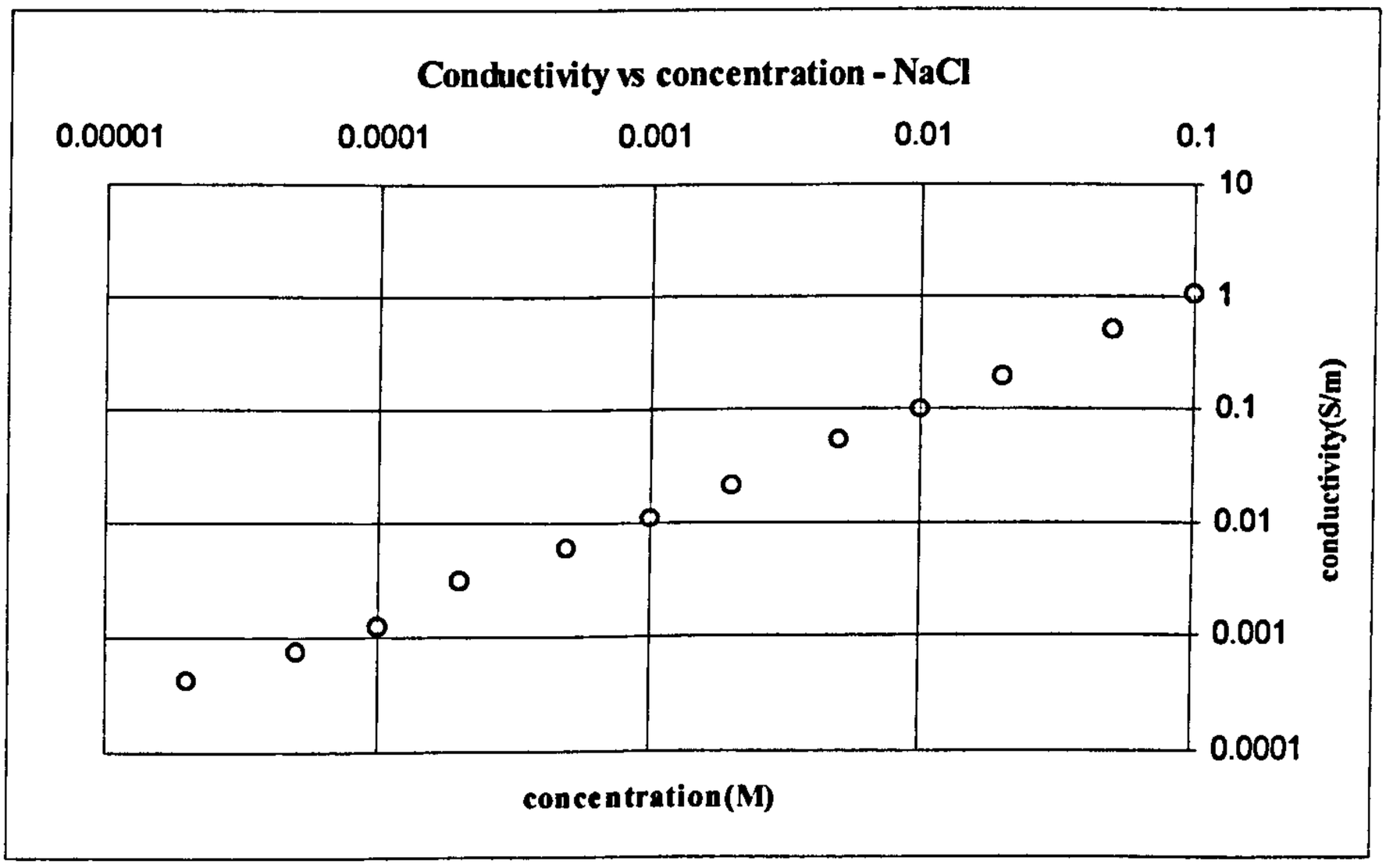

Figure (7.5b) Conductivity in Siemens per metre against concentration in Moles at 21°C (room temperature) for NaCl.

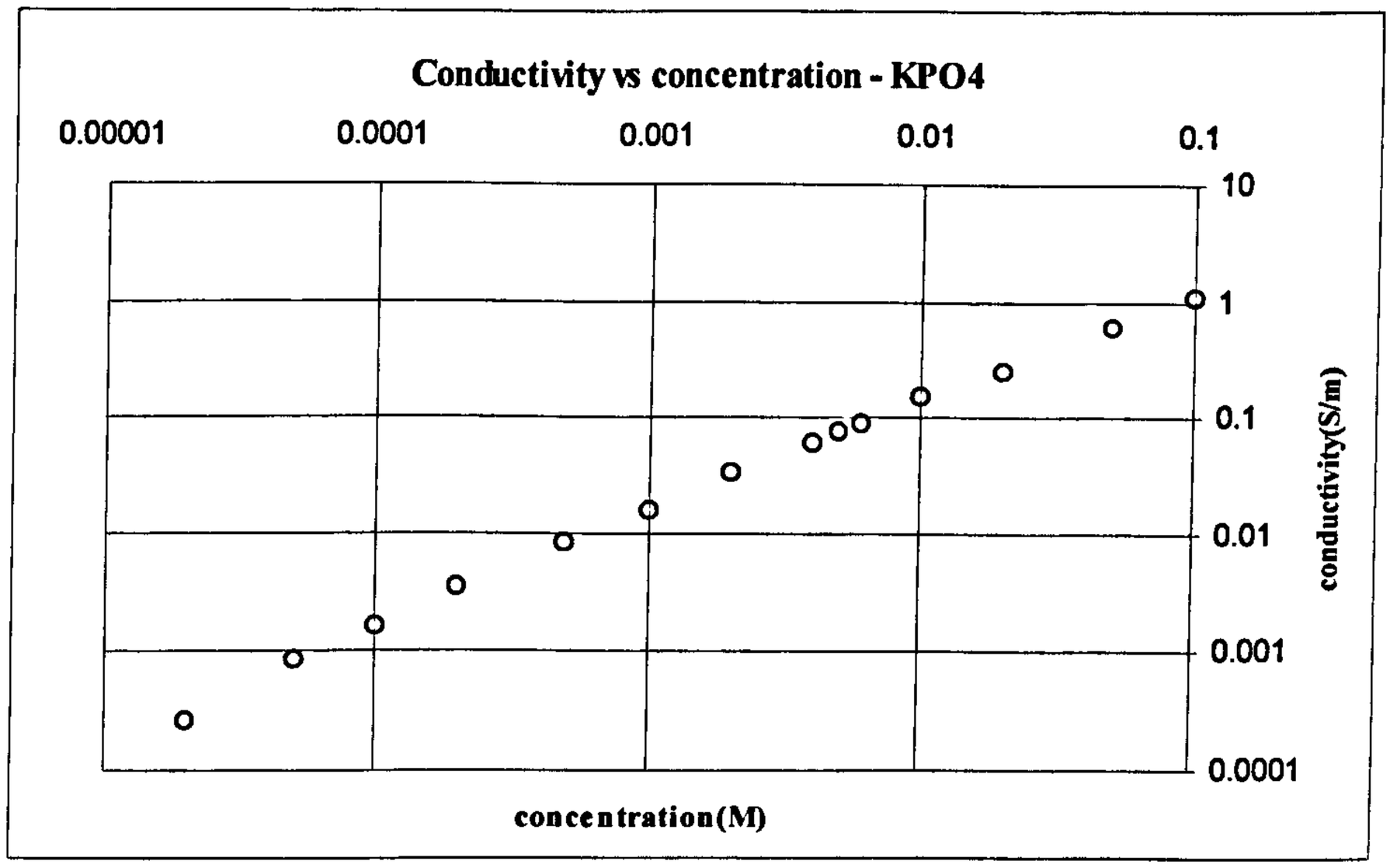

Figure (7.5c) Conductivity in Siemens per metre against concentration in Moles at 21°C (room temperature) for KPO_4.

7.3.2 Latex Sphere surface charge measurements

The electrophoretic mobility of suspensions of the 557, 282 and 93nm diameter spheres was measured using a Coulter particle analyser. The measured distributions in mobilities are shown in Figures (7.6a-c) and for each size have an approximately Gaussian profile. The Coulter particle analyser uses a system of lasers at different angles (as shown on the graph) to determine the velocity of particles and from this data and the applied field, the mobility (see section 4.2.5) is determined.

(7.6a)

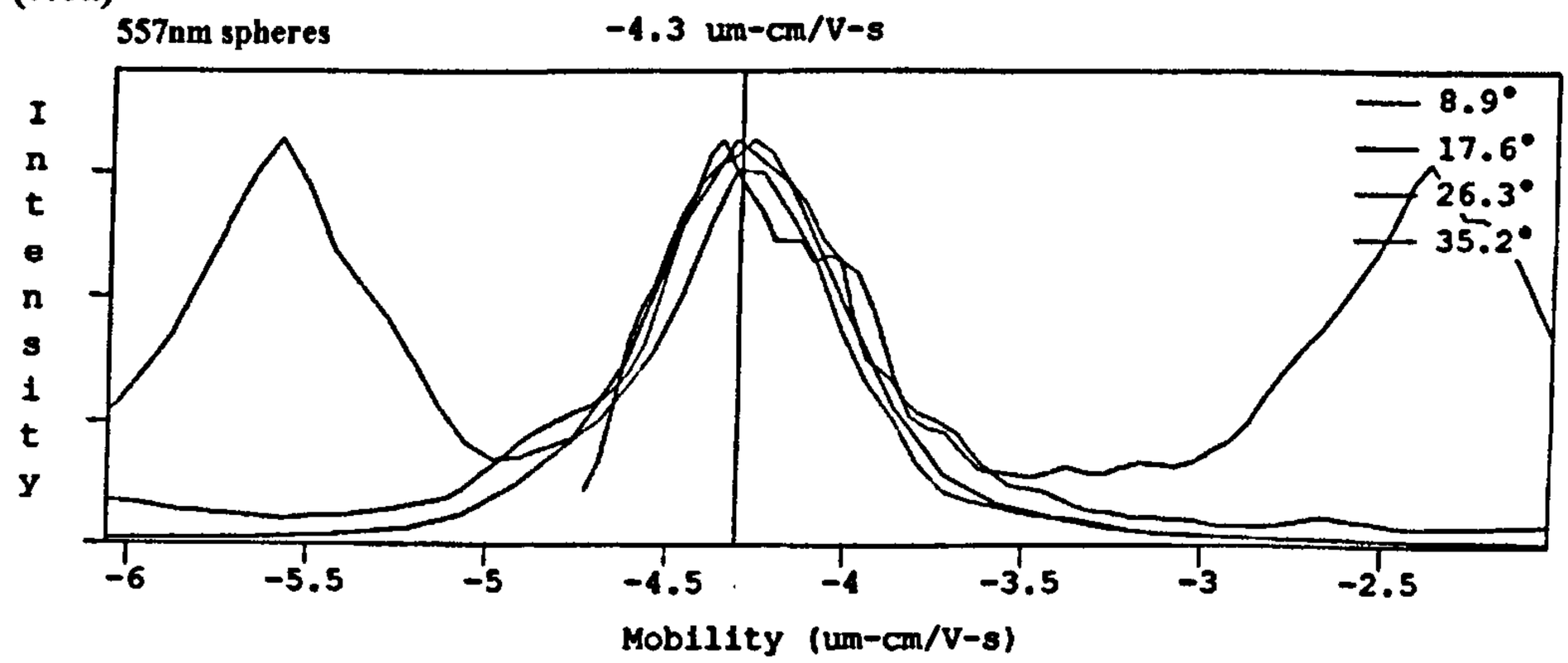

(7.6b)

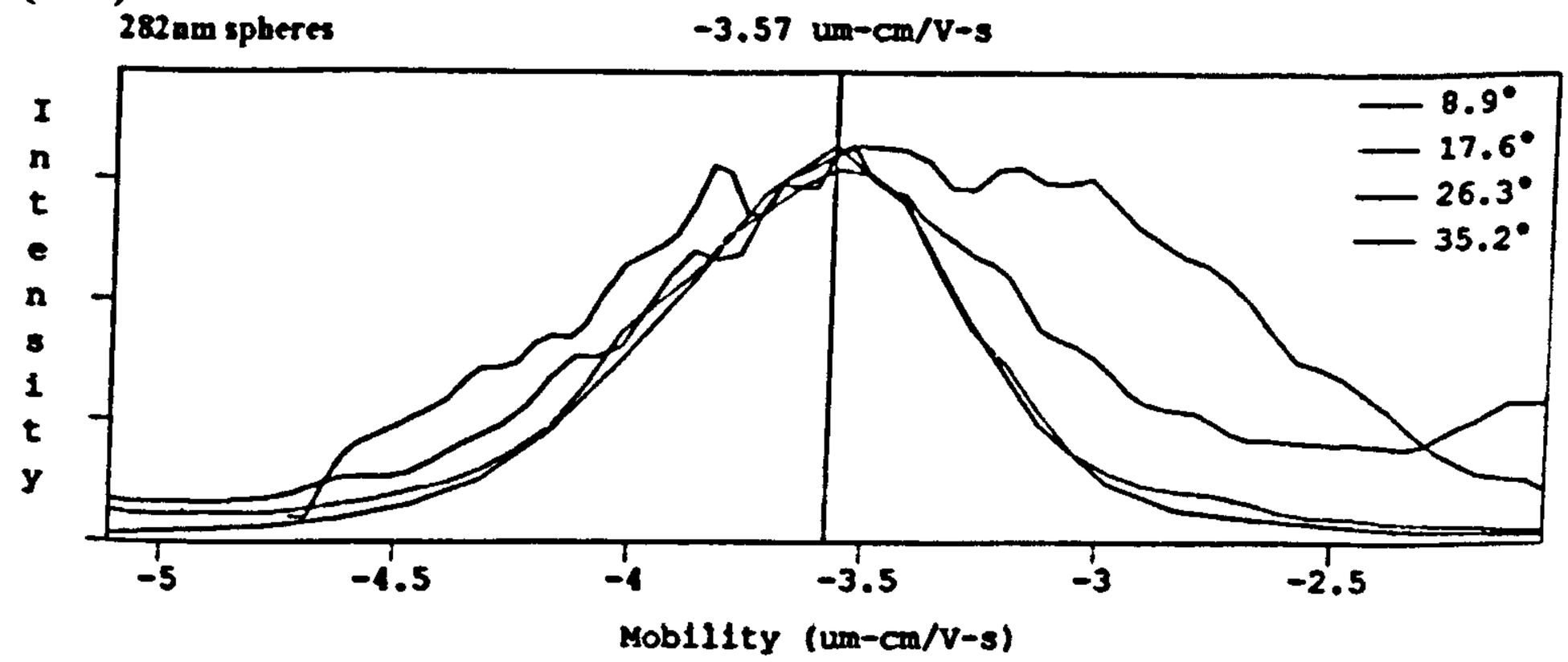

(7.6c)

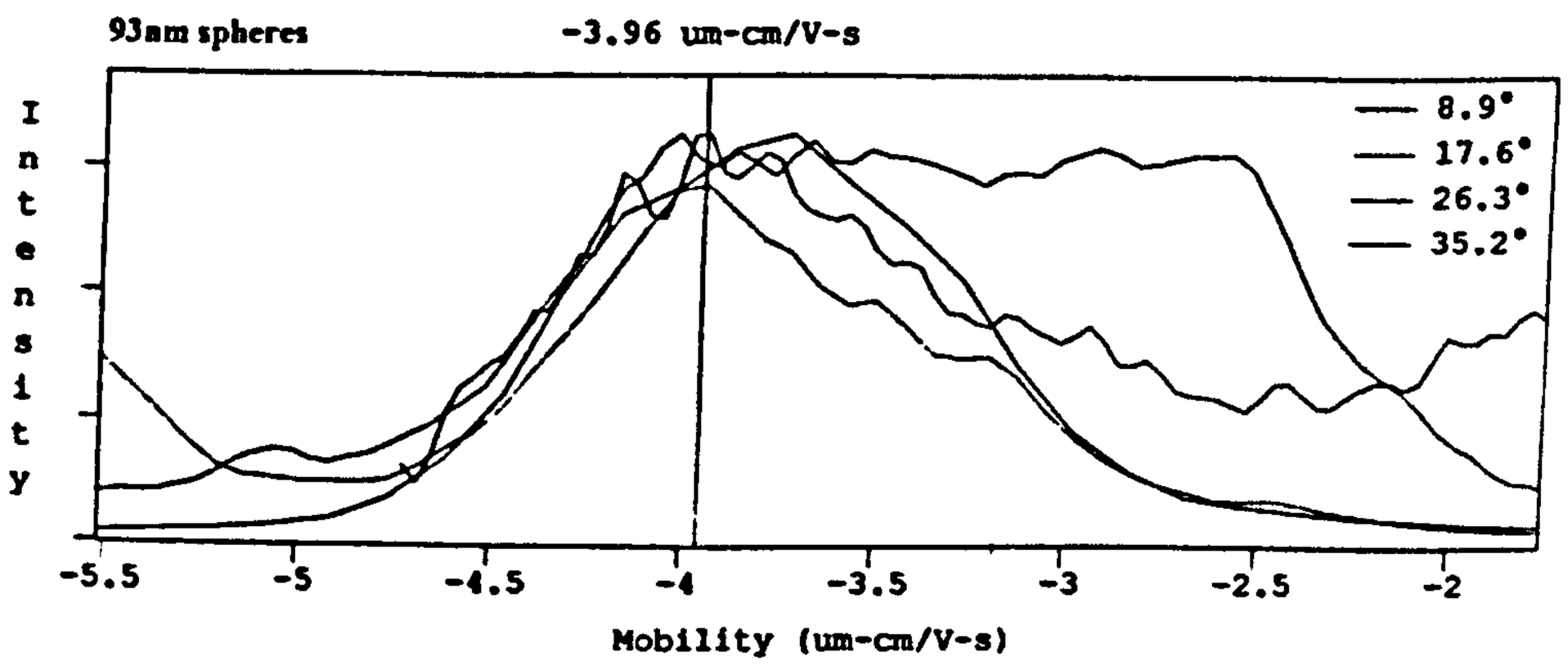

Figure (7.6) Coulter particle analyser measurements of the electrophoretic mobility of the 93, 282 and 557nm diameter latex spheres.

7.3.3 Dielectrophoretic behaviour

The devices described in Chapter Five were used to perform dielectrophoresis experiments on the solutions of latex spheres. The analogue generator (Appendix 5b.4) and the DDS (Appendix 5b.5) were used as generators to provide signals over the range 100Hz - 20MHz with potentials in the range 0-20volts peak to peak.

Figures (7.7) show typical results of dielectrophoresis experiments in hyperbolic polynomial electrodes (section 5.2). In general, the spheres experienced positive dielectrophoresis at low frequencies, changing to negative dielectrophoresis as the frequency was increased.

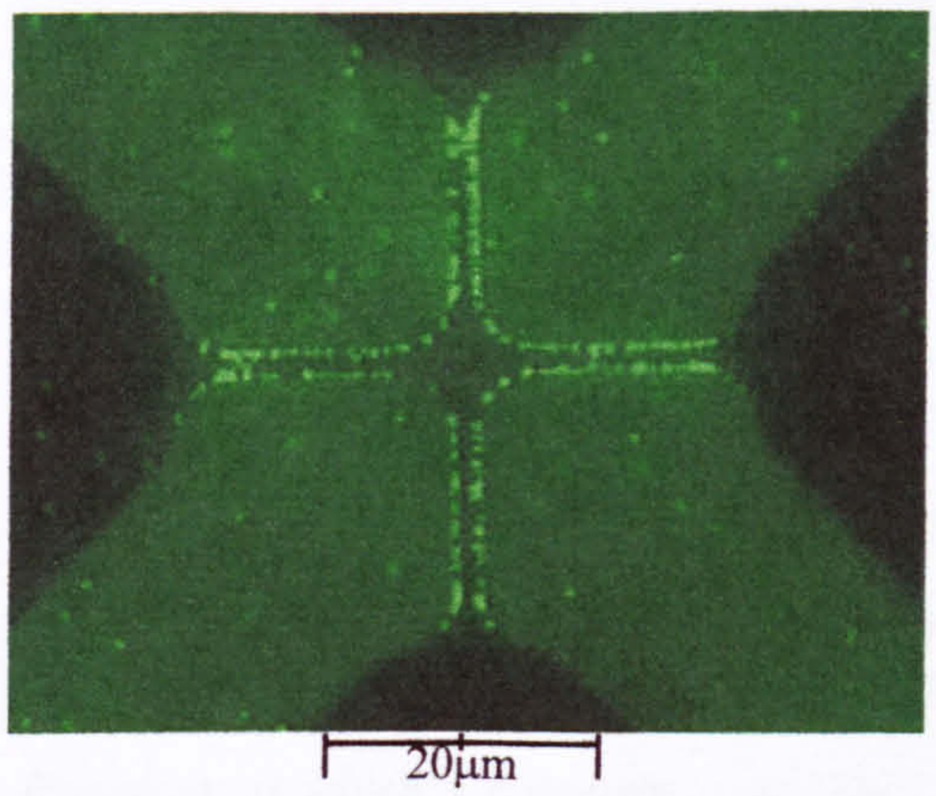

(7.7a) 557nm spheres in 100µM KCl with an applied signal of 5volts peak to peak at 500kHz.

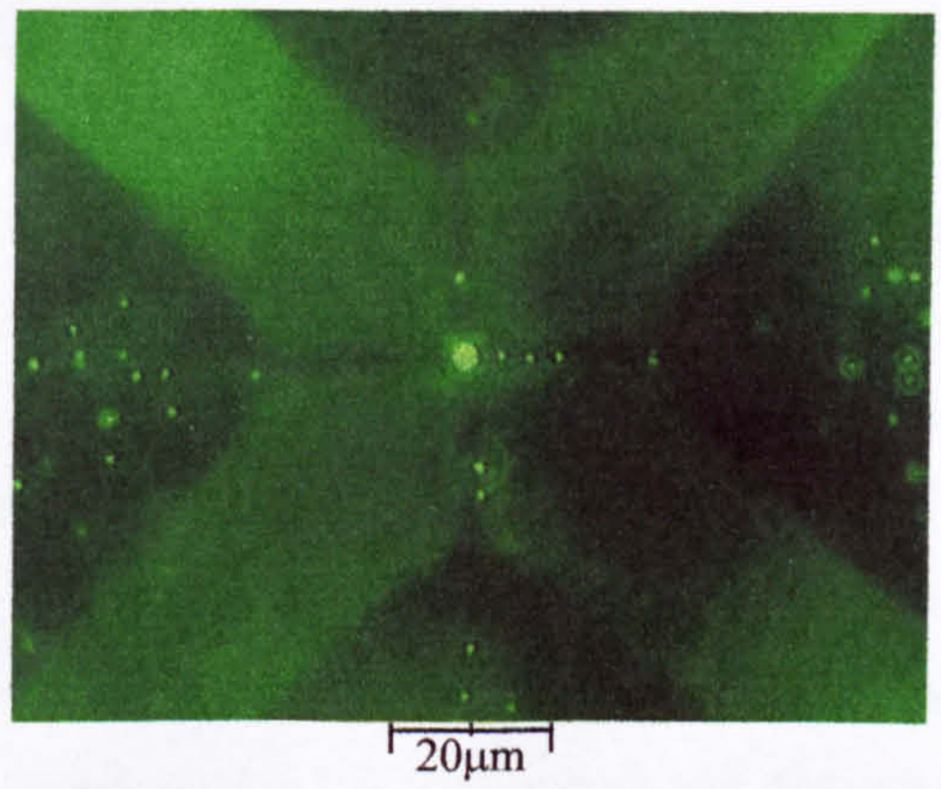

(7.7b) 557nm spheres in 100µM KCl with an applied signal of 5volts peak to peak at 5 MHz.

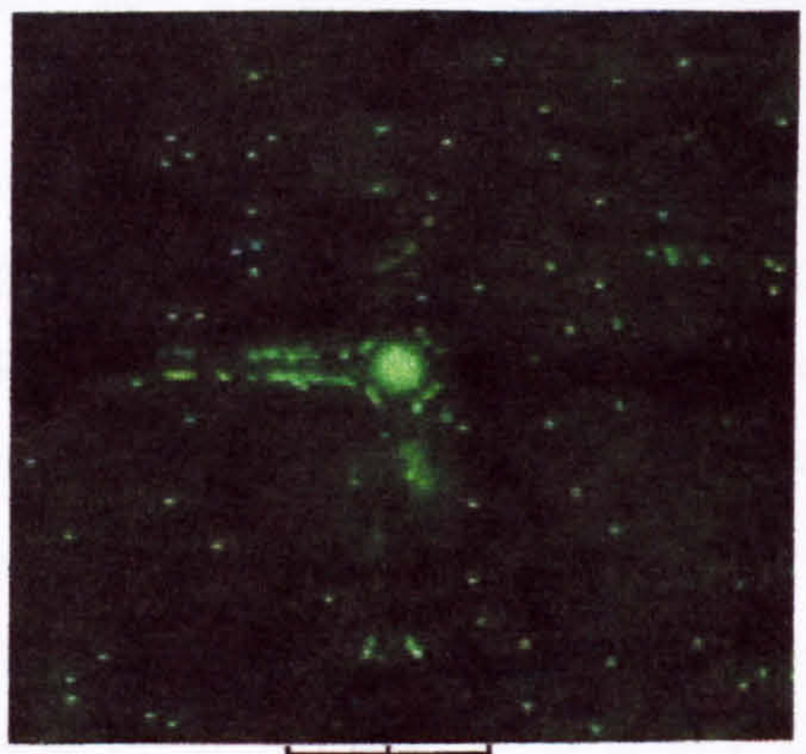

(7.7c) 282nm spheres in 10mM KPO_4 with an applied signal of 4V peak to peak at 1MHz.

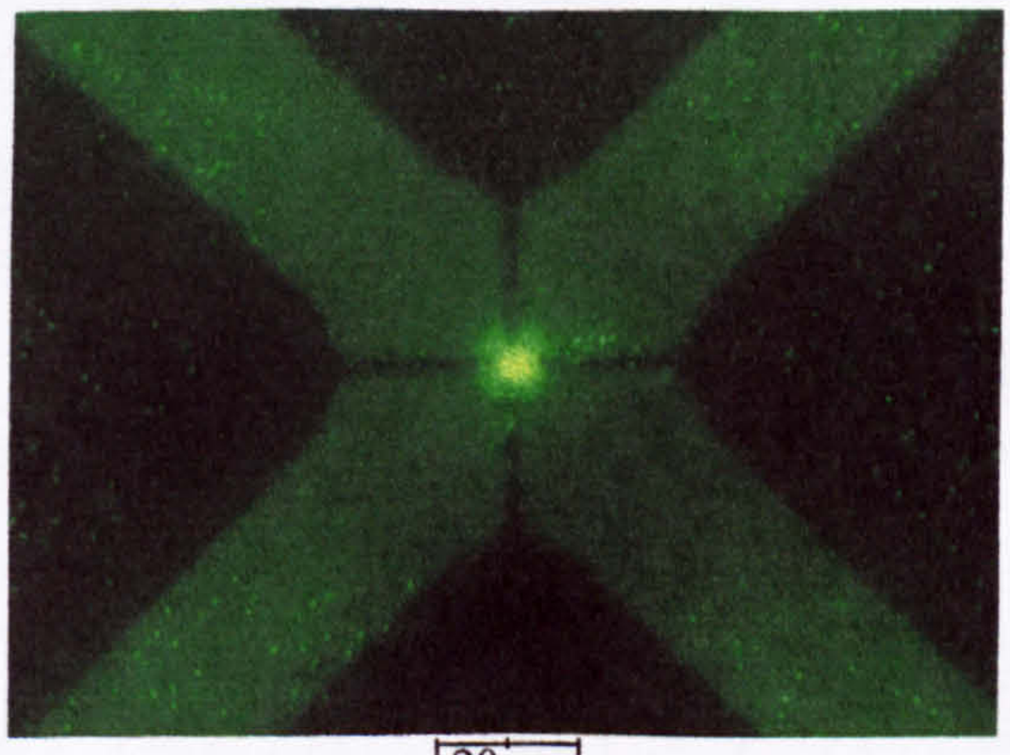

(7.7d) 282nm spheres in 100mM KCl with an applied signal of 8 volts peak to peak at 6MHz.

Figure (7.7) Dielectrophoretic behaviour in hyperbolic polynomial electrodes. The distance across the centre of the electrodes was 6µm in (7.7c) and 7.5µm in (7.7a), (7.7b) and (7.7d).

Figures (7.7a) and (7.7b) show 557nm spheres in 100μM KCl with a conductivity of $1.5mSm^{-1}$ experiencing positive dielectrophoresis at a frequency of 500kHz and negative dielectrophoresis at 5MHz respectively. The electric potential applied to the electrodes was 5 volts peak to peak and the distance across the centre of the electrodes was 7.5μm. Figure (7.7c) shows 282nm spheres experiencing negative dielectrophoresis in 10mM KPO_4 ($\sigma = 152mSm^{-1}$) at 4 volts peak to peak and 1MHz in a hyperbolic array with a centre separation of 6μm. Figure (7.7d) shows 282nm spheres trapping under negative dielectrophoresis in 100μM KCl at 8 volts peak to peak and 6MHz in a hyperbolic array with a centre separation of 7.5μm.

The dielectrophoretic movement of the spheres was rapid, with a response and travel time that decreased with decreasing sphere diameter. The path of the particles followed precisely the pattern expected from the theoretical DEP force plots in Chapter Six. In general, when particles experienced positive DEP in these electrode arrays, they collected at points of high DEP potential energy, which always correspond to high field points since the DEP potential is proportional to the field magnitude squared. When the particles experienced negative DEP, they collected at low field points (which exactly correspond to low DEP potential points) only if the point was completely surrounded by regions of high potential.

If particles were collected using positive dielectrophoresis and the frequency of the applied field was switched rapidly (the DDS can switch frequencies 33 times per second) to a frequency at which the spheres experience negative dielectrophoresis, the subsequent observed movement was exactly as predicted by the theoretical simulation of the electric field. Figure (7.8) shows four time captured video images at approximately 2.5 second time intervals during just such a procedure. The 557nm diameter spheres were suspended in 100μM KCl with a measured medium conductivity of $1.5mSm^{-1}$ and placed on a set of 50μm hyperbolic polynomial electrodes. In Figure (7.8a), the spheres are held at the electrode edges by positive dielectrophoresis at an applied field frequency of 500kHz and a potential of 10volts peak to peak. Figures (7.8b-d) show the captured images of the result of switching the field to 5MHz, where the spheres experience negative dielectrophoresis. As predicted by the field simulation, spheres in the area of the array enclosed by the curved parts of the electrodes are repelled from the electrode edge into the centre of the array. After approximately 10 seconds, the spheres have collected at the centre of the array (Figure 7.8d). In the area of the array where the electrode edges are parallel (or nearly so), the theoretical simulation of the dielectrophoretic force indicates that the particles should move away from the edge perpendicularly. Since the 557nm spheres are about 5 times larger than the thickness of the electrodes, they will experience a force which is an average of the DEP force above the electrodes as well as the force in the plane of the electrodes. As a result, the theoretical simulation suggests that they should experience a force upwards and

away from the electrode edge rather than directly into the centre of the array. Figures (7.8c-d) show that spheres at the edge of the image, where the electrode edges are parallel, do in fact move upwards and away from the electrodes rather than into the centre. The trapped spheres in the centre of the electrode array remained there as long as the electric field was maintained at the same frequency and potential.

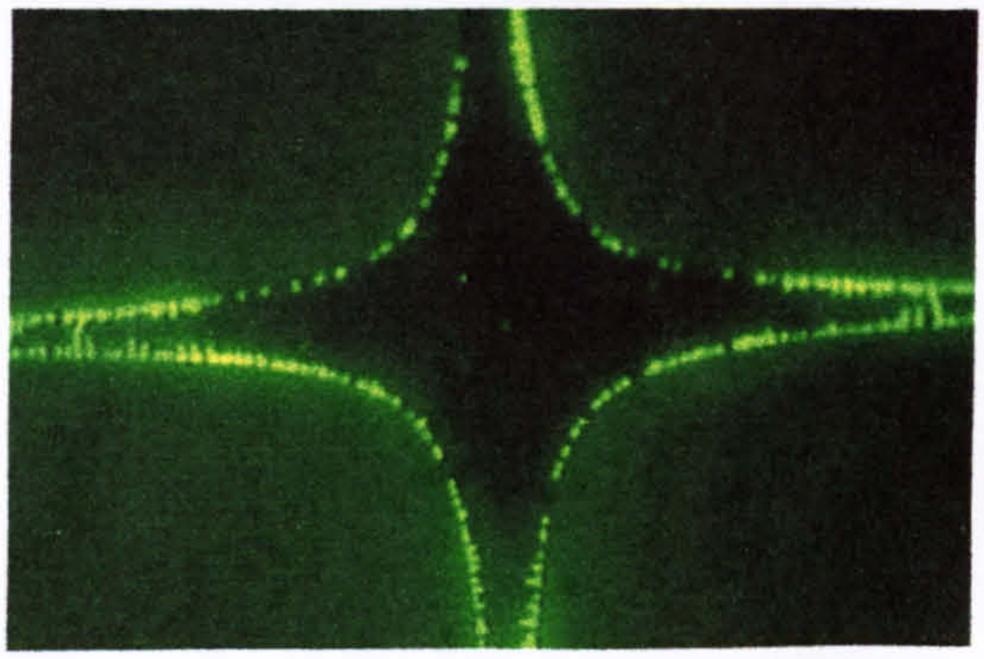

(7.8a)

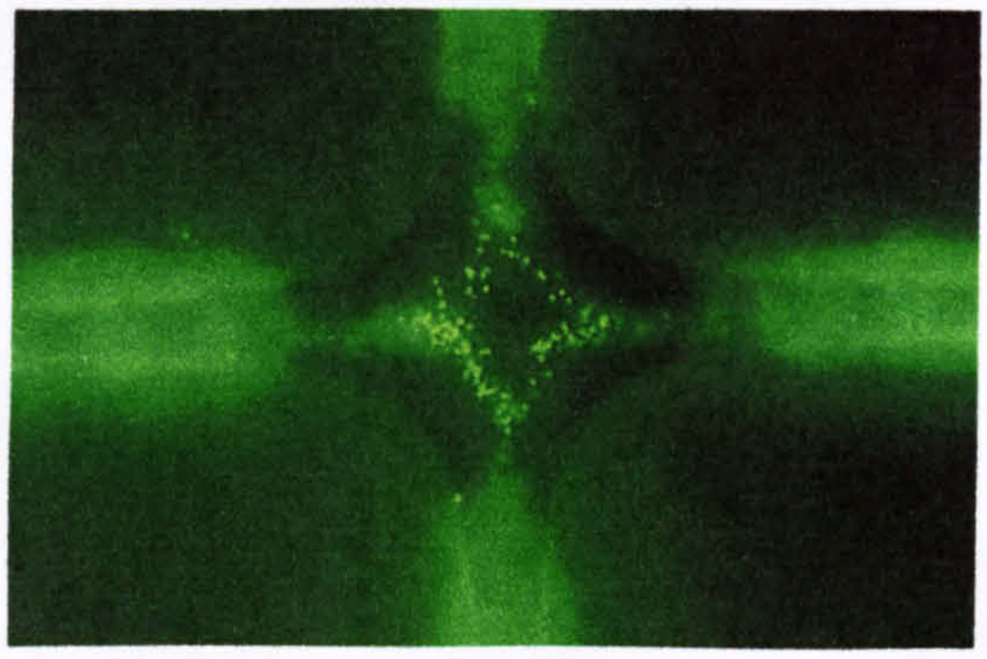

(7.8b)

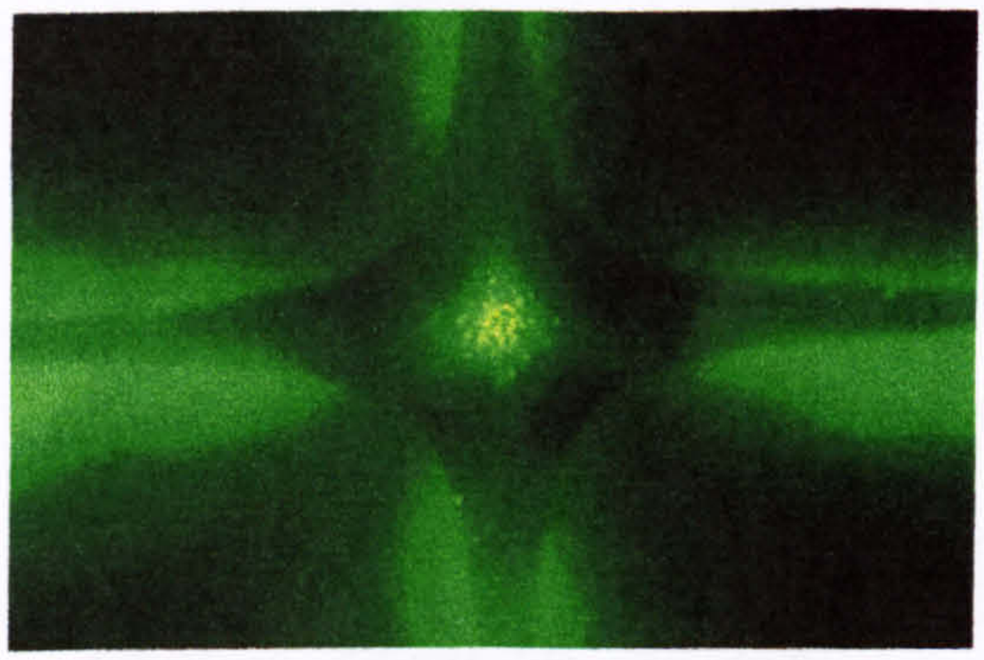

(7.8c)

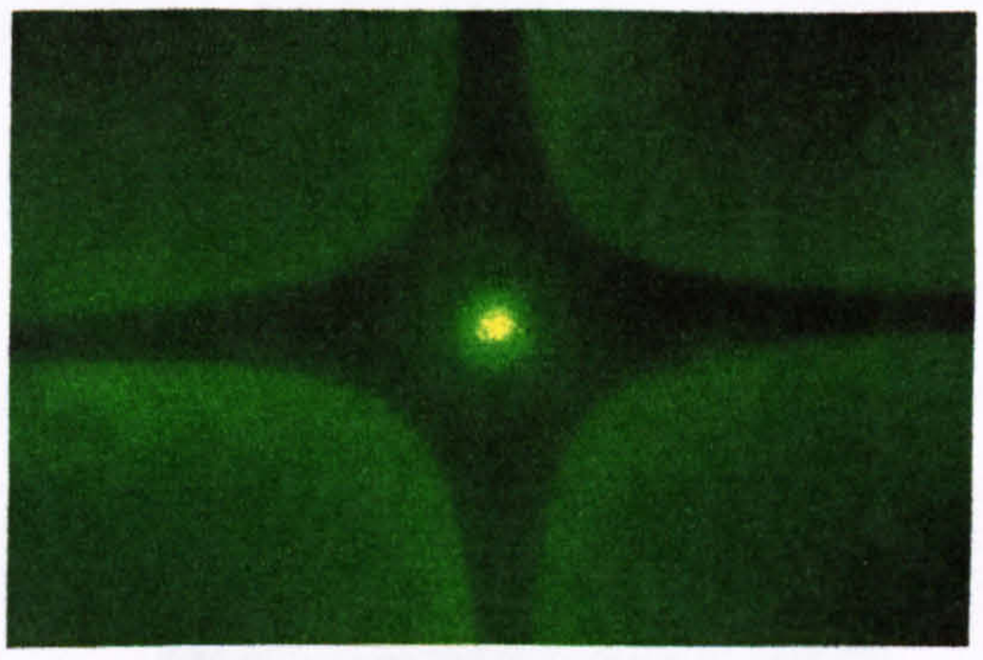

(7.8d)

Figure (7.8) Four captured video images at approximately 2.5 second time intervals of 557nm spheres in 100μM KCl on a set of polynomial electrodes 50μm across the centre. (7.8a) shows particles trapped by positive dielectrophoresis at the electrode edge by an applied signal of 500kHz and 10volts peak to peak. Just after this image was captured, the applied signal was switched to 5MHz and (7.8b-d) show the resulting negative dielectrophoretic movement of the with time. Particles in the central region move inwards to the middle and particles close to where the electrodes run parallel move upwards.

The dielectrophoretic behaviour of the spheres on castellated electrodes also matched the theoretical predictions accurately. Figure (7.9) shows typical results for the 282nm diameter spheres on electrodes manufactured using both photolithography and electron beam lithography (section 5.3). The electrodes in Figures (7.9a-c) are the lighter regions but the electrodes in Figure (7.9d) were back-lit and appear as the darker regions. Figure (7.9a) shows that at low applied potentials, in this case 2.5 volts peak to peak at 500kHz in 35μM KCl (σ =

$0.54mSm^{-1}$), positive dielectrophoretic collection or trapping is observed first at the tips of the castellated features where the highest fields and therefore lowest positive DEP potential energy is found.

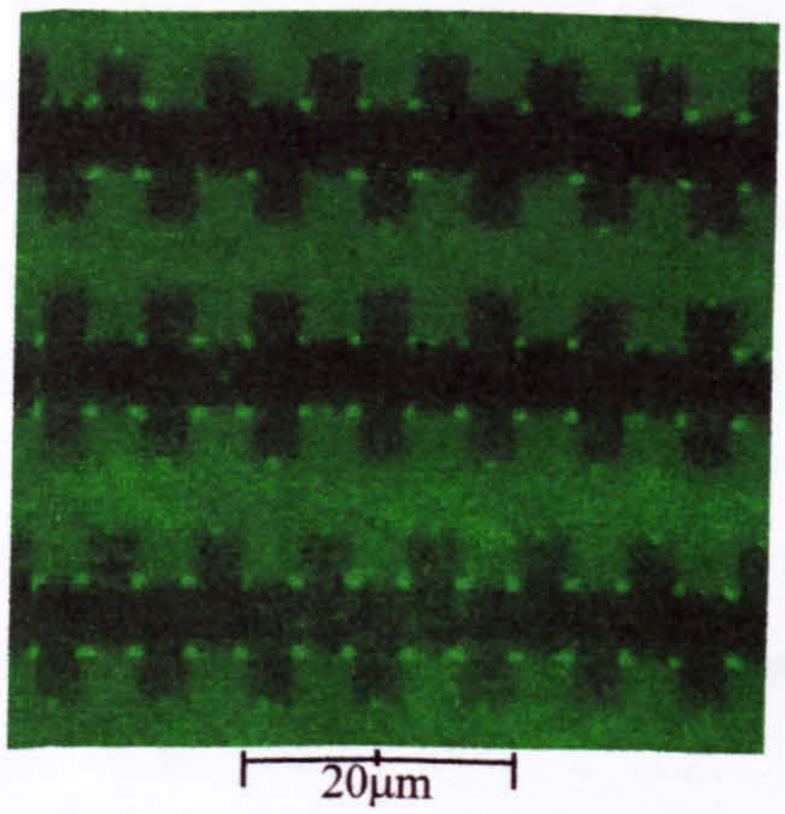

(7.9a) 282nm in 35μM KCl with an applied signal of 2.5 volts peak to peak at 500KHz

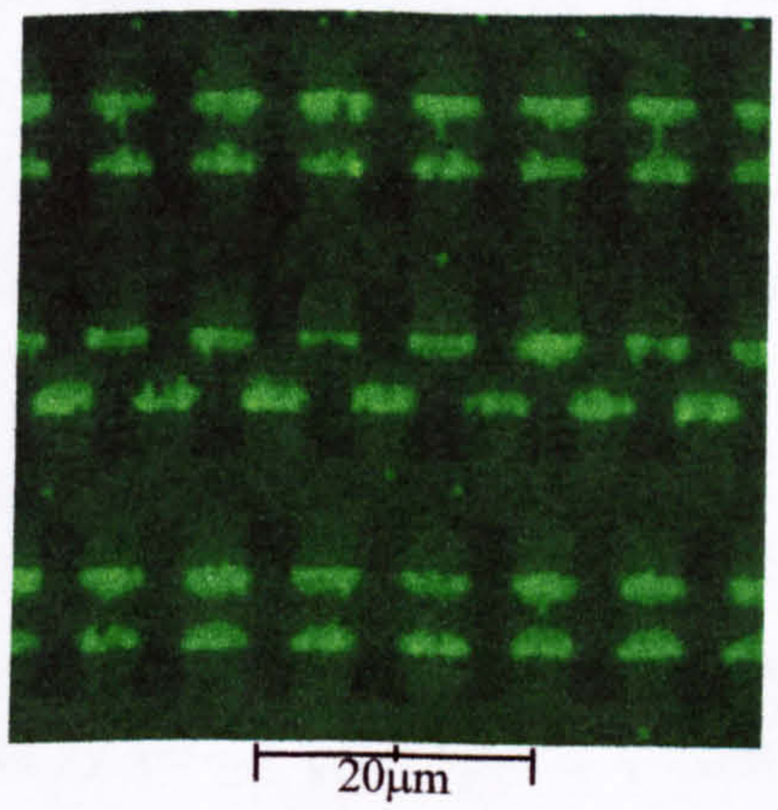

(7.9b) 282nm in 100μM KCl with an applied signal of 8 volts peak to peak at 500kHz.

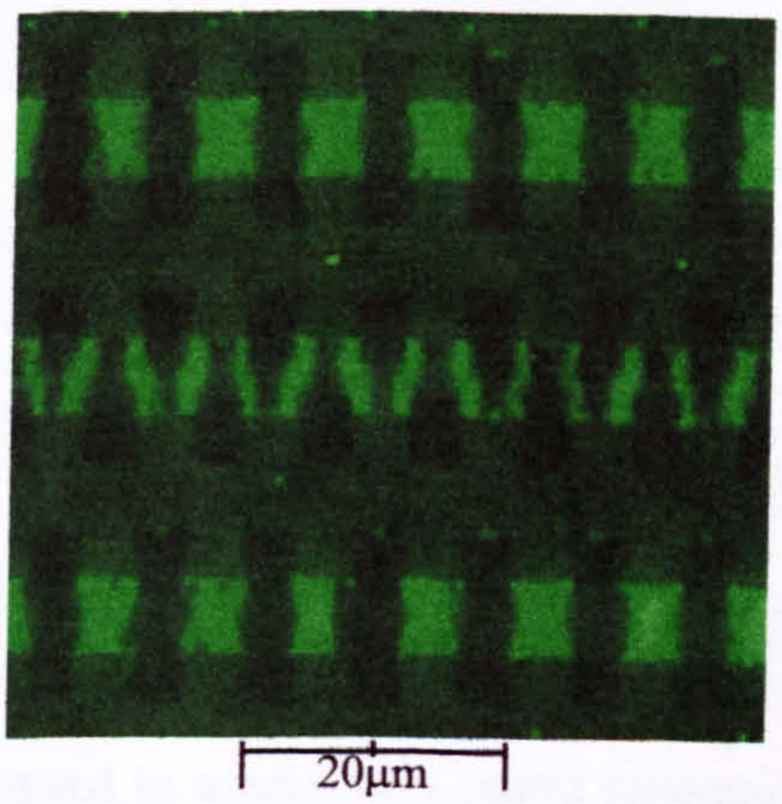

(7.9c) 282nm in 100μM KCl with an applied signal of 8 volts peak to peak at 1MHz.

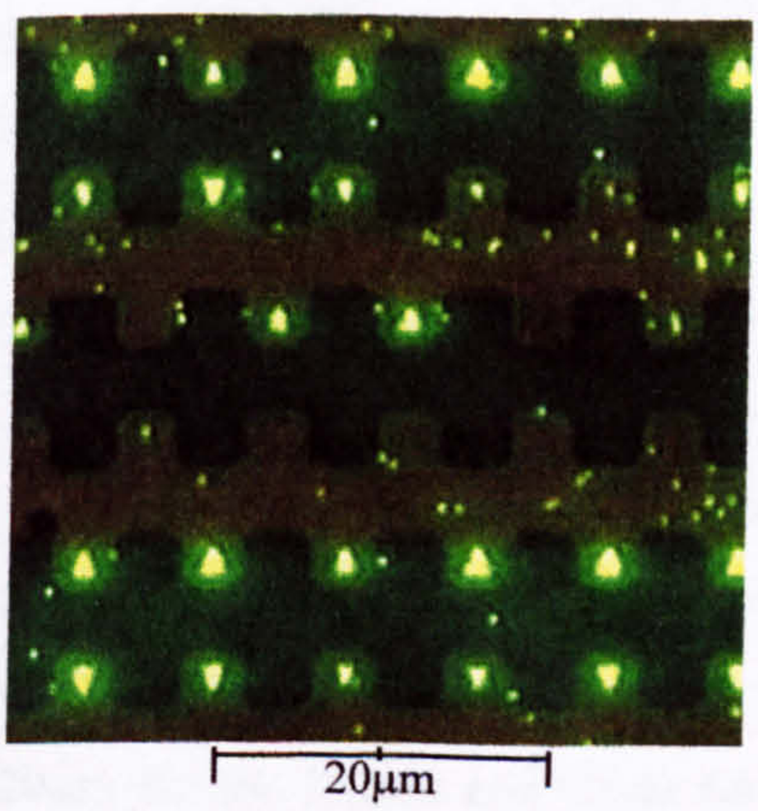

(7.9d) 282nm in 1mM KCl with an applied signal of 8 volts peak to peak at 10MHz.

Figure (7.9) Dielectrophoretic behaviour in castellated electrodes. 282nm spheres experiencing positive dielectrophoresis in electron-beam manufactured electrodes (7.9a-c) and negative dielectrophoresis in photolithographically manufactured electrodes (7.9d). the exact experimental conditions are shown under each figure. The feature and gap sizes of all the electrodes were 4μm. The electrodes are the lighter regions in (7.9a-c) and the darker area in the back-lit image (7.7d)

At higher applied potentials, as shown in Figure (7.9b) for 100μM KCl ($\sigma = 1.50mSm^{-1}$) and a potential of 8 volts peak to peak at 500kHz, more collection was observed along the front edges of the castellations. For the same medium, if the potential is maintained constant but the

frequency is increased to 1MHz, which is close to the frequency at which the behaviour changes from positive DEP to negative DEP, the force decreases and pearl chaining is observed between opposite tips of the electrodes. Negative DEP trapping in the castellated electrodes was difficult to achieve under most circumstances. Under normal experimental conditions, the spheres remained suspended in the medium in a uniform and random manner (due to diffusion, section 4.2.5). When the field was switched on at an appropriate frequency for negative DEP, very little if any trapping was observed. This result was reproducible under all experimental conditions for all the sizes of spheres and confirms the theoretical prediction (Chapter Six) that the negative trap or cage in the castellated electrodes was enclosed and did not extend to a sufficient height above the electrodes to trap particles suspended in solution above approximately 4-5μm. However, the theoretical simulation does indicate that particles close to the electrodes should be trapped by negative DEP. This was tested by attracting the spheres towards the electrodes by positive DEP and switching the field immediately to a frequency for strong negative DEP. Using this method, reproducible negative trapping was achieved in 1mM KCl (σ = 13mSm^{-1}) on a set of 4μm feature and gap size castellated electrodes as shown in Figure (7.9d) for an applied potential of 8 volts peak to peak at a frequency of 10MHz.

Under certain reproducible experimental conditions, there were deviations from the expected behaviour due to DEP and these effects can attributed to convective movement of the fluid. This behaviour is described and discussed in more detail in Chapter Nine under the heading of other forces.

In general, the size of electrodes required to obtain DEP, especially negative DEP, varied with the size of the particle. For example, negative DEP of both 557 nm spheres could be achieved in polynomial electrodes up to 100μm across. No negative trapping of spheres was observed in arrays with centre separations larger then 20μm for the 282nm and 10μm for the 93nm. However, the 4 and 5μm castellated electrode arrays were too small to obtain negative DEP of the 557nm and the 282nm spheres under most circumstances. In this case, large electrodes would probably be more suitable but were not investigated.

7.3.4 Single particle trapping

In the literature [2] a certain amount of importance has been given to the negative dielectrophoretic trapping of single particles. In reference 2, the smallest particle that could be stably trapped was quoted as 650nm diameter. However, it was found that stable single particle trapping could be achieved for a range of particle diameters down to 282nm. Figure (7.10a) shows a captured video image of a single 282nm diameter latex sphere trapped in polynomial electrodes at a frequency of 20 MHz and an applied voltage of 10 volts peak to peak. The suspending medium was 100μM potassium chloride and the conductivity was 1.5mSm^{-1} and the centre separation of the electrodes was 6μm.

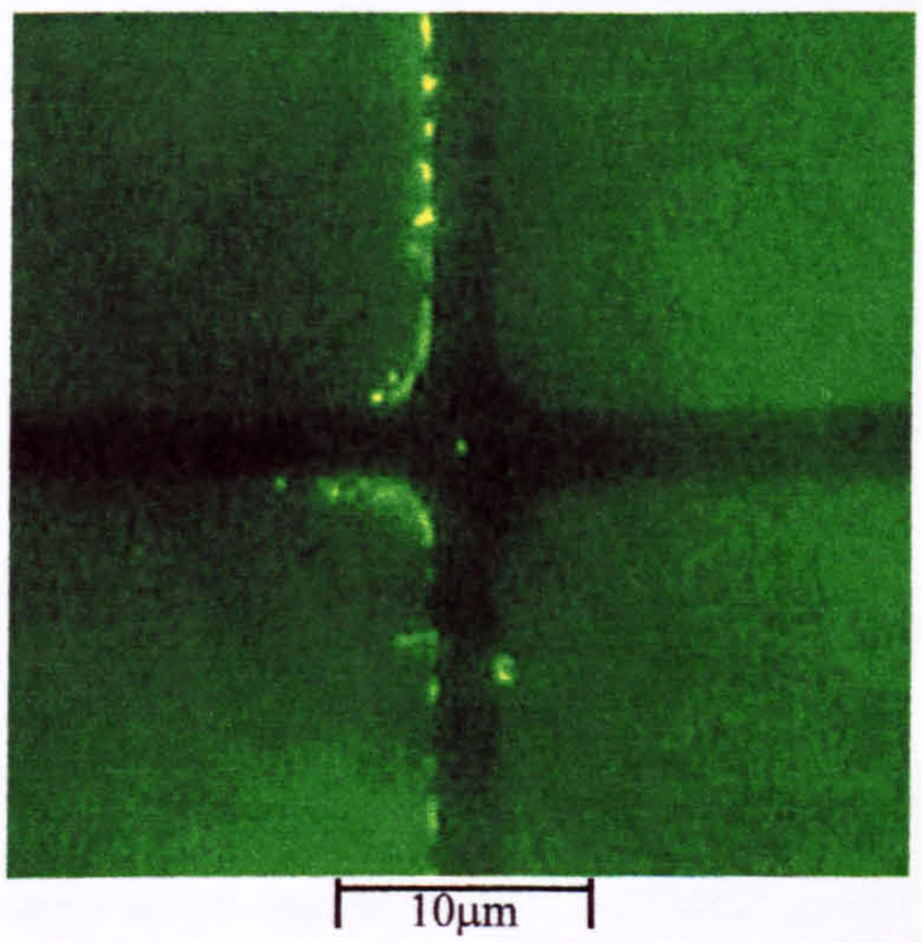

(7.10a) 282nm sphere in 100μM KCl with an applied potential of 10 volts peak to peak at 20MHz

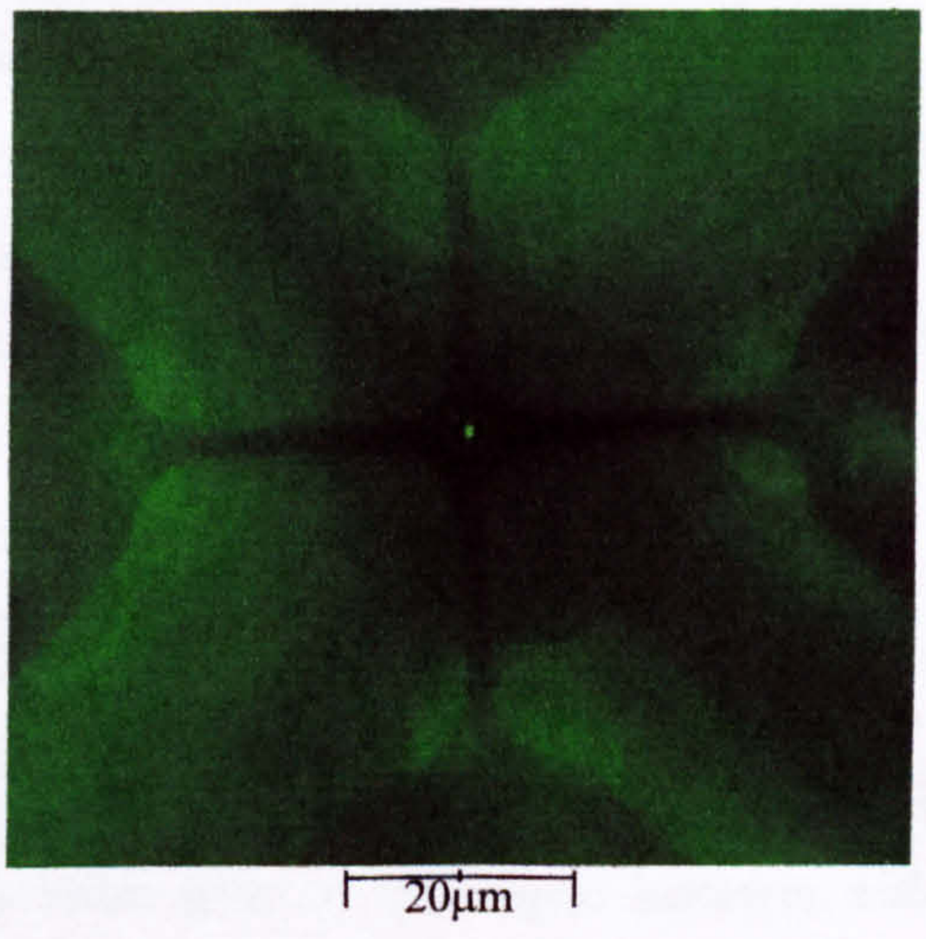

(7.10b) 557nm sphere in 100μM KCl with an applied potential of 10 volts peak to peak at 20MHz

Figure (7.10) Single latex spheres trapping by negative dielectrophoresis in hyperbolic polynomial electrodes. The centre separations of the electrodes were 6μm in (7.10a) and 7.5μm in (7.10b).

The sphere was stably trapped under these conditions as long as the field remained. When the voltage was reduced the sphere moved around in a random manner within a circle defined by a radius from the centre of the electrodes. When the voltage was increased again, the radius decreased until the sphere stopped moving. Figure (7.10b) shows a 557nm sphere trapped in a set of 7.5μm hyperbolic electrodes at a potential of 10volts peak to peak at 20MHz in 100μM KCl.

7.3.5 Dielectrophoretic force zero point measurements

The dielectrophoretic behaviour of four different sizes of latex spheres: 557, 282, 216 and 93nm diameter, was observed in varying concentrations of three different salt solutions and recorded as a function of applied field frequency and solution conductivity. In general, the movement of the spheres at low frequencies was due to positive DEP and at high frequencies was due to negative DEP. The change in behaviour from positive to negative DEP as the applied frequency increases is characterised by a frequency at which the dielectrophoretic force is zero. This zero force point or "*cross-over*" corresponds to the frequency at which the movement of the sphere is no longer governed by the DEP force. For large particles such as cells, it is possible to say that there is no movement at the zero point. However, as was discussed in Chapter Four, for colloidal particles Brownian motion is noticeable. As a result, the range of frequencies over which DEP is not observed was wider than would be expected for particles larger than a micrometre in diameter.

The results of the zero point frequency measurements are shown in the following series of figures, grouped by particle diameter. Figures (7.11), (7.12), (7.13) and (7.14) show the results for the 557, 282, 216 and 93nm diameter spheres respectively. The experimental uncertainties in the measured frequencies were negligible compared to the width of the zero point region and were therefore ignored.

Each figure shows the same general trend. At low medium conductivities, there is a zero point region in the 1-10MHz range and the centre point of this region increases with decreasing particle size. As the medium conductivity is increased, the range remains relatively constant until, at a certain value of σ_m, the zero point region drops to the 100kHz-1MHz range. The zero point region continues to drop slightly as the medium conductivity is increased further.

Another feature of each figure is that there also appears to be a range of conductivities just below the drop-off point where the zero point region increases in frequency with σ_m. This effect is very marked for the smallest size of sphere, both in terms of the size of the conductivity range and in the increase in frequency of the zero point region. As the size of the sphere increases, the size of this effect decreases and for the 557nm spheres, it is noticeable but only slightly. There are also small variations with the composition of the electrolyte, and these effects are more prominent in the high conductivity behaviour.

Zero point region - 557nm in KCl

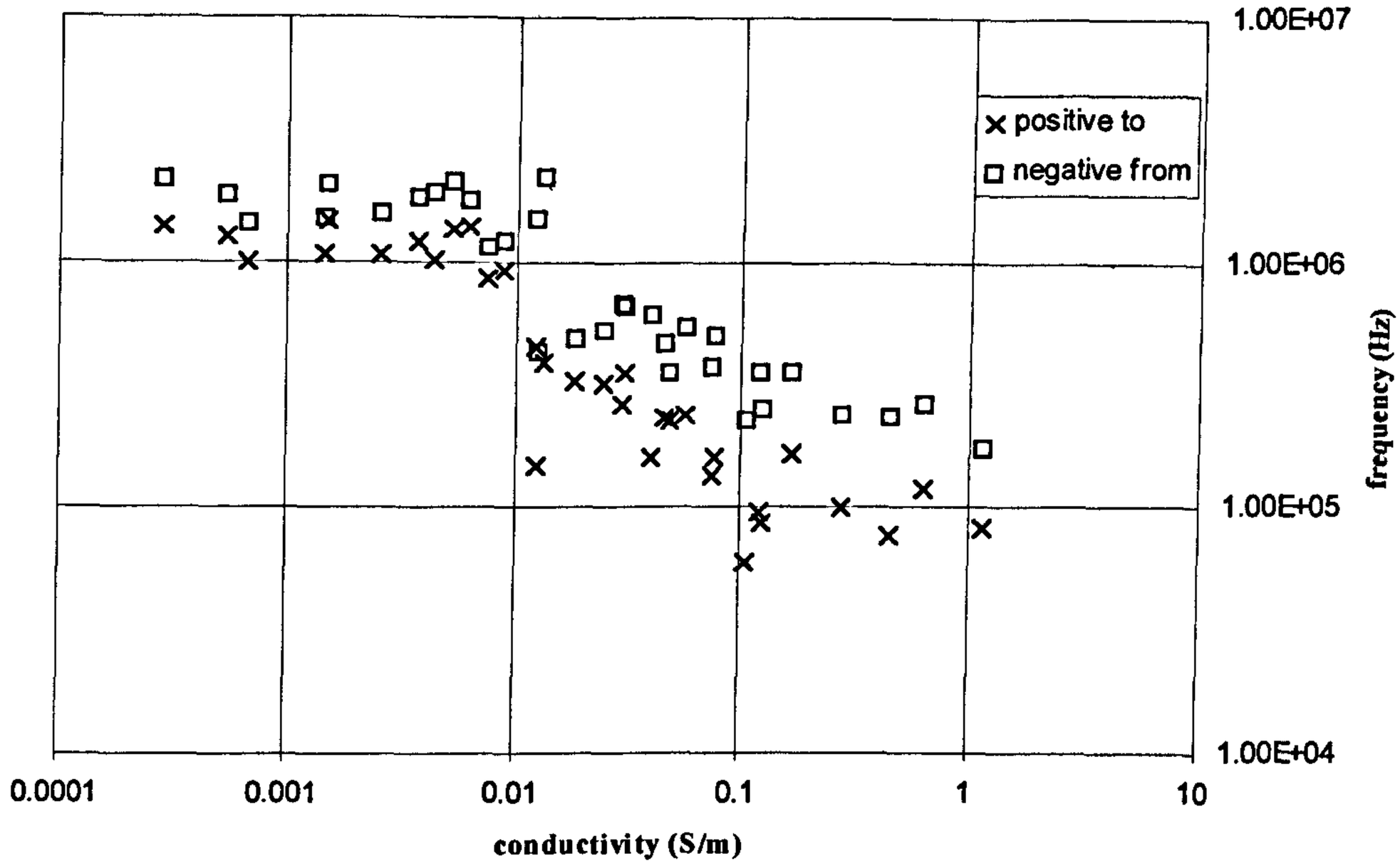

(7.11a)

Zero point region - 557nm in NaCl

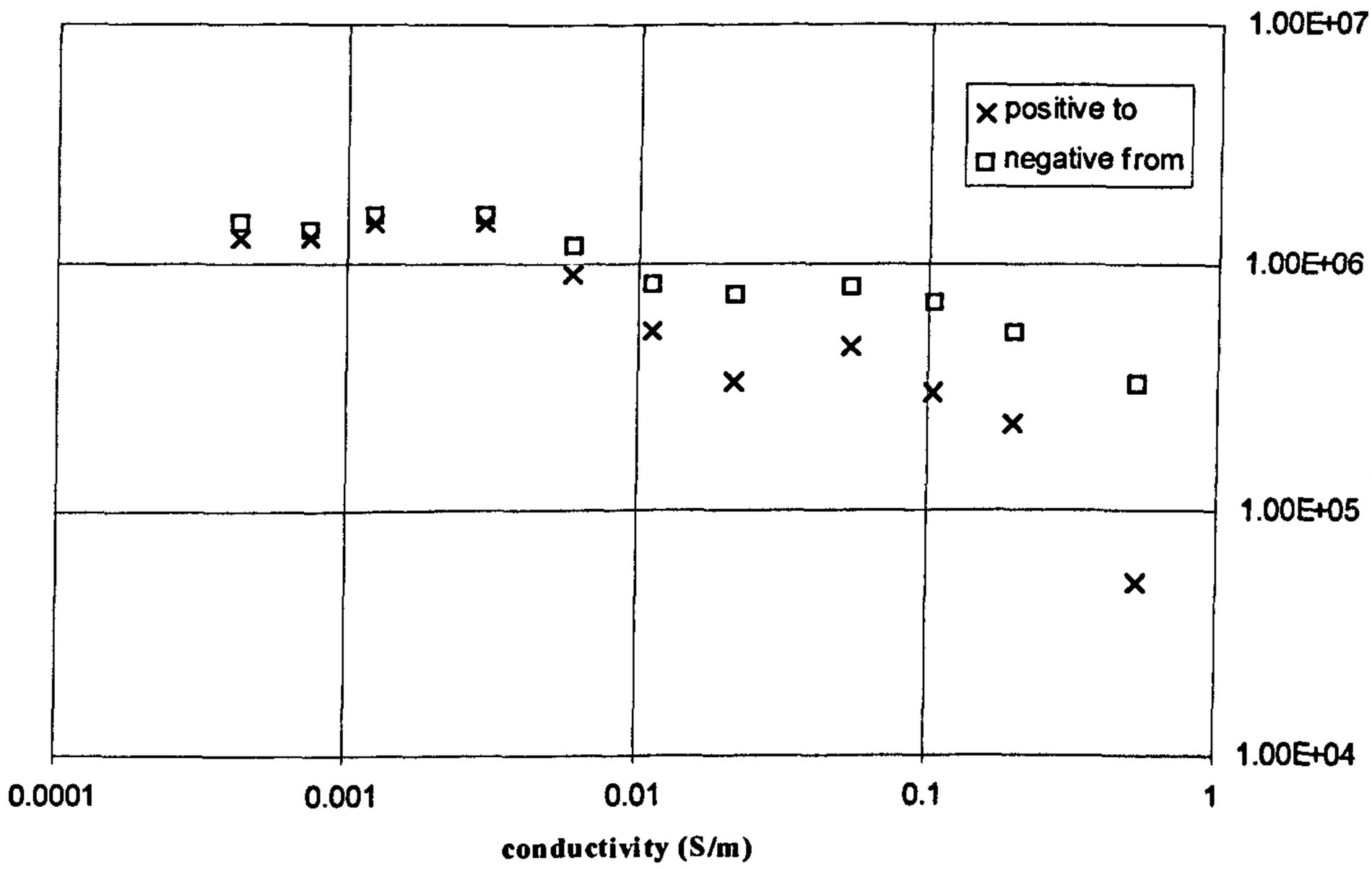

(7.11b)

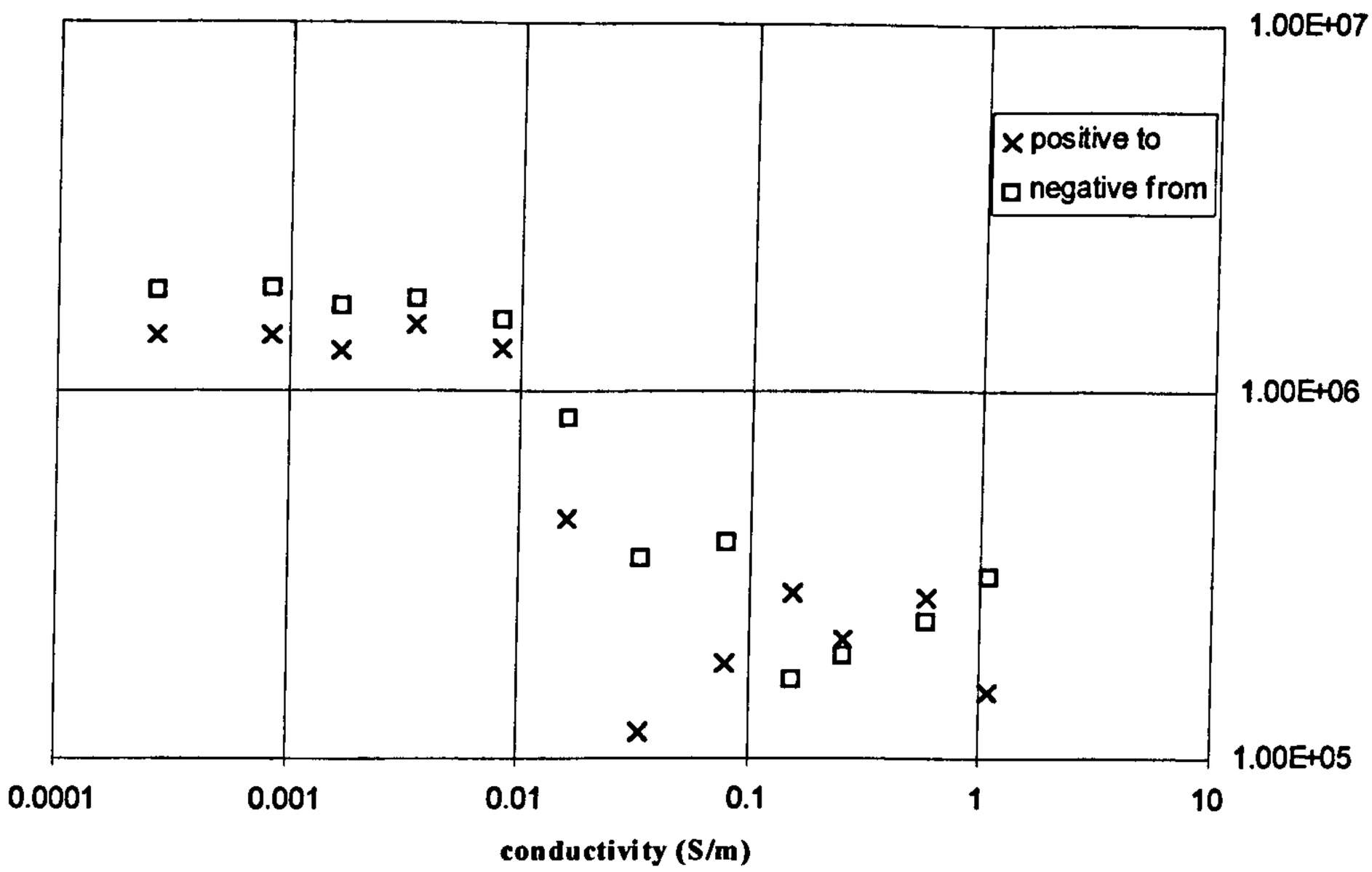

(7.11c)

Figure (7.11) Zero point frequency measurements for the 557nm diameter latex spheres in **(a)** KCl, **(b)** NaCl and **(c)** KPO_4. The crosses represent the frequency at which positive dielectrophoresis ends if the applied frequency is being increased and the square represents the frequency at which negative dielectrophoresis starts.

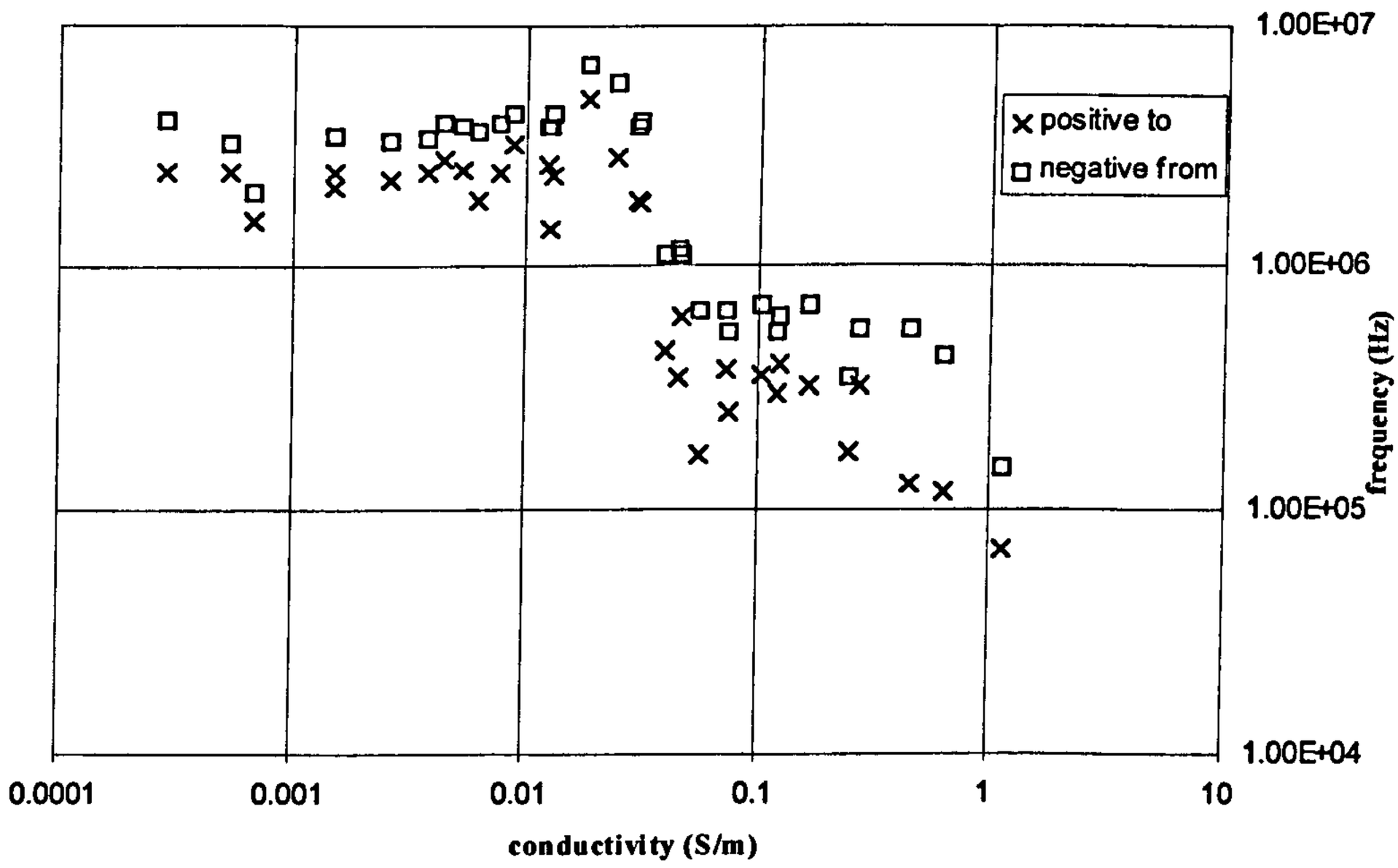

(7.12a)

Zero point region - 282nm in NaCl

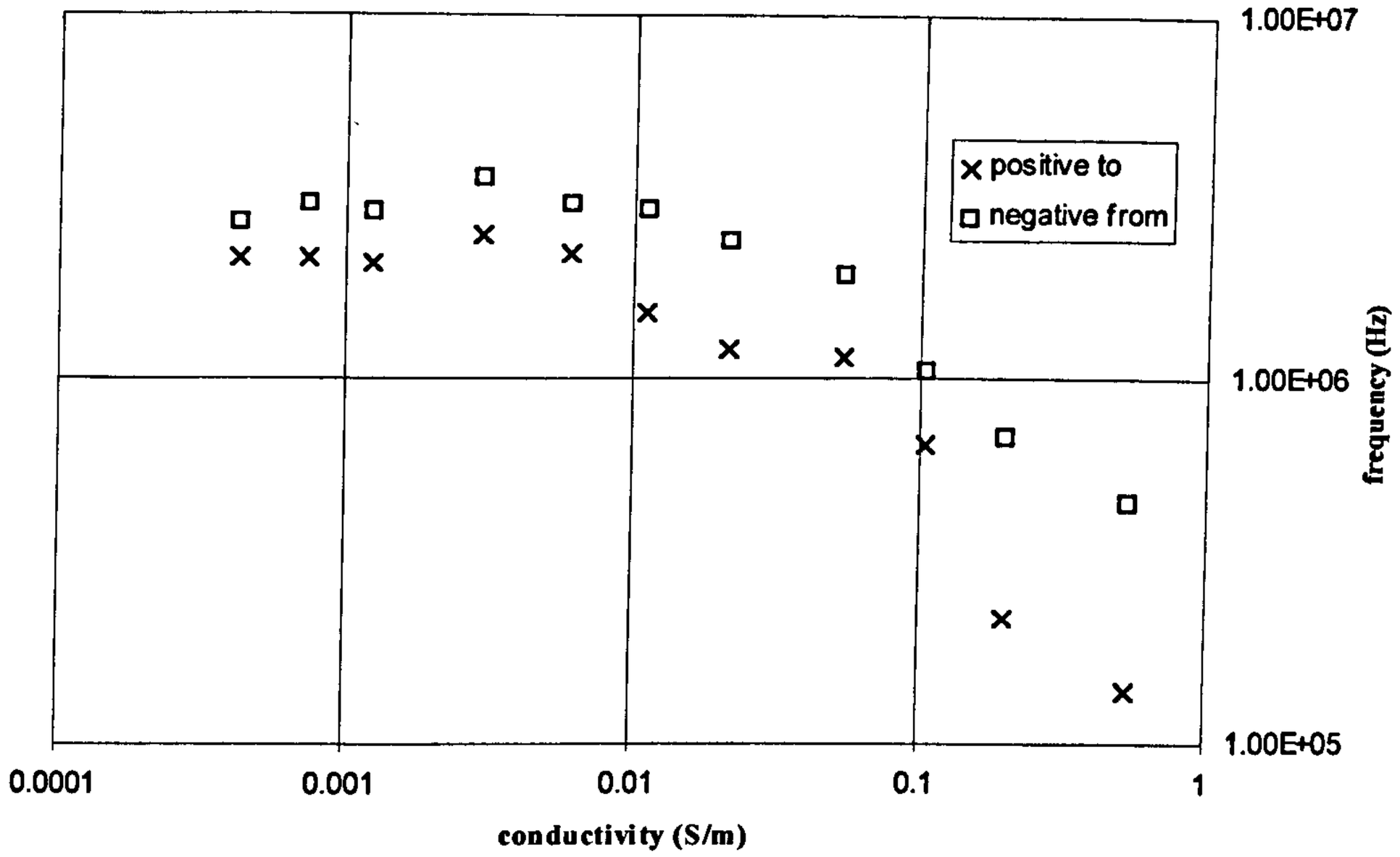

(7.12b)

Zero point region - 282nm in KPO_4

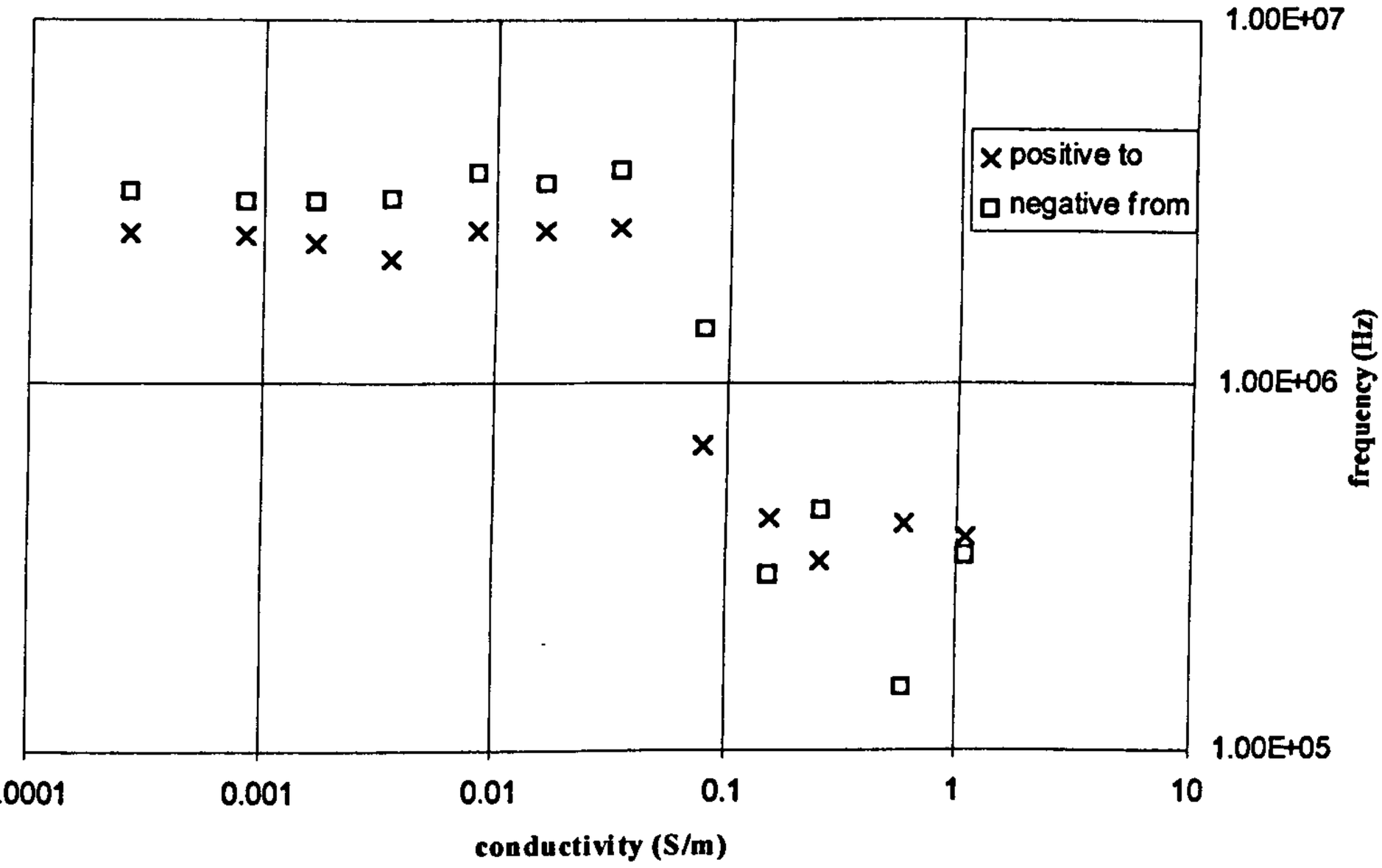

(7.12c)

Figure (7.12) Zero point frequency measurements for the 282nm diameter latex spheres in **(a)** KCl, **(b)** NaCl and **(c)** KPO_4. The crosses represent the frequency at which positive dielectrophoresis ends if the applied frequency is being increased and the square represents the frequency at which negative dielectrophoresis starts.

Zero point region - 216 nm in KCl

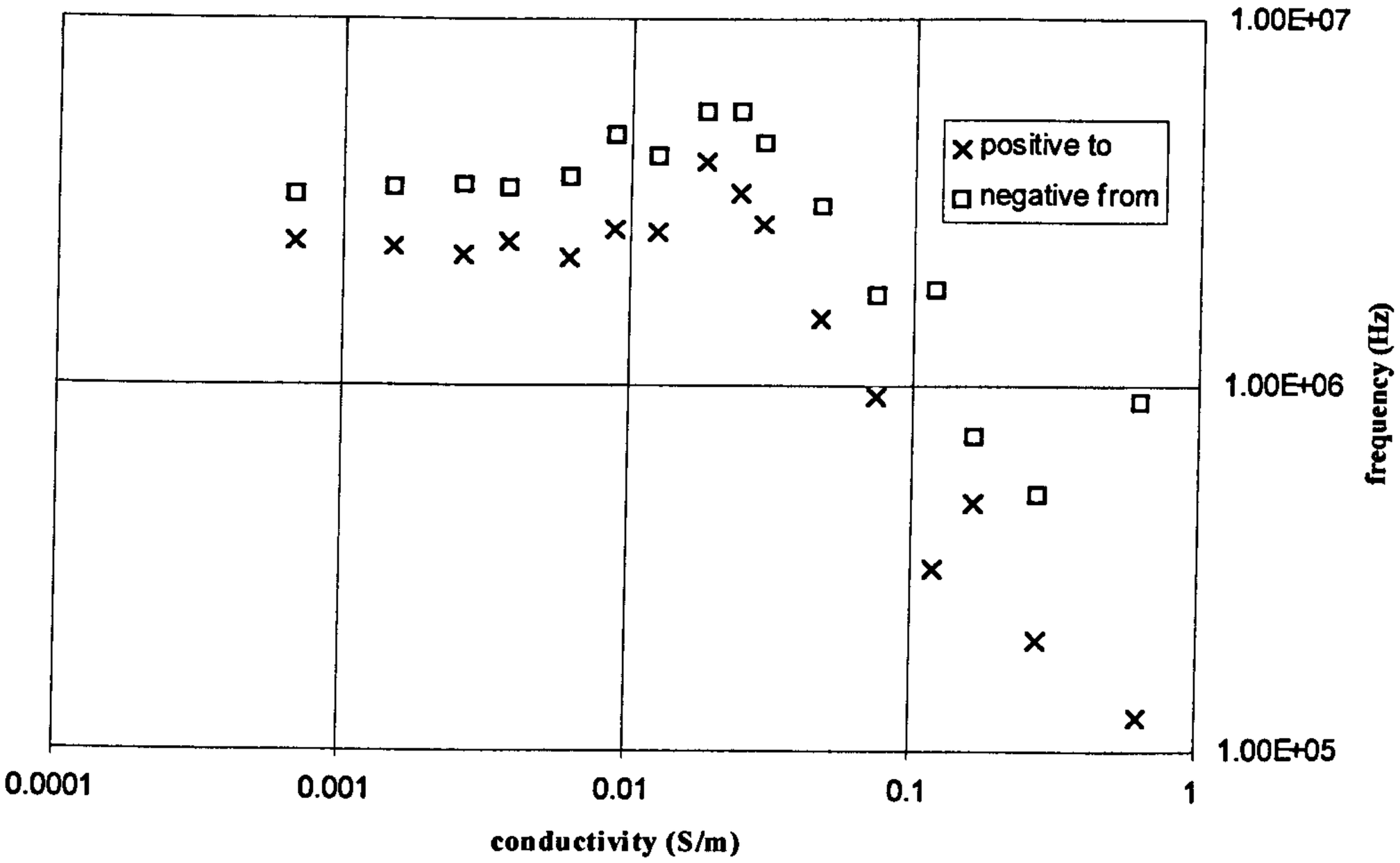

(7.13a)

Zero point region - 216nm in NaCl

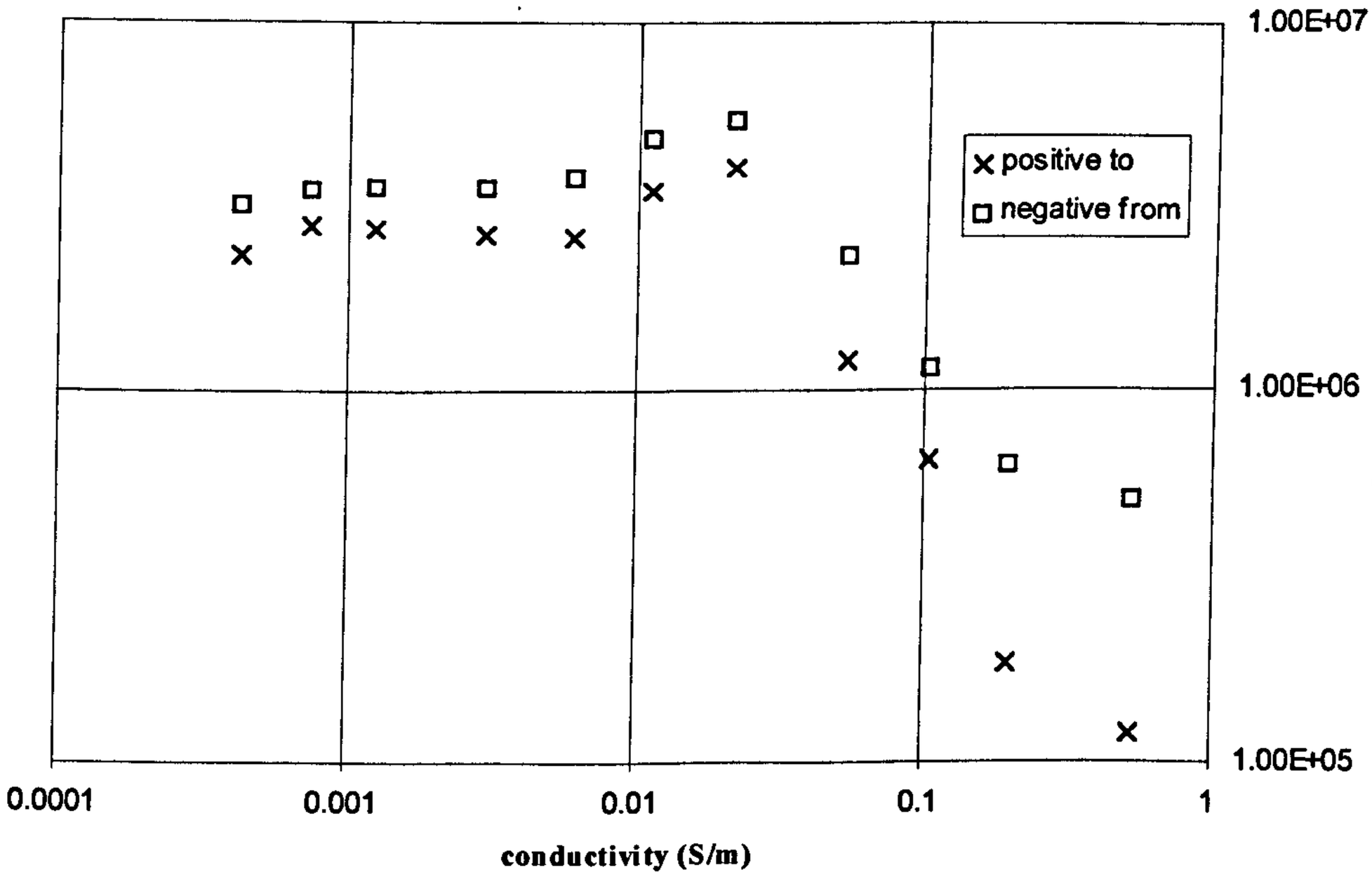

(7.13b)

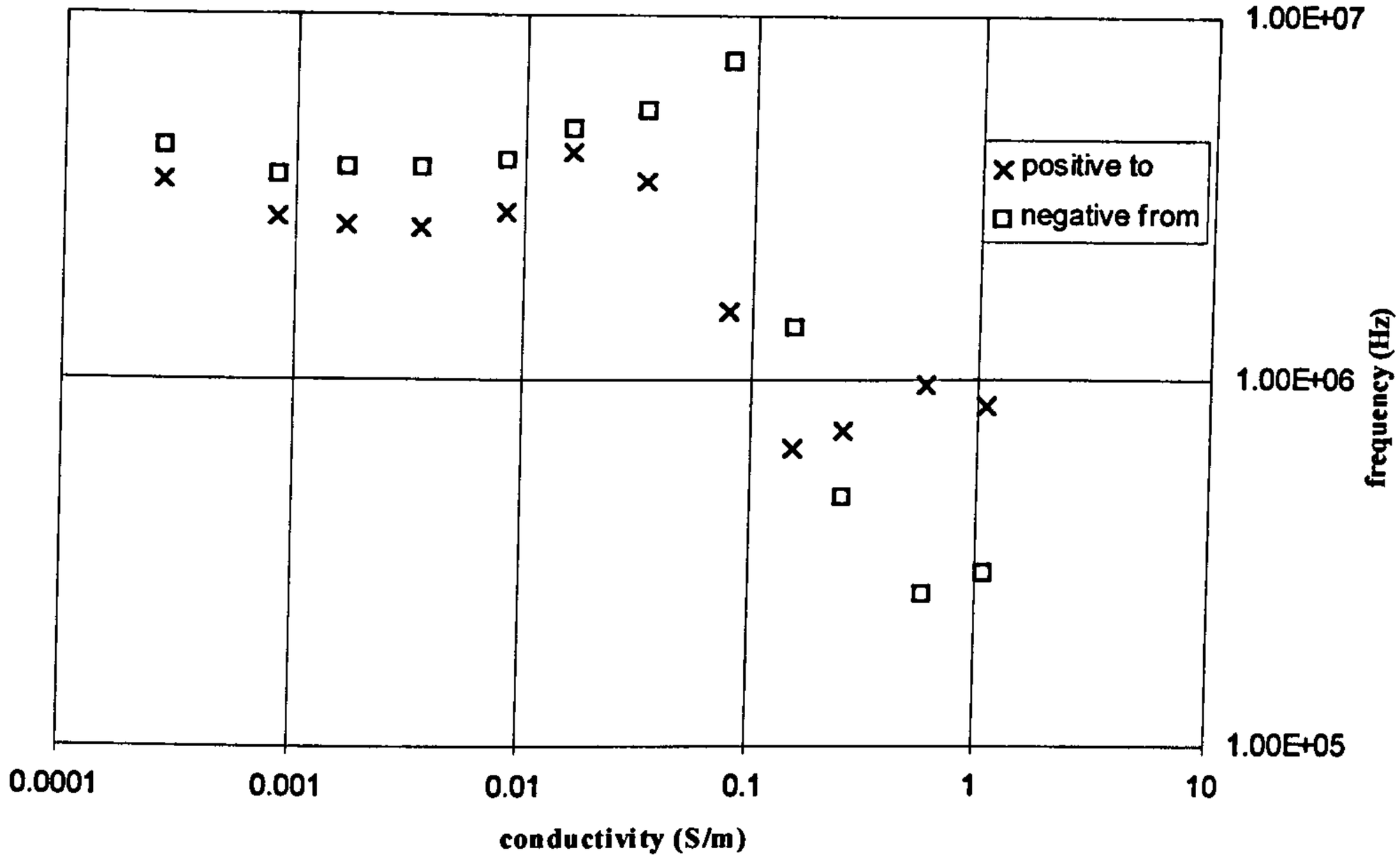

(7.13c)

Figure (7.13) Zero point frequency measurements for the 216nm diameter latex spheres in **(a)** KCl, **(b)** NaCl and **(c)** KPO_4. The crosses represent the frequency at which positive dielectrophoresis ends if the applied frequency is being increased and the square represents the frequency at which negative dielectrophoresis starts.

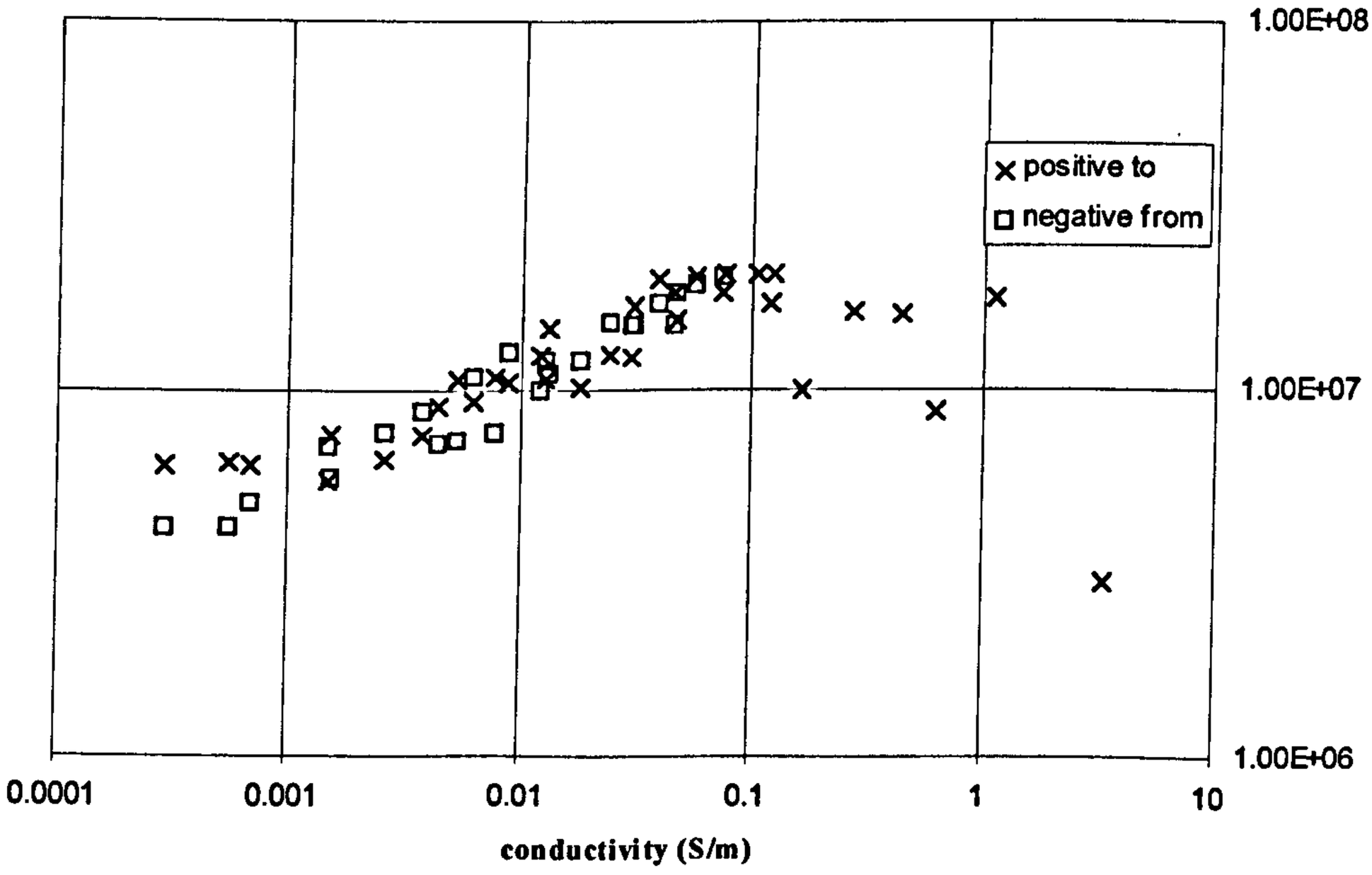

(7.14a)

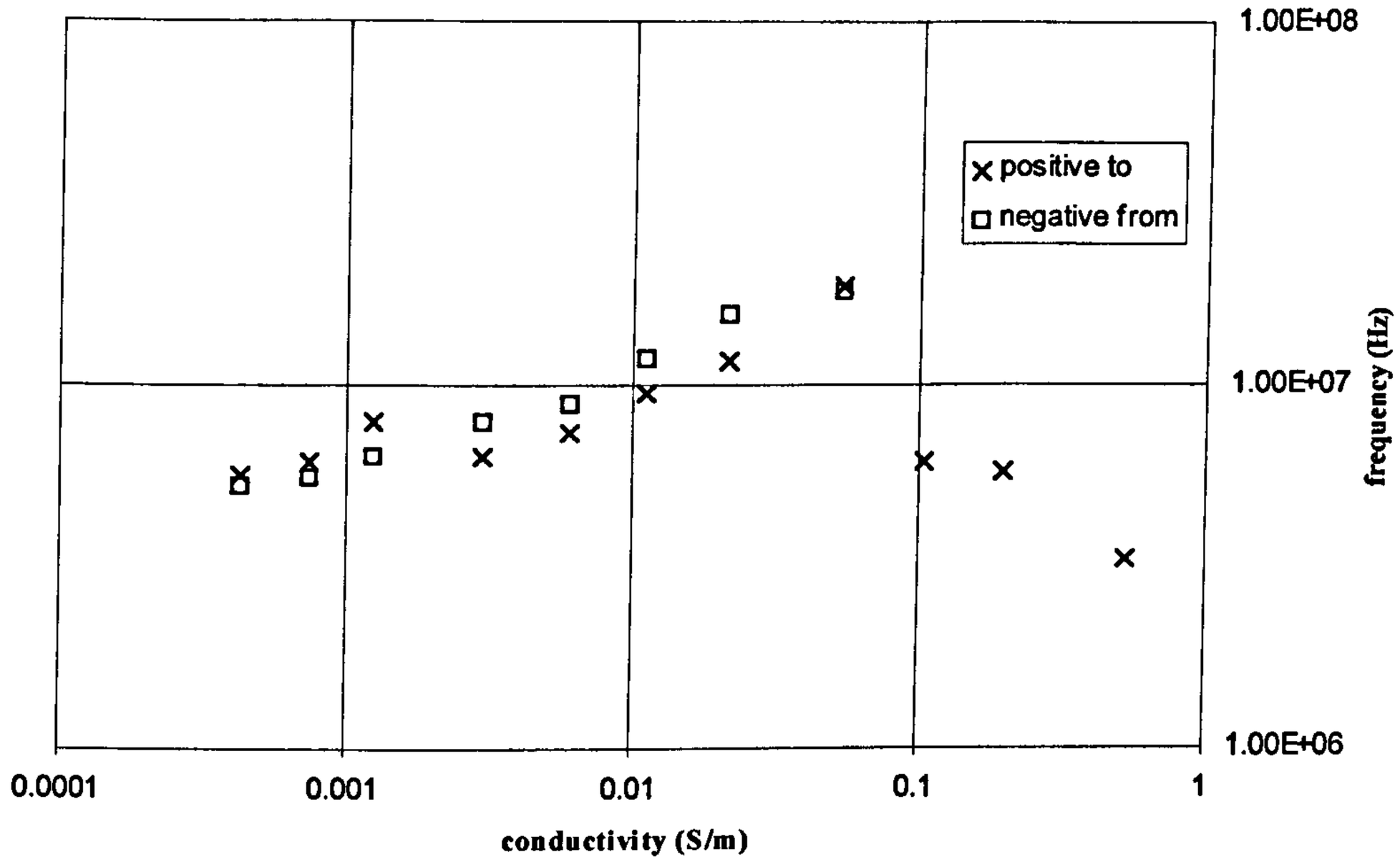

(7.14b)

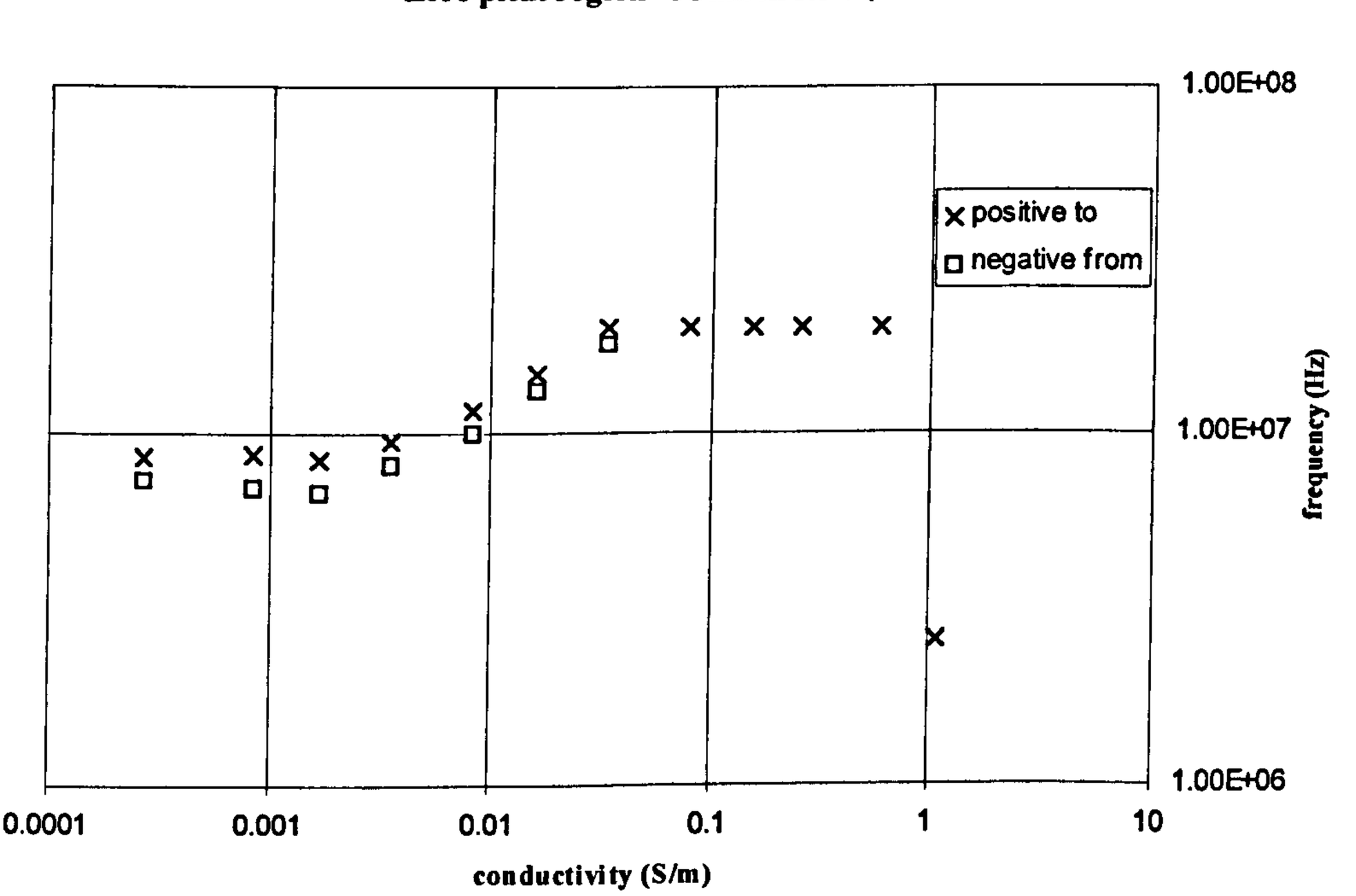

(7.14c)

Figure (7.14) Zero point frequency measurements for the 93nm diameter latex spheres in **(a)** KCl, **(b)** NaCl and **(c)** KPO_4. The crosses represent the frequency at which positive dielectrophoresis ends if the applied frequency is being increased and the square represents the frequency at which negative dielectrophoresis starts.

7.4 Discussion and theoretical comparison

This section presents and compares the experimental measurement of the zero force frequencies in section (7.3.4) with the theory of Chapter Three. The first sub-section deals with the Maxwell-Wagner interfacial polarisation relaxation with particular attention to the surface effects which are so prominent in sub-micrometre particles. The second sub-section looks at the high medium conductivity region where the Maxwell-Wagner relaxation is not responsible for the change from positive to negative dielectrophoresis. It is only in this region that the alpha relaxation can be determined using this method of measuring behaviour. All theoretical work was performed using Matlab (The Mathworks Inc, Natick, MA, USA) and the functions used included in Appendix (7b).

7.4.1 Maxwell-Wagner Interfacial polarisation

The classical Maxwell-Wagner relaxation of the dipole moment of a spherical particle induced by an electric field of constant potential, is governed by the Clausius-Mossotti factor (equation 3.15). As all the other terms in the expression for the dipole (equation 3.17) and the dielectrophoretic force (equation 4.21) do not vary with the frequency of the applied field, the Clausius-Mossotti factor also described the change in the dielectrophoretic force with frequency and medium conductivity.

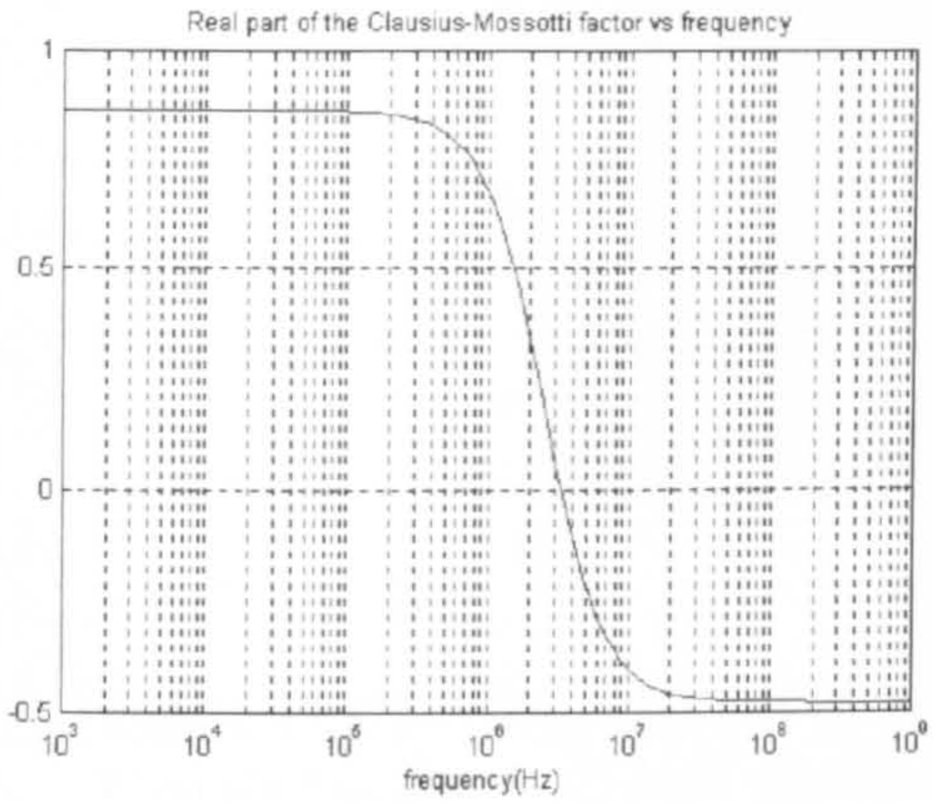

Figure (7.15) The variation of the Clausius-Mossotti factor with frequency for a 282nm diameter sphere of relative permittivity 2.55 and conductivity 20mSm^{-1} suspended in a medium of relative permittivity 78.54 and conductivity 1mSm^{-1}. The zero force frequency was calculated using a binary search algorithm and is shown in the middle of the graph

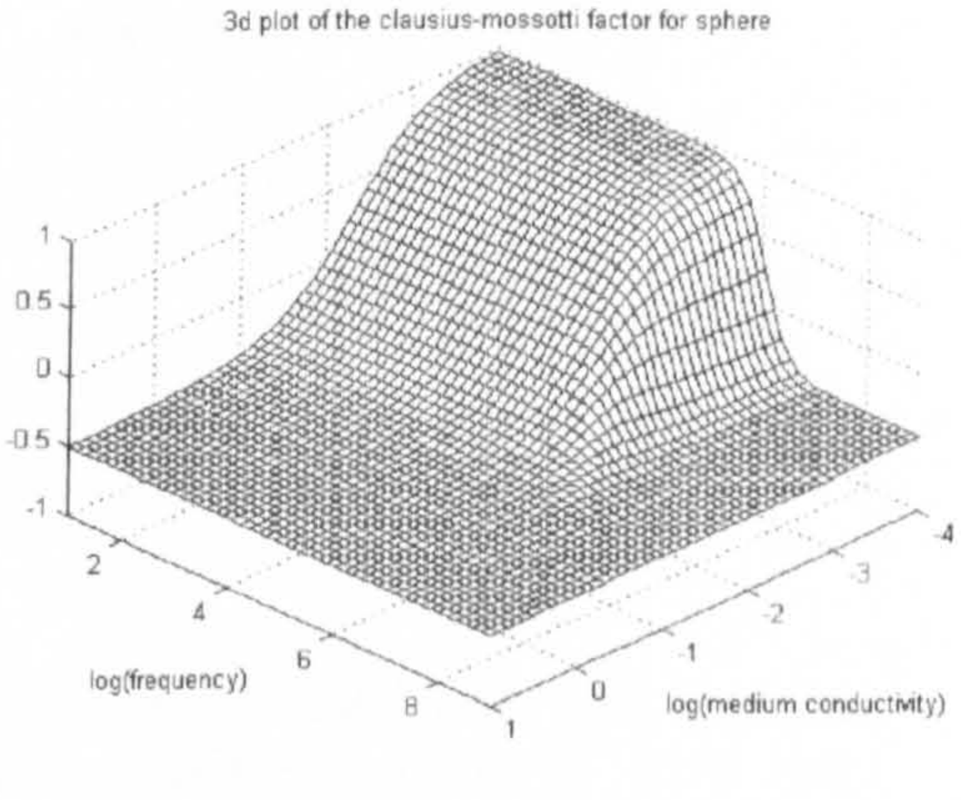

Figure (7.16) The variation of the Clausius-Mossotti factor with frequency and medium conductivity for a 557nm diameter sphere of relative permittivity 2.55 and conductivity 10mSm^{-1} suspended in a medium of relative permittivity 78.54.

Figure (7.15) shows the variation of the real part of the Clausius-Mossotti factor (C-M) with applied field frequency for a 282nm sphere with a permittivity of 2.55 and a conductivity of $20mSm^{-1}$in a medium of permittivity 78.54 (water) and conductivity $1mSm^{-1}$. The C-M factor varies with both the conductivity and permittivity of the particle and the medium and this is shown in Figure (7.16) for a 557nm sphere with relative permittivity 2.55 and conductivity $10mSm^{-1}$ suspended in water. At low medium conductivity and frequency, the theory predicts a value for the real part of the C-M factor of +1. As the frequency of the applied field or the medium conductivity is increased, the C-M factor undergoes a dispersion and the real part falls to a value of approximately -0.5.

The zero force point for dielectrophoresis, corresponds exactly to the point where the real part of the C-M factor equals zero. This value was calculated numerically from the equation for the C-M factor using a simple binary search algorithm. The zero point for the function shown in Figure (7.15) is included on the graph and applying the algorithm to stepped values of medium conductivity, the variation of the zero force frequency can be obtained. Figure (7.17) shows the variation of the zero force frequency with medium conductivity for the C-M factor shown in Figure (7.16).

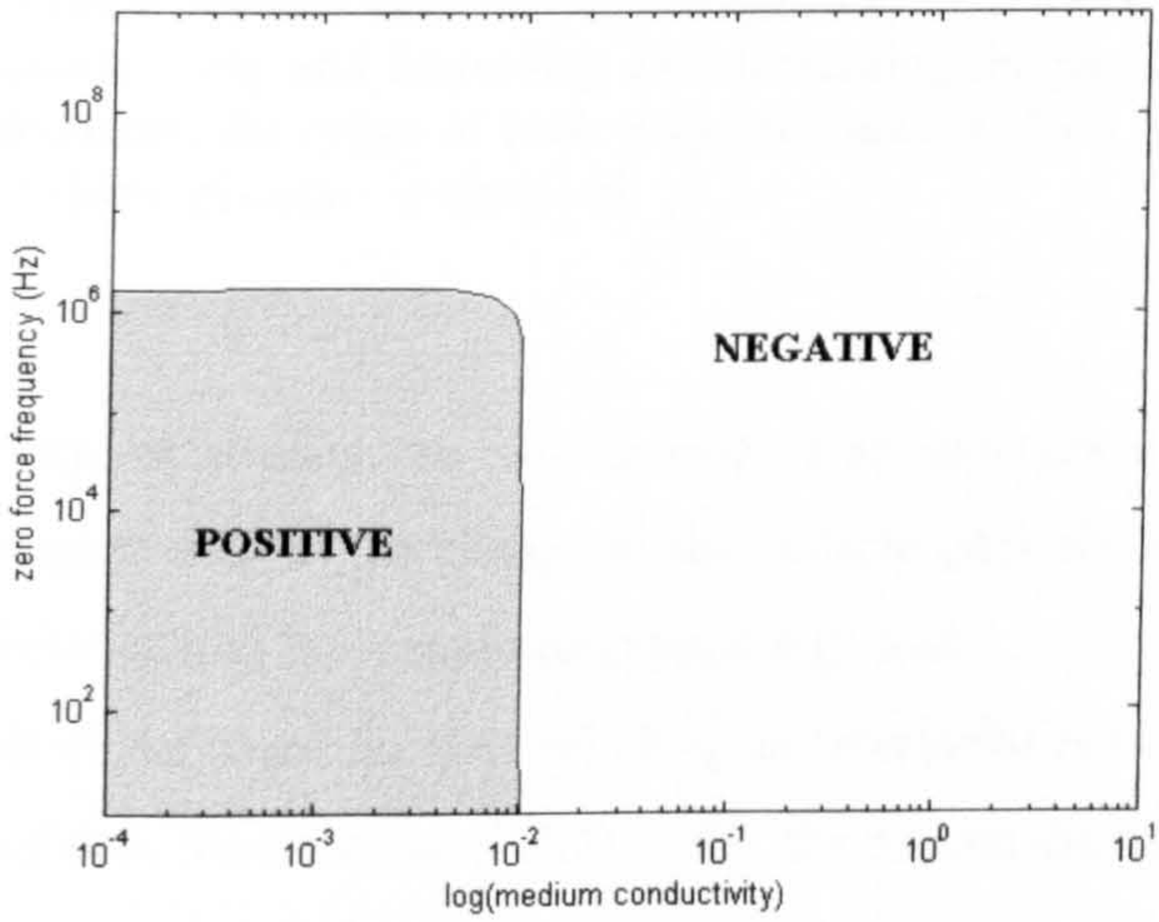

Figure (7.17) The variation of the zero force point (solid line) with medium conductivity for a 557nm diameter sphere of relative permittivity 2.55 and conductivity $10mSm^{-1}$. The relative permittivity of the medium was set to the value for water: 78.54. The figure also shows the type of dielectrophoretic behaviour on either side of the line of zero force.

The measurement of the zero force point for the latex spheres can provide information about the internal dielectric properties of the particle. Figure (7.18) shows the variation of the zero force line with the relative permittivity and conductivity of the 557nm sphere. Increasing the relative permittivity of the sphere increases the zero point frequency for a given medium

conductivity as shown in Figure (7.18a). Altering the conductivity of the sphere also increases the zero force frequency but also extends the range of medium conductivities over which positive dielectrophoresis is observed.

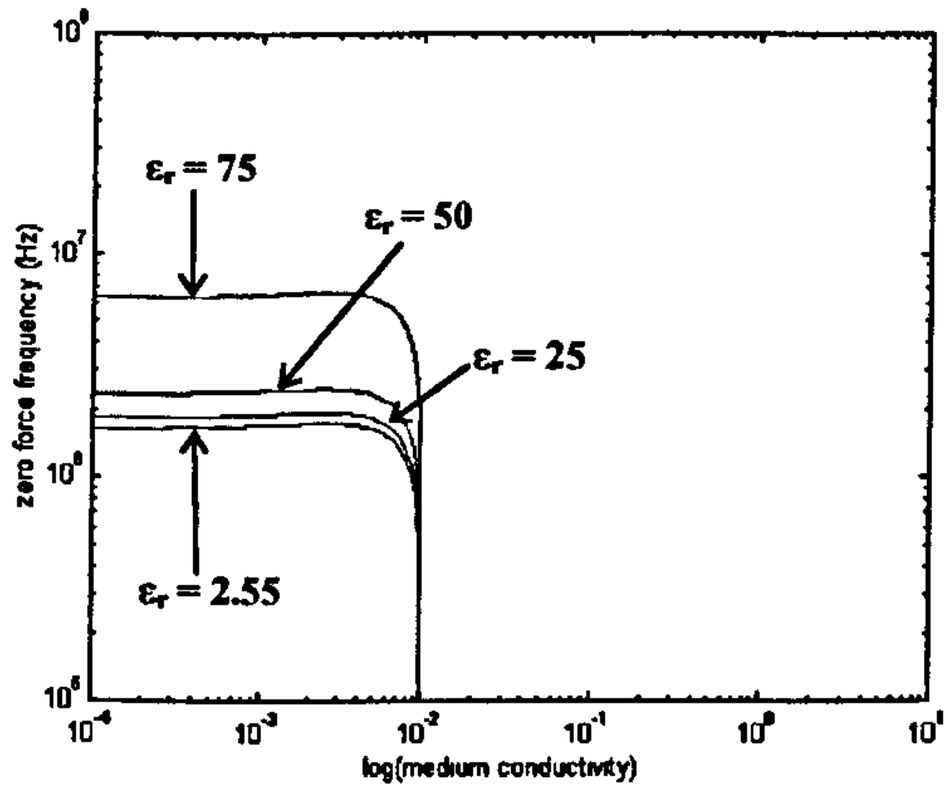

(7.18a) Variation of the zero force line with particle relative permittivity ε_r. The curves are for $\varepsilon_r = 2.55$, 25, 50 and 75 and $\sigma_p = 0.01 Sm^{-1}$.

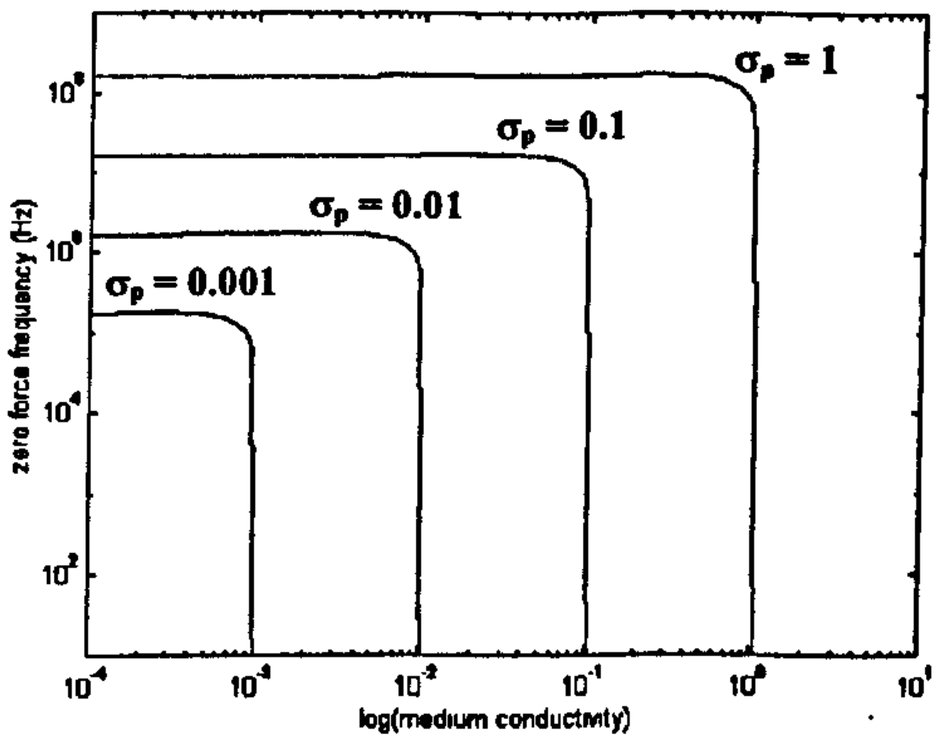

(7.18b) Variation of the zero force line with particle conductivity σ_p. The curves are for $\sigma_p = 0.001$, 0.01, 0.1 and 1 Sm^{-1} and $\varepsilon_p = 2.55$.

Figure (7.18) The variation of the zero force line with particle internal dielectric properties for a 557nm sphere suspended in a medium of relative permittivity 78.54. Changing the particle relative permittivity changes the zero force frequency for a given medium conductivity and increasing and decreasing the particle conductivity, increases and decreases the range of both frequency and medium conductivity over which positive dielectrophoresis is observed.

As the observable effects of altering the two internal parameters are different, they can be determined from a complete map of the change in the dielectrophoretic behaviour of a particle with medium conductivity such as those outlined in section (7.3.4).

The theoretical model based on Maxwell-Wagner interfacial polarisation was compared with each of the sets of data from section (7.3.4). For the 557nm diameter latex spheres, the match was correct for the textbook value of relative permittivity for polystyrene ($\varepsilon_r = 2.55$). The values of the internal conductivity of the particles for the three different salts are shown in table (7.1). For the smaller sizes of spheres there was a departure from the theory which became more noticeable with decreasing particle diameter. As mentioned in section (7.3.4), for the 282nm and 216nm diameter latex spheres, there is a slight rise in zero point frequency just before the dispersion in the conductivity direction. Figure (7.19) shows the results for 282nm spheres in potassium chloride with three theoretical curves. The curves for conductivities 0.0145 and 0.0194 Sm^{-1} describe the zero point behaviour for medium conductivities up to approximately $0.01 Sm^{-1}$. However, these curves do not match the observed dispersion along the conductivity

axis (at higher σ) and this discrepancy cannot be explained by altering the particle permittivity which only moves the curve along the frequency axis. However, the third curve for a particle conductivity of $0.035 Sm^{-1}$ not only matches the observed dispersion along the conductivity but also matches the increase in observed zero force frequency at slightly lower medium conductivities. This suggests that the internal conductivity of the particle rises over this range, giving rise to these anomalous effects.

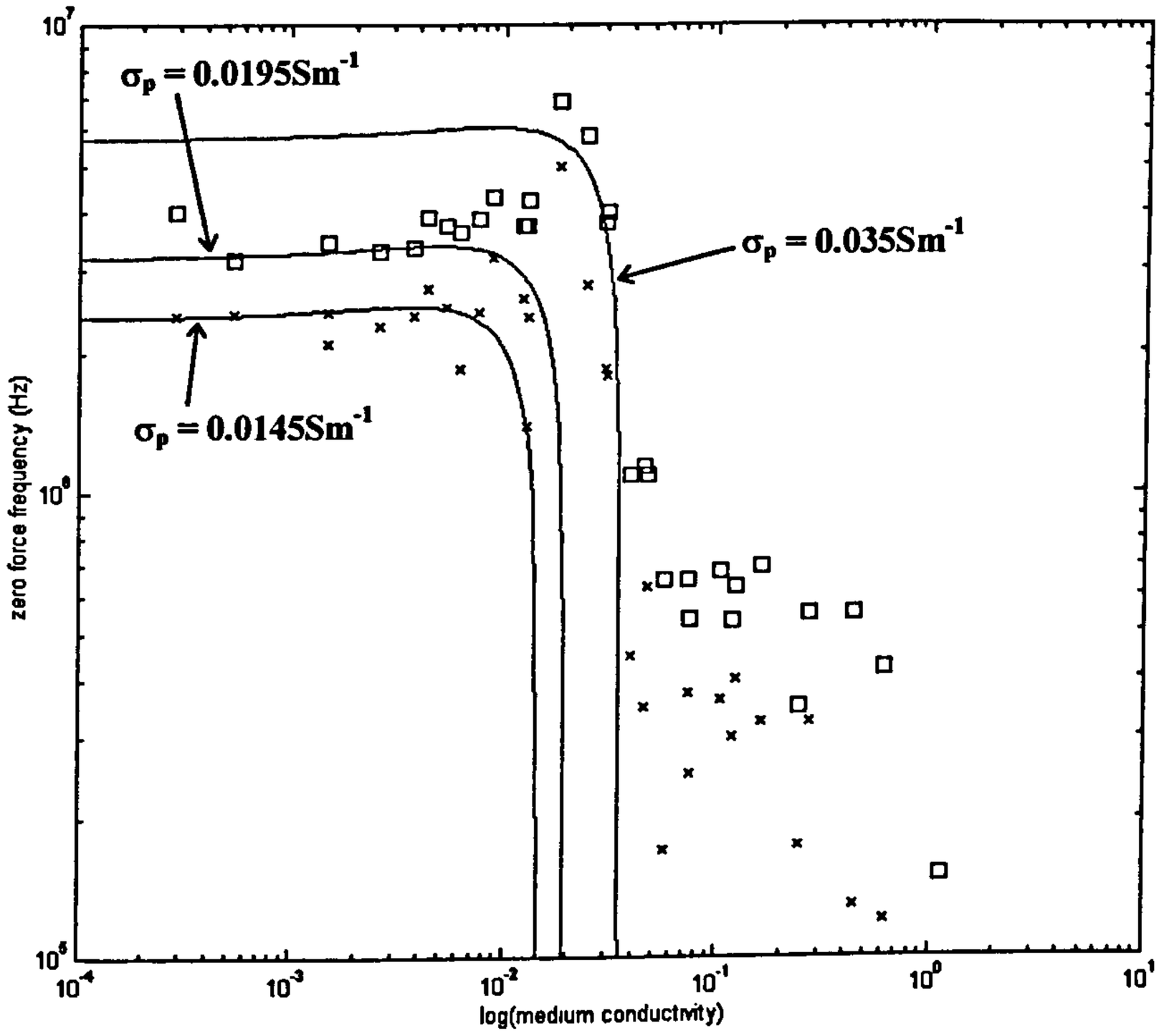

Figure (7.19) The experimental data for 282nm spheres in KCl (Figure 7.12a) with three theoretical zero force lines calculated from Maxwell-Wagner theory. The curves were calculated with a particle relative permittivity of 2.55 and conductivities of 0.0145, 0.0195 and 0.035 Sm^{-1}. The crosses mark frequencies below which positive DEP was observed and the squares mark frequencies above which negative DEP was observed

Since the conductivity of the spheres is dominated by surface effects and the double layer, this may not be an unreasonable assumption. The double layer thickness decreases inversely with the square root of the medium concentration and therefore, approximately with the square root of the medium conductivity. The relationship between medium conductivity σ_m and the concentration is given by the sum over all ions *i* [3]:

$$\sigma_m = \sum_i |z_i| F \mu_i c_i \qquad (7.1)$$

where z_i is the valency, μ_i is the mobility and c_i is the molar concentration of ion i and F is the Faraday constant. The experimentally determined relationship between ion concentration and conductivity (section 7.3.1) matches this equation quite closely.

The anomalous rise is present in the results for all the spheres smaller then 557nm in diameter but is much more prominent in the 93nm spheres which also implies that the effect is caused by the double layer. Figure (7.20) shows a similar graph to Figure (7.19) for the 93nm spheres in potassium chloride. For this size of sphere, the rise in zero force frequency occurs over a very large range and extends the region of positive dielectrophoresis a long way beyond the predictions of the theory. It is worthwhile to note at this point, that there is evidence of another low frequency relaxation at very high medium conductivities, (the α–relaxation).

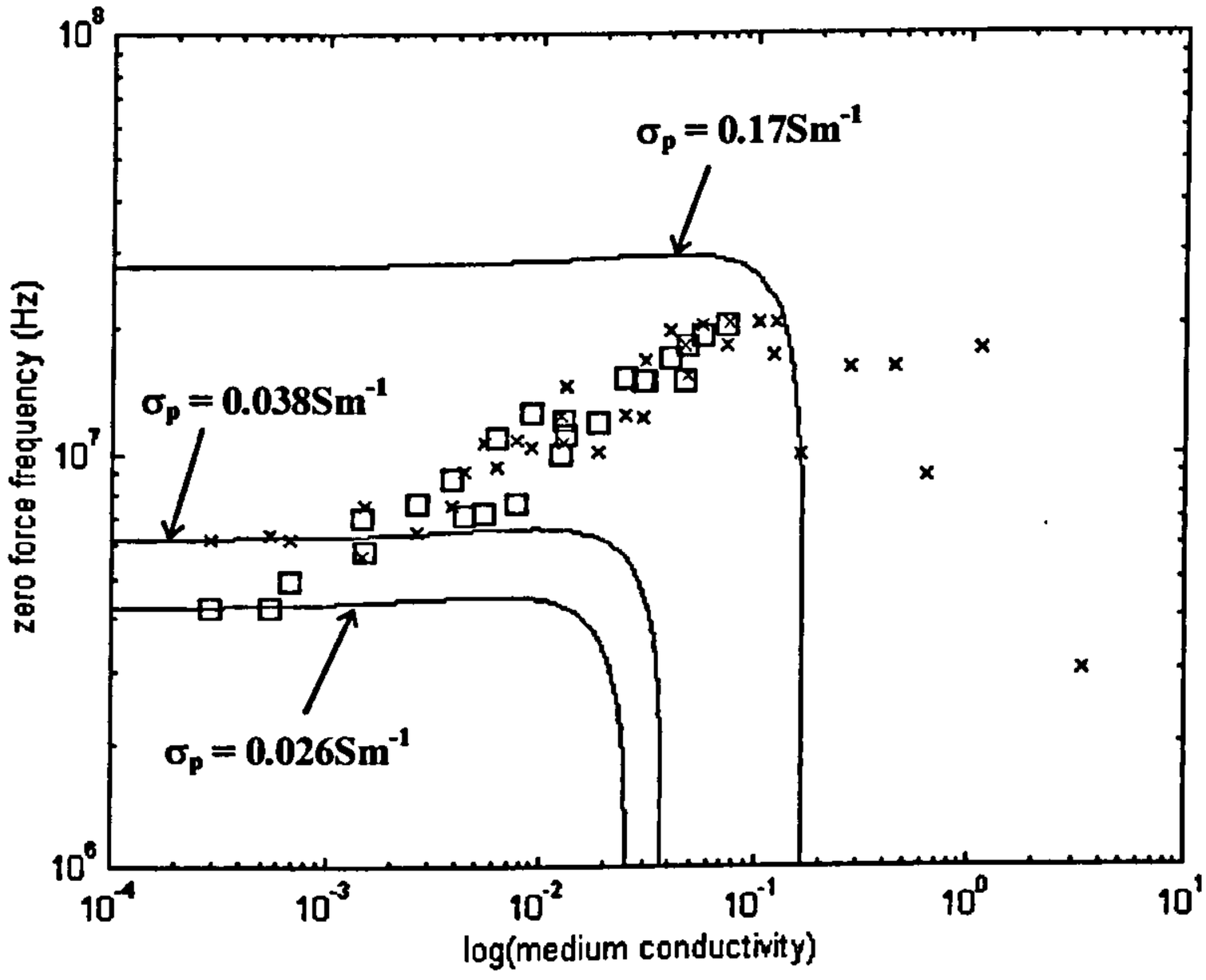

Figure (7.20) The experimental data for 93nm spheres in KCl (Figure 7.14a) with three theoretical zero force lines calculated from Maxwell-Wagner theory. The curves were calculated with a particle relative permittivity of 2.55 and conductivities of 0.026, 0.038 and 0.17 Sm^{-1}.

However, this set of results demonstrates that the rise in zero force frequency cannot be accounted for by a simple increase in particle conductivity. Over two decades along the conductivity axis, the rise along the frequency axis is under a decade. The curve for $0.17Sm^{-1}$ is a good match for the data but a further increase in σ_p cannot account for the data points at higher medium conductivities ($> 0.3Sm^{-1}$).

Table (7.1) shows for each of the smaller sizes of spheres, the average particle conductivity which matches the low medium conductivity points and also the particle conductivity which matches the maximum rise in the zero force frequency.

Table (7.1) Results for particle conductivity obtained by matching the zero force frequency data with the Maxwell-Wagner theory. The first particle conductivity matches the low medium conductivity points and the second value matches the dispersion along the conductivity axis.

Sphere diameter (nm)	salt	low medium σ (mSm^{-1})	σ dispersion value (mSm^{-1})
	KCl	10 ± 2	
557	NaCl	8.4 ± 0.6	
	KPO_4	10 ± 1	
	KCl	17 ± 2.5	35
282	NaCl	15.5 ± 2.5	
	KPO_4	17.5 ± 1.5	37
	KCl	17 ± 3	45 ± 5
216	NaCl	18.5 ± 2.5	42 ± 2
	KPO_4	20 ± 3	45 ± 5
	KCl	32 ± 6	500 - 1000
93	NaCl	35 ± 3	100
	KPO_4	48 ± 4	500 - 1000

A comparison of the values shows that for the largest size of sphere, the KCl and the KPO_4 salts give the same values for particle conductivity but as the size of the particle is reduced, the particle conductivity in KPO_4 is larger than for KCl. This implies that the negative ions in the solution are affecting the surface conductance for smaller diameters. However, it should also be noted that for the 557nm sphere and the 282nm sphere, the particle conductivity for KCl is larger than for NaCl, which is to be expected since the surface conductance depends on the ion mobility and the mobility of the potassium ion is higher than the sodium ion (see Table 7.2). However, for the two smallest sizes of sphere, the values of particle conductivity for NaCl are higher than for KCl. Also, for the 93nm spheres, the apparent position of the dispersion along the conductivity axis is matched by a much lower particle conductivity.

As described in Chapter three, the surface conductance of a particle is related to the ions in solution and the surface charge density of the particle. Using the Helmholtz-Smoluchowski equation and the Gouy-Chapman/Grahame theory of the double layer [4], the electrophoretic mobility, μ, of a spherical particle and its zeta potential, ζ, which are related by the equation:

$$\zeta = \frac{\eta}{\varepsilon_o \varepsilon_r} \mu \tag{7.2}$$

where η is the viscosity, ε_r is the relative permittivity and ε_o is the permittivity of free space. This can be translated into a surface charge density, ρ^s, using the relationship:

$$\left(\rho^s\right)^2 = 2\varepsilon_o \varepsilon_r kT \sum_i n_i \left[e^{-\frac{-z_i e_o \zeta}{kT}} - 1 \right] \tag{7.3}$$

where k is Boltzmann's constant, T is the temperature and e_o is the charge on an electron. The sum in the equation is a sum of all ions i with volume density n_i and valency z_i. Table (7.2) shows the textbook [5] values for the ion diffusion coefficient D_i and the ion mobility μ_i calculated from D_i using the Einstein relation (equation 4.16).

Table (7.2) Textbook value for the diffusion coefficient D from the CRC Handbook [5] for the ions relevant to calculations in this Chapter plus the valency and mobility calculated from D using equation (4.16).

Ion	valency	diffusion coefficient ($\times 10^{-9}$ $m^2 s^{-1}$)	mobility (at 21°C) ($\times 10^{-8}$ $m^2 s^{-1}$)
K^+	1	1.957	7.69
Na^+	1	1.334	5.24
Cl^-	1	2.032	7.99
HPO_4^{2-}	2	0.878	3.45
$H_2PO_4^-$	1	0.879	3.45

Using equations (7.2) and (7.3), the measured distributions in mobilities given in section (7.3.2) were converted into surface charge densities for the 557, 282 and 93nm spheres and the results are shown in Table 7.3.

Table (7.3) Surface charge density determined from the measured sphere mobility using equations (7.1) and (7.2).

sphere diameter (nm)	surface charge density (Cm^{-2})
557	0.038 ± 0.005
282	0.028 ± 0.006
93	0.032 ± 0.008

O'Konski's equation for the surface conductance (equation 3.21) was used to calculate the surface charge density for the four sizes of spheres from the particle conductivity (equation 3.26). For this calculation, the ion mobility was assumed to be the bulk value although the correct value will be lower as the ions may be partially bound to the surface. The internal particle conductivity was also assumed to be zero which is a valid assumption for latex but the presence of the fluoroprobe inside the sphere may result in a non-zero conductivity. The results are shown in Table (7.4) along with the manufacturer's value of surface charge (Appendix 7a).

Table (7.4) Surface charge density determined from the measured particle conductivity using equations (3.21) and (3.26) assuming the ion mobility to be equal to the bulk mobility.

	Surface charge density (Cm^{-2})			
Salt	**KCl**	**NaCl**	**KPO_4**	**App. (7a)**
diameter (nm)				
557	0.0181 ± 20%	0.0223 ± 7%	0.0181 ± 10%	1.85
282	0.0156 ± 15%	0.0208 ± 16%	0.0160 ± 8.6%	0.0483
216	0.0119 ± 17.6%	0.0191 ± 13.5%	0.0140 ± 15%	1.41
93	0.0097 ± 19%	0.0155 ± 8.6%	0.0145 ± 8.5%	0.0209

The results in this table demonstrate that for the two largest sizes, the data seems to match O'Konski's theory where the surface conductance involves only the positive ion in the medium for a negatively charged sphere. The results for the two smaller sphere sizes demonstrate that the results depart from the accepted theory.

For the 557nm spheres, the value of surface charge density is higher for NaCl than for KCl by approximately 23% of the KCl value. The difference between the mobilities of Na^+ and K^+ however, is approximately 32%. The discrepancy between these two figure indicates that there is probably a non-zero internal conductivity for these latex spheres which must be subtracted before calculating the surface charge density.

The particle conductivity consists of a bulk and surface component (equation 3.26). This equation was used to match the data given in Tables (7.1) - (7.3) to the theory, but with the addition of a scaling parameter as follows:

$$\sigma_p = \sigma_{pb} + C_o \frac{2\lambda_s}{a} \tag{7.4}$$

where σ_p is the particle conductivity (composed of the bulk internal conductivity σ_{pb} and the surface conductance λ_s), C_o is a scaling constant and a is the radius of the sphere. It was assumed that σ_{pb} was constant in any solution and that the difference in the measured conductivity given in Table (7.1) was proportional to the difference in the mobilities of the two positive ions involved. Following this calculation through gives a value for σ_{pb} of 5.0mSm^{-1} and a value of C_o of 0.24. The value of C_o is satisfactory as it means either that the counterions at the surface have a lower mobility than the bulk value (by C_o), which is a reasonable assumption, or that the amount of charge associated directly with the surface (contributing to λ_s) is less than predicted by O'Konski's equation (by C_o). The latter might also be a reasonable assumption as for the medium conductivities at which the Maxwell-Wagner relaxation occurs, the double layer is quite large (>10nm). Equation (3.21) gives the amount of excess charge over the bulk in the whole double layer. For a thin double layer, or for a large particle (>1μm), then this can be assumed to be the surface charge giving rise to λ_s as assumed by O'Konski. However, for a colloidal particle surrounded by a double layer with a large diffuse component, it may be necessary to distinguish between the charges close to the slip plane and the charges farther from the surface.

This may also explain the rise in apparent conductance for the smaller particle close to the drop-off point on the conductivity axis. The size of the double layer shrinks as the medium conductivity rises. The charge density increases and the surface conductance might be expected to rise as a result. For the 282nm and the 216nm, the effect is small (and reproducible) but for the 93nm it is large. For the 93nm sphere, the volume of the double layer is large compared to the particle over a large range of medium conductivities and would probably dominate the dielectric properties. For the 282nm and the 216nm, the effect only produces a slight rise.

In order to test this idea, a rise in surface conductance was inserted into the expression for σ_p by adding a term which is inversely proportional to the thickness of the double layer ($1/\kappa$). The thickness of the double layer is generally taken to be the Debye length which is the reciprocal of κ where [4]:

$$\kappa^2 = \frac{e_o^2}{\varepsilon_o \varepsilon_m kT} \sum_i z_i^2 n_i \qquad (7.5)$$

The sum is over all ions i with valency z_i and volume density n_i. Using this equation and the relationship between concentration and conductivity derived from the experimental results in section (7.3.1), equation (7.4) then becomes:

$$\sigma_p = \sigma_{pb} + \frac{2\lambda_s}{a}\left(C_1 + C_2 \kappa a\right) \tag{7.6}$$

where C_1 and C_2 are constants. Figure (7.21a) shows the best fit for this function with the experimental data for the 93nm spheres with C_1 = 0.2 and C_2 = 0.1. The bulk particle conductivity was taken to be zero, the particle relative permittivity was 2.55, the surface charge density was 32mCm^{-2} and the bulk ion mobility values were used. As can be seen, over most of the measured range, the fit to the data is good, with the rise due to the extra function matching the experimental rise accurately. At the high conductivity end, the fit is not good, however the experimental data at these high conductivities is not as reliable and could be due to the α–dispersion.

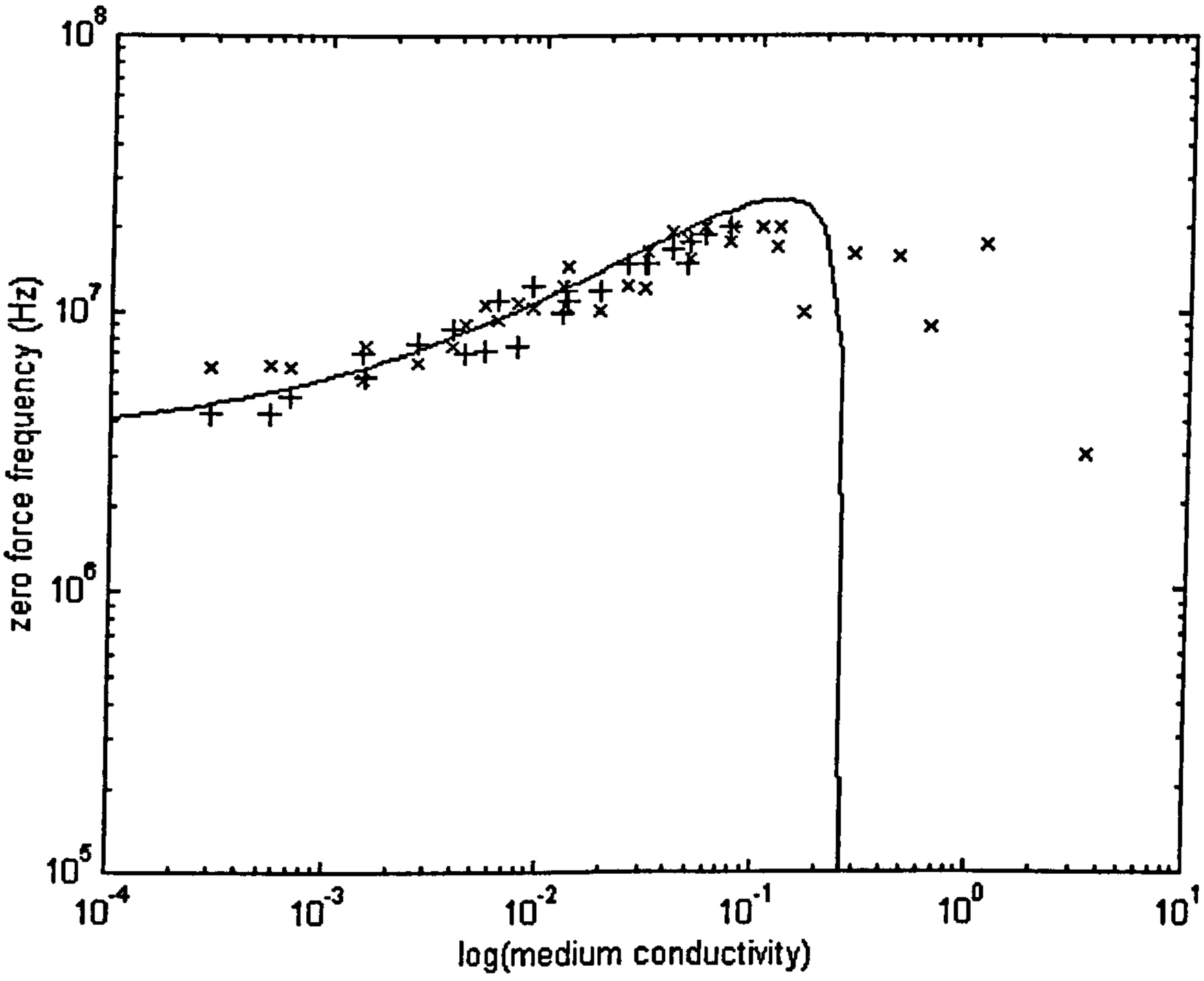

Figure (7.21a) Theoretical fit of the zero force frequency calculated using equation (7.6) for the particle conductivity to the data for 93nm diameter latex spheres in KCl. The bulk particle conductivity was taken to be zero, the surface charge density was 32mCm^{-2} and the bulk ion mobility value was used. The values for the constants in equation (7.6) were C_1 = 0.2 and C_2 = 0.1.

However, although this modification of the surface conductance equation describes the 93nm spheres in KCl quite accurately, it does not describe the data for the other salts or the other sizes of spheres. For the 93nm spheres in NaCl, the slope appears to be steeper than for KCl and for

KPO_4, the problem is more involved. The low conductivity zero force frequency is higher for KPO_4 than for KCl, indicating a higher surface conductance, but the range of conductivity over which this frequency is constant is greater. The result is that the sloping parts of the graphs for the two salts (i.e. where the frequency rises) coincide exactly: the two graphs match where they are sloping but do not match at low conductivities.

The larger sizes of spheres do not match equation (7.6) for the same values of the constants. Figure (7.21b) shows a graph of the modified model for the 282nm spheres in KCl with the experimental data also shown. The value of the surface charge density was $28mCm^{-2}$ and all other parameters, except of course the particle radius, were the same. The dashed line shows the theoretical zero force line for $C_1 = 0.2$ and $C_2 = 0.1$, and the solid line shows the best fit for equation (7.6) with $C_1 = 0.3$ and $C_2 = 0.025$.

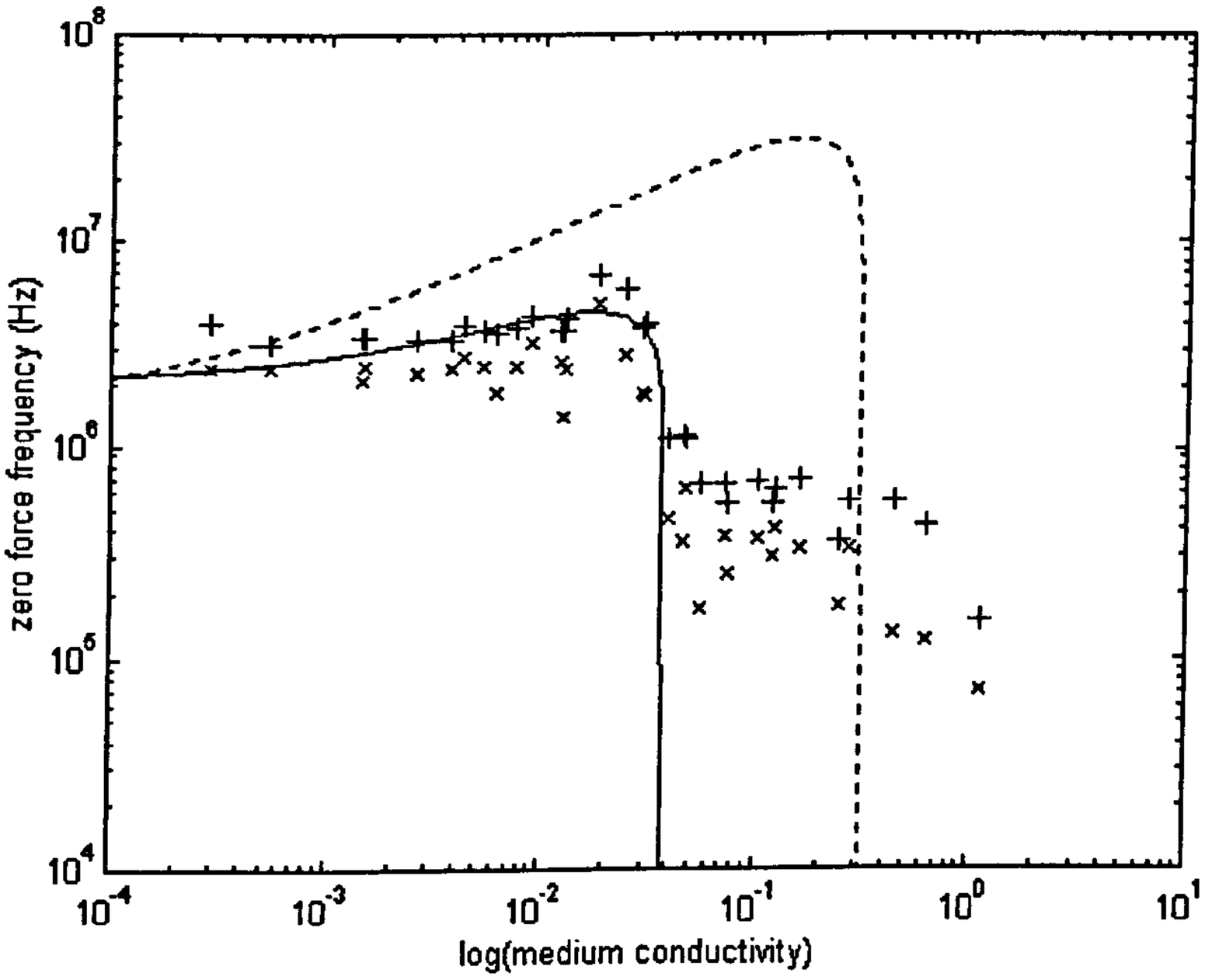

Figure (7.21b) Theoretical fit of the zero force frequency calculated using equation (7.6) for the particle conductivity to the data for 282nm diameter latex spheres in KCl. The bulk particle conductivity was taken to be zero, the surface charge density was $28mCm^{-2}$ and the bulk ion mobility value was used. The values for the constants were $C_1 = 0.2$ and $C_2 = 0.1$ for the dashed line and $C_1 = 0.3$ and $C_2 = 0.025$ for the solid line.

The lack of consistency in the values of C_1 and C_2 with a change in particle size indicates that this function is not the correct one although it is a close match for the smallest size of sphere.

The system was also modelled as a two interface problem with a single elliptical shell added to encompass the inner spherical particle [6]. As can be seen from the theoretical matching section in Chapter Eight, the zero force frequency line for an ellipse as described in

Chapter Three has a similar profile to that shown in Figures (7.21a) and (7.21b). The principle behind this model is that the electric field distorts the double layer around the particle as it polarises. The resulting ellipsoidal shape would be approximately a spherical shell for the 557nm and a prolate ellipsoid for the 93nm as shown in Figure (7.22).

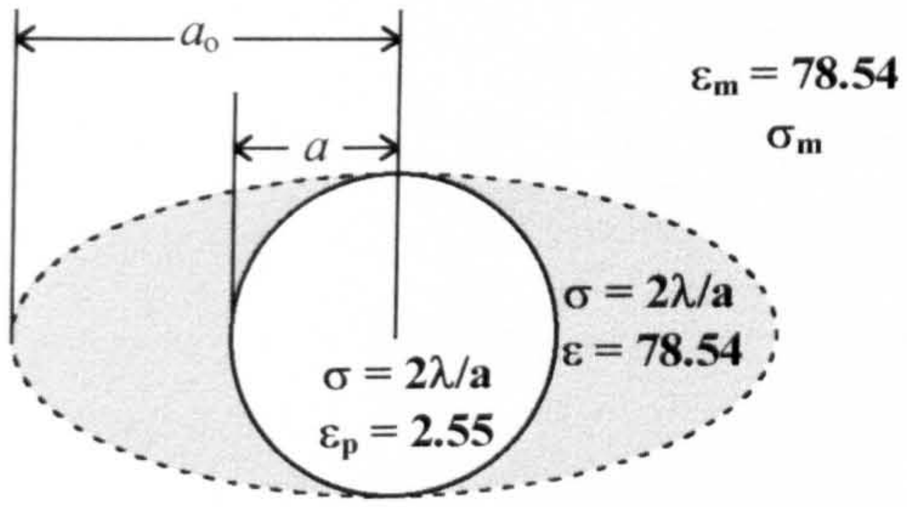

Figure (7.22) Schematic diagram of an ellipse representing the distorted double layer surrounding the spherical particle

The outer shell was assigned a conductivity equal to $2\lambda/a$ and a relative permittivity equal to the bulk medium. The major axis half length a_o was equal to $a+(3/\kappa)$, a value derive from the geometry of the system. Unfortunately, the zero force calculated using this model did not match the experimental data even at low conductivities as shown in Figure (7.23).

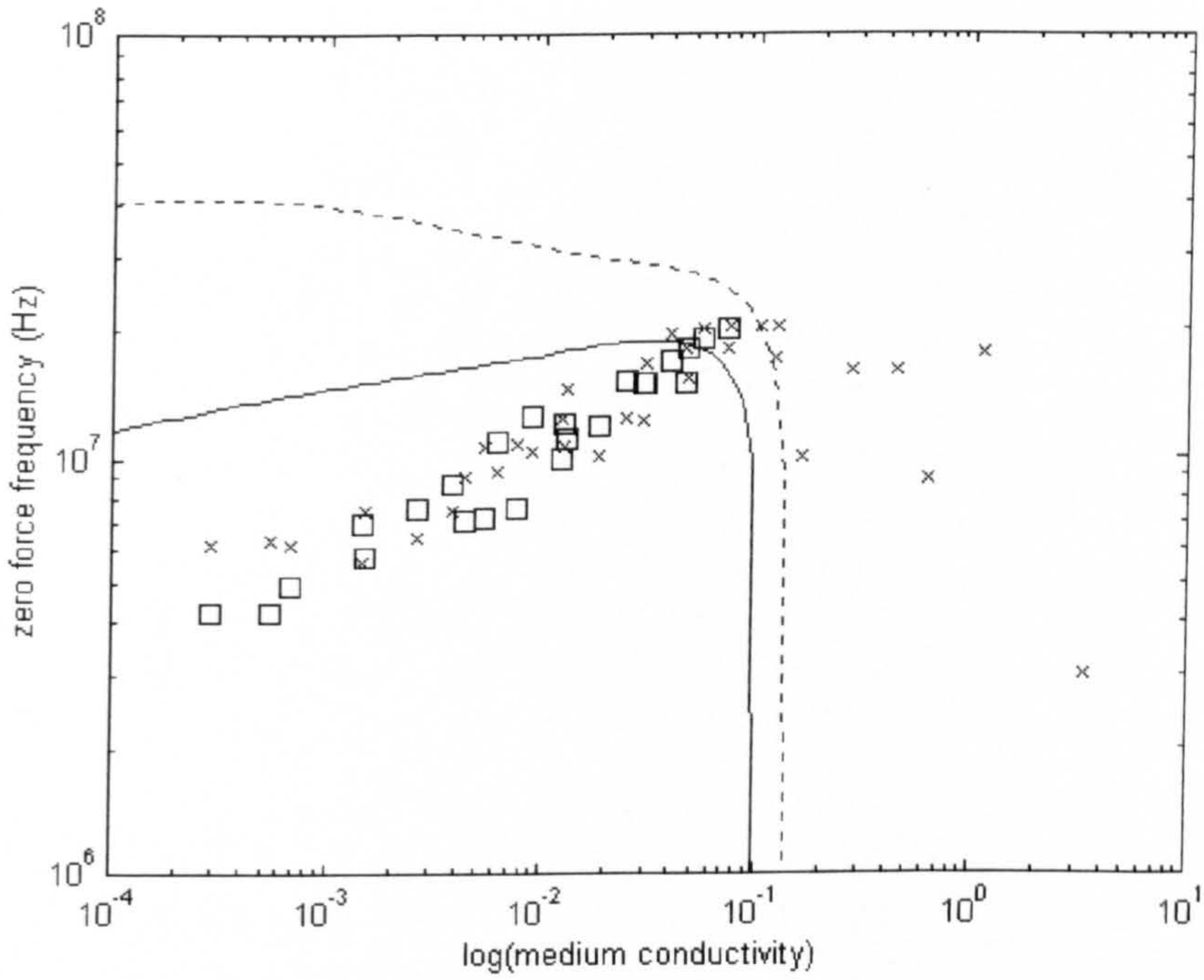

Figure (7.23) Theoretical fit of the zero force frequency calculated from the ellipsoid shell model outlined above. The solid line is the result for a shell conductivity equal to the particle and the dashed line is the result of increasing the conductivity of the shell to $0.5 Sm^{-1}$.

Increasing the conductivity of the shell to 0.5 Sm^{-1} did not improve the fit and decreasing the conductivity reduced the problem to the Maxwell-Wagner interfacial polarisation.

In conclusion, none of the theoretical models proposed here to explain the rise in zero force frequency was successful in fitting all of the data.

7.4.2 The alpha relaxation

As was shown in Figures (7.15)-(7.18), the Maxwell-Wagner interfacial polarisation does not account for the observed and measured dielectrophoretic behaviour at high medium conductivities. The zero force frequency falls off rapidly and the Maxwell-Wagner relaxation frequency (shown in Figure (7.24) for the 282nm spheres in KCl) rises after this drop off. The real part of the Clausius-Mossotti factor is always less than zero in this region of medium conductivity and as a consequence, the expected DEP behaviour would be negative. A simple comparison of the frequencies indicates that the low frequency behaviour cannot be due to interfacial effects for these particles.

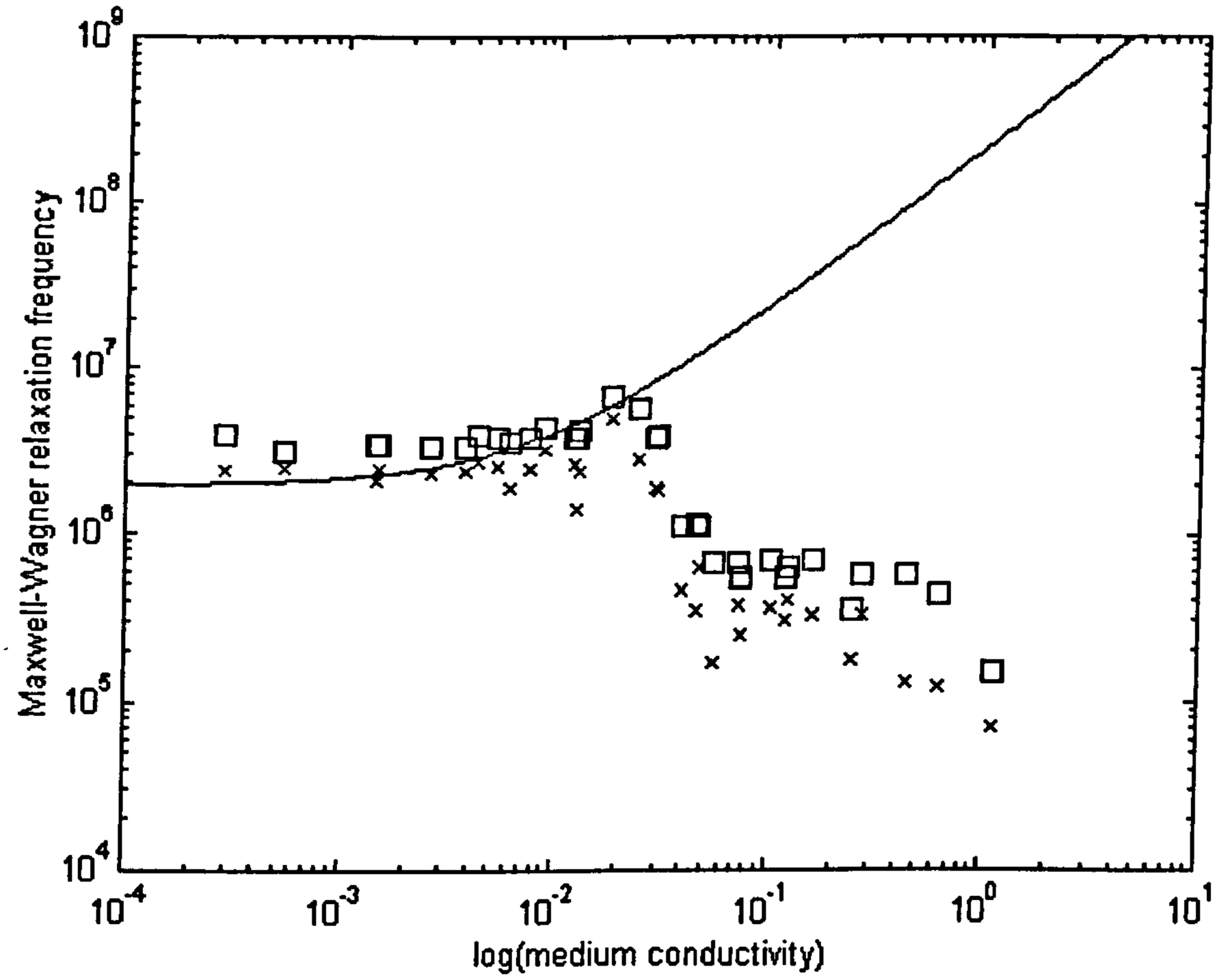

Figure (7.24) The experimental data for the 282nm spheres in KCl and the Maxwell-Wagner relaxation frequency plotted against the medium conductivity in Sm^{-1}.

The experimental data indicates that there is another dispersion at lower frequencies and that it is only seen at higher medium conductivities on a plot of this type. Dielectric mixture data for spheres has been reported in the literature over a number of years and there have been numerous theories published on the subject [3,7-16]. A cross-section of the theories was outlined in Chapter Three and in this sub-section the data is analysed in terms of these theories, together with other related theories. These theories were developed to explain dielectric spectroscopy data and very little has been done in attempting to apply the models to dielectrophoresis data.

The dispersion at low frequencies has consistently been reported as being large (in terms of $\Delta\varepsilon$) but regardless of the size, if it is regarded as independent and therefore separable from the Maxwell-Wagner relaxation, it must be zero after the relaxation is complete. There are two reasons behind this statement. First, the AC response of the ions in a double layer is a classical polarisation relaxation not an interfacial mechanism like the Maxwell-Wagner. This means that after the relaxation, the ions are arranged in their original unperturbed state and there is no induced dipole moment. This would seem to be borne out by the second reason, which is that large low frequency relaxations have been reported for numerous particles (e.g. [16] on electrorotation at low frequencies) but the Maxwell-Wagner relaxation theory still applies to these particles. If the dipole due to the double layer were still present after the relaxation, this would be summed with the Maxwell-Wagner interfacial dipole, which would in turn be distorted from the normal +1 to –1/2 pattern.

The first attempt to model a relaxation of the double layer was made by Schwarz [7] and involved a modification to O'Konski / Maxwell-Wagner surface conductance theory. This model was corrected for low frequency measured surface conductance by Schurr [8] two years later. The parameters of the two models were discussed in Chapter Three and the particle conductivities for the two models are given by equation (3.26) and (3.27) respectively. Figure (7.25) shows the variation of the real part of the polarisation factor from these models as a function of frequency and medium conductivity for 282nm spheres in KCl (with ε_p = 2.55, surface charge density = 28mCm^{-2}).

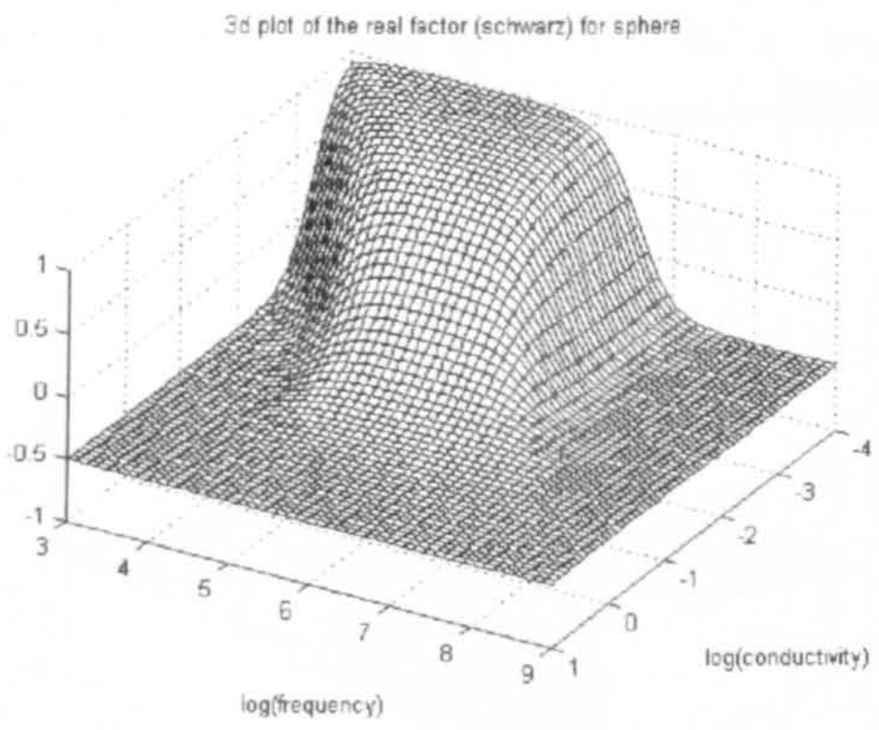

Figure (7.25a) Schwarz model for the α-relaxation for 282nm spheres in KCl (see text for details.

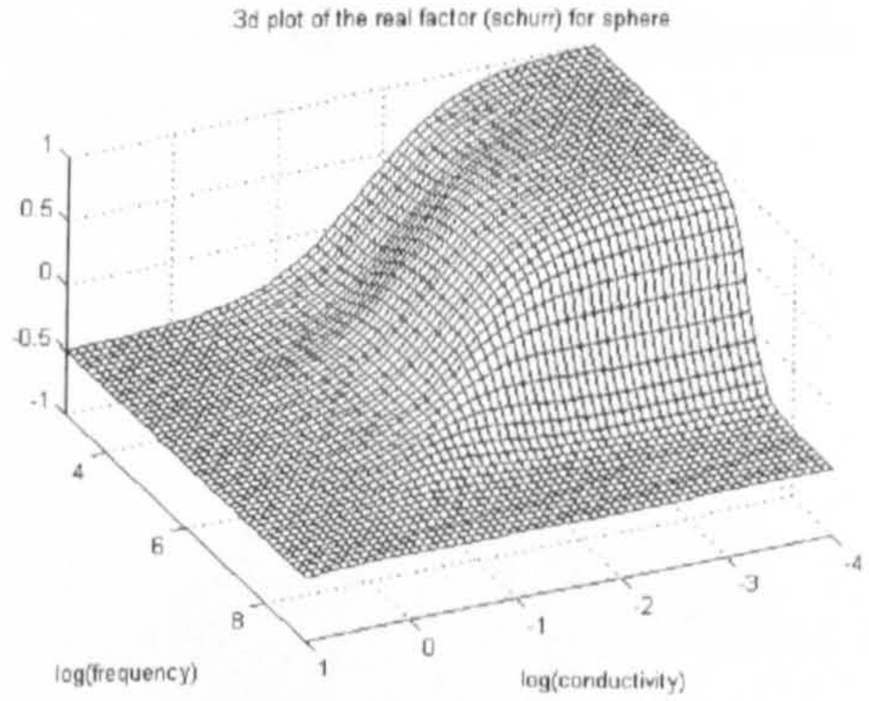

Figure (7.25b) Schurr model for the α-relaxation for 282nm spheres in KCl (see text for details.

The α-dispersion in the dipole moment term for the Schwarz model increases with frequency which is in the wrong direction. The Schurr model shows a similar effect but it is very slight and hardly perturbs the Maxwell-Wagner variation.

The diffuse layer model of Lyklema (section 3.5.2, Appendix (3b), [9]) was modelled over the experimental ranges for the different sphere sizes using the experimentally determined values for permittivity, conductivity, zeta potential etc. The results for the 282nm spheres are shown in Figure (7.26).

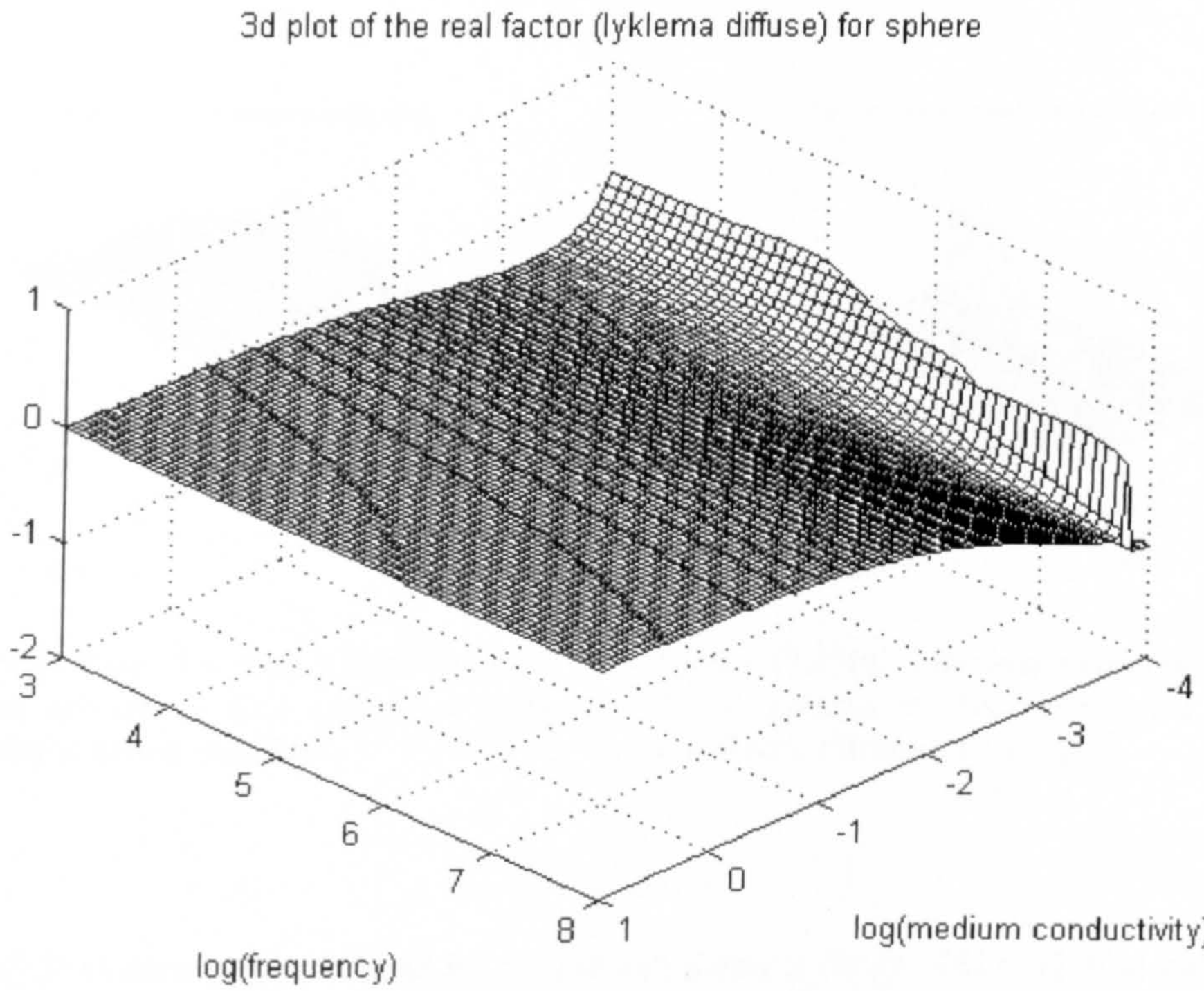

Figure (7.26a) The variation of the real part of the polarisation factor of the diffuse layer for 282nm spheres in KCl, calculated according to the equations in Appendix (3a), with the applied frequency (Hz) and the medium conductivity (Sm^{-1}).

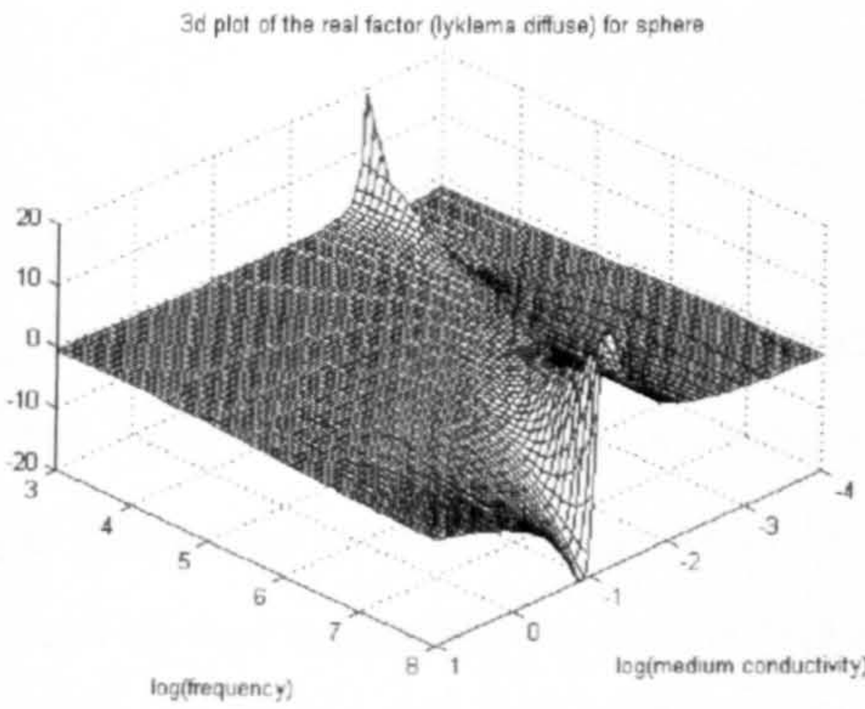

Figure (7.26b) The change in (7.26a) if the zeta potential is assumed to be 0.2V.

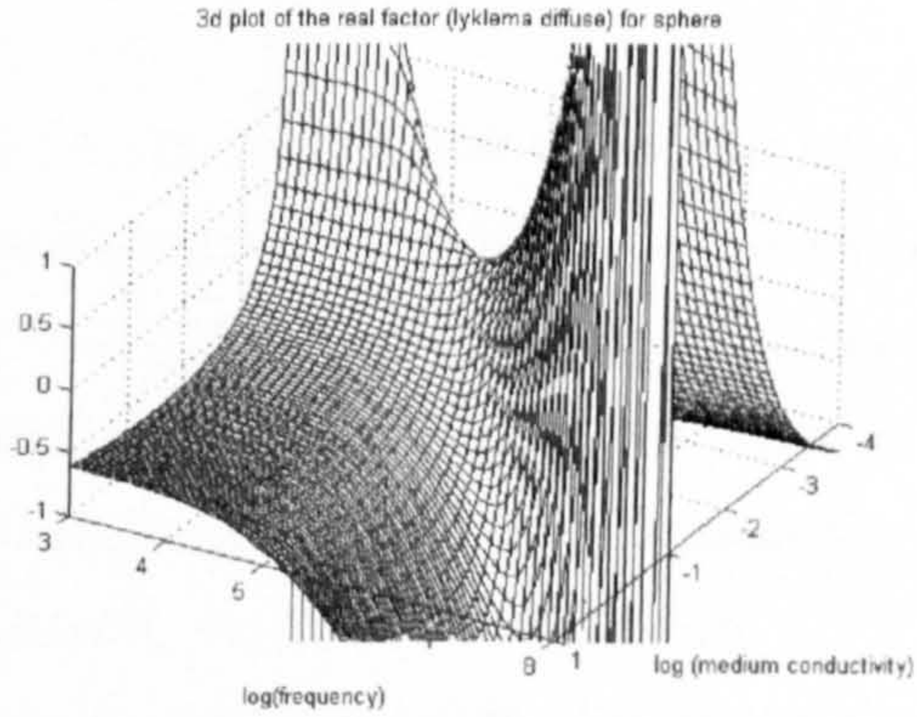

Figure (7.26c) Close up of the change in (7.26a) if the zeta potential is assumed to be 0.2V.

The graph shows a dispersion at very low medium conductivities, but altering parameters to allow for say larger zeta potentials due to induced potential effects, results in a solution that does

not look like a simple dispersion (Figures 7.26b and 7.26c). The value of the dipole does however tend to zero for low zeta potentials and high frequencies as shown in Figure (7.26a). The dispersion which can be seen at low conductivities does not extend to high enough conductivities to account for the observed results. Figure (7.27) shows the results for the 557nm and the 93nm spheres calculated using experimental results.

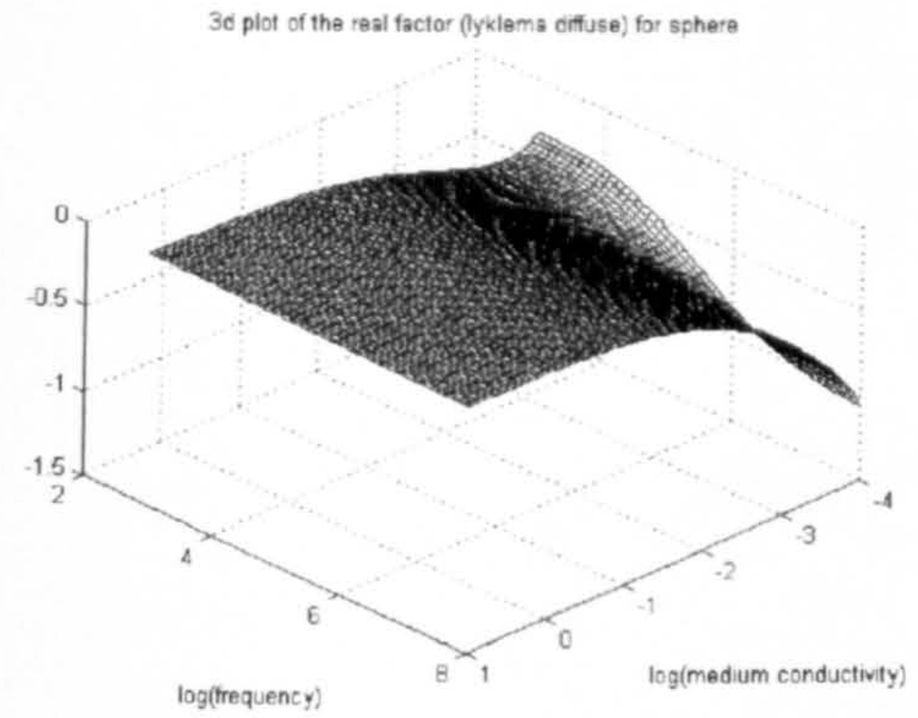

Figure (7.27a) The polarisation factor for 557nm spheres in KCl calculated using Lyklema's diffuse model [9].

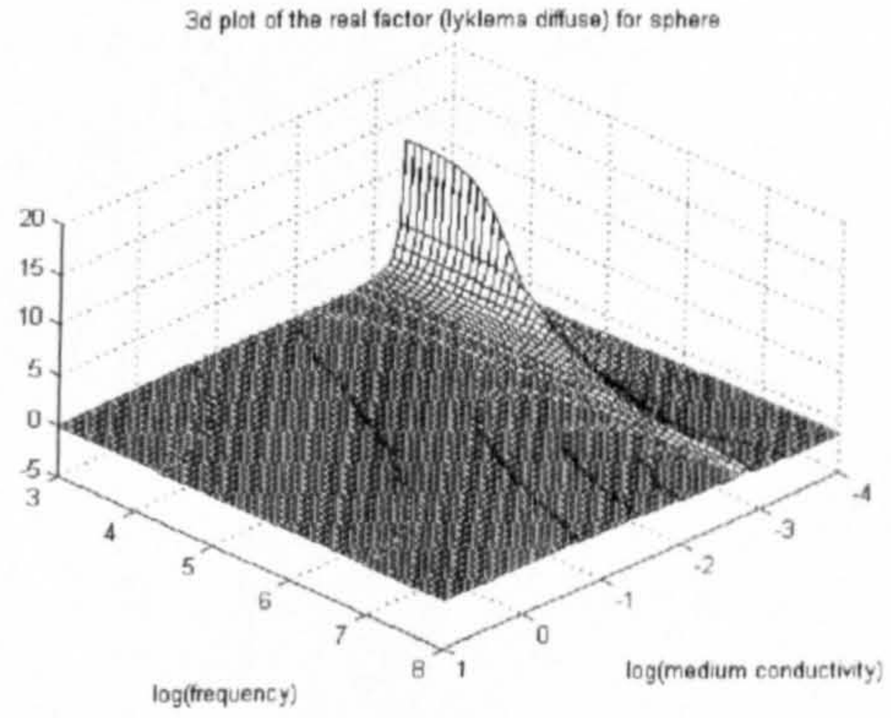

Figure (7.27b) The polarisation factor for 93nm spheres in KCl calculated using Lyklema's diffuse model [9].

Figure (7.27a) shows a similar trend for the 557nm spheres as for the 282 in (7.26a) and Figure (7.27b) shows a large dispersion for the 93nm spheres at a frequency of the order of 10^5Hz. However, in neither of these cases does the dispersion extend far enough along the medium conductivity scale to match the high conductivity DEP results.

The model from Lyklema's book (section 3.5.3, [3]) was modelled for the four sizes of spheres again using the previously determined experimental results for the model parameters. Figure (7.28) shows the model for the 282nm spheres in KCl with different surface potentials. (7.28a) shows the graph for the measured zeta potential of –43mV and is mainly flat except for a slight fluctuation at low conductivities. The zeta potential was increased, a valid assumption if induced surface potentials due to high fields are considered, to –200mV in (7.28b) and –400mV in (7.28c). The distance along the medium conductivity axis that the dispersion extends to increases rapidly with increasing zeta potential and in the third graph, the dispersion extends across the experimental range.

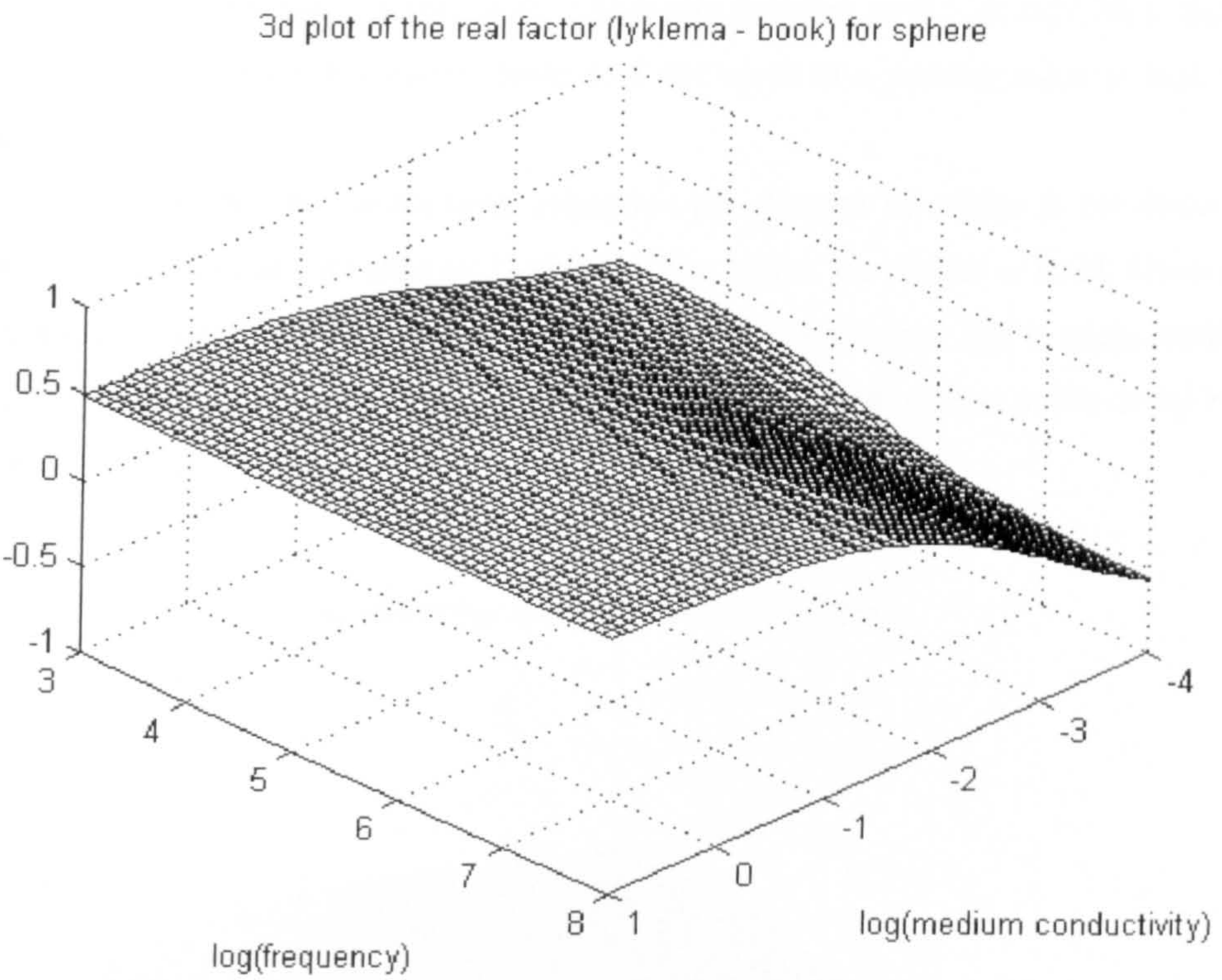

Figure (7.28a) The variation of the real part of the polarisation factor of the double layer for 282nm spheres in KCl, calculated according to [3] with the applied frequency (Hz) and the medium conductivity (Sm^{-1}). The zeta potential was taken to be -43mV.

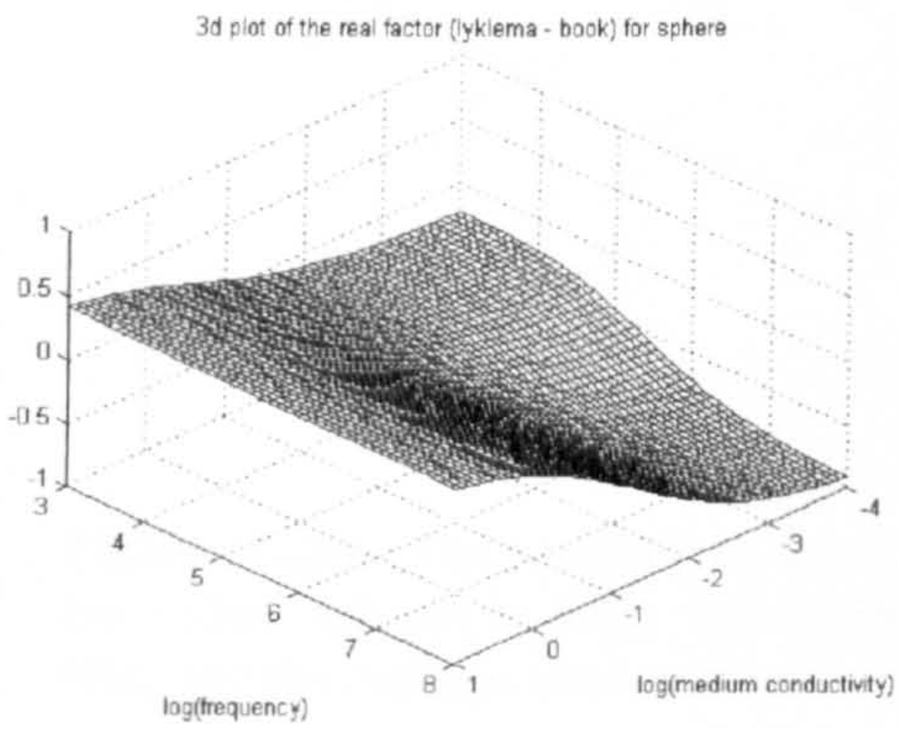

Figure (7.28b) The change in (7.28a) when the zeta potential is increased to a value of -200mV.

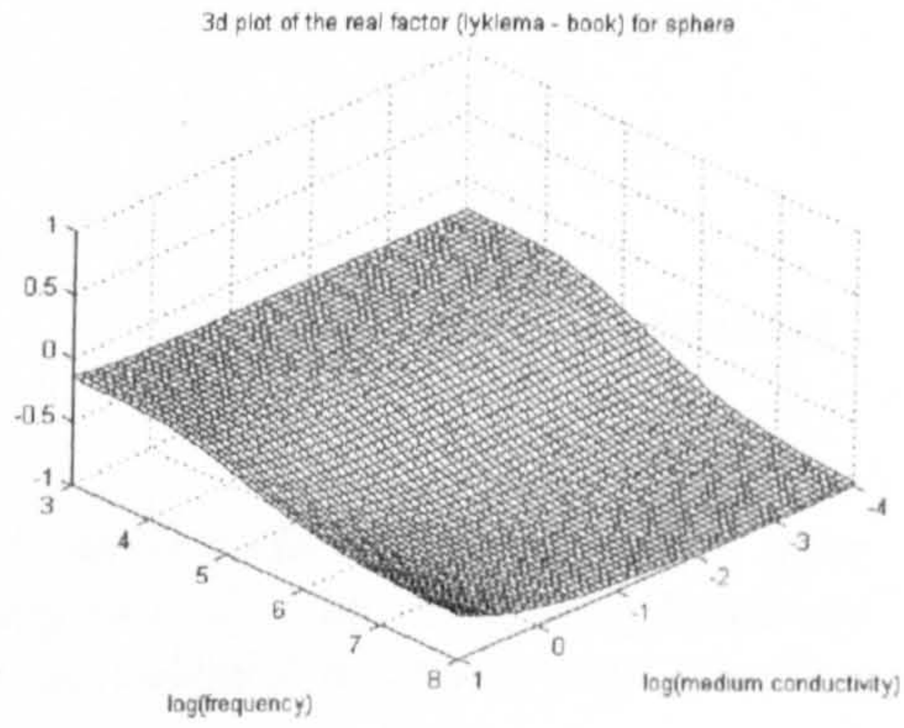

Figure (7.28c) The change in (7.28a) when the zeta potential is increased to a value of -400mV.

The results improve slightly with decreasing particle diameter but for all the sizes of particles, the zeta potential must be increased to produce a dispersion occurring in the correct range of medium conductivities. The other problem with this theory is that the polarisation factor tends to +0.5 at high frequencies in high medium conductivities which does not match with the Maxwell-

Wagner theory. If the dipole is correct for a high zeta potential as in Figure (7.28c), the sum of this dipole and the Maxwell-Wagner dipole does not result in a positive value in high medium conductivities.

The theory for the double layer relaxation put forward by Minor in his thesis [12] is similar to the last model published by Lyklema. The author would like to thank Marcel Minor and Professor Lyklema for forwarding a copy of this thesis in the hope that it might clarify some problems. A plot of the variation with applied field frequency and medium conductivity is shown in Figure (7.29) for 282nm spheres in KCl.

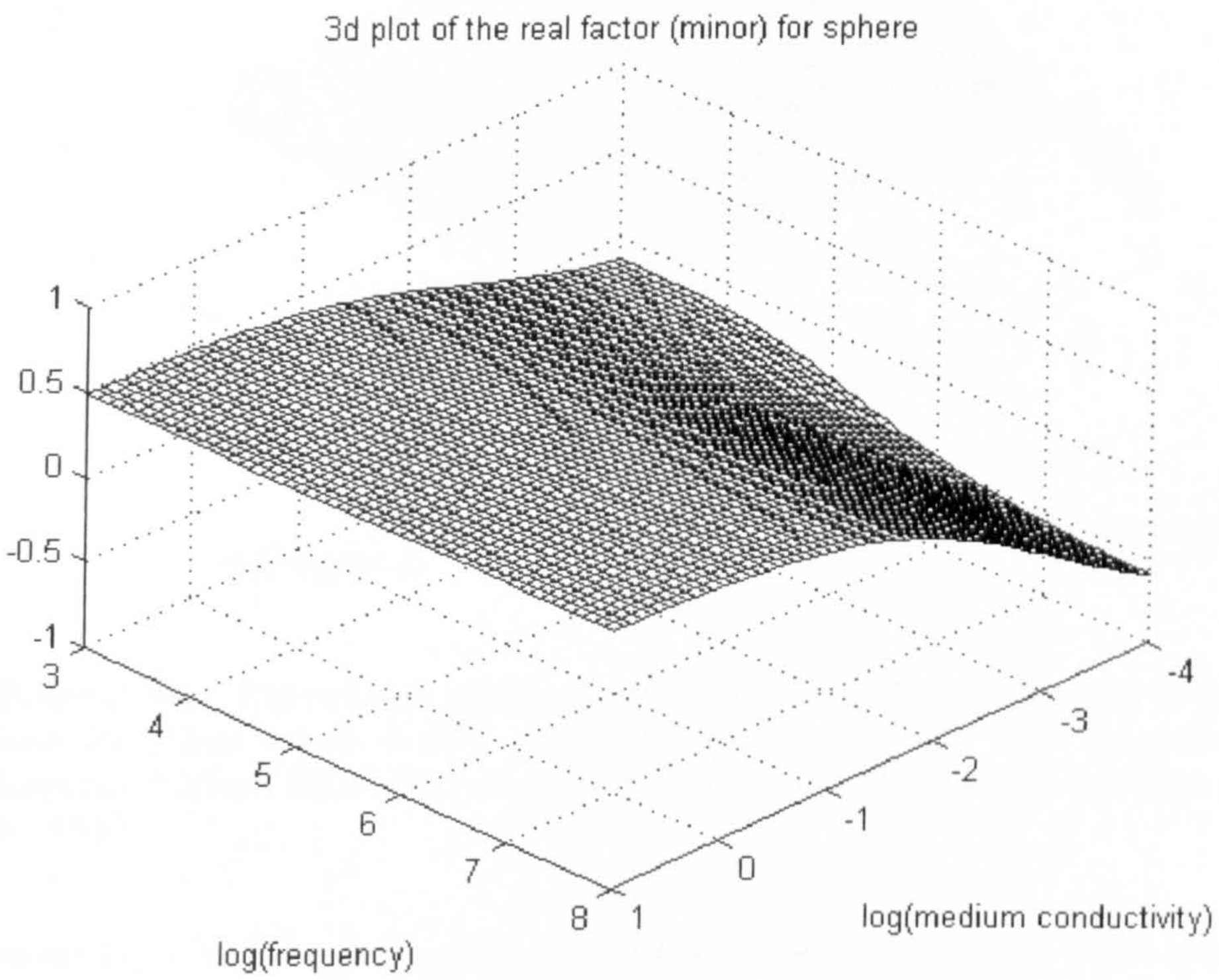

Figure (7.29) The variation of the real part of the dipole moment of the double layer for 282nm spheres in KCl, calculated according to [12] with the applied frequency (Hz) and the medium conductivity (Sm^{-1}). The zeta potential was taken to be -43mV.

Compared to Figure (7.28) there is a slight increase in the distance along the medium conductivity axis over which the dispersion extends, but the variation with particle size is identical to the previous model, Other than that, the model results in the same problems as the previous one when it comes to calculating the total dipole moment of the sphere.

Fixman [13] published a model for a thin double layer which is under the restriction that $\kappa a \ll 1$. This restriction is true in the region where the double layer relaxation is observed for the 557, 282 and 216nm spheres. The equation for the polarisation factor can be found in the

program in Appendix (7a). Figure (7.30) shows the variation of the real part of the frequency varying dipole term with medium conductivity.

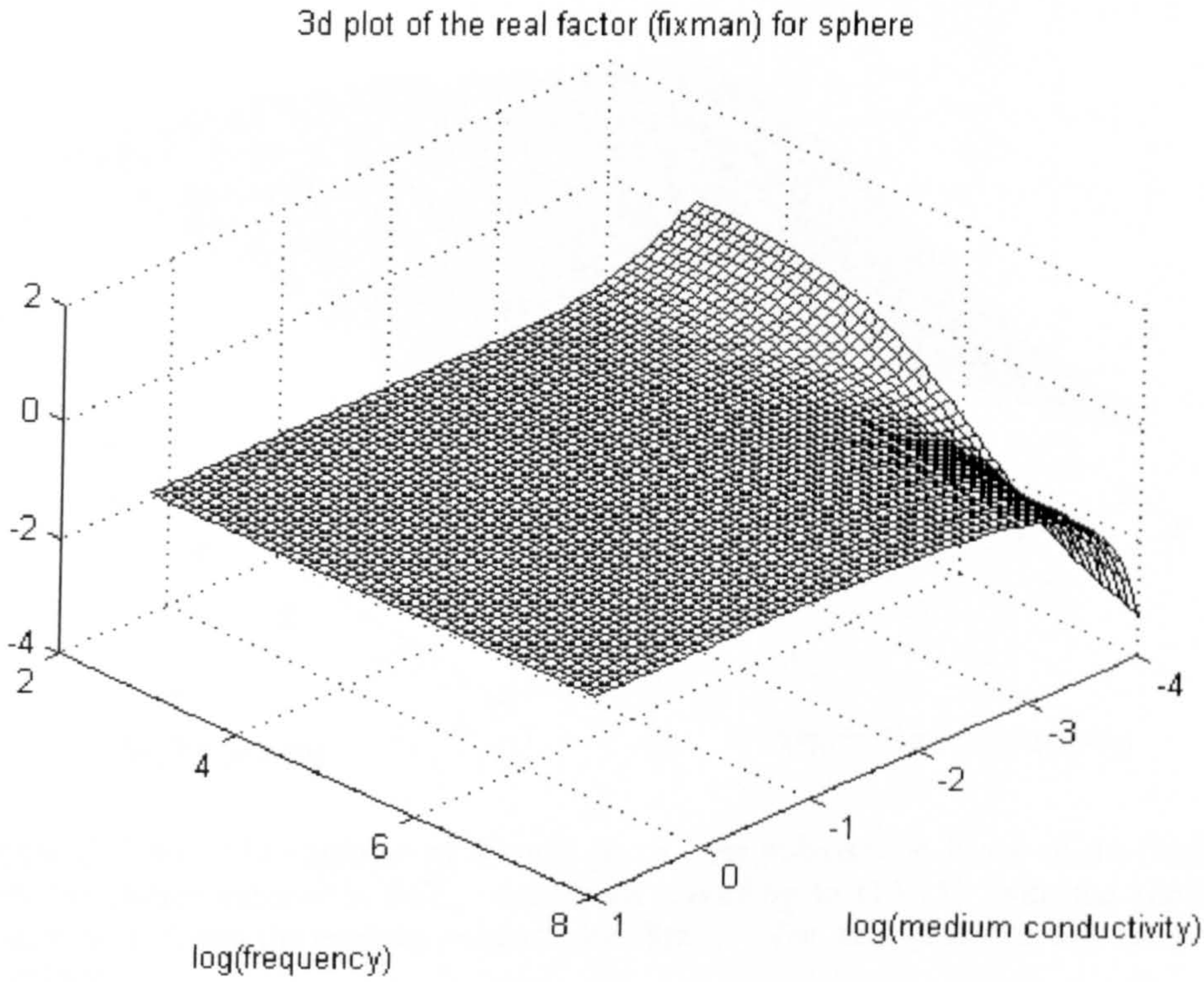

Figure (7.30) The variation of the real part of the polarisation factor of the double layer for 282nm spheres in KCl, calculated according to [13] with the applied frequency (Hz) and the medium conductivity (Sm^{-1}). The zeta potential was taken to be -43mV.

This model has a fairly large dispersion at very low medium conductivities which tends to a values of -0.5 at high conductivities. Again, this would cause difficulties with the total dipole moment when combined with the Clausius-Mossotti factor but the dispersion does not extend along the conductivity axis far enough. The distance does, however, increase with decreasing particle size but under these conditions, the model is no longer valid.

The final model considered here is the model presented by Hinch [14] and expanded by O'Brien [15]. This theory may or may not be an intermediate step between the models of Lyklema and Minor but is worth examining nevertheless. The equation for the dipole is very similar to Lyklema's equation with minor differences and can be found in program form in Appendix (7a). Figure (7.31) shows the variation in the polarisation factor with frequency and medium conductivity for 282nm spheres in KCl.

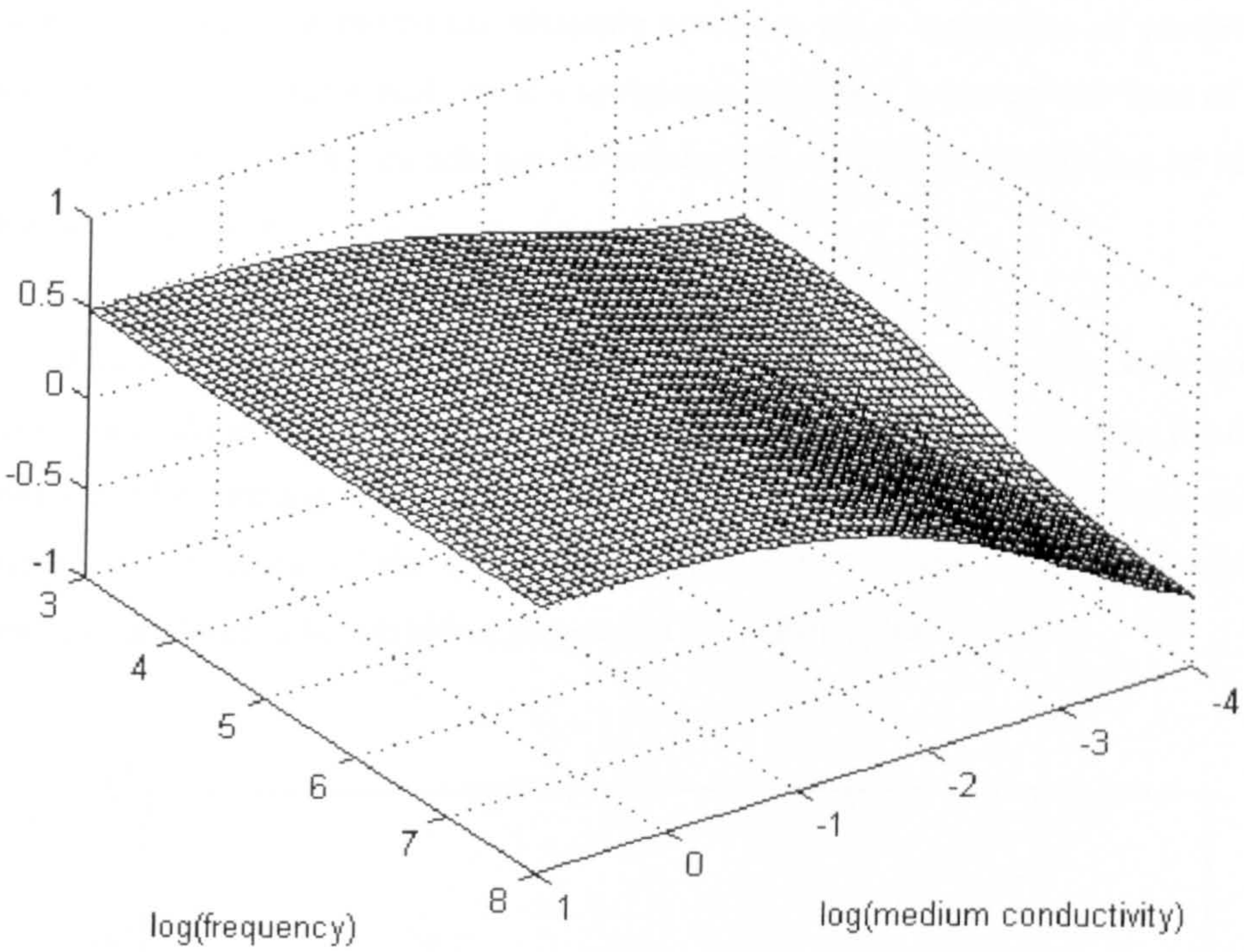

Figure (7.31a) The variation of the real part of the polarisation factor of the double layer for 282nm spheres in KCL, calculated according to [14,15] with the applied frequency (Hz) and the medium conductivity (Sm^{-1}). The zeta potential was taken to be -43mV.

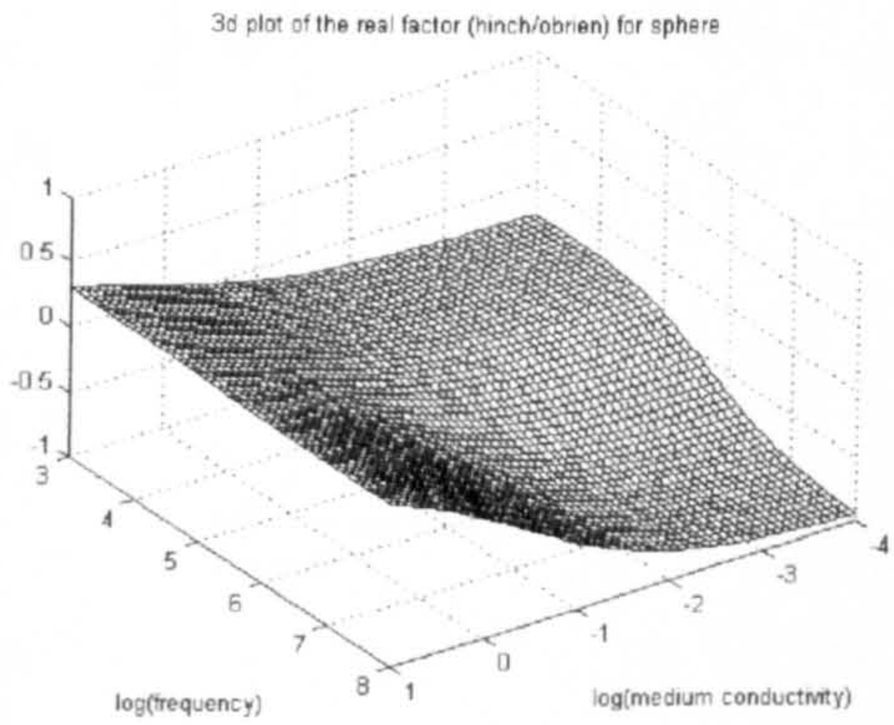

Figure (7.31b) The change in (7.31a) when the zeta potential is increased to a value of -200mV.

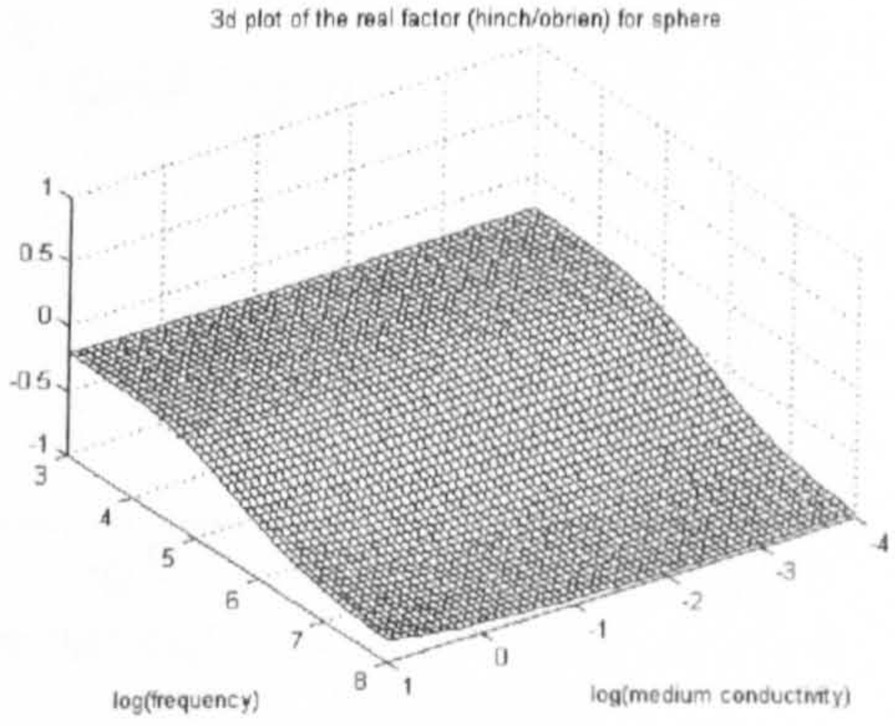

Figure (7.31c) The change in (7.31a) when the zeta potential is increased to a value of -500mV.

As in the models of Lyklema and Minor, the dispersion extended farther along the conductivity axis as particle diameter decreased and increasing the zeta potential also extended this distance. The model still does not have limits suitable for combination with the Clausius-Mossotti factor to give an independent relaxation.

The difficulty with all of these models is that they are generally written as an intermediate step towards obtaining a theoretical dielectric spectrum for a suspension of particles. The researchers who devise the models are not necessarily interested in the correct form of the single particle dipole. None of the models met the criteria that the high frequency limit be zero for the magnitude of the dipole.

In order to determine certain parameters for the problem, the data was modelled by adding an extra dispersion to the Clausius-Mossotti factor. This has been done previously for the purposes of examining low frequency electrorotation results [16]. The parameter of most interest is the frequency of the double layer relaxation. Figure (7.32) shows the major frequencies postulated to be relaxation frequencies for 282nm spheres in KCl.

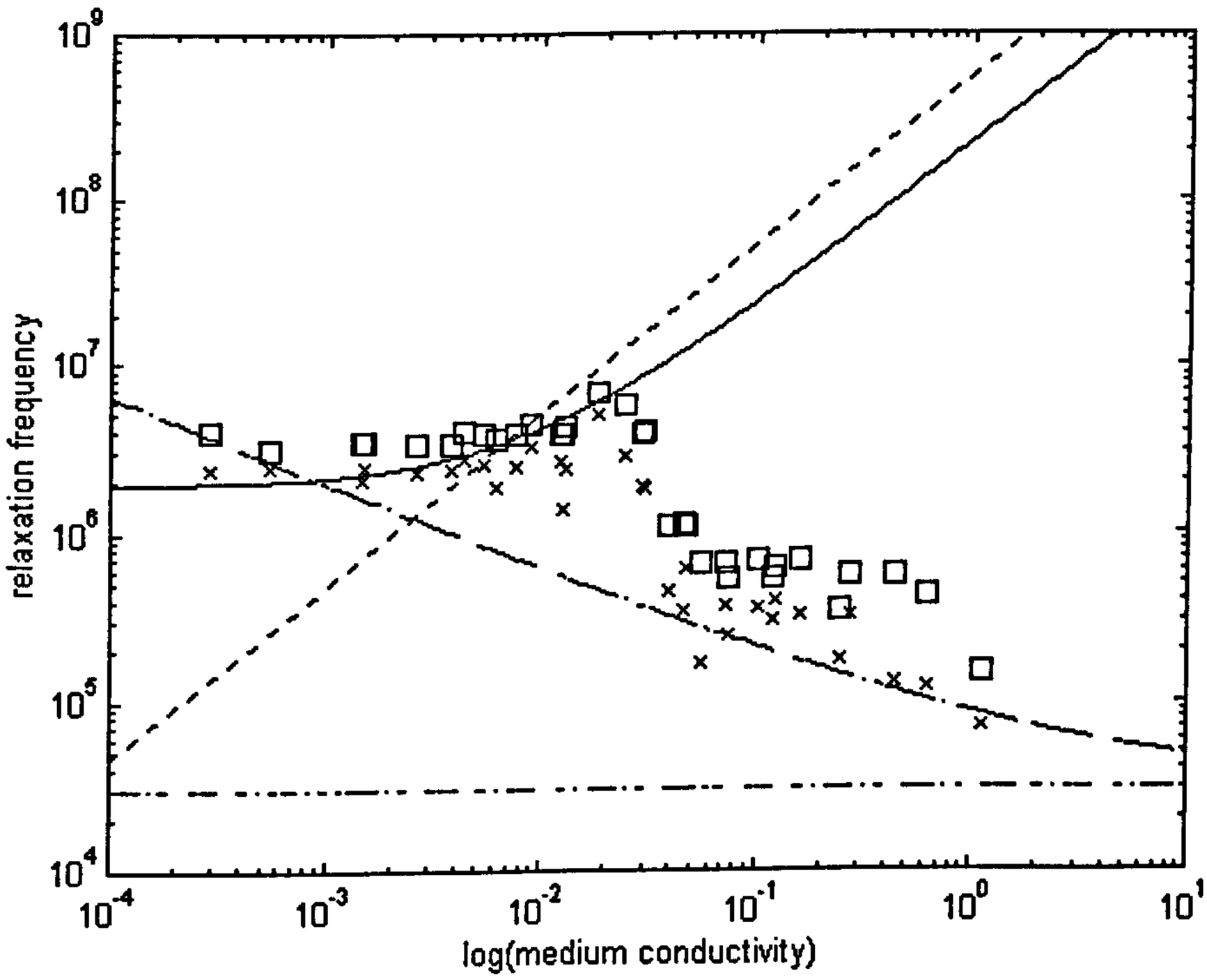

Figure (7.32) Relaxation frequencies for 282nm spheres in KCl. The solid line is the Maxwell-Wagner frequency and the horizontal dot-dash line is the classical α–relaxation frequency (equation 7.7). The heavy-dashed falling line is the modified bound frequency (equation 7.8) and the small-dashed rising line is the radial relaxation frequency (equation 7.9).

The three frequencies shown in this graph (other than the Maxwell-Wagner) are all related, but in different ways to the structure of the double layer. The classical α–relaxation frequency originally postulated by Schwarz [7] is given by:

$$f_{\alpha 1} = \frac{D}{\pi a^2} \tag{7.7}$$

where D is the diffusion coefficient, which may be less than the bulk value, and a is the radius of the particle. The relaxation time for this mechanism is simply the characteristic time associated with movement of charge around the particle. A modified frequency was given by Lyklema [9] for the case of a bound double layer which is influenced by the capacitance of the diffuse part of the double layer:

$$f_{\alpha 2} = \frac{MD}{\pi a^2} \tag{7.8}$$

The parameter M is given in section (3.5.1) where this mechanism is explained further. The third frequency was given by O'Brien [15]:

$$f_{\alpha 3} = \frac{D\kappa^2}{\pi} \tag{7.9}$$

where κ is the reciprocal Debye length. The relaxation time for this mechanism is the characteristic time taken for an ion to move out of the double layer from the surface in a radial direction. As can be seen from Figure (7.32), either $f_{\alpha 1}$ or $f_{\alpha 2}$ could be responsible for the high conductivity dispersion but $f_{\alpha 3}$ could not. However for the 93nm spheres, where the radial distance across the double layer can be of the same order as the radius of the particle, the third relaxation at $f_{\alpha 3}$ may become as prominent as the observed low frequency relaxation. Therefore, the relaxation frequency $f_{\alpha 3}$ could easily account for the observed rise in the zero force point of the 93nm spheres.

Zhou [16] inserted an extra dispersion into the conductivity term of the particle and plotted the resulting Clausius-Mossotti factor. As the low-frequency dispersion is entirely to do with moving charge, this is a reasonable assumption. The equation for the latex sphere particle conductivity is therefore:

$$\sigma_p = \sigma_{pb} + \frac{2\lambda}{a} + \frac{A}{1+(j\omega\tau)^B} \tag{7.10}$$

where A and B are arbitrary constants which describe the shape of the dispersion and τ is the relaxation time. Figure (7.33) shows the Clausius-Mossotti factor for the 282nm spheres with the extra dispersion added. In this case $A = 0.1$ and $B = 1$ and τ is given by equation (7.7).

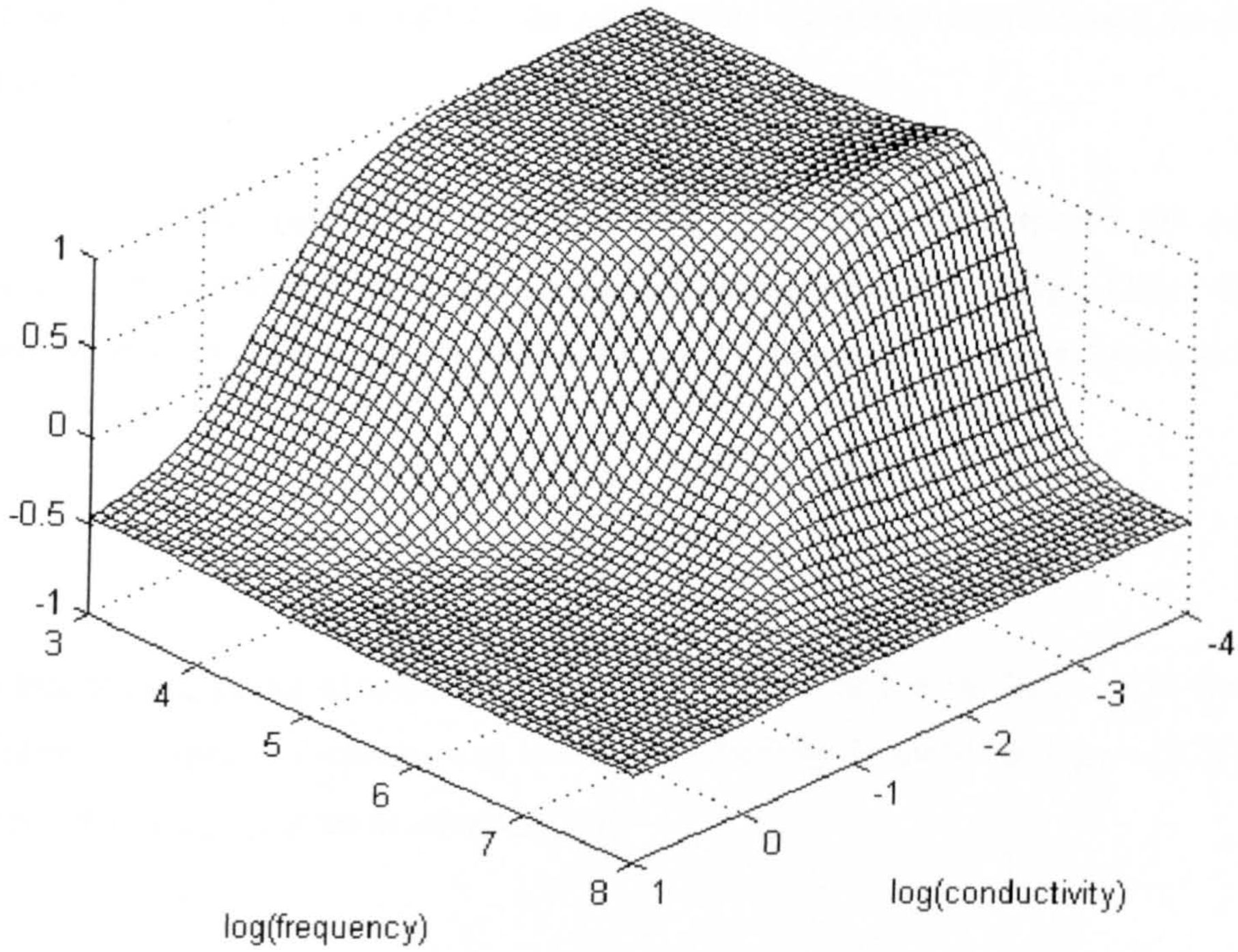

Figure (7.33) Variation of the Clausius-Mossotti factor of a 282nm sphere with the particle conductivity given by equation (7.10) where A=0.1 and B=1.

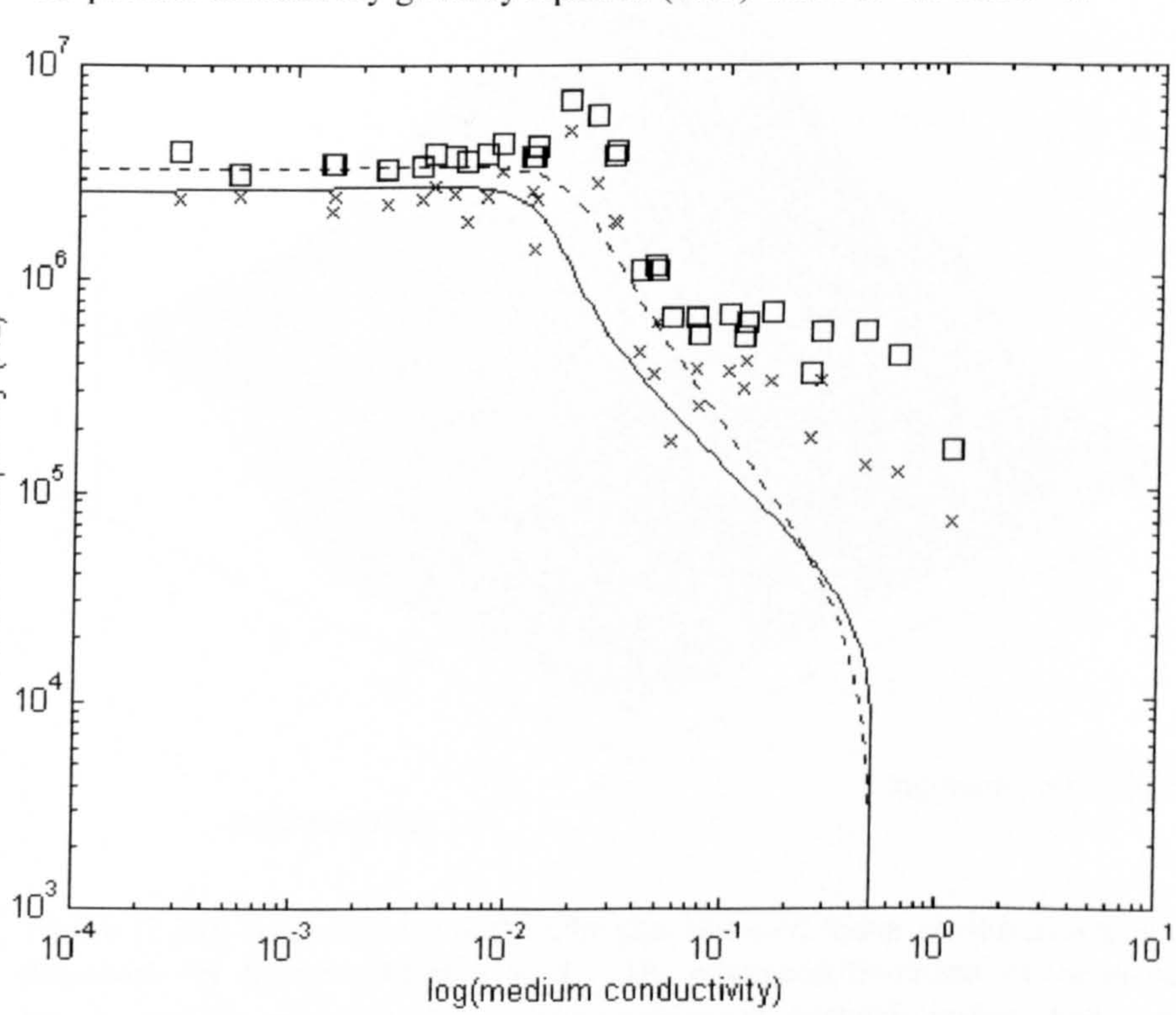

Figure (7.34) The zero force line for the theoretical model shown in (7.33) compared to the experimental results for 282nm in KCl. A was again equal to 0.1 but the solid line is with B = 1 and the dashed line with B = 0.8.

Figure (7.34) shows the theoretical zero force lines for $B = 1$ and 0.8 and $A = 1$ with the experimental data for 282nm in KCl. As can be seen, the theory doesn't match the data to any great degree.

Finally, the experimental data for the 557, 282 and 216nm spheres are analysed in terms of a simple combination of the Clausius-Mossotti factor and a single Debye dispersion. The maximum of the dispersion was taken to be 1 and the minimum value was zero and the term:

$$\frac{1}{1 + j\omega\tau} \tag{7.11}$$

was added to the Clausius-Mossotti factor to give a polarisation scaling factor. The variation of this factor with applied frequency and medium conductivity is shown in Figure (7.35) for the relaxation frequency $f_{\alpha 1}$ given by equation (7.7).

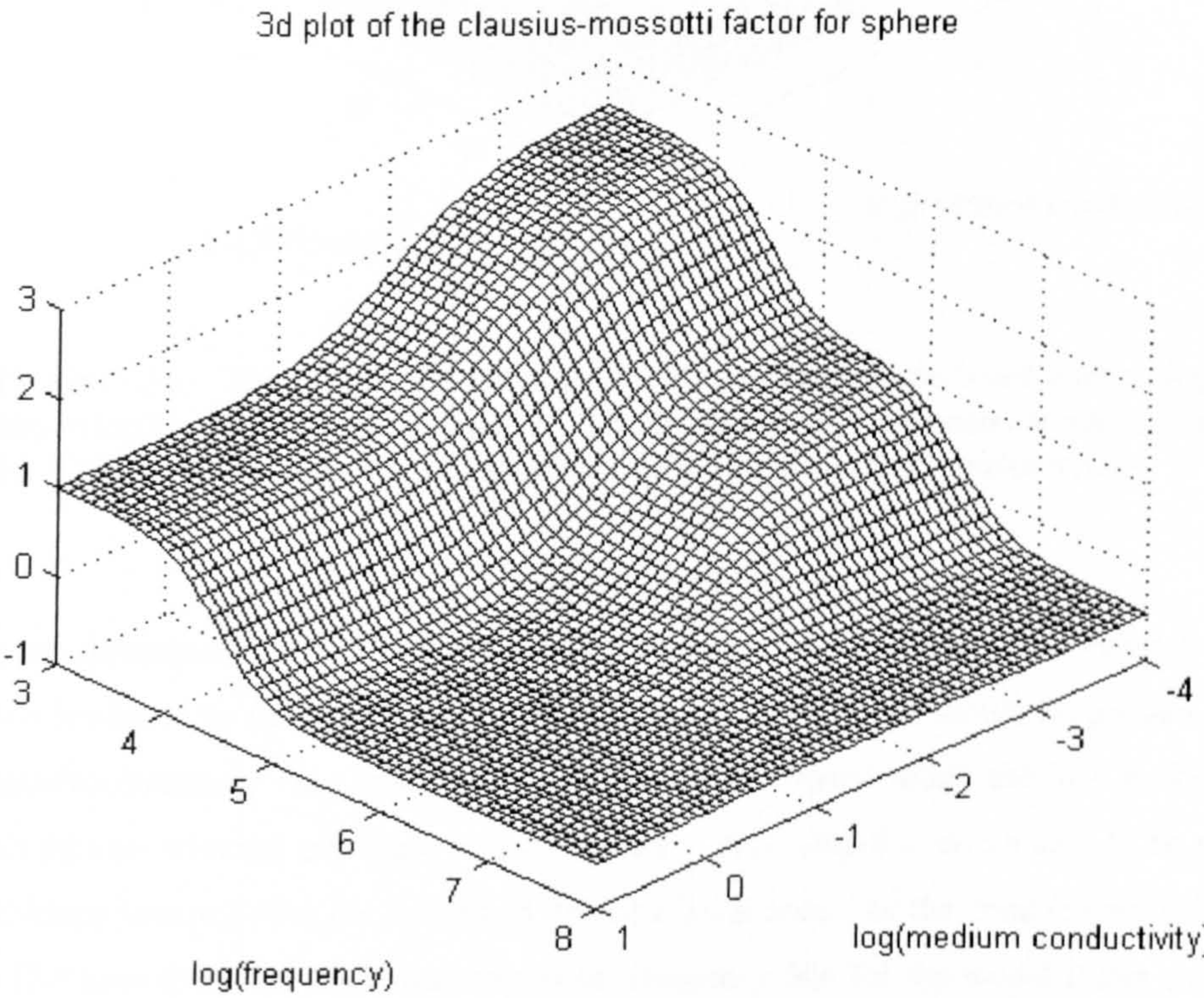

Figure (7.35) The variation of the Clausius-Mossotti factor combined with a single dispersion for 282nm spheres in KCl. The relaxation frequency of the dispersion was $f_{\alpha 1}$ and the variation of the Clausius-Mossotti factor is undisturbed except at low frequencies.

The variation of the Clausius-Mossotti factor is unchanged except at frequencies well below the Maxwell-Wagner relaxation frequency. The variation of this factor if the second frequency, given by equation (7.8) is used instead is shown in Figure (7.36).

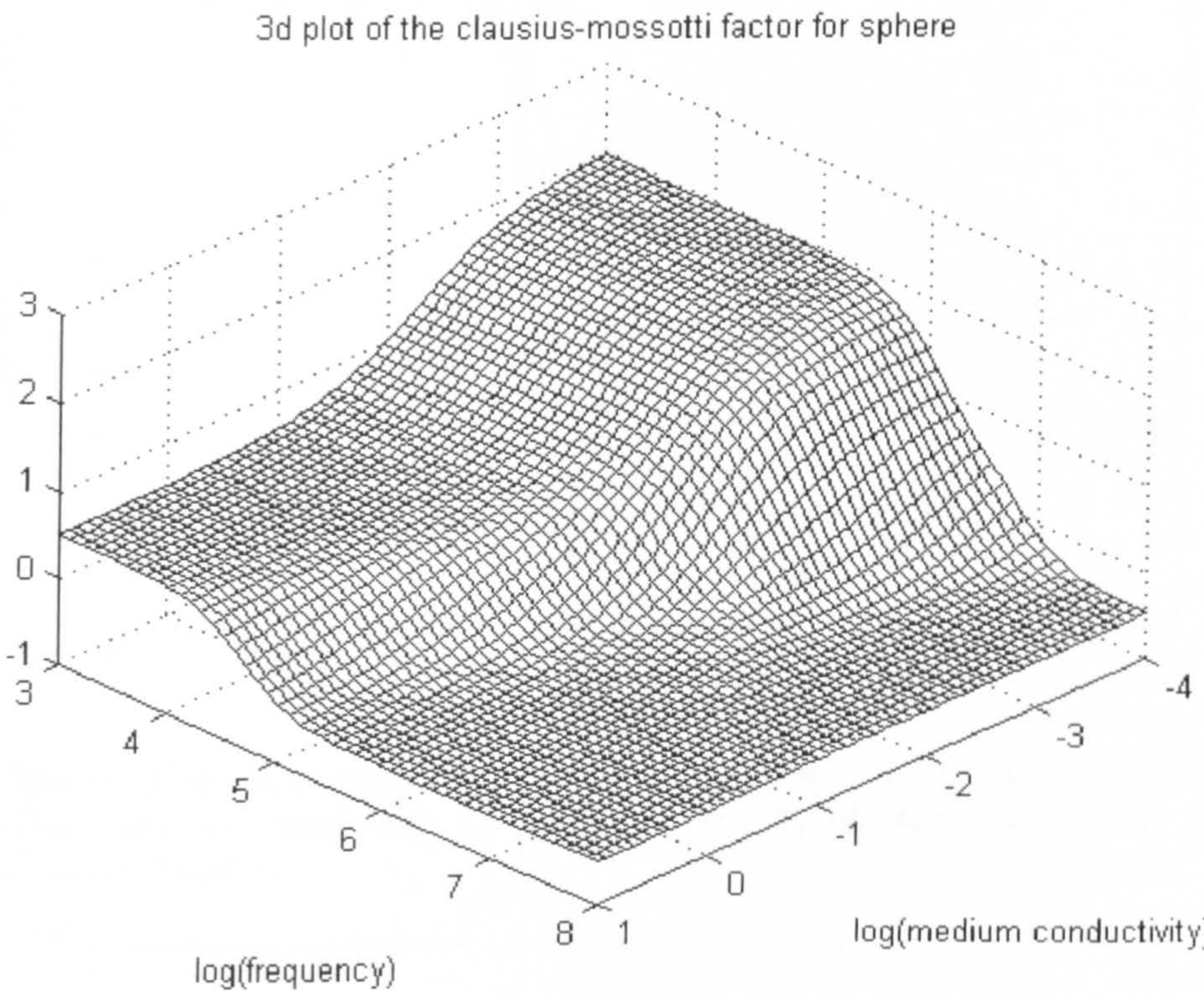

Figure (7.36) The variation of the Clausius-Mossotti factor combined with a single dispersion for 282nm spheres in KCl. The frequency of the dispersion was $f_{\alpha 2}$ and the Clausius-Mossotti factor varied substantially at low medium conductivities.

This figure demonstrates that if the relaxation frequency $f_{\alpha 2}$ is chosen, the Maxwell-Wagner dispersion is altered by the low frequency dispersion. However, it should be pointed out that this relaxation frequency only applies for very thin double layers where the ions in the diffuse layer can interact with the ions close to the surface. This condition is unlikely to be met in a medium where Maxwell-Wagner interfacial polarisation is seen, as the conductivity is too low. Figures (7.37a-c) show the theoretical zero point frequency line for the model above using both relaxation frequencies ($f_{\alpha 1}$ and $f_{\alpha 2}$) compared to the experimental data for the 557, 282 and 216nm spheres.

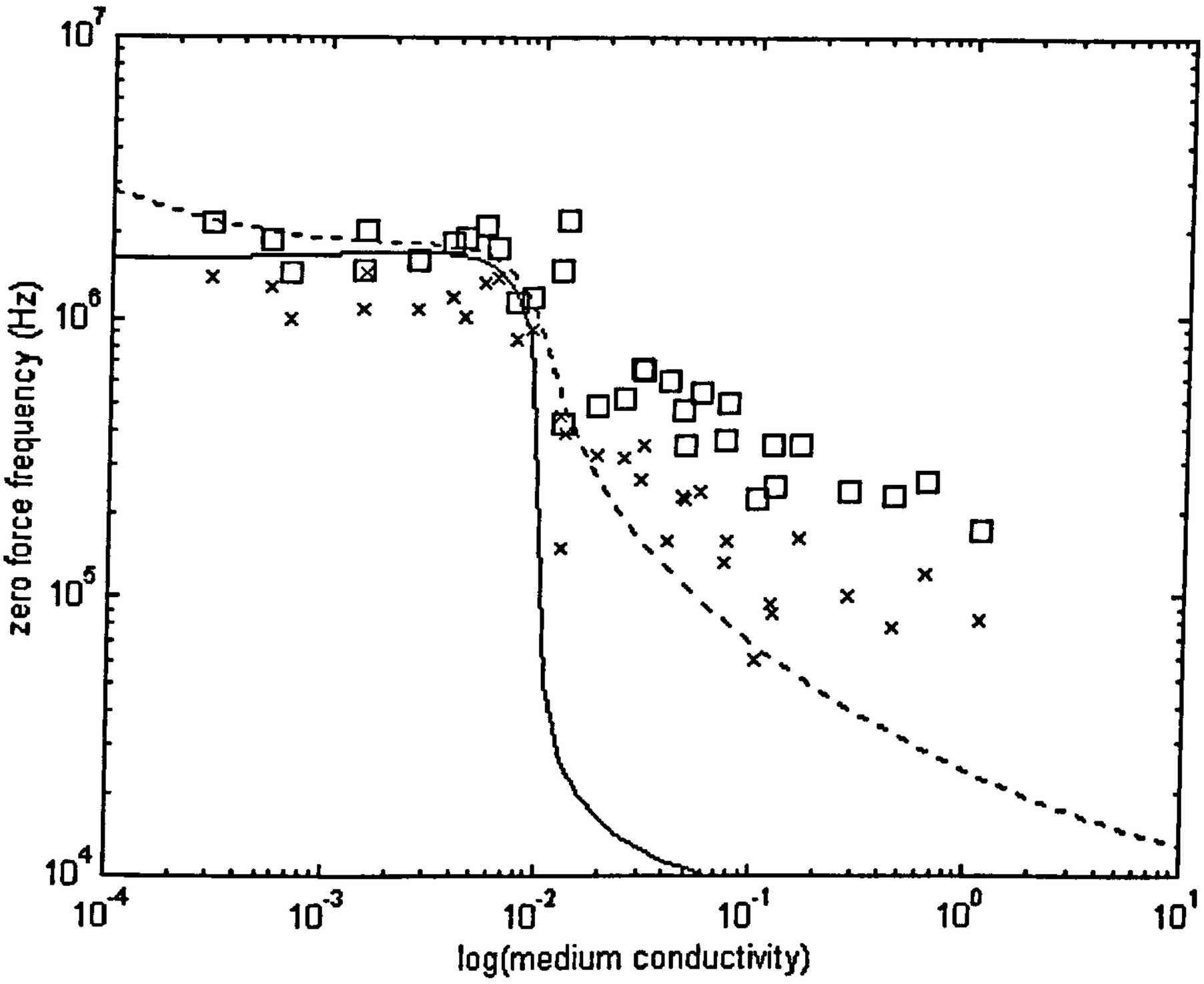

Figure (7.37a) Experimental data for the 557nm spheres in KCl compared to the added dispersion model with $f_{\alpha 1}$ (solid line) and $f_{\alpha 2}$ (dashed line) used as the relaxation frequency.

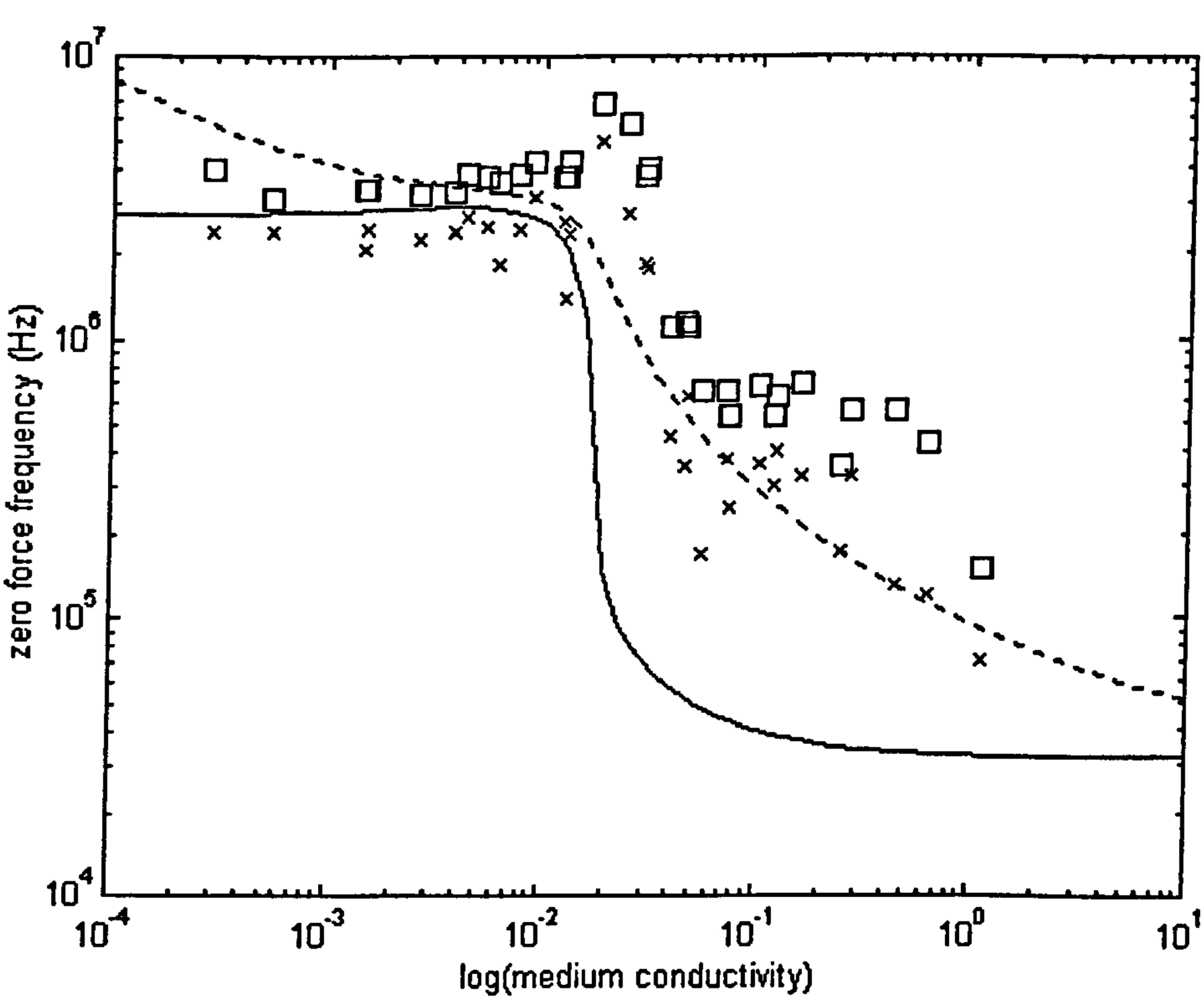

Figure (7.37b) Experimental data for the 282nm spheres in KCl compared to the added dispersion model with $f_{\alpha 1}$ (solid line) and $f_{\alpha 2}$ (dashed line) used as the relaxation frequency.

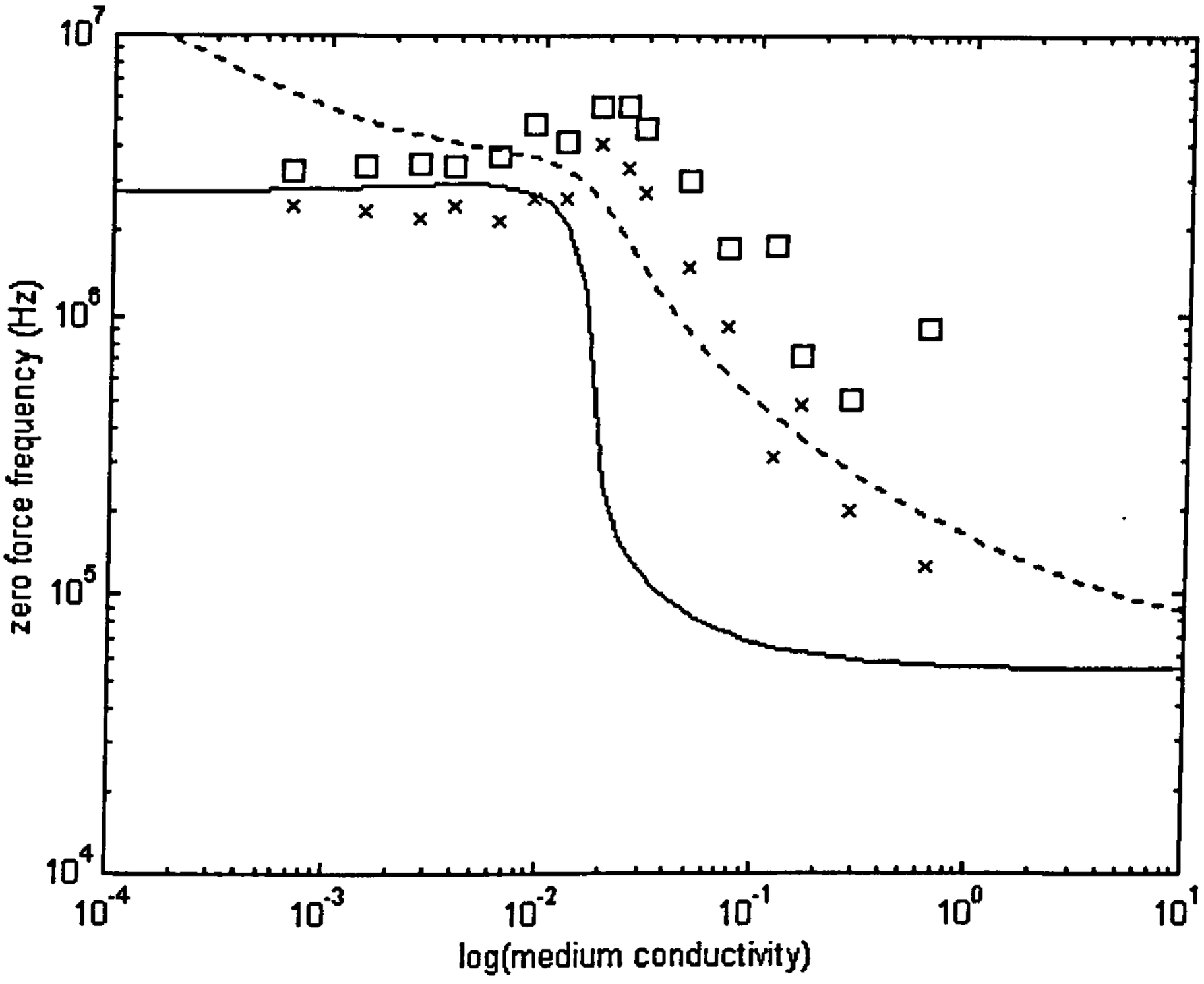

Figure (7.37c) Experimental data for the 216nm spheres in KCl compared to the added dispersion model with $f_{\alpha 1}$ (solid line) and $f_{\alpha 2}$ (dashed line) used as the relaxation frequency.

As can be seen from all three graphs, neither of the relaxation frequencies match the data precisely. Figures (7.37a) and (7.37b) suggest that the zero force frequency should vary less with conductivity than zero force frequency found from $f_{\alpha 2}$ (dashed lines in Figures 7.35). However, this relaxation frequency seems to be of the correct order of magnitude whereas the classical frequency given by equation (7.7) is too low. What is apparent is that the bound layer model of Lyklema is the closest to predicting the order of magnitude at which the relaxation occurs. However, this model is for a bond layer which implies that the ions involved should have a higher diffusion coefficient then the bulk and therefore a lower relaxation frequency.

The measurements performed for this Chapter have demonstrated that sub-micrometre latex spheres are a complicated particle from the point of view of modelling their behaviour. The theories used in the related field of dielectrics do not adequately account for the low frequency behaviour, which can not even be described in simple terms.

Appendix (7a) Latex Sphere information

This appendix contains the background information on the carboxylate modified latex spheres supplied by Molecular Probes, Leiden, The Netherlands.

sphere diameter (nm)	**557±2.0%**	**282±2.6%**	**216±3.8%**	**93±7.4%**
catalogue number	L-5261	L-5241	F-8808	L-5221
lot number	5852	6932	6951	6951
percent solids	2.0%±0.1	2.0%±0.1	2.0%±0.1	2.0%±0.1
density at 20°C (g/m^3)	1.06	1.06	1.06	1.055
surface charge density ($\mu C/cm^2$)	185	4.83	141	2.09
area /charge group (nm^2/group)	0.09	3.32	11	7.65
milliequivalents /gram	0.1953	0.0101	0.3859	0.01327
specific surface area (cm^2/g)	102102	201674	263296	611527
particle number / ml	$2.1x10^{11}$	$1.6x10^{12}$	$3.6x10^{12}$	$405x10^{13}$
approximate dye excitation (nm)	505	490	490	490
approximate dye emission (nm)	515	515	515	515

Appendix (7b) Matlab programs

Functions from section (7.4.1)

DCPLOTTER.M

```
% Consider this a generic model for things to come.

% This script calculates the clausius-mossotti factor
% for a given vector of conductivities . The program
% plots a 3D graph, calculates all the zero points
% and plots them on a 2D graph.

clear all

global ep em eo sp scd mob a;

ep = 2.55; em = 78.54; eo = 8.85e-12;  % permittivity stuff
sp = 0.11; scd = 0; mob = 7.56e-8;     % conductivity stuff
n1 = 1; n2 = 9; N = 100;               % frequency vector numbers
m1 = -4; m2 = 1; M = 200;              % conductivity vector numbers
a = 141e-9;                            % particle radius
particle = 282;                        % a data switch
zerr = 0.01;                           % zero error value (percent)
salt = 1;                              % salt variable ::::
                                % 1 - KCl; 2 - NaCl; 3 - KPO4

% variable definition stage

f = logspace(n1,n2,N);
sigm = logspace(m1,m2,M);

% plotting bit

DCM = []; ICM = [];
for l = 1:M
  sm = sigm(l);
  DIPval = clausmos(f,sm);
  for k = 1:(N-1)
    trans1 = real(DIPval(k));   f1 = f(k);
    trans2 = real(DIPval(k+1)); f2 = f(k+1);
    test = trans1*trans2;
    if test < 0
      error = 101; zerof = [];
      while error > zerr
        shortf = [f1 f2];
        trans1 = real(clausmos(shortf,sm));
              meanf = (f1+f2)/2;
        trans = real(clausmos(meanf,sm));
        test1 = trans*trans1(1);
        test2 = trans*trans1(2);
                        if test1 < 0
                                f2 = meanf; zerof =
(meanf+f1)/2;
                        end
                        if test2 < 0
                        f1 = meanf; zerof = (meanf+f2)/2;
                                end
        error = ((abs(meanf-zerof))*100)/zerof;
      end
        zeros = [zeros zerof];
      end
    end
    DCM = [DCM;real(DIPval)];
    ICM = [ICM,imag(DIPval)];
end

% work out the plotting vector for the zeros
goo = size(zeros);
for kl = 1:(goo(2)-1)
  xover(kl) = zeros(kl+1);
end

for lk = goo(2).M
  xover(lk) = 1;
end

%mesh(log10(sigm),log10(f),DCM');
%Ylabel('log(frequency)')
%Xlabel('log(medium conductivity)')
%axis([m1 m2 n1 n2 -1 1])
%Title('3d plot of the clausius-mossotti factor for sphere')
%view(135,45)

%figure
loglog(sigm,xover)
Xlabel('log(medium conductivity)')
Ylabel('zero force frequency (Hz)')
axis([1e-4 1e1 1e1 1e9])

hold on
switch particle
case 557,
  data557; loglog(conddata,posdata,'kx'); loglog(conddata,negdata,'ks');
  axis([1e-4 1e1 1e4 1e7])
case 282,
  data282; loglog(conddata,posdata,'kx'); loglog(conddata,negdata,'ks');
  axis([1e-4 1e1 1e5 1e7])
case 216,
  data216; loglog(conddata,posdata,'kx'); loglog(conddata,negdata,'ks');
  axis([1e-4 1e1 1e5 1e7])
case 93,
  data93; loglog(conddata,posdata,'kx'); loglog(conddata2,negdata,'ks');
  axis([1e-4 1e1 1e6 1e8])
end

hold off
```

CLAUSMOS.M

```
function [R1] = clausmos(freq,sigm)

% This function plots the maxwell-wagner interfacial
% polarisation terms for a prolate ellipsoidal particle. There
% are of course three - because there are three axes.

% The function needs the following variables defined as global
% ep - particle perm, em - medium perm, sp - particle cond
% scd - surface charge dens, u - mobility, a - particle radius
% eo - perm of free space

global ep em eo sp a R kB qo T F tau zeta eta scd mob kappa D z;

% dipole calculation

w = 2.*pi.*freq;
surfc = (2*mob*scd/a);
sigp = sp + surfc;
ems = em*eo - j.*(sigm./w);
eps = ep*eo - j.*(sigp./w);

dipole = (eps-ems)./(eps + (2.*ems));

R1 = dipole;

% end of function
```

CMPLOTTER.M

```
% This script calculates the maxwell-wagner for a spherical
% particle given a single value for the conductivity, then
% plots a 2d graph of the factor vs f and writes the zero
% force point on the graph.

clear all

global ep em eo sp scd mob a;

ep = 2.55; em = 78.54; eo = 8.85e-12;  % permittivity stuff
sp = 0.02; scd = 0; mob = 7.56e-8;     % conductivity stuff
n1 = 3; n2 = 9; N = 100;               % frequency vector numbers
m1 = -4; m2 = 1; M = 100;              % conductivity vector numbers
a = 141e-9;                            % particle radius
zerr = 0.01;                           % zero error value (percent)

% variable definition stage

f = logspace(n1,n2,N);
sm = 1;

DIPval = clausmos(f,sm);
zeros = [];
for k = 1:(N-1)
  trans1 = real(DIPval(k));   f1 = f(k);
  trans2 = real(DIPval(k+1)); f2 = f(k+1);
  test = trans1*trans2;
  if test < 0
    error = 101; zerof = [];
    while error > zerr
      shortf = [f1 f2];
      trans1 = real(clausmos(shortf,sm));
            meanf = (f1+f2)/2;
      trans = real(clausmos(meanf,sm));
      test1 = trans*trans1(1); test2 = trans*trans1(2);
                          if test1 < 0
                                  f2 = meanf; zerof =
(meanf+f1)/2;
                          end
                          if test2 < 0
        f1 = meanf; zerof = (meanf+f2)/2;
       end
                                  error = ((abs(meanf-
zerof))*100)/zerof;
                          end
     zeros = [zeros,zerof];
   end
end
dip = real(DIPval);
semilogx(f,dip);
Title('Real part of the Clausius-Mossotti factor vs frequency')
Xlabel('frequency(Hz)')
% test for number of zeros
fmmm = size(zeros);
if fmmm(1)>0
  for l = 1:fmmm(1)
    zpos = fmmm(1); zval = zeros(zpos);
    inst = num2str(zval);
    text(zval,0.1,inst);
  end
end
```

CMSPECIAL.M

```
function [R1] = clausmos(freq,sigm)

% This function plots the maxwell-wagner interfacial
% polarisation terms for a prolate ellipsoidal particle. There
% are of course three - because there are three axes.

% The function needs the following variables defined as global
% ep - particle perm, em - medium perm, sp - particle cond
% scd - surface charge dens, u - mobility, a - particle radius
% eo - perm of free space

global ep em eo sp scd mob a kappa;

% dipole calculation

w = 2.*pi.*freq;
%surfc = (2*mob*scd/(a + (10/kappa)));
surfc = (2*mob*scd/a)*(0.2 + 0.1*(a*kappa));
sigp = sp + surfc;
ems = em*eo - j.*(sigm./w);
eps = ep*eo - j.*(sigp./w);

dipole = (eps-ems)./(eps + (2.*ems));

R1 = dipole;

% end of function
```

DCMSPECIAL.M

```
% Consider this a generic model for things to come.

% This script calculates the clausius-mossotti factor
% for a given vector of conductivities . The program
% plots a 3D graph, calculates all the zero points
% and plots them on a 2D graph.

clear all

global ep em eo sp scd mob a kappa;

ep = 2.55; em = 78.54; eo = 8 85e-12;   % permittivity stuff
sp = 0.00; scd = 0.038; mob = 7.56e-8; % conductivity stuff
n1 = 1; n2 = 9; N = 50;     % frequency vector numbers
m1 = -4; m2 = 1; M = 60;    % conductivity vector numbers
a = 141e-9;                 % particle radius
particle = 282;             % a data switch
zerr = 0.01;                % zero error value (percent)
salt = 1;                   % salt variable ::::
                            % 1 - KCl;  2 - NaCl;  3 -

KPO4
kB = 1.38e-23; T = 295;
Na = 6.022e26; qo = 1.6e-19; z = 1;


% variable definition stage

f = logspace(n1,n2,N);
sigm = logspace(m1,m2,M);

% plotting bit

DCM = [];  ICM = [];
for l = 1:M
  sm = sigm(l);

  Conc = 0.0852*(sm^1.0245);          % equation from experimental
data - KCl
kappa = sqrt((2*(z^2)*(qo^2)*Na*Conc)/(em*eo*kB*T));

DIPval = cmspecial(f,sm);
for k = 1:(N-1)
  trans1 = real(DIPval(k));   f1 = f(k);
  trans2 = real(DIPval(k+1)); f2 = f(k+1);
  test = trans1*trans2;
  if test < 0
    error = 101; zerof = [];
    while error > zerr
      shortf = [f1 f2];
      trans1 = real(cmspecial(shortf,sm));
            meanf = (f1+f2)/2;
      trans = real(cmspecial(meanf,sm));
      test1 = trans*trans1(1);
      test2 = trans*trans1(2);
                              if test1 < 0
                              f2 = meanf; zerof = (meanf+f1)/2;
                              end
                              if test2 < 0
                              f1 = meanf; zerof = (meanf+f2)/2;
                                        end
      error = ((abs(meanf-zerof))*100)/zerof;
    end
      zeros = [zeros zerof];
  end
end
DCM = [DCM;real(DIPval)];
ICM = [ICM,imag(DIPval)];
end

% work out the plotting vector for the zeros
goo = size(zeros);
for kl = 1:(goo(2)-1)
  xover(kl) = zeros(kl+1);
end
for lk = goo(2):M
  xover(lk) = 1;
end

%mesh(log10(sigm),log10(f),DCM');
%Ylabel('log(frequency)')
%Xlabel('log(medium conductivity)')
%axis([m1 m2 n1 n2 -1 1])
%Title('3d plot of the clausius-mossotti factor for sphere')
%view(135,45)

%figure
loglog(sigm,xover)
Xlabel('log(medium conductivity)')
Ylabel('zero force frequency (Hz)')
axis([1e-4 1e1 1e1 1e9])

hold on
switch particle
case 557,
  data557; loglog(conddata,posdata,'kx'); loglog(conddata,negdata,'k+');
  axis([1e-4 1e1 1e4 1e7])
case 282,
  data282; loglog(conddata,posdata,'kx'); loglog(conddata,negdata,'k+');
  axis([1e-4 1e1 1e4 1e7])
case 216,
  data216; loglog(conddata,posdata,'kx'); loglog(conddata,negdata,'k+');
  axis([1e-4 1e1 1e5 1e7])
case 93,
  data93; loglog(conddata,posdata,'kx'); loglog(conddata2,negdata,'k+');
  axis([1e-4 1e1 1e5 1e8])
end

hold off
```

MAXWAGFREQ.M

```
% Consider this a generic model for things to come.

% This script calculates the clausius-mossotti factor
% for a given vector of conductivities . The program
% plots a 3D graph, calculates all the zero points
% and plots them on a 2D graph.

clear all

global ep em eo sp scd mob a;

ep = 2.55; em = 78.54; eo = 8.85e-12;  % permittivity stuff
sp = 0.017; scd = 0; mob = 7.56e-8;    % conductivity stuff
n1 = 1; n2 = 9; N = 100;               % frequency vector numbers
m1 = -4; m2 = 1; M = 200;              % conductivity vector numbers
a = 141e-9;                            % particle radius
particle = 282;                        % a data switch
zerr = 0.01;                           % zero error value (percent)
salt = 1;
            % salt variable :::: % 1 - KCl;  2 - NaCl;  3 - KPO4

% variable definition stage

f = logspace(n1,n2,N);
sigm = logspace(m1,m2,M);

% plotting bit

TAU = [];
for l = 1:M
  sm = sigm(l);
  DIPval = MaxWag(f,sm);
  TAU = [TAU DIPval];
end

loglog(sigm,TAU)
Xlabel('log(medium conductivity)')
Ylabel('Maxwell-Wagner relaxation frequency')
axis([1e-4 1e1 1e4 1e9])

hold on
switch particle
case 557,
  data557; loglog(conddata,posdata,'kx'); loglog(conddata,negdata,'ks');
case 282,
  data282; loglog(conddata,posdata,'kx'); loglog(conddata,negdata,'ks');
case 216,
  data216; loglog(conddata,posdata,'kx'); loglog(conddata,negdata,'ks');
case 93,
  data93; loglog(conddata,posdata,'kx'); loglog(conddata2,negdata,'ks');
end

hold off
```

MAXWAG.M

```
function [R1] = MaxWag(freq,sigm)

% This function plots the maxwell-wagner interfacial
% polarisation terms for a prolate ellipsoidal particle. There
% are of course three - because there are three axes.

% The function needs the following variables defined as global
% ep - particle perm, em - medium perm, sp - particle cond
% scd - surface charge dens, u - mobility, a - particle radius
% eo - perm of free space

global ep em eo sp scd mob a kappa;

% dipole calculation

w = 2*pi*freq;
surfc = (2*mob*scd/a);
sigp = sp + surfc;
ems = em*eo;
eps = ep*eo;

dipole = (eps+(2*ems))./(sigp + (2.*sigm));

R1 = 1./(2.*pi.*dipole);

% end of function
```

Functions from section (7.4.2)

Ref [7/8]

SCHWARZPLOTTER.M

```
% This script calculates the lyklema 1 polarisation factor
% for a given vector of conductivities . The program
% plots a 3D graph, calculates all the zero points
% and plots them on a 2D graph.

clear all

global ep em eo sp a R kB qo T F tau zeta eta scd mob kappa D z;

ep = 2.55; em = 78.54; eo = 8.85e-12;  % permittivity stuff
sp = 0.0; D = 1.957e-9; z = 1;         % conductivity stuff
n1 = 3; n2 = 9; N = 50;     % frequency vector numbers
m1 = -4; m2 = 1; M = 60;               % conductivity vector numbers
a = 141e-9;                            % particle radius
zerr = 0.01;                           % zero error value (percent)
R = 8.3145; T = 295; F = 9.6485e4;     % more constants
kB = 1.38e-23;                         % boltzmann's constant
zeta = 0.05; qo = 1.6e-19; % zeta potential / electron
eta = 8.4e-4;                          % viscosity of water
Na = 6.022e26;
                        % Avogadro's number in SI units
mob = 7.56e-8;
scd = 0.028;
% variable definition stage

f = logspace(n1,n2,N);
sigm = logspace(m1,m2,M);

% plotting bit

DCM = []; ICM = [];
for l = 1.M
  sm = sigm(l);
  Conc = 0.0852*(sm^1.0245);
          % equation from experimental data - KCl
  tau = (a*a)/(2*D);
  kappa = sqrt((2*z*z*qo*qo*Na*Conc)/(em*eo*kB*T));
  DIPval = schwarz(f,sm);
  for k = 1:(N-1)
    trans1 = real(DIPval(k));  f1 = f(k);
    trans2 = real(DIPval(k+1)); f2 = f(k+1);
    test = trans1*trans2;
    if test < 0
      error = 101; zerof = [];
      while error > zerr
        shortf = [f1 f2];
        Conc = 0.0852*(sm^1.0245);
        tau = (a*a)/(2*D);
                                    kappa =
sqrt((2*z*z*qo*qo*Na*Conc)/(em*eo*kB*T));
        trans1 = real(schwarz(shortf,sm));
        meanf = (f1+f2)/2;
        Conc = 0.0852*(sm^1.0245);
        tau = (a*a)/(2*D);
                                    kappa =
sqrt((2*(z^2)*(qo^2)*Na*Conc)/(em*eo*kB*T));
        trans = real(schwarz(shortf,sm));
        test1 = trans*trans1(1);
        test2 = trans*trans1(2);
                        if test1 < 0
                        f2 = meanf; zerof = (meanf+f1)/2;
                        end
                        if test2 < 0
                        f1 = meanf; zerof = (meanf+f2)/2;
                        end
        error = ((abs(meanf-zerof))*100)/zerof;
      end
      zeros = [zeros zerof];
    end
  end
  DCM = [DCM;real(DIPval)];
  ICM = [ICM,imag(DIPval)];
end

% work out the plotting vector for the zeros
goo = size(zeros);
for kl = 1:(goo(2)-1)
  xover(kl) = zeros(kl+1);
end
for lk = goo(2):M
  xover(lk) = 1;
end

mesh(log10(sigm),log10(f),DCM');
Ylabel('log(frequency)')
Xlabel('log(conductivity)')
axis([m1 m2 n1 n2 -1 1])
%Title('3d plot of the real factor (schwarz) for sphere')
Title('3d plot of the real factor (schurr) for sphere')
view(135,45)

%figure
%mesh(log10(sigm),log10(f),ICM');
%Ylabel('log(frequency)')
%Xlabel('log(medium conductivity)')
%axis([m1 m2 n1 n2 -1 1])
%Title('3d plot of the imaginary factor (schwarz) for sphere')
%view(135,45)

%figure
%loglog(sigm,xover)
%Xlabel('log(medium conductivity)')
%Ylabel('zero force frequency (Hz)')
%axis([1e-4 1e1 1e5 1e8])
```

SCHWARZ.M

```
function [R1] = schwarz(freq,sigm)

% This function plots the maxwell-wagner + Schwarz/Schurr interfacial
% polarisation terms for a prolate ellipsoidal particle. There
% are of course three - because there are three axes.

% The function needs the following variables defined as global
% ep - particle perm, em - medium perm, sp - particle cond
% scd - surface charge dens, u - mobility, a - particle radius
% eo - perm of free space

global ep em eo sp a R kB qo T F tau zeta eta scd mob kappa D z;

% dipole calculation

w = 2.*pi.*freq;
surfc = (2*mob*scd/a);
efac = tau./(1 + (w.*w.*tau.*tau));
sfac = (w.*tau.*tau)./(1 + (w.*w.*tau.*tau));
ems = em*eo - j.*(sigm./w);
%Scharwz
%eps = ep*eo + (surfc.*efac) - j.*((sp./w) + (surfc.*sfac));
%Schurr
eps = ep*eo + (surfc.*efac) - j.*((sp./w) + (surfc./w) + (surfc.*sfac));

dipole = (eps-ems)./(eps + (2.*ems));

R1 = dipole;

% end of function
```

Ref [9]

DLYK2PLOTTER.M

```
% This script calculates the lyklema diffuse polarisation factor
% for a given vector of conductivities . The program
% plots a 3D graph, calculates all the zero points
% and plots them on a 2D graph.

clear all

global em eo a qo kB R F T zeta eta kappa D z;

ep = 2.55; em = 78.54; eo = 8.85e-12;  % permittivity stuff
sp = 0; D = 1.957e-9; z = 1;           % conductivity stuff
n1 = 3; n2 = 8; N = 50;    % frequency vector numbers
m1 = -4; m2 = 1; M = 100;              % conductivity vector numbers
a = 46.5e-9;                           % particle radius
zerr = 0.01;                           % zero error value (percent)
R = 8.3145; T = 295; F = 9.6485e4;     % more constants
kB = 1.38e-23;                         % boltzmann's constant
zeta = -0.0457; qo = 1.6e-19;          % zeta potential / electron
eta = 8.4e-4;                          % viscosity of water
Na = 6.022e26;
                        % Avogadro's number in SI units
% variable definition stage

f = logspace(n1,n2,N);
sigm = logspace(m1,m2,M);

% plotting bit

DCM = []; ICM = [];
for l = 1:M
  sm = sigm(l);
  Conc = 0.0852*(sm^1.0245);% equation from experimental - KCl
  kappa = sqrt((2*(z^2)*(qo^2)*Na*Conc)/(em*eo*kB*T));
  DIPval = lyk2(f,sm);
  for k = 1:(N-1)
    trans1 = real(DIPval(k));   f1 = f(k);
    trans2 = real(DIPval(k+1)); f2 = f(k+1);
    test = trans1*trans2;
    if test < 0
      error = 101; zerof = [];
      while error > zerr
        shortf = [f1 f2];
        Conc = 0.0852*(sm^1.0245);
        tau = (a*a)/(2*D);
kappa = sqrt((2*(z^2)*(qo^2)*Na*Conc)/(em*eo*kB*T));
        trans1 = real(lyk2(shortf,sm));
        meanf = (f1+f2)/2;
        Conc = 0.0852*(sm^1.0245);
        tau = (a*a)/(2*D);
kappa = sqrt((2*(z^2)*(qo^2)*Na*Conc)/(em*eo*kB*T));
        trans = real(lyk2(meanf,sm));
        test1 = trans*trans1(1);
        test2 = trans*trans1(2);
                              if test1 < 0
                              f2 = meanf; zerof = (meanf+f1)/2;
                              end
                              if test2 < 0
                              f1 = meanf; zerof = (meanf+f2)/2;
                                        end
        error = ((abs(meanf-zerof))*100)/zerof;
      end
      zeros = [zeros zerof];
    end
  end
  DCM = [DCM,real(DIPval)];
  ICM = [ICM,imag(DIPval)];
end

% work out the plotting vector for the zeros
goo = size(zeros);
for kl = 1:(goo(2)-1)
  xover(kl) = zeros(kl+1);
end
for lk = goo(2):M
  xover(lk) = 1;
end

mesh(log10(sigm),log10(f),DCM');
Ylabel('log(frequency)')
Xlabel('log(medium conductivity)')
%axis([m1 m2 n1 n2 -2 1])
Title('3d plot of the real factor (lyklema diffuse) for sphere')
view(135,45)

%figure
%loglog(sigm,xover)
%Xlabel('log(medium conductivity)')
%Ylabel('zero force frequency (Hz)')
%axis([1e-4 1e1 1e5 1e8])
```

LYK2.M

```
function [R1] = lyk1(freq,sigm)

% The function needs the following variables defined as global
% ep - particle perm, em - medium perm, sp - particle cond
% scd - surface charge dens, u - mobility, a - particle radius
% eo - perm of free space

global em eo a qo kB R F T zeta eta kappa D z;

% basics

ka = kappa*a;
w = 2.*pi.*freq;
m = 2*eo*em*R*R*T*T/(3*eta*D*F*F);
tau = a*a/(2*D);
DW = sqrt(w.*tau);

% simplification things

Fac1 = F*zeta/(R*T);
Fac2 = cosh(Fac1*(z/4));
Fac3 = cosh(Fac1*(z/2));

% The factors - reverse order to dipole

I3minus = -((3*Fac3) - exp(z*Fac1) - 2)/Fac3;
I3plus = -((3*Fac3) - exp(-1*z*Fac1) - 2)/Fac3;
I2cminus = ((2/z)*Fac1) - ((4/(z*z))*(1 - exp((z/2)*Fac1))) -
(16*log(Fac2));
I2cplus = ((2/z)*Fac1) - ((4/(z*z))*(1 - exp(-1*(z/2)*Fac1))) -
(16*log(Fac2));
I2minus = (2*Fac1) + ((4/z)*(1 - exp((z/2)*Fac1)));
I2plus = (2*Fac1) - ((4/z)*(1 - exp(-1*(z/2)*Fac1)));
I1minus = -2*exp((z*Fac1) - 1);
I1plus = -2*exp(-1*((z*Fac1) + 1));

alpha1minus = (z/ka)*(I1minus + I3minus);
alpha1plus = (z/ka)*(I1plus + I3plus);
alphacminus = (1/ka)*(((3/2)*m*I2cminus) - I1minus);
alphacplus = (1/ka)*(((3/2)*m*I2cplus) - I1plus);
alphaminus = (1/ka)*(((3/2)*m*I2minus) + (z*I1minus));
alphaplus = (1/ka)*(((3/2)*m*I2plus) - (z*I1plus));

A2 = ((z - alphaminus)*(1 + alpha1plus)) + ((z + alphaplus)*(1 +
alpha1minus));
A1 = ((z - alphaminus)*(1 + alphacplus)) + ((z + alphaplus)*(1 +
alphacminus));
a2 = (alphaplus*(1 + alpha1minus)) - (alphaminus*(1 + alpha1plus));
a1 = (alphaplus*(1 + alphacminus)) - (alphaminus*(1 + alphacplus));

% dipole calculation

numer = (a1.*(1 + DW)) + j.*((a1.*DW) + (a2.*DW.*DW));
denom = (A1.*(1 + DW)) + j.*((A1.*DW) + (A2.*DW.*DW));

dipole = - (3/2)*(numer./denom);

R1 = dipole;

% end of function
```

DLYK1PLOTTER.M

```
% This script calculates the lyklema 1 polarisation factor
% for a given vector of conductivities. The program
% plots a 3D graph, calculates all the zero points
% and plots them on a 2D graph.

clear all

global ep em eo sp a R kB qo T F tau zeta eta kappa D z;

ep = 2.55; em = 78.54; eo = 8.85e-12;  % permittivity stuff
sp = 0; D = 1.957e-9; z = 1;           % conductivity stuff
n1 = 3; n2 = 8, N = 50;    % frequency vector numbers
m1 = -4; m2 = 1; M = 60;               % conductivity vector numbers
a = 46.5e-9;                           % particle radius
zerr = 0.01;                           % zero error value (percent)
R = 8.3145; T = 295; F = 9.6485e4;     % more constants
kB = 1.38e-23;                         % boltzmann's constant
zeta = 0.0514; qo = 1.6e-19;           % zeta potential / electron
eta = 8.4e-4;                          % viscosity of water
Na = 6.022e26;             % Avogadro's number in SI units

% variable definition stage

f = logspace(n1,n2,N);
sigm = logspace(m1,m2,M);

% plotting bit

DCM = []; ICM = [];
for l = 1:M
  sm = sigm(l);
  Conc = 0.0852*(sm^1.0245);
            % equation from experimental data - KCl
  tau = (a*a)/(2*D);
  kappa = sqrt((2*z*z*qo*qo*Na*Conc)/(em*eo*kB*T));
  DIPval = lyk1(f,sm);
for k = 1:(N-1)
  trans1 = real(DIPval(k));  f1 = f(k);
  trans2 = real(DIPval(k+1)); f2 = f(k+1);
  test = trans1*trans2;
  if test < 0
    error = 101; zerof = [];
    while error > zerr
      shortf = [f1 f2];
      Conc = 0.0852*(sm^1.0245);
      tau = (a*a)/(2*D);
kappa = sqrt((2*z*z*qo*qo*Na*Conc)/(em*eo*kB*T));
      trans1 = real(lyk1(shortf,sm));
      meanf = (f1+f2)/2;
      Conc = 0.0852*(sm^1.0245);
      tau = (a*a)/(2*D);
kappa = sqrt((2*(z^2)*(qo^2)*Na*Conc)/(em*eo*kB*T));
      trans = real(lyk1(meanf,sm));
      test1 = trans*trans1(1);
      test2 = trans*trans1(2);
                        if test1 < 0
                        f2 = meanf; zerof = (meanf+f1)/2;
                        end
                        if test2 < 0
                        f1 = meanf; zerof = (meanf+f2)/2;
                                end
      error = ((abs(meanf-zerof))*100)/zerof;
    end
    zeros = [zeros zerof];
  end
end
DCM = [DCM,real(DIPval)];
  ICM = [ICM;imag(DIPval)];
end

% work out the plotting vector for the zeros
goo = size(zeros);
for kl = 1:(goo(2)-1)
  xover(kl) = zeros(kl+1);
end
for lk = goo(2):M
  xover(lk) = 1;
end

mesh(log10(sigm),log10(f),DCM');
Ylabel('log(frequency)')
Xlabel('log(medium conductivity)')
axis([m1 m2 n1 n2 -1 1])
Title('3d plot of the real factor (lyklema - book) for sphere')
view(135,45)

%figure
%mesh(log10(sigm),log10(f),ICM');
%Ylabel('log(frequency)')
%Xlabel('log(medium conductivity)')
%axis([m1 m2 n1 n2 -1 1])
%Title('3d plot of the imaginary factor (lyklema 1) for sphere')
%view(135,45)

%figure
%loglog(sigm,xover)
%Xlabel('log(medium conductivity)')
%Ylabel('zero force frequency (Hz)')
%axis([1e-4 1e1 1e5 1e8])
```

LYK1.M

```
function [R1] = lyk1(freq,sigm)

% This function plots the Lyklema book polarisation

% The function needs the following variables defined as global
% ep - particle perm, em - medium perm, sp - particle cond
% scd - surface charge dens, u - mobility, a - particle radius
% eo - perm of free space

global ep em eo sp a R kB qo T F tau zeta eta kappa D z;

% dipole calculation

w = 2.*pi.*freq;
wtau = w.*tau;
gamma = 1 - (((wtau.^1.5)-(j.*wtau))./((1+(wtau.^0.5)).*(1+wtau)));
m = (2*eo*em*kB*kB*T*T)/(3*eta*qo*qo*D);
%m = ((R*T/F)^1.5)*((2*eo*em)/(3*eta*D))  WRONG!!!
Dud =
(2./(kappa.*a)).*(1+((3.*m)./(z.^2))).*cosh(((z.*F.*zeta)./(2.*R.*T))-
1);

dipole = 0.5 - (3.*Dud)./(2.*(1 + Dud.*(1+gamma)));

R1 = dipole;

% end of function
```

Ref [12]

DMINOR1PLOTTER.M

```
% This script calculates the minor Ch3 polarisation factor
% for a given vector of conductivities . The program
% plots a 3D graph, calculates all the zero points
% and plots them on a 2D graph.

clear all

global em eo a kB qo R T F tau zeta eta kappa mob D z Theta h;

ep = 2.5; em = 78.54; eo = 8.85e-12;    % permittivity stuff
sp = 0; D = 1.9e-9; z = 1;              % conductivity stuff
n1 = 3; n2 = 8; N = 50;    % frequency vector numbers
m1 = -4; m2 = 1; M = 60;                % conductivity vector numbers
a = 141e-9;                             % particle radius
zerr = 0.01;                            % zero error value (percent)
R = 8.3145; T = 295; F = 9.6485e4;      % more constants
kB = 1.38e-23;                          % boltzmann's constant
zeta = -0.0429; qo = 1.6e-19;           % zeta potential / electron
eta = 8.4e-4;                           % viscosity of water
Na = 6.022e26;          % Avogadro's number in SI units
mob = 7.69e-8; D = 1.957e-9;
Theta = 1;
h = 0;

% variable definition stage

f = logspace(n1,n2,N);
sigm = logspace(m1,m2,M);

% plotting bit

DCM = []; ICM = [];
for l = 1:M
  sm = sigm(l);
  Conc = 0.0852*(sm^1.0245);
            % equation from experimental data - KCl
  tau = (a*a)/(2*D);
  kappa = sqrt((2*(z^2)*(qo^2)*Na*Conc)/(em*eo*kB*T));
  DIPval = minor1(f,sm);
  for k = 1:(N-1)
    trans1 = real(DIPval(k));  f1 = f(k);
    trans2 = real(DIPval(k+1)); f2 = f(k+1);
    test = trans1*trans2;
    if test < 0
      error = 101; zerof = [];
      while error > zerr
        shortf = [f1 f2];
        Conc = 0.0852*(sm^1.0245);
        tau = (a*a)/(2*D);
kappa = sqrt((2*(z^2)*(qo^2)*Na*Conc)/(em*eo*kB*T));
        trans1 = real(minor1(shortf,sm));
        meanf = (f1+f2)/2;
        Conc = 0.0852*(sm^1.0245);
        tau = (a*a)/(2*D);
kappa = sqrt((2*(z^2)*(qo^2)*Na*Conc)/(em*eo*kB*T));
        trans = real(minor1(meanf,sm));
        test1 = trans*trans1(1);
        test2 = trans*trans1(2);
                        if test1 < 0
                        f2 = meanf; zerof = (meanf+f1)/2;
                        end
                        if test2 < 0
                        f1 = meanf; zerof = (meanf+f2)/2;
                                end
      error = ((abs(meanf-zerof))*100)/zerof;
    end
      zeros = [zeros zerof];
    end
  end
  DCM = [DCM;real(DIPval)];
  ICM = [ICM;imag(DIPval)];
end

% work out the plotting vector for the zeros
goo = size(zeros);
for kl = 1:(goo(2)-1)
  xover(kl) = zeros(kl+1);
end
for lk = goo(2):M
  xover(lk) = 1;
end

mesh(log10(sigm),log10(f),DCM');
Ylabel('log(frequency)')
Xlabel('log(medium conductivity)')
axis([m1 m2 n1 n2 -1 1])
Title('3d plot of the real factor (minor) for sphere')
view(135,45)

%figure
%mesh(log10(sigm),log10(f),ICM');
%Ylabel('log(frequency)')
%Xlabel('log(medium conductivity)')
%axis([m1 m2 n1 n2 -1 1])
%Title('3d plot of the imaginary factor (lyklema 1) for sphere')
%view(135,45)

%figure
%loglog(sigm,xover)
%Xlabel('log(medium conductivity)')
%Ylabel('zero force frequency (Hz)')
%axis([1e-4 1e1 1e5 1e8])
```

MINOR1.M

```
function [R1] = minor1(freq,sigm)

% This function plots the minor Ch3 polarisation

global em eo a kB qo R T F tau zeta eta kappa mob D z Theta h;

% dipole calculation

w = 2.*pi.*freq;
wt = w.*tau;
%m2 = (2*eo*em*kB*kB*T*T)/(3*eta*qo*qo*D);
m2 = (2*eo*em*kB*T*z)/(3*eta*mob*qo);
Du2 = (2/(a*kappa))*(1 + Theta + ((3*m2)/(z*z)))*(exp((-
z*qo*zeta)/(2*kB*T)) - 1);
gamma = ((wt.^(1.5)) + (i.*wt))./((1 + sqrt(wt)).*(1 + wt));

numer = 3*Du2*(1 + h);
denom = 2.*(2 + (Du2.*(2 - (gamma.*(1-h)))));

dipole = 0.5 - (numer./denom);

R1 = dipole;

% end of function
```

DFIX1PLOTTER.M

```
% This script calculates the fixman polarisation factor
% for a given vector of conductivities . The program
% plots a 3D graph, calculates all the zero points
% and plots them on a 2D graph.

clear all

global em eo a T kB zeta eta kappa z D qo;

ep = 2.5; em = 78.54; eo = 8.85e-12;    % permittivity stuff
sp = 0; D = 1.9e-9; z = 1;              % conductivity stuff
n1 = 3; n2 = 8; N = 50;    % frequency vector numbers
m1 = -4; m2 = 1; M = 60;                % conductivity vector numbers
a = 46.5e-9;                            % particle radius
zerr = 0.01;                            % zero error value (percent)
R = 8.3145; T = 295; F = 9.6485e4;      % more constants
kB = 1.38e-23;                          % boltzmann's constant
zeta = -0.0457; qo = 1.6e-19;           % zeta potential / electron
eta = 8.4e-4;                           % viscosity of water
Na = 6.022e26;                          % Avogadro's number in SI
units
% variable definition stage

f = logspace(n1,n2,N);
sigm = logspace(m1,m2,M);

% plotting bit

DCM = []; ICM = [];
for l = 1:M
  sm = sigm(l);
  Conc = 0.0852*(sm^1.0245);
            % equation from experimental data - KCl
  tau = (a*a)/(2*D);
  kappa = sqrt((2*(z^2)*(qo^2)*Na*Conc)/(em*eo*kB*T));
  DIPval = fix1(f,sm);
for k = 1:(N-1)
  trans1 = real(DIPval(k));  f1 = f(k);
  trans2 = real(DIPval(k+1)); f2 = f(k+1);
  test = trans1*trans2;
  if test < 0
    error = 101; zerof = [];
    while error > zerr
      shortf = [f1 f2];
      Conc = 0.0852*(sm^1.0245);
      tau = (a*a)/(2*D);
kappa = sqrt((2*(z^2)*(qo^2)*Na*Conc)/(em*eo*kB*T));
      trans1 = real(fix1(shortf,sm));
      meanf = (f1+f2)/2;
      Conc = 0.0852*(sm^1.0245);
      tau = (a*a)/(2*D);
kappa = sqrt((2*(z^2)*(qo^2)*Na*Conc)/(em*eo*kB*T));
      trans = real(fix1(meanf,sm));
      test1 = trans*trans1(1);
      test2 = trans*trans1(2);
                        if test1 < 0
                        f2 = meanf; zerof = (meanf+f1)/2;
                        end
                        if test2 < 0
                        f1 = meanf; zerof = (meanf+f2)/2;
                                  end
      error = ((abs(meanf-zerof))*100)/zerof;
      end
      zeros = [zeros zerof];
    end
  end
  DCM = [DCM,real(DIPval)];
  ICM = [ICM;imag(DIPval)],
end

% work out the plotting vector for the zeros
goo = size(zeros);
for kl = 1:(goo(2)-1)
  xover(kl) = zeros(kl+1);
end
for lk = goo(2):M
  xover(lk) = 1;
end
mesh(log10(sigm),log10(f),DCM');
Ylabel('log(frequency)')
Xlabel('log(medium conductivity)')
%axis([m1 m2 n1 n2 -1 1])
Title('3d plot of the real factor (fixman) for sphere')
view(135,45)

%figure
%mesh(log10(sigm),log10(f),ICM');
%Ylabel('log(frequency)')
%Xlabel('log(medium conductivity)')
%axis([m1 m2 n1 n2 -1 1])
%Title('3d plot of the imaginary factor (lyklema 1) for sphere')
%view(135,45)

%figure
%loglog(sigm,xover)
%Xlabel('log(medium conductivity)')
%Ylabel('zero force frequency (Hz)')
%axis([1e-5 1e10 1e1 1e10])
```

FIX1.M

```
function [R1] = fix1(freq,sigm)

% This function plots the fixman polarisation
% The function needs the following variables defined as global
% ep - particle perm, em - medium perm, sp - particle cond
% scd - surface charge dens, u - mobility, a - particle radius
% eo - perm of free space

global em eo a T kB zeta eta kappa z D qo;

% dipole calculation

alpha = kappa*a;
delta = 0.1715;              % for KCl apparently
w = 2.*pi.*freq;
%wr = (w.*(7.136e-10))./(kB.*T.*kappa.*kappa);  % value for water
wr = w.*((6.*pi.*eta.*qo.*qo)./(kB.*kB.*T.*T.*D.*kappa.*kappa));
lambda = sqrt(i.*delta.*wr);
x = lambda.*alpha;
zetar = (qo*zeta)/(kB*T);

z1 = z;       z2 = -z;
Zed1 = z1/(z1*z1);Zed2 = z2/(z1*z1);
K1 = tanh(z1*zetar/4);     K2 = tanh(z2*zetar/4);
I1thing = -(4*K1)/(1+K1);I2thing = -(4*K2)/(1+K2);
I11 = 16*((K1/(1+K1))-log(1+K1));    I22 = 16*((K2/(1+K2))-
log(1+K2));
I12 = -8*log(1-(K2*K2));                  21 = -8*log(1-(K1*K1));
IFac1 = (3*delta*Zed1)/(2*z1);IFac2 = (3*delta*Zed2)/(2*z2);
A11 = I1thing-(IFac1*I11);A22 = I2thing-(IFac2*I22);
A12 = -(IFac2*I12);                       A21 = -(IFac1*I21);
L1 = z1-((2/alpha)*(A11 + A12)*z2);  L2 = z2-((2/alpha)*(A21 +
A22)*z1);
J1 = -(2*z1)-((2/alpha)*(A11 + A12)*z2);
J2 = -(2*z2)-((2/alpha)*(A21 + A22)*z1);
H1 = ((1./alpha).*(2+(2.*x)+(x.*x))) +
((2./(alpha*alpha)).*(1+x).*(A11+A12));
H2 = ((1./alpha).*(2+(2.*x)+(x.*x))) +
((2./(alpha*alpha)).*(1+x).*(A21+A22));

alpha3 = alpha*alpha*alpha;

numer = (L1.*H2)-(L2.*H1);
denom = (J1.*H2)-(J2.*H1);

dipole = (numer./denom);

R1 = dipole;

% end of function
```

Ref [14,15]

DOBRIENPLOTTER.M

```
% This script calculates the lyklema 1 polarisation factor
% for a given vector of conductivities . The program
% plots a 3D graph, calculates all the zero points
% and plots them on a 2D graph.

clear all

global ep em eo sp a kB T qo tau zeta eta kappa D z;

ep = 2.5; em = 78.54; eo = 8.85e-12;   % permittivity stuff
sp = 0;  z = 1;                        % conductivity stuff
n1 = 3; n2 = 8; N = 50;     % frequency vector numbers
m1 = -4; m2 = 1; M = 60;               % conductivity vector numbers
a = 46.5e-9;                           % particle radius
zerr = 0.01;                           % zero error value (percent)
R = 8.3145; T = 295; F = 9.6485e4;     % more constants
kB = 1.38e-23;                         % boltzmann's constant
zeta = 0.0457; qo = 1.6e-19;           % zeta potential / electron
eta = 8.4e-4;                          % viscosity of water
Na = 6.022e26;                         % Avogadro's number in SI
units
D = 1.957e-9;

% variable definition stage

f = logspace(n1,n2,N);
sigm = logspace(m1,m2,M);

% plotting bit

DCM = []; ICM = [];
for l = 1.M
  sm = sigm(l);
  Conc = 0.0852*(sm^1.0245);
          % equation from experimental data - KCl
tau = (a*a)/(2*D);
kappa = sqrt((2*(z^2)*(qo^2)*Na*Conc)/(em*eo*kB*T));
DIPval = obrien(f,sm);
  for k = 1:(N-1)
  trans1 = real(DIPval(k));   f1 = f(k);
  trans2 = real(DIPval(k+1)); f2 = f(k+1);
  test = trans1*trans2;
  if test < 0
    error = 101; zerof = [];
    while error > zerr
      shortf = [f1 f2];
      Conc = 0.0852*(sm^1.0245);
kappa = sqrt((2*(z^2)*(qo^2)*Na*Conc)/(em*eo*kB*T));
      trans1 = real(obrien(shortf,sm));
      meanf = (f1+f2)/2;
      Conc = 0.0852*(sm^1.0245);
kappa = sqrt((2*(z^2)*(qo^2)*Na*Conc)/(em*eo*kB*T));
      trans = real(obrien(meanf,sm));
      test1 = trans*trans1(1);
      test2 = trans*trans1(2);
                          if test1 < 0
                          f2 = meanf; zerof = (meanf+f1)/2;
                          end
                          if test2 < 0
                          f1 = meanf; zerof = (meanf+f2)/2;
                                  end
      error = ((abs(meanf-zerof))*100)/zerof;
    end
    zeros = [zeros zerof];
  end
end
  DCM = [DCM,real(DIPval)];
  ICM = [ICM;imag(DIPval)];
end

% work out the plotting vector for the zeros
goo = size(zeros);
for kl = 1:(goo(2)-1)
  xover(kl) = zeros(kl+1);
end
for lk = goo(2).M
  xover(lk) = 1;
end
mesh(log10(sigm),log10(f),DCM');
Ylabel('log(frequency)')
Xlabel('log(medium conductivity)')
axis([m1 m2 n1 n2 -1 1])
Title('3d plot of the real factor (hinch/obrien) for sphere')
view(145,45)

%figure
%mesh(log10(sigm),log10(f),ICM');
%Ylabel('log(frequency)')
%Xlabel('log(medium conductivity)')
%axis([m1 m2 n1 n2 -1 1])
%Title('3d plot of the imaginary factor (lyklema 1) for sphere')
%view(135,45)

%figure
%loglog(sigm,xover)
%Xlabel('log(medium conductivity)')
%Ylabel('zero force frequency (Hz)')
%axis([1e-4 1e1 1e5 1e8])
```

OBRIEN.M

```
function [R1] = obrien(freq,sigm)

% This function plots the Lyklema book polarisation

% The function needs the following variables defined as global
% ep - particle perm, em - medium perm, sp - particle cond
% scd - surface charge dens, u - mobility, a - particle radius
% eo - perm of free space

global ep em eo sp a kB T qo tau zeta eta kappa D z;

% dipole calculation

w = 2.*pi.*freq;
iwt = i.*w.*tau;
m = (2*eo*em*kB*kB*T*T)/(3*eta*qo*qo*D);
beta = (2/(kappa*a))*(1 +
((3*m)/(z*z)))*exp((qo*z*zeta)/(2*kB*T));
delta = (1 + sqrt(iwt))./(1 + sqrt(iwt) + (iwt./2));

dipole = 0.5 - (1.5).*(beta./(2 + beta.*(1 + delta)));

R1 = dipole;

% end of function
```

Ref [16]

XFENGPLOTTER.M

```
% This script calculates the polarisation factor from ref 16
% for a given vector of conductivities . The program
% plots a 3D graph, calculates all the zero points
% and plots them on a 2D graph.

clear all
global ep em eo sp a R kB qo T F tau zeta eta scd mob kappa D z;

ep = 2.55; em = 78.54; eo = 8.85e-12;  % permittivity stuff
sp = 0.017; D = 1.957e-9; z = 1;       % conductivity stuff
n1 = 3; n2 = 8; N = 50;    % frequency vector numbers
m1 = -4; m2 = 1; M = 200;              % conductivity vector numbers
a = 141e-9;                            % particle radius
zerr = 0.01;                           % zero error value (percent)
R = 8.3145; T = 295; F = 9 6485e4;     % more constants
kB = 1.38e-23;                         % boltzmann's constant
zeta = 0.05; qo = 1.6e-19; % zeta potential / electron
eta = 8.4e-4;                          % viscosity of water
Na = 6.022e26;                         % Avogadro's number in SI
units
mob = 7.69e-8;
scd = 0.0;
salt = 1;                              % salt variable ::::
particle = 282;                        % a data switch
% variable definition stage

f = logspace(n1,n2,N);
sigm = logspace(m1,m2,M);

% plotting bit

DCM = []; ICM = [];
for l = 1 M
  sm = sigm(l);
  Conc = 0.0852*(sm^1.0245);% equation from experimental - KCl
  tau = (a*a)/(2*D);
  kappa = sqrt((2*z*z*qo*qo*Na*Conc)/(em*eo*kB*T));
  DIPval = xfeng(f,sm);
  for k = 1 (N-1)
    trans1 = real(DIPval(k));   f1 = f(k);
    trans2 = real(DIPval(k+1)); f2 = f(k+1);
    test = trans1*trans2;
    if test < 0
      error = 101; zerof = [];
      while error > zerr
        shortf = [f1 f2];
        Conc = 0.0852*(sm^1.0245);
        tau = (a*a)/(2*D);
kappa = sqrt((2*z*z*qo*qo*Na*Conc)/(em*eo*kB*T));
        trans1 = real(xfeng(shortf,sm));
        meanf = (f1+f2)/2;
        Conc = 0.0852*(sm^1.0245);
        tau = (a*a)/(2*D);
kappa = sqrt((2*(z^2)*(qo^2)*Na*Conc)/(em*eo*kB*T));
        trans = real(xfeng(meanf,sm));
        test1 = trans*trans1(1);
        test2 = trans*trans1(2);
                              if test1 < 0
                              f2 = meanf; zerof = (meanf+f1)/2
                              end
                              if test2 < 0
                              f1 = meanf; zerof = (meanf+f2)/2;
                                        end
          error = ((abs(meanf-zerof))*100)/zerof;
        end
        zeros = [zeros zerof];
      end
    end
    DCM = [DCM;real(DIPval)];
    ICM = [ICM;imag(DIPval)];
end

% work out the plotting vector for the zeros
goo = size(zeros);
for kl = 1:(goo(2)-1)
  xover(kl) = zeros(kl+1);
end
for lk = goo(2):M
  xover(lk) = 1;
end

mesh(log10(sigm),log10(f),DCM');
Ylabel('log(frequency)')
Xlabel('log(conductivity)')
axis([m1 m2 n1 n2 -1 1])
Title('3d plot of the real factor (zhou) for sphere')
view(135,45)
%figure
%mesh(log10(sigm),log10(f),ICM');
%Ylabel('log(frequency)')
%Xlabel('log(medium conductivity)')
%axis([m1 m2 n1 n2 -1 1])
%Title('3d plot of the imaginary factor (schwarz) for sphere')
%view(135,45)
figure
loglog(sigm,xover,'b-.')
Xlabel('log(medium conductivity)')
Ylabel('zero force frequency (Hz)')
axis([1e-4 1e1 1e5 1e8])

hold on
switch particle
case 557,
  data557; loglog(conddata,posdata,'kx'); loglog(conddata,negdata,'ks');
  axis([1e-4 1e1 1e4 1e7])
case 282,
  data282; loglog(conddata,posdata,'kx'); loglog(conddata,negdata,'ks');
  axis([1e-4 1e1 1e3 1e7])
case 216,
  data216; loglog(conddata,posdata,'kx'); loglog(conddata,negdata,'ks');
  axis([1e-4 1e1 1e5 1e7])
case 93,
  data93; loglog(conddata,posdata,'kx'); loglog(conddata2,negdata,'ks');
  axis([1e-4 1e1 1e6 1e8])
end
hold off
```

XFENG.M

```
function [R1] = schwarz(freq,sigm)

% This function plots the maxwell-wagner + Schwarz/Schurr interfacial
% polarisation terms for a prolate ellipsoidal particle. There
% are of course three - because there are three axes.

% The function needs the following variables defined as global
% ep - particle perm, em - medium perm, sp - particle cond
% scd - surface charge dens, u - mobility, a - particle radius
% eo - perm of free space

global ep em eo sp a R kB qo T F tau zeta eta scd mob kappa D z;

% dipole calculation

A = 0.5;
palpha = 0.8;
w = 2.*pi.*freq;
surfc = (2*mob*scd/a);
sigp = sp + surfc + (A./(1 + ((j.*w.*tau).^palpha)));
ems = em*eo - j.*(sigm./w);
eps = ep*eo - j.*(sigp./w);

dipole = (eps-ems)./(eps + (2.*ems));

R1 = dipole;

% end of function
```

DISP2PLOTTER.M

```
% This script calculates the clausius-mossotti factor
% for a given vector of conductivities . The program
% plots a 3D graph, calculates all the zero points
% and plots them on a 2D graph.

clear all
global ep em eo sp a R kB qo T F tau1 zeta eta scd mob kappa D z;

ep = 2.55; em = 78.54; eo = 8.85e-12;   % permittivity stuff
sp = 0.017; scd = 0; mob = 7.56e-8;     % conductivity stuff
n1 = 3; n2 = 8, N = 50;     % frequency vector numbers
m1 = -4; m2 = 1; M = 60;                % conductivity vector numbers
a = 46.5e-9;                            % particle radius
D = 1.957e-9; scd = 0; zeta = 0.0514;
R = 8.3145; T = 295; F = 9.6485e4;      % more constants
kB = 1.38e-23;                          % boltzmann's constant
qo = 1.6e-19;                           % electron
eta = 8.4e-4;                           % viscosity of water
Na = 6.022e26;                          % Avogadro's number in SI
units
z = 1;
particle = 93;                          % a data switch zero off
zerr = 0.01;                            % zero error value (percent)
salt = 1;                               % salt variable ::::
                                % 1 - KCl; 2 - NaCl; 3 - KPO4
% variable definition stage

f = logspace(n1,n2,N);
sigm = logspace(m1,m2,M);

% plotting bit

DCM = []; ICM = [];
for l = 1:M
  sm = sigm(l);
  Conc = 0.0852*(sm^1.0245);
            % equation from experimental data - KCl
  kappa = sqrt((2*z*z*qo*qo*Na*Conc)/(em*eo*kB*T));
            Cd = eo*em*kappa*cosh(F*zeta/(2*R*T));
            ML = 1 + (F*zeta/(R*T*Cd));
  tau1 = a*a/(2*D*ML);
  %tau1 = a*a/(2*D);
  %tau1 = 1/(2*D*kappa*kappa);
  DIPval = cm2disp(f,sm);
  for k = 1:(N-1)
    trans1 = real(DIPval(k));  f1 = f(k);
    trans2 = real(DIPval(k+1)); f2 = f(k+1);
    test = trans1*trans2;
    if test < 0
      error = 101; zerof = [];
      while error > zerr
        shortf = [f1 f2];
Conc = 0.0852*(sm^1.0245);% equation from experimental - KCl
 kappa = sqrt((2*z*z*qo*qo*Na*Conc)/(em*eo*kB*T));
Cd = eo*em*kappa*cosh(F*zeta/(2*R*T));
ML = 1 + ((F*zeta)/(R*T*Cd));
        tau1 = a*a/(2*D*ML);
        %tau1 = a*a/(2*D);
        %tau1 = 1/(2*D*kappa*kappa);
            trans1 = real(cm2disp(shortf,sm));
            meanf = (f1+f2)/2;
Conc = 0.0852*(sm^1.0245);% equation from experimental - KCl
  kappa = sqrt((2*z*z*qo*qo*Na*Conc)/(em*eo*kB*T));
Cd = eo*em*kappa*cosh(F*zeta/(2*R*T));
ML = 1 + (F*zeta/(R*T*Cd));
      tau1 = a*a/(2*D*ML);
                                %tau1 = a*a/(2*D);
%tau1 = 1/(2*D*kappa*kappa);
      trans = real(cm2disp(meanf,sm));
test1 = trans*trans1(1);
test2 = trans*trans1(2);
                    if test1 < 0
                    f2 = meanf; zerof = (meanf+f1)/2;
                    end
                    if test2 < 0
                    f1 = meanf; zerof = (meanf+f2)/2;
                                end
error = ((abs(meanf-zerof))*100)/zerof;
      end
      zeros = [zeros zerof];
    end
  end
  DCM = [DCM,real(DIPval)];
  ICM = [ICM;imag(DIPval)];
end

% work out the plotting vector for the zeros
goo = size(zeros);
for kl = 1:(goo(2)-1)
  xover(kl) = zeros(kl+1);
end
for lk = goo(2):M
  xover(lk) = 1;
end

%mesh(log10(sigm),log10(f),DCM');
%Ylabel('log(frequency)')
%Xlabel('log(medium conductivity)')
%axis([m1 m2 n1 n2 -1 3])
%Title('3d plot of the clausius-mossotti factor for sphere')
%view(135,45)

%figure
loglog(sigm,xover,'b:')
Xlabel('log(medium conductivity)')
Ylabel('zero force frequency (Hz)')
axis([1e-4 1e1 1e1 1e9])

hold on
switch particle
case 557,
  data557; loglog(conddata,posdata,'kx'); loglog(conddata,negdata,'ks');
  axis([1e-4 1e1 1e4 1e7])
case 282,
  data282; loglog(conddata,posdata,'kx'); loglog(conddata,negdata,'ks');
  axis([1e-4 1e1 1e4 1e7])
case 216,
  data216; loglog(conddata,posdata,'kx'); loglog(conddata,negdata,'ks');
  axis([1e-4 1e1 1e4 1e7])
case 93,
  data93; loglog(conddata,posdata,'kx'); loglog(conddata2,negdata,'ks');
  axis([1e-4 1e1 1e5 1e8])
end
hold off
```

CM2DISP.M

```
function [R1] = cm2disp(freq,sigm)

% This function plots the maxwell-wagner interfacial
% polarisation terms for a prolate ellipsoidal particle. There
% are of course three - because there are three axes.

% The function needs the following variables defined as global
% ep - particle perm, em - medium perm, sp - particle cond
% scd - surface charge dens, u - mobility, a - particle radius
% eo - perm of free space

global ep em eo sp a R kB qo T F tau1 zeta eta scd mob kappa D z;

% dipole calculation

Constant=1;
w = 2.*pi.*freq;
surfc = (2*mob*scd/a);
sigp = sp + surfc;
ems = em*eo - j.*(sigm./w);
eps = ep*eo - j.*(sigp./w);

dipole1 = (eps-ems)./(eps + (2.*ems));
dipole2 = Constant./(1 + (j.*w.*tau1));
dipole = dipole1 + dipole2;

R1 = dipole;

% end of function
```

References

1. N.G.Green and H.Morgan (1997)
   Journal of Physics D: Applied Physics **30** 2626-2633
2. T.Muller, A.Gerardino, T.Schnelle, S.G.Shirley, F.Bordoni, G.de Gasperis, R.Leoni and G.Fuhr (1996)
   Journal of Physics D: Applied Physics **29** 340-349
3. J.Lyklema (1991) *Fundamentals of Interface and Colloid Science*
   Academic Press Ltd, London
4. P.C.Hiemenz (1986) *Principles of Colloid and Surface Chemistry*
   Marcel Dekker, New York
5. CRC Handbook of Chemistry and Physics 74ed. (1993-1994)
   CRC Press (David R. Lide, editor)
6. T.Kakutani, S.Shibatani and M.Sugai (1993)
   Bioelectrochemistry and Bioenergetics **31** 131-145
7. G.Schwarz (1962)
   Journal of Physical Chemistry **66** 2636-2642
8. J.M.Schurr (1964)
   Journal of Physical Chemistry **68** 2407-2413
9. J.Lyklema, S.S.Duhkin and V.N.Shilov (1983)
   Journal of Electroanalytical Chemistry **143** 1-21
10. M.M.Springer, A Korteweg and J.Lyklema (1983)
    Journal of Electroanalytical Chemistry **153** 55-66
11. J.Lyklema, M.M.Springer, V.N.Shilov and S.S.Duhkin (1986)
    Journal of Electroanalytical Chemistry **198** 19-26
12. M.Minor (1997) *Thesis: Published and unpublished work*
    University of Wageningen, The Netherlands
13. M.Fixman (1983)
    Journal of Chemical Physics **78** 1483-1491
14. E.J.Hinch, J..Sherwood, W.C.Chew and P.N.Sen (1984)
    Journal of the Chemical Society: Faraday Transactions **80** 535-551
15. R.W.O'Brien (1986)
    Journal of Colloid and Interface Science **113** 81-93
16. X-F.Zhou, G.H.Markx, R.Pethig and I.M.Eastwood (1995)
    Biochimica et Biophysica Acta **1245** 85-93

Chapter Eight

Results and discussion: Tobacco Mosaic Virus

8.1 Tobacco Mosaic Virus

Tobacco Mosaic Virus (TMV) is a cylindrical, unenveloped plant virus (Figure 8.1) [1,2]. Its internal structure is shown schematically in Figure (8.2). The TMV virion is a straight rigid tubule of length 300nm long and 9nm radius composed of 2130 identical coat protein units close packed in a helical form of pitch 2.3nm and $16\frac{1}{3}$ units per turn around a central cylindrical canal of radius 2nm. Around the canal there is also a single strand of RNA consisting of 6395 nucleotides follows the same helix, with 49 nucleotides per turn (3 per coat protein) and a radius of 4nm. The charge groups on the RNA are associated with groups of opposite charge near the inner surface of the coat protein units.

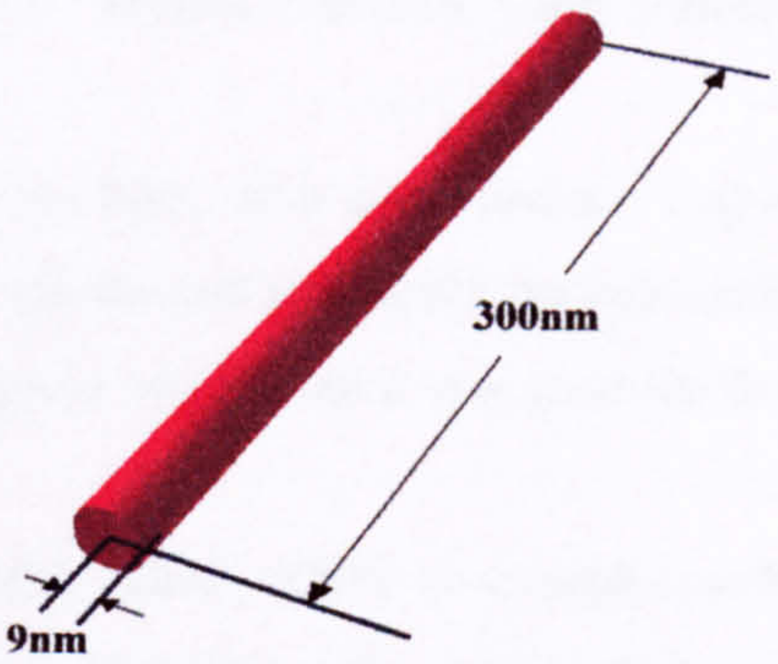

Figure (8.1) Dimensions and approximate shape of a single TMV virion

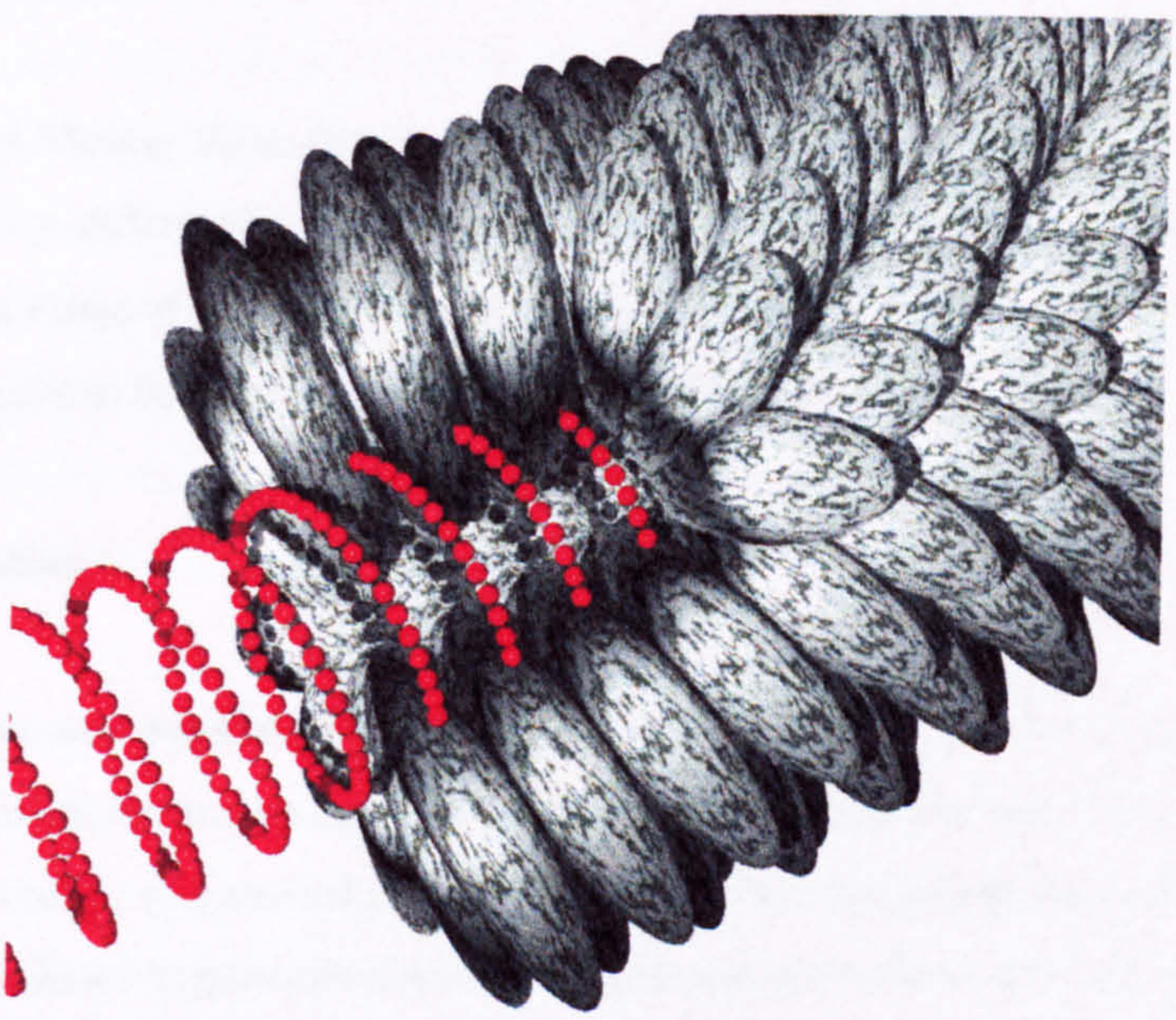

Figure (8.2) Cut-away schematic of the helical internal structure of TMV. There are 2130 individual coat proteins arranged in a helix of with $16\frac{1}{3}$ units per turn and a single strand of helical RNA of radius 4nm running through the protein units

The molecular weight of the RNA strand is 2.05×10^6 and a single coat protein, which consists of a chain of 158 amino acids, has a molecular weight of 1.75×10^4. A single TMV virion has a molecular weight of 3.93×10^7.

This part of the project was carried out with the invaluable assistance of Dr J.J.Milner (Div. Biochemistry and Molecular Biology, University of Glasgow) and the original stock of TMV inoculum was kindly donated by Professor T.M.A. Wilson (Scottish Crop Research Institute, Invergowrie, Scotland).

TMV is the most well-known and studied plant virus and, as a consequence, a great deal is known about its internal structure [2]. It has also been the test subject for the application of AC electric fields to small biological particles as long ago as 1939 when it was used for field orientation experiments [3].

Equivalent in volume to a spherical particle of radius 26nm, TMV is a much smaller particle than any previously studied using dielectrophoresis. It is also a long thin cylinder, a shape which has not been looked at in terms of experimental and theoretical comparisons. Both of these properties makes it an ideal and innovative particle for study in this project. Sections of the results and discussion in this Chapter have been published in the Journal of Biochemical and Biophysical Methods [4] and in the Journal of Electrostatics [5].

8.2 Preparation

Tobacco Mosaic Virus (Strain U1) was raised in *Nicotiana tabacum cv Petite Havana* SR1, purified by differential centrifugation, chemically labelled with a fluorescent tag and resuspended in a range of different buffer concentrations for dielectrophoresis experiments. The following sub-sections detail each step of the preparation procedure.

8.2.1 Purification

The virus was purified using differential centrifugation [6]. The weights and volumes given are appropriate for processing a 100g sample of leaves infected with TMV.

The procedure was carried out using 10mM potassium phosphate buffer (KPO_4) at pH 7.0, prepared by dissolving enough potassium dihydrogen phosphate (KH_2PO_4) to make a 10mM solution and adding 10mM potassium hydroxide to adjust the pH to the required value. This was kept on ice as a stock solution for the entire procedure.

0.2% thioglycollic acid and 1mM ethylenediaminetetra-acetic acid disodium salt(EDTA) (to improve yield) was added to 200ml of the KPO_4 buffer. This was added to the 100g sample of leaves which was shredded into a food mixer. The mixture was blended until it was of uniform pale green consistency and run into a beaker through four layers of muslin to remove large plant components. An equal volume of 1:1 butanol(C_4H_9OH)/chloroform($CHCl_3$) was added (200ml) and the 400ml mixture was stirred for 10 minutes. The butanol/chloroform is an

organic solvent and is not miscible in the KPO_4. After stirring, the suspension was poured quickly (to avoid phase separation) into two 250ml centrifuge bottles. The bottles were put in a Beckman JA-14 rotor and spun at 6krpm (7,000g) for 10 minutes in a Beckman J2-21 centrifuge.

The suspension in the bottles was separated into two phases by the centrifuge: the lower dark green layer consisting of the butanol/chloroform contained the cell remnants and other heavy material while the upper pale, slightly cloudy layer contained mainly virus. The upper layer was carefully removed from the lower and placed in 25ml ultracentrifuge bottles. The bottles were then placed in a Sorval T-865 rotor and spun in a Sorval Combi-plus ultra-centrifuge at 50krpm (200,000g) for 45 minutes to separate the virus from the solution, which could contain virus and protein fragments. After spinning, each of the bottles had a large white pellet at the base. The clear liquid was removed carefully and the pellet was resuspended in 3ml of the original 10mM KPO_4 with 1mM EDTA. The EDTA helped to prevent aggregation of the virions and as a result improved the yield. The samples from all the bottles were placed in a 250ml centrifuge bottle which was spun in the Beckman rotor at 7krpm (9,000g) for 10 minutes. After spinning, the clear liquid was carefully removed from the large pellet and placed in a 25ml ultra-centrifuge bottle. This bottle was again spun in the Sorval centrifuge at 50krpm (200,000g) for 45 minutes. This slow spin removes organic components which are heavier than the virus, while the fast spin removes lighter components. The slow/fast cycle can be repeated until the sample is satisfactorily pure. After the fast spin, the clear liquid was carefully removed and the pellet was resuspended in 5.5ml of 10mM KPO_4.

The virus concentration was determined using an ultraviolet spectrometer. The absorption at 260nm was measured and the published extinction coefficient of 3.0 used to determine the concentration, which was found to be 16.33 mg/ml.

8.2.2 Fluorescence labelling

Initial attempts at labelling the virus using NHS-rhodamine (Sigma) (a standard protein reagent bought commercially), which reacts with Lysine groups proved unsuccessful. The procedure was performed as instructed by the manufacturer, a reaction occurred and a solution containing labelled protein was produced. However, DEP experiment produced no visible results and no pellet could be produced with ultra-centrifugation. This indicated that no virus was present but that there was labelled protein. Testing in an electrophoresis gel gave a single clear band at the molecular weight of the TMV coat protein but no heavier components. Further literature research revealed that the positive charge of the only accessible Lysine surface group is important to the stable structure of the virus [7,8]. The labelling procedure was performed at pH8.8 where the amine group presumably has a tendency to become less positively charged.

This would destabilise the virus which would denature, resulting in free coat protein appearing in solution [8] and no intact virions.

As a consequence, an alternative method of fluorescently labelling TMV was devised with the assistance of Professor J. Coggins and Ms. S. Hardie (Div Biochemistry and Molecular Biology, University of Glasgow) from reference 7.

The virus was labelled with either the fluoroprobe Rhodamine B (Sigma) or the compound Rhodamine B amine (Sigma), the chemical structures of which are shown in Figure (8.3). In the first procedure, the fluoroprobe was converted into an active ester which was then directly coupled to the amine group of the lysine amino acid in the TMV coat protein. In the second procedure, the carboxyl groups on the surface of the virus were converted into active esters and then directly coupled to the amine group on the Rhodamine B amine compound. Both procedures used a carbodiimide coupling reagent to create the active ester.

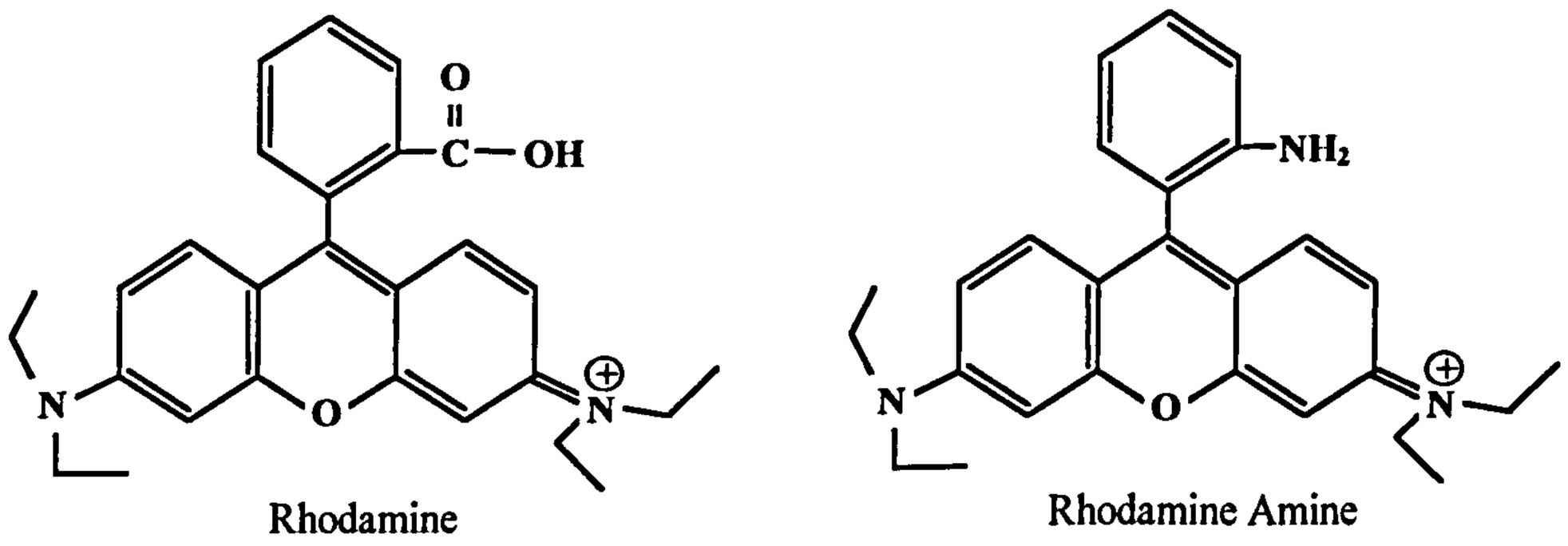

Rhodamine Rhodamine Amine

Figure (8.3) Structure of the Rhodamine and the Rhodamine amine fluoroprobes

The first procedure (*scheme 1*) was carried out as follows and is shown schematically in Figure (8.4). 48mg of Rhodamine B (10mM) compound was mixed 11.5mg N-hydroxysuccinimide (10mM) in 10ml of purified water. The pH was measured at 2.5 and then adjusted to 4.75 (the optimum coupling reaction pH) using 0.1M sodium hydroxide (NaOH). The mixture was stirred and 9.6mg 1-ethyl-3-(3-dimethylaminpropyl)carbodiimide (EDCI) (10mM) was added, giving a steady increase in pH as the reaction occurred. The pH was continually adjusted to 4.75 using 0.1M hydrogen chloride (HCl). After 20 minutes, the pH stabilised indicating that the chemical reaction had ceased. 5ml of this solution was then added to 0.1M triethanolamine (TEA) and stirred while the remaining 5ml of reagent was added. The pH of the resulting TEA buffered reagent solution was measured at 7.2, a suitable pH for the virus.

The virus was labelled in several batches to allow testing for successful labelling. 0.1ml of TMV in KPO_4 (at 10mg/ml) was added to 0.2ml of the 0.1M TEA buffer, 0.2ml of purified water and 0.5ml of the reagent in TEA buffer. The amounts of each component were chosen to

give an excess of the reagent. The mixture was stirred overnight at room temperature and the labelled virus was separated from the excess reagent by gel filtration on Sephadex G-10. The virus was then concentrated by ultracentrifugation in a Sorval ultracentrifuge at 50krpm (200,000g) for 1hour and stored at –70°C until required.

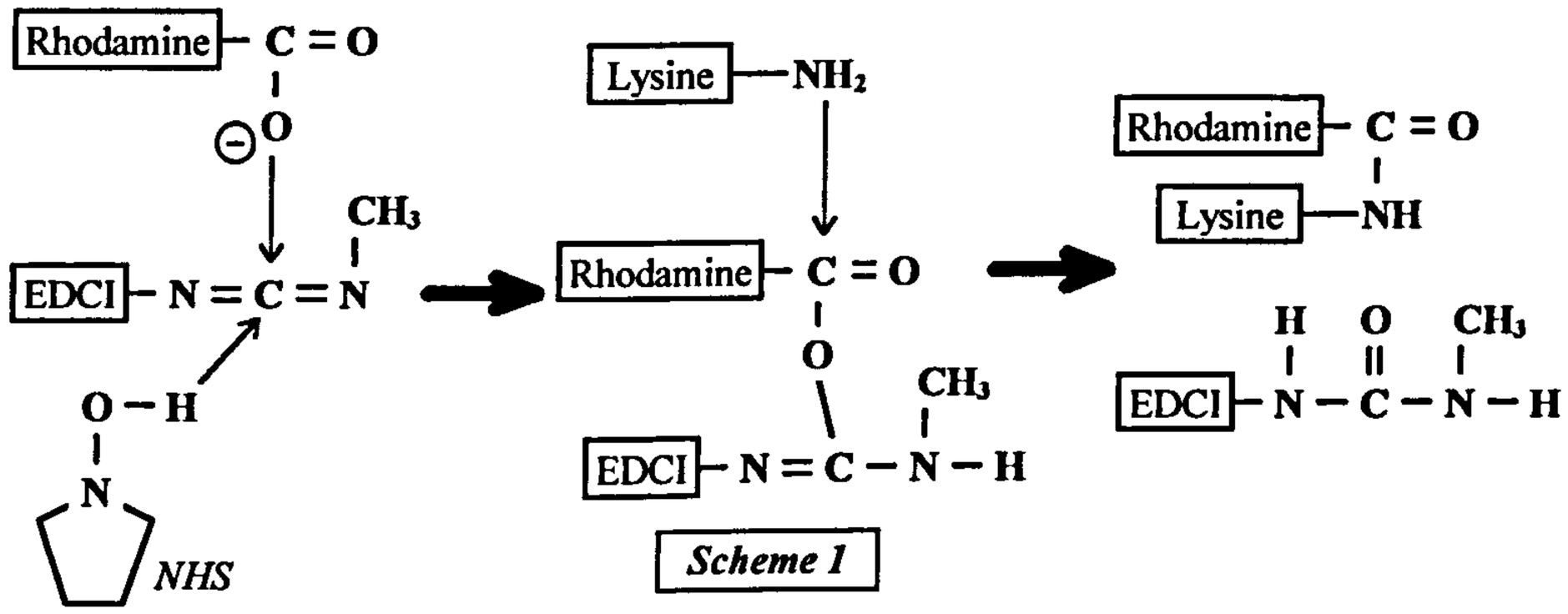

Figure (8.4) Diagram of the reactions in the rhodamine labelling procedure. The NHS (see text) gives up a proton to the active ester during the first reaction. The active ester then couples with the NH_2 on the Lysine to give a Lysine-rhodamine final product.

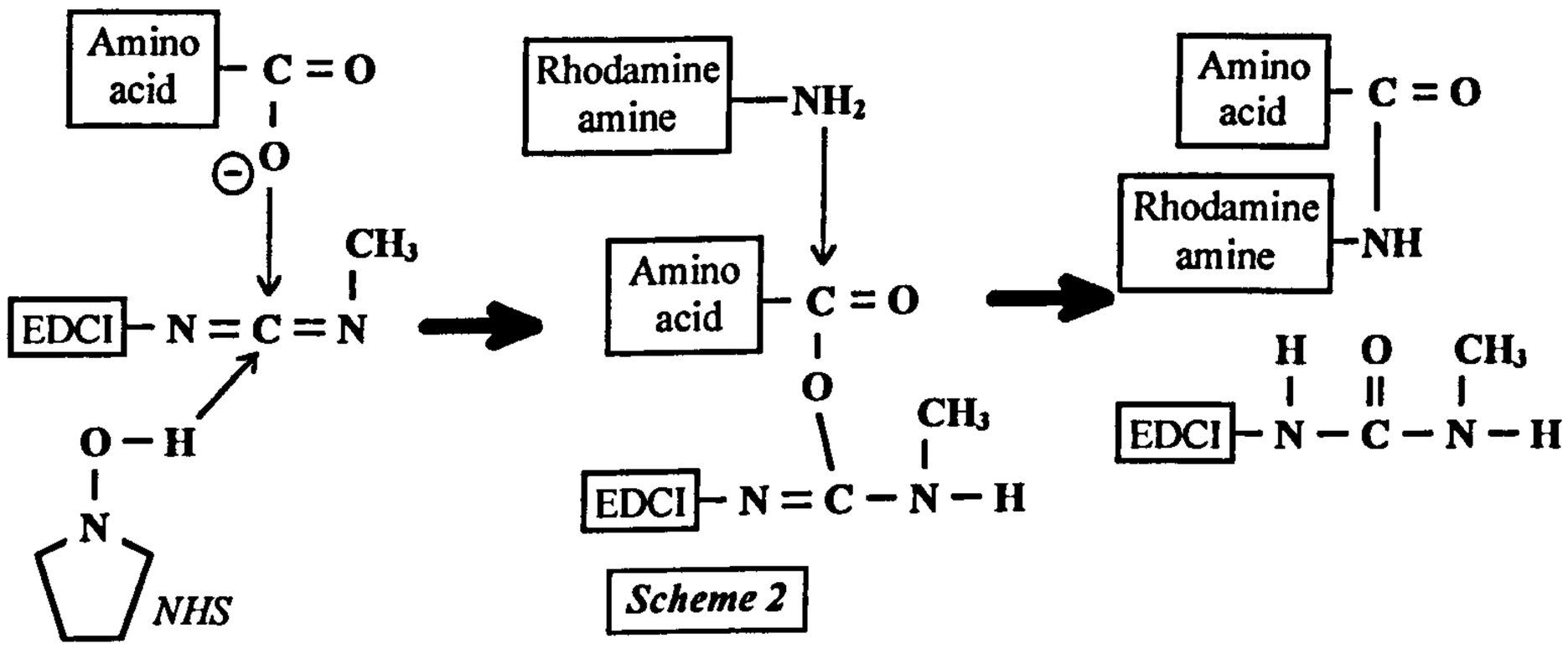

Figure (8.5) Diagram of the reactions in the rhodamine amine labelling procedure. The NHS (see text) gives up a proton to the active ester which is formed from the virus via a number of carboxylate containing amino acids in the coat protein. The ester then couples directly with the rhodamine amine to form a compound of rhodamine and the amino acid.

The second procedure (*scheme 2*) was carried out as follows and is shown schematically in Figure (8.5). 1ml of a 10mg/ml TMV sample was added to 2ml of purified water and stirred with 2ml of TEA buffer, 11.5mg of N-hydroxysuccinimide and 10.5mg of EDCI. The pH was measured at approximately 5.8. 50mg of rhodamine amine was added to 25ml of purified water

and 5ml of the rhodamine solution was then added to the solution of activated virus and stirred overnight. The labelled virus was separated from the excess reagents and concentrated as for the first procedure and then stored at -70°C.

The first procedure resulted in brighter particles indicating more successful coupling than for the second procedure. There is only a single amine group on the surface of each TMV coat protein and there are several carboxylate groups per coat protein which would suggest that the second procedure would be more successful. However, the rhodamine amine is not very water soluble and the resulting solution is of a lower concentrations than the rhodamine B. As a consequence, it is difficult to have a large excess of rhodamine amine over the active carboxylate groups in the same manner as the first procedure (which has a large excess of rhodamine B to TMV amine groups. The second procedure (scheme 2) results in more stable fluorescing TMV virions. Virus labelled by the first procedure (scheme 1) broke up with time.

8.2.3 Sample preparation

Potassium phosphate buffer was used as the suspending medium for the DEP experiments. A 1M stock solution was prepared from 1M monopotassium dihydrogen phosphate (Sigma) and 1M dipotassium monohydrogen phosphate (Sigma) mixed in a 1:1 ratio. The stock solution was then sterilised by autoclave and the pH was measured at 7.2 ± 0.1. Different concentrations of suspending buffer were prepared from the stock solution using purified water and re-sterilised. Samples of the virus were spun down at 50krpm (200,000g) for 1 hour in the Sorval Combi-plus ultra-centrifuge and re-suspended in the different solutions.

8.3 Results

8.3.1 Buffer conductivity measurements

The electrical conductivity of the different potassium phosphate solutions was measured using the HP bridge and cell (Appendix 5b.1). The results of the conductivity measurement of potassium phosphate are described in detail in Chapter Seven. The graph of the conductivity versus concentration at 21°C (experimental temperature) is shown in Figure (8.6). The uncertainty in the conductivity is too small to be seen on a log-log plot of this nature but the marked circles can be considered sufficient indication of the errors.

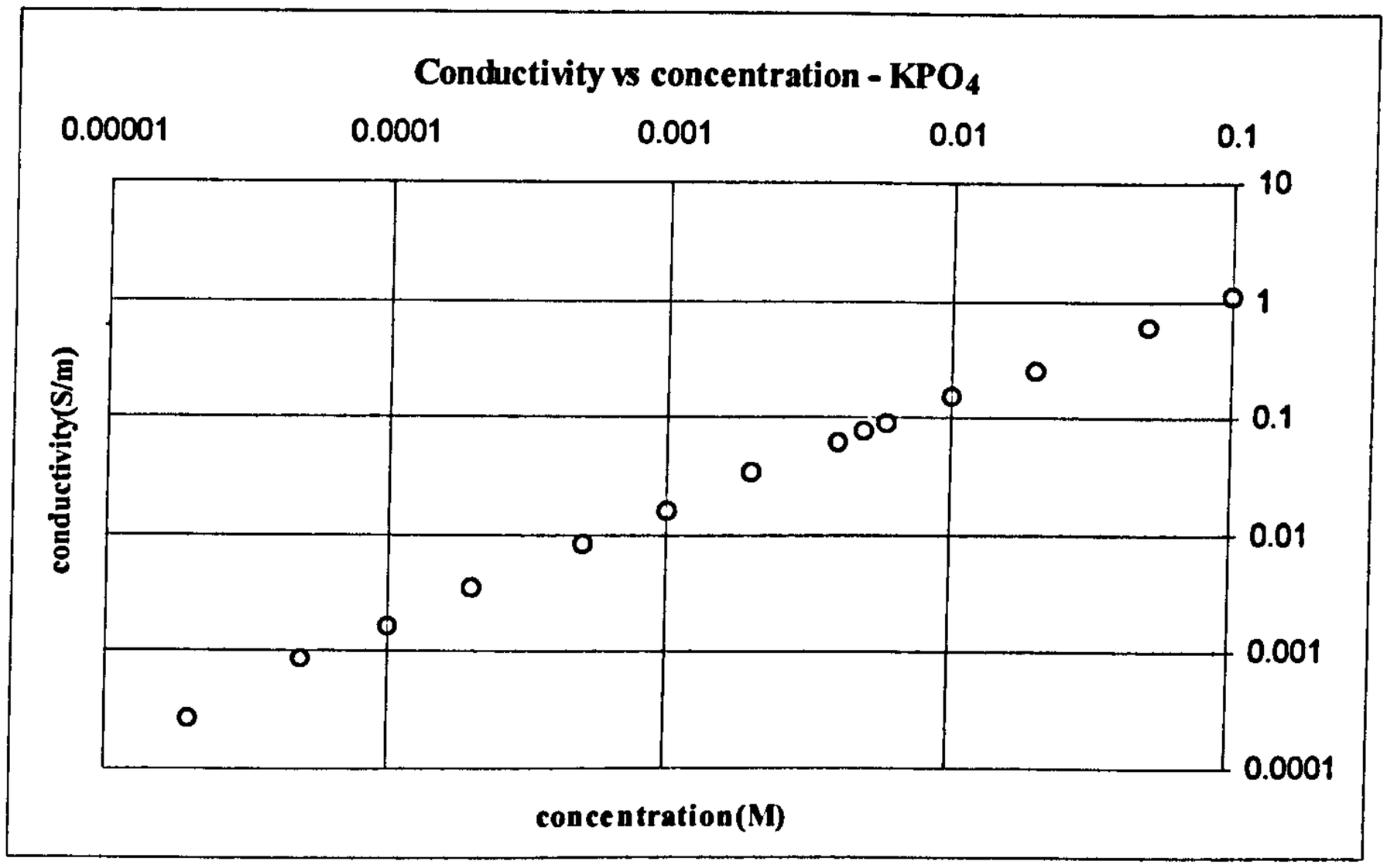

Figure (8.6) Measured values of the conductivity (S/m) versus concentration (M) for the potassium phosphate solutions used in this Chapter. The uncertainty in the values is too small to be seen on this scale and the circle is considered to be sufficient indication of the error.

8.3.2 Dielectrophoretic behaviour

The devices described in Chapter Five were used to perform dielectrophoresis experiments on the different TMV samples. Both the analogue generator (Appendix 5b.4) and the DDS (Appendix 5b.5) were used to provide signals over the ranges 100Hz-20MHz and 0-20volts peak-peak.

In general, during an experiment, single virions could not be resolved against the background fluorescence. However, increases in local concentration were readily observed for positive DEP and under certain experimental conditions, for negative DEP.

Positive dielectrophoresis was observed at low frequencies in all but highest medium conductivities. The areas where the particles collected were the regions of highest field strength as indicated by the solutions for the dielectrophoretic force (Chapter Six). Figures (8.7a-c) are scanned photographs of Rhodamine modified TMV experiencing positive DEP. The applied potential was 4 volts peak to peak, the frequency was 100kHz and the medium conductivity was 16.2mSm^{-1}. The photographs were taken using a microscope mounted with a Nikon camera and high speed black and white film (3200 ASA), approximately 1 minute after the field was applied. Positive collection was observed a few seconds after the application of the field and the intensity of the bright region increased with time. The dark regions in Figures (8.7a-c) are the electrodes and the intensity of the fluorescence in the gaps of the triangular electrodes (8.7a) and the

castellated electrodes (8.7b) is a good approximation of the distribution of the positive DEP force magnitude. Removing the field resulted in a rapid diffusion of the virions back into the medium within approximately ten seconds.

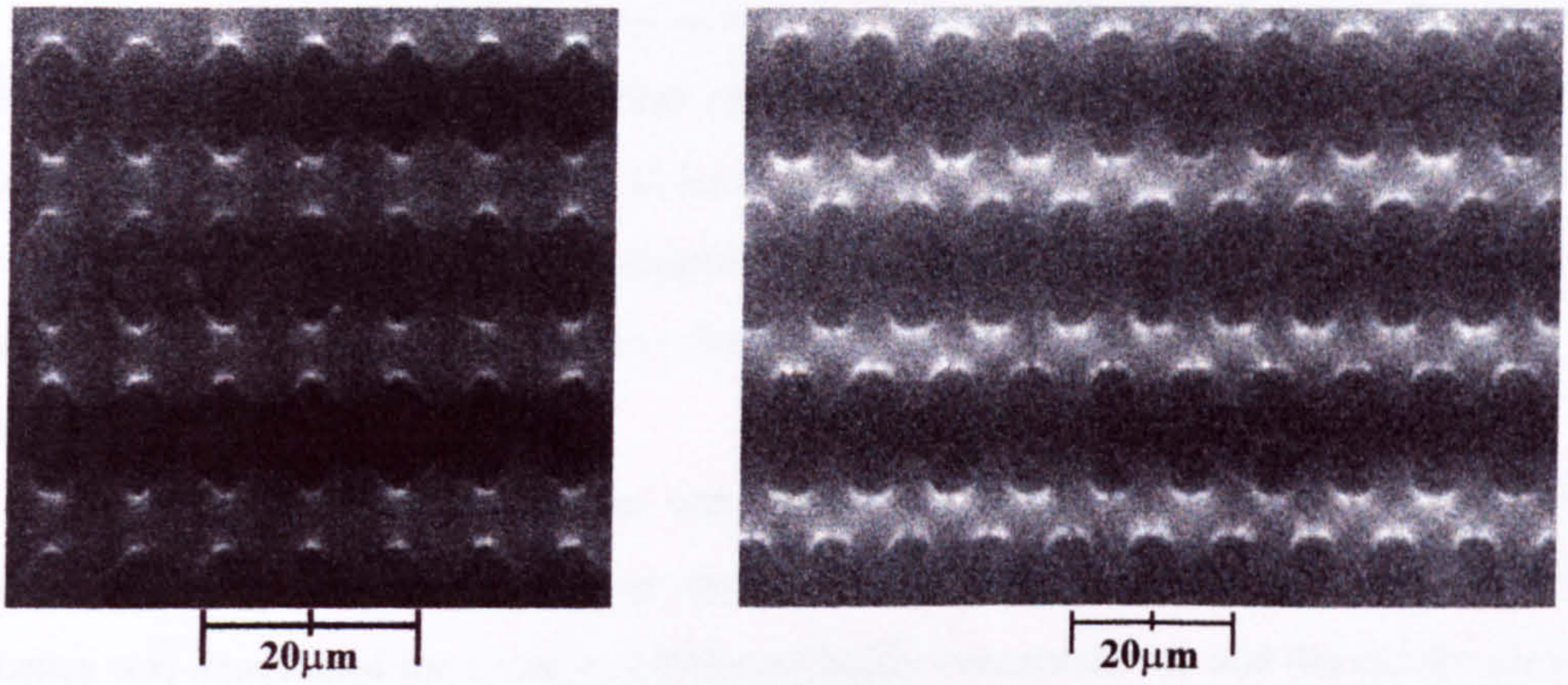

(8.7a) **(8.7b)**

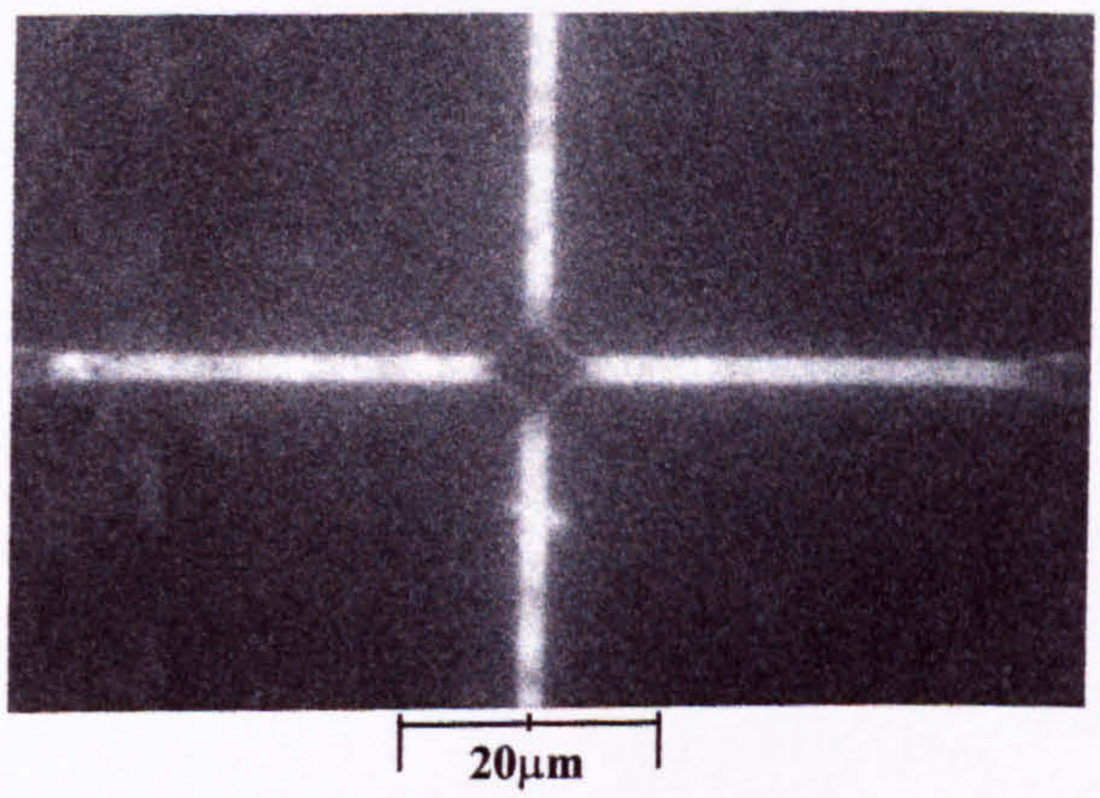

(8.7c)

Figure (8.7) Positive dielectrophoresis of TMV in: **(a)** triangular electrodes with a feature and gap size of 4μm; **(b)** castellated electrodes with a feature and gap size of 5μm and **(c)** polynomial electrodes with a centre separation of 6μm and a gap size of 2μm. The applied field frequency was 100kHz, the potential was 4 volts peak to peak and the medium conductivity was 16.2mSm^{-1}.

Negative dielectrophoresis was difficult to observe under most experimental conditions. Negative DEP trapping was achieved in the smallest size (6μm) of polynomial electrodes but the bright region was impossible to render in a form that could be reproduced here. Negative DEP was also observed as an increased rate of diffusion from the electrode edges after collection by positive DEP. By collecting the virions at the edges with a suitable frequency for positive DEP and switching the frequency, negative DEP could be observed as rapid repulsion from the electrode edge.

8.3.3 Dielectrophoresis zero force point measurements

The dielectrophoretic behaviour of Rhodamine and Rhodamine amine labelled TMV in potassium phosphate buffer pH7.2 was observed and recorded as a function of applied frequency and medium conductivity. At low frequencies, in general, collection of virions due to positive DEP at local DEP potential maxima was observed. At high frequencies, negative DEP was observed, either by trapping of TMV in local DEP potential minima or by repulsion from high field regions. The observation of negative dielectrophoresis was clarified if necessary by attracting virions to high field regions with positive DEP and switching the applied field frequency.

The dielectrophoretic behaviour was observed to change from positive to negative at a frequency where the force magnitude was zero and neither type of DEP occurred. The zero force frequency was determined for a range of different buffer concentrations and the results are shown in Figures (8.8a) and (8.8b) for TMV labelled according to scheme 1 and 2 respectively.

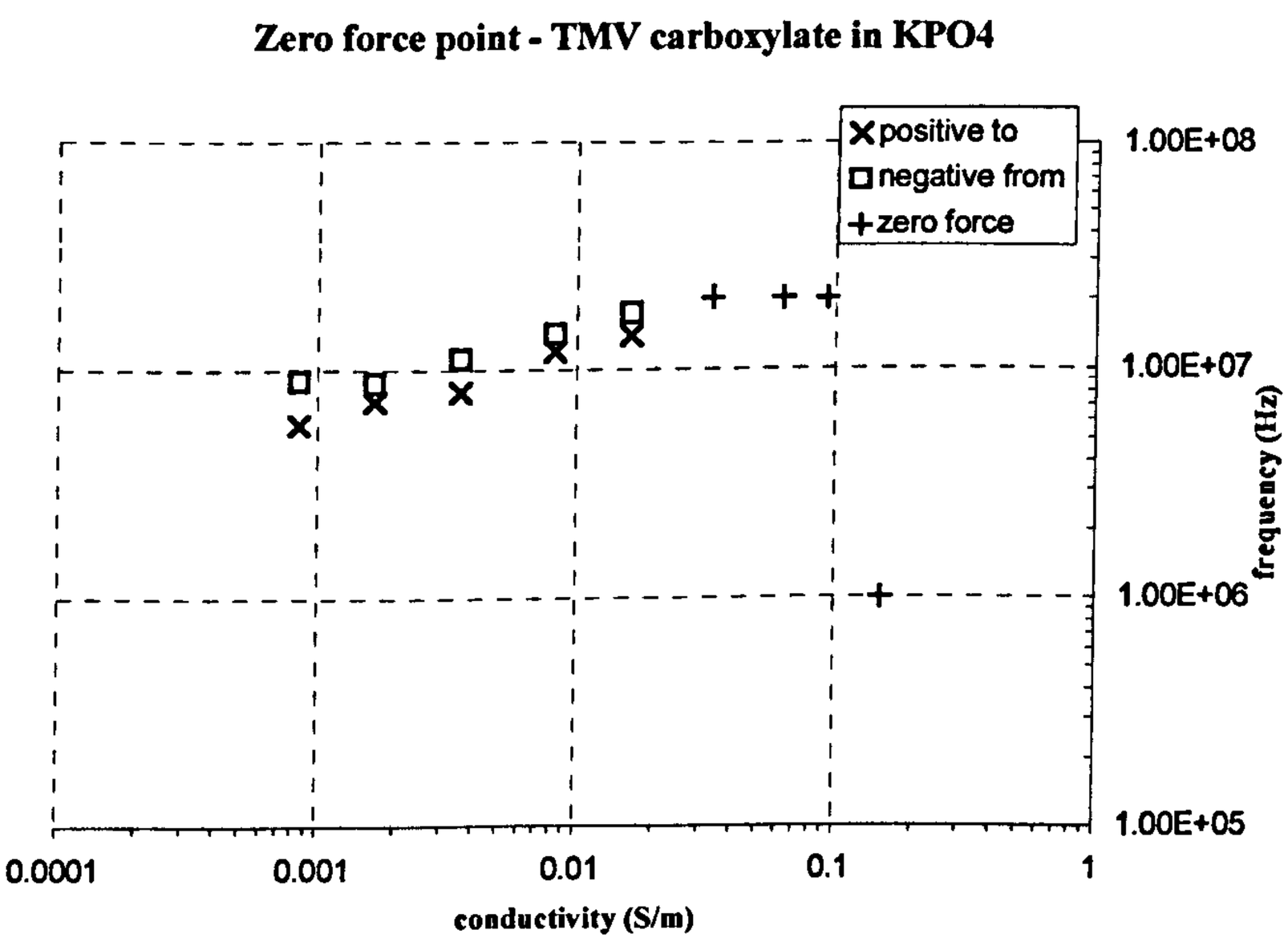

Figure (8.8a) Zero force frequency measurements for TMV labelled by scheme 1. The squares represent the frequencies above which negative DEP is observed by trapping of virions in the centre of a set of polynomial electrodes and the crosses represent the frequency below which positive DEP is observed. For conductivities above 20-30mSm^{-1}, negative trapping was not observed and the crosses show the maximum value at which positive DEP was observed.

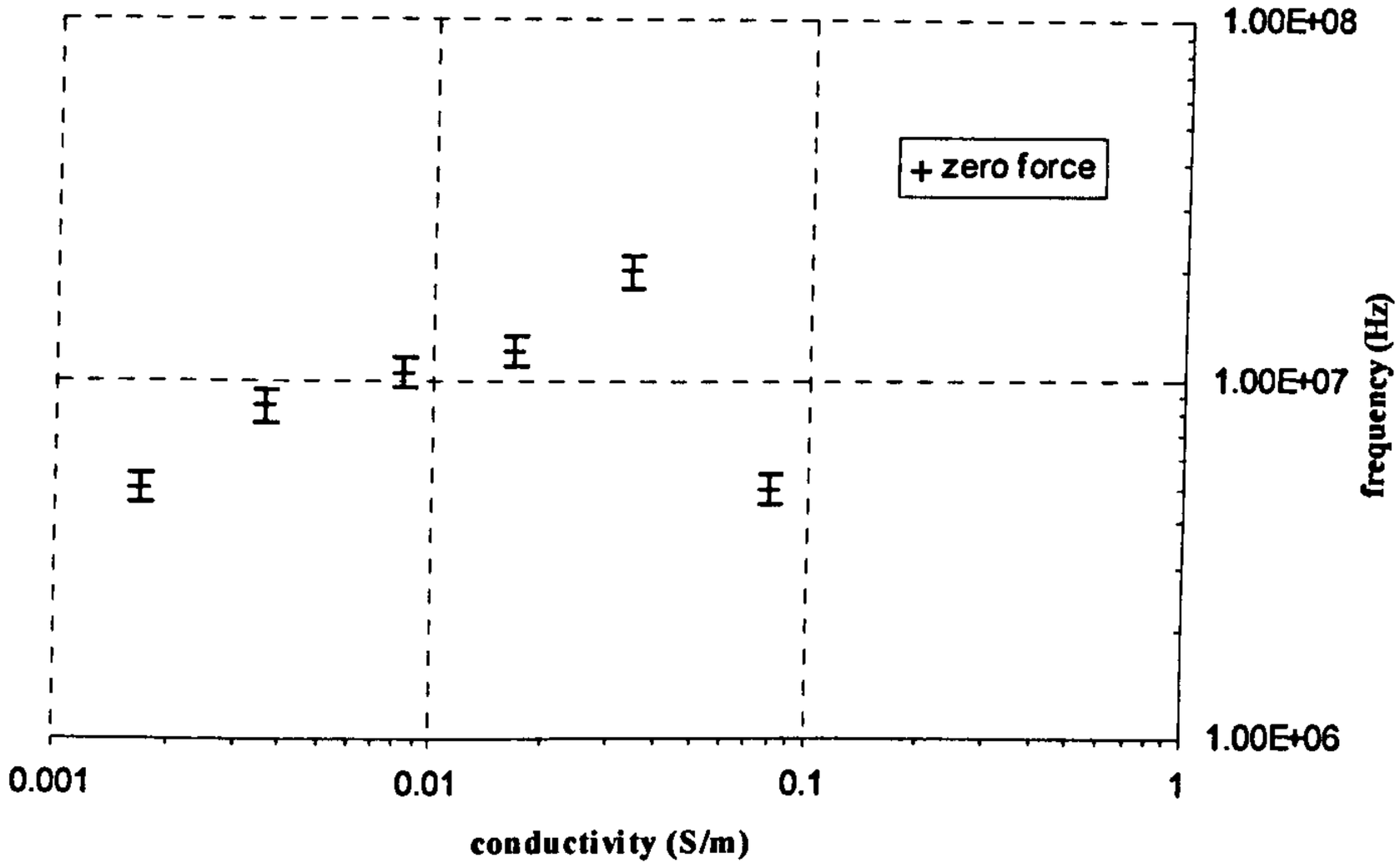

Figure (8.8b) Zero force frequency measurements for TMV labelled by scheme 2. The crosses with error bars represent the zero force point measurement. Below this point positive DEP was observed and above this point repulsion from the electrode edges due to negative DEP was observed. During this series of experiments, negative DEP trapping was not observed.

There are slight differences between the two graphs which can be attributed to the fact that the dielectric properties of the particles are dependent on the net surface charge in a similar manner to the latex spheres (Chapter Seven). The chemical labelling techniques alter the surface charge characteristics of the particles and the differences in the labelling procedures probably result in different surface charge densities on the virions.

8.3.4 Dielectrophoresis threshold force measurements

The threshold potential required to observe positive dielectrophoresis was measured. Samples of Rhodamine amine labelled TMV in KPO_4 were used on an array of 4μm triangular electrodes. The frequency of the applied field was kept at 100kHz and the potential increased until positive dielectrophoretic collection and/or movement was seen in the gap between the electrodes approximately 1μm from the tip of the triangular feature along the line joining opposing tips. This distance was chosen to ensure that the numerically determined field strengths would correspond to the field strengths expected from the more rounded physical electrode features.

Figure (8.9) shows the peak to peak potentials at which positive DEP was observed as a function of medium conductivity. As can be seen, the necessary potential increases with

increasing medium conductivity corresponding to a decrease in the susceptibility or polarisation factor. Comparison between this data and the numerically modelled field in order to determine the absolute force is discussed in section (8.4.2).

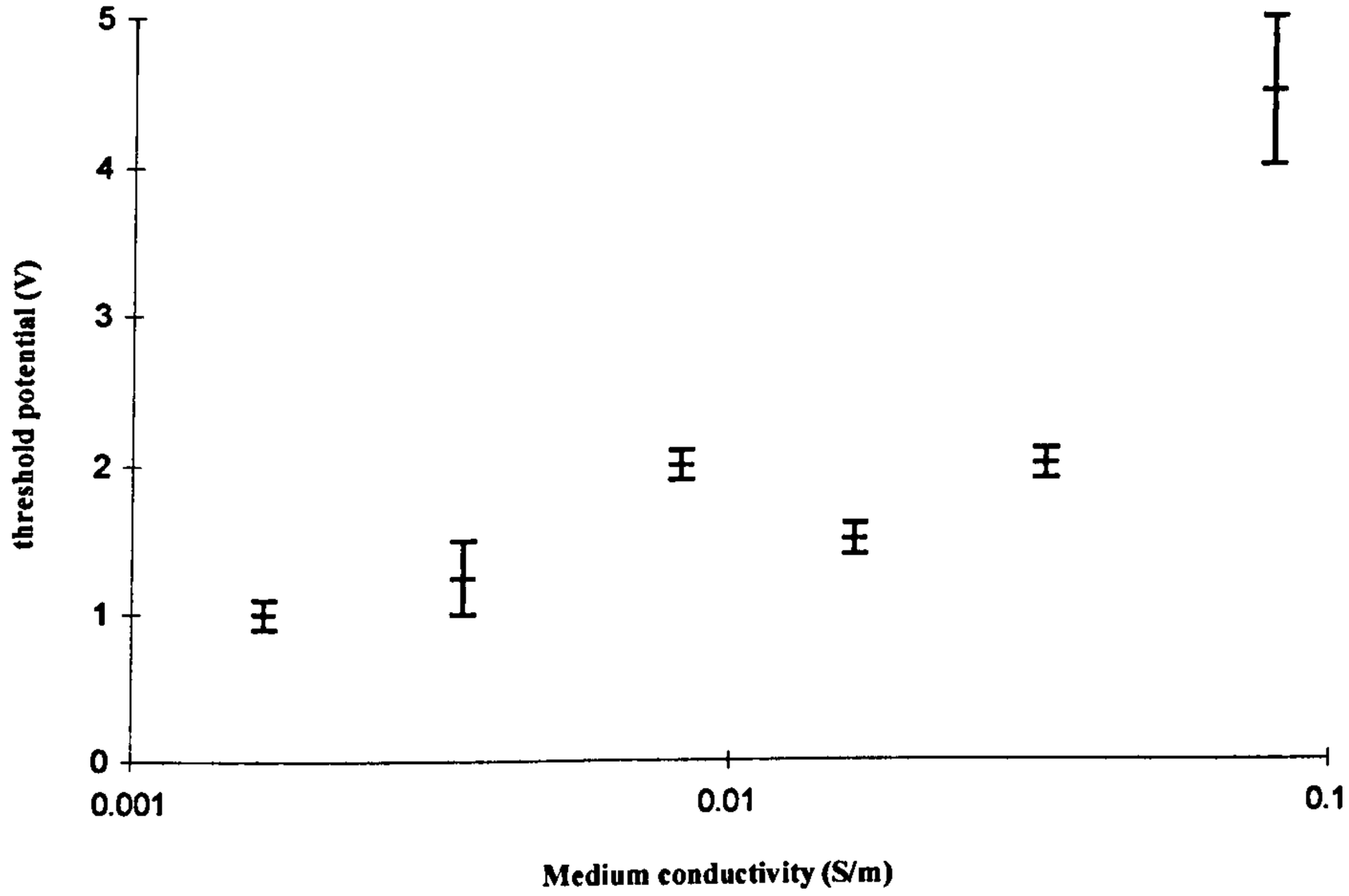

Figure (8.9) Variation of the threshold potential (in volts peak to peak) above which positive DEP is observed as a function of medium conductivity (in Sm^{-1}) for the Rhodamine amine labelled TMV. The threshold voltage increases with increasing medium conductivity.

8.4 Discussion and theoretical comparison

This section discusses the comparison of the results in sections (8.3.3) and (8.3.4) with the theoretical model of the prolate ellipsoidal particle presented in Chapter Three. The dipole relaxation mechanism is assumed to be Maxwell-Wagner polarisation at the interface between the surface of the TMV protein coat and the medium. The theoretical work was carried out in Matlab (The Mathworks Inc, Natick, MA, USA) and the functions used are included in Appendix (8a). The calculation of function zeros was performed using a simple numerical binary search method.

8.4.1 Zero force frequencies

There are two distinct theories which can be applied to model the theoretical variation of the prolate ellipsoid. The simplest method is to model TMV as a rod with the major axis length

a very much greater than the minor axes lengths b and c and use equation (3.55). However, it would be more valid to consider the actual dimensions of TMV and use an ellipsoid model with a = 150nm and $b = c$ = 9nm and equation (3.50). For the second case, the integral in equation (3.51) must be solved which is not a simple task, however Kakutani [9] provided an approximation for the case of the prolate ellipsoid. Assuming the major axis is aligned along the x-axis without loss of generalisation, the depolarising factors along the three axes are given by:

$$\mathrm{A_x} = \frac{1}{\left(G_{ab}^2 - 1\right)}\left[\left(\frac{G_{ab}}{\sqrt{G_{ab}^2 - 1}}\right)\ln\left(G_{ab} - \sqrt{G_{ab}^2 - 1}\right) - 1\right] \tag{8.1}$$

and:

$$\mathrm{A_y} = \mathrm{A_z} = \frac{1}{2}\left(1 - \mathrm{A_x}\right) \tag{8.2}$$

where ln() indicates the natural log of and the factor $G_{ab} = a/b$. In either case the variation in the susceptibilities (equations 3.50 and 3.55) completely describes the variation with frequency of the dielectrophoretic force, as all other terms in the dipole equation (equation (3.18) and the expression for the DEP force (equation (4.21) do not vary with the frequency of the applied field. Therefore, the zero point in the function that describes the particle susceptibility for a particular medium conductivity and permittivity is exactly equivalent to the zero dielectrophoretic force frequency for the medium.

The variation in the susceptibility for a rod of length 300nm with medium conductivity and applied frequency is shown in Figure (8.10). In this plot, the rod relative permittivity was 50, the medium relative permittivity was 78.54 and the particle conductivity 0.1 Sm^{-1}. As can be seen in Figure (8.10a), the value of the susceptibility can rise to approximately 1000 for low frequencies and low medium conductivities compared to a maximum of 1 for the Clausius-Mossotti factor for the sphere. The same graph with the vertical axis expanded to the range –1 to 1 is shown in Figure (8.10b). As is apparent from this figure, at high frequencies, the value of the susceptibility falls to the negative of the ratio of the particle to medium permittivities, which is approximately –3/8 in this case. Along the axis for the medium conductivity, the value of the susceptibility falls to –1 for high values. Figure (8.10c) shows the zero force line and the regions of positive and negative DEP behaviour for the rod and Figure (8.10d) shows the variation of this line with particle permittivity and conductivity. Increasing and decreasing the particle permittivity increases and decreases the zero force frequency without altering the point along the medium conductivity axis at which the zero force line drops off. Increasing and decreasing the particle conductivity, respectively increases and decreases the size of the positive

DEP region (and vice versa for the negative DEP region). As a result, the dielectric properties of the virions can be determined in the same manner as for the latex spheres.

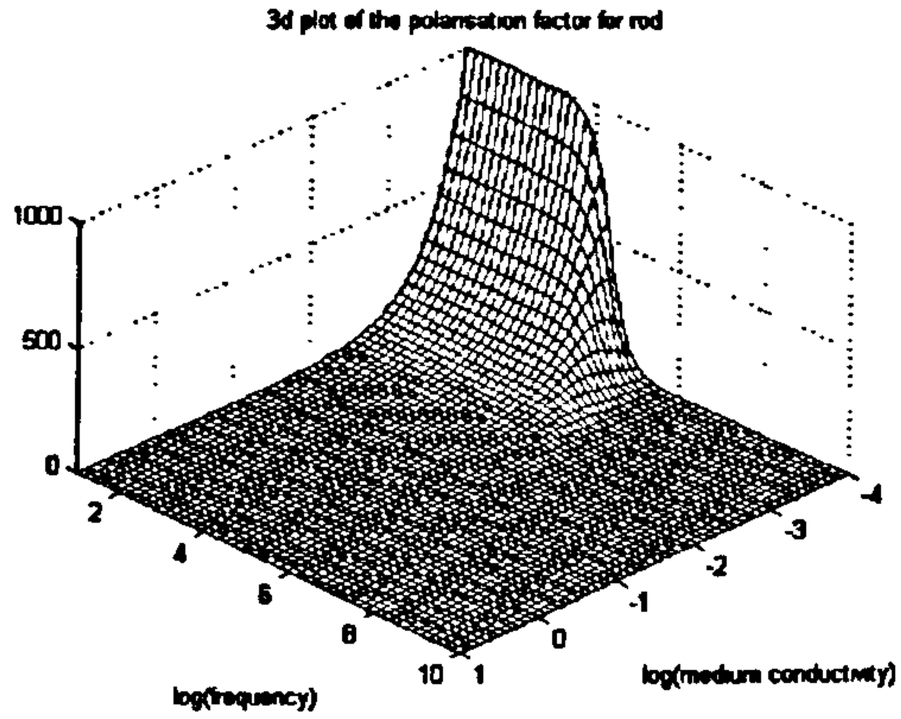

Figure (8.10a) Plot of the susceptibility or polarisation factor for a thin rod of length 300nm. For details of the dielectric properties of the rod and the medium see the text. The susceptibility of the particle, indicated by the vertical axis, rises to approximately 1000 at low frequencies and medium conductivities.

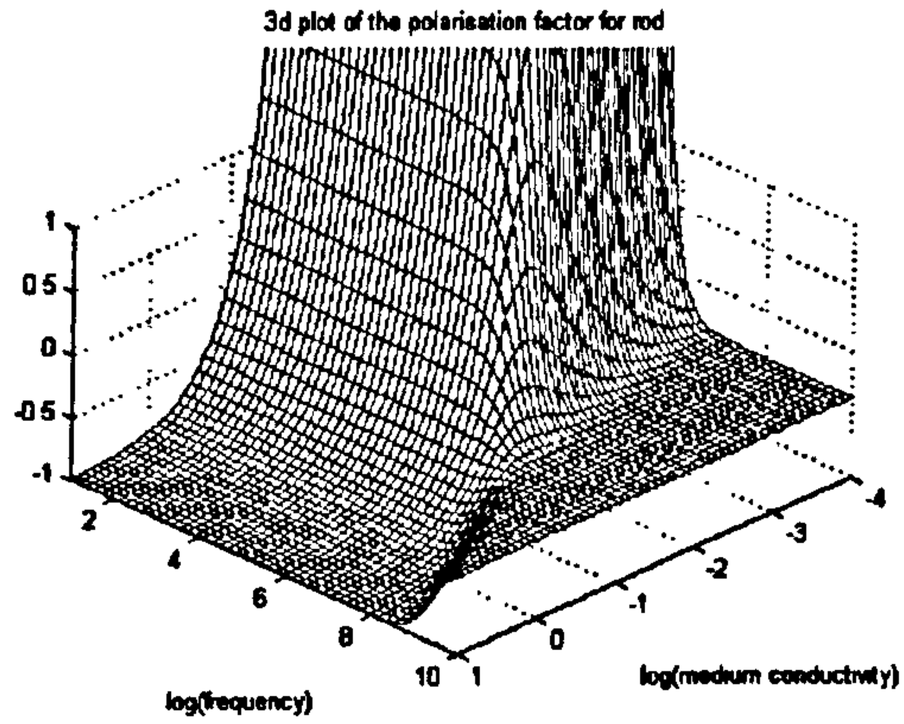

Figure (8.10b) Plot of the susceptibility or polarisation factor for a thin rod of length 300nm with the vertical axis expanded to show the region around zero. The susceptibility of the particle falls to –1 at high medium conductivities and to –3/8 at high frequencies.

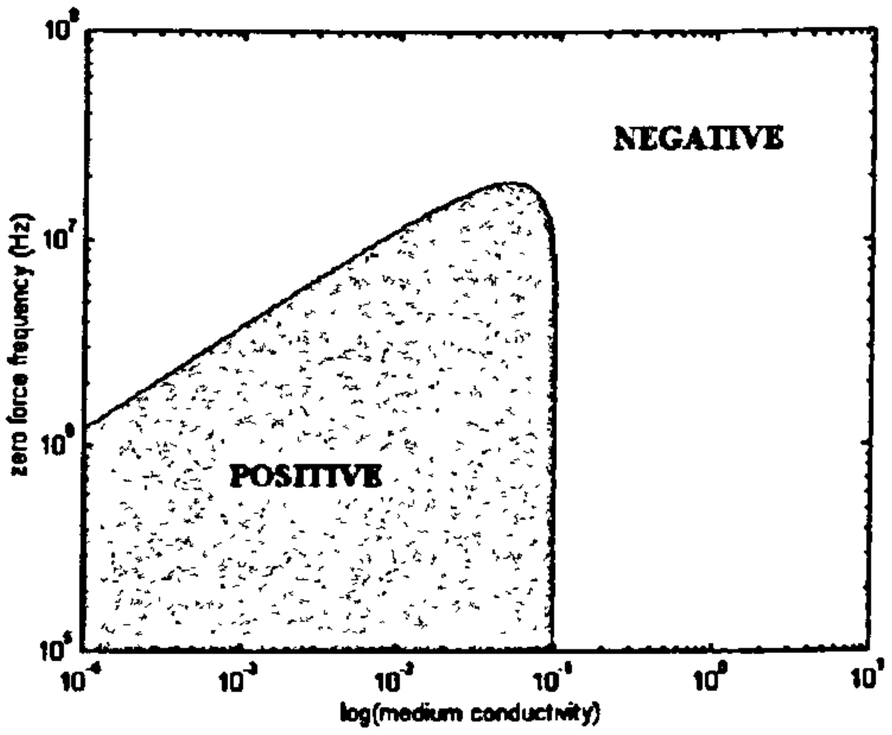

Figure (8.10c) Plot of the zero force line and the regions of positive and negative DEP for the rod susceptibility as shown in (8.10a) and (8.10b).

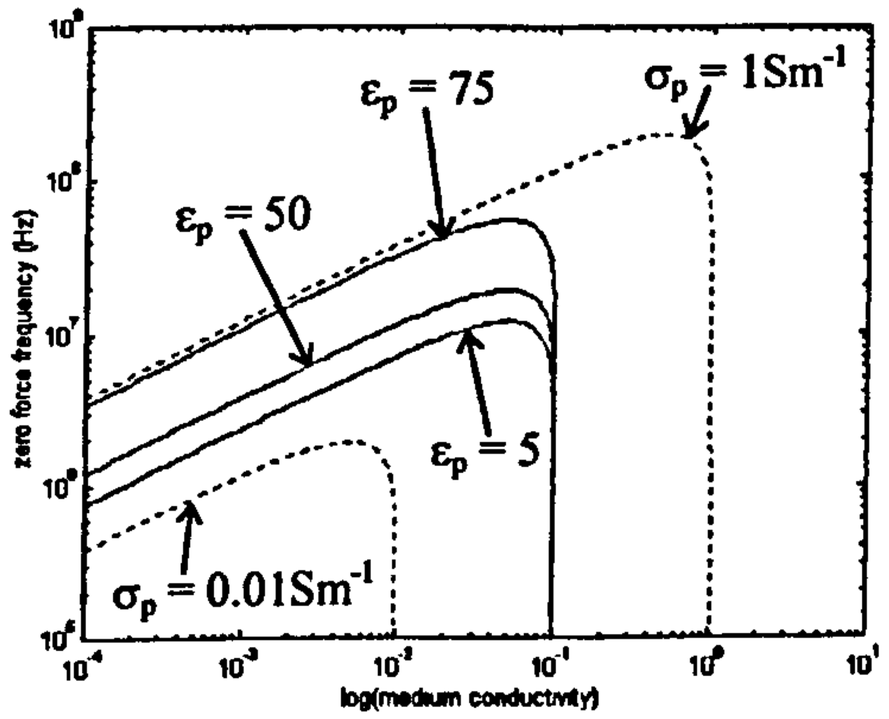

Figure (8.10d) Plot of the variation of the zero force line with particle dielectric properties. The three solid lines are for $\sigma_p = 0.1$ Sm^{-1} and $\varepsilon_p = 5,50,75$ and the two dashed lines are for $\varepsilon_p = 50$ and $\sigma_p = 1$ and 0.01 Sm^{-1}.

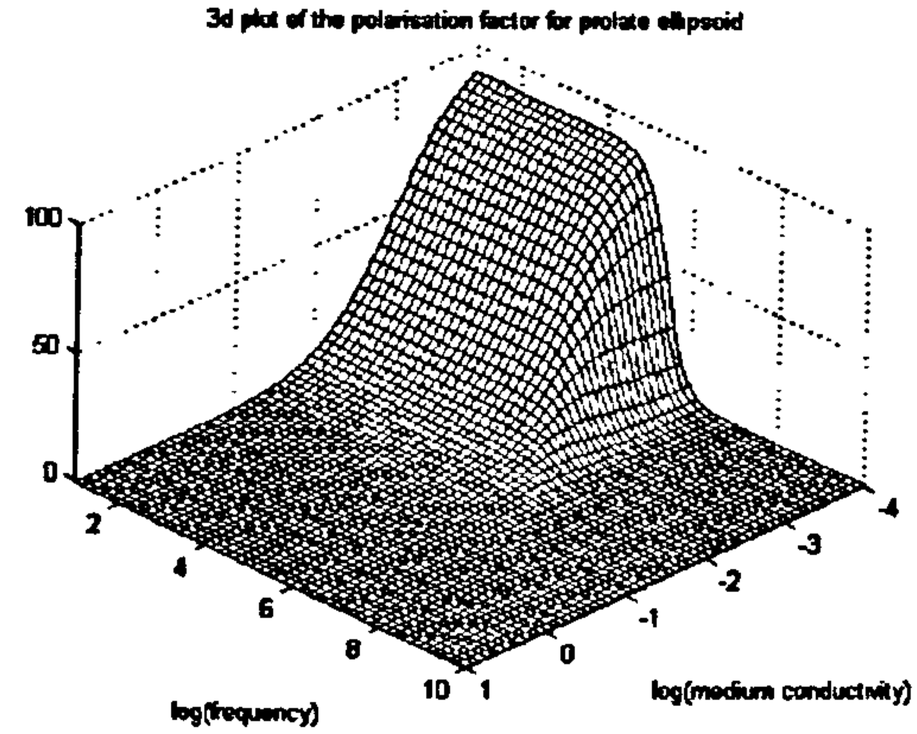

Figure (8.11a) Plot of the susceptibility or polarisation factor for an ellipsoidal particle with a=150nm and b=9nm. For details of the dielectric properties of the particle and the medium see the text. The susceptibility of the particle, indicated by the vertical axis, rises to approximately 100 at low frequencies and medium conductivities.

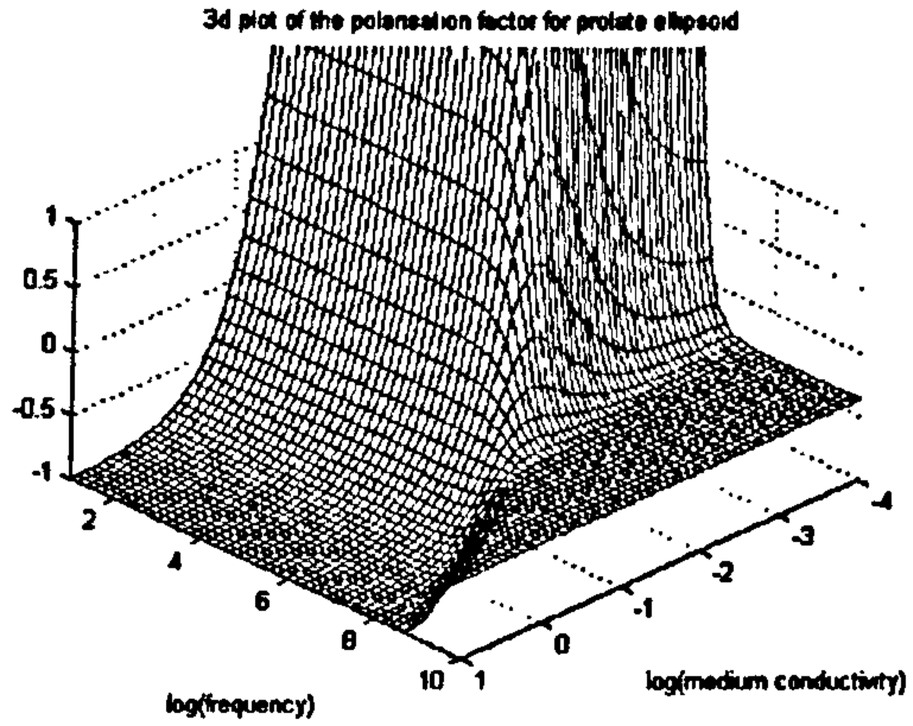

Figure (8.11b) Plot of the susceptibility or polarisation factor for an ellipsoidal particle with the vertical axis expanded to show the region around zero. The susceptibility of the particle falls to –1 at high medium conductivities and to –3/8 at high frequencies.

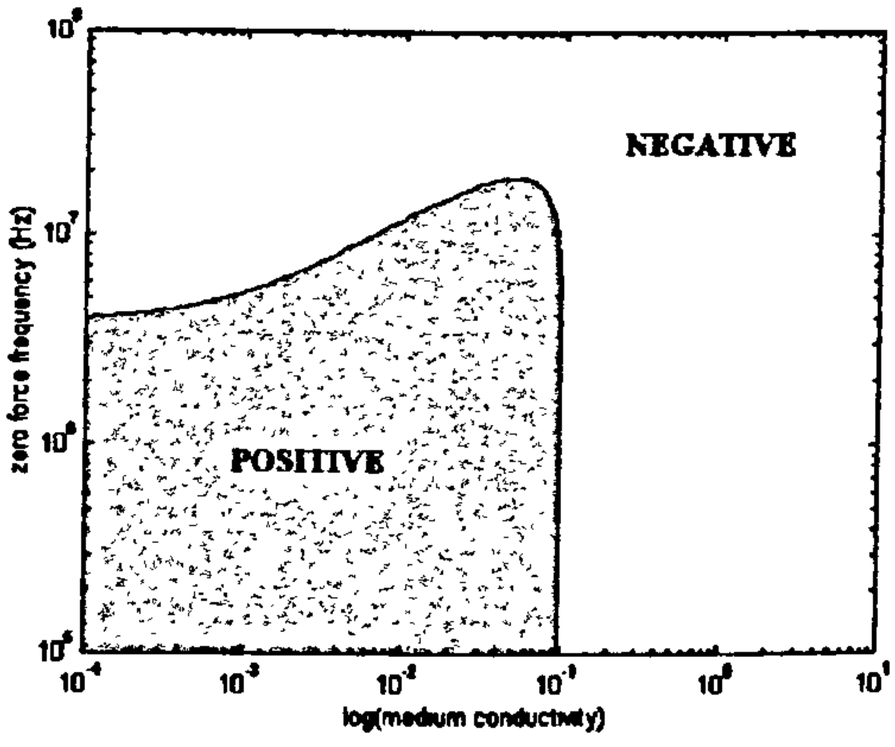

Figure (8.11c) Plot of the zero force line and the regions of positive and negative DEP for the ellipsoid susceptibility as shown in (8.11a) and (8.11b).

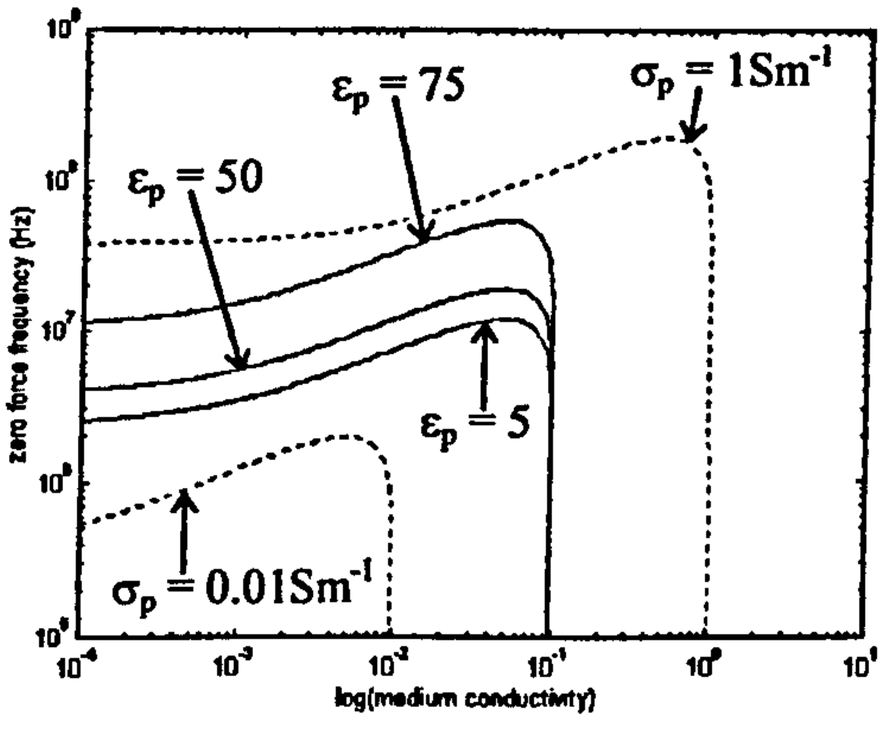

Figure (8.11d) Plot of the variation of the zero force line with particle dielectric properties. The three solid lines are for σ_p = 0.1 Sm^{-1} and ε_p = 5,50,75 and the two dashed lines are for ε_p = 50 and σ_p = 1 and 0.01 Sm^{-1}.

Figure (8.11) shows the variation of the susceptibility or polarisation factor for a prolate ellipsoid according to equation (3.50). The dielectric properties of the particle and the medium were varied in the exactly the same manner as for the rod in Figure (8.10). The results are similar to the rod with two noticeable differences. The susceptibility reaches a maximum defined by the ratio $1/A_x$ which is in this case approximately 100. The high frequency value for the susceptibility is still –3/8 and the high conductivity value is –1. The zero force line also has a different profile, following the same pattern for higher medium conductivities but tending to a

constant frequency as the medium conductivity decreases. Figure (8.12) shows the difference between the zero force line for the rod (solid line) and ellipsoid (dashed line). The permittivity of the particle and medium were 50 and 78.54 respectively and the particle conductivity was $0.1Sm^{-1}$. The lines follow the same path at higher medium conductivities but diverge at low frequencies as the zero force line for the ellipsoid tends to a constant frequency.

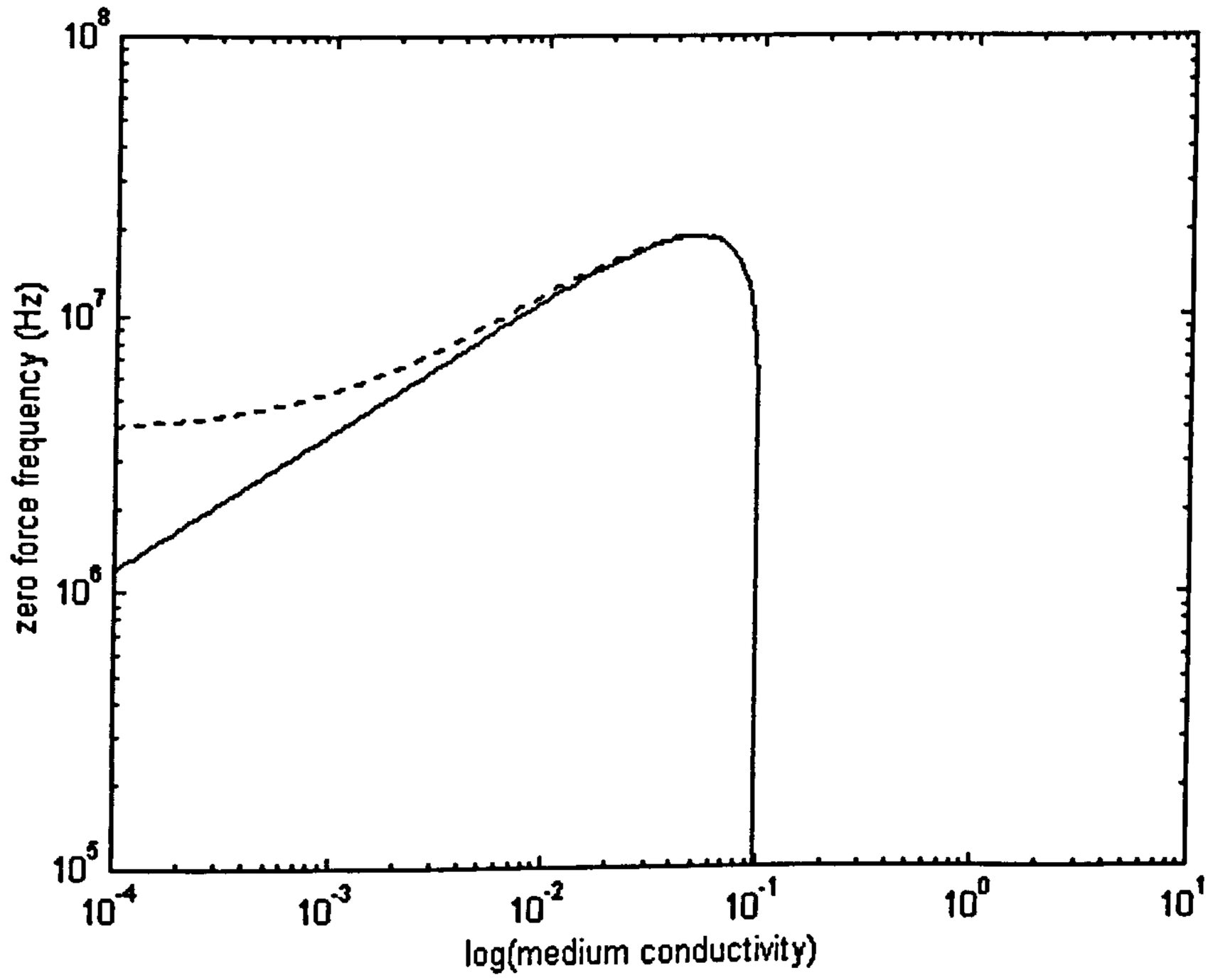

Figure (8.12) Plot of the zero force frequency with medium conductivity for a rod (solid line) and an ellipsoid (dashed). The rod length was 300nm and the ellipsoid had a major axis half length of 150nm and minor axis half lengths of 9nm. The particle permittivity and conductivity were 50 and $0.1Sm^{-1}$ respectively and the medium permittivity was 78.54.

It is apparent from both models that the force on a particle with the dimensions of a TMV virion due to dielectrophoresis is going to be much greater than for a sphere of the same volume at low frequencies and medium conductivities.

The measured zero force points were compared with the theory and the values for the particle permittivity and conductivity determined. The best fit for the Rhodamine labelled TMV was using the ellipsoid model as the rod model did not match the data at all points. The ellipsoid fit is shown in Figure (8.13) demonstrating a tendency towards a fixed frequency as the medium conductivity decreases.

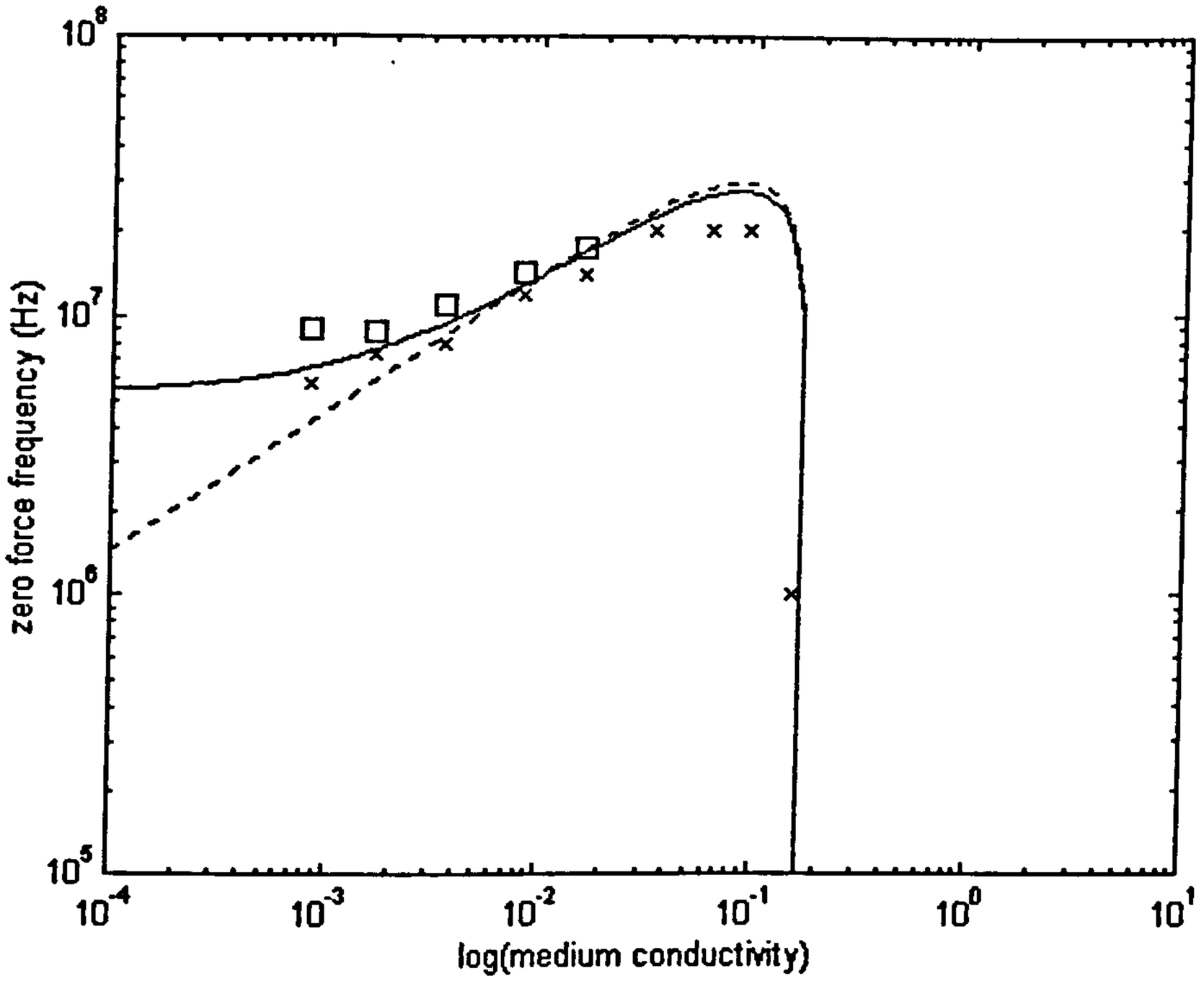

Figure (8.13) Theoretical matching line from the ellipsoid model (solid line) with the results for the TMV labelled by scheme 1 (Rhodamine). The particle relative permittivity was set to 40 and the conductivity set to 0.17 Sm^{-1}. The medium relative permittivity was 78.54. The dashed line is the best fit line for the rod model with the values for the parameters as given in Table (8.1).

The values for particle relative permittivity and conductivity determined from this match were 0.17 ± 0.01 Sm^{-1} and 40 ± 5 respectively. Matching the rod model to the higher medium conductivity points and neglecting the low σ_m points gave values of 0.17 ± 0.02 Sm^{-1} and 45 ± 8 respectively. However, this was not considered a sufficiently accurate theoretical model. The results of the theoretical comparison are shown in Table (8.1).

The best fit for the TMV labelled with Rhodamine amine was obtained with the rod model due to the unsatisfactory fit of the ellipsoid model at low medium conductivities. The values for particle conductivity and relative permittivity determined from this match were 0.085 ± 0.003 Sm^{-1} and 55 ± 5 respectively. Matching the ellipsoid model to this data gave values of 0.085 ± 0.005 Sm^{-1} and 55 ± 10 for σ_p and ε_p respectively. The two models agree on the values for the relative permittivity and conductivity but the fit for the rod model was considerably more accurate than the ellipsoid model. The results for this comparison are summarised in Table (8.1) along with the results for the Rhodamine labelled TMV.

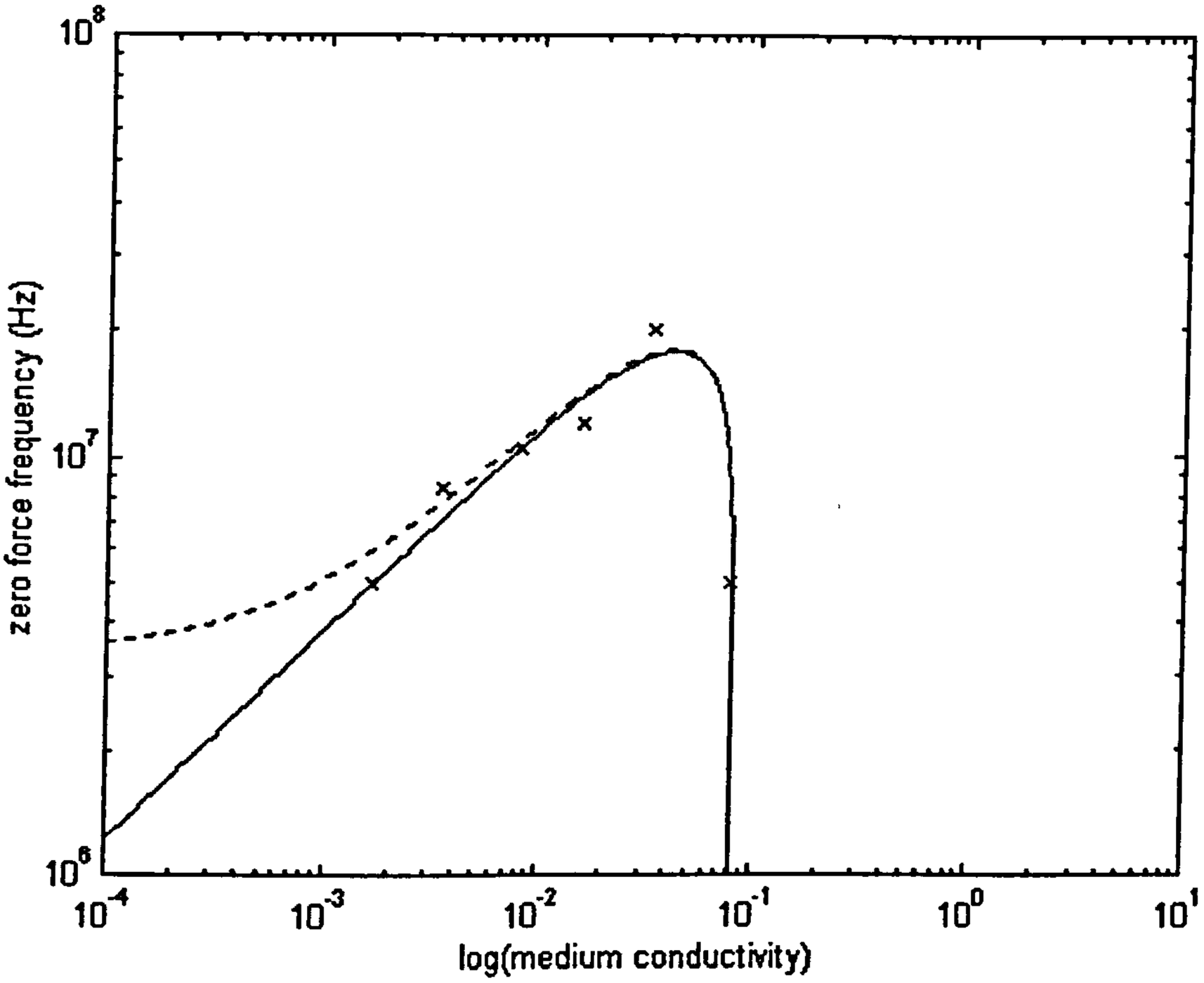

Figure (8.14) Theoretical matching line from the rod model (solid line) with the results for the TMV labelled by scheme 2 (Rhodamine amine). The particle relative permittivity was set to 55 and the conductivity set to 0.085 Sm^{-1}. The medium relative permittivity was 78.54 and the dashed line is the best fit (see Table 8.1) for the ellipsoid model.

Table (8.1) Summary of data comparison results for the rhodamine labelled TMV and the Rhodamine amine labelled TMV for the rod and the ellipsoid model.

label	model	σ_p (Sm^{-1})	ε_p
Rhodamine	ellipsoid	0.17 ± 0.01	40 ± 5
scheme 1	rod	0.17 ± 0.02	45 ± 8
Rhodamine amine	rod	0.085 ± 0.003	55 ± 5
scheme 2	ellipsoid	0.085 ± 0.005	55 ± 10

TMV virions are unenveloped and can be considered to be a solid protein object with a given surface charge density. The high value of the particle conductivity is therefore likely to arise from the counterions associated with the surface charge moving along the surface as well as charges moving inside the particle. As mentioned previously, the different labelling procedures result in a different surface charge distribution which could account for the difference in the conductivity values for the two types of TMV. High values for the relative permittivity and

conductivity have been reported previously for a similar unenveloped plant virus, Alfalfa Mosaic Virus [10].

8.4.2 Threshold force

The absolute DEP force $\underline{\mathbf{F}}_{DEP}$ can be derived from equation (4.21) and the expression for the susceptibility of the particle. The force equation is:

$$\underline{\mathbf{F}}_{DEP} = -\frac{2\pi abc}{3}\varepsilon_m \mathrm{Re}\{\chi\}\nabla|\underline{\mathbf{E}}|^2 \tag{8.3}$$

where a, b, c are the half lengths of the axes, ε_m is the medium permittivity and χ is the susceptibility or polarisation factor (equation 3.50 or 3.55). $\nabla|\underline{\mathbf{E}}|^2$ is calculated numerically for the different electrode shapes as discussed in Chapter Six.

The force on a TMV virion can be calculated from equation (8.3) given the magnitude of $\nabla|\underline{\mathbf{E}}|^2$ at a point. The threshold potential required to induce observable positive DEP of TMV was measured as a function of medium conductivity (section 4.3.4) at a constant frequency of 100kHz. Thermal effects will be considerable on TMV as it is equivalent in volume to a sphere of approximately 26nm radius and below the threshold, it was assumed that these effects were dominant. The electric field was numerically calculated for a triangular electrode with feature and gap size equal to 4μm. The value of $\left|\nabla|\underline{\mathbf{E}}|^2\right|$ at a distance of 1μm from the tip for each applied potential was determined. Typically, for a peak to peak potential of 2 volts, $\left|\nabla|\underline{\mathbf{E}}|^2\right|$ at 1μm had an average value of 10^{17} V^2m^{-3}. The maximum value for the same solution was approximately 10^{21} V^2m^{-3} at the tip and the minimum value along the line between the tips was 10^{16} V^2m^{-3} in the centre.

In addition to the simple dielectrophoretic force, the torque on the particle must be considered. The equations described previously all assume that the major axis is aligned with the electric field. However, an ellipsoid at a random orientation to the field, experiences a torque which tends to align one of the axes with the field [5]. As was shown in [5] and [11], the regions of frequency and medium conductivity in which the major axis is not aligned with the field can be calculated. For the rod, the torque component at any point always acts to align the major axis with the field. From calculations based on [5,11], when the rod is oriented with one of the minor axes parallel to the field, the torque is zero but the particle is in an unstable equilibrium. For the prolate ellipsoid, from [11], the torque acts to orient the major axis with

the field for medium conductivities greater than $0.1Sm^{-1}$ and for all frequencies. For conductivities less than $0.1Sm^{-1}$, the torque acts to align a minor axis with the field in a narrow frequency window from approximately 5-50MHz. Therefore, for the purpose of calculating the DEP force at 100kHz, the particle can be assumed to be oriented with the major axis parallel to the electric field.

The threshold field data can be analysed by plotting $\left|\nabla|\underline{E}|^2\right|$ for each medium conductivity against $1/\chi$. This is shown in Figure (8.15) for a susceptibility given by the rod model with the particle dielectric properties determined in section (8.4.1). The gradient of this plot is:

$$F_{thr} \Big/ \left(\frac{2\pi abc}{3}\right) \tag{8.4}$$

where F_{thr} is the threshold force. Using equation (8.4) a threshold force value of $F_{thr} = 1.12\times10^{-15}$ N (± 52%) was calculated, equivalent to an rms value of 5.6×10^{-16} N. The same calculation was performed for the ellipsoid model and the threshold force found to be $F_{thr} = 1.05\times10^{-15}$ N (± 47%) which is equivalent to an rms value of 5.3×10^{-16} N.

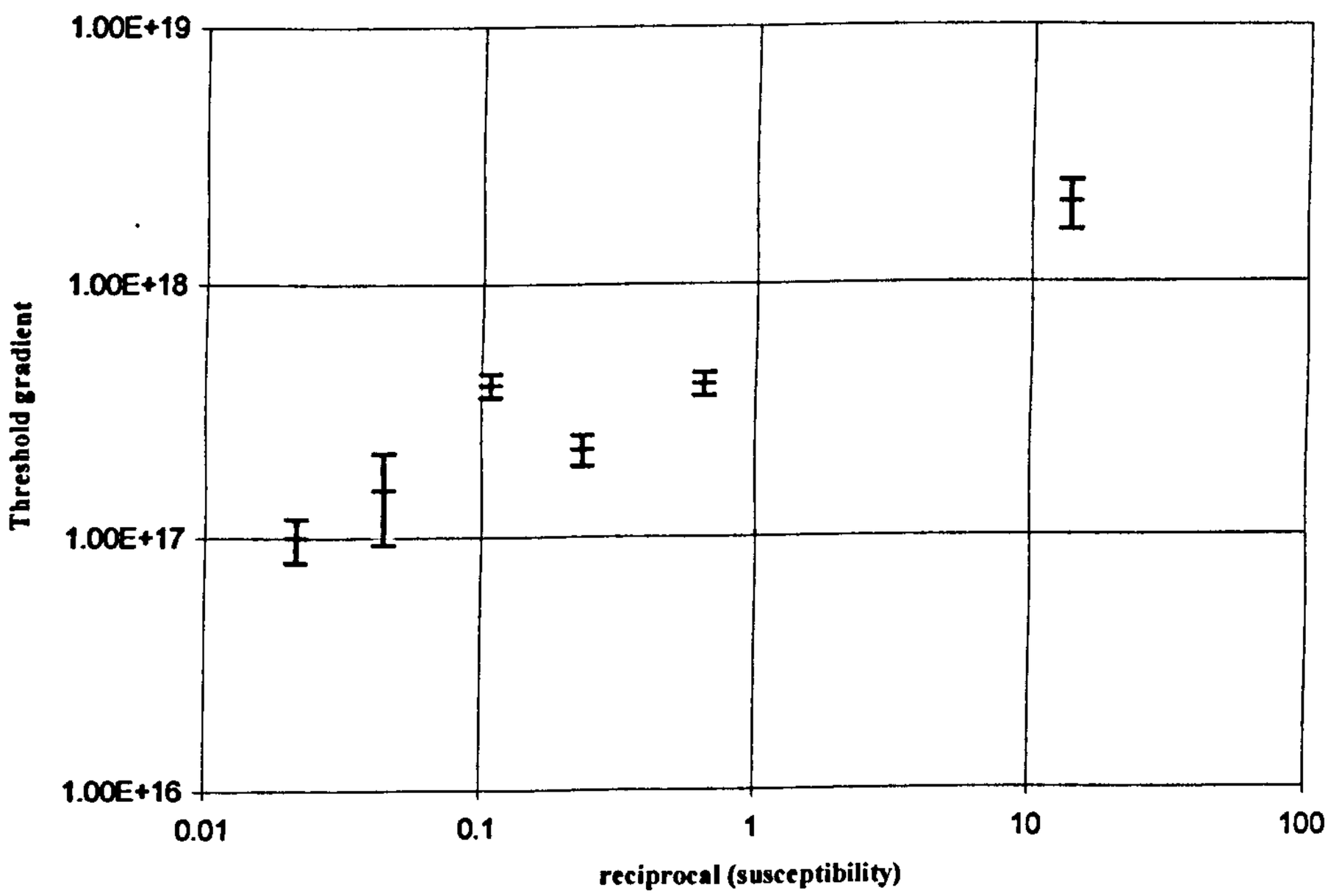

Figure (8.15) A plot of $\nabla|\underline{E}|^2$ at the threshold potential against the reciprocal of the particle susceptibility from the rod model given by equation (3.55). The threshold potential was defined to be the potential at which positive DEP is observed.

The calculated value for the force is much lower than would be expected from the thermal diffusion arguments used to predict threshold forces previously [12,13]. One possible error is the volume term in equation (8.3) and (8.4). The high value of particle conductivity for TMV was deduced to arise from surface charge and associated counterions (section (8.4.1). If a noticeable proportion of these counterions are in a diffuse layer around the particle, the additional volume equal to the surface area times the Debye length should be considered. In the lowest medium conductivity measured, the Debye length is large compared to the particle radius, the volume of the particle is increased by a factor of approximately 20 and the force is therefore increased by the same amount to approximately 1×10^{-14} N. However, even allowing for this correction, the estimated force is orders of magnitude lower than expected from the arguments of Pohl [12].

The force required to overcome thermal effects is discussed further in Chapter Nine.

Appendix (8a) Matlab functions

This appendix contains the functions used to plot the functions for the susceptibility and zero force frequencies for a rod and a prolate ellipsoid in section (8.4).

Rod plotting script

```
% This script calculates the clausius-mossotti factor for a
% prolate spheroid which has become a rod of length a
% given a vector of conductivities . The program
% plots a 3D graph, calculates all the zero points
% and plots them on a 2D graph.

clear all

global ep em eo sp scd mob a;

ep = 55; em = 78.54; eo = 8.85e-12;          % permittivity
stuff
sp = 0.085; scd = 0.0; mob = 7.56e-8;        % conductivity
stuff
n1 = 1; n2 = 10; N = 50;                     % frequency
vector numbers
m1 = -4; m2 = 1; M = 200;          % conductivity vector numbers
a = 150e-9;                                  % particle radius
zerr = 0.01;                                 % zero error value
(percent)
label = 2;                                   % switch
rhodamine amine (2) or rhodamine (1)

% variable definition stage

f = logspace(n1,n2,N);
sigm = logspace(m1,m2,M);

% plotting bit

DCM = []; ICM = [];
for l = 1:M
  sm = sigm(l);
  DIPval = MWrod(f,sm);
  for k = 1:(N-1)
    trans1 = real(DIPval(k));   f1 = f(k);
    trans2 = real(DIPval(k+1)); f2 = f(k+1);
    test = trans1*trans2;
    if test < 0
      error = 101; zerof = [];
      while error > zerr
        shortf = [f1 f2];
        trans1 = real(MWrod(shortf,sm));
         meanf = (f1+f2)/2;
        trans = real(MWrod(meanf,sm));
        test1 = trans*trans1(1);
        test2 = trans*trans1(2);
                    if test1 < 0
                    f2 = meanf; zerof = (meanf+f1)/2;
                    end
                    if test2 < 0
                    f1 = meanf; zerof = (meanf+f2)/2;
                    end
        error = ((abs(meanf-zerof))*100)/zerof;
      end
      zeros = [zeros zerof];
    end
  end
  DCM = [DCM,real(DIPval)];
  ICM = [ICM,imag(DIPval)];
end

% work out the plotting vector for the zeros
goo = size(zeros);

for kl = 1:(goo(2)-1)
  xover(kl) = zeros(kl+1);
end
for lk = goo(2):M
  xover(lk) = 1;
end

%mesh(log10(sigm),log10(f),DCM');
%Ylabel('log(frequency)')
%Xlabel('log(medium conductivity)')
%axis([m1 m2 n1 n2 -1 1])
%Title('3d plot of the polarisation factor for rod')
%view(135,45)

%figure
loglog(sigm,xover)
Xlabel('log(medium conductivity)')
Ylabel('zero force frequency (Hz)')
axis([1e-4 1e1 1e5 1e8])

hold on
switch label
case 1
  dataTMV; loglog(conddata,posdata,'kx');
loglog(conddata(1:5),negdata,'ks');
  axis([1e-4 1e1 1e5 1e8])
case 2
  dataTMV; loglog(conddata,posdata,'kx');
  axis([1e-4 1e1 1e5 1e8])
end
hold off
```

Rod susceptibility function

```
function [R1] = MWrod(freq,sigm)

% This function plots the maxwell-wagner interfacial
% polarisation terms for a prolate ellipsoidal particle. There
% are of course two - because there are three axes, two of which
% have the same answer.

% The function needs the following variables defined as global
% ep - particle perm, em - medium perm, sp - particle cond
% scd - surface charge dens, u - mobility, eo - perm of free space
% a - virus particle length

global ep em eo sp scd mob a;

% dipole calculation

w = 2*pi*freq;
surfc = 2*mob*scd/a;
sigp = sp + surfc;
ems = em*eo - j.*(sigm./w);
eps = ep*eo - j.*(sigp./w);

dipole = (eps-ems)./ems;

R1 = dipole;

% end of function
```

Prolate ellipsoid plotting script

```
% This script calculates the clausius-mossotti factor for a
% prolate spheroid with axes radii a > b = c
% given a vector of conductivities . The program
% plots a 3D graph, calculates all the zero points
% and plots them on a 2D graph.

clear all

global ep em eo sp scd mob a b c;

ep = 45; em = 78.54; eo = 8.85e-12;          % permittivity
stuff
sp = 0.16; scd = 0.0; mob = 7.56e-8;         % conductivity
stuff
n1 = 1; n2 = 10; N = 50;                     % frequency
vector numbers
m1 = -4; m2 = 1; M = 200;          % conductivity vector numbers
zerr = 0.01;                                 % zero error value
(percent)
label = 1;                                   % switch
rhodamine amine (2) or rhodamine (1)
a = 150e-9; b = 9e-9; c = 9e-9;

% variable definition stage

f = logspace(n1,n2,N);
sigm = logspace(m1,m2,M);

% plotting bit

DCM = []; ICM = [];
for l = 1:M
  sm = sigm(l);
  DIPval = MWellipse(f,sm);
  for k = 1:(N-1)
    trans1 = real(DIPval(k));  f1 = f(k);
    trans2 = real(DIPval(k+1)); f2 = f(k+1);
    test = trans1*trans2;
    if test < 0
      error = 101; zerof = [];
      while error > zerr
        shortf = [f1 f2];
        trans1 = real(MWellipse(shortf,sm));
         meanf = (f1+f2)/2;
        trans = real(MWellipse(meanf,sm));
        test1 = trans*trans1(1);
        test2 = trans*trans1(2);
                    if test1 < 0
                    f2 = meanf; zerof = (meanf+f1)/2;
                    end
                    if test2 < 0
                    f1 = meanf; zerof = (meanf+f2)/2;
                    end
        error = ((abs(meanf-zerof))*100)/zerof;
      end
      zeros = [zeros zerof];
    end
  end
  DCM = [DCM,real(DIPval)];
  ICM = [ICM,imag(DIPval)];
end

% work out the plotting vector for the zeros
goo = size(zeros);
for kl = 1:(goo(2)-1)
  xover(kl) = zeros(kl+1);
end
for lk = goo(2):M
  xover(lk) = 1;
end

%mesh(log10(sigm),log10(f),DCM');
%Ylabel('log(frequency)')
%Xlabel('log(medium conductivity)')
%axis([m1 m2 n1 n2 -1 100])
%Title('3d plot of the polarisation factor for prolate ellipsoid')
%view(135,45)

%figure
loglog(sigm,xover)
Xlabel('log(medium conductivity)')
Ylabel('zero force frequency (Hz)')
axis([1e-4 1e1 1e5 1e8])

hold on
switch label
case 1
  dataTMV; loglog(conddata,posdata,'kx');
loglog(conddata(1:5),negdata,'ks');
  axis([1e-4 1e1 1e5 1e8])
case 2
  dataTMV; loglog(conddata,posdata,'kx');
  axis([1e-4 1e1 1e5 1e8])
end
hold off
```

Prolate ellipsoid function

```
function [R1,R2,R3] = MWellipse(freq,sigm)

% This function plots the maxwell-wagner interfacial
% polarisation terms for a prolate ellipsoidal particle. There
% are of course three - because there are three axes.

% The function needs the following variables defined as global
% ep - particle perm, em - medium perm, sp - particle cond
% scd - surface charge dens, u - mobility, eo - perm of free space
% a b c - the comparitive radii but b must equal c

global ep em eo sp scd mob a b c;

% dipole calculation

w = 2*pi*freq;
surfc = 2*mob*scd/a;
sigp = sp + surfc;
ems = em*eo - j.*(sigm./w);
eps = ep*eo - j.*(sigp./w);

% calculate the directional volume terms

qe = a/b;
inter = ((qe*qe) - 1);
Ax = (((qe/sqrt(inter))*log(qe + sqrt(inter)))-1)/inter;
Ay = (1-Ax)/2;
Az = (1-Ax)/2;

Xdipole = (eps-ems)./((Ax.*(eps-ems)) + ems);
Ydipole = (eps-ems)./((Ay.*(eps-ems)) + ems);
Zdipole = (eps-ems)./((Az.*(eps-ems)) + ems);

R1 = Xdipole;
% end of function
```

References

1. M.Zaitlin and H.C.Israel (1975)
   CMI AAB Description of plant viruses No.**151**
2. R.E.F.Mathews (1981) *Plant Virology*
   Academic Press, London
3. M.A.Lauffer (1939)
   Journal of the American Chemical Society **61** 2412-2416
4. N.G.Green, H.Morgan and J.J.Milner (1997)
   Journal of Biochemical and Biophysical Methods **35** 89-102
5. H.Morgan and N.G.Green (1997)
   Journal of Electrostatics **42** 279-293
6. H.Boedker and N.S.Simmons (1958)
   Journal of the American Chemical Society **80** 2550-2556
7. R.N.Perham and J.O.Thomas (1971)
   Journal of Molecular Biology **62** 415-418
8. T.M.A.Wilson and R.N.Perham (1985)
   Virology **140** 21-27
9. T.kakutani, S.Shibatani and M.Sugai (1993)
   Bioelectrochemistry and Bioenergetics **31** 131-145
10. F.Van der Touw, J.W.H.Breide and M.Mandel (1973)
    Biopolymers **12** 111-119
11. R.D.Miller and T.B.Jones (1993)
    Biophysical Journal **64** 1588-1595
12. H.A.Pohl (1978) *Dielectrophoresis*
    Cambridge University Press, Cambridge
13. M.Washizu, S.Suzuki, O.Kurosawa, T.Nishizaka and T.Shinohara (1994)
    IEEE Transactions on Industry Applications **30** 835-843

Chapter Nine

Results and discussion: Particle movement

9.1 Introduction

A particle in solution undergoing dielectrophoresis (DEP) experiences a number of forces other than the dielectrophoretic force, $\underline{F}_{DEP}$ as described in Chapter Four. Summarising, these are: the buoyancy force $\underline{F}_B$ related to the gravitational force and the difference in the particle and solution densities; a random thermal force $\underline{F}_{RAND}$ from Brownian motion; the diffusion force $\underline{F}_{DIFF}$, related to the thermal energy of the system and the concentration gradient, if any; and the viscous drag force $\underline{F}_{DRAG}$ due to the fluid. The total force $\underline{F}_T$ on the particle is given by the sum:

$$\underline{F}_T = \underline{F}_{DEP} + \underline{F}_B + \underline{F}_{RAND} + \underline{F}_{DIFF} + \underline{F}_{DRAG} \qquad (9.1)$$

For DEP on the super-micrometre scale, for example DEP separation of cells [1-3], the effects of forces other than buoyancy and drag are generally ignored in the total force equation. If the cell is more dense than the suspending medium, the buoyancy force acts downwards and the cell sinks until it comes to rest on the glass substrate or on the electrodes and the buoyancy force can also be neglected. In this case there is, of course, an extra drag term due to the friction between the cell and the surface.

On the sub-micrometre scale, thermal forces cannot be ignored. Thermal effects must be considered in order to explain for example, why there is a threshold DEP force required to initiate movement (Chapter Eight). If the force equation consisted only of the DEP term and a drag term acting against it, then DEP should be observed for all applied field strengths but it is not. Section (9.2) presents and discusses a definition pertinent to this problem.

An additional effect observed clearly on the sub-micrometre scale [4,5] is fluid flow caused by a combination of electrical and thermal effects. The high electric fields in DEP electrodes can cause strong fluid flow, which in turn adds to the drag term in the total force equation. The drag term in equation (9.1) as applied to cell DEP is only valid for a static fluid, which is not necessarily true for the sub-micrometre scale and in certain circumstances the super-micrometre scale as well. Section (9.3) discusses fluid flow patterns and the observational evidence for such, as well as clarifying previously reported "unexplained" DEP phenomena which can be completely explained in terms of fluid flow [2,3].

9.2 Observations of forces and Brownian motion.

An energy based argument can be used to describe the balance, or lack of, between the dielectrophoretic energy (equation 4.22) and the thermal energy of a particle (which is of the order of kT) by numerically comparing the two energies [6]. However, experiments have consistently shown that the values of electric field strength predicted by this method which are necessary to overcome the effects of thermal energy are too high. The problem with this method is that it simply balances the thermal energy with the dielectrophoretic potential at a point whereas the force is the gradient of the potential. As a result, it is better to consider the force instead.

9.2.1 Definition: An 'Observably Deterministic Force'

An energy method can be used to describe the force necessary to trap colloidal particles as above, however, it is forces and potential gradients which are most important for dielectrophoresis, especially on the sub-micrometre scale

In this section for the sake of experimental analysis, an '*observably deterministic*' force is defined for a **single** colloidal particle over a time interval Δt. A colloidal particle is defined in physical chemistry to be a particle whose size is between the limits 1nm and 1μm. In this range, the particle is small enough to be significantly affected by Brownian motion but still large enough so that the medium it is suspended in can be assumed to be a continuum.

The system is taken to be sufficiently large so that the boundary conditions do not affect the particle over a time interval Δt. At time $t = 0$, the particle position is recorded by an observer and its position at this time can be represented by a delta function at position $x = 0$. Over a period of time, the particle experiences a random force which gives rise to stochastic movement of the particle (Chapter Four). As a result, the position of the particle after some time can only be represented by a probability distribution of possible positions around a mean value. In this specific case, the position of the particle after time Δt is represented by a Gaussian displacement distribution (with zero mean) and standard deviation (from equation 4.8) given by:

$$\sigma_x = (6D\Delta t)^{1/2} \tag{9.2}$$

where D is the particle diffusion coefficient given by $D = kT/f$ (equation 4.13) and f is the friction factor for the particle.

Assume that the particle experiences an arbitrary uniform force F and that the force has been applied for a time prior to t = 0 sufficient for the system to reach steady state. The particle therefore moves at a terminal velocity given by:

$$v = \frac{F}{f} \tag{9.3}$$

In the steady state, over the time interval Δt, the displacement is given by $\Delta x = v\Delta t$ and substituting for v from equation (9.3) gives:

$$\Delta x = \frac{F}{f}\Delta t \tag{9.4}$$

At $t = 0$, the particle position is represented by a delta function at $x = 0$. For $t > 0$, the particle moves only under the influence of the force F and Brownian motion. After time Δt, the position of the particle is represented by a Gaussian distribution with mean position given by equation (9.4) and a standard deviation given by equation (9.2). In simple terms, this means that if the particle is observed for the second time after Δt, there is a 67% chance of finding it within a sphere of radius σ_x around the mean position Δx. If the radius of the sphere is equal to three standard deviations, the probability is now 99.7%.

For the definition of an observable deterministic force, a displacement of $\Delta x = 3 \times \sigma_x$ is considered a sufficient limit to determine whether the particle has moved due to the force F over the time interval Δt. Substituting this displacement (using equation 9.2) into equation (9.4) gives:

$$\frac{F}{f}\Delta t = 3(6D\Delta t)^{1/2}$$

which can be rearranged in terms of the force and the time interval:

$$F\Delta t^{1/2} = (54kTf)^{1/2} \tag{9.5}$$

This gives the threshold force required to be '*observably deterministic*' for a particle of friction factor *f* over a time interval Δt. Figure (9.1) shows the variation of F with Δt for a spherical particle of radius *a*, in a medium of viscosity 8.4×10^{-4} Nsm^{-2} at a temperature of 295K.

Increasing the time interval (for the same particle) decreases the threshold force. Also, since this is a statistical definition, increasing the number of observations, by either repeated

observations of the same particle or by looking at several non-interacting particles, also decreases the threshold force. The equation produced by considering the case of multiple observations is not discussed here.

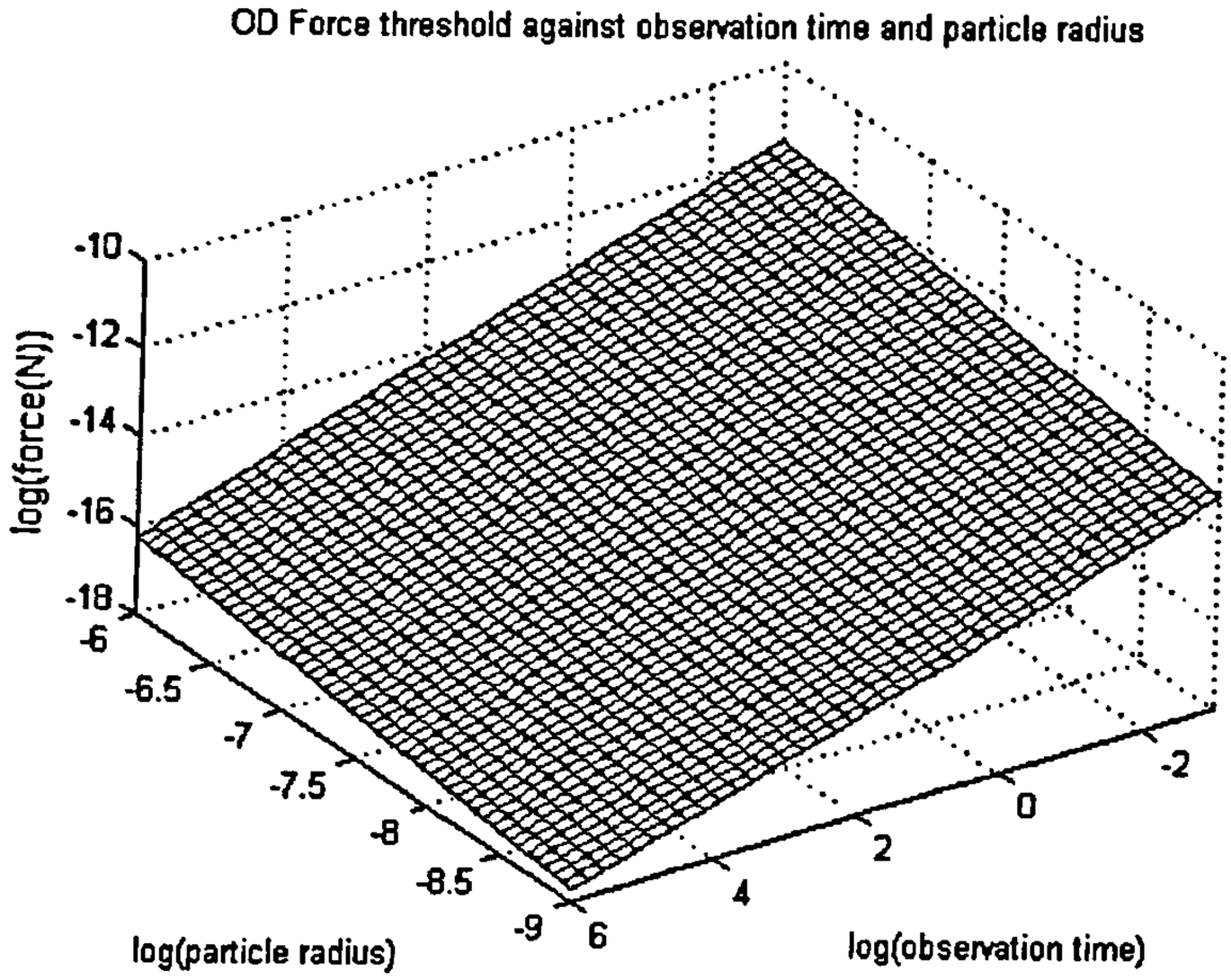

Figure (9.1) Diagram of the variation of the observably deterministic force threshold with observation time and particle radius in the colloidal domain. The value along the vertical axis is the log of the threshold force and all three axes are $\log_{10}$ of the appropriate value.

The next section compares values of forces for latex spheres and TMV obtained from experimental observations with the force predicted by this theory.

9.2.2 The dielectrophoretic force.

Figure (9.2a) shows a theoretical plot of the value of the observational force threshold F against time interval Δt for the four sizes of latex spheres used in the experiments detailed in Chapter Seven. The predicted size of force for an observation time of approximately 1-10 seconds is of the order of 10^{-14}N which can be achieved for the 282nm spheres with $\left|\nabla|\underline{E}|^2\right| = 3\times10^{14}V^2m^{-3}$. This value of the gradient of the dielectrophoretic potential can easily be obtained in a set of experimental electrodes.

Figure (9.2b) shows a plot of the theoretical force threshold for Tobacco Mosaic Virus. The predicted value for the threshold is ~ 3-8$\times10^{-15}$N for an observation time of between 1 and 10 seconds which agrees with the measured threshold force of 6×10^{-16}N in Chapter Eight if the volume of the virus is assumed to include the double layer. The calculation was performed using

the friction factor for an ellipsoid as outlined in section (4.2.2) and the correction factor (equation 4.4) was determined to be 1.86.

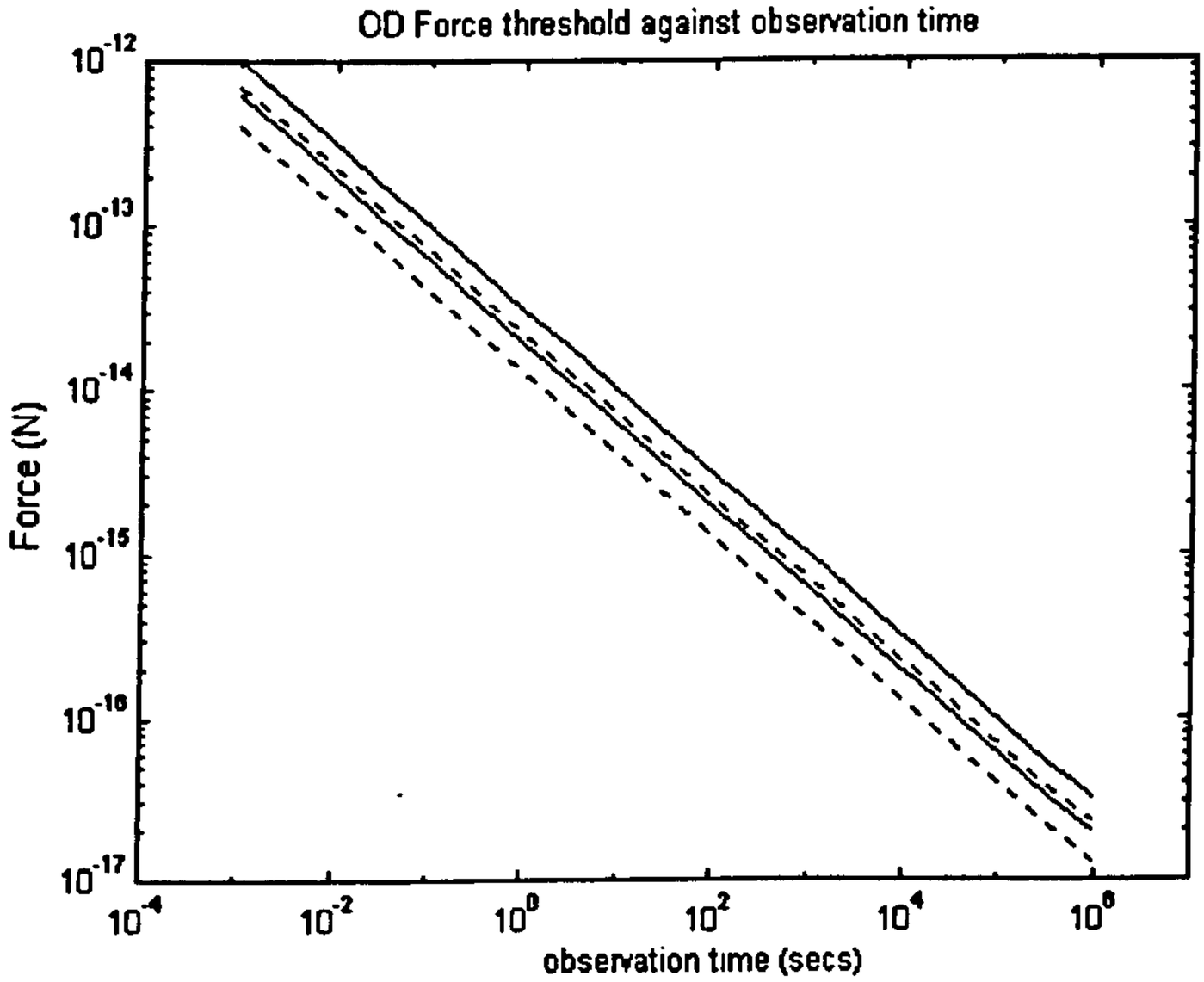

Figure (9.2a) Theoretical diagram of the variation of the observably deterministic threshold force for the four sizes of latex spheres used in Chapter Seven. The upper solid line is for the 557nm, the lower solid line is for the 216nm, and the upper and lower dashed lines are for the 282nm and 93nm spheres respectively. As can be seen, the threshold force, plotted along the y-axis decreases with particle radius.

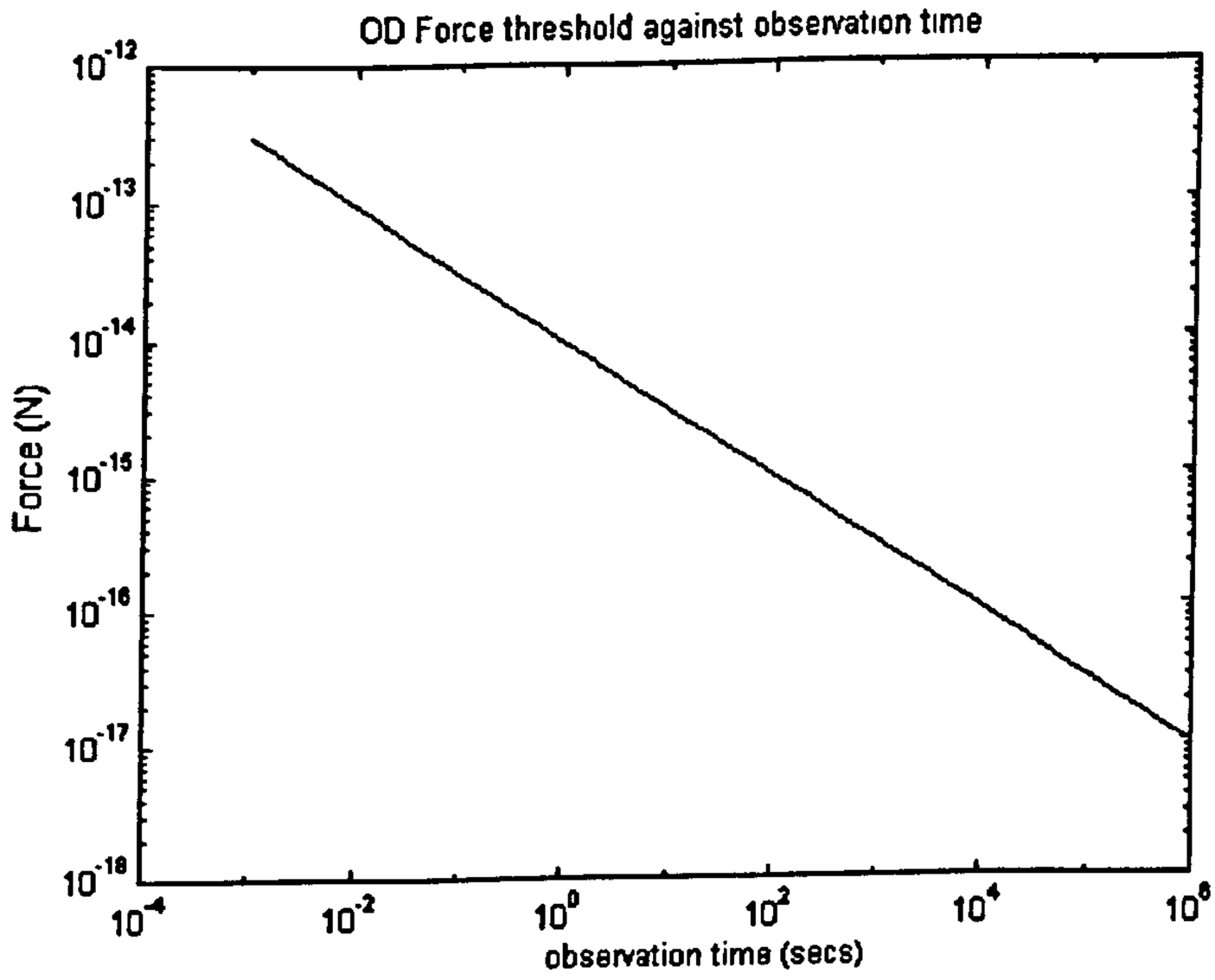

Figure (9.2b) Theoretical diagram of the variation of the observably deterministic force threshold for TMV. The threshold force plotted along the y-axis decreases with increasing time of observation.

9.3 Fluid movement in microelectrode arrays

Fluid flow caused by the electric field in microelectrodes has been reported previously [4,5], without a detailed attempt being made to characterise the behaviour. It has been described both as a disruptive effect or something which assists dielectrophoretic collection in the case of polynomial electrodes [4]. Dielectrophoresis on the sub-micrometre scale is affected by convection to a greater degree than for larger systems and as a result the effect of fluid movement cannot be ignored. Controlled fluid movement can in fact be used as a practical means of separation independently of dielectrophoresis as shown in Chapter Ten.

Work on elucidating the mechanism responsible for fluid flow is being carried out in a collaborative project with the University of Sevilla. This work is not part of this thesis, but the results are worthy of inclusion.

The charge relaxation frequency of a liquid is given by $2\pi f_0 = 1/\tau = \sigma/\varepsilon$. Power dissipation in a liquid gives rise to temperature gradients which in turn produce inhomogeneities in the permittivity and conductivity of the liquid. As a result, volume forces occur, driving fluid motion. At low frequencies, below a threshold frequency f_0, coulomb forces dominate, whereas at high frequencies, above f_0, dielectric forces (from permittivity gradients) dominate. The threshold frequency at which both forces are equal is given by [5]:

$$2\pi f_0 = \frac{1}{\tau}\left|\frac{\frac{\partial\sigma}{\sigma\partial T}}{\frac{\partial\varepsilon}{\varepsilon\partial T}}\right|^{\frac{1}{2}} \tag{9.6}$$

The coulomb force is approximately ten times stronger than the dielectric force [5].

This section describes the different convection patterns observed in the micro electrode arrays used during the course of this work and the resulting observed particle movement. The frequency ranges in which each pattern is seen is detailed as well as the effect of altering the frequency and potential of the applied field.

9.3.1 Low frequency fluid flow

At frequencies below f_0, fluid movement was observed moving onto the electrode surface. Figure (9.3) shows a representation of a gap between two parallel electrodes and the observed fluid motion. The fluid moves onto and parallel to the electrode surface along a path which is perpendicular to the edge of the electrode.

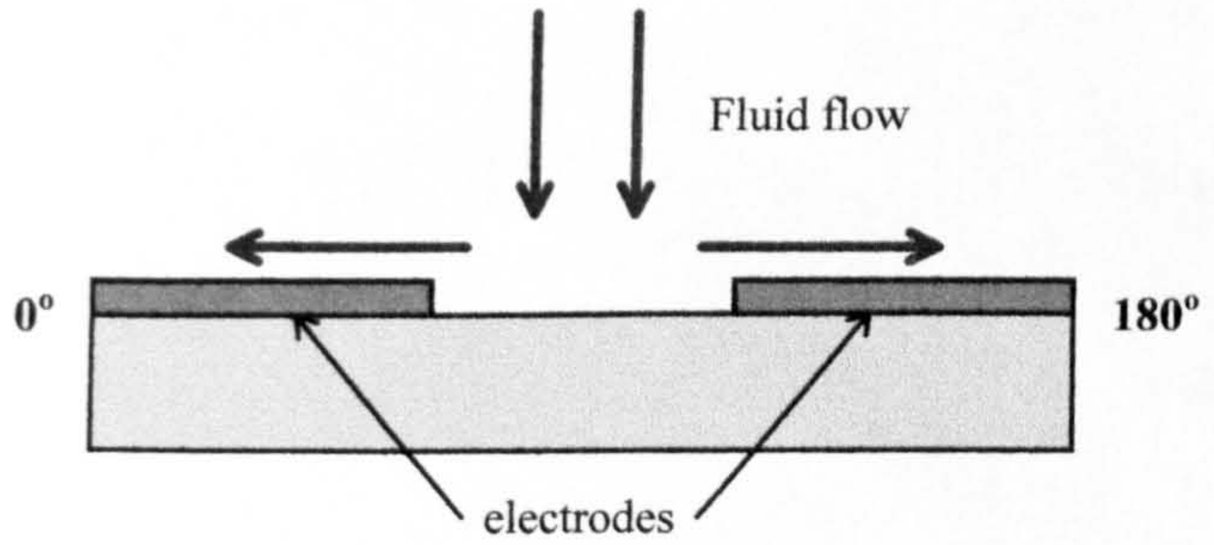

Figure (9.3) Approximate fluid flow observed at the edges of electrodes at frequencies below f_0.

This fluid flow occurred at any electrode edge and the velocity of the flow increased both with decreasing frequency and increasing potential. According to the theory [5], this flow velocity reaches a plateau as the frequency is decreased but in these type of microelectrode arrays, it was difficult to determine an absolute flow velocity. This type of flow was seen at higher frequencies in media of higher conductivity as the charge relaxation frequency is correspondingly higher.

In microelectrode arrays, the observation of this flow is complicated by the geometry of the electrodes. The flow velocity was proportional to the electric field strength in some manner and the flow pattern was complicated by the shape of the electrode edges. In hyperbolic electrodes, the flow was readily observed when the latex spheres experienced positive dielectrophoresis. The DEP force pulled the particles towards the electrode edge and the drag force from the fluid flow pushed them away. This is shown schematically in Figure (9.4) with the flow patterns for one electrode only being drawn for simplicity.

Figure (9.4a) shows the flow at a low potential and the line along which the fluid flow balances the DEP force is close to the electrode edge. If the potential is high, as shown in Figure (9.4b), the fluid velocity is highest where the field is strongest (see Chapter Six), the fluid has a higher velocity over a greater distance and the particles are pushed well onto the electrodes. Figure (9.5) shows a photograph of 557nm diameter spheres on a set of 10μm hyperbolic polynomial electrodes at 100kHz 12 volts peak to peak in 1mM KCl. Fluid flow is very apparent and the particles are being pushed well away from the centre of the array into the centre of the individual electrodes

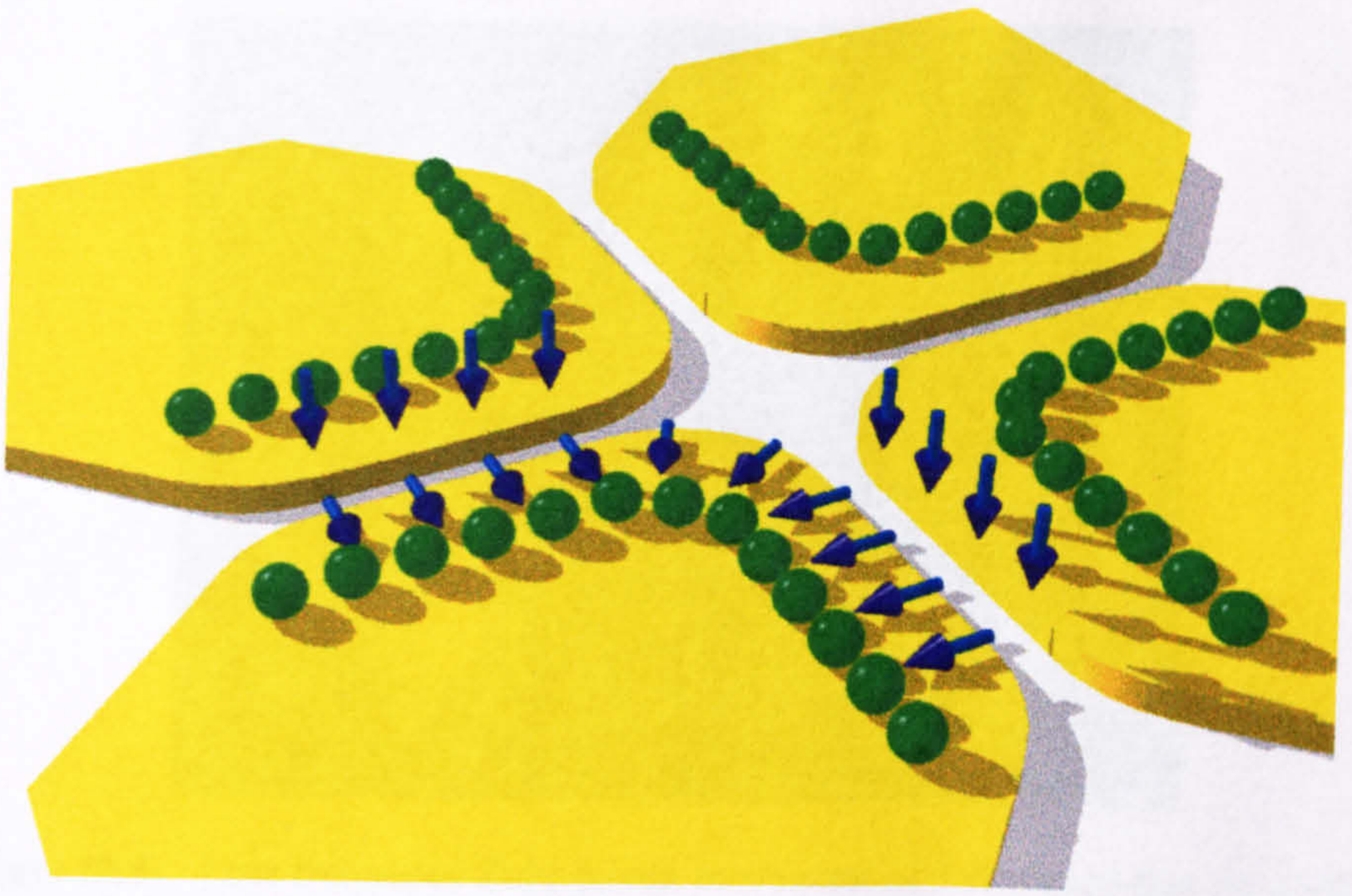

(9.4a) Fluid flow (blue arrows) and approximate particle position on a set of hyperbolic electrodes at low potentials and $f < f_0$.

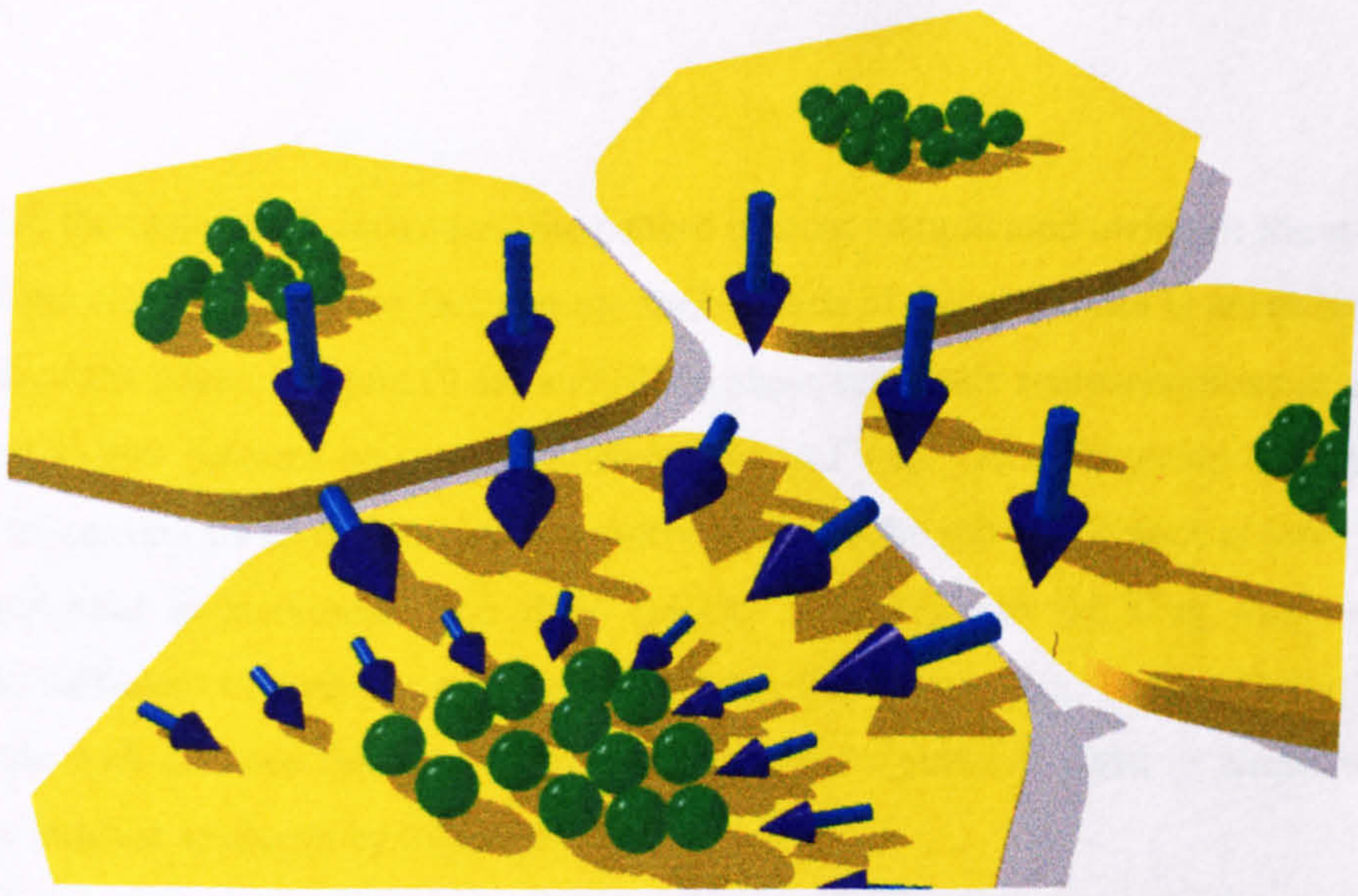

(9.4b) Fluid flow (blue arrows) and approximate particle position on a set of hyperbolic electrodes at high potentials and $f < f_0$.

Figure (9.4) Schematic diagram of the low frequency fluid flow direction close to the electrode edge on one of the four electrodes in the hyperbolic polynomial design. The approximate particle positions at which the drag force and the positive DEP force balance are indicated.

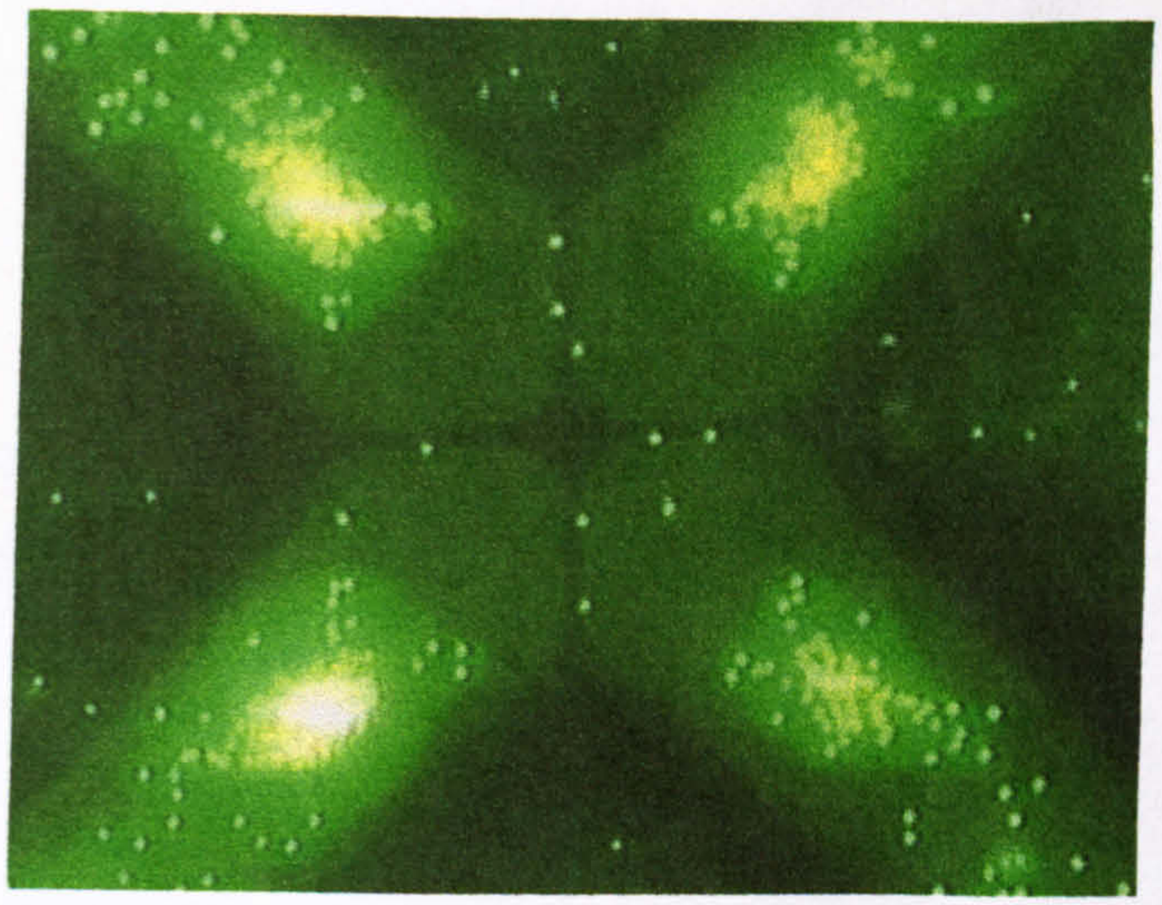

Figure (9.5) Low frequency fluid driven movement of 557nm spheres on a set of hyperbolic polynomial electrodes with a centre separation of 10μm. A few spheres can be seen stuck to the edge of the electrodes by positive DEP but the majority are being pushed on top of the electrodes by the movement of fluid from the edges onto the surface.

On the castellated electrodes, the pattern is more complicated owing to the symmetrical nature of the electrodes and the fact that the surface area of the electrodes is small compared to the length of the edges. Figure (9.6a) and (9.6b) show schematic representations of a high and low potential flow patterns on castellated electrodes at $f < f_0$. At a frequency low enough for this type of convection to be prominent, positive DEP of the spheres is seen at low potentials. As the potential is increased, the fluid velocity increases and the drag force reaches a magnitude sufficient to push the particles away from the edges. The fluid velocity decreases very rapidly with distance from the electrode edge and the particles settle at points where the two forces balance as shown by Figure (9.6a).

As the potential is further increased, the particles are pushed into the centre of the electrodes where they settle into formations dictated by the flow patterns. The fluid moves in from all edges into the centre of the electrode, then up and out into the bulk. The particles remain along the axis of symmetry of the electrodes, presumably under the influence of gravity, positive DEP and possibly, the formation of a stagnation region. This is shown schematically in figure (9.6b) and by experimental results shown in Figure (9.7) which show the effect of increasing the potential on 93nm diameter latex spheres in a set of 4μm castellated electrodes.

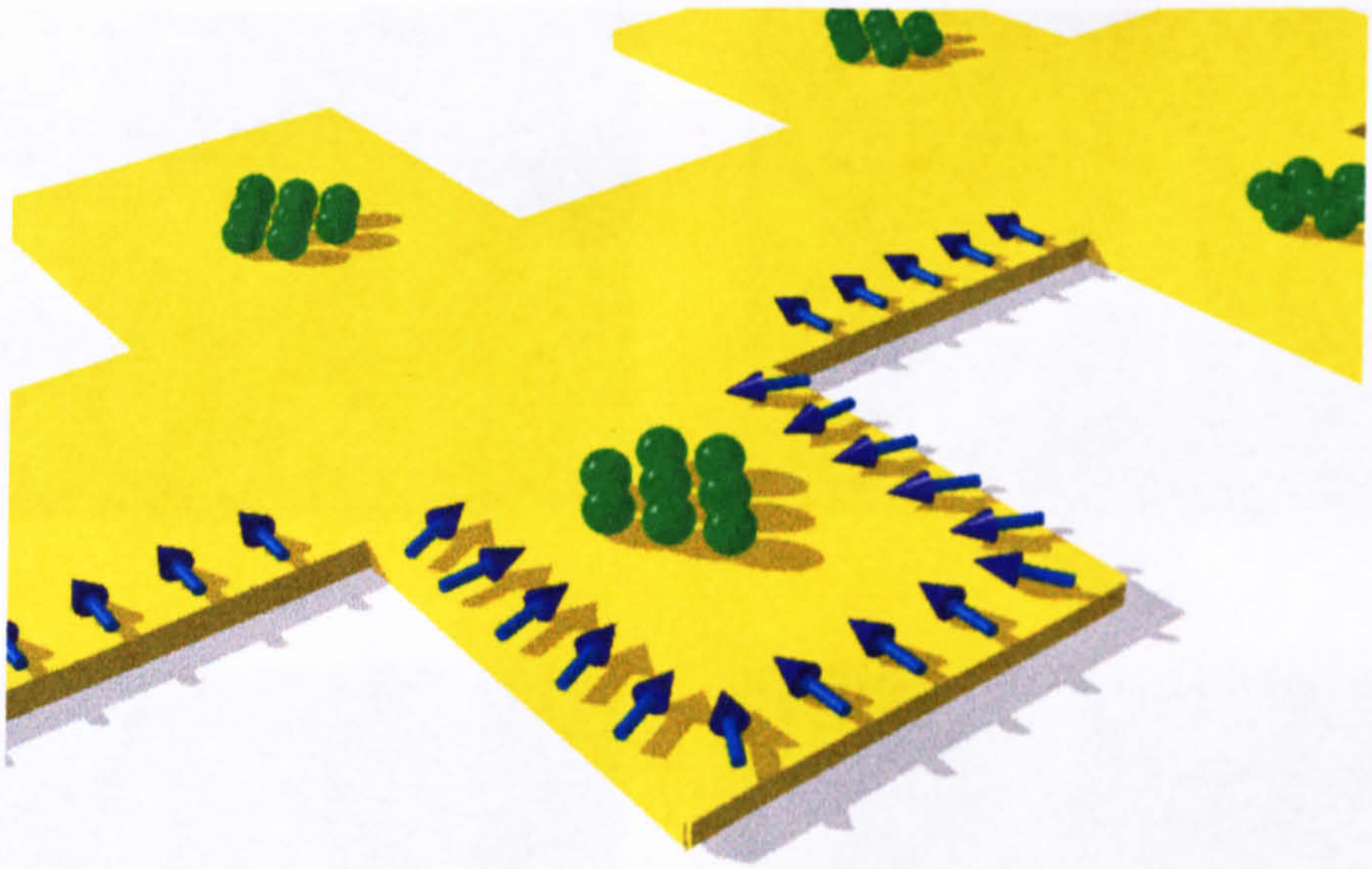

(9.6a) Fluid flow (blue arrows) and approximate particle position on a set of hyperbolic electrodes at low potentials and $f < f_0$.

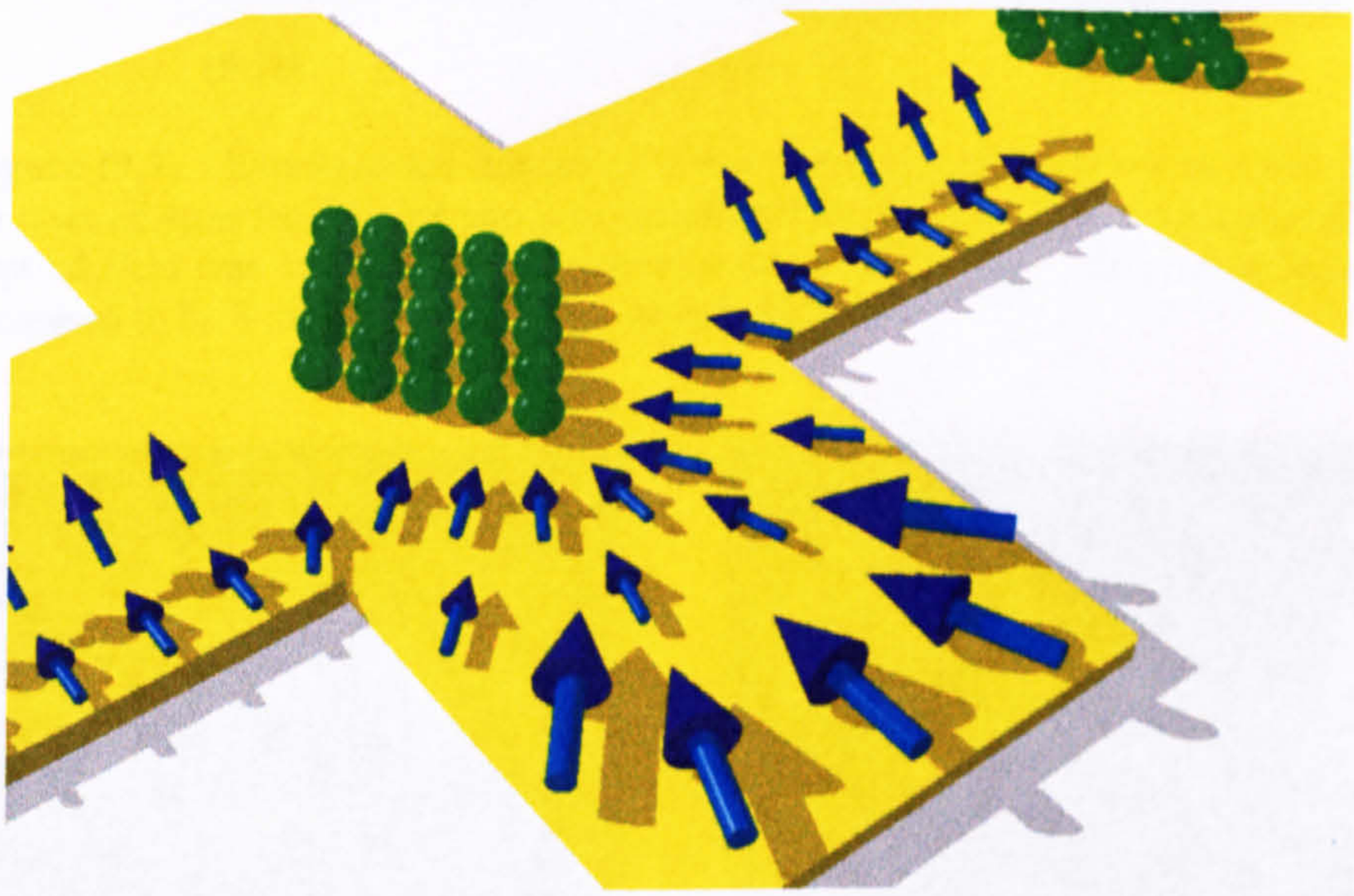

(9.6b) Fluid flow (blue arrows) and approximate particle position on a set of hyperbolic electrodes at high potentials and $f < f_0$.

Figure (9.6) Schematic diagram of the low frequency fluid flow direction close to the electrode edge on one of the features on a set of castellated electrodes. The approximate particle positions at which the drag force and the positive DEP force balance are indicated.

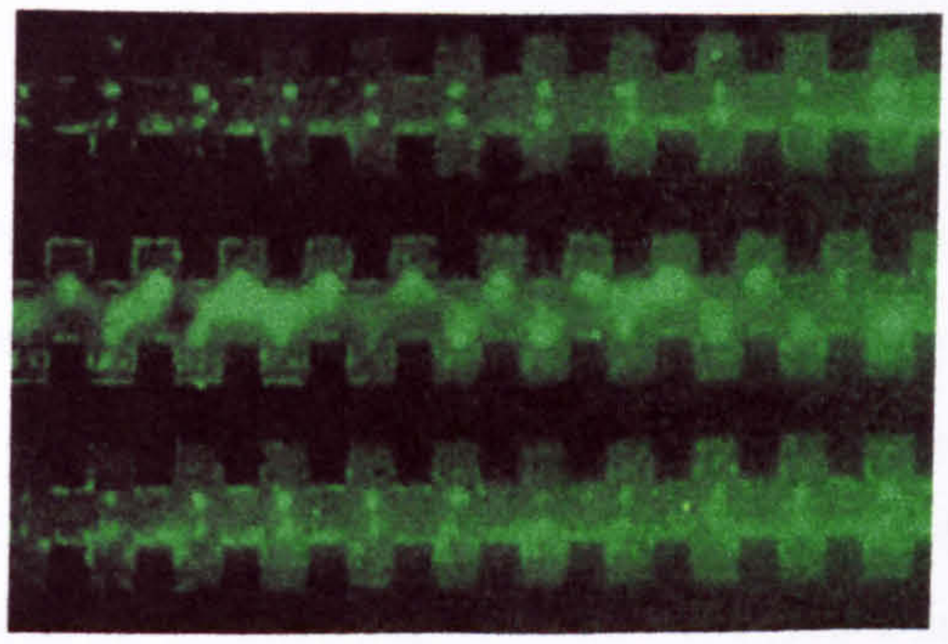

(9.7a)

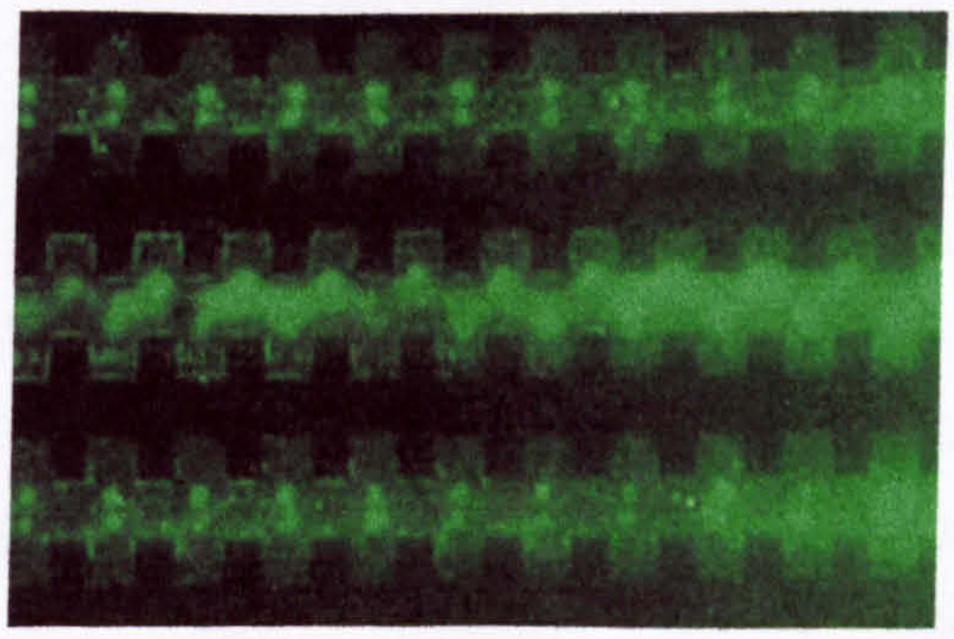

(9.7b)

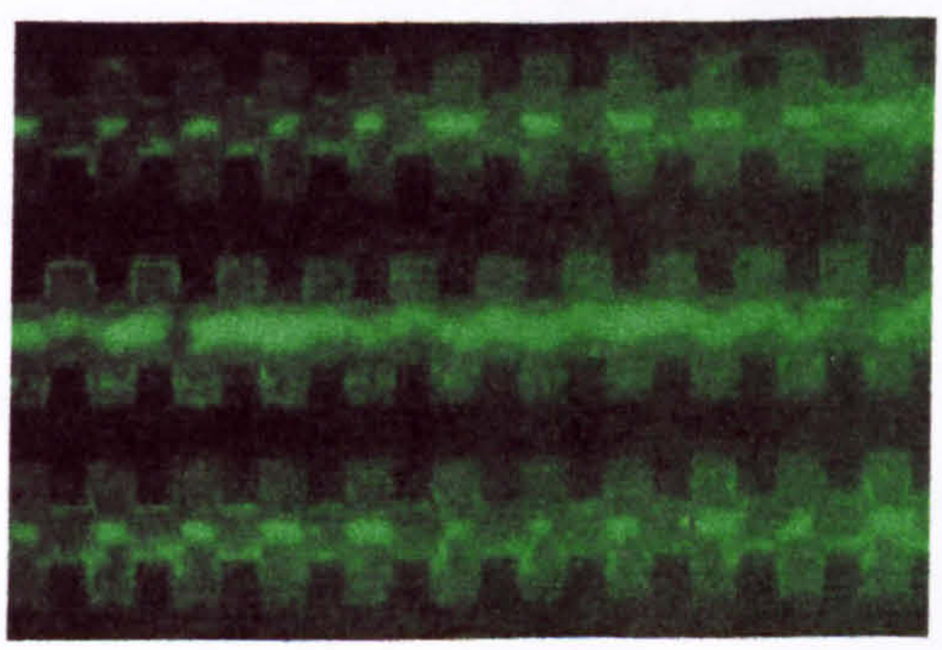

(9.7c)

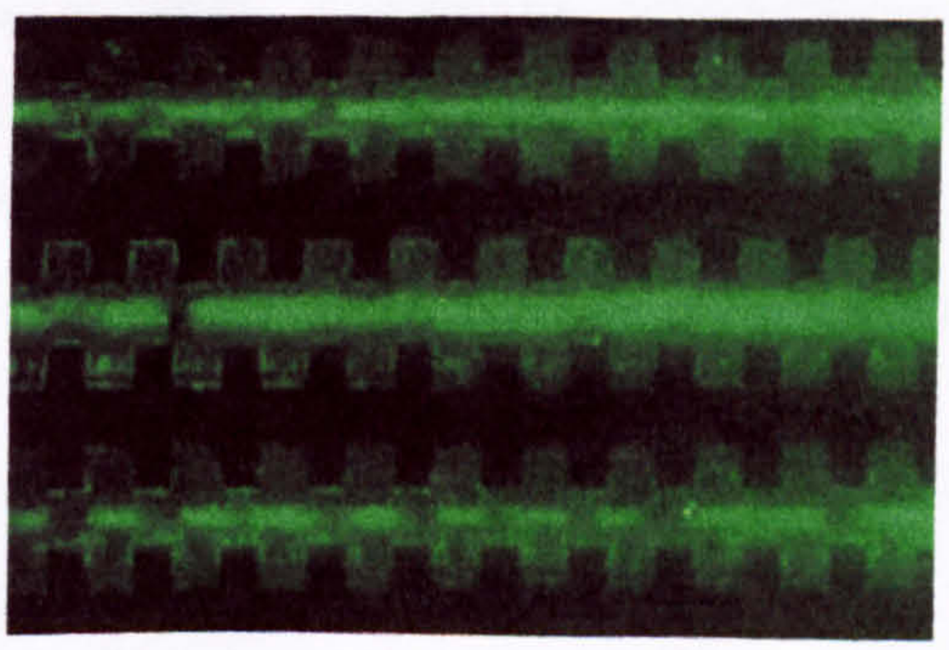

(9.7d)

Figure (9.7) Experimental images of 93nm diameter latex spheres in 1mM KCl on a set of 4μm feature and gap size castellated electrodes. The frequency of the applied field was 100kHz and the potential was 4volts peak to peak in **(9.7a)** and increased to 6, 8 and 10 volts peak to peak in **(9.7b-d)**.

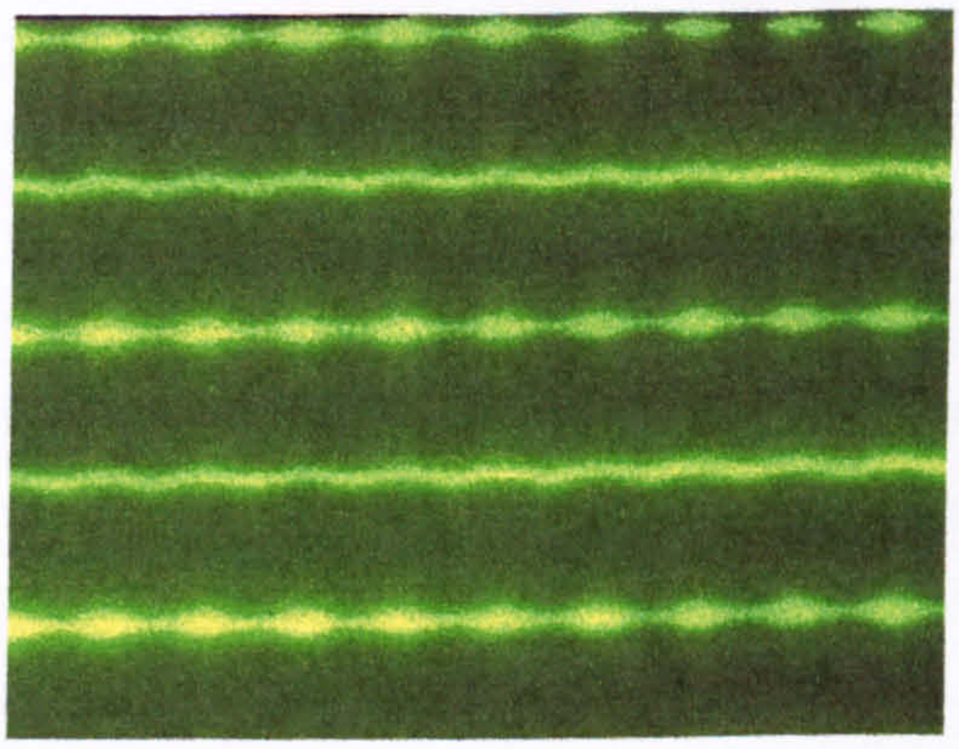

(9.8a) 557 nm spheres in 50μM KCl at an applied frequency of 100kHz and 5 volts peak to peak.

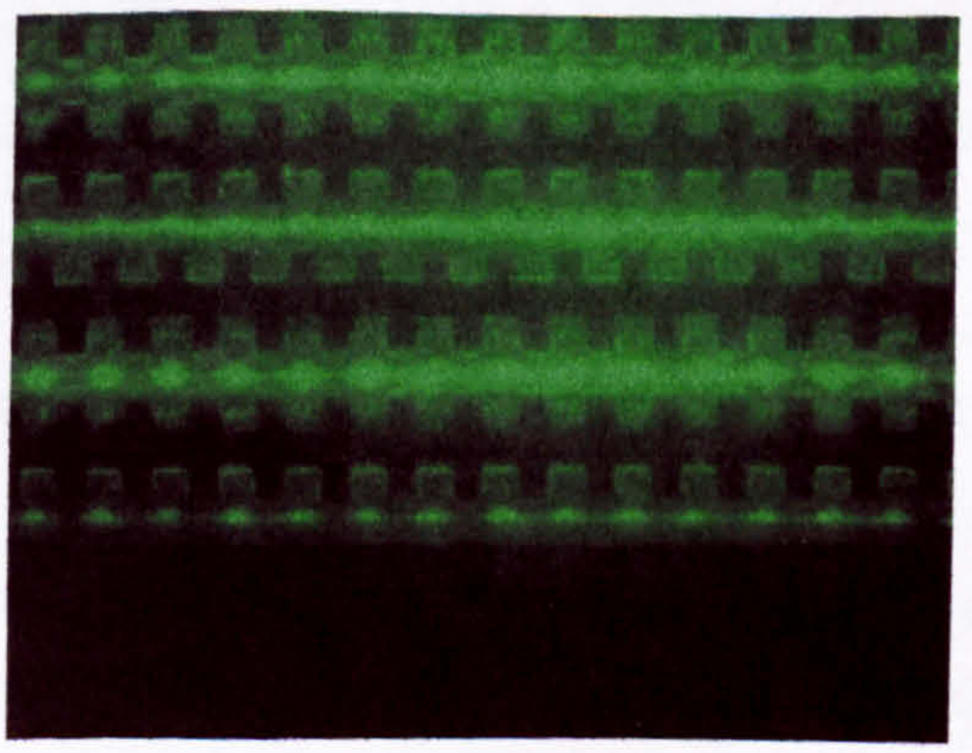

(9.8b) 93 nm spheres in 50μM KCl at an applied frequency of 100kHz and 5 volts peak to peak.

Figure (9.8) Experimental images of latex spheres on a set of 4μm castellated electrodes forming in the diamond formation reported previously [2,3]. As can be seen from (9.8b), there are a few spheres still experiencing positive DEP while most are pushed into the centre by fluid flow

The diamond formation shown in Figure (9.6b) and (9.8b) for 93nm latex spheres has been reported previously for cells on castellated electrodes [2,3]. Here, the effect is seen at lower frequencies (owing to the fact that cells are much larger) and also occurs for cells that are experiencing negative dielectrophoresis. The reason that the particles which move into the centre of the electrodes are those which are experiencing negative DEP in this case rather than positive is that the trapping force for the former is much lower than for the latter. There is also the fact that the negative trap does not exist after a certain height above the electrodes (see Chapter Six). For the spheres, the movement into diamond shapes on top of the electrodes occurs while they are experiencing positive dielectrophoresis. At low potentials, they are trapped at the electrode edges by positive DEP as shown in Chapter Seven. As the potential is increased, they move into the centre of the electrodes in the manner described above. The Clausius-Mossotti factor does not vary with the potential of the applied signal (for linear dielectrics), so the movement cannot be due to dielectrophoresis.

This form of fluid flow is reproducible and was observed over a wide range of medium conductivities and appears to occur only below the charge relaxation time (or f_0) of the liquid.

9.3.2 High frequency fluid flow

The second type of fluid flow occurred at high frequencies, possibly only above f_0. It was most noticeable in the polynomial electrodes as the flow enhanced the collection of particles by negative dielectrophoresis in the centre of the electrodes. However, it also levitated the particles above the surface of the electrodes which distinguished it from DEP. The fluid movement in this case seemed to be in the opposite direction to the flow in Figure (9.3) but also operated on a larger scale. The flow develops into convection patterns and the position and shape of these patterns varies with frequency and voltage. They occur in macroscopic areas of high field, such as the centre of an electrode array, rather than microscopic high field points like the electrode edges. For the case of the polynomial electrodes, this meant that the flow moved into the centre of the electrodes from a long distance beyond the array and then up along a line perpendicular to the centre of the array. The scale of the flow pattern increased with increasing frequency and potential as shown by Figures (9.9a) and (9.9b). A levitated ball of particles trapped by negative DEP and levitated by fluid flow was seen above the centre of the electrodes. If the potential was increased further, the drag force from the flow increased to the point where the particles were levitated too high and could no longer be held in the trap so that they diffused out into the medium.

For sufficiently high potentials and/or frequencies, the flow pattern was such that particles moving into the array were carried up and out of the array again before reaching the

centre. If a single particle was trapped in the centre of the array as shown in Section (7.3.4), the centre of the electrodes could be blocked off from the bulk medium by this method ensuring that the single particle remained undisturbed as shown in Figure (9.9b).

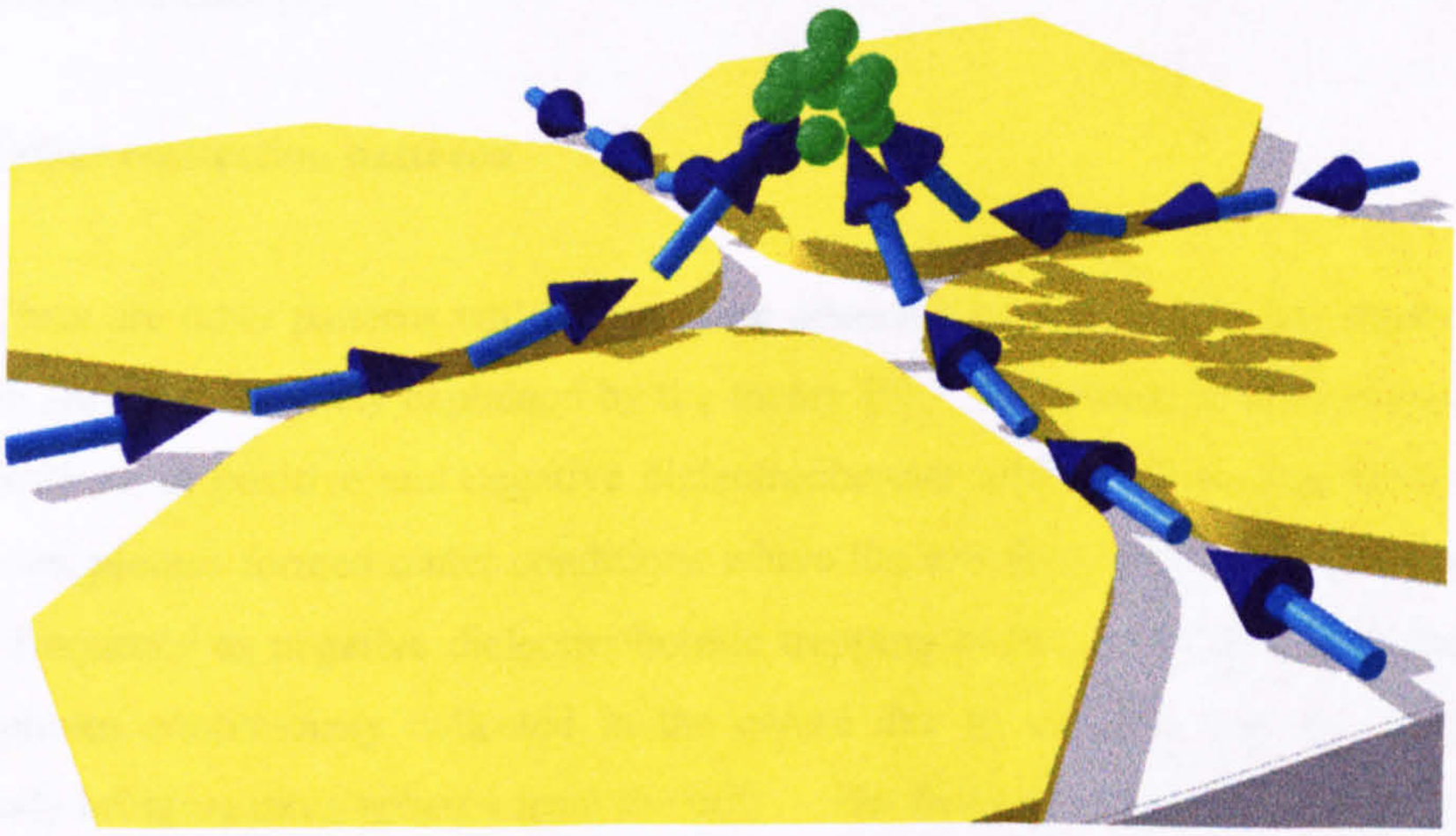

(9.9a) Diagrammatic representation of the observed fluid flow (blue arrows) and approximate particle position on a set of hyperbolic electrodes at $f > f_0$.

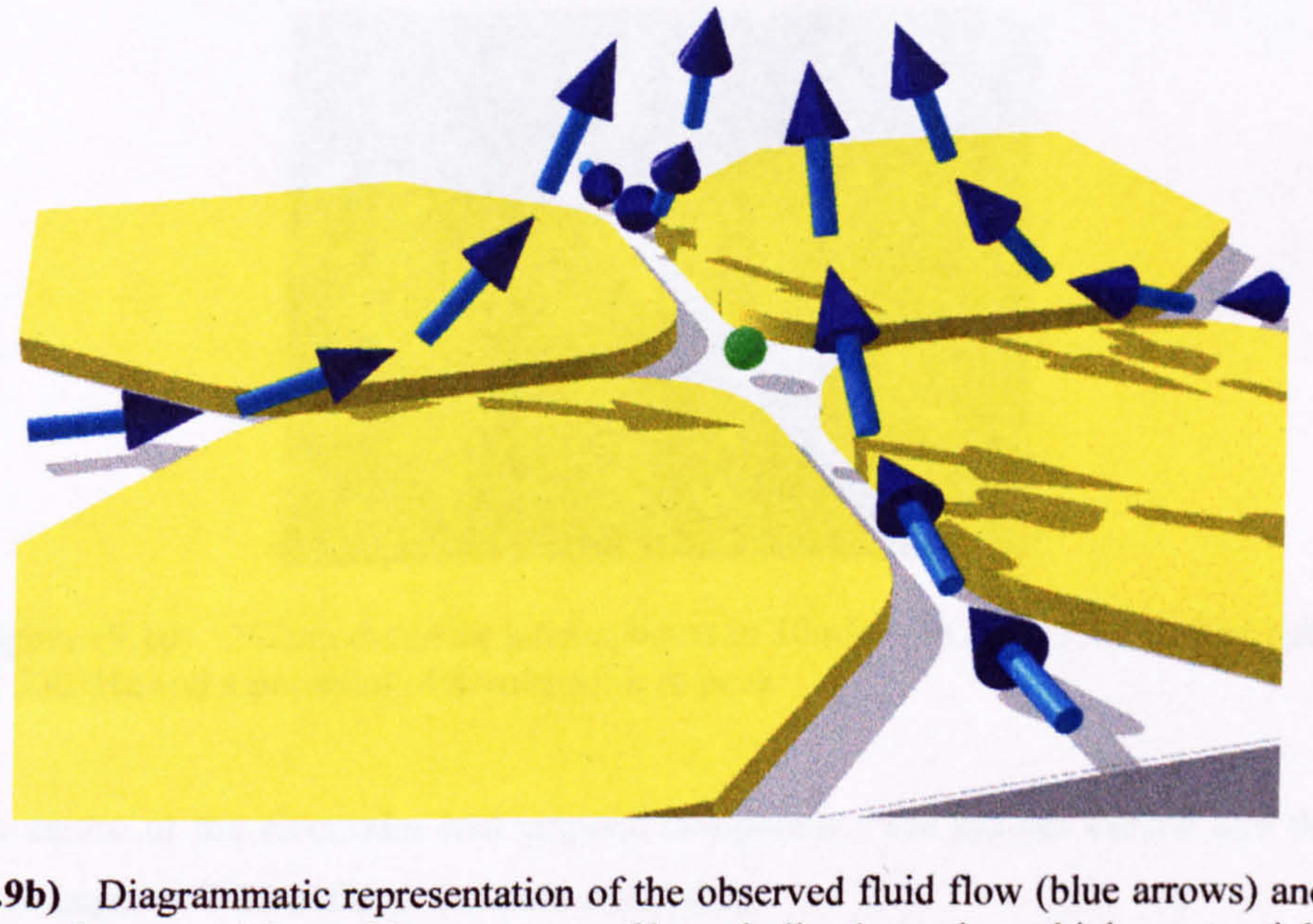

(9.9b) Diagrammatic representation of the observed fluid flow (blue arrows) and approximate particle positions on a set of hyperbolic electrodes at higher potentials and/or frequencies than in (9.5a). The trapping of a particle at the centre as shown does not occur when the fluid is moving in this manner. The particle must first be trapped at a lower frequency and/or potential.

Figure (9.9) Schematic diagram of the high frequency fluid flow in a set of hyperbolic polynomial electrodes. The fluid movement in general is along the gaps between the electrodes, up and out of the centre of the array.

Fluid movement was also seen in castellated and triangular electrodes at the same frequencies and this produced a general movement of liquid upwards over the array, coupled with movement of fluid from regions outside the electrode arrays. Experimental images of this effect are difficult to obtain with a microscope but have been reported previously by other researchers in the field [4].

9.3.3 Other convection patterns

There are other patterns which have been observed on occasion in the electrode arrays and which are not adequately explained by the theory [5]. They seem to arise mainly because of combinations of positive and negative dielectrophoresis and the flow drag force. Figure (9.10) shows plumes formed under conditions where the low frequency fluid flow occurred at the same frequency as negative dielectrophoretic trapping in the centre of the electrodes. A ball of spheres continuously collected in the centre due to the fact that the fluid flow is continuously bringing more spheres from the bulk. The ball expanded until it was big enough for the outermost spheres to feel the effects of the fluid flow. Above a certain size the ball collapsed and the spheres shot out in plumes along the symmetry line of the electrodes.

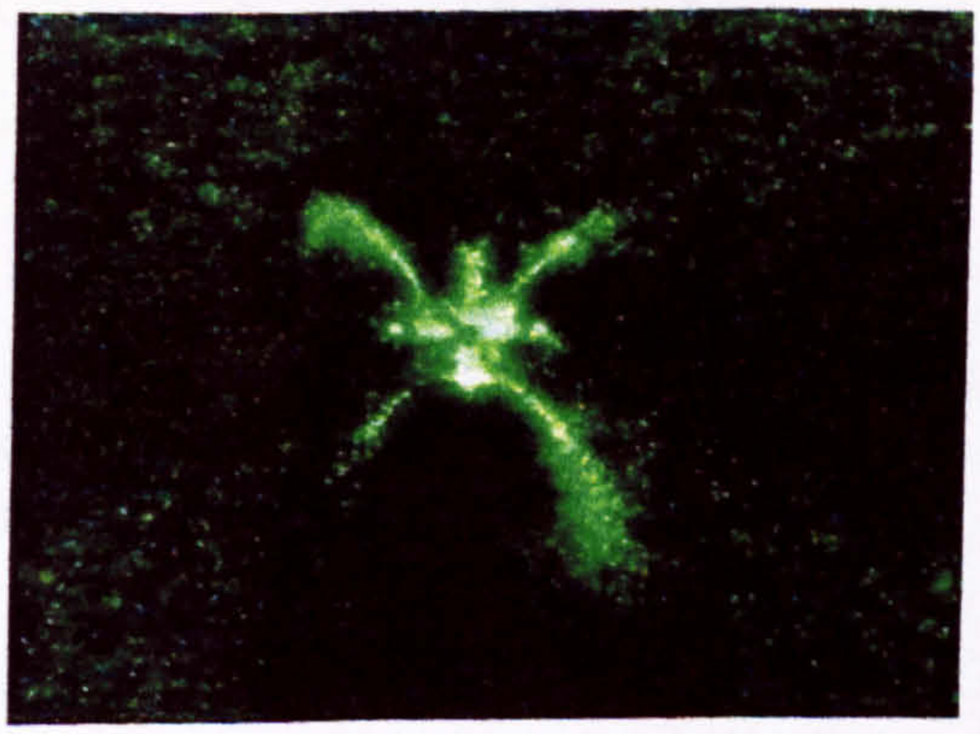

Figure (9.10) 282nm diameter latex spheres in 10mM KPO_4 with an applied field of 500kHz and a potential of 8 volts peak to peak

Once the centre of the electrodes had emptied completely, the plumes ceased and the cycle repeated as negative DEP collection started once more.

Another, reproducible effect seemed to occur when the high frequency fluid flow regime coincided with the zero force region of the particles being used. This effect is shown schematically in Figure (9.11) and is almost certainly due to a balance of forces in some way. The effect occurred close to and above the zero DEP force region, so that it occurred when the particles were experiencing negative dielectrophoresis. The particles at the four points also moved rapidly in a vertical circular motion across the gap. Under typical experimental

conditions, as the frequency of the applied field was increased the collection region moved inwards until all the particles fell into the centre of the electrodes. In high concentrations of spheres (approximately 0.02% by volume) and at a constant field frequency and amplitude, the collection regions moved inwards as the number of particles increased. Once the region was sufficiently close to the centre of the electrodes, some of the particles fell into the negative trap. The remainder, now that the number of particles in the collection had decreased, moved back to its original position and the cycle repeated.

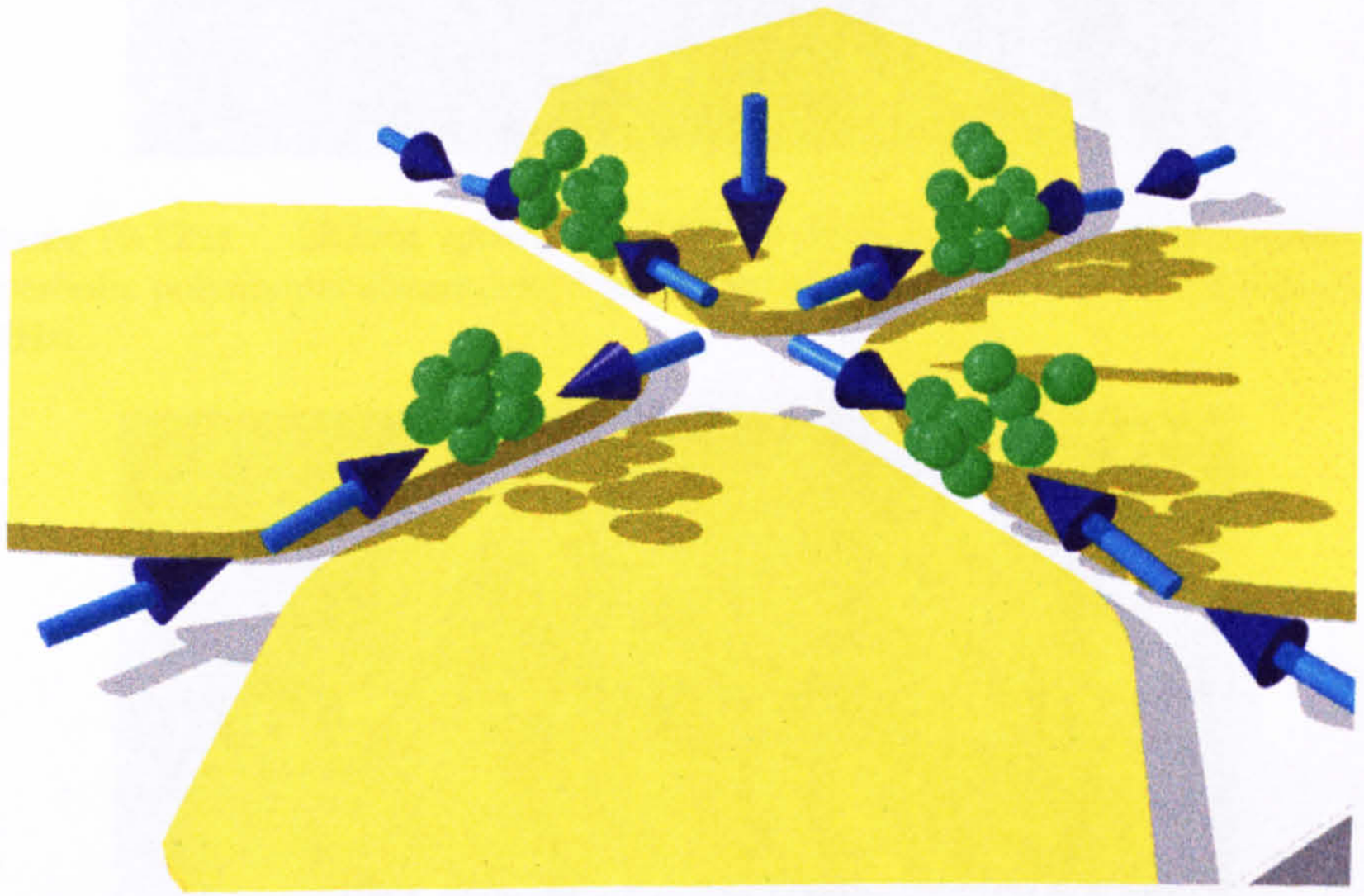

Figure (9.11) Schematic representation of the formation of collections of particles in the high field regions of the electrode array at frequencies when they are undergoing negative dielectrophoresis

Figures (9.12) show experimental images of this effect for a variety of conditions outlined in the diagram legends. Figure (9.12a) shows a typical result for 282nm spheres in 100μM KCl at an applied frequency of 6MHz and a potential of 5 volts peak to peak. There is negative DEP collection in the centre and four bright points of fluid flow collection above each electrode gap. Figure (9.12b) shows 557nm spheres in 500μM KCl in a set of hyperbolic polynomial electrode with centre separation 10μm. The applied field was 3MHz and the potential was 5 volts peak to peak. There are a few spheres experiencing negative DEP in the centre and the four collection regions but there are also collection points away from the electrodes along the lines of the electrode gap. At these points, there is fluid flow into the array along these line but there is also repulsion by negative DEP and a number of particles sit in these four regions under the balance of two forces.

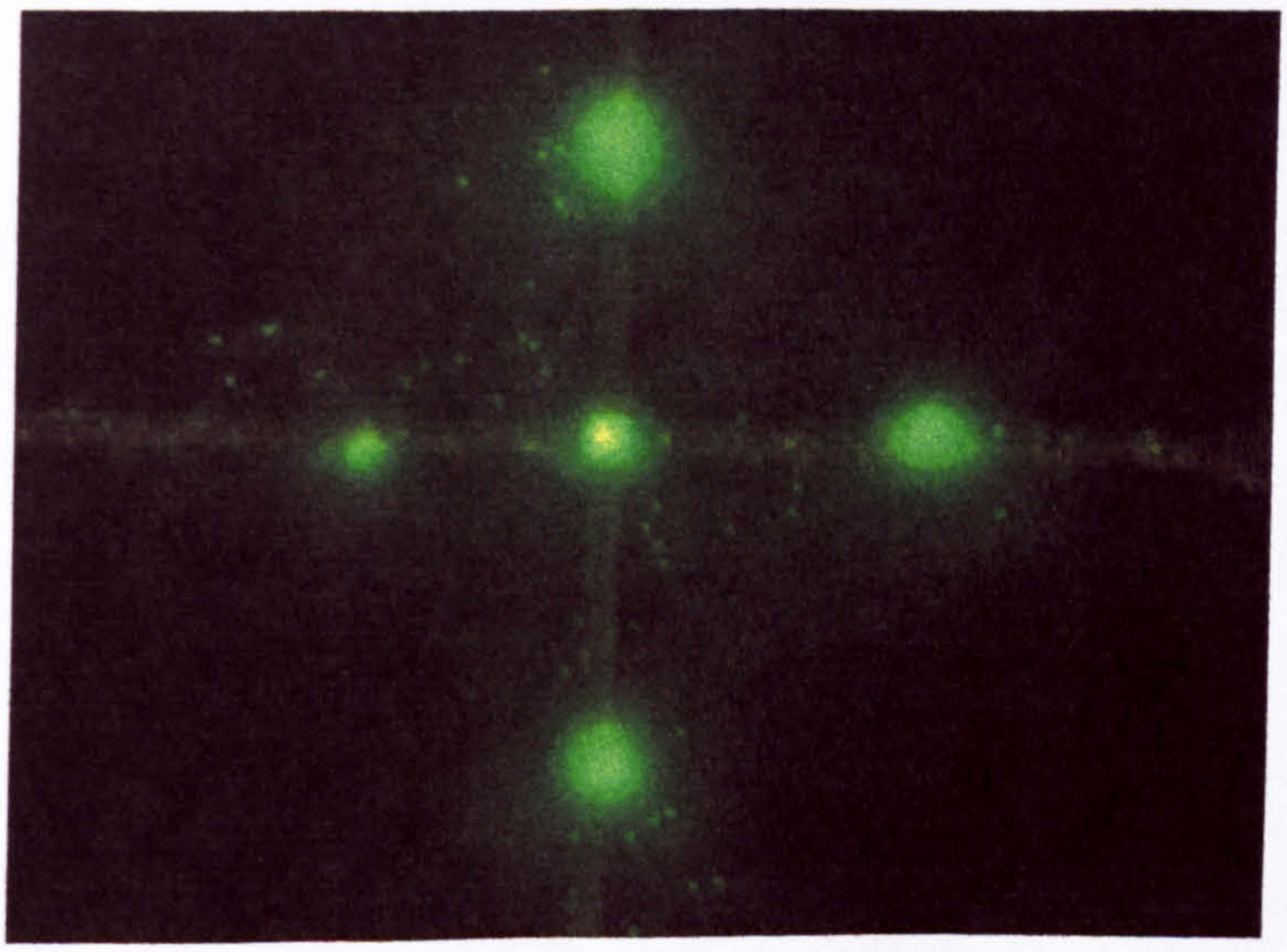

Figure (9.12a) 282nm spheres in 100mM KCl in a set of 6μm separation hyperbolic polynomial electrodes. The applied potential was 5volts peak to peak at 6MHz.

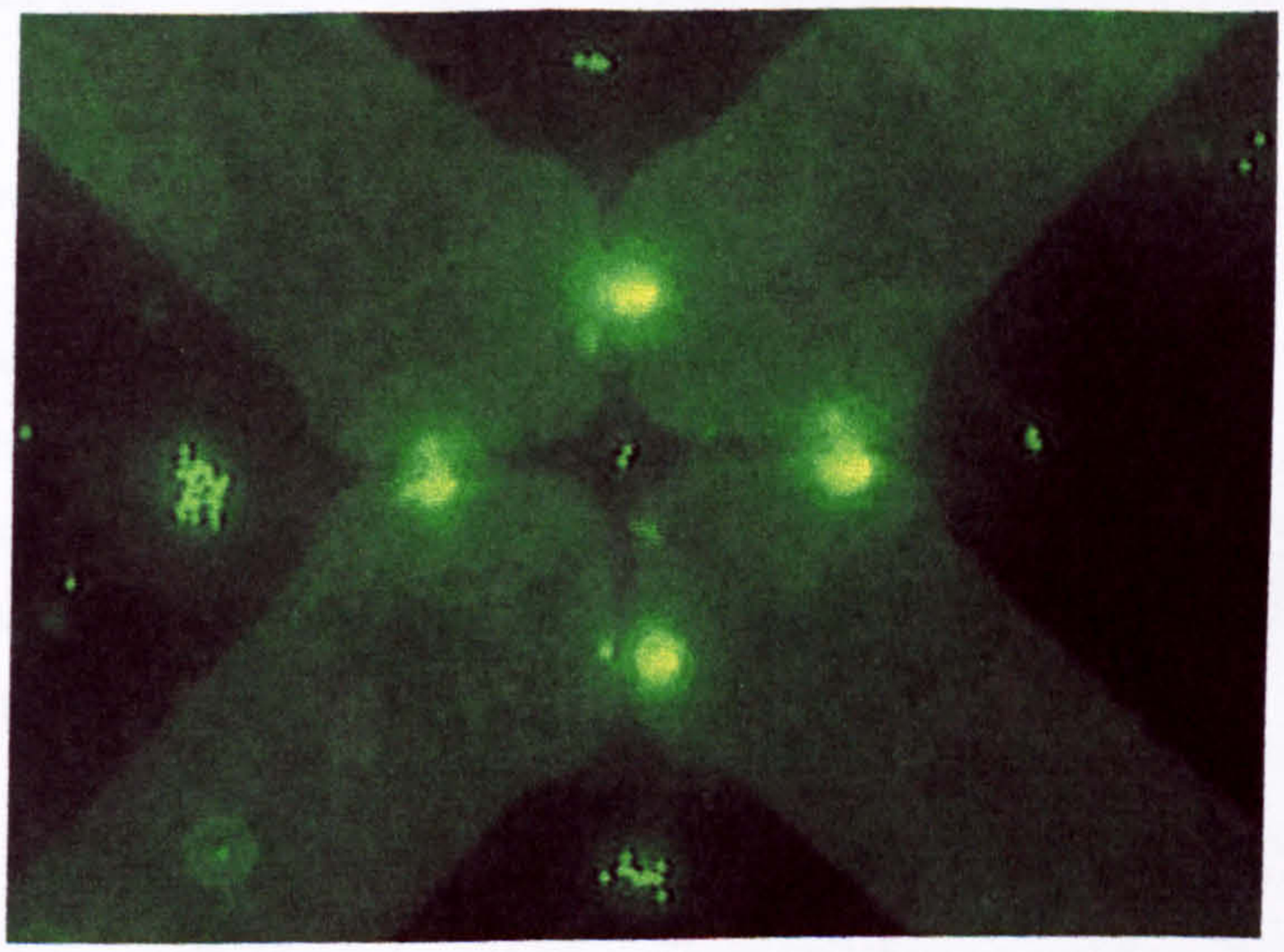

Figure (9.12b) 557nm spheres in 500mM KCl in a set of 10-μm separation hyperbolic polynomial electrodes. The applied potential was 5volts peak to peak at 3MHz.

As can be seen from Figure (9.12c), the apparently homogeneous balls of particles are in fact made up of two separate collection regions, one spinning over each electrode on either side of the gap. This set of electrodes was damaged during an experiment and as a result, there are imperfections on the edges of the electrode which disrupt the uniform distribution of the electric field in the gap

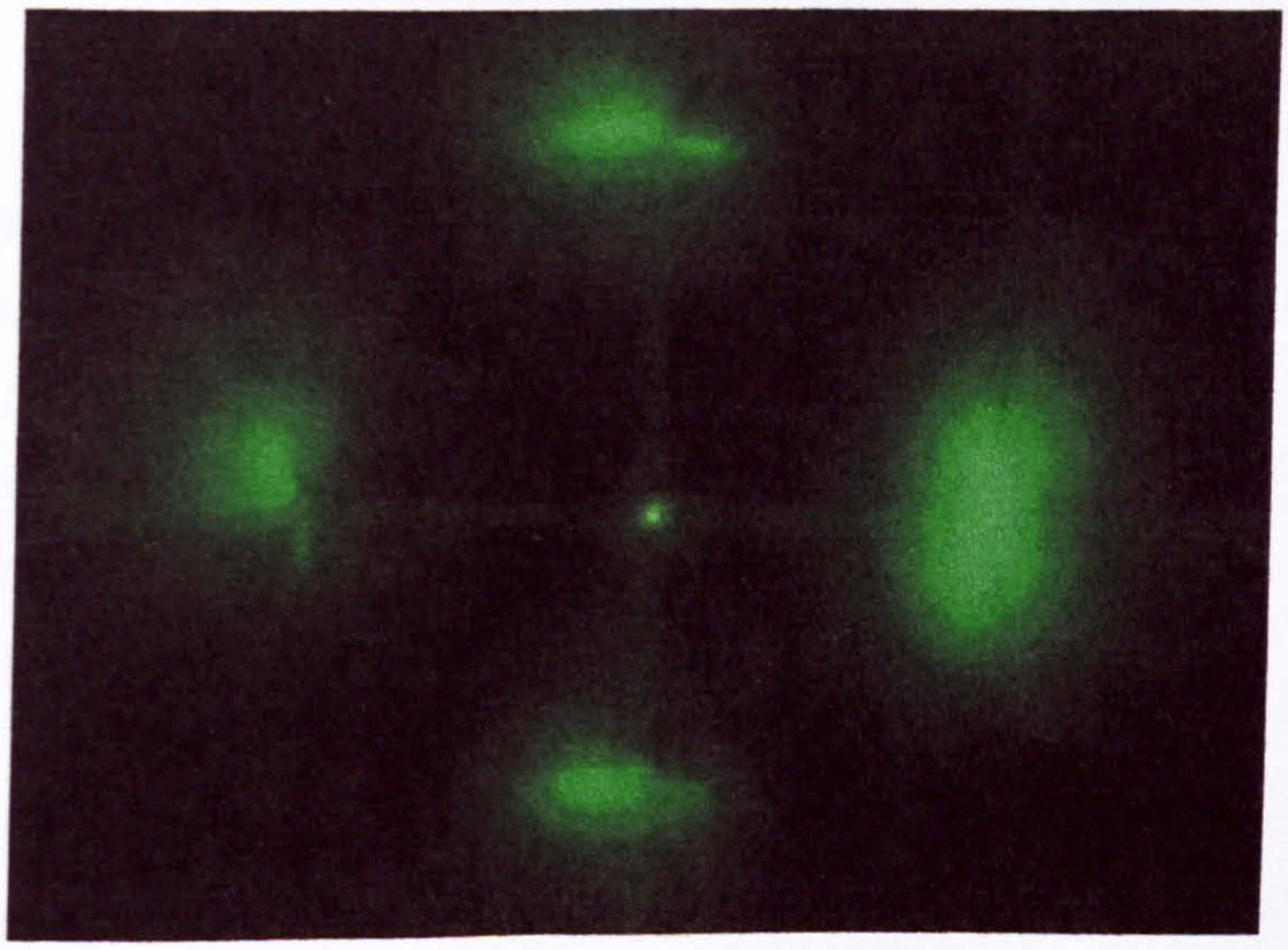

Figure (9.12c) 282nm spheres in 100μM KCl on a damaged set of 6μm electrodes. The applied potential was 12 volts peak to peak at 6MHz and the four collection regions can be seen breaking up into two distinct regions one on either side of the gap.

9.3.4 Summary

As has been described, fluid effects are noticeable and reproducible on the sub-micrometre scale but to a certain extent are predictable. The applied electric field heats the fluid and the resulting gradients of conductivity and permittivity give rise to fluid movement.

The low frequency motion occurs below a frequency approximately equal to the charge relaxation frequency and is probably due to coulomb forces arising from gradients in conductivity. The flow patterns are small scale and follow the geometry of the electrodes precisely.

The high frequency effect occurs above f_0 and can probably be assigned to the dielectric forces and the gradient in the permittivity. The latter effect looks like thermal convection, since the fluid rises in the general area where heat is being produced and presumably descends again in another region. The flow is affected by the geometry of the electrodes but not in the same microscopic way as the low frequency flow and therefore has a much larger typical scale associated with it.

Some conclusions have been drawn about the reasons for the frequency regimes in which each type of convection is observed but further theoretical work is required to obtain a detailed picture of the patterns and the expected frequency regimes. Such theoretical work was outside the scope of this thesis but is being carried on in collaboration with the University of Sevilla.

References

1. P.R.C.Gascoyne, Y.Huang, R.Pethig, J.Vykoukal and F.F.Becker (1992)
   Measurement Science and Technology **3** 439-445
2. R.Pethig, Y.Huang, X-B.Wang and J.P.H.Burt (1992)
   Journal of Physics D: Applied Physics **22** 881-888
3. G.H.Markx, M.S.Talary and R.Pethig (1994)
   Journal of Biotechnology **32** 29-37
4. T.Muller, A.Gerardino, T.Schnelle, S.G.Shirley, F.Bordoni, G.De Gasperis, R.Leoni and G.Fuhr (1996)
   Journal of Physics D: Applied Physics **29** 340-349
5 A.Ramos, H.Morgan, N.G.Green and A.Castellanos
   Journal of Physics D: Applied Physics (submitted)
6. H.A.Pohl (1978) *Dielectrophoresis*
   Cambridge University Press, Cambridge

Chapter Ten

Separation

Results and discussion: Dielectrophoretic separation

Results and discussion: Dielectrophoretic/Hydrodynamic separation

Results and discussion: Design of Travelling Wave Dielectrophoretic separators

10.1 Introduction to separation

Of equal importance to particle characterisation in the development of sub-micrometre dielectrophoresis, is the capability to physically separate different types of particles based on their dielectric properties. In Chapter One, the practical applications that dielectrophoresis has been used for were summarised. However, although the dielectrophoretic properties of sub-micrometre particles have been characterised, little work has been done on applying dielectrophoresis in a practical manner.

This chapter presents the results of nano-scale dielectrophoretic separation based on existing dielectrophoretic techniques as well as a new technique based on the fluid movement characterised in this thesis (Chapter Nine). The last section summarises work carried out on designing large scale particle separators based on the related technique of travelling wave dielectrophoresis.

10.2 Dielectrophoretic separation

The contents of this section were published in the Journal of Physics D: Applied Physics Volume 30 (1997) pL41-L44 under the title:

Dielectrophoretic Separation of Nano-particles

N.G.Green and H.Morgan

Abstract: It is shown for the first time that it is possible to separate a population of nanoparticles into two subpopulations solely on the basis of their dielectric properties. Using nanofabricated electrode arrays it has been shown that a solution of 93nm diameter latex beads with a distribution of surface charge can be separated by the application of non-uniform AC electric fields (dielectrophoresis). The mixture separated into two distinct populations, one experiencing positive dielectrophoresis and the other negative dielectrophoresis.

10.2.1 Introduction

The movement of polarisable particles in non-uniform fields, termed dielectrophoresis by Pohl [1], has been exploited as a rapid non-invasive tool for the diagnosis and separation of mammalian cells and micro-organisms [2]. It has found practical applications in medicine for separating cancer cells from blood [3], enriching CD34+ cells in bone marrow samples [4] and for detecting the viability of pathogenic organisms in water [5].

Separation of particles is based on the fact that when placed in a non-uniform AC electric field, polarised particles experience a variable translational force, depending on the applied field frequency. For particles whose polarisability is greater than the medium, the movement is to regions of high field strength, whereas particles whose polarisability is less than the medium move to the region of lowest field strength. Because the particle's polarisation is frequency dependent, the net force is also frequency dependent. Therefore, by judicious choice of suspending medium conductivity and applied frequency, even particles with very similar dielectric properties can be efficiently separated.

The sum total of the forces on a given particles is: $F_{total} = F_{deterministic} + F_{random}$. The deterministic force is the sum of the sedimentation, hydrodynamic and dielectrophoretic forces. The random force is due to Brownian motion and for particles with a diameter of the order of 100nm, this force is considerable. The mean free path of the movement is inversely dependent on mass, implying that decreases in the particle diameter require significant increases in the applied electrostatic energy (or field strength). The stable trapping of viruses and beads has been

demonstrated previously [6-9]. Here, it is shown that nanometre scale latex spheres can be both stably trapped in nanofabricated electrode arrays and, *more importantly*, that a heterogeneous mixture can be separated into two populations using dielectrophoresis.

10.2.2 Experimental procedure and results

Experiments were conducted on charged latex spheres of 93nm diameter, using planar electrodes manufactured by electron beam lithography. The applied electric field strength was 2.5×10^5 Vm^{-1} and the suspending medium conductivity was $0.018Sm^{-1}$. Large electric field strengths cause localised heating of electrode structures which in turn gives rise to discontinuities in conductivity, permittivity and viscosity of the medium. The result is the inception of convective currents around electrodes which can disrupt experiments. In order to reduce these effects as much as possible, the size of the electrode structure must be minimised to maintain a low ratio of volume to surface area. Therefore, sub-micron electrodes structures were used and the field strength was kept low enough so that, while there was inevitable power dissipation in the medium, no convective currents were observed.

A photograph of part of the nano-fabricated planar electrode arrays is shown in Figure (10.1). This array had a feature periodicity of 6μm and an electrode gap of 4μm. This electrode design was chosen because of the high electric field gradient regions produced between adjacent tips, together with well defined low field gradient regions in the bays (Chapter Six, [10]). The electrodes were fabricated using direct-write electron-beam lithography (Leica EBPG-HR5 beam writer) onto chromium plated mask plates (Hoya Corporation) followed by lift off in acetone (Appendix 5a.5). The electrode arrays were constructed on substrates 35mm by 25mm in size, with active areas covering a few hundred square millimetres.

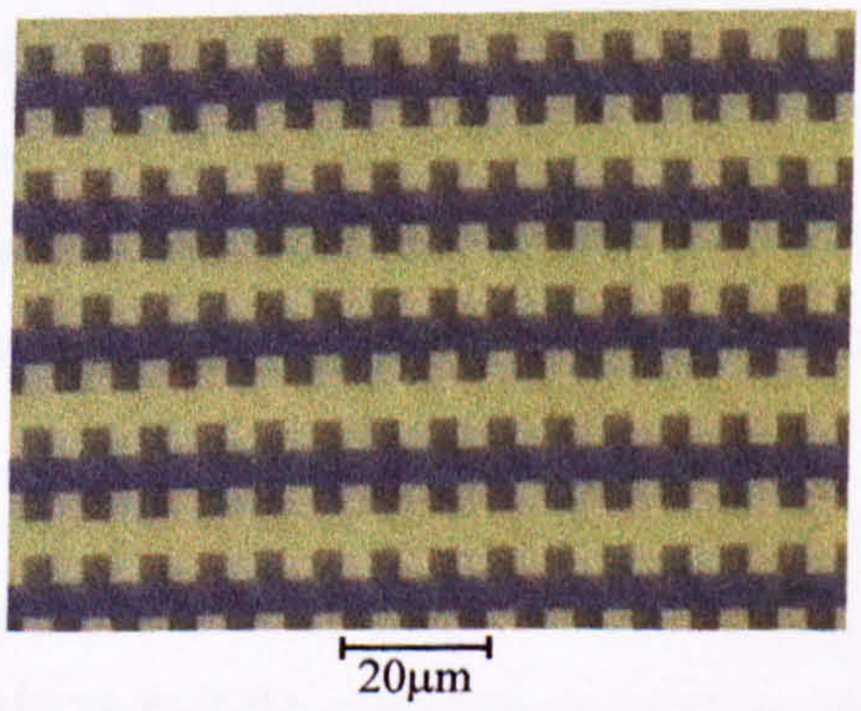

Figure (10.1) Photograph of a 4μm feature and gap size castellated dielectrophoresis electrode. The electrode was manufactured using direct-write electron-beam lithography.

Although the electrodes are not nanometres in size, the use of nanofabrication methods was critical in maintaining reproducible and well defined features in order to generate the required field gradients. Figure (10.2) is a colour coded three-dimensional electric field plot for a small region of the electrode array taken in a plane parallel to, and 100nm above, the plane of the electrodes. The plot was obtained using a finite element method (Ansoft Corporation, Pittsburgh, PA, USA) and clearly shows that regions of maximum and minimum field strength occur at the tips of electrodes and in the bays respectively, in agreement with earlier 2D calculations [11].

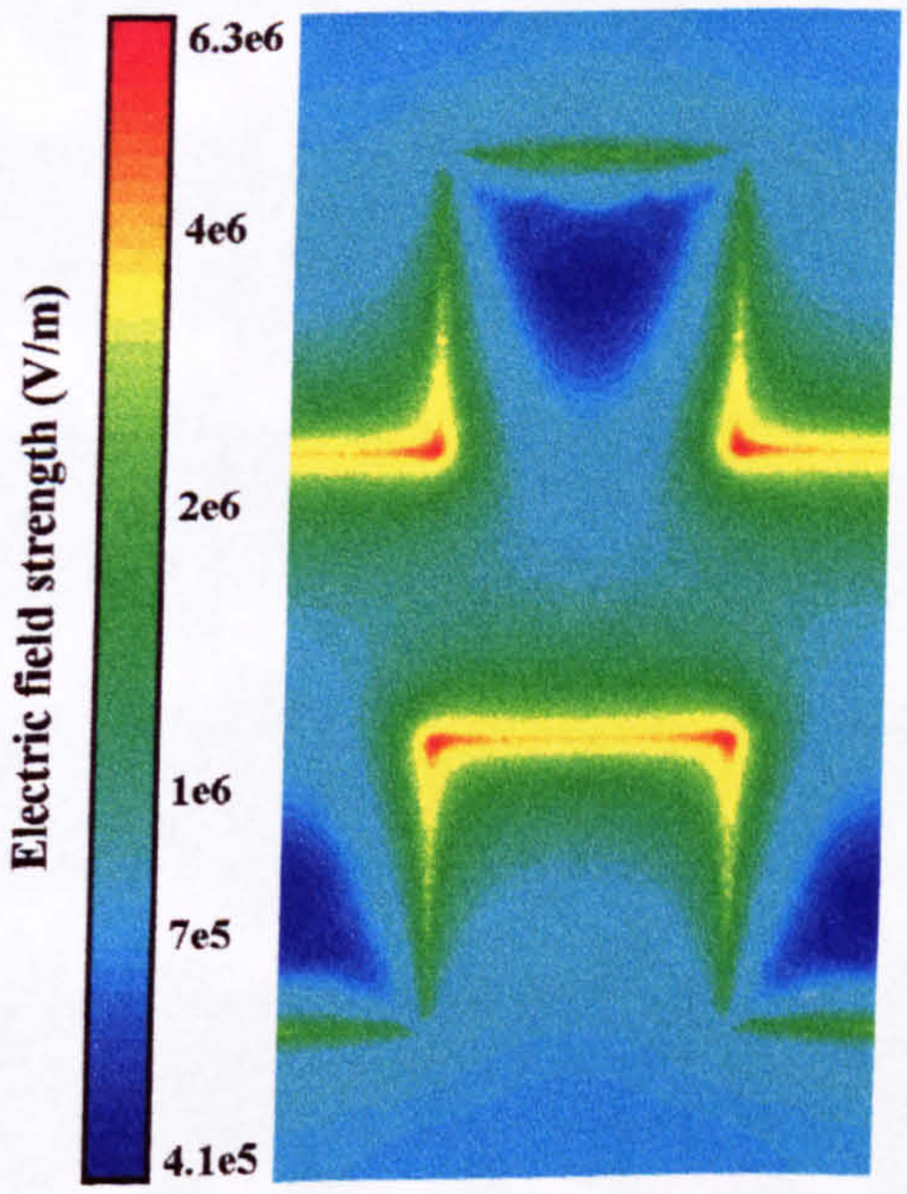

Figure (10.2) A colour coded three dimensional plot of the electric field distribution for a castellated electrode array showing regions of maximum and minimum field strength on a logarithmic scale. This plot corresponds to a plane 100nm above the upper surface of the electrodes.

A potential of 1V peak-peak was applied between adjacent electrodes, equivalent to a field strength of 2.5×10^5 Vm^{-1}. The frequency of the applied field could be varied from 100Hz to 250MHz. The beads were carboxylate modified latex (Molecular Probes, Eugene, Oregon, USA), loaded with fluorescent dye, and the suspending medium was 1mM potassium phosphate buffer, pH 7.1. Images of the beads in the electrode arrays were collected using fluorescence microscopy (Nikon Microphot) and high-speed black and white film.

At frequencies well below 20MHz (1kHz-1MHz) all the beads moved to regions of maximum field gradient at the tips of the electrodes, consistent with the polarisability of the particle exceeding the medium. Similarly at frequencies >20MHz (20MHz-250MHz) all the beads collected at low field gradient regions in the electrode bays or were repelled from the electrodes. Such an observation is consistent with that expected from dielectric studies of latex

particles (Chapter Seven, [12]). However, at frequencies in the region of 20MHz a clear separation of the beads into two distinct populations was seen, as shown in Figure (10.3). Collection of the beads occurred within a few seconds and beads remained stably trapped on the electrode array for an indefinite period of time. Removal of the field caused the particles to instantly disperse back into the medium.

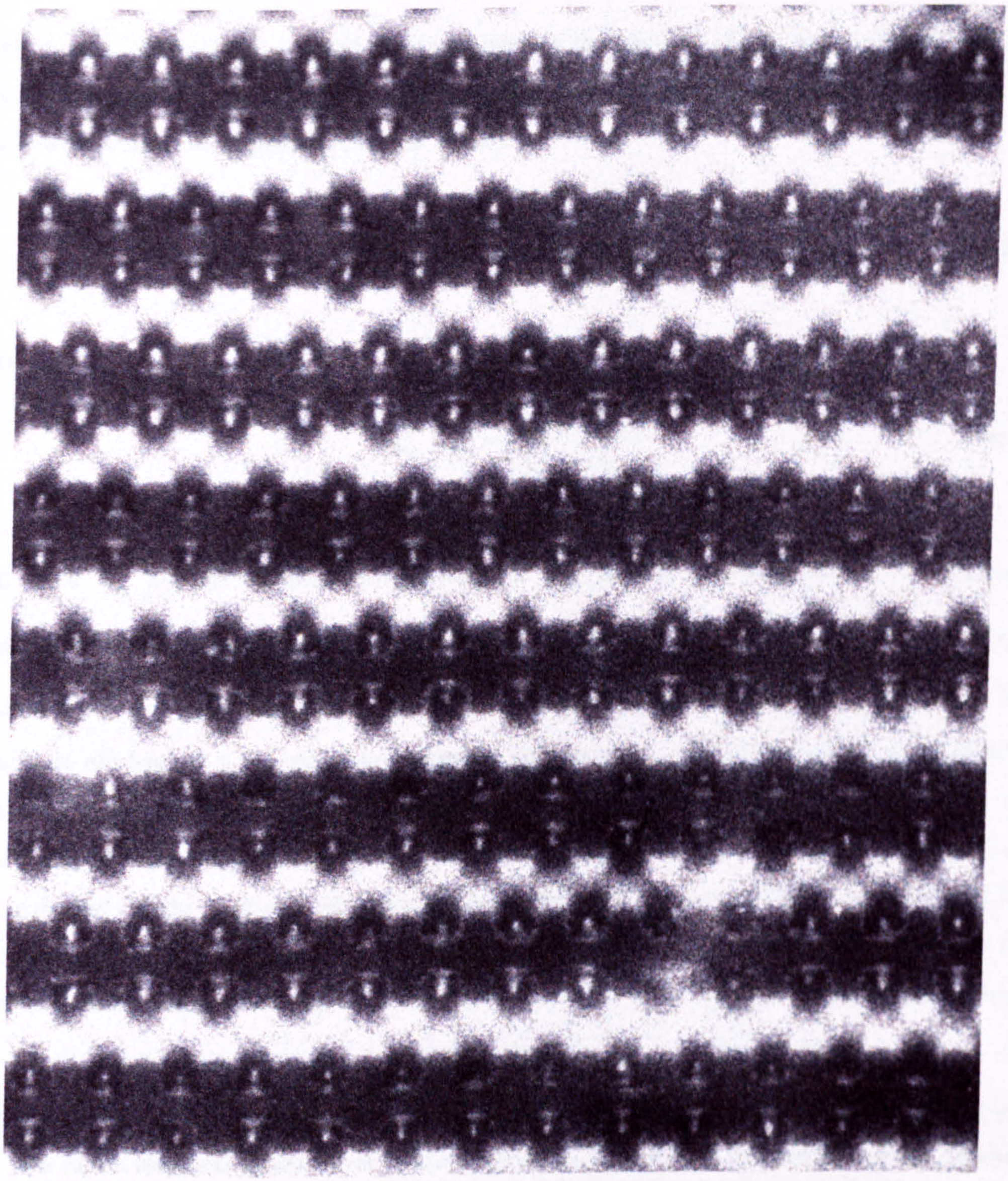

Figure (10.3) A photograph showing separation of a heterogeneous mixture of 93nm diameter fluorescently loaded latex beads into subpopulations. Beads with lower surface charge move to the low field regions between the electrode fingers, whilst beads with the higher surface charge are trapped at the electrode tips. The photograph was taken with 3200 ASA black and white film and a Nikon Microphot fluorescence microscope. The electrode gap is 4μm and the applied field is $2.5\times10^{5}Vm^{-1}$.

10.2.3 Discussion

The instantaneous dielectrophoretic force on a particle, $\underline{\mathbf{F}}(\omega)$, is given by (Chapter Four, [13]):

$$\underline{\mathbf{F}}(\omega) = \mathrm{Re}\{(\underline{\mathbf{m}}(\omega).\nabla)\underline{\mathbf{E}}\} \tag{10.1}$$

where $\underline{\mathbf{m}}(\omega)$ is the (field) induced dipole moment of the particle, $\underline{\mathbf{E}}$ the RMS electric field and Re{} indicates only the real part. For a sphere, the induced dipole moment is given by the following well-known equation (Chapter Three):

$$\underline{\mathbf{m}} = 4\pi\varepsilon_m f\left(\varepsilon_p^*, \varepsilon_m^*\right) a^3 \underline{\mathbf{E}} \tag{10.2}$$

where:

$$f\left(\varepsilon_p^*, \varepsilon_m^*\right) = \left(\frac{\varepsilon_p^* - \varepsilon_m^*}{\varepsilon_p^* + 2\varepsilon_m^*}\right) \tag{10.3}$$

ε_p^* and ε_m^* are the complex permittivities of the particle of radius a and the medium, respectively. A general complex permittivity is given by $\varepsilon^* = \varepsilon - j(\sigma/\omega)$ where ε is the real permittivity, σ is the conductivity, $j = \sqrt{-1}$ and ω is the angular frequency. Therefore, for particles of identical size exposed to a constant field gradient, the induced dipole moment and, as a consequence, the magnitude and sign of the dielectrophoretic force, depends on the difference between the polarisability of the particle and the medium. The dielectrophoretic force is governed by the real part of this expression and, for latex particles, is dominated by conductivity effects. The conductivity of a colloidal particle consists of two components: a bulk and a surface component (Chapter Three, [14,15]) and is given by $\sigma_p = \sigma_s + 2K_s/a$, where σ_s is the bulk conductivity of the particle of radius a, which can be assumed to be approximately zero for latex spheres. The surface conductance, K_s, arises from the movement of ions in the electrical double layer and is directly proportional to the surface charge density. Therefore, for latex beads the sign and magnitude of the dielectrophoretic force is governed almost exclusively by surface conductivity effects. Independent measurements of the electrophoretic mobility of the beads were made with a Coulter particle analyser. A Gaussian spread in the mobilities with a mean of -3.8 ± 0.6 μm-cm$V^{-1}s^{-1}$ was observed. Using the Helmholtz-Smoluchowski equation [16] and the Gouy-Chapman and Grahame theory of the

double layer [17] this spread in mobility was translated into a spread in surface charge density around a mean of $-3.3(+1, -0.7)\mu Ccm^{-2}$. The variation in $f\left(\varepsilon_p^*, \varepsilon_m^*\right)$ and therefore the relative magnitude of the dielectrophoretic force was calculated as a function of frequency using the mean and the half point in the Gaussian spread in electrophoretic mobility. The results are shown in Figure (10.4).

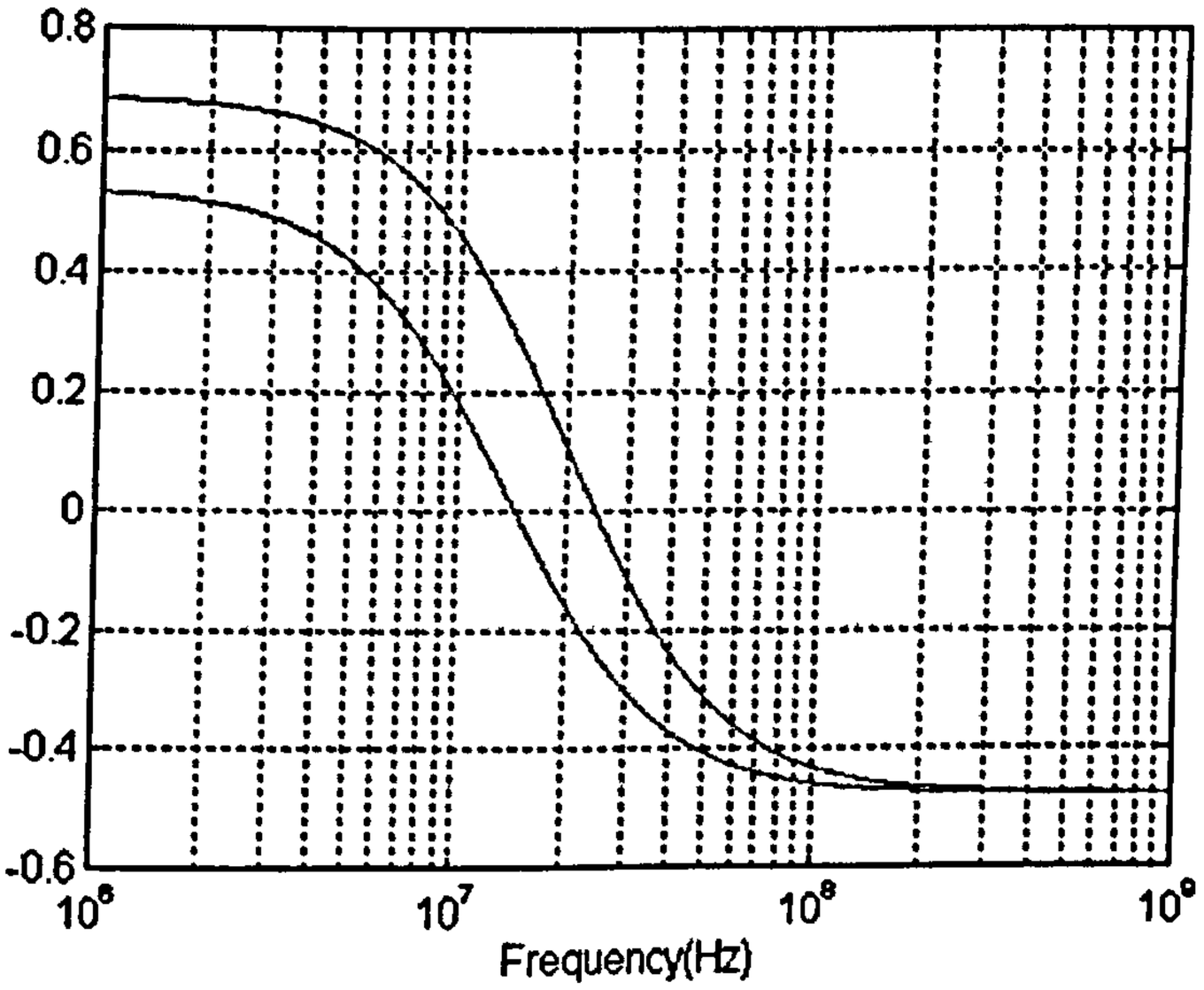

Figure (10.4) A theoretical plot of the variation in $f\left(\varepsilon_p^*, \varepsilon_m^*\right)$ which is directly proportional to the dielectrophoretic force for a given size of particle as a function of frequency for 93nm latex beads. The two curves correspond to force plots calculated with value of surface charge density at the half widths of the Gaussian spread as measured directly with a Coulter particle zeta potential analyser.

In the calculation of this data the diameter of the beads was taken as 93nm, a value confirmed by electron microscopy. It can be seen that at a frequency of 20MHz, the force on the beads is either positive or negative depending on the absolute value of the surface charge density. This figure shows that, at this frequency, the beads divide into two populations with one moving to the high-field region (positive DEP) and the other to the low-field region (negative DEP) as seen experimentally. Therefore, for a mixture of beads with slightly different values of surface charge density ±20% around the mean, the mixture rapidly separates into two sub-populations as seen in Figure (10.3).

It is conceivable that separation of the beads may occur due to the formation of aggregates due to dipole-dipole interactions which will then have different dielectric properties. This phenomenon is likely to depend on the concentration of the beads on the electrode array. However, we did not observe the formation of aggregates before the beads separated.

Separation was extremely rapid, within seconds of applying the field, and furthermore all of the beads dispersed into single entities upon removal of the electric field.

The beads trapped at field gradient maxima, by positive DEP, are held by a stronger force than those experiencing negative DEP [10]. As demonstrated by Markx *et al* [18], physical separation of a mixture of particle into two populations can be achieved by subjecting the electrode array to a flow of liquid of sufficient pressure to remove particles trapped at field minima leaving the other particles trapped at the electrode tips. The remaining beads can then be removed by switching off the field and flushing fresh liquid across the electrodes.

10.2.4 Conclusion

Our experiments clearly show that it is indeed possible to separate nanometre scale particles according to their dielectric properties alone. Since it is virtually impossible to separate small particles of similar size but with different biological properties, nanoscale dielectrophoresis may find new applications in separating a range of structures such as chromosomes, viruses, DNA and macromolecules.

10.3 Separation through combination of Dielectrophoresis and hydrodynamic flow

The contents of this section have been submitted to the Journal of Physics D: Applied Physics under the title:

Separation of Sub-micrometre Particles Using a Combination of Dielectrophoretic and Electrohydrodynamic Forces

N.G.Green and H.Morgan

Abstract: The controlled spatial separation of sub-micrometre particles by a combination of dielectrophoretic and electrohydrodynamic forces is demonstrated for the first time. Using planar micro-electrode arrays a mixture of two differently sized particles (93nm and 216nm diameter latex spheres) has been separated into constituent components. The particles separate into distinct bands, spatially separated from each other. The separation pattern is reproduced across the entire electrode array, indicating that the method could be used as a means of rapid nano-particle separation, processing and positioning.

10.3.1 Introduction

The controlled movement of particles in solution can be achieved by a variety of methods. In spatially non-uniform AC electric fields, dielectric particles move as a consequence of the interaction of the applied field gradient and the dipole induced in the particle. This movement was termed dielectrophoresis (DEP) by Pohl [1] and is currently being successfully exploited for the manipulation, characterisation and separation of cells and micro-organisms [3,19]. More recently, through the use of advanced micro-electrode fabrication techniques, DEP manipulation has been applied to the sub-micrometre world to characterise and separate a range of particles such as latex spheres, macromolecules, DNA and virues [8,9,20-24]. The high electric fields required to initiate the dielectrophoretic movement of such small particles also results in fluid movement due to electrohydrodynamic (EHD) effects. This fluid movement acts on the particles through the viscous drag force.

The total force on a polarisable particle in a non-uniform AC field can be written as the sum of a number of independently acting forces:

$$\underline{\mathbf{F}}_{total} = \underline{\mathbf{F}}_{DEP} + \underline{\mathbf{F}}_{viscous} + \underline{\mathbf{F}}_{other} \qquad (10.4)$$

Apart from the DEP force and the viscous force, the other forces include sedimentation and random thermal forces (which drive diffusion when it occurs). For particles of diameter less than 1μm, thermal effects are important, but as has been demonstrated previously (Chapter Seven and Section (10.2)) [4-10] the DEP force can be sufficient to produce particle movement. The dielectrophoretic force can be written as:

$$\underline{\mathbf{F}}_{DEP} = \mathrm{Re}\{(\underline{\mathbf{m}}(\omega).\nabla)\underline{\mathbf{E}}\} \tag{10.5}$$

where $\underline{\mathbf{E}}$ is the electric field, Re{} indicates the real part of and $\underline{\mathbf{m}}(\omega)$ is the field induced dipole moment of the particle. For a homogeneous dielectric sphere, this is given by:

$$\underline{\mathbf{m}}(\omega) = 4\pi\varepsilon_m a^3 f(\omega)\underline{\mathbf{E}} \tag{10.6}$$

where ω is the angular field frequency, a the particle radius and $f(\omega)$ the Clausius-Mossotti factor given by:

$$f(\omega) = \frac{\left(\varepsilon_p^* - \varepsilon_m^*\right)}{\left(\varepsilon_p^* + 2\varepsilon_m^*\right)} \tag{10.7}$$

where ε_p^* and ε_m^* are the complex permittivities of the particle and the medium respectively. The complex permittivity is $\varepsilon^* = \varepsilon - j(\sigma/\omega)$ where $j = \sqrt{-1}$, ε is the permittivity and σ is the conductivity of the dielectric. The time averaged DEP force is found by substituting equation (10.6) into (10.5) and is given by:

$$\left\langle \underline{\mathbf{F}}_{DEP} \right\rangle = 2\pi\varepsilon_m a^3 \mathrm{Re}\left\{f(\omega)\right\} \nabla \left|\underline{\mathbf{E}}_{rms}\right|^2 \tag{10.8}$$

where $\nabla\left|\underline{\mathbf{E}}_{rms}\right|^2$ is the gradient of the square of the *rms* electric field. The Clausius-Mossotti factor not only depends on the electrical parameters of the particle and medium, but also on the frequency of the applied field. The variation in this factor results in a frequency dependent dielectrophoretic force that is unique to a particular particle type. As a consequence, dielectrophoresis can be used as an effective means of separating particles solely according to their dielectric properties and size.

For a spherical particle in a fluid of viscosity η , the viscous drag force in equation (10.4) is given by Stoke's law (Chapter Four):

$$\underline{\mathbf{F}}_{\text{viscous}} = 6\pi\eta a\underline{\mathbf{v}} \tag{10.9}$$

where $\underline{\mathbf{v}}$ is the velocity of the particle. Under the influence of an electric field, heat is generated in the medium resulting in local temperature gradients, which in turn give rise to gradients in the conductivity and permittivity of the medium. These gradients can induce fluid movement, and experiments show that for a given set of parameters (applied voltage, medium conductivity, frequency, electrode geometry, etc.) the resulting flow pattern has a reproducible pattern [25]. The drag force exerted by the moving fluid must therefore be considered in the total force on a particle (equation 10.4).

In this communication, we demonstrate the manner in which electrohydrodynamic and dielectrophoretic forces can be combined and used as a means of separating particle types.

10.3.2 Experimental

Experiments were performed using planar gold electrodes fabricated on glass or quartz substrates by direct-write electron beam lithography (Appendix 5a). In brief, the electrode pattern was written onto mask plates (Hoya Corporation) using electron beam lithography (Leica EBPG HR5 beamwriter). After development, a gold layer was evaporated over the patterned resist and lift-off was performed in acetone to remove excess resist and gold. The remaining chrome underlayer was then removed using a chemical wet etch.

The finished electrodes were 25x25mm in size with an active area covering a few hundred square millimetres. An photograph of part of the electrode array used in this work is shown in Figure (10.1) where the dimensions of the electrodes were 4μm between opposite and nearest neighbour castellations. Although the electrode dimensions were not in the nano-scale, accurate feature definition was required, so the lithographic resolution has to be 100nm or less. Such feature definition is essential to generate the high field gradients necessary for sub-micrometre dielectrophoresis. The electric field patterns for these electrodes have been published elsewhere [Chapter Six, 24] and an example can be seen in Figure (10.2).

The particles used in the experiments were carboxylate modified latex spheres (Molecular Probes, Eugene, Oregon, USA). The spheres had a net negative charge and were supplied pre-loaded with a fluorescent dye. The suspending medium was potassium chloride and experimental images were recorded using fluorescence microscopy (Nikon Microphot) and a video recording/capture system (Appendix 5b).

A sample consisting of a 1:1 mixture of yellow-green 93nm diameter spheres and red 216nm diameter spheres suspended in 1mM KCl (conductivity 13mSm^{-1}) was prepared and

pipetted onto the electrode array. An AC signal was applied to the electrode and varied in the ranges: 100Hz to 20MHz and 0 to 20 volts peak to peak.

10.3.3 Results and discussion

At frequencies greater than 500kHz, our experiments indicated that particles behaved in a manner consistent with conventional dielectrophoretic theory. Particles experienced either positive or negative forces depending on whether the particles were more or less polarisable than the medium [26]. At 500kHz, both the 93nm and the 216nm spheres experienced positive dielectrophoresis. However, as the frequency was decreased further, both particles continued to experience positive dielectrophoresis but fluid flow became more apparent. It was also observed that, at any given frequency, increasing the potential increased the velocity of the fluid (measured indirectly by observing the movement of the spheres). The movement of the fluid exerted a viscous drag on the particles and at a certain threshold fluid velocity, it was observed that the particles moved with the fluid flow in a direction that drove them onto the electrode surface and away from the electrode edge. For frequencies below 500kHz the direction of the flow was constant, parallel to the substrate surface and perpendicular to the edge of the electrodes. This is shown schematically in Figure (10.5).

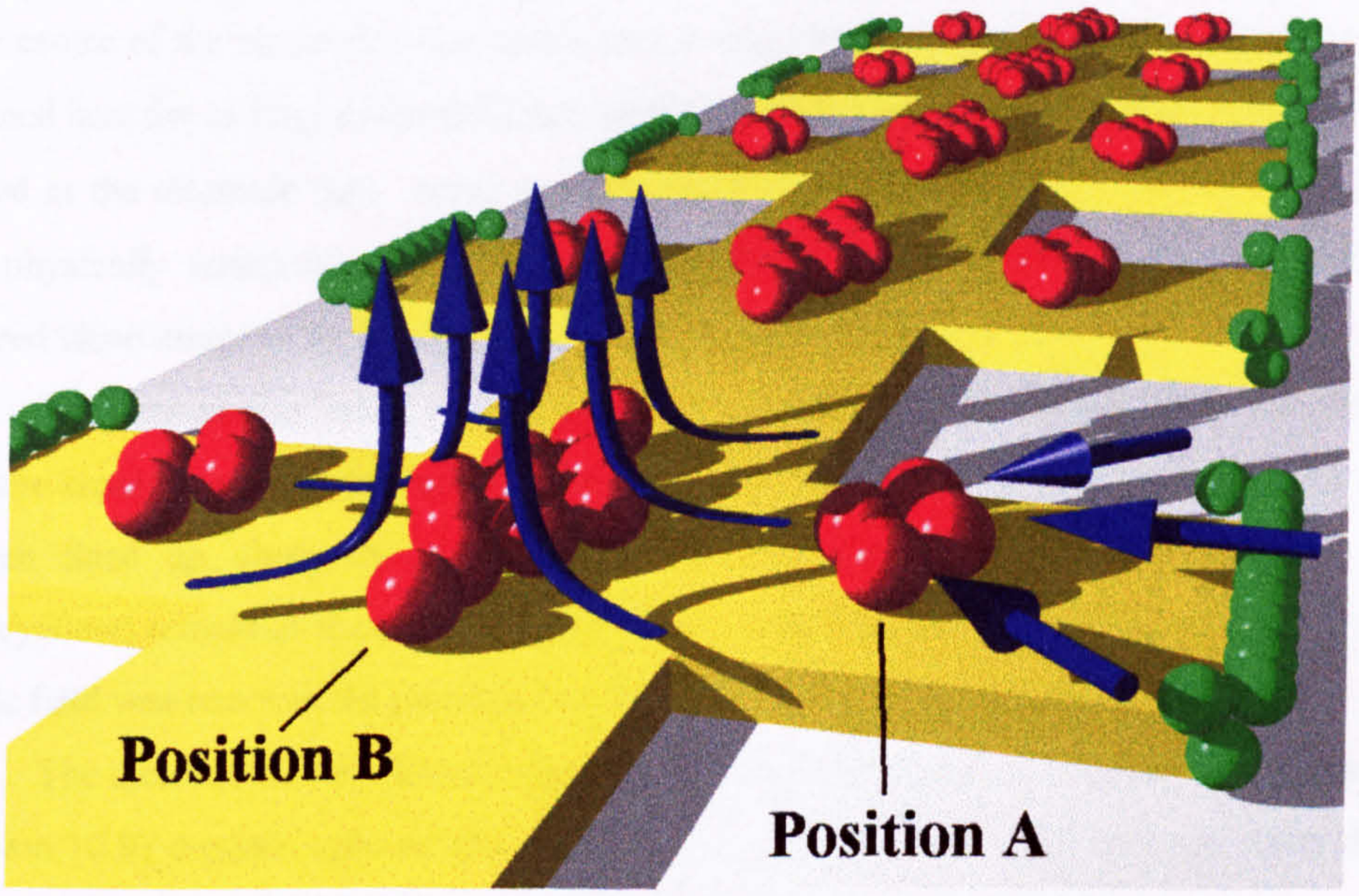

Figure (10.5) Schematic illustration of the fluid flow patterns observed on the microelectrodes at frequencies below 500kHz. Fluid moves in from the electrode edges with the flow lines running parallel to the substrate. At the centre of the electrode the converging flows move upwards perpendicular to the substrate. Spheres which are not held by dielectrophoretic forces, experience a viscous drag and are pushed into the centre where they settle at the stagnation point.

At a frequency of 100kHz and with a potential difference of 1 volt peak to peak, all the particles collected at the high field points on the electrodes under the influence of positive dielectrophoresis. Increasing the potential to a voltage of 8 volts peak to peak, produced an increase in the fluid movement and it was observed that the 216nm diameter spheres moved in towards the central region of the metal. The particles moved a certain fixed distance from the edge and this was dependent on the applied potential: presumably the particles settled at the point at which the positive dielectrophoretic force and the viscous drag force balanced each other. This is represented by position A in Figure (10.5) and, for a constant potential, the particles were observed to remain in this state indefinitely. Reducing the potential resulted in a reduction in the fluid velocity and the spheres moved back to the high field points at the edges of the electrodes.

At a frequency of 100kHz and a potential of between 10 and 15 volts peak to peak, the fluid flow patterns from opposite edges of the electrode converged, and the 126nm diameter particles were pushed into the plane of symmetry running along and perpendicular to the surface of the electrodes. This region corresponds to a minimum in the electric field (and a corresponding minimum in the dielectrophoretic potential) across the electrode. The fluid moved upwards along this plane, but the particles remained at the minimum due to a combination of the influence of gravity, positive dielectrophoresis and/or a stagnation point in the fluid flow. These observations are represented schematically by position B in Figure (10.5). The collection point in the centre of the electrodes was stable and it was observed that the 216nm diameter spheres remained here for as long as the field was applied. At the same time the 93nm spheres remained trapped at the electrode tips, under positive dielectrophoretic forces, so that the two particles were physically separated. The separation is shown schematically by Figure (10.5) and a captured video image of the experimental result is shown in Figure (10.6).

This image was taken a few seconds after applying the 100kHz field and shows the complete separation of the mixture into sets of bands. The 216nm spheres fluoresce red and can be seen lined up along the symmetry axis of the electrodes, while the 93nm spheres (green/yellow) remain at the electrode edges under a positive dielectrophoretic force. When the electric field was removed the particles rapidly dispersed into the medium.

The dielectrophoretic force (equation 10.8) depends on the volume and the viscous force (equation 10.9) depends only on the radius. As a consequence, although the 93nm diameter spheres experience a smaller viscous force than the 216nm (approximately 2.3 times), they will also experience a much smaller dielectrophoretic force (by a factor of 12). This implies that the smaller particles should move preferentially under the influence of viscous drag rather than the larger, contrary to our observations. This paradox can be explained by considering the relative values of the Clausius-Mossotti factor (equation 10.7) for the two sizes of sphere.

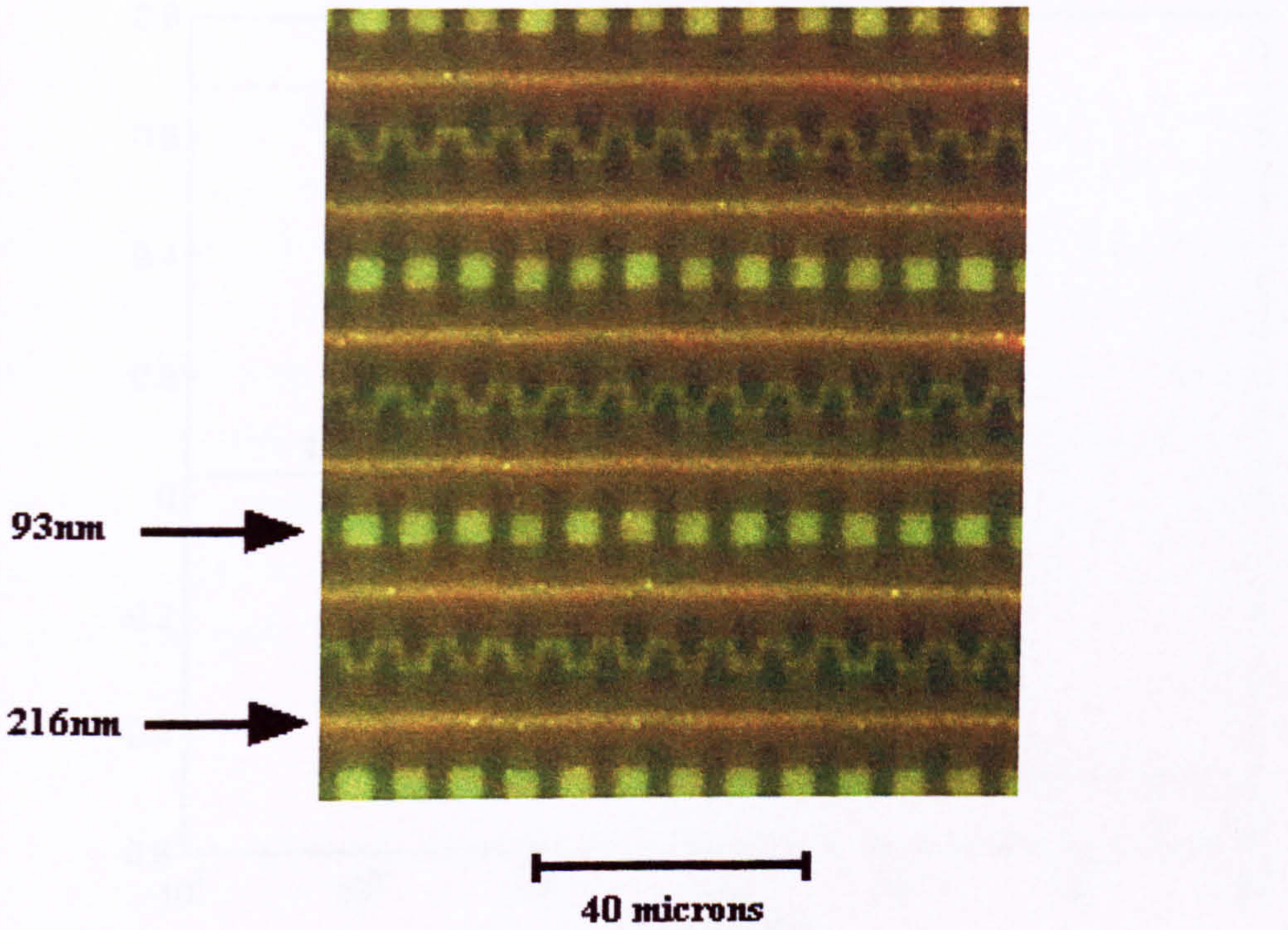

Figure (10.6) Fluorescence video image showing the separation of red 216nm and yellow-green 93nm diameter latex spheres under the influence of combined dielectrophoretic and electrohydrodynamic forces in the micro electrode array shown in Figure (10.1). The larger spheres move into the centre of the electrode and form long continuous ribbons at the field minimum, while the smaller spheres remain trapped at the electrode tips under positive dielectrophoresis. This image shows the 93nm spheres forming long pearl chains from one electrode to the opposite neighbour.

The conductivity of a latex sphere is given by the sum of the bulk conductivity and the surface conductivity $\sigma_p = \sigma_b + 2K_s/a$, where K_s is the surface conductance, σ_b the bulk conductivity (approximately zero for latex) and a the particle radius [14,15]. The surface conductance for the particle was obtained by measuring the frequency at which the force on the particle goes to zero (Chapter Seven) i.e. the frequency at which $\mathrm{Re}\{K(\omega)] = 0$. For the 93nm spheres, the value of K_s has been obtained previously [section (10.2),24] and is $K_s = 2.64\mathrm{nS}$. Measurements of the frequency at which the force is zero for the 216nm particles were made in 0.1mM KCl and this frequency was found to be 3MHz. Assuming that the particle permittivity is 2.5 (Chapter Seven), then the surface conductance was then calculated as $K_s = 0.9\mathrm{nS}$. Using this data, a plot of the frequency variation of the Clausius-Mossotti factor for both the 93nm and 216nm spheres was produced and is shown in Figure (10.7).

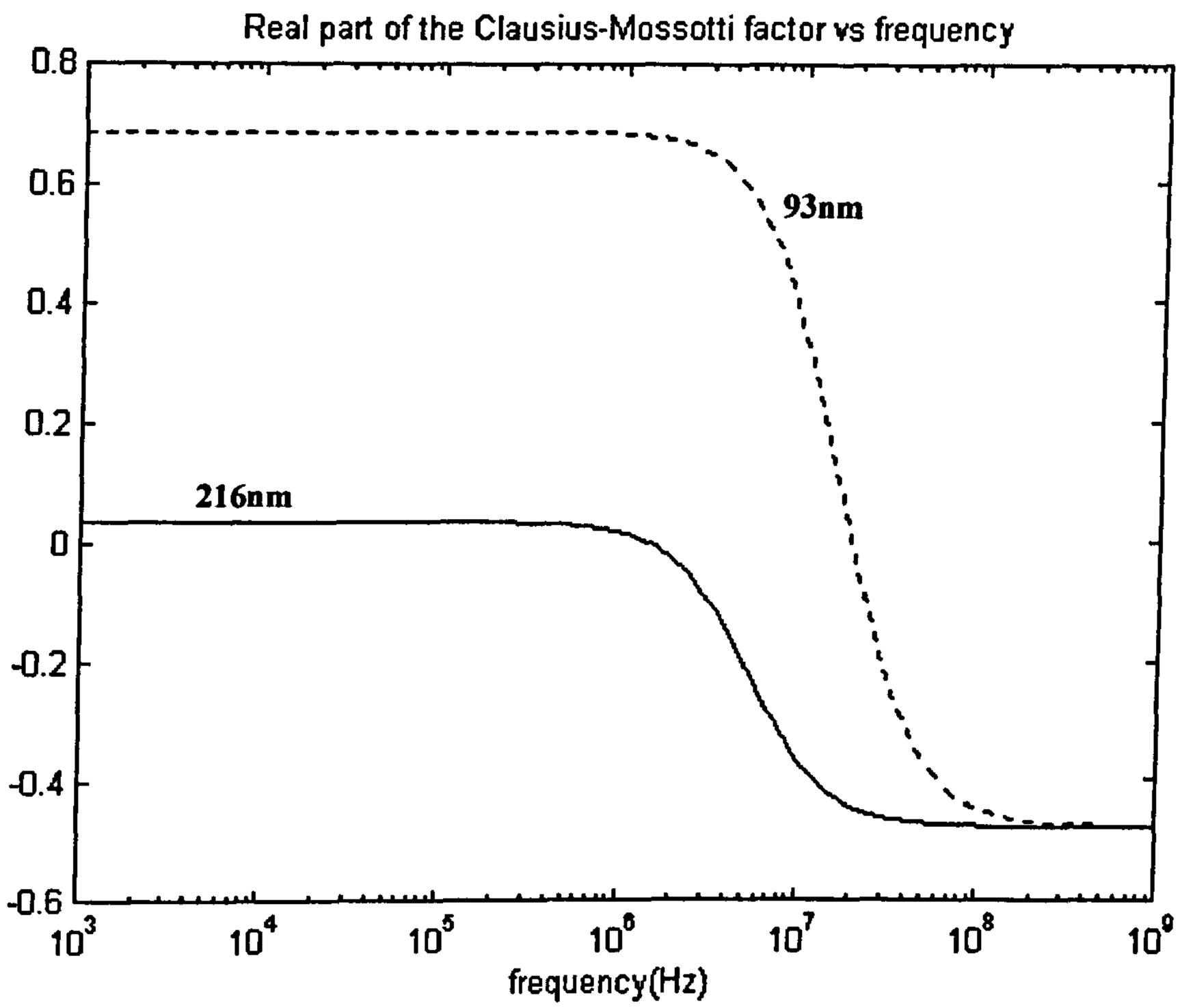

Figure (10.7) A Clausius-Mossotti plot showing the variation in the polarisability of the 216 and 93nm diameter spheres as a function of frequency. This plot was computed with $K_s = 2.64nS$ for the 93nm spheres, $K_s = 0.9nS$ for the 216nm spheres and a medium conductivity of $13mSm^{-1}$. At frequencies below 1MHz, both particles experience positive dielectrophoresis, but the polarisability is much greater for the 93nm spheres so that the force is approximately 20 times greater than for the 216nm spheres.

It is clear from the plot that at low frequencies (<1MHz) both particles experience positive dielectrophoretic forces but the magnitude of the Clausius-Mossotti factor for the 93nm sphere is approximately 20 times large than for the 216nm particle. Allowing for the difference in particle volumes, this means that the dielectrophoretic force on the 93nm particle is at 1.5 times greater than on the 216nm particle over a range of frequencies up to 1MHz. However, the viscous drag force on the 93nm particles is 2.3 times smaller. The net balance of forces therefore is such that the larger particles move away from the electrode edges under the influence of EHD flow and are separated out from the smaller particles that remain trapped under a dominant positive dielectrophoretic force.

10.3.4 Conclusion

In conclusion, it has been demonstrated that the physical separation of two types of sub-micrometre particles can be achieved using a combination of dielectrophoretic and electrohydrodynamic forces. In this case, the spheres are spatially separated in the micro-electrode array in a predictable manner. In combination with other separation techniques which are based exclusively on the dielectric properties of particles [section (10.2), 24], it should be possible to spatially separate a heterogeneous mixture consisting of a range of sub-micrometre particles into constituent particle types. This would have major advantages in being able to process and analyse small numbers of particles entirely "on chip" rather than use a range of different techniques.

10.4 Travelling Wave Dielectrophoresis: separators

This section presents a summary of design and testing on travelling wave dielectrophoresis separators. Parts of this work were published in journals [27,28] and presented at Micro- and Nano- engineering 1996 in Glasgow and the Micromechanics Europe meeting 1997 in Southampton.

10.4.1 Introduction

A travelling electric field can be generated by applying AC potentials, with staggered phases sequentially, to arrays of parallel electrodes. This is shown schematically in Figure (10.8) for a four-phase signal. The ability of this arrangement to propel microparticles was first described by Masuda et al [29,30] and it has since developed into a reliable technique for the characterisation of bioparticles like cells [31-33]. The technique is referred to as travelling wave dielectrophoresis (TWD). Versatile particle micro-manipulators based on this principle have been developed [34] and the technique can be used to separate different types of cells [28,35]. The theory for the TWD force has been thoroughly examined [32,33,36] and simulated using numerical methods [37]. In addition, the same technique has also been used in micro-systems for electrohydrodynamic pumping of fluid [38,39].

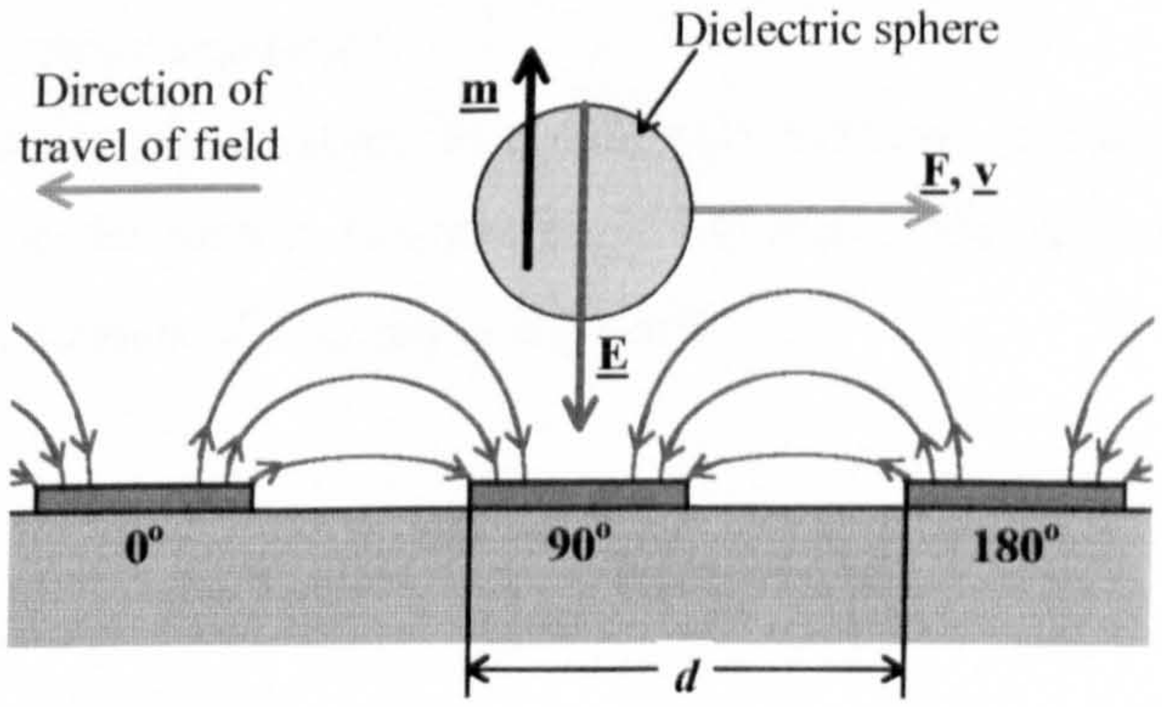

Figure (10.8) A diagram showing the dipole moment **m** in a particle induced by a travelling electric field **E**. The travelling electric field is generated by four phases, 0°, 90°, 180°, 270° applied sequentially to an array of parallel electrodes. Under appropriate conditions, the particle is levitated above the electrodes by negative DEP and the particle experiences a translational force **F** due to the phase lag between **m** and the moving field.

The TWD force on a spherical particle is given by the equation

$$F_{TWD} = -\frac{4\pi^2 \varepsilon_m a^3}{\lambda} \mathrm{Im}\{f_{CM}\} \underline{E}^2 \qquad (10.10)$$

where ε_m is the medium permittivity, a is the radius of the sphere and λ is the wavelength of the travelling wave. For a set of uniformly spaced electrodes, λ is given by the number of phases in the signal multiplied by the periodic spacing of the electrodes, which for the electrodes shown schematically in Figure (10.8) is $4d$. E is the applied electric field, Im{} indicates the imaginary part of and f_{CM} is the Clausius-Mossotti factor given by equation (10.7) which describes the frequency dependent behaviour of the induced dipole. Owing to the large number of variable factors in equation(10.10) as well as the frequency dependence of equation(10.7), TWD is an extremely versatile technique for separating different particle types from a mixture, since even equally sized particles with slightly different dielectric properties can be distinguished. It is important to note that the particle also experience positive and negative dielectrophoresis as well as the TWD force [36]. Unhindered movement due to TWD will occur if the particles are repelled from the electrodes by negative DEP.

Practical TWD separators for biotechnological applications have not yet been developed owing to the small scale of the electrode arrays. The efficiency of a TWD separator depends on the differences between particle types and the number of electrodes in the array. Therefore, for particles of similar properties, longer arrays (in terms of numbers of electrodes) are required to achieve one hundred percent separation.

In addition to this consideration, as equation (10.9) shows, in the steady state condition, where viscous drag on the particle balances the TWD force, the terminal velocity v_{TWD} of a spherical particle in a medium of viscosity η is given by:

$$v_{TWD} = -\frac{2\pi \varepsilon_m a^2}{3\eta\lambda} \mathrm{Im}\{f_{CM}\} \underline{E}^2 \qquad (10.11)$$

For sub-micrometre particles, the velocity of travel will be higher than for a cell since the electric field will need to be higher to dominate over thermal effects. As a consequence of the increased velocity, the arrays for TWD separation of sub-micrometre particles will need to be longer than for super-micrometre particles to achieve the same degree of separation.

This section describes the application of multi-layer fabrication techniques [35] to the manufacture of long arrays of parallel electrodes and the design of electrode arrays to achieve

separation of particles both in the sub-micrometre and cell size ranges. The technique allows arrays with 25,000 electrodes or more to be manufactured as opposed to the approximately 100 that single layer surface lithography allows.

10.4.2 Electrode design and fabrication

Conventional single layer fabrication (as described in Chapter Five) as used to manufacture TWD arrays has inherent problems which limit the number of electrodes. The need to separately connect each electrode to one of three or more phases limits the number of electrodes in the array to approximately 100. If, however, the need to connect **every** individual electrode to the signal source is removed, the number of electrodes in the array is unlimited. Figure (10.9) shows a schematic representation of the two cases for a four phase signal source similar to the type used for experimentation in this section. In Figure (10.9a), the large bonding pads limit the number of electrodes in the centre since each electrode must be attached to a separate pad. In Figure (10.9b), the array has an upper layer of four power rails which are connected in turn to every fourth electrode and this reduces the number of bonding pads to just four.

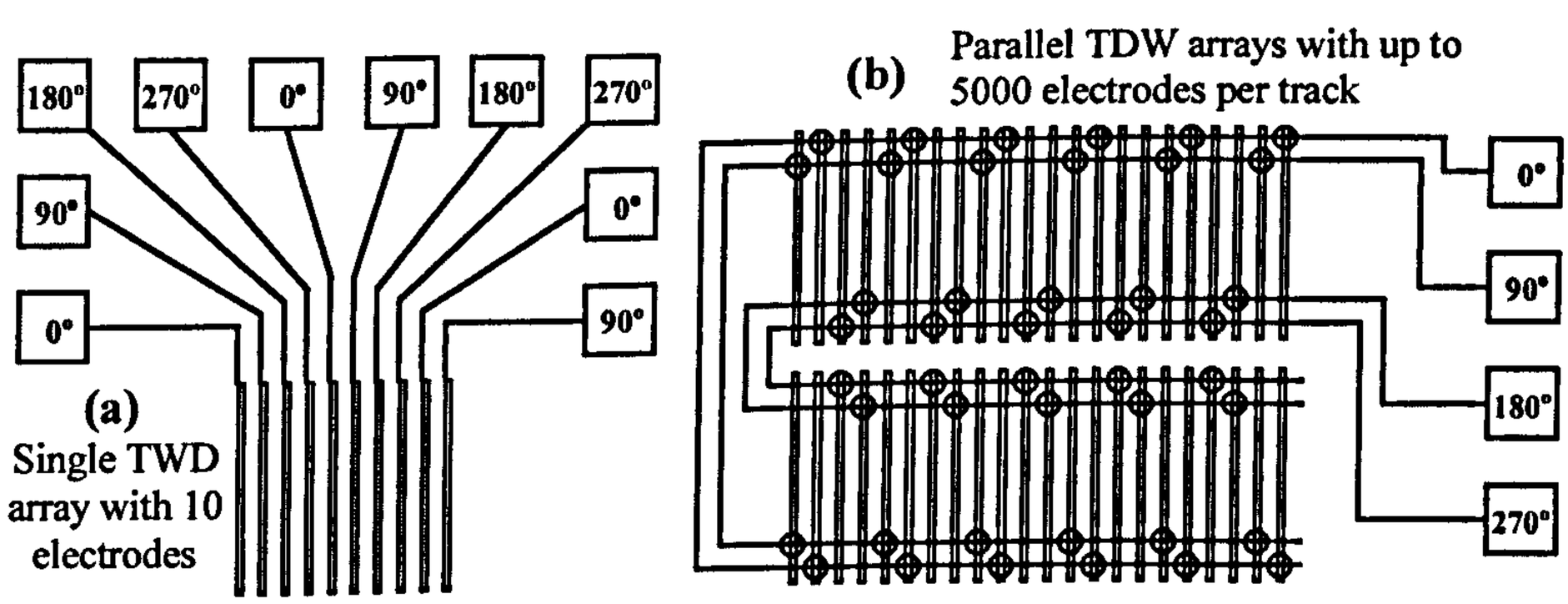

Figure (10.9) A schematic drawing of two designs of TWD array for operation with a four phase signal. **(a)** shows a ten electrode array constructed using conventional single layer lithography with each electrode separately connected to one of four phases. **(b)** shows an array designed for multi-layer lithography where the number of electrodes is limited only by the size of the substrate.

The number of electrodes in the second design of array is limited only by the physical size of the substrate that the array is manufactured on.

Three designs of electrodes were produced. The first was a simple straight array consisting of 200 10μm wide electrodes, and the second consisted of 25 parallel arrays of 1000 10μm electrodes similar to the schematic diagram in Figure (10.9b). The electrode periodicity in

each of these designs was 20μm. The third design is shown schematically in Figure (10.10) and consisted of three tracks in the form of a Y. The principle behind separation of two particle types A and B on such an array is also shown [40]. On the single track on the left, two frequencies I and II are multiplexed. Particle type A experiences negative DEP and a TWD force at frequency I and particle type B experiences the same with frequency II. The two frequencies are chosen so that A and B do not respond to frequencies II and I respectively. The mixture of particles A and B move from the left under TWD until it reaches the junction. On the right hand part of the array, there are two tracks of electrodes each of which has a single frequency applied. In principle [40], the mixture will separate as particle type A moves along the track with frequency I applied and type B moves along the other track.

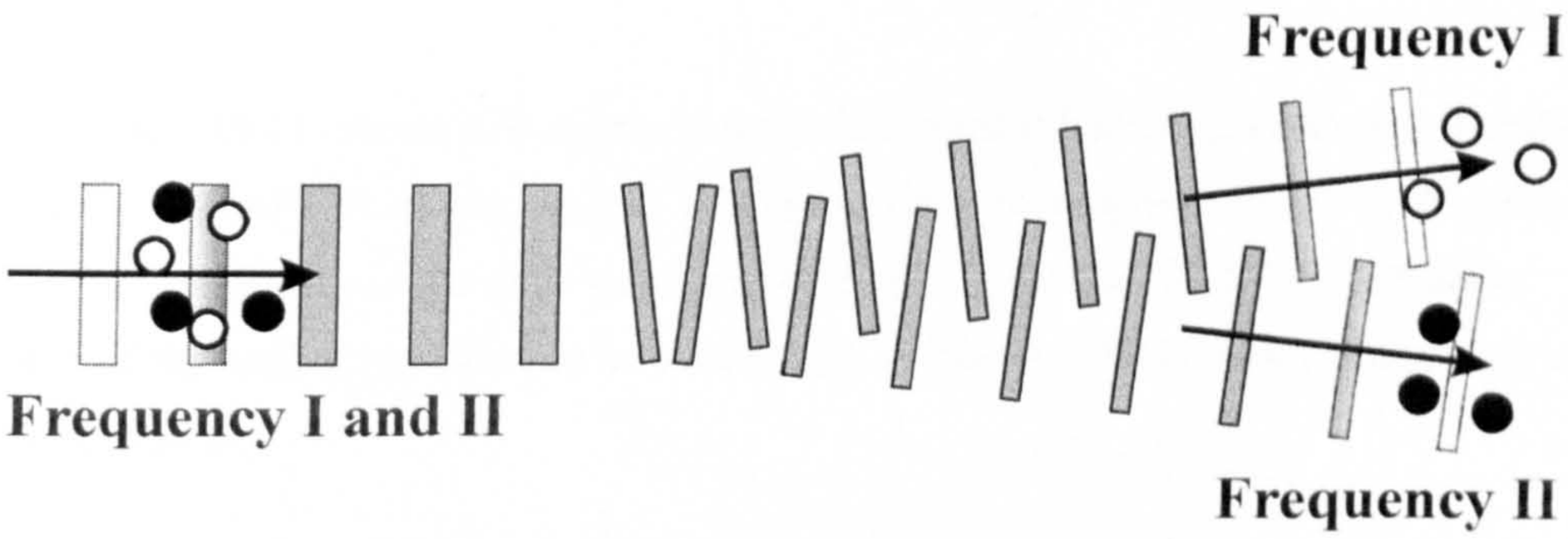

Figure (10.10) Schematic diagram of separation on a Y-shaped electrode. On the left a mixture of particle types A and B move under the influence of frequencies I and II. At the junction, the mixture separates with particle type A moving along the upper track under the influence of frequency I and type B moving along the other track. Further details can be found in the text and [40].

The manufacturing process is described in detail in Appendix (10a) and employs two standard single layer processes:

(a) Metal electrodes were manufactured on the substrate by photolithography (Appendix 5a.3).

(b) An insulating layer of Si_3N_4 was deposited over the entire substrate. Reactive ion etching was used to make connecting holes through the insulator over each electrode and also to open up a track over the active region of the electrodes (the Y shape in Figure (10.10) for example).

(c) The power rails were then produced on top of the insulator by photolithography, the evaporation of the metal producing the connection through the holes to the electrodes on the bottom.

(d) A protecting layer of insulator was then deposited over the entire substrate and the track over the active area opened up again.

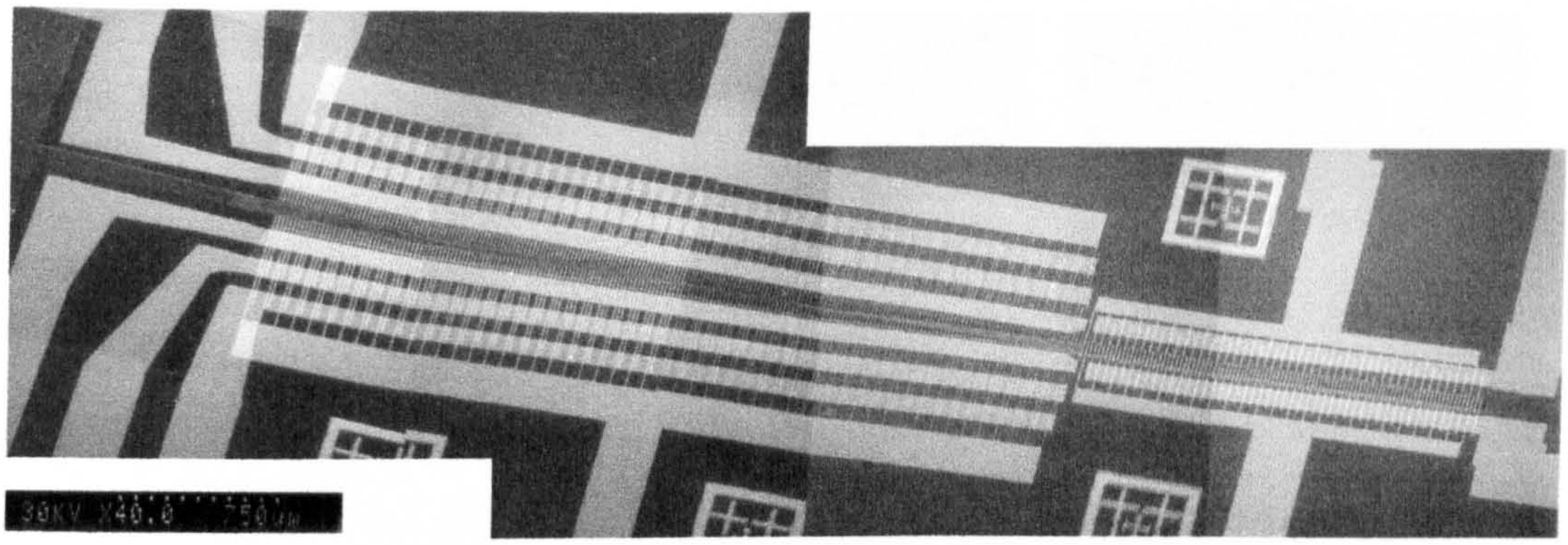

Figure (10.11) A composite image comprising four scanning electron micrographs of a Y-electrode array manufactured using the multi-layer procedure outlined here.

Figure (10.11) shows a Y-electrode array fabricated using this procedure. The digital synthesiser (Appendix 5b.4) was used to provide a four phase signal: (0^o-90^o-180^o-270^o) and was attached to the array in the same manner as described in Chapter Five for DEP arrays. The frequency of the applied signal could be varied from 100Hz to 20MHz with potentials up to 12 volts peak to peak.

10.4.3 Results and discussion

The manufacturing procedure was found to be moderately efficient, with unforeseen array design problems being adjusted as testing proceeded. Testing also provided information about the optimum thickness necessary for each layer to obtain efficient and reliable connection across the insulator. The electrodes and the power rails were 120nm thick and the insulating layer was approximately 200nm. The upper insulating layer was made as thick as possible as long as a track could still be opened along the active area of the array.

Straight electrode arrays were used to perform successful separation of blood into two cell types [28]. The Y array was also tested using latex spheres obtained from Molecular Probes (Oregon, USA) of diameter 10µm. Smaller latex spheres were also used but the rate of travel along the array was too great to capture clear images. Figure (10.12) shows typical results using the 10µm spheres on different arms of the array. As yet however, separation of the type outlined in Figure (10.10) has not been achieved Figures (10.12a-c) show spheres moving under the influence of TWD and positive DEP on the Y-electrode in 1mM KCl

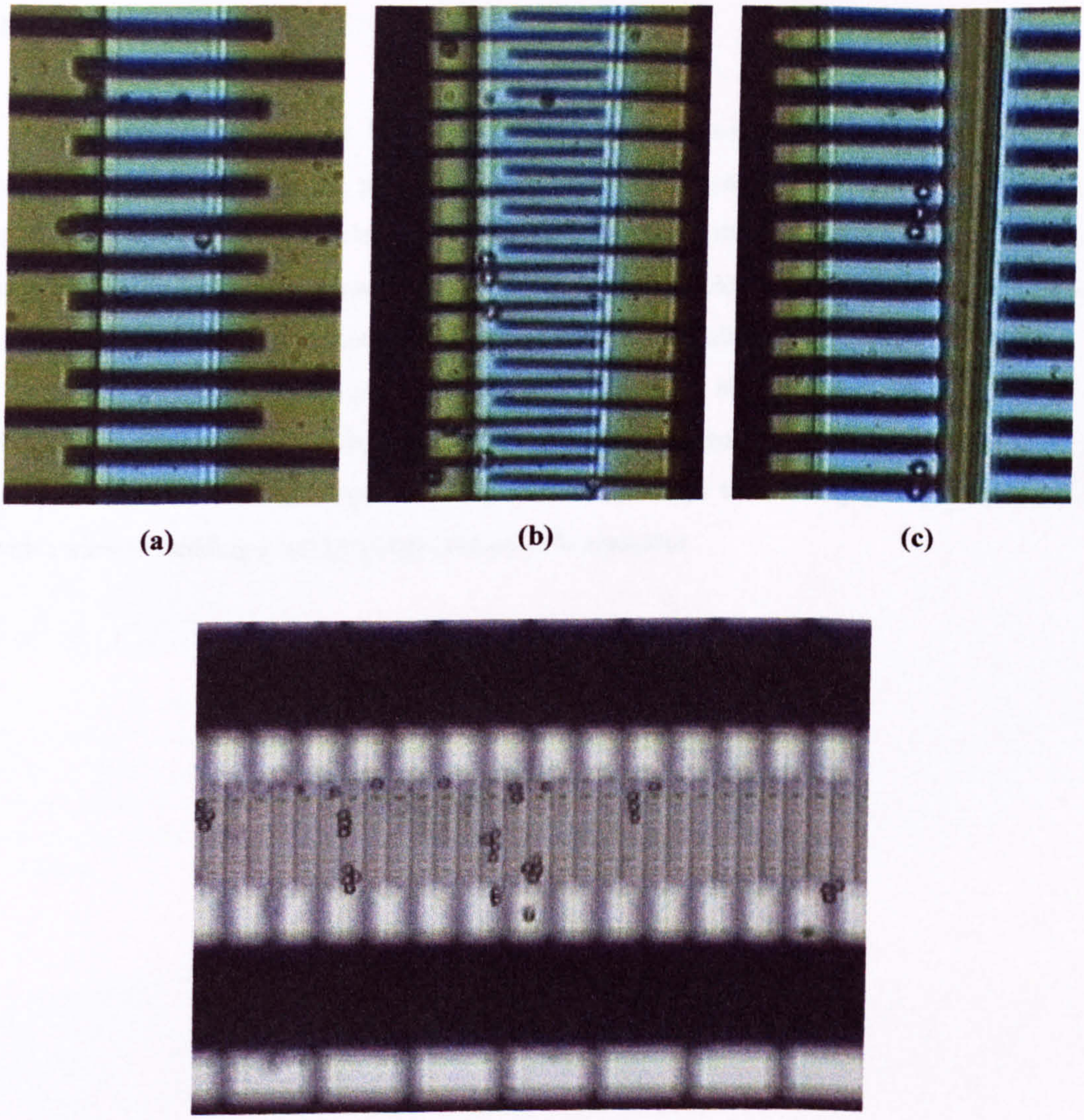

(a) (b) (c)

(d)

Figure (10.12) Ten micrometre diameter latex spheres moving on the Y-electrode shown in Figure (10.11). In (a), (b), and (c), spheres start on the single track, move to the junction then along the left hand track under the influence of a 800kHz 12 volts peak to peak signal. In (d), the spheres are moving under the influence of TWD at 10MHz and 12 volts peak to peak. The suspending medium was 100μM KCl and the array is out of focus due to the fact that the sphere are levitated by negative DEP to approximately 7 micrometres.

In the experiment shown in Figure (10.12), the lower and left hand arms of the array were attached to the same signal source. The spheres moved up the lower arm and then along the left hand arm in exactly the predicted manner.

10.4.4 Conclusion

In conclusion, it has been demonstrated that electrodes designed and manufactured according to the multi-layer procedure outlined in previous sub-sections can successfully manipulate and separate particles using travelling wave dielectrophoresis. The straight arrays have proved to be the most successful both for large particles and sub-micrometre particles, although for the latter, the structure of the electrodes must be altered to improve results.

By this method, even particles with small differences in size and/or dielectric properties may be separated using electrode arrays of an appropriate design. The multi-layer procedure can be applied to manufacture complicated TWD electrode arrays to be designed and manufactured with a view to building a working real-time particle separator.

Appendix (10a) Fabrication outline

Layer 1. Electrodes are fabricated onto the substrate using photolithography.

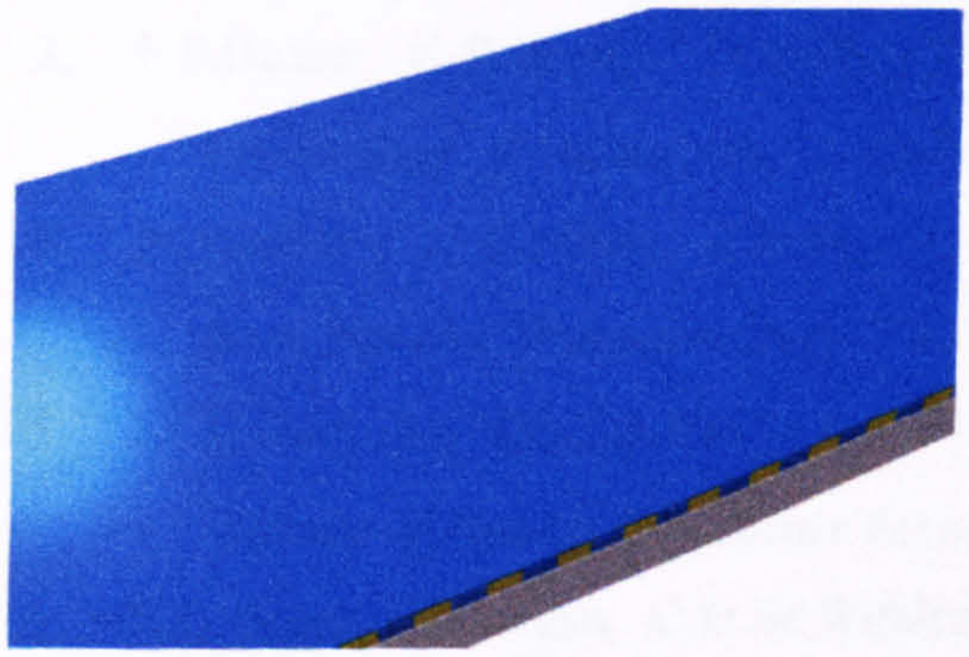

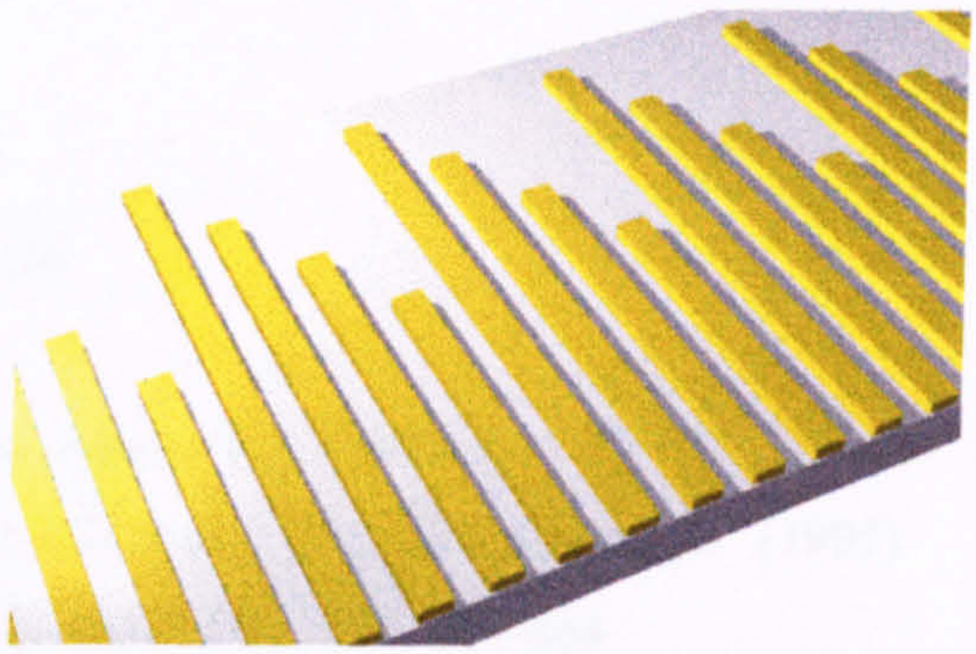

Layer 2. Silicon Nitride is deposited as an insulator between layers 1 and 3.

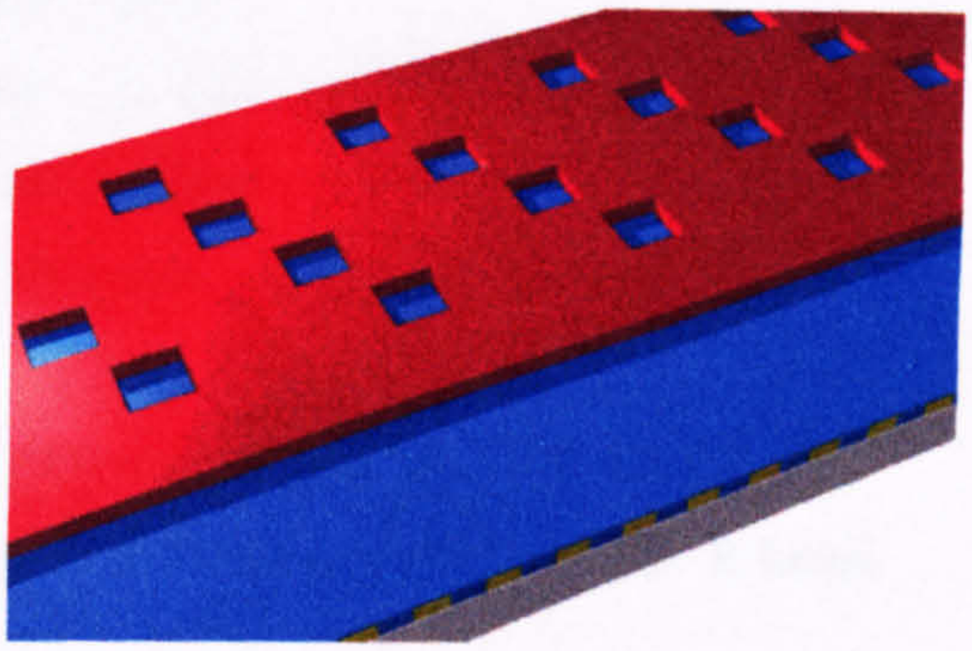

Layer 2. A layer of resist is spun onto the silicon nitride and patterned using ultra violet exposure followed by development. The mask pattern contains the connecting holes and the track to be etched over the active area of the electrodes.

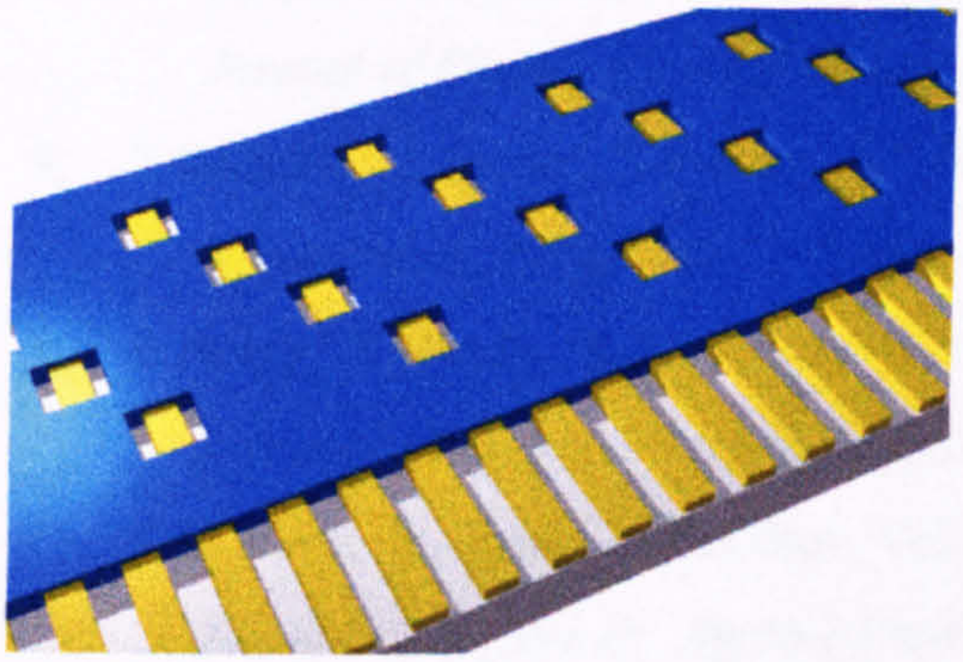

Layer 2. The pattern in the resist is transferred to the silicon nitride by dry-etching leaving a single connecting hole over each electrode.

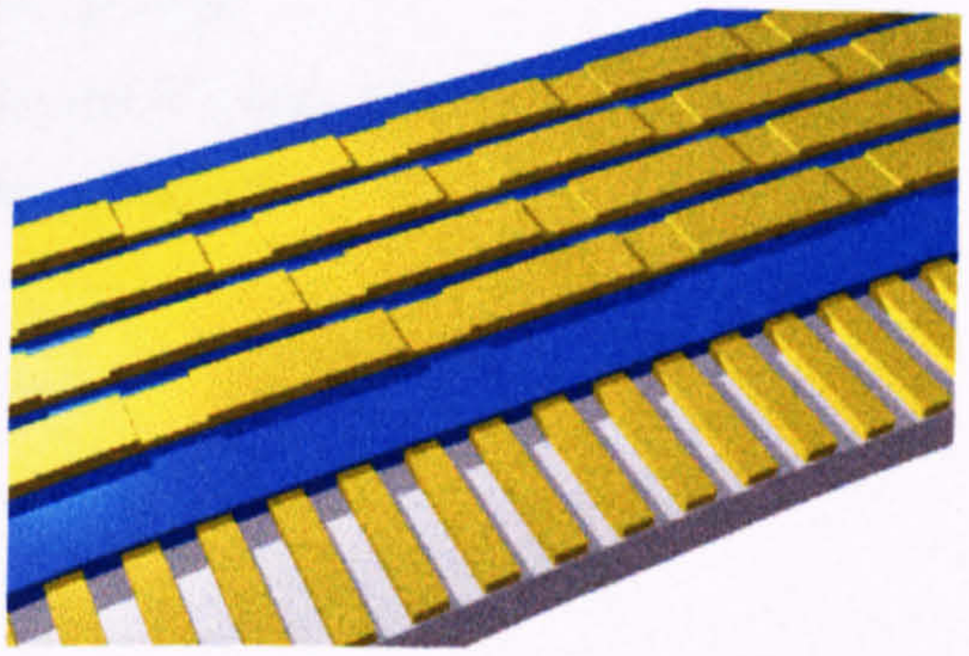

Layer 3. The power rails are fabricated on top of the insulator by photolithography. The evaporation deposits metal through the holes forming the necessary connections.

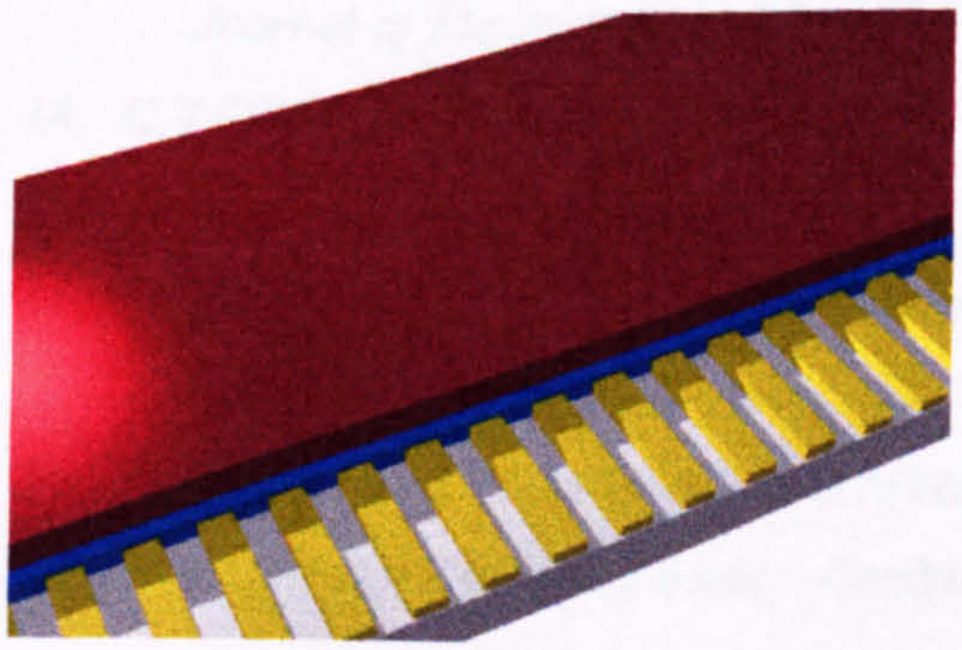

Layer 4. A second protective insulating layer is added and the track is again etched away over the active area of the electrodes.

References

1. H.A.Pohl (1978) *Dielectrophoresis*
   Cambridge University Press, Cambridge UK
2. R.Pethig (1991)
   Automation in Biotechnology (ed I.Karube, Amsterdam, Elsevier) 159-185
3. F.F.Becker, X-B.Wang, Y.Huang, R.Pethig, J.Vykoukal and P.R.C.Gascoyne (1995)
   Proceedings of the National Academy of Sciences, USA **92** 860-864
4. M.Stephens, M.S.Talary, R.Pethig, A.K.Burnett and K.I.Mills (1996)
   Bone Marrow Transplantation **18** 777-782
5. J.P.H.Burt, R.Pethig, A.Parton and D.Dawson (1995)
   Institute of Physics Conference Series **143** 381-384
6. N.G.Green, H.Morgan, C.D.W.Wilkinson and J.J.Milner (1995)
   Proc. St Andrews meeting, Animal & Cell Abstracts, St Andrews, UK **C2.18** p77
7. G.Fuhr (1995)
   Proc. St Andrews meeting, Animal & Cell Abstracts, St Andrews, UK **C2.17** p77
8. T.Muller, A.Gerardino, T.Schnelle, S.G.Shirley, F.Bordoni, G.de Gasperis, R.Leoni and G.Fuhr (1996)
   Journal of Physics D: Applied Physics **29** 340-349
9. T.Schnelle, T.Muller, S.Fiedler, S.G.Shirley, K.Ludwig, A.Hermann and G.Fuhr (1996)
   Naturwissenschaften **83** 172-176
10. R.Pethig, Y.Huang, X-B.Wang and J.P.H.Burt (1992)
    Journal of Physics D: Applied Physics **24** 881-888
11. X-B.Wang, Y.Huang, J.P.H.Burt, G.H.Markx and R.Pethig (1993)
    Journal of Physics D: Applied Physics **26** 1278-1285
12. S.Sasaki, A.Ishikawa, and T.Hanai (1981)
    Biophys. Chem. **14** 45-53
13. M.Washizu (1992)
    Journal of Electrostatics **29** 177-188
14. C.T.O'Konski (1960)
    Journal of Physical Chemistry **64** 605-619
15. W.M.Arnold, H.P.Schwan and U.Zimmerman (1987)
    Journal of Physical Chemistry **91** 5093-5098
16. W.B.Russel, D.A.Saville and W.R.Schoual (1991) *Colloidal Dispersions, Chapter 7*
    Cambridge University Press, Cambridge

17. D.C.Grahame (1947)
Chemical Review **41** 441-501

18. G.H.Markx, Y.Huang, X-F.Zhou and R.Pethig (1994)
Microbiology **140** 585-591

19. R.Pethig (1996)
Critical Reviews in Biotechnology **16** 331-348

20. M.Washizu, S.Suzuki, O.Kurosawa, T.Nishizaka and T.Shinohara (1994)
IEEE Transactions on Industry Applications **30** 835-843

21. H.Morgan and N.G.Green (1997)
Journal of Electrostatics **42** 279-293

22. T.Muller, S.Fiedler, T.Schnelle, K.Ludwig, H.Jung and G.Fuhr (1996)
Biotechnology techniques **4** 221-226

23. N.G.Green, J.J.Milner and H.Morgan (1997)
Journal of Biochemical and Biophysical methods **35** 89-102

24. N.G.Green and H.Morgan (1997)
Journal of Physics D: Applied Physics **30** L41-L44

25. A.Ramos, H.Morgan, N.G.Green and A.Castellanos
Journal of Physics D: Applied Physics (Submitted)

26. N.G.Green and H.Morgan (1997)
Journal of Physics D: Applied Physics **30** 2626-2633

27. N.G.Green, M.P.Hughes, W.Monaghan and H.Morgan (1997)
Microelectronic Engineering **35** 421-424

28. H.Morgan, N.G.Green, M.P.Hughes, W.Monaghan and T.C.Tan (1997)
Journal of Micromechanics and Microengineering **7** 65-70

29. S.Masuda, M.Washizu and M.Iwadare (1987)
IEEE Transactions on Industry Applications **23** 474-480

30. S.Masuda, M.Washizu and I.Kawabate (1988)
IEEE Transactions on Industry Applications **24** 217-222

31. G.Fuhr, R.Hagedorn, T.Muller, W.Benecke, B.Wagner and J.Gimsa (1991)
Studia Biophysica **140** 79-102

32. R.Hagedorn, G.Fuhr, T.Muller and J.Gimsa (1992)
Electrophoresis **13** 49-54

33. Y.Huang, X-B.Wang, J.A.Tame and R.Pethig (1993)
Journal of Physics D: Applied Physics **26** 1528-1535

34. G.Fuhr, S.Fiedler, T.Muller, T.Schnelle, H.Glaser, T.Lisec and B.Wagner (1994)
Sensors and Actuators A **41-42** 230-239

35. M.S.Talary, J.P.H.Burt, J.A.Tame and R.Pethig (1996)
Journal of Physics D: Applied Physics **29** 2198-2203

36. X-B.Wang, Y.Huang, F.F.Becker and P.R.C.Gascoyne (1994)
Journal of Physics D: Applied Physics **27** 1571-1574

37. M.P.Hughes, R.Pethig and X-B.Wang (1996)
Journal of Physics D: Applied Physics **29** 474-482

38. G.Fuhr, R.Hagedorn, T.Muller, W.Benecke and B.Wagner (1992)
Journal of Micromechanical Systems **VI** 141-146

39. G.Fuhr, T.Schnelle and B.Wagner (1994)
Journal of Micromechanics and Microengineering **4** 217-226

40. S.Bush (1997)
Electronics Weekly 28 May p14

Conclusion and future prospects

Conclusion and future prospects

This thesis contains the results of the first thorough investigation of sub-micrometre dielectrophoresis, both in terms of the experimental equipment required and the measurement of dielectric properties, as well as analysis of new effects which have been observed. That Dielectrophoresis can be applied and used for characterisation on this scale has been incontrovertibly shown. Furthermore, sub-micrometre dielectrophoresis can be used as a practical means of separating even nano-scale particles.

The manufacturing techniques of photolithography and electron-beam lithography were used to manufacture suitable electrode arrays for dielectrophoretic studies (Chapter Five). E-beam techniques in particular were used to produce electrode structures with the detail necessary to generate high electric fields using low applied potentials. Experimental observations indicated that dielectrophoretic manipulation of small particles using such arrays could be improved if further work on the relationship between the size of the particle and the *necessary* size of the electrode features is carried out.

Numerical simulations (Chapter Six) of electric fields in the arrays were performed and found to accurately determine the behaviour of particles. For example, simulation of the hyperbolic polynomial electrodes showed that the "trap" for negative dielectrophoresis in the centre of the array is most efficient close to the surface and that the trapping force diminishes rapidly with height. Above a certain height, the trap cannot hold particles in the presence of a competing force, even if the second force is slight. This was confirmed by experimental observations of particles under the influence of fluid flow which occurs in high frequency AC fields (section 9.3.2), where the flow was observed to push particles upwards and out of the trap. Simulation of the castellated electrodes also demonstrated that planar electrodes can produce three-dimensional field "cages", a type of trap that previously was thought to require three dimensional electrode structures.

Measurements of the dielectrophoretic behaviour of sub-micrometre particles were also carried out for the first time (Chapters Seven and Eight). This data was used to characterise the dielectric properties of these particles.

Chapter Seven showed that experimental measurements of frequency-dependent dielectrophoretic behaviour of sub-micrometre latex spheres indicated that the theory of interfacial polarisation is incomplete when applied on this scale. For spheres at the upper end of the sub-micrometre scale (0.5-1μm), the Clausius-Mossotti factor can be successfully applied to predict the experimentally measured zero force spectrum for the high frequency dispersion. However, for particles below approximately 0.5μm in diameter, an increasing deviation from this fit was observed and the data could not be successfully explained using the

simple models available in the literature. For particles on the boundary of the nano-scale (<100nm), the deviation from theory is most apparent at high frequencies and dominates the particle behaviour. These effects were not observed previously by other workers as this is the first time the properties of single sub-micrometre particles have been examined thoroughly. Previous publications have focused on a single medium conductivity and have not analysed the changes in DEP and/or dielectric properties of the particle with conductivity. The dielectric properties of the particles are heavily influenced by surface conductance effects which are not accurately described by current theory for this size of particle.

The low frequency α–relaxation was also measured and the theories from the literature examined. The frequency of the dispersion was found to agree closely with experimental data if the relaxation of a bound or thin double layer model was used, a reasonable assumption for high medium conductivities. However, none of the dipole expressions contained in the literature match either the experimental observations or what would be expected to exist for a physical system. This may be because these theories have been derived as the first step towards a model for explaining the dielectric spectra of particle suspensions. Since there have previously been no measurements on single particles, the expression for a single dipole derived in these theories has remained untested. Further work, both theoretical and experimental, is required in this particular area to more fully understand these mechanisms and several publications are being prepared based on the work outlined in this thesis on this topic (Chapter Seven).

Zero force measurements together with threshold force measurements (Chapter Eight) were performed on a biological particle, tobacco mosaic virus (TMV). TMV is volumetrically equivalent to sphere 52nm in diameter and can be classed as nano-scale. It is rod-shaped, an extreme shape which has not been studied using dielectrophoresis previously. The theory of interfacial polarisation around such a shape was shown to match the experimental observations very well. The threshold field required to initiate dielectrophoretic movement was determined by observation, and the force required to overcome thermal effects calculated. This force was much smaller than expected from the energy balance arguments that have previously been used to define the field strengths necessary for dielectrophoresis in contention with diffusion. To clarify this inconsistency, a new definition was presented in section (9.2) for the "observably deterministic force" threshold required to overcome Brownian motion for a single particle. The force values predicted by this definition matched the experimentally determined value more accurately. Further work is planned in this area but the successful characterisation of TMV indicates that the identification and characterisation of nano-scale viruses by DEP is an achievable goal.

The dielectrophoretic properties of sub-micrometre particles are dominated by surface properties so that these particles are ideal systems for use in affinity separation technology. To this end, the separation of almost identical nano-scale particles using dielectrophoresis on planar electrodes has been successfully demonstrated (section 10.2). These simple experiments showed that all the advantages of manipulation and separation that have so effectively been demonstrated and applied for large particles such as cells and bacteria can be applied on the sub-micrometre scale. The possibilities for biotechnological applications in this particular area are numerous, since particles with only slightly different dielectric properties can be distinguished and physically separated using this technique.

Chapter Nine presented preliminary experimental observations of fluid flow caused by high strength electric fields in microelectrode arrays. Previously uncharacterised in the literature, these effects were described in detail for specific electrode shapes and arrangements (section 9.3), along with the frequency regimes in which each type was observed. Theoretical and experimental work is currently being carried out to accurately determine flow patterns and forces for the fluids used in dielectrophoresis. Two papers on this subject have been submitted and this particular aspect of sub-micrometre dielectrophoresis has the potential to be a valuable enhancement to established techniques. Section (10.3) describes a preliminary experiment on separation using a combination of dielectrophoresis and controlled fluid flow using a castellated electrode array where sub-micrometre particles of different sizes were separated. The possibilities of applying this technique for separation purposes, either exclusively or in combination with other techniques (such as DEP) means that a new type of manipulation technology is now available for study and use.

In conclusion, this thesis has achieved the stated aim of developing dielectrophoresis for use in the sub-micrometre scale. The characterisation, manipulation and separation of particles has been demonstrated, both by dielectrophoresis and by new electrohydrodynamic techniques discovered and developed during the course of these studies. As a consequence of this work, the field of dielectrophoresis has been widened extensively to enable its application to particles such as latex spheres, viruses, DNA and macromolecules. Such an application could lead to more rapid and sensitive manipulation and separation technologies for sub-micrometre and nano-scale bioparticles.

Publications arising from this thesis

Journal publications:

1. N.G.Green, M.P.Hughes, W.Monaghan and H.Morgan (1997)
   Large-area multi-electrode arrays for dielectrophoretic fractionation
   Microelectronic Engineering **35** 421-424
2. N.G.Green and H.Morgan (1997)
   Dielectrophoretic separation of nano-particles
   Journal of Physics D: Applied Physics **30** L41-44
3. H.Morgan, N.G.Green, M.P.Hughes, W.Monaghan and T.C.Tan (1997)
   Large-area travelling-wave dielectrophoresis particle separator
   Journal of Micromechanics and Microengineering **7** 65-70
4. N.G.Green and H.Morgan (1997)
   Dielectrophoretic investigations of sub-micrometre latex spheres
   Journal of Physics D: Applied Physics **30** 2626-2633
5. N.G.Green, H.Morgan and J.J.Milner (1997)
   Manipulation and trapping of sub-micron bioparticles using dielectrophoresis
   Journal of Biochemical and Biophysical Methods **35** 89-102
6. H.Morgan and N.G.Green (1997)
   Dielectrophoretic manipulation of rod-shaped bioparticles
   Journal of Electrostatics **42** 279-293
7. N.G.Green and H.Morgan (1998)
   Separation of sub-micrometre particles using a combination of Dielectrophoretic and Electrohydrodynamic forces
   Journal of Physics D: Applied Physics (submitted)
8. A.Ramos, H.Morgan, N.G.Green and A.Castellanos (1998)
   AC Electrokinetics: A review of forces in microelectrode structures
   Journal of Physics D: Applied Physics (submitted)

9. N.G.Green, M.P.Hughes and H.Morgan

   Dielectrophoresis and an "observably deterministic force"

   in preparation

10. N.G.Green and H.Morgan

    Dielectrophoresis of sub-micrometre latex spheres I: experimental measurements

    in preparation

Conference presentations

1. N.G.Green, H.Morgan, C.D.W.Wilkinson and J.J.Milner

   Dielectrophoresis of viral particles: preliminary investigations

   presented at SEB Annual meeting, St Andrews, UK 1995

   Proc. SEB. annual meeting, Animal & Cell Abstracts, St. Andrews, UK **C2.18** p77

2. N.G.Green and H.Morgan

   Dielectrophoresis of nano-scale particles

   presented at IUTAM Summer School on Electrohydrodynamics, Udine, Italy 1996

3. N.G.Green, M.P.Hughes, W.Monaghan and H.Morgan

   Large-area multi-electrode arrays for dielectrophoretic chromatography

   presented at MNE '96, Glasgow, UK 1996

4. N.G.Green, H.Morgan and J.J.Milner

   Dielectrophoresis of Tobacco Mosaic Virus

   presented at Biophysical Society Meeting '97, New Orleans, USA 1997

   Biophysical Journal **72** p.MP448

5. N.G.Green, W.Monaghan and H.Morgan

   New electrode arrays for particle manipulation and separation using travelling wave dielectrophoresis

   presented at MME '97, Southampton, UK 1997